

The University of Sheffield



Investigation of Torque and Torque Ripple in Dual Three-Phase Permanent Magnet Synchronous Machines for Electric Vehicles

Shensheng Wang

A thesis submitted for the degree of Doctor of Philosophy

Department of Electronic and Electrical Engineering

The University of Sheffield

Mappin Street, Sheffield, S1 3JD, UK

September 2023

ABSTRACT

Permanent magnet (PM) synchronous machines (PMSMs) are featured with high torque density, high power density, and high efficiency. Compared with conventional single three-phase (STP) PMSMs, dual three-phase (DTP) PMSMs exhibit some additional advantages, such as better fault-tolerant, power sharing, and torque capabilities, as well as better efficiency performance. This thesis investigates the electromagnetic performance of DTP PMSMs, with particular reference to torque capability and torque ripple for electric vehicle applications.

A generic winding configuration technique of DTP PMSMs is firstly developed based on the star of slots. Different slot/pole number combinations, phase shift angles, and coil pitch numbers are all considered. Thus, for PMSMs with any slot/pole number combination, all feasible DTP winding configurations can be quickly obtained with the proposed method. For 48-slot/8-pole PMSMs, which are widely utilized in electric vehicles, two feasible DTP winding configurations, i.e., single-layer full-pitched one and double-layer short-pitched one, are proposed and compared under healthy and three-phase open-circuit conditions. It is found that the double-layer short-pitched DTP winding configuration is the preferred DTP winding configuration.

Further, the concept of “attenuation factors”, which is utilized in STP PMSMs with stator shifting, to describe the effects of stator shifting angle on different magnetomotive force (MMF) orders, is extended to DTP PMSMs by considering spatial and time shifting angles together. Similarly, the instantaneous torque separation method in STP PMSMs is also extended to DTP PMSMs by considering the cross-coupling effects within and between the two winding sets. In addition, the effects of AIPM rotors, which are under extensive investigation in STP PMSMs, on the electromagnetic performance of DTP PMSMs are evaluated. It reveals that the application of AIPM rotors to DTP PMSMs can enhance average torque but increase iron loss and decrease overall efficiency in various operating conditions. Hence, AIPM rotors are not recommended for DTP PMSMs in electric vehicles.

Finally, a simplified approach to estimate torque performance of PMSMs with rotor skew is developed. With the simplified approach, the effectiveness of rotor skew in STP and DTP surface PMSMs (SPMSMs) and interior PMSMs (IPMSMs) are investigated. The optimal skew angles for STP and DTP PMSMs accounting for the effect of load can be obtained, which are especially important for IPMSMs.

ACKNOWLEDGMENTS

First and foremost, I would like to express my sincerest thanks to my supervisor, Professor Zi-Qiang Zhu, for his invaluable guidance, meticulous help, and unconditional support during my PhD study at Sheffield. It is a great honour for me to be one of his PhD students. In the last several years, I encountered unprecedented problems and challenges in both academic and life. Prof. Zhu always encourages and supports me no matter what condition I am in. It is impossible for me to complete this thesis without his help. Furthermore, I would like to extend my sincere gratitude to Dr. Zhenping Xia, for her warmest care and encouragement in my hardest period.

The research work was conducted with the sponsorship from IMRA UK research centre, Toyota Group. I would like to thank them for their financial and technical support. Especially, I would like to thank all the colleagues there, Mr. Adam Pride, Dr. Rajesh Deodhar, Dr. Juntao Shi, and Mr. Chiaki Umemura, for their insights and help in manufacturing and testing the prototype machines. I really enjoyed and missed the coastline of Brighton.

I would also like to thank Dr. Dawei Liang, Dr. Yang Xiao, Dr. Bo Shao, Dr. Ji Qi, Mr. Yan Jia, and all my fellows in the Electrical Machines and Drives Group for their inspired suggestions, generous help, and precious companionship. It is a pity that I cannot list all your names in this short acknowledgment. It is you make my life in Sheffield so wonderful and memorable. Wish you all the best in both career and life.

With all my sincerity, I would like to take this opportunity to thank all my past teachers in Nanjing Normal University and Southeast University. The knowledge they imparted to me has become stepping stone to this PhD degree. I will always remain grateful to Prof. Heyun Lin and Dr. Hui Yang, who motivated and encouraged me to pursue a PhD degree.

Finally, sincerest thanks to my parents, my parents-in-law and my entire family. Without the constant support and encouragement from them, this journey would not have been possible. Special thanks to my wife, Mrs. Ziwei Zhou, for her unconditional love and personal sacrifices owing to my study abroad. Whenever I am feeling down, their belief that I can succeed always gives me the courage to tackle any difficulty.

CONTENTS

| | |
|---|-------------|
| ABSTRACT..... | I |
| ACKNOWLEDGMENTS..... | II |
| CONTENTS..... | III |
| NOMENCLATURE | VIII |
| CHAPTER 1 General Introduction | 1 |
| 1.1 Introduction..... | 1 |
| 1.2 STP PMSMs..... | 2 |
| 1.2.1 Stator Winding Configurations | 3 |
| 1.2.2 Rotor PM Configurations..... | 5 |
| 1.2.3 Stator PM Machines..... | 12 |
| 1.2.4 Summary..... | 14 |
| 1.3 DTP PMSMs | 15 |
| 1.3.1 Multiphase PMSMs | 16 |
| 1.3.2 DTP Winding Configuration and Stator Shifting Technique | 28 |
| 1.3.3 Phase Shift Angle in DTP Windings | 34 |
| 1.3.4 Star-delta and Dual Inverter Drives | 42 |
| 1.3.5 Summary of DTP PMSMs in Existing Literature | 46 |
| 1.4 Scope of Research and Contributions of the Thesis | 48 |
| CHAPTER 2 Developments of Various DTP PMSM Topologies | 53 |
| 2.1 Introduction..... | 53 |
| 2.2 Winding Assignments and Winding Factors of DTP PMSMs | 54 |
| 2.2.1 Star of Slots..... | 54 |
| 2.2.2 Distribution Factor and Phase Shift Angle..... | 56 |
| 2.2.3 Pitch Factor and Coil Pitch | 77 |

| | |
|---|------------|
| 2.2.4 Resultant Winding Factor | 81 |
| 2.3 Attenuation Factor for Two Three-Phase Winding Sets..... | 83 |
| 2.3.1 Attenuation Factor Caused by Spatial Shifting..... | 83 |
| 2.3.2 Attenuation Factor Caused by Spatial and Time Shifting..... | 87 |
| 2.4 FE and Experimental Validation | 93 |
| 2.4.1 Machine and Winding Configuration..... | 93 |
| 2.4.2 FE Validation | 94 |
| 2.4.3 Experimental Validation..... | 96 |
| 2.5 Conclusion | 99 |
| CHAPTER 3 Comparison of Different Winding Configurations for Dual Three-Phase PMSMs in Electric Vehicles | 100 |
| 3.1 Introduction..... | 100 |
| 3.2 Winding Configurations..... | 103 |
| 3.2.1 Winding Arrangements | 104 |
| 3.2.2 Winding Specifications | 106 |
| 3.3 Electromagnetic Performance under Healthy Condition | 111 |
| 3.3.1 Winding Factor..... | 112 |
| 3.3.2 Open-circuit (OC) performance | 113 |
| 3.3.3 Torque Performance | 120 |
| 3.3.4 Loss and Efficiency..... | 133 |
| 3.3.5 Summary..... | 139 |
| 3.4 Electromagnetic Performance under 3-phase OC Condition..... | 140 |
| 3.4.1 Winding Layouts..... | 140 |
| 3.4.2 Torque Performance | 141 |
| 3.4.3 Loss and Efficiency..... | 144 |
| 3.5 Summary | 145 |

| | |
|--|------------|
| 3.6 Experimental Validation..... | 145 |
| 3.7 Conclusion | 148 |
| CHAPTER 4 Torque Separation for Dual Three-Phase PMSMs using Frozen Permeability Method | 151 |
| 4.1 Introduction..... | 151 |
| 4.2 Machine Configurations..... | 152 |
| 4.3 Analytical Modelling and Torque Components for DTP PMSMs | 154 |
| 4.4 Torque Separation Method for DTP PMSMs..... | 156 |
| 4.4.1 Calculate Relative Permeability Distribution | 156 |
| 4.4.2 Excitation Configurations of Different Cases | 157 |
| 4.4.3 Flux Linkage Components of Different Cases..... | 158 |
| 4.4.4 Torque Separation and Reproduction..... | 160 |
| 4.5 Comparison of Torque Components in STP and DTP PMSMs | 163 |
| 4.6 Experimental Validation..... | 166 |
| 4.7 Conclusion | 166 |
| CHAPTER 5 Influence of Load on Effectiveness of Rotor Skew in STP IPMSMs and SPMSMs..... | 167 |
| 5.1 Introduction..... | 167 |
| 5.2 Machine Configurations..... | 169 |
| 5.3 Simplified Torque Estimation Approach..... | 171 |
| 5.3.1 Torque Characteristics without Rotor Skew | 171 |
| 5.3.2 Simplified Torque Estimation Approach..... | 176 |
| 5.3.3 Verification with Conventional Approach | 179 |
| 5.4 Influences of Load in Rotor Continuous Skew | 183 |
| 5.4.1 Optimal Current and Skew Angles for Specific Load Condition | 183 |
| 5.4.2 Effects of Load in Interior and Surface PMSMs | 189 |
| 5.5 Influences of Load in Rotor Step Skew | 196 |

| | |
|---|------------|
| 5.5.1 Simplified Torque Estimation Approach in Rotor Step Skew | 196 |
| 5.5.2 Effects of Load in Interior and Surface PMSMs | 197 |
| 5.6 Experimental Validation..... | 205 |
| 5.7 Conclusion | 208 |
| CHAPTER 6 Influence of Load on Effectiveness of Rotor Skew in DTP IPMSMs and SPMSMs..... | 209 |
| 6.1 Introduction..... | 209 |
| 6.2 Machine Configurations..... | 210 |
| 6.3 Torque Characteristics without Rotor Skew | 211 |
| 6.4 Influences of Load in PMSMs with Rotor Continuous Skew..... | 219 |
| 6.4.1 Selection of Optimal Current Angle and Optimal Skew Angle for Specific Load Condition..... | 219 |
| 6.4.2 Effects of Load on Optimal Current Angle | 226 |
| 6.4.3 Effects of Load on Optimal Skew Angle | 227 |
| 6.4.4 Effects of Load on Torque Characteristics with Conventional and Optimal Skew Angles | 231 |
| 6.5 Influences of Load in PMSMs with Rotor Step Skew | 234 |
| 6.5.1 Effects of Load on Optimal Current Angle | 235 |
| 6.5.2 Effects of Load on Optimal Skew Angle | 237 |
| 6.5.3 Effects of Load on Torque Characteristics with Optimal Skew Angles..... | 241 |
| 6.6 Experimental Validation..... | 243 |
| 6.7 Conclusion | 244 |
| CHAPTER 7 Analysis of Torque Characteristics in Dual Three-Phase PMSMs with Asymmetric IPM Rotor | 245 |
| 7.1 Introduction..... | 245 |
| 7.2 Machine Configuration and Operation Principle | 247 |
| 7.2.1 Machine Configuration | 247 |

| | |
|---|------------|
| 7.2.2 Operation Principle | 249 |
| 7.3 Electromagnetic Performance under Healthy Condition | 251 |
| 7.3.1 Open-Circuit Characteristics..... | 251 |
| 7.3.2 Torque Characteristics..... | 255 |
| 7.3.3 Loss and Efficiency..... | 261 |
| 7.4 Electromagnetic Performance under 3-ph OC Condition..... | 270 |
| 7.4.1 Torque Characteristics..... | 270 |
| 7.4.2 Loss and Efficiency..... | 274 |
| 7.5 Experimental Validation..... | 275 |
| 7.6 Conclusion | 281 |
| CHAPTER 8 General Conclusion and Future Work | 282 |
| 8.1 General Conclusion..... | 282 |
| 8.1.1 General Winding Configuration Technique of DTP PMSMs | 282 |
| 8.1.2 Extension of Some Analysing Methods to DTP PMSMs | 285 |
| 8.1.3 Comparison of some design techniques in STP and DTP PMSMs | 287 |
| 8.2 Future Work | 290 |
| REFERENCES..... | 291 |
| APPENDIX I PUBLICATIONS RESULTED FROM PHD STUDY | 317 |

NOMENCLATURE

Symbol

| | | |
|-----------------|---|---------------|
| A | Cross-section area of conductor | mm^2 |
| f_{base} | Frequency at based speed | Hz |
| I_a | Amplitude of phase current | A |
| I_d | Amplitude of d -axis current | A |
| I_q | Amplitude of q -axis current | A |
| k | Number of spokes per phase in the star of slots | |
| K_a | Attenuation factor | |
| K_d | Distribution factor | |
| K_p | Pitch factor | |
| K_w | Winding factor | |
| l | Length of conductor | mm |
| l_a | Stator axial length | mm |
| l_{cd} | Distance between two coil sides | mm |
| l_{ew} | Length of end-winding | mm |
| N_s | Number of slots | |
| n_s | Number of spokes in the star of slots | |
| p | Pole pair number | |
| P_{Cu} | Copper loss | W |
| $P_{Eddy-base}$ | Eddy current loss at base speed | W |
| $P_{Hyst-base}$ | Hysteresis loss at base speed | W |
| P_{Fe} | Iron loss | W |
| P_{Me} | Mechanical loss | W |
| P_{in} | Input power | W |
| P_{out} | Output power | W |
| r_e | Equivalent radius of end-winding | mm |
| R_{ph} | Phase resistance | Ohm |
| t | Electrical periodicity number | |
| T_{direct} | Torque obtained from finite element analysis directly | Nm |

| | | |
|---------------|--|------------|
| T_{em} | Electromagnetic torque | Nm |
| T_{pm} | PM torque component | Nm |
| T_{rel} | Reluctance torque component | Nm |
| T_{mr} | Torque component caused by magnets and stator reluctance | Nm |
| U_{dc} | Terminal direct current voltage | V |
| ν | Harmonic order | |
| y | Coil pitch number | |
| α | Spatial shifting angle in space | Elec. Deg. |
| β | Phase shifting angle in time | Elec. Deg. |
| θ_{sk} | Skew angle | Elec. Deg. |
| ρ | Electrical resistivity of conductor | Ohm/mm |

Acronym

| | |
|----------|--------------------------------------|
| AC | Alternating current |
| AIPM | Asymmetric interior permanent magnet |
| Back-EMF | Back electromotive force |
| BLAC | Brushless alternating current |
| BLDC | Brushless direct current |
| CPSR | Constant power speed range |
| DC | Direct current |
| DL | Double layer |
| DS | Double layer short-pitched |
| DTP | Dual three-phase |
| EMF | Electromotive force |
| EV | Electric vehicle |
| FE | Finite element |
| FEA | Finite element analysis |
| FSCW | Fractional-slot concentrated winding |
| HEV | Hybrid electric vehicle |
| ID | Inner diameter |
| IM | Induction machines |

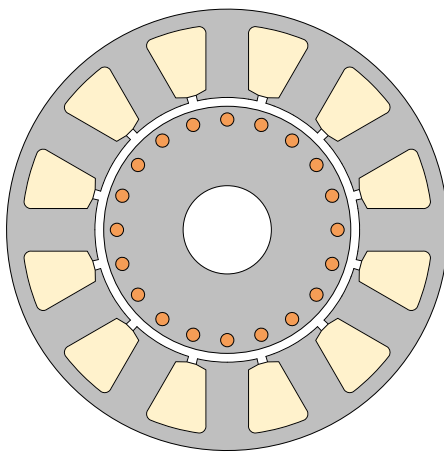
| | |
|-----------|--|
| IPM | Interior permanent magnet |
| IPMSM | Interior permanent magnet synchronous machine |
| MMF | Magnetomotive force |
| MTPA | Maximum torque per ampere |
| Non-OW | Non-overlapping |
| OC | Open-circuit |
| OD | Outer diameter |
| OW | Overlapping |
| PM | Permanent magnet |
| PMA-SynRM | Permanent magnet assisted-synchronous reluctance machine |
| PMSM | Permanent magnet synchronous machine |
| PWM | Pulse width modulation |
| SF | Single layer full-pitched |
| SL | Single layer |
| SPM | Surface permanent magnet |
| SPMSM | Surface permanent magnet synchronous machine |
| SRM | Switched reluctance machine |
| STP | Single three-phase |
| SynRM | Synchronous reluctance machine |
| THD | Total harmonic distortion |
| TTP | Triple three-phase |

CHAPTER 1

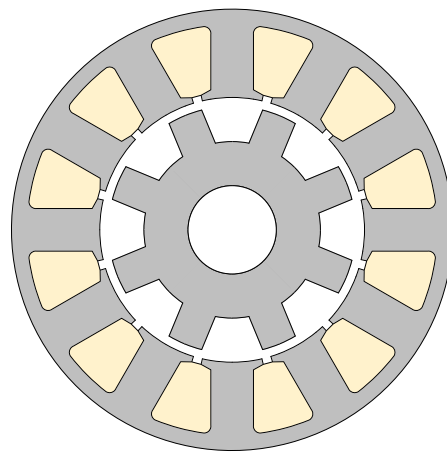
GENERAL INTRODUCTION

1.1 Introduction

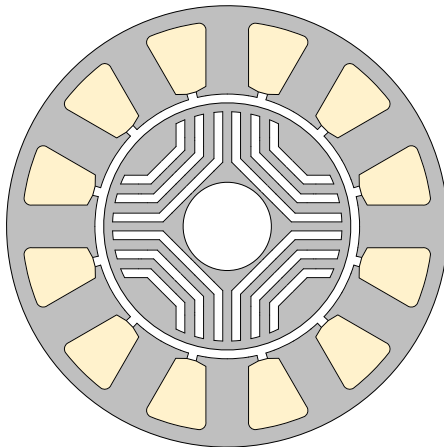
Electrical machines are a device that converts electrical energy into mechanical energy or vice versa. They have been widely applied to power generating, mining, manufacturing, aerospace, locomotives, electric vehicles, domestic appliances, and hand tools, etc. After over two centuries of research and development, numerous types of electrical machines have been developed. The popular technologies include induction machines (IMs), switched reluctance machines (SRMs), synchronous reluctance machines (SynRMs), and permanent magnet (PM) synchronous machines (PMSMs), as shown in Fig. 1.1.



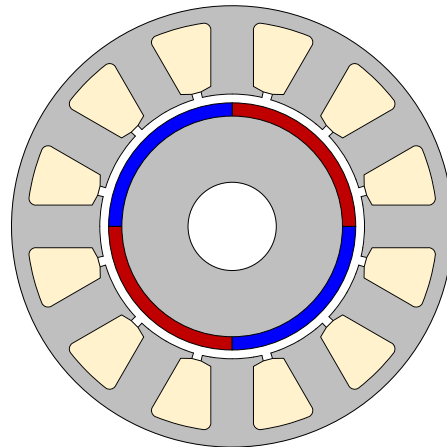
(a) Induction machine (IM)



(b) Switched reluctance machine (SRM)



(c) Synchronous reluctance machine (SynRM)



(d) Permanent magnet synchronous machine (PMPM)

Fig. 1.1 Cross-sections of different types of electric machines.

Among these four machine technologies shown in Fig. 1.1, PMSMs are inherently more efficient and have higher power/torque density due to PM excitation [ZHU07]. Hence, over last 40 years, PMSMs have been extensively investigated and applied, and will be the focus of research in this thesis.

The development of PMSMs depends on the development of PM materials. In 1931, the first aluminium-nickel-cobalt (AlNiCo) magnet was invented by Mishima, and then, in the early 1950s, Philips developed the first hard ferrite magnet [MCC87]. From then on, AlNiCo magnet and ferrite magnet were widely researched and employed in PMSMs. For example, some PMSMs utilizing AlNiCo and ferrite magnets were reported in [MER47] [SAU51] [BRA52] and [DOU59]. A milestone on the performance of PMs occurred in the late 1960s, when various rare-earth magnets, especially samarium-cobalt (SmCo) magnet, were discovered. Furthermore, in the early 1980s, neodymium-iron-boron (NdFeB) magnet was invented by General Motors and Sumitomo Special Metals independently and almost simultaneously. NdFeB magnets have inherent high coercivity (H_c), high remanence (B_r), and high energy product (BH_{max}). Today, NdFeB magnets are still the strongest PM material in the world. PMSMs equipped with NdFeB magnets can achieve high efficiency, high power/torque density, high reliability, and robustness simultaneously [RAH12].

In this thesis, electromagnetic performance of multiphase PMSMs, more specifically, dual three-phase (DTP) PMSMs, will be investigated, with reference to torque and torque ripple characteristics for electric vehicle applications. In this chapter, the winding and rotor configurations in conventional single three-phase (STP) PMSMs will be introduced in Section 1.2. In Section 1.3, DTP PMSMs are compared with other multiphase PMSMs. Finally, the research scope and major contributions of this thesis are presented in Section 1.4.

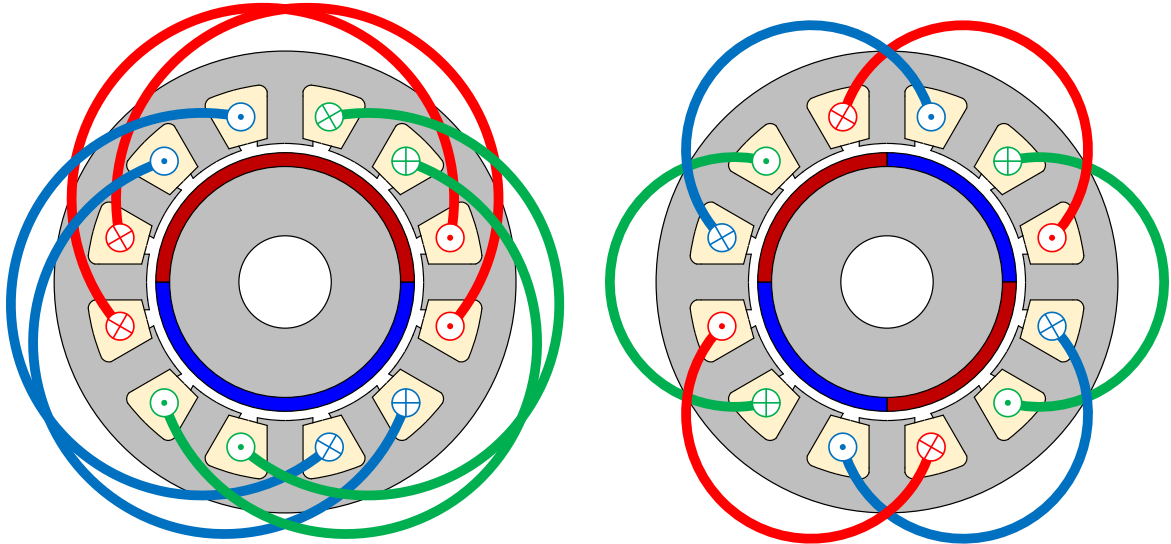
1.2 STP PMSMs

In this section, various stator and rotor configurations of STP PMSMs will be introduced and reviewed. It should be mentioned that although numerous new topologies have been proposed in STP PMSMs in the last decades, such as external rotor, stator PM, claw pole rotor, axial flux, etc., the review will mainly focus on the most conventional type of PMSMs, i.e., the external slotted stator with internal PM rotor type.

1.2.1 Stator Winding Configurations

In the slotted stator of STP PMSM, the coils of three-phase armature windings are accommodated in slots to produce a rotary magnetic field. For any STP PMSM, the detailed winding connection is determined by its slot/pole number combination and can be obtained by using the star of slots [HEN94] [BIA06a] [PYR08]. In general, stator windings can be categorised into two groups, i.e., overlapping winding (OW) and non-overlapping winding (non-OW).

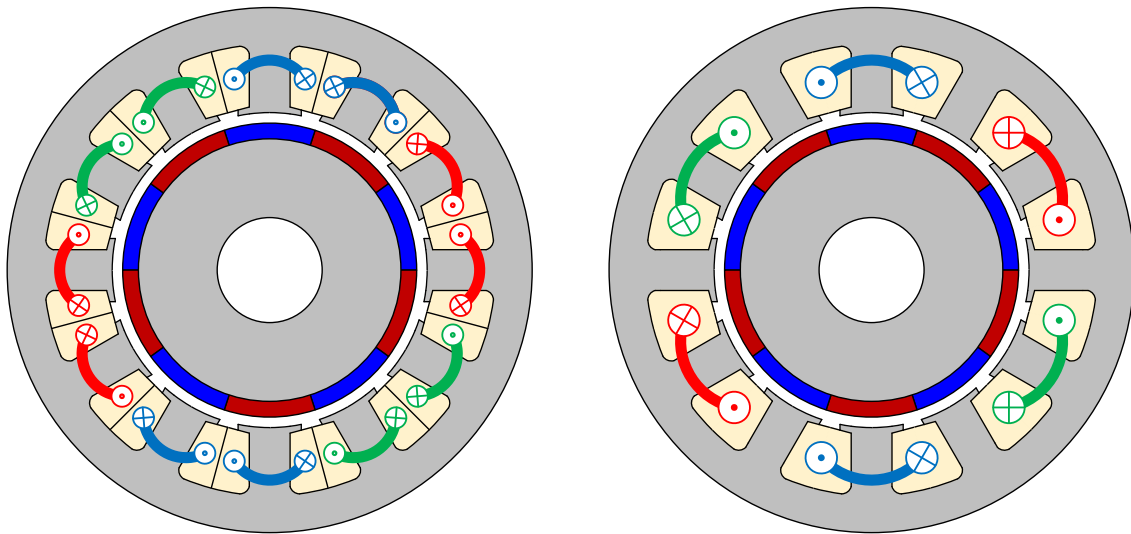
In OW, the coil pitch is almost matching the pole pitch, and hence, OWs can be widely utilized in STP PMSMs with the slot number per pole per phase ≥ 1 . According to the winding layout, OWs can be further classified into distributed winding and concentrated winding, as shown in Fig. 1.2 (a) and (b), respectively. The possible concentrated windings are given in a paper [LIB04]. It can be seen that in distributed windings, the coils of the same phase and/or different phases are overlapped with each other. In general, the coil pitch number of OW is ≥ 2 , and OW always has relatively long end-windings. Hence, OW can result in a high winding factor and can better utilize reluctance torque component [ELR10]. However, the long end-windings of OW also cause a high copper loss and a low torque density, and to solve these issues, non-OW was introduced.



(a) Distributed windings (12-slot/2-pole) (b) Concentrated windings (12s-slot/4-pole)

Fig. 1.2 Winding configurations of overlapping windings.

Non-OWs are suitable for STP PMSMs with the slot number per pole per phase < 1 . In non-OWs, all the coils are wound around stator teeth without any overlapping, as shown in Fig. 1.3. Since the slot number per pole per phase is fractional and the coils are all concentrated, this kind of windings is also known as fractional-slot concentrated winding (FSCW). Compared with OW, FSCW configuration can shorten end-windings, reduce copper loss, improve slot fill factor, and ease manufacturing, and hence, FSCW configuration is very popular and has been widely researched all over the world since the early 2000s [CRO02] [MAG03] [ISH06] [BIA06b] [MAG07] [ELR10]. It also should be noticed that FSCW can be further classified into all teeth wound (double layer, DL) and alternate teeth wound (single layer, SL) types, as shown in Fig. 1.3 (a) and (b), respectively [ISH06] [ELR08]. In addition, although some higher winding layer numbers (e.g., 3, 4) also have been proposed and researched in FSCW PMSMs [CIS10a] [RED15] [WAN15a], considering the difficulties in manufacturing multilayer windings, in practice, only SL and DL winding configurations are usually utilized in FSCW PMSMs.



(a) All teeth wound (double layer)

(b) Alternate teeth wound (single layer)

Fig. 1.3 Winding configurations of non-overlapping (concentrated) windings.

In general, it can be summarized that the winding layout of a STP PMSM is mainly determined by its slot/pole number combination. According to the coil pitch number, stator windings can be categorised into OW and non-OW. OW could be either distributed winding or concentrated winding, but non-OW is always concentrated winding.

1.2.2 Rotor PM Configurations

In PMSMs, besides armature windings in stators, rotor PM configurations also play an important role in the resultant electromagnetic performances. In this sub-section, the rotor configurations in STP PMSMs will be briefly reviewed. As mentioned before, only internal radial flux PM rotors will be included in the review.

1.2.2.1 Surface PM (SPM)

Among all PM rotor topologies in STP PMSMs, surface PM (SPM) is the most widely used one due to its simple structure. In SPM rotors, magnets are bonded to the outside surface of rotors using mechanical methods or adhesives. According to the shape of rotor lamination, SPM rotors can be further categorized into surface mounted and surface inset types, as shown in Fig. 1.4 (a) and (b), respectively.

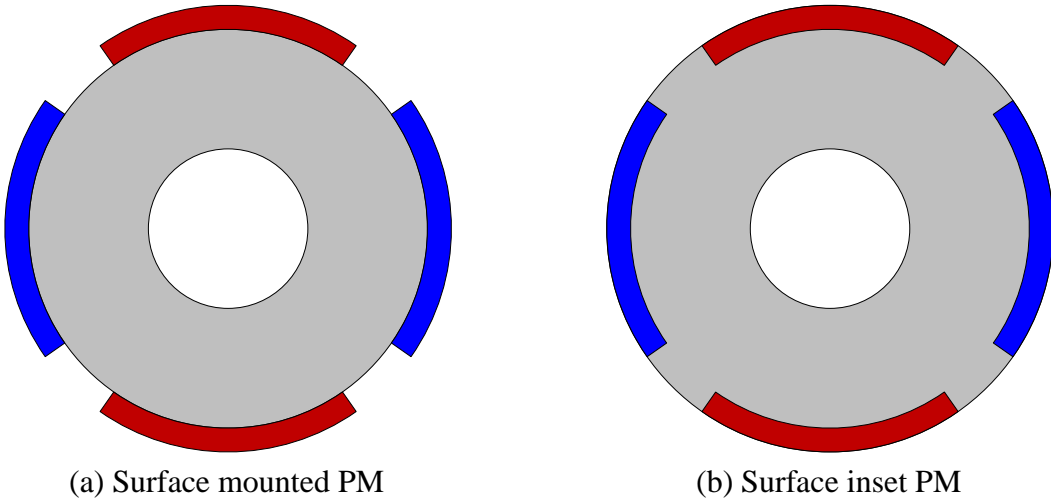


Fig. 1.4 Rotor configurations of SPM rotors.

Since the relative permeability of magnets is very similar to that of air, the d - and q -axis inductances in surface mounted PM rotors are almost the same, but the d - and q -axis inductances in surface inset PM rotors are different. Hence, surface mounted PM rotors exhibit very limited magnetic saliency and rely almost completely on PM torque component to produce torque, but surface inset PM rotors can benefit from reluctance torque component.

In the last decades, numerous analyses were made to further improve the electromagnetic performances of STP SPM machines. Some typical methods are illustrated in Fig. 1.5, including magnet shaping [LI88] [ZHU92] [LI03], magnet segmentation [POL99] [ATA00],

magnet Halbach array [HAL80] [ZHU01], and combining with flux barriers [CHA96] [ION98] [BIA00]. It should be mentioned that although these methods were proposed based on SPM rotors, they are widely applicable for all kinds of PM rotors.

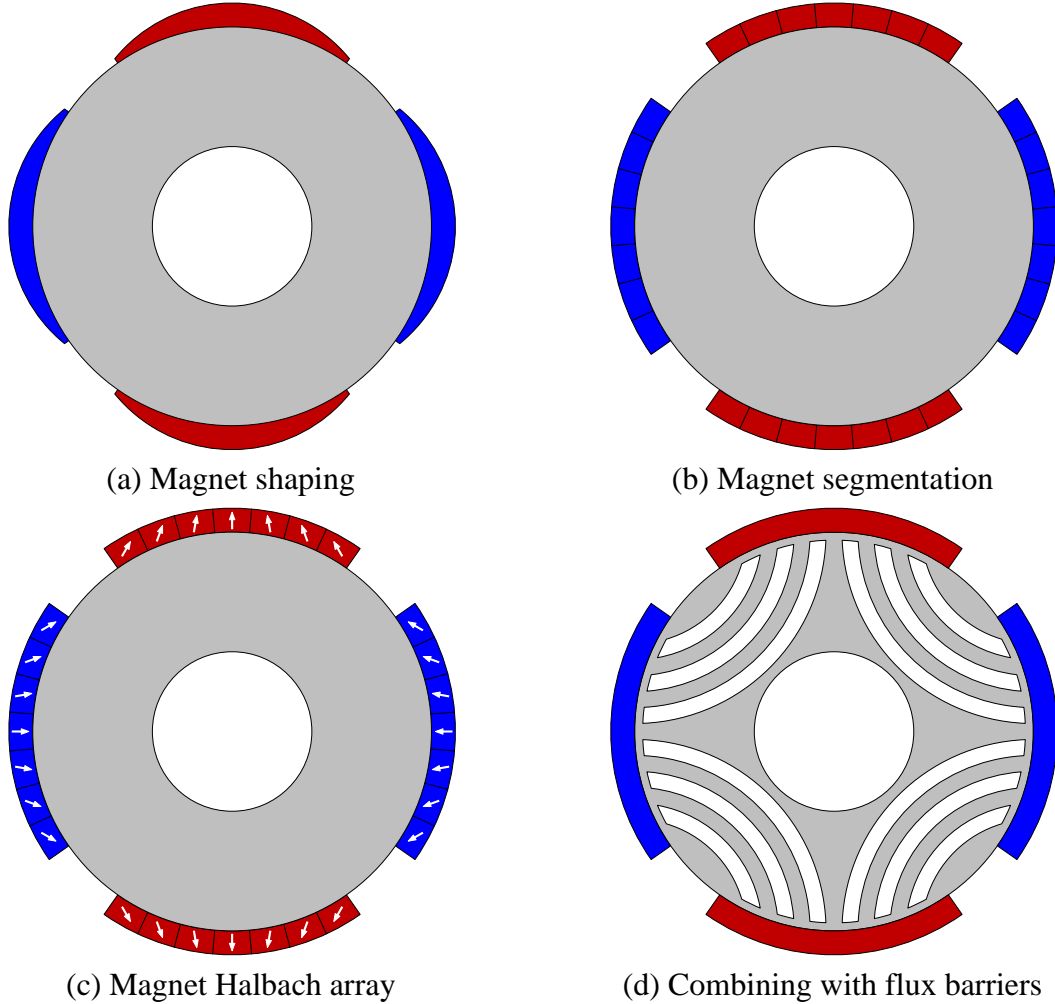


Fig. 1.5 Typical methods to improve electromagnetic performances in SPM rotors.

However, the magnets in SPM rotor are exposed directly to the armature reaction field, which can lead to a significant PM eddy current loss in the magnets. Hence, it is always necessary to examine the PM demagnetization withstand capability and thermal performance in machine design process. Additionally, as the magnets are affixed to the exterior rotor surface, SPM rotors have weaker mechanical strength than IPM counterparts, and the weakened mechanical strength limits the maximum speed of SPM machines. Thus, SPM rotors, especially those for high-speed applications, are required to be equipped with rotor retention bonds or retaining sleeves [BIN06] [ZHO06].

1.2.2.2 Interior PM (IPM)

In interior PM (IPM) rotor, PMs are embedded inside rotors, and hence, IPM rotor has better mechanical strength than its SPM counterpart. In addition, the magnets can be shielded effectively from the armature reaction field, and thus, the eddy current loss and demagnetization risk in the magnets in IPM rotor are smaller than those in SPM rotor. Another prominent feature of IPM rotor is the high rotor saliency ratio. In IPM rotor, the q -axis inductance is larger than the d -axis inductance. Hence, IPM machines can utilize PM and reluctance torque components simultaneously. A further advantage of IPM rotor is that they are more suitable for flux weakening control method, as the d -axis inductance in IPM rotor is usually larger than that in SPM counterpart. Thus, the constant power speed range (CPSR) of IPM machine can be extended by using flux weakening control method and the IPM machine can be operated at higher speed. Generally speaking, IPM rotors are more robust than SPM rotors, and more suitable for high-speed applications.

In the last decades, especially after the invention of NdFeB magnet in 1982 and commercialization in 1984, numerous analyses have been made based on PMSMs with IPM rotors [STR52] [HAN57] [HON80] [HON82] [RAH85] [JAH86] [JAH87] [SCH90] [SOO02]. In this sub-section, various IPM rotor topologies are briefly reviewed. As there are many degrees of freedom in designing IPM rotors, these rotor topologies are grouped according to the number of PM layers in the review.

The single layer IPM rotor is the simplest type of IPM rotors. In each rotor pole, the single layer magnets can be arranged in different shapes. The most conventional shapes include I-, V-, and U-shape, and thus, the corresponding I-, V-, and U-type single layer IPM rotors can be obtained, as shown in Fig. 1.6 (a), (b), and (c), respectively. Among the three rotors, the I-type IPM rotor has a simple construction, but the V- and U-type IPM rotors can enhance flux focusing effect and improve torque capability. It should be noticed that the spoke-type IPM rotor, as shown in Fig. 1.6 (d), in which the magnets are circumferentially magnetized, can also be seen as a special kind of single layer V-type rotor and are also grouped into the single layer IPM rotor in the review. The spoke-type IPM rotor can also achieve flux focusing effect but suffer from its relatively higher flux leakages. The I-, V-, U-, and spoke-type IPM rotors are compared based on electric vehicle machines in [LIU16]. The research results indicate that the I-type rotor has the highest average torque, but the worst CPSR; the spoke-type rotor has the

widest CPSR, but the lowest average torque; the V- and U-type rotors show similar torque capability at high-speed region, both higher than the I-type counterpart, but the V-type rotor has higher average torque than the U-type counterpart at low-speed region. Considering that V-type rotor layout can make full use of the rotor space to further increase PM volume, the V-type IPM rotor is more recommended for electric vehicles with comprehensive consideration [LIU16] [YAN17a].

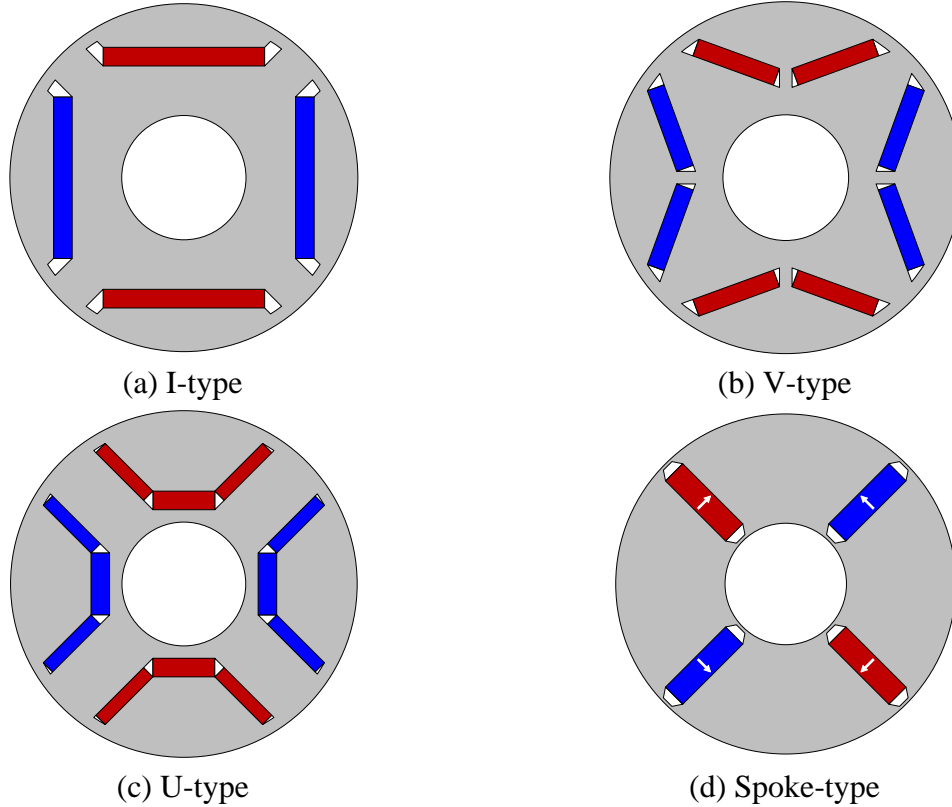
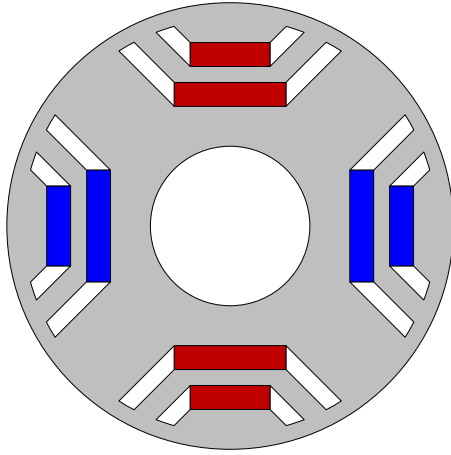
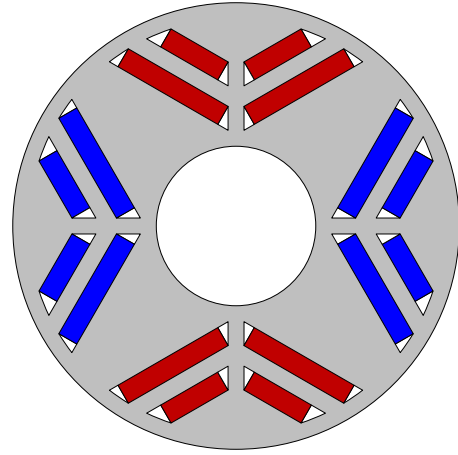


Fig. 1.6 Rotor configurations of single layer IPM rotors.

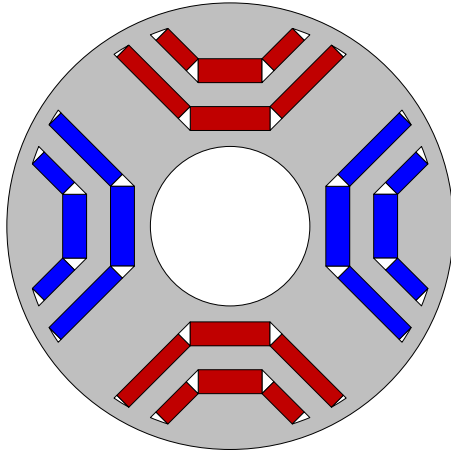
When the PM layer number is 2, the double layer magnets can be combined by two single layer magnets. Based on the single layer I-, V-, and U-type magnet layouts, double I-, double V-, double U-, I+V-, I+U-, and V+U-type IPM rotors were proposed and analysed in papers [LOV02] [CHE14b] [CHE15] [KIM13] [HON98] [ZHU18] [HU17a] [HAN10], as presented in Fig. 1.7. With the double layer magnet disposition, the rotor saliency ratio can be enhanced. In addition, the rotor flux field can also be optimized as there are more degrees of freedom in double layer IPM rotor, which can help to reduce torque ripple and iron loss. Among these double layer IPM rotor topologies, the I+V-type, which is also called as delta-type, attracts more attention as it can provide a better torque capability than its single layer counterparts without too much sophistication in rotor construction [HON98].



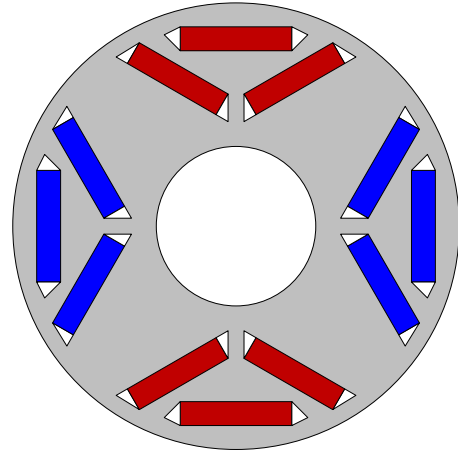
(a) Double I-type



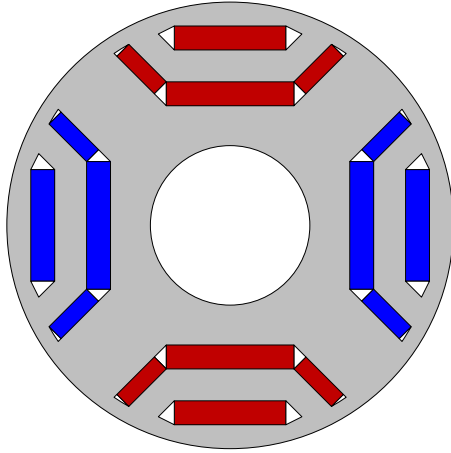
(b) Double V-type



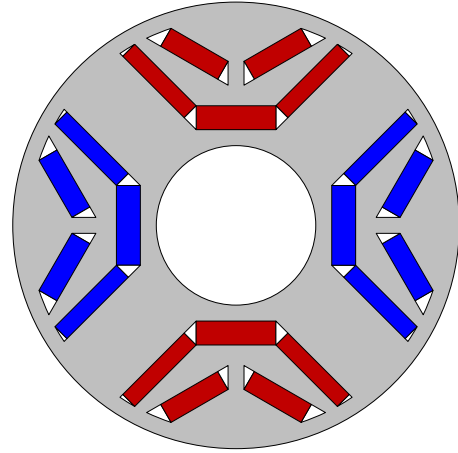
(c) Double U-type



(d) I+V(delta)-type



(e) I+U-type



(f) V+U-type

Fig. 1.7 Rotor configurations of double layer IPM rotors.

Besides double layer IPM rotor, the PM layer number can further be increased to 3. For example, a triple I-type IPM rotor is designed in [BOL04] by inserting three magnets in a synchronous reluctance PM machine with triple layer flux barriers, as shown in Fig. 1.8 (a). In this kind of machines, the rotors have multilayer flux barriers, and can be seen as reluctance

rotors. The interior magnets are inserted to improve the electromagnetic performance of the original synchronous reluctance machine. Hence, this kind of machines are also called as PM assisted-synchronous reluctance machine (PMA-SynRM). Based on the concept of “PMA-SynRM Machine”, many multilayer IPM rotors were proposed [BIA06c] [ARM09] [PEL10] [BAR12] [GUG13]. Another example of triple layer IPM rotors is presented in Fig. 1.8 (b), which is composed by I-, V-, and U-type magnets [HU18] [ZHU18]. Compared with conventional V- and Delta-type counterparts, the triple layer rotor design shows the lowest total harmonic distortion in air-gap flux density, and thus, the iron loss can be reduced and the overall efficiency can be improved significantly. However, considering the difficulties and the high cost in manufacturing complicated IPM rotors, in practice, the PM layer number is usually limited under 3.

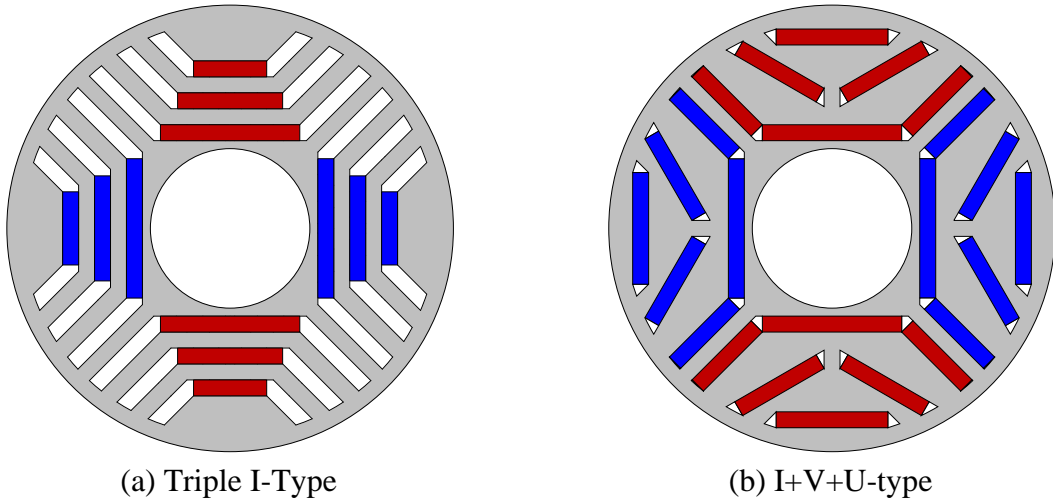


Fig. 1.8 Rotor configurations of triple layer IPM rotors.

It should be mentioned that with the increase of PM layer number, the piece number of magnets is also increased, and thus, some high energy but expensive NdFeB magnets can be replaced by low-energy but much cheaper ferrite magnets without much sacrifice on resultant electromagnetic performance [LI19a]. This kind of IPM rotors, which utilize different magnet materials simultaneously, are also be known as hybrid IPM rotor [ZHU17a] [JEO19]. In multilayer IPM rotor, the concept of “hybrid IPM rotor” makes the arrangement of magnets more flexible, but more complicated as well.

1.2.2.3 Asymmetric IPM (AIPM)

An attractive advantage of IPM rotor is that it can utilize both PM and reluctance torque components together to produce average torque and hence to improve the ratio of torque per PM volume. However, with the conventional symmetrical IPM rotors, maximum PM and reluctance torque components are achieved at different current advancing angles [JAH86]. To solve this issue, asymmetric IPM (AIPM) rotor topologies were proposed in recent years to enhance the torque capability of PMSM by making the current advancing angles to achieve maximum PM and reluctance torque components close to each other. In this part, some important AIPM rotor topologies are reviewed according to different design concepts. The detailed operating principle and existing topologies of AIPM rotors are summarized and reviewed in [ZHU22]. Typical AIPM rotor topologies are shown in Fig. 1.9.

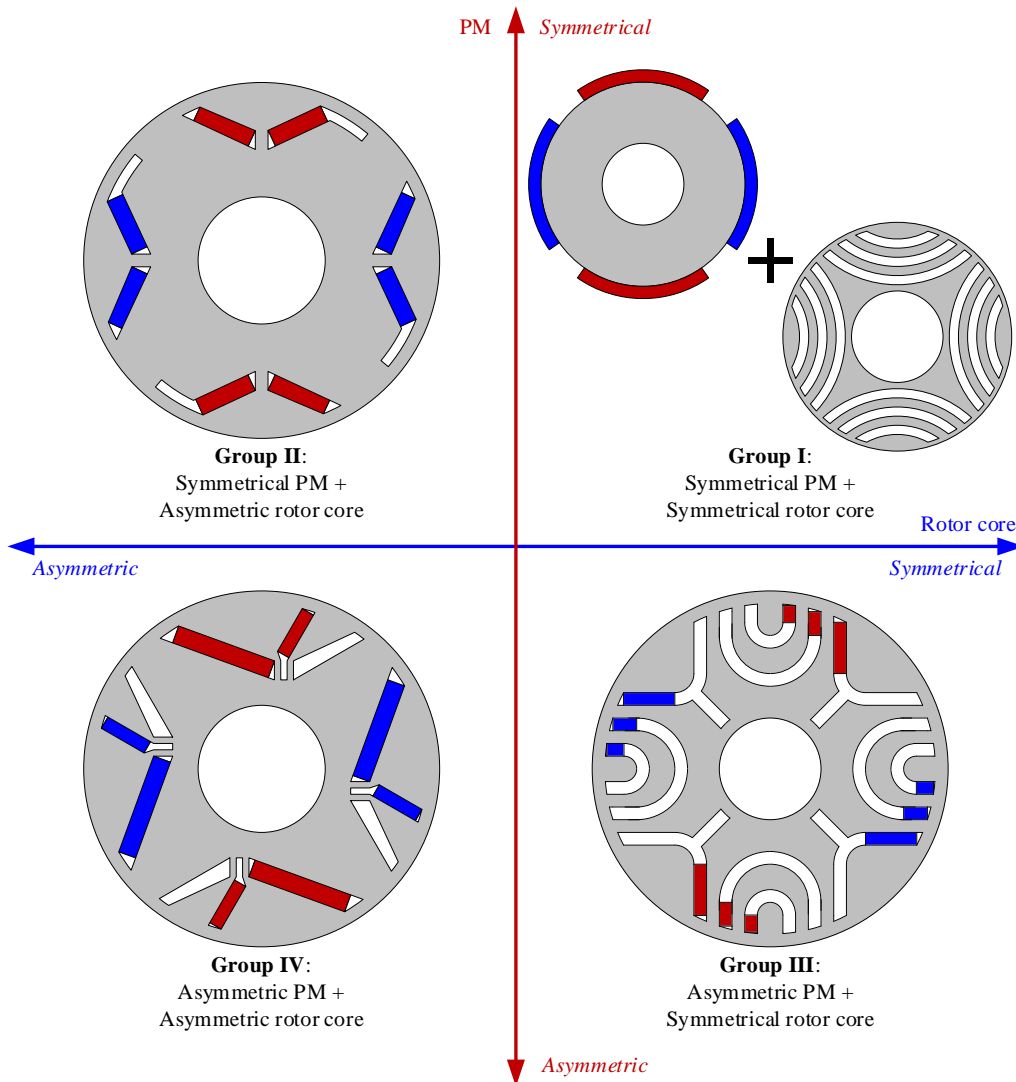


Fig. 1.9 Rotor configurations of AIPM rotors.

All AIPM rotors can be grouped into four groups according to symmetries and asymmetries of magnets and rotor cores. In Group I, both PM and rotor core are symmetrical. To make the current advancing angles closer to achieve maximum PM and reluctance torque components, the rotors of Group I are usually composed by two parts, i.e., PM part and reluctance part, and the two rotor parts are shifted by a specific displacement angle. This kind of rotors are also known as hybrid rotor [CHA96] [YAN17b]. In Group II, the AIPM rotor has symmetrical PMs, but asymmetric rotor core. The asymmetric rotor core is usually achieved by adding additional flux barriers [ZHA14]. In Group III, the rotor core is symmetrical, but the PM layout is asymmetric. This kind of AIPM rotors is usually obtained based on the concept of “PMA-SynRM”, by inserting magnets asymmetrically in symmetrical reluctance rotor core [XIN19]. Finally, the magnets and flux barriers can be designed without any consideration of symmetries, and thus, Group IV of AIPM rotors, with asymmetric magnets and rotor cores can be obtained [XIA21].

It is found that the torque density of PMSM with conventional IPM rotor can be further enhanced by using AIPM rotor. Additionally, AIPM machines can show competitive CPSR and flux weakening capability with conventional IPM counterparts [XIA21]. However, the demerits of AIPM rotor mainly include iron loss, efficiency, thermal characteristics, noise, and vibration. The design of AIPM rotor needs more comprehensive considerations.

1.2.3 Stator PM Machines

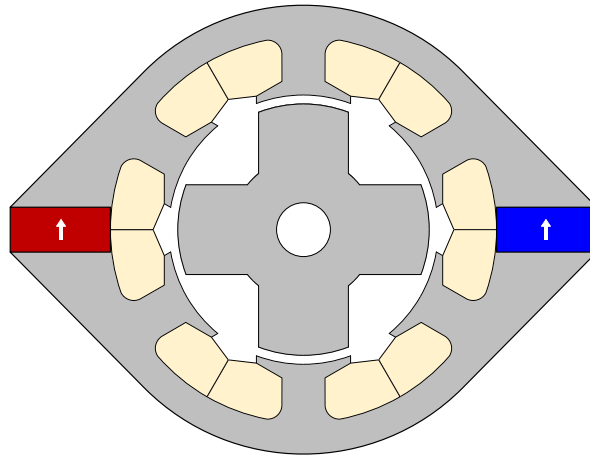
In the previous sub-sections 1.2.1 and 1.2.2, the stator windings and rotor PM configurations of conventional internal rotor-PM machines were reviewed. In fact, in STP PMSMs, PMs can also be embedded in the stators. In the recent decades, stator-PM machines have also been developed very quickly and attracted much attention [ZHU07] [CHE11a] [ZHU12].

Compared with rotor-PM machines, the advantages of stator-PM machines include:

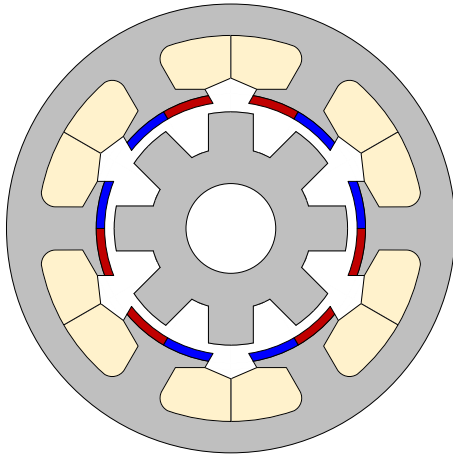
- Stator-PM machines utilize salient pole rotors, which are simple, robust, cheap and easy to produce, and suitable for high-speed applications;
- Stator-PM machines usually have concentrated windings, which have short end-windings and can help to reduce copper loss;

- Magnets are located in stators, and thus, more effective cooling methods can be adopted and the thermal management can be easier, which benefits the machines when running in heavy-load condition.

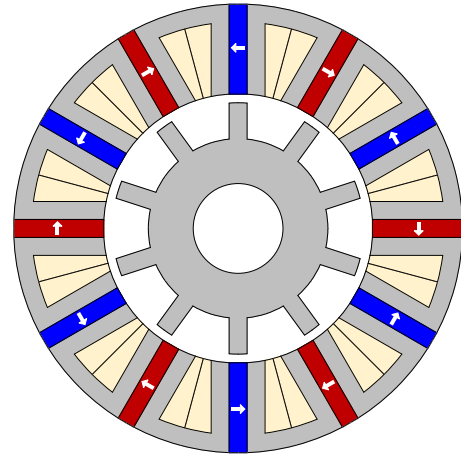
According to the positions of PMs, there are generally three types of stator-PM machines, i.e., doubly salient machine (PMs are located in stator yoke), flux reversal machine (PMs are located on stator bore), switched flux PM machines (PMs are located inside stator teeth), as shown in Fig. 1.10.



(a) Double salient machine [LIA95]



(b) Flux reversal machine [WAN99]



(c) Switched flux machine [HOA97]

Fig. 1.10 Cross-sections of STP stator-PM machines.

Fig. 1.10(a) presents a STP doubly salient PM machine, which was proposed in [LIA95], following an earlier single-phase version [SAY83]. To make the phase number 3, the magnets are placed every three teeth. However, due to the machine topology and PM locations, the flux-linkages in all coils are unipolar, and hence, the torque density of doubly salient machine is relatively poor compared with other PMSMs [CHE11a].

Fig. 1.10(b) presents a STP flux reversal machine, which was proposed in [WAN99], and based on the single-phase counterparts introduced in [DEO97]. In flux reversal machine, a pair of PMs are mounted on the inner surface of every stator tooth. When rotor rotates, the flux-linkages in all coils are bipolar, making flux reversal machine has higher torque density than its doubly salient counterpart [CHE11a]. Due to the special PM position, the PM assembling in flux reversal machine is relatively simpler than other kinds of stator-PM machines, but it also makes the magnets more vulnerable to partial irreversible demagnetization [ZHU07].

Fig. 1.10(c) presents a STP switched flux machine, which was firstly proposed in [HOA97]. In this kind of machines, the PMs are sandwiched between U-shaped stator segments. Every coil is wound around two stator pieces and a circumferentially magnetized PM. With the rotation of rotor, the phase flux-linkages are bipolar, which makes switched flux machines have high torque densities. In addition, as the magnets are circumferentially magnetized in switched flux machine, the flux-focusing effect is evident. Thus, even ferrite magnets can achieve good electromagnetic performances with switched flux machine topologies.

It should be mentioned that Fig. 1.10 only shows three typical stator-PM machine topologies. Most of stator-PM machines can be grouped into these three types. In general, stator-PM machines have high power/torque density, high efficiency, and robust rotor structure. It can be seen as a potential alternative to conventional rotor-PM machines.

1.2.4 Summary

In this section, the stator windings and rotor PM configurations of STP rotor-PM machines are briefly reviewed. The topologies of STP stator-PM machines are simply introduced.

It can be summarized that PMSMs all have high power/torque densities and high efficiencies. SPM machines are featured with their simple rotor structure; IPM machines are featured with better torque per PM volume, good flux weakening capability and wider CPSR; stator-PM machines are featured with their stationary magnets and robust rotors. Hence, different kinds of PMSMs are suitable for different applications.

In electric vehicles and hybrid electric vehicle applications, a constant output torque capability over a wide speed range is the most important requirement [RAH12]. As IPM machines have superior torque/power density, high efficiency, wide CPSR, and high rotor robustness, IPM

machine is an appealing candidate for electric vehicles. In Table 1.1, the electrical machines equipped in some commercial electric vehicles are summarized [AGA20]. It can be seen that almost all commercial electric vehicles choose IPM machines. 48-slot/8-pole is the most popular slot/pole number combination and the V-type IPM rotor is the most popular rotor configuration in these applications.

Table 1.1 Electrical machines in commercial EV/HEVs [AGA20]

| Electric vehicle (year) | Machine type | Slot/pole combination | Winding type | Rotor configuration |
|-------------------------|--------------|-----------------------|--------------|---------------------|
| Toyota Camry (2007) | IPMSM | 48/8 | OW | V-type |
| Toyota Prius (2010) | IPMSM | 48/8 | OW | V-type |
| Nissan Leaf (2012) | IPMSM | 48/8 | OW | Delta-type |
| Toyota Camry (2012) | IPMSM | 48/8 | OW | V-type |
| Tesla Model S (2013) | IM | N/A | OW | Squirrel case |
| Chevrolet Spark (2014) | IPMSM | 72/12 | OW | Double V-type |
| Honda Accord (2014) | IPMSM | 12/8 | Non-OW | I-type |
| Honda Acura (2016) | IPMSM | 18/12 | Non-OW | V-type |
| BMW i3 (2016) | IPMSM | 72/12 | OW | Double I-type |
| Chevrolet Volt (2016) | IPMSM | 72/12 | OW | V-type |
| Tesla Model 3 (2017) | IPMSM | 54/6 | OW | V-type |
| Toyota Prius (2017) | IPMSM | 48/8 | OW | Delta-type |
| Nissan Leaf (2017) | IPMSM | 48/8 | OW | Delta-type |
| Chevrolet Bolt (2017) | IPMSM | 48/8 | OW | Double V-type |

1.3 DTP PMSMs

Nowadays, three-phase PMSMs have been widely adopted in almost all fields, from power generating, automation, electric vehicles, to domestic appliances. However, the researches of other multiphase (phase number > 3) PMSMs are also developed rapidly at the same time, since multiphase PMSMs have advantages of better torque capability, better fault tolerant capability, higher reliability and lower rating per phase [LEV08] [SAL19] [ZHU21a], and hence, multiphase PMSMs are especially suitable for the applications with special requirements on high power and high reliability, such as more-electric aircrafts, marine propulsion, locomotive traction and electric vehicles [MEC04] [BEN11] [CAO12] [YAN19a] [WAN22]. In this section, multiphase PMSMs will be briefly reviewed, with focus on DTP PMSMs. The design techniques, which are usually utilized in DTP PMSMs, i.e., stator shifting, variable phase shifting angle, and star-delta winding connection, will be reviewed in more details, with some

examples from existing papers. At the end of this section, the DTP machine topologies from existing papers will be summarized according to slot/pole number combinations.

1.3.1 Multiphase PMSMs

In this sub-section, the machine topologies of multiphase (phase number > 3) PMSMs will be reviewed, with particular focus on six- (dual three-) phase PMSMs. A list of the references covering PMSMs of different phase numbers will be provided at the end of this sub-section.

An example of four-phase PMSMs can be found in [MEC04]. A four-phase 8-slot/6-pole SPM machine was designed for an engine fuel pump in an aircraft in that paper, as shown in Fig. 1.11. A series of tests were carried out on this machine in a fully functional pump, and the fault tolerant capability of this four-phase SPM machine was validated.

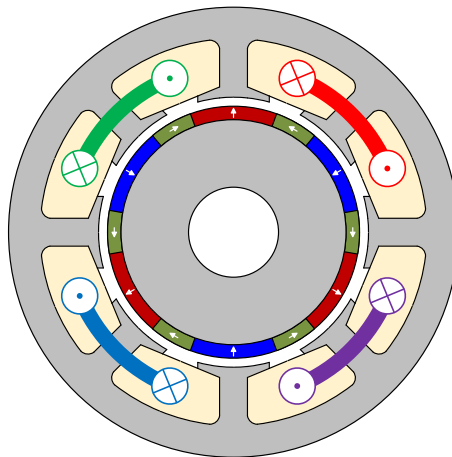
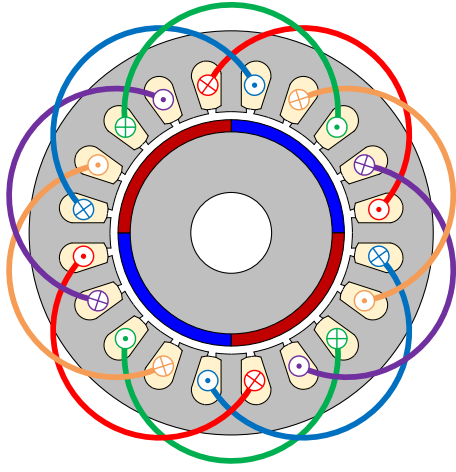
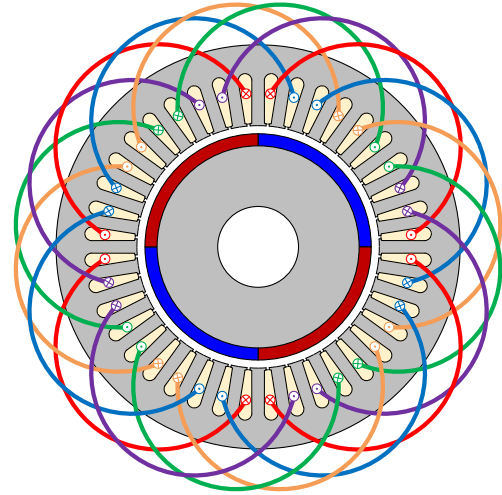


Fig. 1.11 Cross-section of four-phase 8-slot/6-pole SPM (Halbach array) machine in [MEC04].

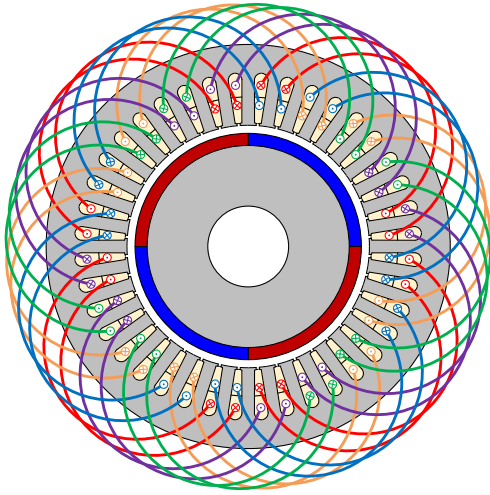
For five-phase PMSMs, Parsa and Toliyat made some important contributions. In [PAR05], they designed three five-phase PMSMs, i.e., 20-slot stator with single layer windings, 40-slot stator with single layer windings, and 40-slot stator with double layer windings, all combined with 4-pole rotors, as shown in Fig. 1.12(a) to (c). The mathematical model and the vector control method of five-phase PMSMs were also presented in [PAR05]. Then, a fault-tolerant control strategy for five-phase PMSMs was introduced in [PAR07], based on a 15-slot/4-pole IPM machine, as shown in Fig. 1.12(d). With the proposed fault-tolerant scheme, the five-phase PMSMs can continue to work safely even under the loss of up to two phases without any additional hardware requirements.



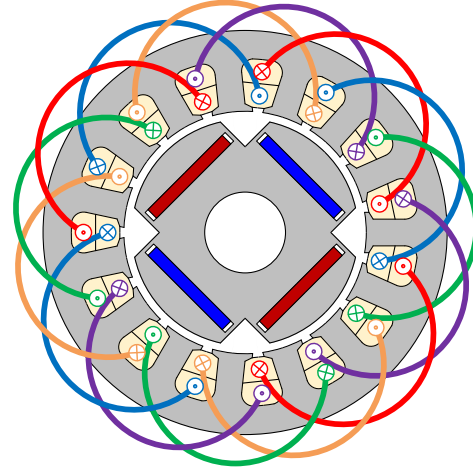
(a) 20-slot/4-pole SPM machine with single layer windings



(b) 40-slot/4-pole SPM machine with single layer windings



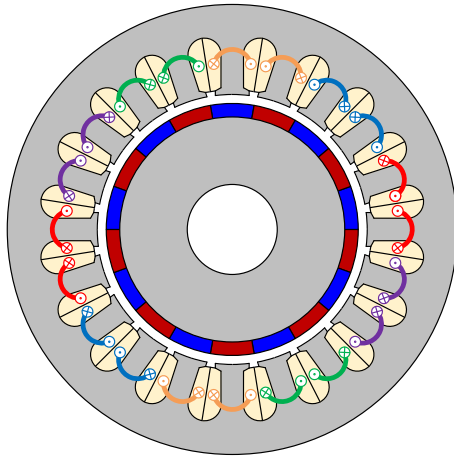
(c) 40-slot/4-pole SPM machine with double layer windings



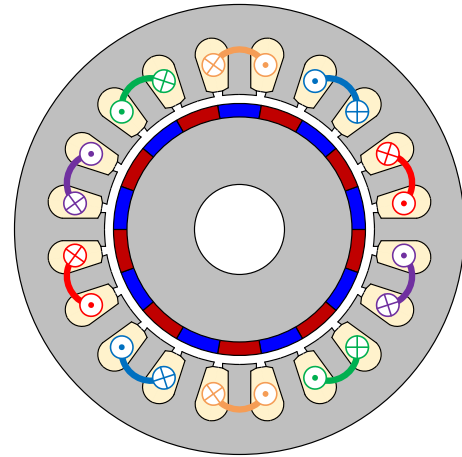
(d) 15-slot/4-pole IPM machine with double layer windings

Fig. 1.12 Cross-sections of five-phase PMSMs in [PAR05] and [PAR07].

Besides distributed windings in [PAR05] and [PAR07], five-phase PMSMs can also be equipped with concentrated windings. In [BIA08], two five-phase 20-slot/18-pole SPM machines with single layer and double layer windings respectively, were introduced. Proper current control strategies for five-phase PMSMs were derived analytically and adopted. The performances of the two machines were compared under various post-fault conditions. It was found that with the proposed current control strategies, both single layer and double layer windings can achieve satisfactory post-fault performances.



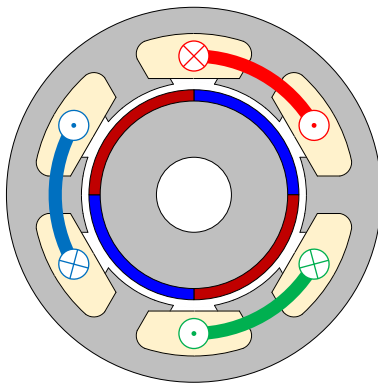
(a) 20-slot/18-pole SPM machine with double layer windings



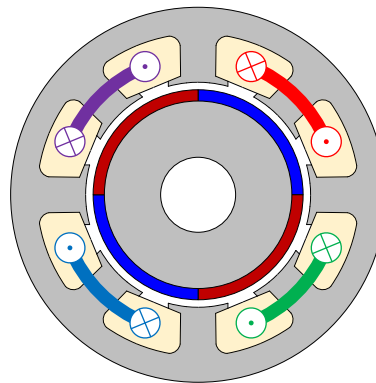
(b) 20-slot/18-pole SPM machine with single layer windings

Fig. 1.13 Cross-sections of five-phase PMSMs in [BIA08].

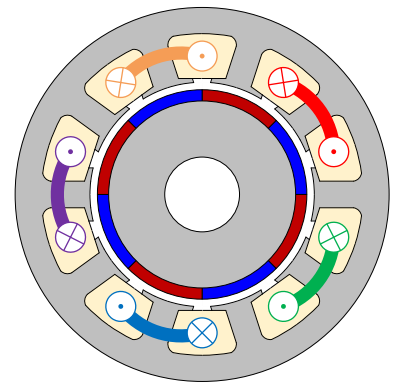
In [GOP00], to present the effects of phase number on fault tolerant capability in PMSMs, three PMSMs with three, four, and five phases were designed and compared, as shown in Fig. 1.14. Various faults that could occur were discussed and some possible control strategies after these faults were presented. The three PMSMs were compared under normal and open-circuit conditions. The results demonstrate that the fault-tolerant capability of PMSMs can be significantly improved by increasing phase number but considering the high cost and the additional complexity when using high phase number, the optimal phase number in fault-tolerant PMSMs is suggested to be five.



(a) 3-phase 6-slot/4-pole SPM machine



(b) 4-phase 8-slot/4-pole SPM machine



(c) 5-phase 10-slot/8-pole SPM machine

Fig. 1.14 Cross-sections of multi-phase PMSMs in [GOP00].

Another comparison of three-, four-, and five-phase PMSMs was presented in [LI17], by considering the effects of modular stator design. In that paper, three-phase 12-slot/10-pole, four-phase 16-slot/12-pole, and five-phase 20-slot/18-pole SPM machines with modular and

un-modular stators were designed and compared, as shown in Fig. 1.15. It is found that the main sub-harmonics in multiphase PMSMs can be reduced by employing modular stators. It also demonstrates that in multiphase PMSMs with modular stators, the resultant electromagnetic performances are affected significantly by the flux gap between stator modules. When slot number $>$ pole number, the flux gap only has negative effects on the electromagnetic performance; but when slot number $<$ pole number, the flux gap could improve the electromagnetic performance. The general conclusions summarized in this paper are widely applicable for other multiphase PMSMs with modular stators.

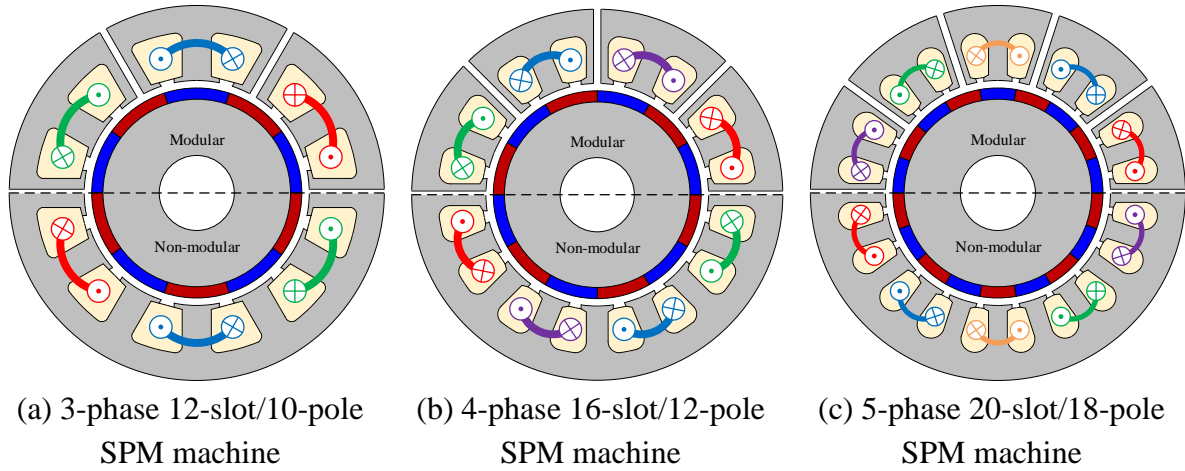
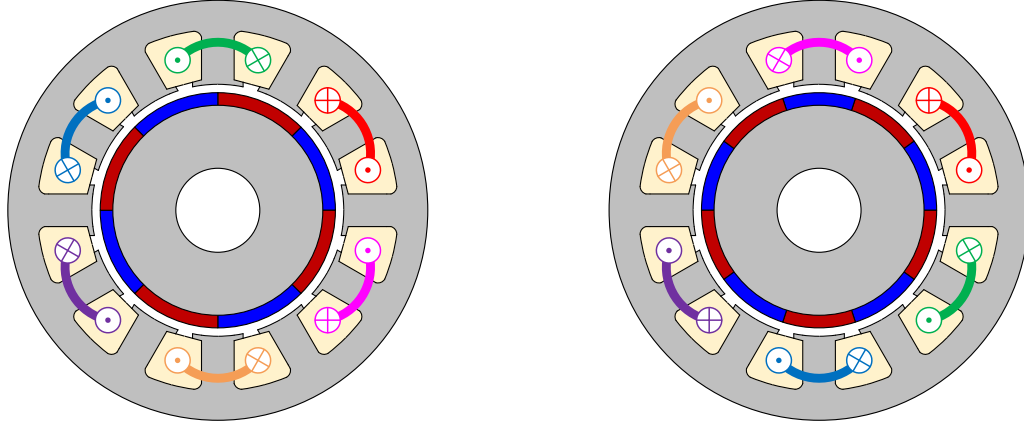


Fig. 1.15 Cross-sections of multi-phase PMSMs in [LI17].

Six-phase PMSMs were also initially proposed for aerospace applications [JAC96] [MEC96] [HAY98] [RAI98]. A six-phase 12-slot/8-pole SPM machine was introduced in [JAC96] and [MEC96], as shown in Fig. 1.16(a). The fault-tolerant operation of this machine was discussed in [HAY98]. [RAI98] presented another feasible topology of six-phase fault-tolerant PMSMs, i.e., 12-slot/10-pole SPM machine, as shown in Fig. 1.16(b). It should be mentioned that in order to achieve better fault-tolerant performance, both six-phase PMSMs shown in Fig. 1.16 utilize single layer windings and each phase was supplied from separate H bridge, to realize more effective electrical, magnetic, thermal, and physical isolation between phases.



(a) 12-slot/8-pole SPM machine with single layer windings [JAC96] [MEC96]

(b) 12-slot/10-pole SPM machine with single layer windings [RAI98]

Fig. 1.16 Cross-section of six-phase SPM machines.

Although multiphase PMSMs have superior fault-tolerant capabilities than conventional three-phase counterparts, the requirements of customized multiphase drives still increase the cost and limit the developments of multiphase PMSMs. In recent decades, as dual three-phase (DTP) machine topologies can make a balance between fault tolerance and the adoption of standard three-phase components, DTP PMSMs have attracted much more attention.

In [BAR10], the electromagnetic performance of the 12-slot/10-pole PMSM with different DTP winding configurations were analysed and compared under healthy and three-phase open-circuit (OC) conditions. The DTP winding configurations are shown in Fig. 1.17. Both single layer and double layer windings were considered, and both SPM and IPM rotors were also considered in that paper. It can be found that no matter with SPM or IPM rotor, the DL-3 (phase shift = 30°) configuration shows the best performance under both healthy and faulty conditions.

More feasible slot/pole combinations of DTP PMSMs were analysed based on the star of slots in [BAR11a], but only concentrated windings (coil pitch = 1) and phase shift = 30° were considered. It was found that among all slot/pole number combinations, 24-slot/20-pole and 24-slot/22-pole are two more promising candidates, as shown in Fig. 1.18. The electromagnetic performances of DTP 24-slot/20-pole and 24-slot/22-pole IPM machines are further compared. The 24-slot/22-pole machine can be equipped with single layer and double layer windings, but the 24-slot/20-pole machine can only use double layer windings. The comparison results show that the 24-slot/22-pole machine with double layer windings exhibits higher average torque, lower torque ripple, and lower mutual coupling. The 24-slot/20-pole machine exhibits lower rotor loss in healthy conditions and lower temperature rise in faulty conditions.

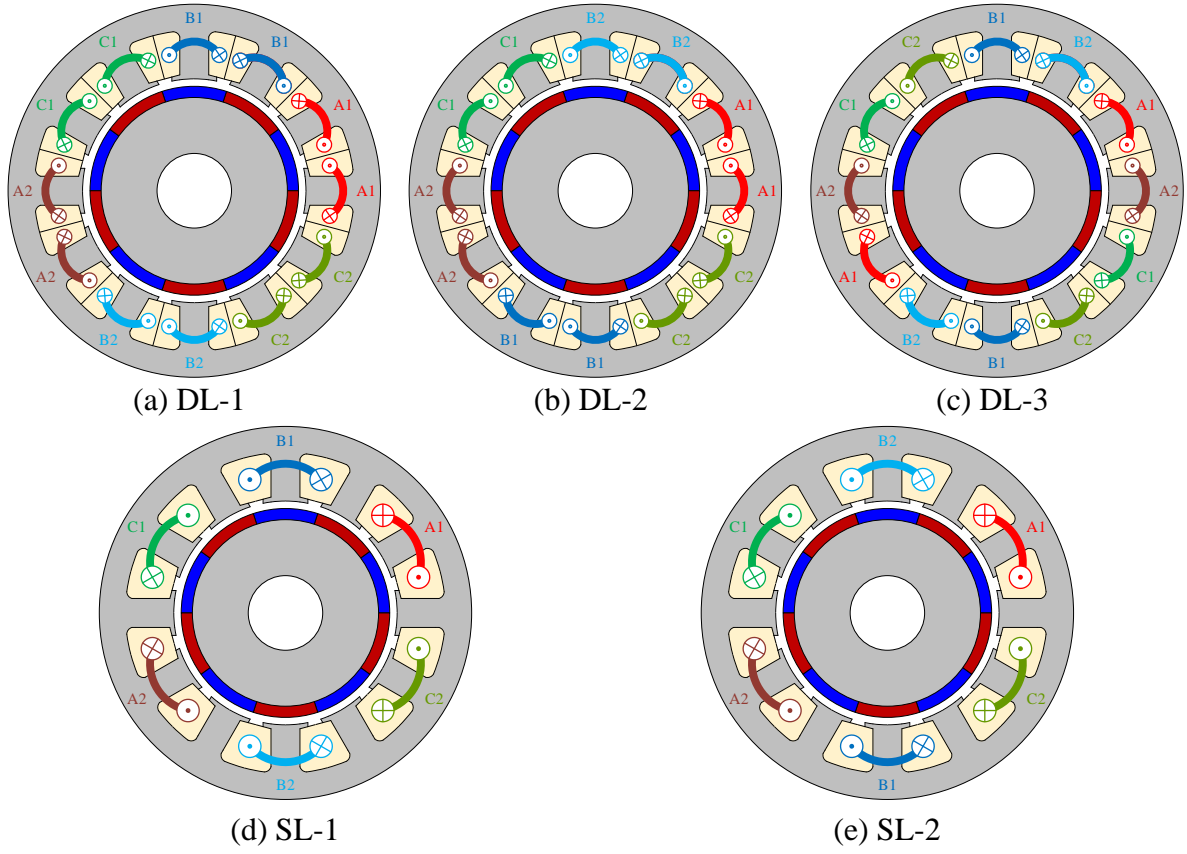


Fig. 1.17 Cross-sections of DTP 12-slot/10pole SPM machine with different DTP winding configurations in [BAR10].

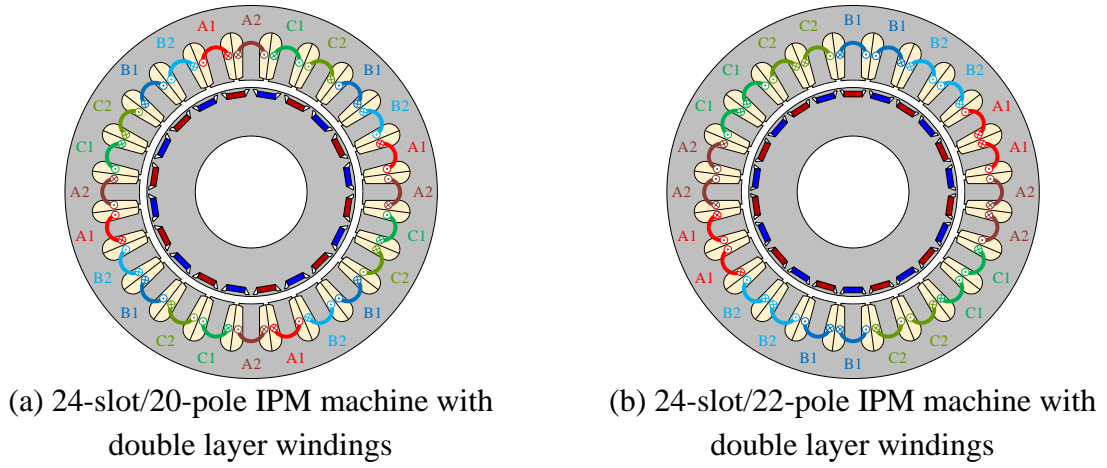


Fig. 1.18 Cross-sections of DTP IPM machines in [BAR11a].

The DTP 24-slot/22-pole combination was also analysed in [ZHE12], in an external SPM rotor machine, both single layer and double layer windings were considered, as shown in Fig. 1.19. It was found that compared with single layer windings, double layer windings can suppress MMF harmonics, reduce iron and PM loss, and lower thermal rise in magnets. In order to obtain flexibilities of post-fault control, the machine was designed to be supplied with six separate H-bridges. Then, the fault-tolerant control strategies for the DTP 24-slot/22-pole SPM machine were discussed. With the proposed control strategies, the machine can be kept operating with up to two phases open circuited.

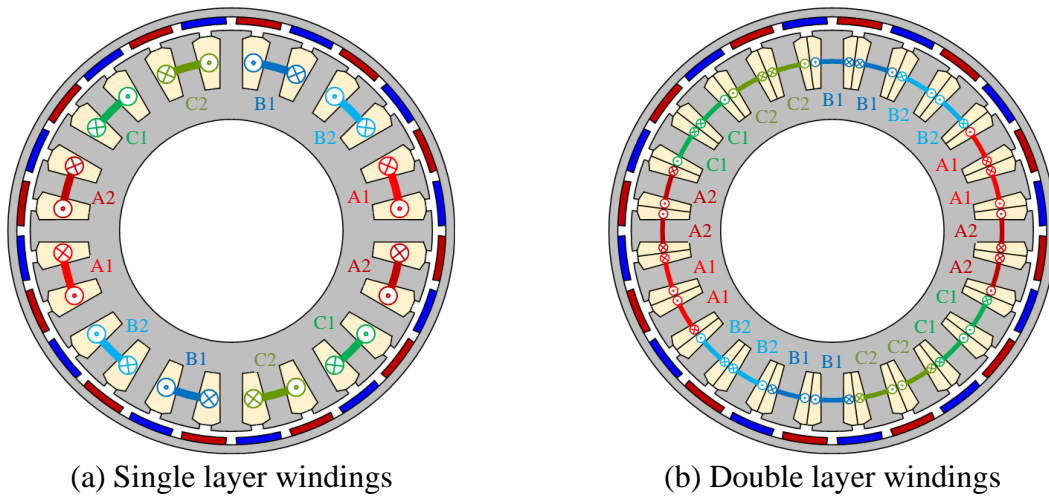


Fig. 1.19 Cross-sections of DTP 24-slot/22-pole machines with external SPM rotors in [ZHE12].

Besides the DTP PMSMs shown in Fig. 1.19, Zheng also proposed a six-phase 24-slot/14-pole machine with external SPM rotor in [ZHE13], as shown in Fig. 1.20. Similar to the machines shown in Fig. 1.16, the proposed machine has single layer windings and two adjacent coils belong to the same phase, and thus, the automatic coil winding and modular stator can be feasible. Additionally, in the proposed machine, different phases are electrically, magnetically, thermally, and physically isolated, which benefits the machine's fault-tolerant capability. Furthermore, unequal stator tooth widths were utilized in the machine, which can improve the winding factor of the working harmonic significantly. Thus, the proposed six-phase 24-slot/14-pole external rotor machine can be a suitable candidate for electric vehicle applications.

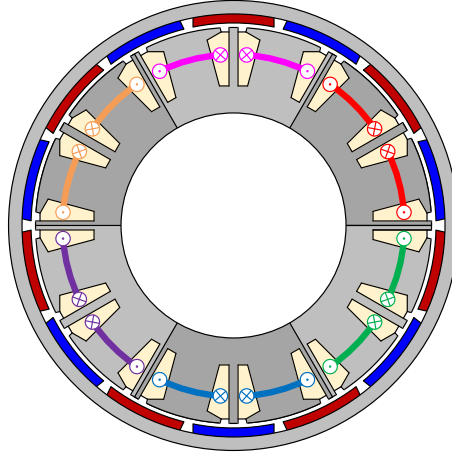


Fig. 1.20 Cross-section of six-phase 24-slot/14-pole machine with single layer windings, modular stator, unequal stator tooth widths, and external SPM rotor in [ZHE13].

Another example of DTP PMSMs was given in [WAN14a]. It was found that for STP PMSMs with slot number = pole number ± 1 , although the MMF harmonic contents are relatively abundant, all the odd or even harmonics can be simply eliminated by doubling the slots and three-phase windings. Thus, a DTP 18-slot/8-pole machine and a DTP 36-slot/8-pole machine can be proposed based on the STP 9-slot/8-pole machine, as shown in Fig. 1.21. For the STP 9-slot/8-pole PMSM, the working harmonic is the 4th harmonic; with the proposed method, all the odd MMF harmonics in the 9-slot/8-pole PMSM can be eliminated in the DTP 18-slot/8-pole PMSM. Further, all the 2nd, 6th, 10th, 14th, 18th, 22nd, ... MMF harmonics can be eliminated by changing the DTP 18-slot/8-pole PMSM into a DTP 36-slot/8-pole PMSM. Hence, the undesirable MMF harmonics can be effectively reduced by the proposed DTP winding configuration.

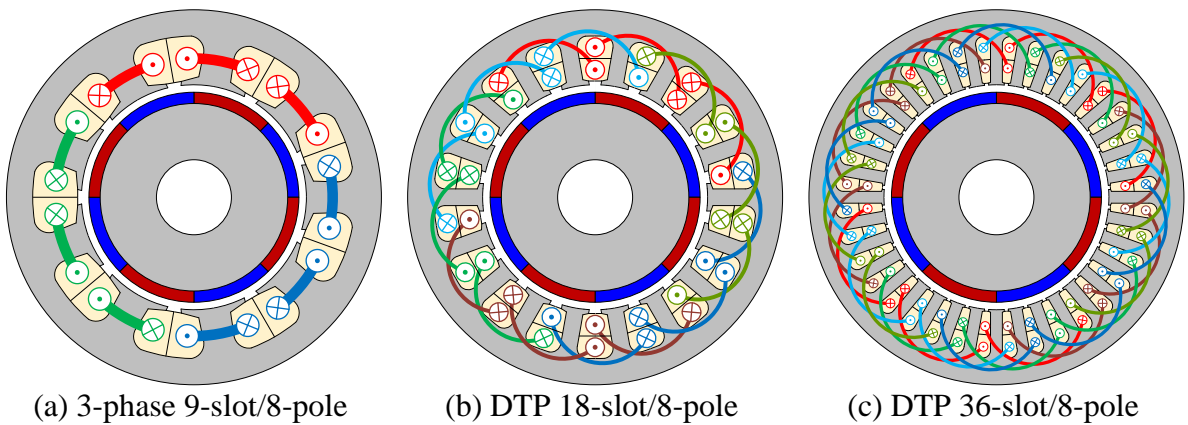


Fig. 1.21 Cross-section of DTP SPM machines in [WAN14a].

More machine topologies of DTP PMSMs will be reviewed in the following sub-sections when introducing related design techniques. It also should be mentioned that although the DTP winding connections are obtained using different methods in different papers, the winding arrangements can still be generally summarized based on the star of slots. The more detailed instructions about arranging DTP windings will be provided in Chapter 2.

As mentioned in [GOP00] [CAO12], a system of more than five phases is generally considered undesirable, because it becomes overly complex and expensive. Multiphase PMSMs with phase number > 5 can only be practical when using multiple three-phase winding configurations, such as six- (dual three-) phase, nine- (triple three-) phase, and twelve- (quadruple three-) phase winding configurations. As there are very few papers on seven-phase PMSMs, the cross-sections of seven-phase PMSMs will not be shown here, but the literature on seven-phase PMSMs can still be found in the reference list in the end of this sub-section.

For practical nine-phase PMSMs, the windings are supplied from triple three-phase (TTP) drives. A typical TTP machine topology was given in [RUB12], as shown in Fig. 1.22. The fault-tolerant control strategies for the TTP 18-slot/16-pole SPM machine were derived and validated. The machine is equipped with single layer windings and the phase shift between the three three-phase winding sets is 40° .

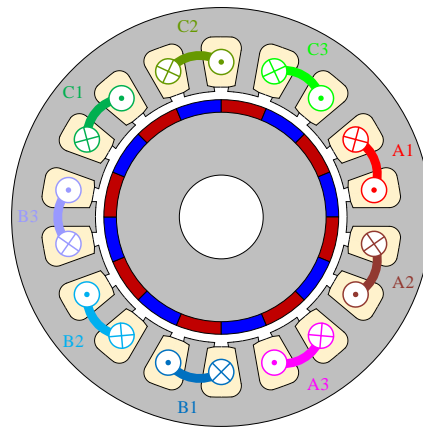


Fig. 1.22 Cross-sections of TTP 18-slot/16-pole SPM machine with single layer windings [RUB12].

In [CHE16], a TTP 18-slot/14-pole IPM machine with double layer windings was designed, as shown in Fig. 1.23. The phase shift angle between the three three-phase winding sets is selected as 20° to reduce MMF harmonics. With the TTP winding configuration, all the subharmonics and some higher order harmonics in the TTP 18-slot/14-pole IPM machine are eliminated. The proposed machine exhibits a high efficiency over wide torque and speed range.

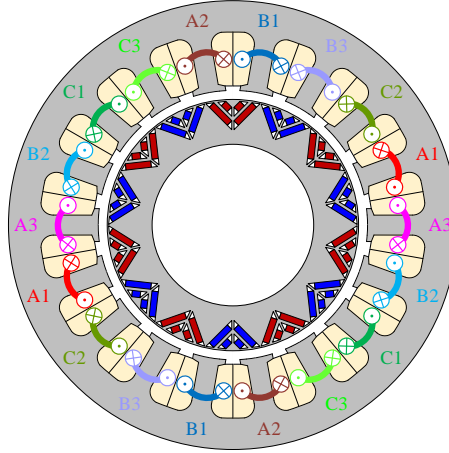


Fig. 1.23 Cross-sections of TTP 18-slot/14-pole IPM machine with double layer windings (Phase shift = 20°) [CHE16].

Overall, from the brief review of multiphase (phase number > 3) PMSMs given in this subsection, it can be concluded that multiphase winding configurations can truly improve the fault-tolerant capability in conventional three-phase PMSMs, but also increase the complexity of the whole system. Considering the high cost of customized multiphase drives and the complexities in fault-tolerant control strategies, multiple three-phase, especially DTP winding configuration is extremely advantageous compared with other multiphase counterparts. The advantages of DTP winding configuration in PMSMs can be generally concluded as:

- They can make a balance between machine's fault tolerant capability and standard three-phase components;
- They can improve torque performance in both average torque and torque ripple compared with conventional three-phase counterparts;
- They can reduce space MMF harmonic contents, which can help to reduce eddy current loss, lower iron loss, and improve efficiency;
- When fault occurs in one three-phase winding set, the machine can be run with the left three-phase winding set, with a much less complicated control scheme;
- It is possible to realize a power sharing between DTP winding sets.

DTP PMSMs will be the focus of this thesis and will be further introduced in more technical details in this section. Key papers in literature on multiphase PMSMs are summarized in Table 1.2 for reference, mainly according to the number of phases.

Table 1.2 Summary of references on multiphase PMSMs

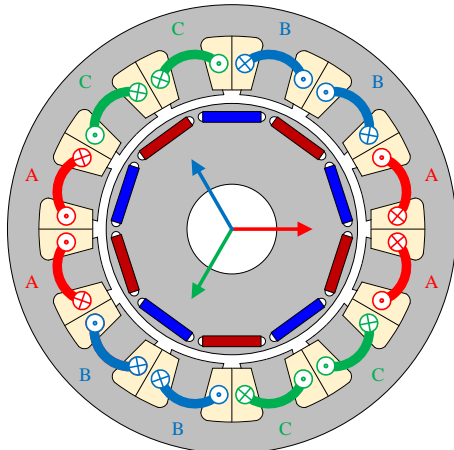
| Number of Phases | Reference | Slot/Pole combination | Rotor type | Features |
|------------------|-----------|-----------------------|-------------|--|
| 4 | [MEC04] | 8/6 | SPM | SL/Concentrated |
| | [LI17] | 16/12 | SPM | Modular stator design |
| 5 | [PAR05] | 20/4 & 40/4 | SPM | SL and DL/Distributed |
| | [PAR07] | 15/4 | IPM | DL/Coil pitch = 3 |
| | [BIA08] | 20/18 | SPM | SL or DL/Concentrated |
| | [SCU09] | 180/58 | SPM | SL/Distributed |
| | [ZHE11] | 40/42 | SPM | SL/Concentrated Phase separation physically |
| | [CHE11b] | 20/18 | IPM | SL/Concentrated Outer spoke-type IPM rotor |
| | [LIU12] | 20/62 | SPM | SL/Concentrated Vernier machine |
| | [WAN14b] | 10/8 | SPM | DL/Concentrated Rotor PM shaping |
| | [WAN14c] | General | SPM/IPM | DL/ Coil pitch = 1 or 2 |
| | [ABD15] | 20/18 | SPM | Dual five phase/DL |
| | [ABD16c] | 40/18 | IPM | DL/ Coil pitch = 2 |
| | [ZHA17a] | 20/18 | IPM + EE | DL/Concentrated Hybrid-excitation |
| | [CHE20a] | 20/14 | IPM | DL/Concentrated Saliency ratio improvement |
| | [HUA22] | 60/22 | SPM | Mixed SL & DL/Coil pitch = 2 or 3 |
| 6 | [MAT10] | 24/2 | SPM/IPM | SL/Distributed DTP, 0 deg. |
| | [BAR10] | 12/10 | SPM/IPM | SL & DL/Concentrated DTP, 0/30 deg. |
| | [DAJ11] | 24/10 | IPM | DL/Coil pitch = 2 STP or DTP, 0 deg. Unequal tooth width |
| | [ZHE12] | 24/22 | SPM | SL & DL/Concentrated DTP, 30 deg. |
| | [ZHE13] | 24/14 | SPM | SL/Concentrated DTP, 30 deg. Unequal tooth width |
| | [PAT14] | 18/8 | IPM | DL/Coil pitch = 2 DTP, 0/20/40 deg. |

| | | | | |
|--|----------|-----------------|-----|---|
| | [ABD15] | 12/10 | SPM | DL/Star-delta DTP, 30 deg. |
| | [ABD16a] | 24/10 | SPM | DL/Coil pitch = 2 DTP, 30 deg. |
| | [ABD16b] | 12/10 | IPM | Four-layer/Concentrated DTP, 30 deg. |
| | [DEM16] | 78/12 | SPM | SL/Distributed DTP, 27.7 deg. |
| | [DEM17] | 78/24 | SPM | SL/Coil pitch = 2 DTP, 0 deg. |
| | [XU18] | 24/10 | SPM | DL/Coil pitch = 2 DTP, 0/15/30 deg. |
| | [XU19] | 24/22 | SPM | DL/Concentrated DTP, 0/15/30 deg. |
| | [ZHU19] | 24/14 | IPM | DL/Concentrated DTP, 30 deg. |
| | [LI19b] | 42/32 | SPM | DL/Concentrated DTP, 30 deg. Modular machine design |
| | [LI19c] | 42/32 192/32 | SPM | DL/Concentrated & SL/Distributed DTP, 30 deg. Modular machine design |
| | [LI20a] | General | SPM | DL/Concentrated DTP, 30 deg. Modular machine design |
| | [LI20b] | 24/22 | SPM | DL/Concentrated DTP, 0/15/30/60 deg. Consequent pole rotor |
| | [WAN20b] | 24/10 | SPM | DL/Coil pitch = 2 DTP, 90 deg. Unequal conductors each turn side |
| | [WAN20c] | 24/10 | SPM | DL/Concentrated DTP, 82.7 deg. Unequal conductors each turn side |
| | [XU18] | 24/10 24/14 | SPM | DL/Coil pitch = 2 DTP, 0/15/30 deg. |
| | [GUO22] | 30/14 | SPM | DL/Coil pitch = 2 DTP, 0 deg. Unequal turns per coil |

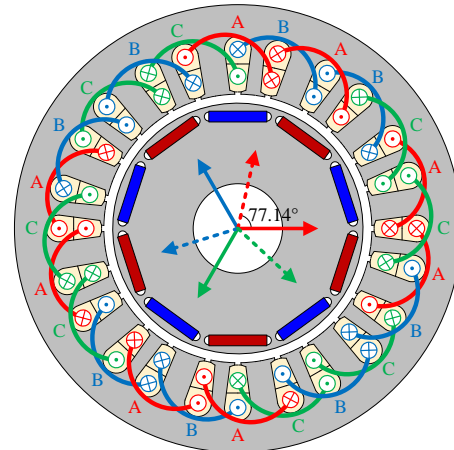
| | | | | |
|----|----------|--------|-----|---|
| 7 | [LOC07] | 14/4 | SPM | DL/Concentrated Axial-flux machine |
| | [SCU20] | 14/4 | SPM | DL/Concentrated |
| 9 | [RUB12] | 18/16 | SPM | DL/Concentrated TTP (40 deg.) |
| | [CHE14a] | 18/14 | SPM | DL/Concentrated TTP (20 deg.) |
| | [WAN19] | 36/6 | IPM | SL/Full-pitched TTP (0 deg.) |
| | [ABD18] | 9/8 | IPM | DL/Distributed 9-phase 6-terminal connection |
| | [DEM19] | 117/36 | SPM | DL/Coil pitch = 3 TTP (27.6 deg.) |
| | [KAN22] | 54/6 | IPM | DL/Distributed TTP (20 deg.) |
| 11 | [DAJ21] | 11/10 | SPM | DL/Concentrated |
| 12 | [DAM13] | 96/94 | SPM | DL/Concentrated Four three-phase |
| | [SHA20] | 48/44 | SPM | DL/Concentrated Four three-phase |

1.3.2 DTP Winding Configuration and Stator Shifting Technique

The stator shifting technique was introduced in [DAJ11] to reduce the undesirable MMF harmonics in FSCW PMSMs. The technique is achieved by doubling the number of slots and doubling the windings, then shifting the two winding sets in a specific shifting angle. To reduce some specific harmonic orders, some specific shifting angles are required, and hence, the unequal stator tooth widths may be utilized in the machine. The technique was validated in a 12-slot/10pole PMSM, and the PMSM was changed into a 24-slot/10-pole PMSM after stator shifting with shifting angle = 77.14° in mech., as shown in Fig. 1.24(a) and (b), respectively. The FE and experimental results show that the stator shifting technique can effectively reduce or even completely cancel un-wanted MMF harmonic orders. However, it should be mentioned that in a STP PMSM after stator shifting, although the armature windings are composed by two three-phase winding sets, the STP PMSM after stator shifting is still a STP PMSM as the coils of the two winding sets are still connected in series and fed by one inverter.



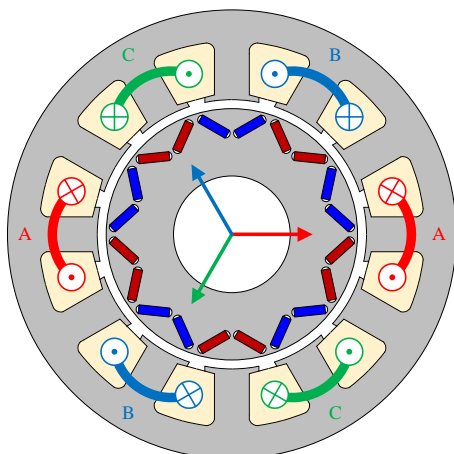
(a) 12-slot/10-pole PMSM (before stator shifting)



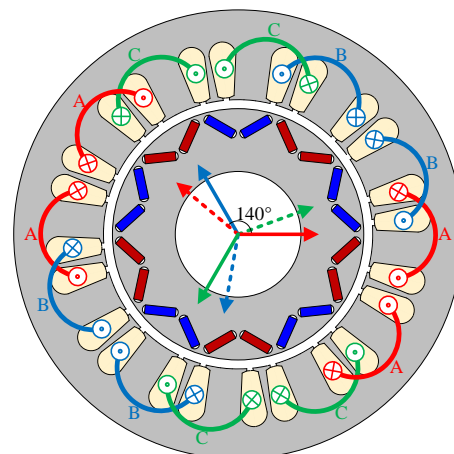
(b) 24-slot/10-pole PMSM (after stator shifting)

Fig. 1.24 Cross-sections of PMSMs before and after using stator shifting technique [DAJ11].

In [RED14], the stator shifting technique was researched in more depth. The effects of stator shifting angle on different MMF harmonic orders were explained by the attenuation factor. The attenuation factor is generic and can be applied to all slot/pole combinations. From the analyses of the attenuation factor, 76° and 140° , both in mech., were chosen to reduce the 7th and 1st harmonics, respectively. Then, the effects of different stator shifting angles on the resultant electromagnetic performance were evaluated in a 12-slot/10-pole IPMSM, both single layer and double layer windings were considered. The stator shifting technique exhibits good performance in reducing iron loss, improving torque density and efficiency.



(c) 12-slot/10-pole PMSM (before stator shifting)



(d) 24-slot/10-pole PMSM (after stator shifting 140° in mech.)

Fig. 1.25 Stator shifting in 24-slot/10-pole IPM machine [RED14].

The concept of stator shifting was also employed in DTP PMSMs. In [ABD16a], a DTP 24-slot/10-pole PMSM was proposed based on a DTP 12-slot/10-pole PMSM by using stator shifting concept with shifting angle $=75^\circ$ (or 5 slots), as shown in Fig. 1.26. As the DTP winding configuration can eliminate the 1st MMF harmonic and the stator shifting technique can reduce the 7th harmonic, the combination of DTP winding configuration and stator shifting technique can result in a fault-tolerant capability and a very good torque and efficiency performance in the proposed DTP 24-slot/10-pole PMSM. A comparative study between the proposed machine and its three-phase counterpart with the same slot/pole number combination is also carried out in [ABD16a], which confirms that the proposed DTP machine exhibits higher torque density and higher efficiency than its three-phase counterpart.

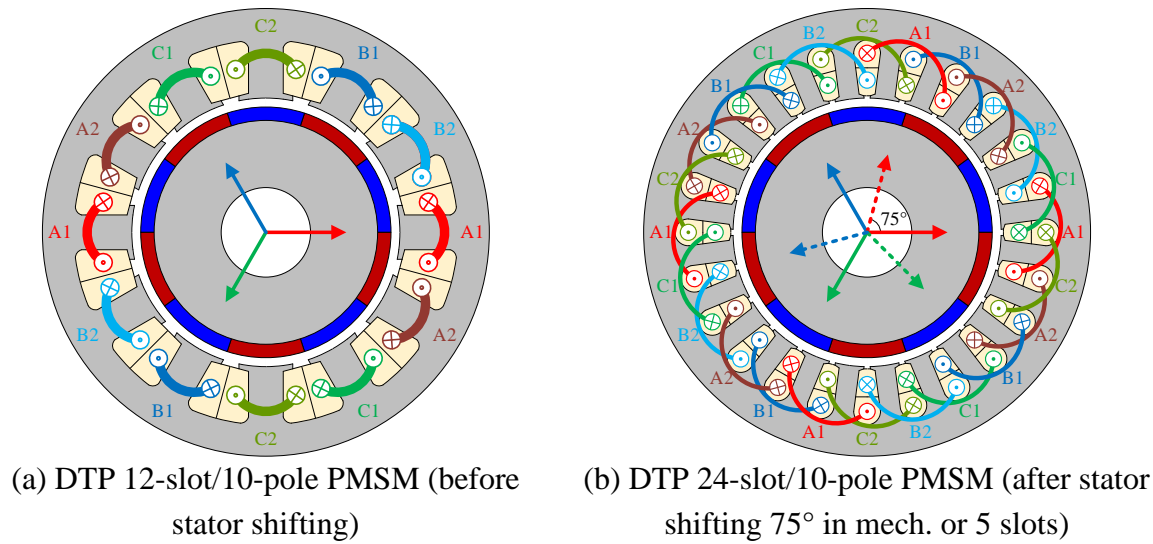
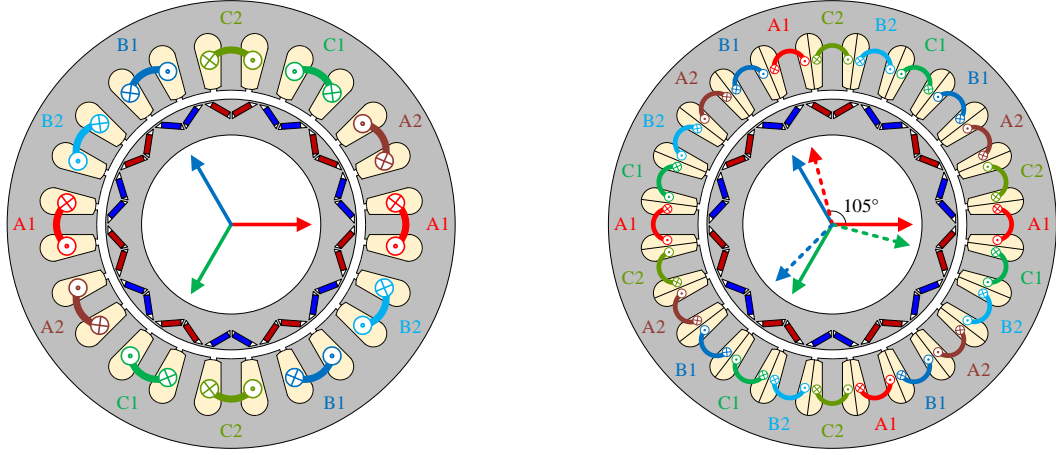


Fig. 1.26 DTP PMSMs before and after stator shifting [ABD16a].

Similar to [ABD16a], a DTP 24-slot/14-pole PMSM with SL windings was modified into a DTP 24-slot/14-pole PMSM with DL windings by using stator shifting technique (stator shifting angle $= 105^\circ$ or 7 slots) in [ZHU19]. As shown in Fig. 1.27, the stator shifting angle is 105° or 7 slots in this case. Different from [ABD16a], coil pitch = 1 was selected in [ZHU19]. Because IPM rotor was utilized in that paper, the machine can benefit from the reluctance torque component although it is rather limited, which compensates the relatively lower winding factor. It reveals that concentrated windings still can be utilized in DTP PMSMs after stator shifting.



(a) DTP 24-slot/14-pole IPMSM with SL windings (before stator shifting)

(b) DTP 24-slot/14-pole IPMSM with DL windings (after stator shifting)

Fig. 1.27 Stator shifting in DTP 24-slot/14-pole IPM machine [ZHU19].

Based the aforementioned papers, the stator shifting technique utilized in STP and DTP PMSMs can be summarized in Table 1.3. The detailed winding configurations and features of the stator shifting techniques are all listed in the table.

Table 1.3 Summary of stator shifting techniques in existing literature

| Paper | Machine topology | | Shifting angle (° in Mech.) | Features |
|----------|------------------|------------|--------------------------------|---|
| | Before | After | | |
| [DAJ11] | 12s10p STP | 24s10p STP | 77.14° | <ul style="list-style-type: none"> • Unequal tooth width • Eliminate 7th harmonic |
| [RED14] | 12s10p STP | 24s10p STP | 76° and 140° | <ul style="list-style-type: none"> • Unequal tooth width • Single and double layer windings • Different harmonic orders reduced by different stator shifting angles • Generalized approach proposed |
| [ABD16a] | 12s10p DTP | 24s10p DTP | 75° (5 slots) | <ul style="list-style-type: none"> • 1st harmonic eliminated by DTP • 7th harmonic reduced by stator shifting |
| [ZHU19] | 12s14p DTP | 24s14p DTP | 105° (7 slots) | <ul style="list-style-type: none"> • Concentrated windings utilized after shifting • 1st harmonic eliminated by DTP • 5th harmonic reduced by stator shifting |

However, it should be noticed that when combining DTP winding configuration and stator shifting technique together in [ABD16a] [ZHU19], the windings before stator shifting already were DTP windings. The stator shifting only take the spatial shifting between the two winding sets into consideration. In fact, the two winding sets can also be designed using two three-phase winding sets with spatial shifting in space, and time shifting in currents synchronously. For

example, in [PAT13], a STP 9-slot/8-pole IPM machine was modified into a DTP 18-slot/8-pole IPM machine, various spatial shifting angles between the two winding sets were considered, and thus, the shifting angles between the currents in the two winding sets would also be different, as shown in Fig. 1.28.

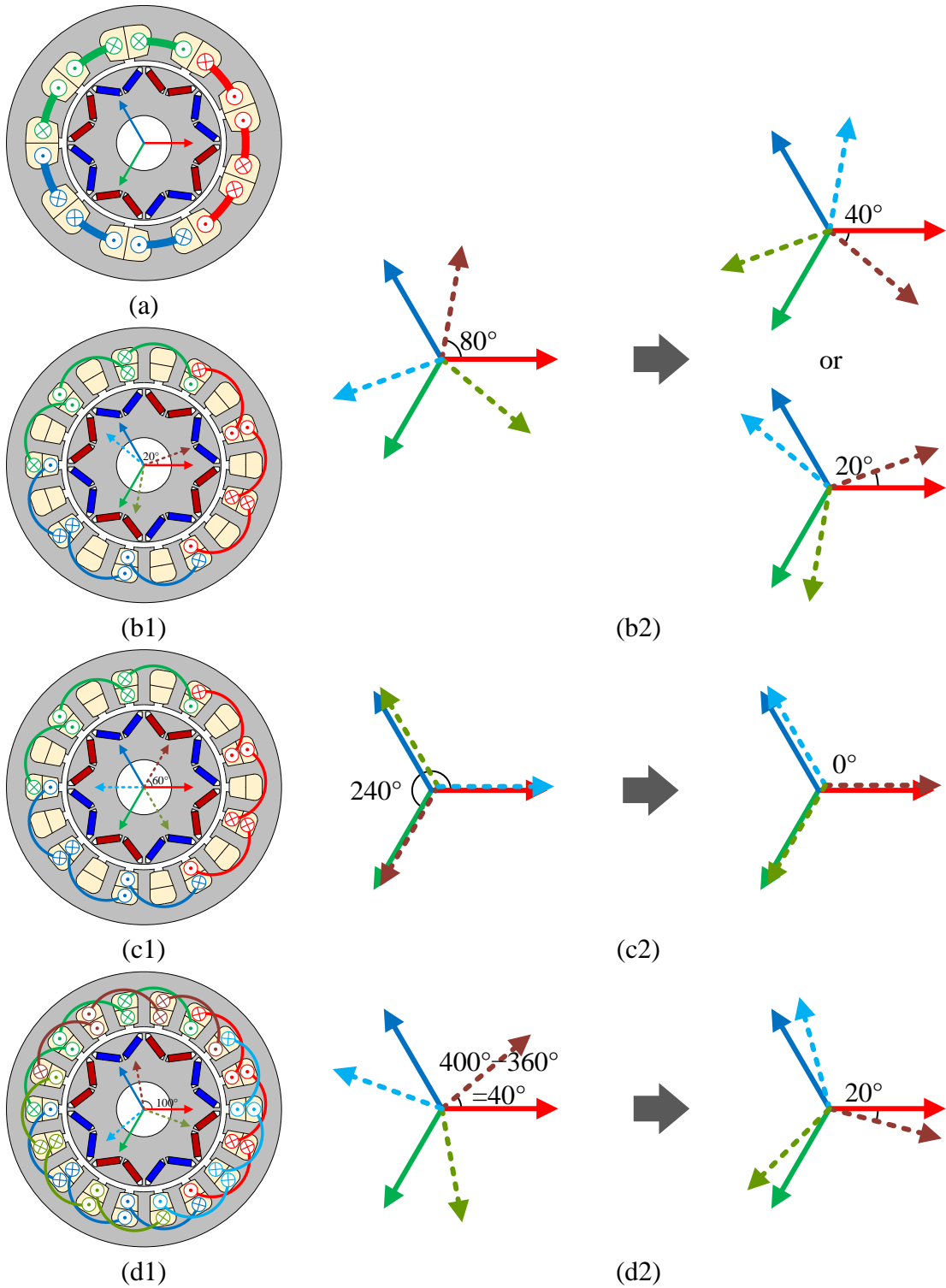


Fig. 1.28 Various phase shift angles in DTP 18-slot/8-pole SPM machine [PAT13].

In Fig. 1.28, for different winding configurations, the spatial shifting angles between the two winding sets are shown in (b1), (c1), and (d2); and the time shifting angles between the currents of the two windings sets are shown in (b2), (c2), and (d2). By changing phase order, all these feasible DTP winding configurations are be further classified into three categories, according to phase shift angle = 0° , 20° , or 40° . In that paper, it was further found 20° is the optimal phase shift angle for the benchmark 118-slot/8-pole IPM machine considering torque, loss, and efficiency characteristics of different phase shift angles.

Similarly, in [CHE17], two DTP winding configurations, i.e., coil pitch = 1 and 2, were discussed and compared in 24-slot/14-pole SPMSMs, as shown in Fig. 1.29. It is found that winding factors are too small when coil pitch = 1. To maintain the winding factors, it is suggested that coil pitch number should be doubled after stator shifting. However, it also highlighted that as the two three-phase winding sets are shifted by 15° in space, for the working harmonic order (7th harmonic), the currents in the two winding sets are shifted by 105° in time. By changing phase order, the 105° shifting angle can also be seen as a 15° phase shift angle. Hence, the proposed DTP machines in [CHE17] can be regarded as DTP PMSMs with phase shift angle = 15° .

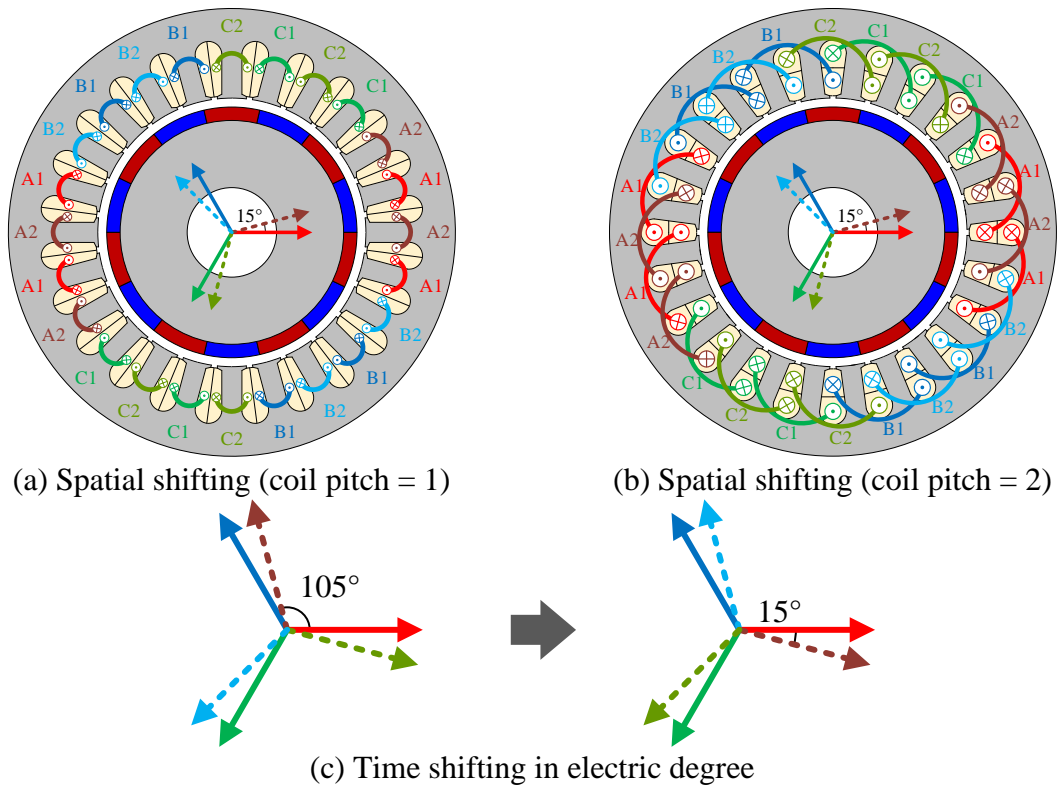


Fig. 1.29 Phase shifting angles in DTP 24-slot/14-pole SPM machines [CHE17].

To evaluate the effects of spatial and time shifting angles on the resultant MMF harmonic contents in multiple three-phase PMSMs, a generic approach to calculate the MMF harmonic contents was proposed in [CHE14a]. The multiple three-phase windings were designed to reduce the MMF harmonics in PMSMs. With the proposed approach, three-phase, six-phase (DTP), nine-phase (TTP) winding configurations were designed in an 18-slot/14-pole PMSM, as shown in Fig. 1.30.

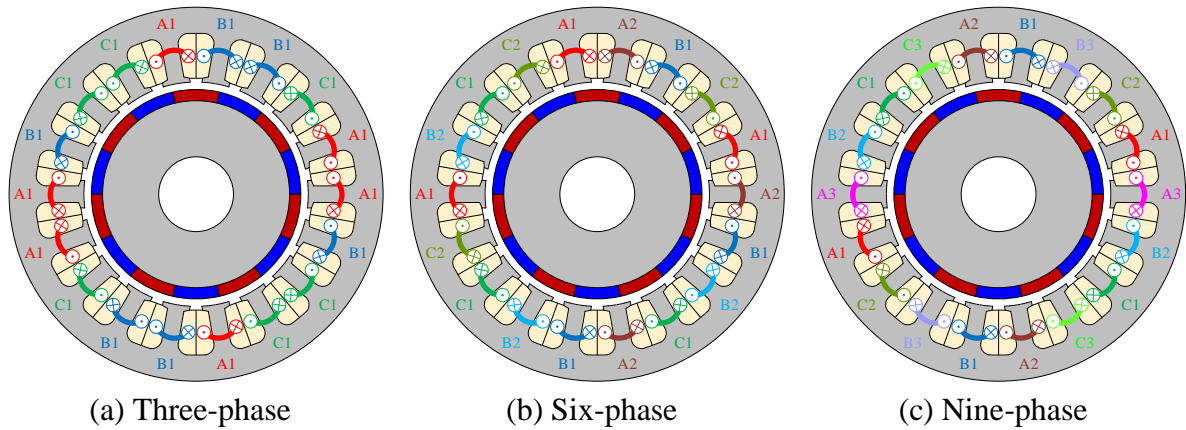


Fig. 1.30 Multiple three-phase 18-slot/14-pole SPM machines [CHE14a].

As the effects of spatial and time shifting angles on different MMF harmonic orders cannot be evaluated by the attenuation factor proposed in [RED14], based on [RED14] and [CHE14a], the attenuation factor will be extended in Chapter 2 by considering spatial and time shifting angles simultaneously.

1.3.3 Phase Shift Angle in DTP Windings

In DTP PMSMs, feasible phase shift angles are mainly determined by the slot/pole number combinations. According to existing literature, the phase shift angles for PMSMs with different slot numbers are summarized in Table 1.4. The detailed instruction about how to achieve these phase shift angles will be given in Chapter 2. In this sub-section, only the effects of different phase shift angles on the resultant electromagnetic performances in PMSMs with different slot/pole number combinations will be briefly introduced. The papers marked in bold in Table 1.4, will be chosen as examples to show these effects.

Table 1.4 Summary of phase shift angles techniques in existing literature

| Slot number | Pole number and phase shift angles |
|-------------|---|
| 12-slot | <ul style="list-style-type: none"> • 10-pole: 0°/30° [BAR10] • 10-pole: 30° [ABD15] |
| 18-slot | <ul style="list-style-type: none"> • 8-pole: 0°/20°/40° [PAT13] [PAT14] • 10-pole: 20° [DAJ12] • 14-pole: 0°/20°/40° [CHE14a] |
| 24-slot | <ul style="list-style-type: none"> • 10-pole: 30° [ABD16a] • 14-pole: 30° [ZHU19] • 14-pole: 15° [CHE17] • 10-pole: 0°/15°/30° [XU18] • 20-pole: 30° [BAR11a] • 22-pole: 30° [BAR11a] [ZHE12] • 22-pole: 0°/15°/30° [XU19] |
| 36-slot | <ul style="list-style-type: none"> • 34-pole: 10°/20°/30°/40°/50°/60° [DHU18] |
| 48-slot | <ul style="list-style-type: none"> • 8-pole: 30° [YAN19a] [WAN22] • 22-pole: 0°/7.5°/15°/30°/45° [ZHU21b] [SUN22] |

From Table 1.4, it can be seen that 30° is the most popular phase shift angle in DTP PMSMs. In [BAR10], 30° phase shift angle is compared with 0° phase shift angle in a 12-slot/10-pole PMSM, as shown in Fig. 1.17(a) to (c). It demonstrates that the DTP winding configuration with 30° phase shift angle can result in better average torque and torque ripple performance under healthy, open-circuit and short-circuit conditions.

Besides the advantages on electromagnetic performance, another advantage of DTP winding configuration with 30° phase shift angle is that the researches on the control of 30° phase shift angle are much more mature. Numerous control strategies were proposed based on DTP PMSMs with phase shift angle = 30° [ZHA95] [KAL13] [WAN15b] [REN15] [KAR17] [HU17b] [YAN22] [SHA23].

For 18-slot PMSMs, as mentioned previously in sub-section 1.3.2, the $0^\circ/20^\circ/40^\circ$ phase shift angles were researched and compared in a DTP 18-slot/8-pole PMSM in [PAT13], as shown in Fig. 1.28.. By comparing the reduction effects of different phase shift angles on MMF harmonic contents, 20° was chosen as the optimal shift angle in the DTP 18-slot/8-pole PMSM.

Phase shift angle

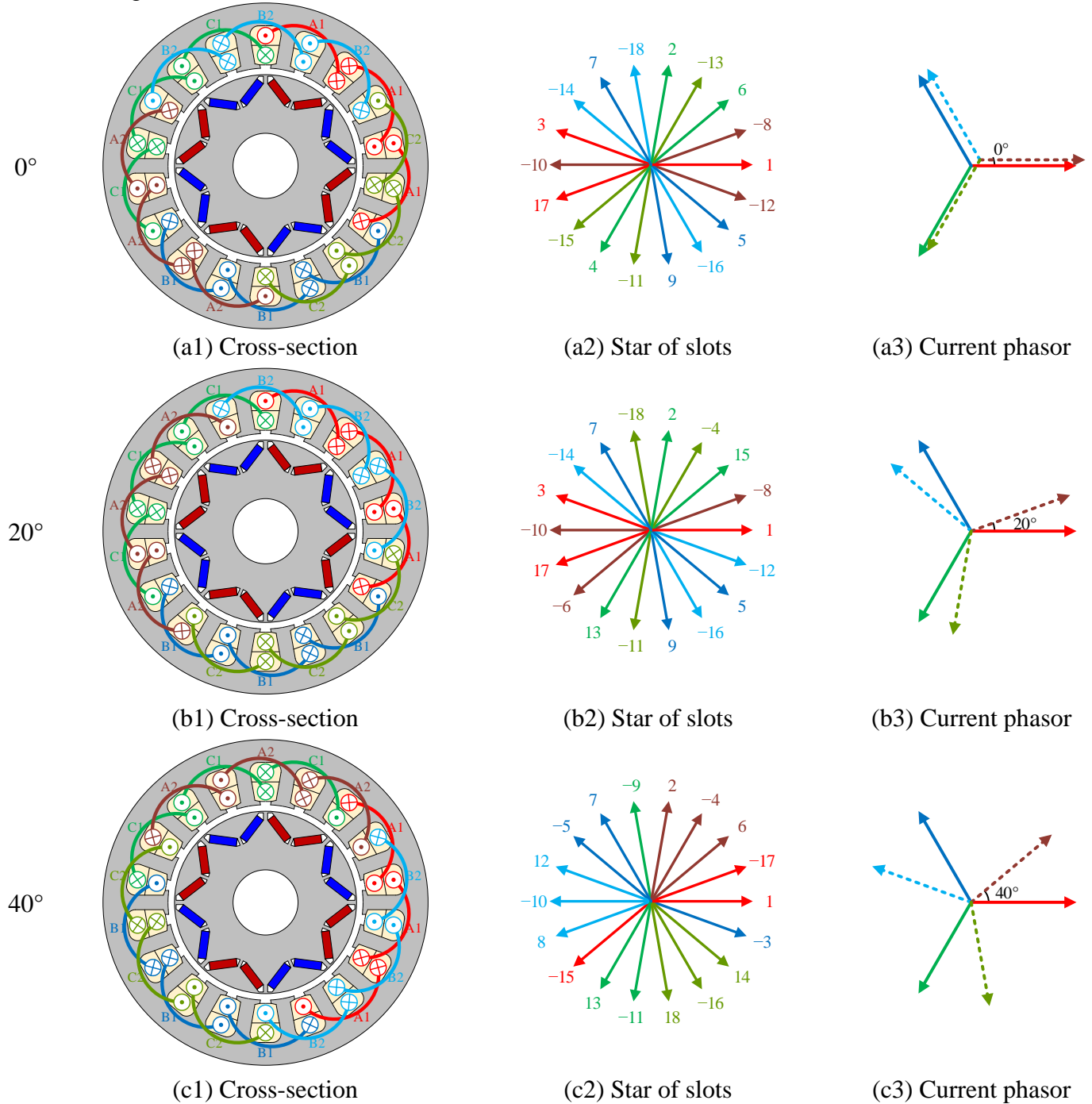


Fig. 1.31 DTP 18-slot/8-pole IPM machine [PAT13].

For 24-slot DTP PMSMs, feasible phase shift angles include 0° , 15° , and 30° . In [XU18] and [XU19], the three feasible phase shift angles were compared in DTP PMSMs with coil pitch = 2 (24-slot/10-pole) and coil pitch = 1 (24-slot/22-pole), respectively, as shown in Fig. 1.32 and Fig. 1.33.

Phase shift angle

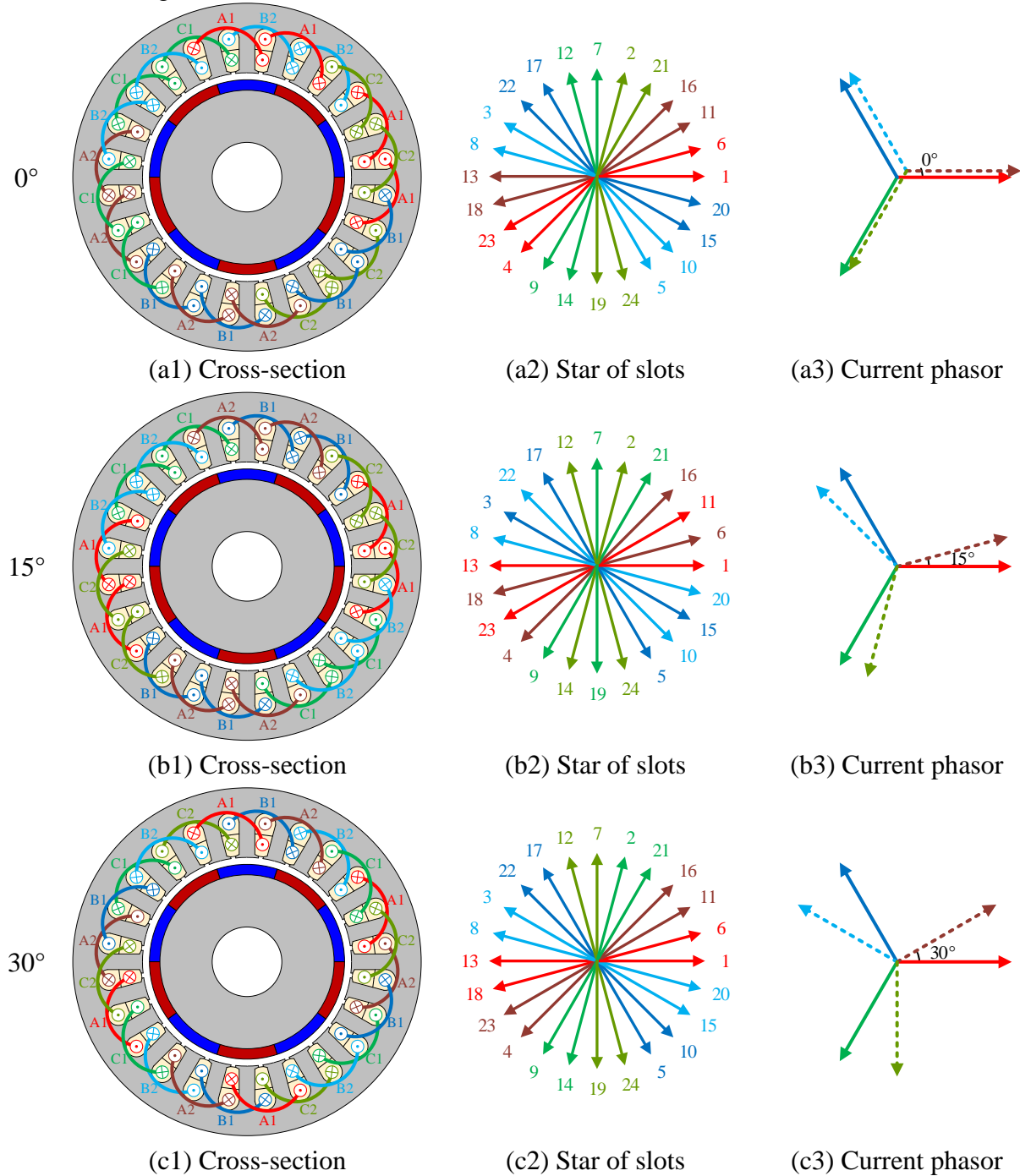


Fig. 1.32 DTP 24-slot/10-pole SPM machines [XU18].

Phase shift angle

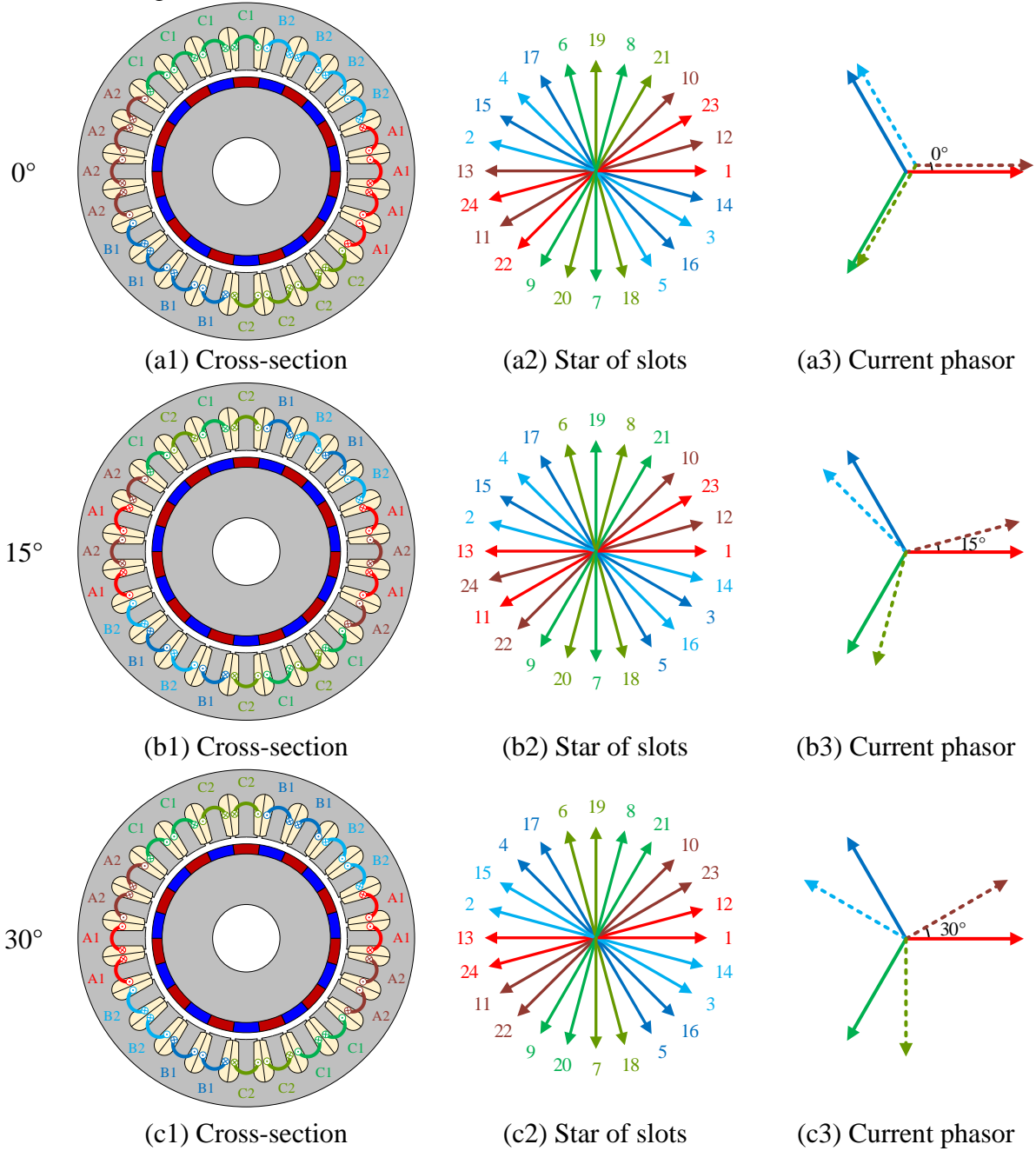
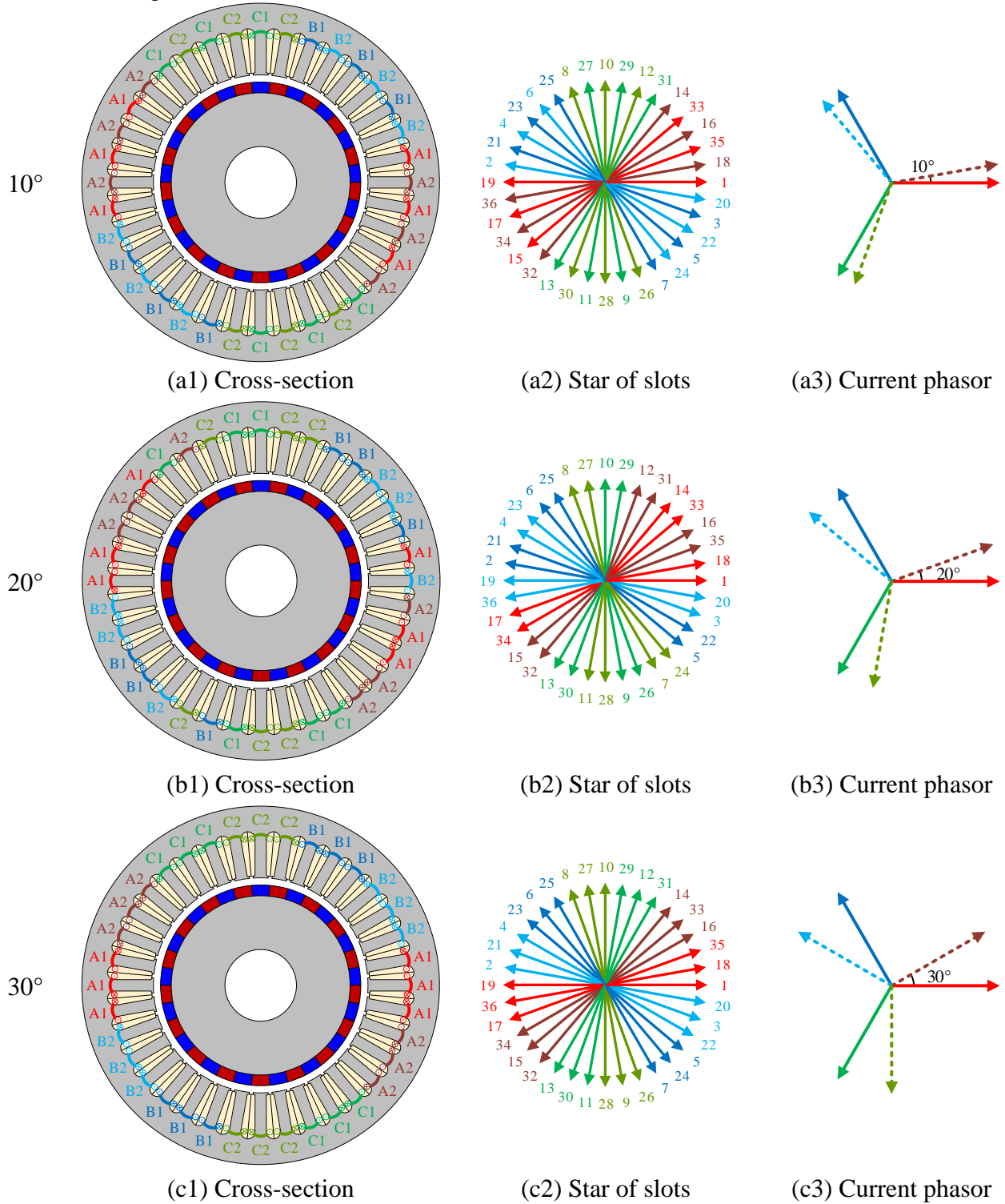


Fig. 1.33 DTP 24-slot/22-pole SPM machines [XU19].

The investigation shows that under healthy condition, the 15° configuration has a comparable electromagnetic performance to the 30° configuration, better than the 0° counterpart. In the DTP 24-slot/10-pole PMSM, the 15° configuration has the lowest SC current, smallest braking torque, and the best PM demagnetization withstand capability under three-phase short-circuit condition. In the DTP 24-slot/22-pole PMSM, the 15° configuration suffers less from the cross-coupling saturation effects, and thus, has better over-rating capability and better PM irreversible demagnetization withstand capability under 3-phase open-circuit condition.

For 36-slot PMSM, various feasible phase shifting angles ($10^\circ/20^\circ/30^\circ/40^\circ/50^\circ/60^\circ$) are compared in a 36-slot/34-pole FSCW DTP PMSM in [DHU18]. Overall, the 30° configuration is the best one in terms of average torque, torque ripple, MMF harmonics, iron loss and eddy current loss, but the 10° configuration has the best demagnetization withstanding capability.

Phase shift angle



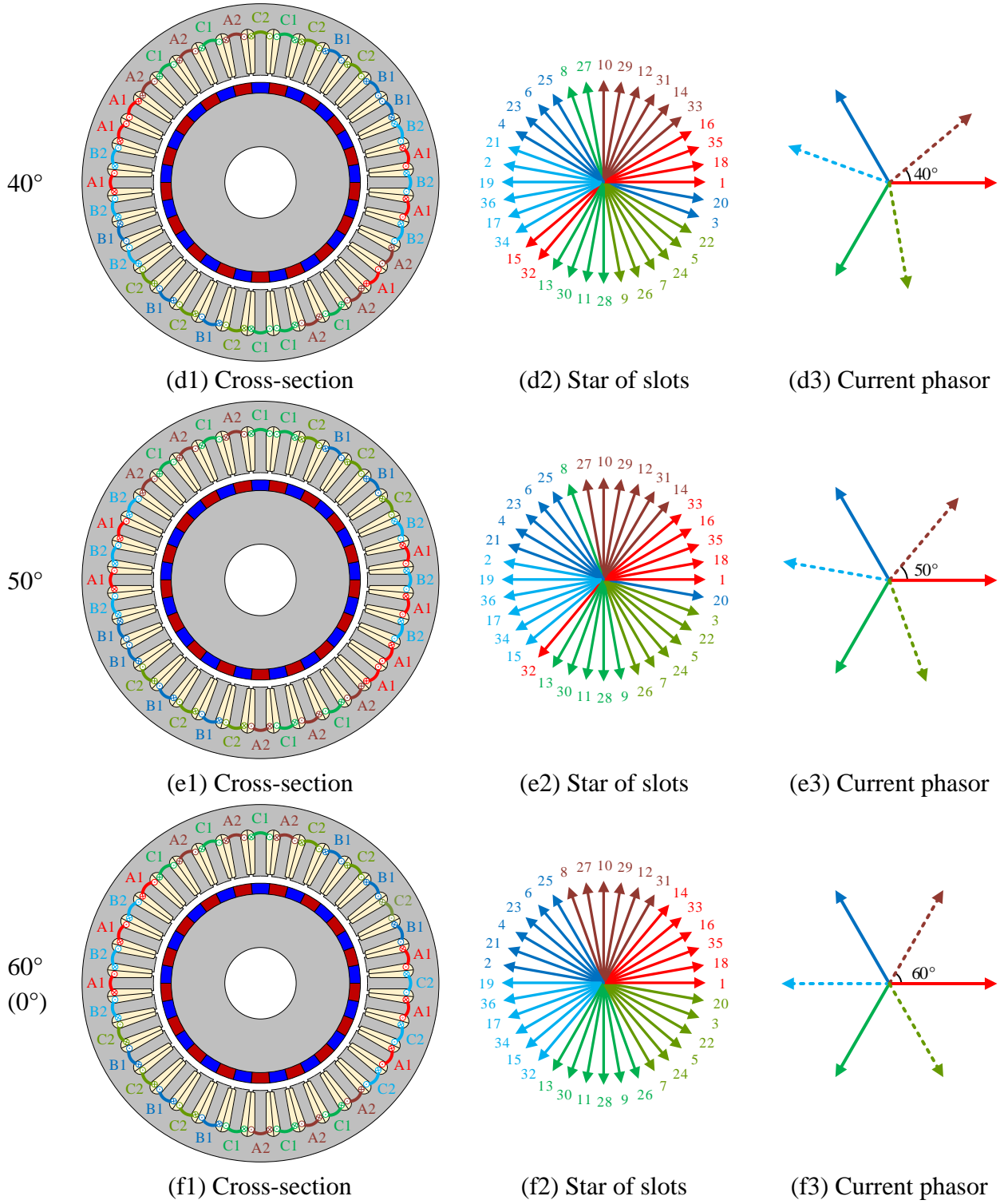


Fig. 1.34 Winding selections in DTP 36-slot/34-pole PMSM considering different phase shift angles [DHU18].

For 48-slot PMSM, there are even more feasible phase shift angles, including 7.5° , 15° , 22.5° , 30° , 45° , etc. In a 48-slot/22-pole DTP PMSM, the effects of different phase shift angles on various electromagnetic performances, including torque, torque ripple, eddy-current loss, radial force, vibration behaviour, inductance, and short-circuit current were investigated in [ZHU21b] and [SUN22]. The investigation reveals that the 7.5° and 30° configurations, as shown in Fig. 1.35 are better than other counterparts among all feasible phase shift angles. To be more specific, the 30° configuration exhibits better torque capability, lower vibration and lower eddy-current loss than the 7.5° counterpart. Overall, 30° phase shift angle is still recommended for 48-slot PMSMs.

Phase shift angle

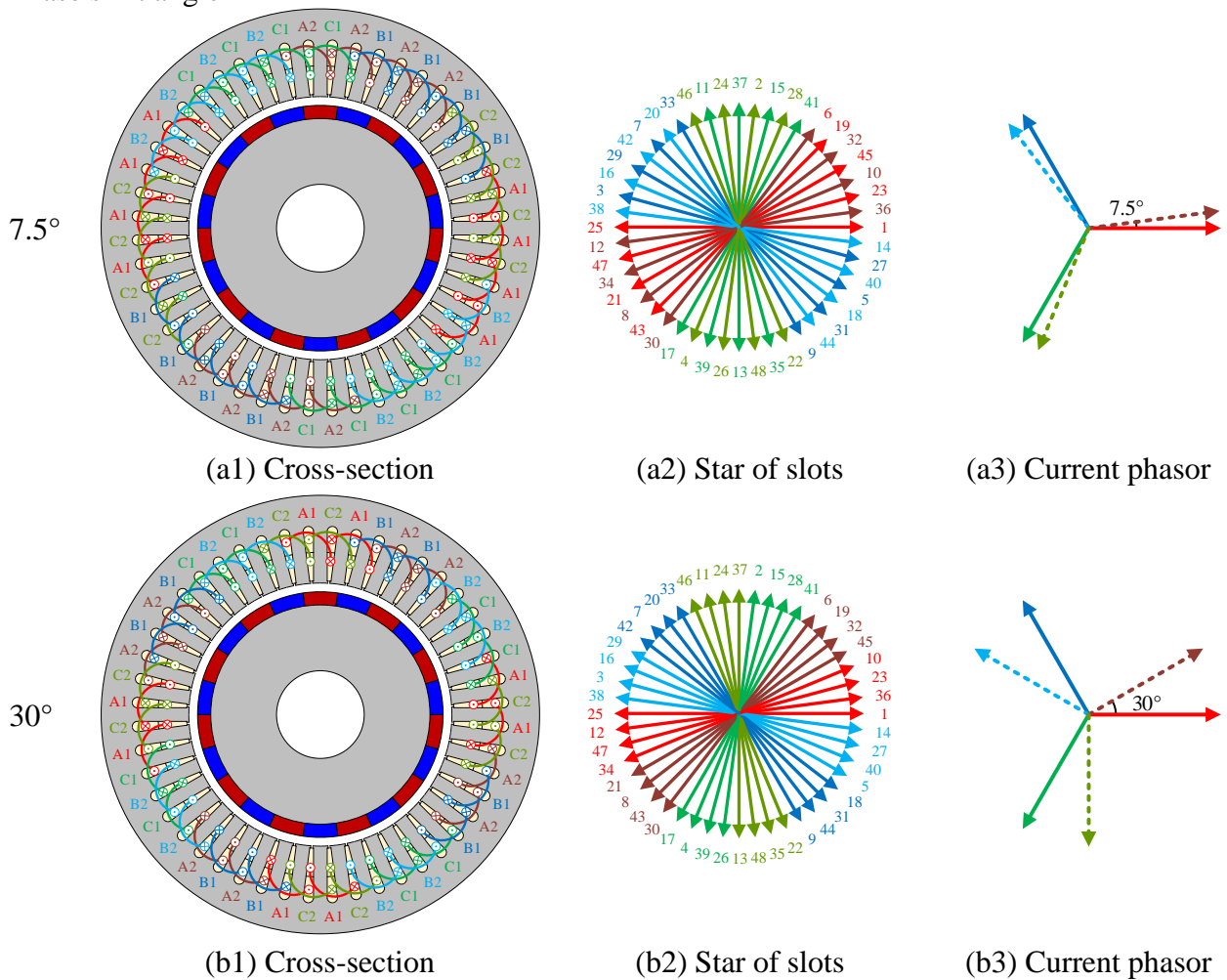


Fig. 1.35 DTP 48-slot/22-pole SPM machine [ZHU21b] [SUN22].

1.3.4 Star-delta and Dual Inverter Drives

Star-delta winding connection has been analysed in IMs for a long time [HUG70] [CHE98] [CIS10b]. In recent years, the star-delta winding connection was introduced in PMSMs to reduce space MMF harmonics. As windings in star-delta winding connections can be categorized into Y- (star-) windings and Δ - (delta-) windings, and there is an inherent phase shift angle (30°) between the currents in Y-windings and Δ -windings. The star-delta windings can be regarded as a special kind of DTP windings.

An example of star-delta windings in PMSMs was introduced in [DAJ13]. In that paper, the star-delta windings were implemented in an 18-slot/10-pole PMSM to reduce the sub- and super-order MMF harmonics simultaneously, as shown in Fig. 1.36. It can also be seen that among the 18 stator teeth, 6 were wound with Y-windings, and 12 were wound with Δ -windings. The Y- and Δ -windings are not balanced under this condition.

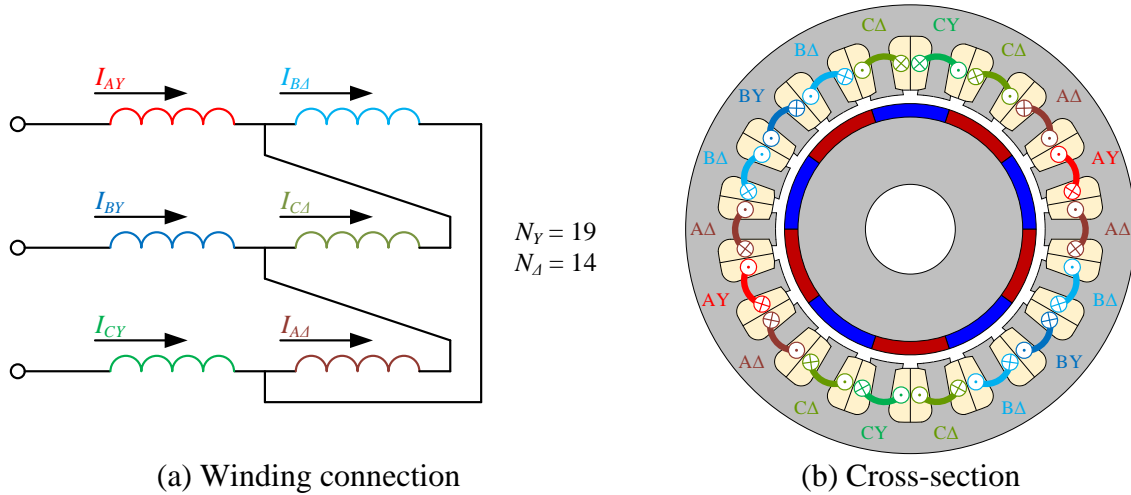


Fig. 1.36 18-slot/10-pole IPM machine with star-delta windings [DAJ13].

Another example with balanced Y- and Δ -windings was introduced in [ABD15]. The winding connections and the cross-section of the 12-slot/10-pole PMSM are shown in Fig. 1.37. In star-delta winding connections, the currents in Y-windings are $\sqrt{3}$ times of those in Δ -windings. Hence, to ensure the Y- and Δ -windings produce equivalent MMF, the number of turns in Δ -windings should be $\sqrt{3}$ times of that in Y-windings. It also should be noticed that the resultant winding layout shown in Fig. 1.37(b) [ABD15] looks identical to that shown in Fig. 1.17(c) [BAR10], which reveals that when using star-delta winding connection, the resultant winding layout is identical to that using conventional DTP windings with 30° phase shift.

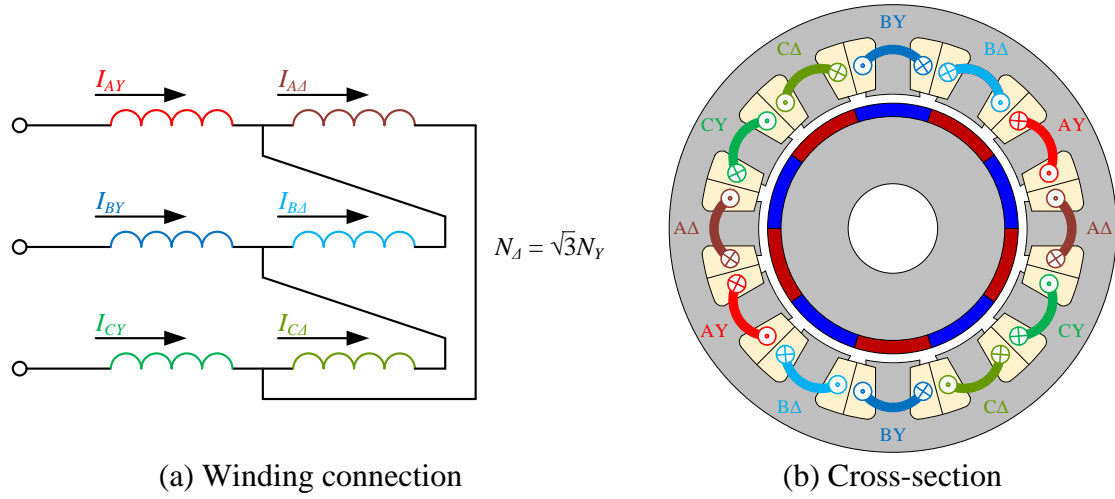


Fig. 1.37 12-slot/10-pole SPM machine with star-delta windings [ABD15].

Based on the 12-slot/10-pole PMSM with star-delta windings given in [ABD15], the stator shifting technique was utilized in [ISL20] to further reduce sub- and super-order MMF harmonics. A 24-slot/10-pole PMSM with star-delta windings and stator shifting technique was proposed, as shown in Fig. 1.38, in which stator shifting angle is 75° in mech. As the 1st MMF harmonic can be eliminated by the star-delta winding configuration, and the 7th harmonic can be reduced by stator shifting, the combination of star-delta winding configuration and stator shifting can achieve good performance in total harmonic distortion reduction, magnetic loss reduction along with torque density and power factor improvements.

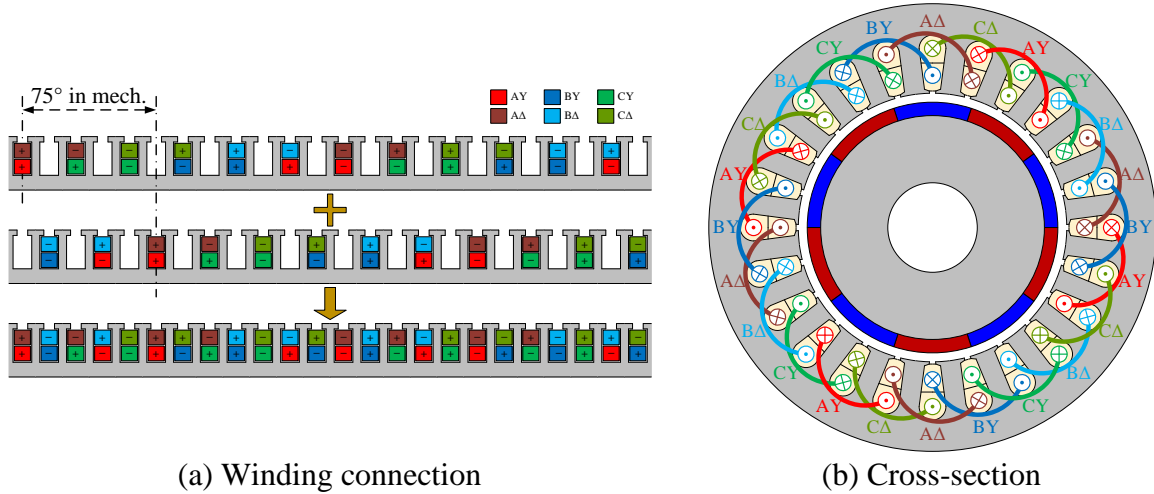


Fig. 1.38 24-slot/10-pole SPM machine with star-delta windings and stator shifting technique [ISL20].

In [RUD23], the star-delta winding connection was combined with conventional dual inverter DTP winding configuration. The proposed 24-slot/10-pole PMSM, as shown in Fig. 1.39, has two winding sets with a 15° phase shift angle, which can eliminate the 7th MMF harmonic, and

each winding set was star-delta connection, which can eliminate the 1st MMF harmonic. Thus, the two largest MMF harmonics which cause iron loss can be totally cancelled by the combination of DTP and star-delta winding connections. The proposed winding configuration shows comparable average torque and efficiency to the 12-slot/10-pole DTP counterpart, but lower torque ripple and lower PM eddy current losses.

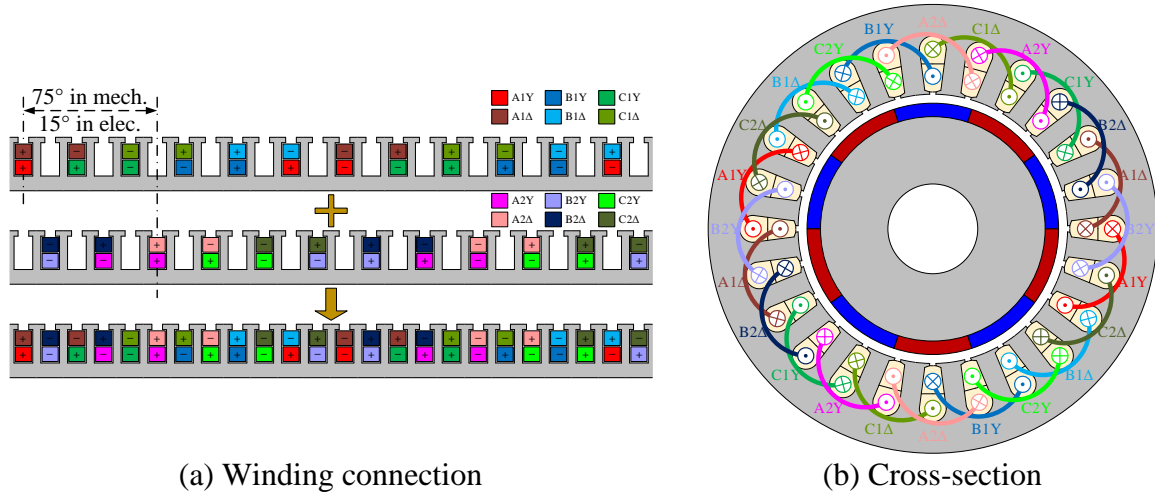


Fig. 1.39 24-slot/10-pole SPM machine with DTP star-delta windings [RUD23].

A generic analysis of the effects of star-delta winding connection on stator MMF harmonics was reported in [ZHA18a], considering different phase numbers. For a m -phase PMSM with slot number = N_s , the general relationship between N_s , m , and harmonic order, ν , can be described as follows:

- When $N_s/4m$ is an integer, the star-delta winding connection is feasible;
- When $N_s/4m$ is odd, the $\nu = 4mk \pm 1$ (k is an integer) orders MMF harmonics are eliminated;
- When $N_s/4m$ is even, the $\nu = 2mk \pm 1$ (k is an integer) orders MMF harmonics are eliminated.

Based on [ZHA18a], when PMSMs are equipped with star-delta winding connections, the eliminations of harmonic orders in different slot/pole number combinations are summarized in Table 1.5. In the table, the blue orders are the working harmonic orders, and the red orders are the harmonic orders that can be totally eliminated by star-delta winding connections. It should be noticed that only some slot/pole number combinations are chosen in the table as examples to show the harmonic elimination effects. In fact, the eliminations of MMF harmonic orders

caused by the star-delta winding configurations are widely applicable for other slot/pole number combinations. The feasibilities of different slot/pole number combinations in DTP PMSMs will be further discussed in Chapter 2.

Table 1.5 Elimination of MMF harmonic orders with star-delta winding connections
($N_s/4m = h$ is odd)

| Slot-pole | Elimination MMF harmonic order |
|----------------------------------|---|
| 12/10 | <u>1</u> , <u>5</u> , <u>7</u> , <u>11</u> , <u>13</u> ,17,19, <u>23</u> , <u>25</u> ,29,31, <u>35</u> , <u>37</u> ,41,43, <u>47</u> , <u>49</u> |
| 36/34 | <u>1</u> , <u>5</u> , <u>7</u> , <u>11</u> , <u>13</u> , <u>17</u> ,19, <u>23</u> , <u>25</u> ,29,31, <u>35</u> , <u>37</u> ,41,43, <u>47</u> , <u>49</u> |
| 16/14 | <u>1</u> ,3,5, <u>7</u> ,9,11,13, <u>15</u> , <u>17</u> ,19,21,23,25,27,29, <u>31</u> , <u>33</u> ,35,37,39,41,43, <u>47</u> , <u>49</u> |
| 48/46 | <u>1</u> ,3,5,7,9,11,13, <u>15</u> , <u>17</u> ,19,21, <u>23</u> , <u>25</u> ,27,29, <u>31</u> , <u>33</u> ,35,37,39,41,43, <u>47</u> , <u>49</u> |
| 20/18 | <u>1</u> , <u>9</u> ,11, <u>19</u> , <u>21</u> ,29,31, <u>39</u> , <u>41</u> ,49 |
| 60/58 | <u>1</u> , <u>9</u> ,11, <u>19</u> , <u>21</u> , <u>29</u> ,31, <u>39</u> , <u>41</u> ,49 |
| (N _s /4m = h is even) | |
| Slot-pole | Elimination MMF harmonic order |
| 24/22 | 1, <u>5</u> , <u>7</u> , <u>11</u> ,13, <u>17</u> , <u>19</u> ,23,25, <u>29</u> , <u>31</u> ,35,37, <u>41</u> , <u>43</u> ,47,49 |
| 48/46 | 1, <u>5</u> , <u>7</u> ,11,13, <u>17</u> , <u>19</u> , <u>23</u> ,25, <u>29</u> , <u>31</u> ,35,37, <u>41</u> , <u>43</u> ,47,49 |
| 32/30 | 1,3,5, <u>7</u> , <u>9</u> ,11,13, <u>15</u> ,17,19,21, <u>23</u> , <u>25</u> ,27,29,31,33,35,37, <u>39</u> , <u>41</u> ,43,47,49 |
| 64/62 | 1,3,5, <u>7</u> , <u>9</u> ,11,13,15,17,19,21, <u>23</u> , <u>25</u> ,27,29, <u>31</u> ,33,35,37, <u>39</u> , <u>41</u> ,43,47,49 |
| 40/38 | 1, <u>9</u> , <u>11</u> , <u>19</u> ,21, <u>29</u> , <u>31</u> ,39,41, <u>49</u> |
| 80/78 | 1, <u>9</u> , <u>11</u> ,19,21, <u>29</u> , <u>31</u> , <u>39</u> ,41, <u>49</u> |

Based on the aforementioned references, the advantages and disadvantages of star-delta and dual inverter DTP winding configurations can be generally summarized in Table 1.6. As a significant advantage of DTP PMSMs is the fault-tolerant capability, and only when DTP PMSMs are fed by dual inverter, the machines can continue to run after any fault in one three-phase winding set, dual inverter DTP winding connection is more popular in DTP PMSMs.

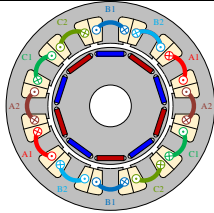
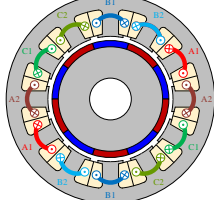
Table 1.6 Comparison of star-delta and dual inverter DTP winding configurations

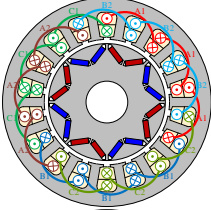
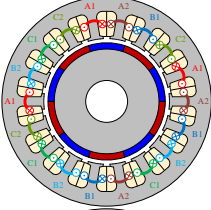
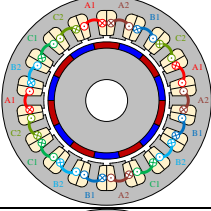
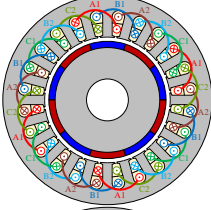
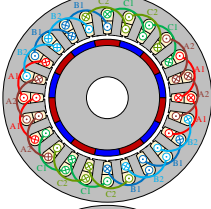
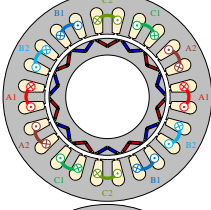
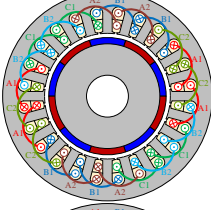
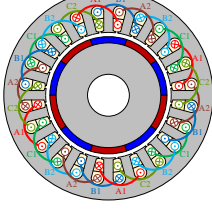
| | Star-delta | Dual inverter |
|---------------|--|--|
| Advantages | <ul style="list-style-type: none"> • Simple connection • More compact inverter size • Cheaper | <ul style="list-style-type: none"> • Better fault-tolerant capability • Commercial three-phase inverter utilized • More mature control strategies • More feasible phase shift angle • Equal turn numbers per coil • Shared rating suitable for high power conditions |
| Disadvantages | <ul style="list-style-type: none"> • Fixed phase shift angle • Unequal turn numbers per coil • Limited rating in one inverter • Poor fault-tolerant capability | <ul style="list-style-type: none"> • More devices required • Larger inverter size • More expensive |

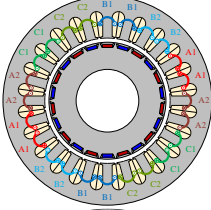
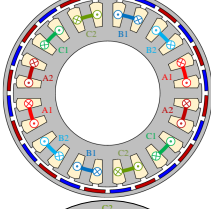
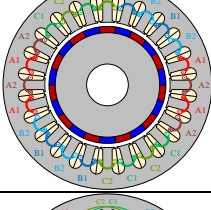
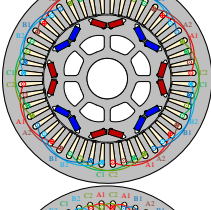
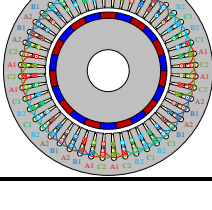
1.3.5 Summary of DTP PMSMs in Existing Literature

In this section, the developments of multiphase PMSMs were simply reviewed, with special focus on DTP PMSMs. The popular design techniques utilized in DTP PMSMs were also introduced and reviewed. Based on the review, the machine topologies of the DTP PMSMs introduced in existing literature can be summarized in Table 1.7. The topologies are listed according to slot number and pole number, and the features of each design are also given in the table.

Table 1.7 Various DTP PMSM topologies in existing literature

| Slot number | Paper | Topology | Features |
|-------------|--------------------|---|--|
| 12-slot | [BAR09] [BAR10] |  | <ul style="list-style-type: none"> • 12-slot/10-pole • Phase shift = 30° • Coil pitch = 1 • IPM & SPM rotor |
| 12-slot | [ABD15] |  | <ul style="list-style-type: none"> • 12-slot/10-pole • Phase shift = 30° • Coil pitch = 1 • Star-delta connection • SPM rotor |

| | | | |
|---------|--------------------|---|---|
| 18-slot | [PAT13] [PAT14] |  | <ul style="list-style-type: none"> • 18-slot/8-pole • Phase shift = $0^\circ/20^\circ/40^\circ$ • Coil pitch = 2 • IPM rotor |
| 18-slot | [DAJ12] |  | <ul style="list-style-type: none"> • 18-slot/10-pole • Phase shift = 20° • Coil pitch = 1 • SPM rotor |
| 18-slot | [CHE14a] |  | <ul style="list-style-type: none"> • 18-slot/14-pole • Phase shift = $0^\circ/20^\circ/40^\circ$ • Coil pitch = 1 • SPM rotor |
| 24-slot | [ABD16a] |  | <ul style="list-style-type: none"> • 24-slot/10-pole • Phase shift = 30° • Stator shifting = 75° • Coil pitch = 2 • SPM rotor |
| 24-slot | [CHE17] |  | <ul style="list-style-type: none"> • 24-slot/14-pole • Phase shift = 30° • Stator shifting = 105° • Coil pitch = 2 • SPM rotor |
| 24-slot | [ZHU19] |  | <ul style="list-style-type: none"> • 24-slot/14-pole • Phase shift = 30° • Stator shifting = 105° • Coil pitch = 1 • IPM rotor |
| 24-slot | [XU18] |  | <ul style="list-style-type: none"> • 24-slot/10-pole • Phase shift = $0^\circ/15^\circ/30^\circ$ • Coil pitch = 2 • SPM rotor |
| 24-slot | [FEN21] |  | <ul style="list-style-type: none"> • 24-slot/10- & 14-pole • Phase shift = $0^\circ/15^\circ/30^\circ$ • Coil pitch = 2 • SPM rotor |

| | | | |
|---------|---------------------|---|--|
| 24-slot | [BAR11a] |  | <ul style="list-style-type: none"> • 24-slot/20- & 22-pole • Phase shift = 30° • Coil pitch = 1 • IPM rotor |
| 24-slot | [ZHE12] |  | <ul style="list-style-type: none"> • 24-slot/22-pole • Phase shift = 30° • Coil pitch = 1 • Outer SPM rotor • Single & double layer |
| 24-slot | [XU19] |  | <ul style="list-style-type: none"> • 24-slot/22-pole • Phase shift = $0^\circ/15^\circ/30^\circ$ • Coil pitch = 1 • SPM rotor |
| 48-slot | [WAN22] |  | <ul style="list-style-type: none"> • 48-slot/8-pole • Phase shift = 30° • Coil pitch = 6 (SL) or 5 (DL) • IPM rotor |
| 48-slot | [ZHU21b] [SUN22] |  | <ul style="list-style-type: none"> • 48-slot/22-pole • Phase shift = $7.5^\circ/15^\circ/30^\circ/45^\circ$ • Coil pitch = 2 • SPM rotor |

It should be mentioned that Table 1.7 only summaries some typical DTP machine designs in existing literature. Due to the rapid developments in this area, some new topologies may not be included in the table. A more detailed general analysis on all feasible slot/pole number combinations and feasible phase shift angles will be presented in Chapter 2.

1.4 Scope of Research and Contributions of the Thesis

In this thesis, the electromagnetic performances of DTP PMSMs are analysed with particular reference on torque and torque ripple performances for electrical vehicles applications. Some general research approaches in designing and analysing DTP PMSMs will be proposed. The effects of some design techniques on the resultant electromagnetic performances in DTP PMSMs will be investigated based on a benchmark Prius 2010 machine. The contents of each chapter are summarized as follows:

Chapter 1: The machine topologies of multiphase PMSMs are briefly reviewed, with particular emphasis on DTP PMSMs. The design techniques, which are usually utilized in DTP PMSMs, i.e., stator shifting, variable phase shift angles, and star-delta connections are introduced with examples from existing papers. Finally, various typical DTP PMSM machine topologies in existing literature are summarized according to slot number.

Chapter 2: The feasibility and winding arrangement of DTP winding configuration in PMSMs are analysed systematically based on the star of slots. Different slot/pole number combinations, different phase shift angles, different coil pitch numbers are all considered. In addition, the concept of “attenuation factor” is extended in DTP PMSMs, to describe the effects of spatial and time shifts between the two winding sets on different MMF harmonic orders, by considering spatial and time shifting angles simultaneously. The analyses shown in this chapter are FE and experimentally validated in a 24-slot/22-pole PMSM.

Chapter 3: In this chapter, two DTP winding configurations, i.e., single-layer full-pitched one (DTP-SF) and double-layer short-pitched one (DTP-DS) are proposed for a benchmark 48-slot/8-pole Prius 2010 machine. The electromagnetic performances of the Prius machine with STP, DTP-SF, and DTP-DS winding configurations compared in detail under various conditions. The comparison shows that DTP-DS winding configuration is advantageous in average torque, torque ripple, and efficiency, especially under high-speed and three-phase open-circuit conditions. Hence, it is suggested that DTP-DS winding configuration is preferred for DTP PMSMs utilized in electrical vehicles. A Prius machine with the proposed DTP-DS windings is fabricated and tested to verify the FE analyses.

Chapter 4: The torque separation method to separate instantaneous torque components in STP PMSMs is extended into DTP PMSMs. The cross-coupling effects within and between different winding sets are all considered. An example is conducted based in a Prius machine with DTP-DS windings. It is found that the reluctance produced by the mutual inductance between the two winding sets contributes the most in the resultant output torque. Since the benchmark machine is the same with that in Chapter 3, the FE results shown in chapter can still be validated by the experiments reported in Chapter 3.

Chapter 5: This chapter proposes a simplified approach to estimate torque performance of PMSMs after rotor continuous skew, and then the influences of load on the effectiveness of

rotor skew in STP IPMSM (Prius machine) and SPMSM are investigated. It is found that the effectiveness of rotor skew depends on electric loading and magnetic saturation, and hence, it is less effective in IPMSM than in SPMSM. The conventional skew angle, i.e., one on-load torque ripple periodicity, only works well in SPMSM under light-load conditions. For SPMSM under heavy-load conditions or IPMSM under all load conditions, a better skew angle can be found. In this chapter, some FE predicted results, which are calculated based on STP Prius machine are validated by experiments, which verifies the correctness of the FE method utilized in this chapter.

Chapter 6: This chapter uses the simplified approach to examine the influences of load on the effectiveness of rotor in DTP IPMSM (the Prius machine with DTP-DS windings) and SPMSM. Similarly, the effectiveness of rotor skew depends on electric loading and magnetic saturation. However, due to the different MMF harmonic contents, the conventional skew angle in DTP PMSMs is smaller, and it can work well in DTP SPMSMs over all load conditions, but for DTP IPMSM, a better skew angle still can be found.

Chapter 7: This chapter investigates the effects of AIPM rotor in DTP PMSMs, and compared with those in STP PMSMs. It reveals that the average torque can be enhanced significantly by using AIPM rotor, and the average torque improvement in DTP PMSMs is even higher than that in STP PMSMs. However, AIPM rotor shows higher iron loss and lower efficiency under slow-speed conditions. The application of AIPM rotors to electric vehicles may be limited. The FE analyses presented in chapter are experimentally validated on a small-scale prototype.

Chapter 8: General conclusions are given based on the previous chapters, and the future work based on this thesis are also proposed.

The main contributions of this thesis can be summarized as follows:

- Generic winding arrangement method of DTP PMSMs, considering different slot/pole number combinations, different phase shift angles, and different coil pitch numbers;
- For 48-slot/8-pole IPMSMs, which are widely utilized in electric vehicles, it is found that the double-layer short-pitched DTP winding configuration is the preferred DTP configuration;
- Extension of attenuation factor in STP PMSMs to DTP PMSMs by considering both spatial

and time shifting angles;

- Extension of instantaneous torque separation method in STP PMSMs to DTP PMSMs;
- Development of a simplified approach to estimate torque performance of PMSMs with rotor continuous skew;
- Derivation of optimal skew angles in STP and DTP SPMSMs and IPMSMs accounting for the effects of loads, which is especially important for IPMSMs.
- Investigation of AIPM rotor in DTP PMSMs, it reveals that the application of AIPM rotors to DTP PMSMs in electric vehicles may be limited and less attractive than the application to STP PMSMs.

The research scope and chapter arrangement are illustrated in Fig. 1.40.

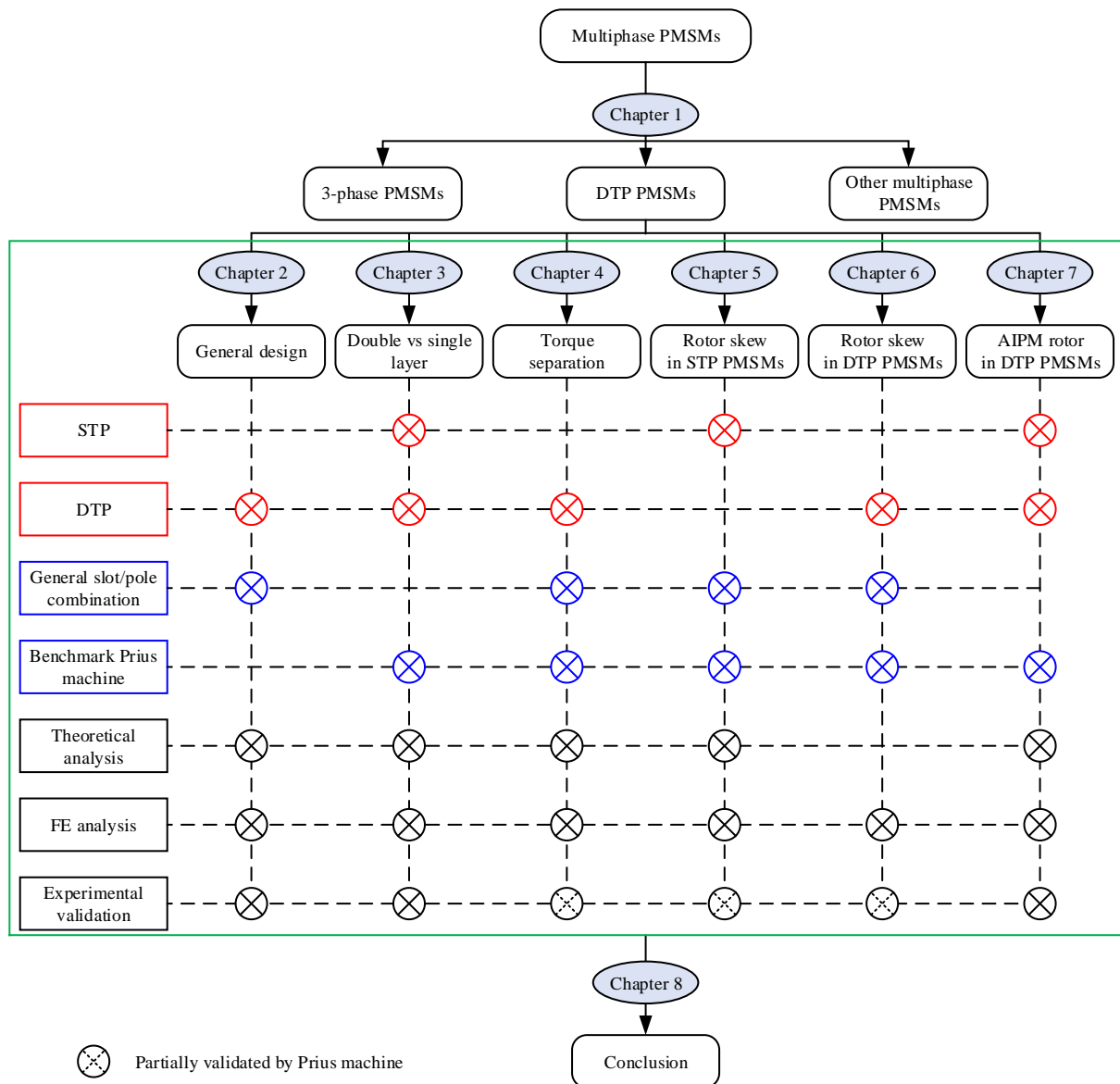


Fig. 1.40 Research scope and chapter arrangement.

CHAPTER 2

DEVELOPMENTS OF VARIOUS DTP PMSM TOPOLOGIES

Compared with conventional STP PMSMs, DTP PMSMs are featured with better fault-tolerant capability, improved torque capability, reduced torque pulsations and reduced power rating per inverter. However, not all DTP PMSMs have all these advantages at the same time. It still depends on the winding configuration of the DTP PMSMs. In this chapter, many feasible winding configurations for DTP PMSMs are described according to different slot/pole number combinations. The feasible winding layouts and the phase shift angles (β) between the two winding sets are analysed based on the star of slots in DTP PMSMs. Winding factors are calculated for different DTP winding configurations. Distribution factors considering different phase shift angles and pitch factors considering different coil pitch numbers are all covered. Besides the winding factors for one winding set, the effects of two winding sets on the resultant stator MMF harmonics are also considered by using attenuation factors. The attenuation factors are also calculated for different DTP PMSM topologies. Based on the foregoing analyses, the resultant performance of DTP PMSMs with different slot/pole number combinations, different phase shift angles, and different coil pitch numbers can be predicted by the winding factors and the attenuation factors, and thus, some appropriate DTP PMSM topologies can be quickly obtained.

2.1 Introduction

Compared with conventional STP PMSMs, DTP PMSMs are advantageous for many industrial applications that require high power rating, smooth torque, high power/torque density, and fault-tolerant capability etc. In the last decades, there are various technical and review papers that discuss the topologies, modelling methods, control strategies, pulse-width-modulation (PWM) techniques, and applications of DTP PMSMs [LEV08] [SAL19] [ZHU21a].

However, most of existing papers only focus on the performances of specific machine topologies, and few of them provide general introductions and analyses of DTP winding configurations considering different slot/pole number combinations, different phase shift

angles, and different coil pitch numbers. In [BAR11a], the feasibilities of DTP winding configurations in PMSMs with different slot/pole number combinations were discussed. However, only fractional-slot concentrated windings with 30° phase shift angle are considered. In [XU18], more feasible phase shift angles (0° and slot-pitch angle) were considered and compared for different slot/pole number combinations, but the winding layouts of different winding configurations and the selection of coil pitch number still have not been discussed comprehensively.

Based on the existing papers, a general summary of winding assignments of DTP PMSM winding configurations considering different slot/pole number combinations, different phase shift angles, and different coil pitch numbers were given in [ZHU21a]. This chapter is further extended based on [ZHU21a], besides 0° , 30° , and slot-pitch angle phase shift angles, some special phase shift angles are also discussed. Different phase shift angles are presented and explained with detailed examples, including stars of slots and resultant winding layouts. In addition to the winding assignments and the winding factors of the two winding sets in DTP PMSMs, the effects of the two winding sets on each other are also investigated and described by using an attenuation factor, considering both spatial and time shifts between the two winding sets.

This chapter is organised as follows. Section 2.2 shows the winding assignments of DTP windings in DTP PMSMs. The calculations of winding factors are also given in Section 2.2. Section 2.3 focuses on the attenuation factor for two winding sets in DTP PMSMs. An example of DTP PMSMs with different phase shift angles was given in Section 2.4, the calculated winding factors and attenuation factors are validated by FE and experimental results.

2.2 Winding Assignments and Winding Factors of DTP PMSMs

2.2.1 Star of Slots

In a PMSM, the electromotive force (EMF) phasors induced in conductors in different slots can be represented geometrically, as a star of slots. As every coil has two coil sides, when all coils share the same coil pitch (also known as coil span or coil throw), the star of slots can further represent the EMF phasors induced in different coils. Hence, the star of slots can be widely utilized in determining winding assignments of different phases in PMSMs with

different slot/pole number combinations [HEN94] [PYR08]. Based on the resultant winding assignments, distribution factors can also be calculated from the star of slots. In this chapter, the winding assignments and winding factors of DTP windings in DTP PMSMs are obtained based on the star of slots. Different phase shift angles (the angle displacement between the two winding sets) are considered (phase shift angles are all in electric degree in the thesis). It also should be mentioned that to simplify the descriptions, the following analyses are conducted in PMSMs with double-layer windings. For the PMSMs with single-layer windings, the number of spokes in the star of slots will be halved [BIA06a], but the approaches introduced in this chapter are still applicable.

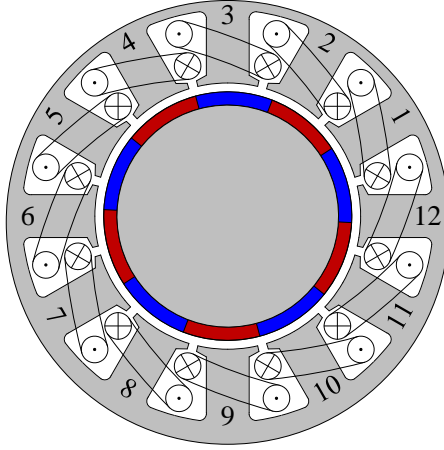
For a PMSM with slot number, N_s , and pole number, $2p$, the electrical periodicity number, t , can be computed as the greatest common divisor (GCD) between N_s and p ,

$$t = \text{GCD}(N_s, p) \quad (2.1)$$

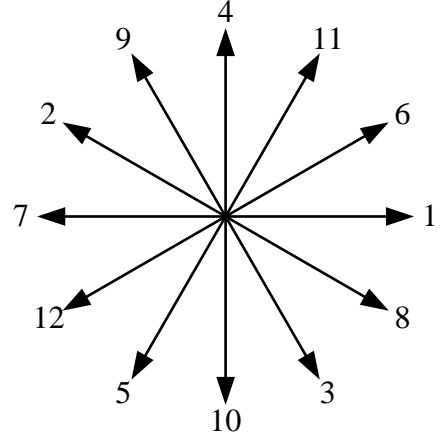
For a N_s -slot/ $2p$ -pole PMSM with double layer windings, the number of coils is N_s . Due to the electrical periodicity, the number of spokes in the star of slots, n_s , is N_s/t , and each spoke stands for t EMF phasors.

In the following analyses, the winding assignments in DTP PMSMs will mainly focus on the conditions with $t = 1$. For the conditions with $t \geq 2$, the winding assignments can be duplicating the winding connections obtained from the conditions with $t = 1$. In addition, when t is even and the windings in one electrical periodicity can be assigned into three phases, the whole armature windings can also be split into two three-phase winding sets directly according to electrical periodicity.

In this chapter, the slots are firstly numbered anticlockwise and the coils are numbered according to the number of slots where their upper coil sides located in. Adjacent slots are displaced by $360^\circ/N_s$ in mechanical, and thus, when taking rotor pole pair number, p , into consideration, the the EMF phasors of adjacent coils are displaced by $360^\circ \cdot p/n_s$ in electric. Then, for any PMSM, the star of slots can be drawn according to slot number, N_s and the pole number, $2p$. Two examples are given in Fig. 2.1 ($N_s = 12$, $2p = 10$) and Fig. 2.2 ($N_s = 9$, $2p = 10$). Both cross-sections and stars of slots are provided. For both 12-slot/10-pole and 9-slot/10-pole PMSMs, t equals 1, and thus, the number of spokes in the star of slots, n_s , equals 12 and 9 respectively, as shown in Fig. 2.1 (b) and Fig. 2.2 (b).

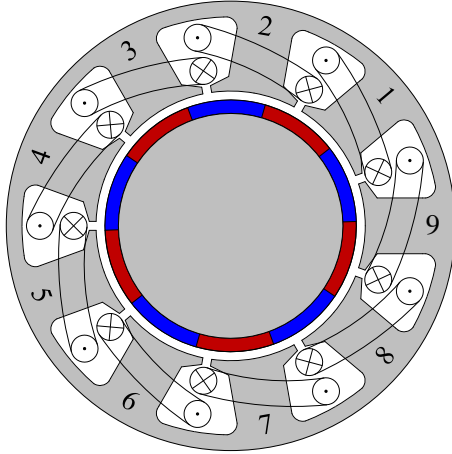


(a) Cross-section

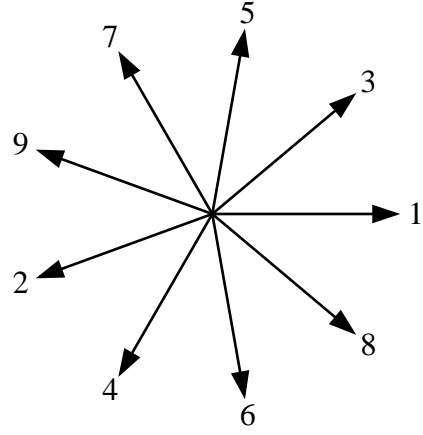


(b) Star of slots

Fig. 2.1 Cross-section and star of slots of 12-slot/10-pole PMSM with double-layer windings.



(a) Cross-section



(b) Star of slots

Fig. 2.2 Cross-section and star of slots of 9-slot/10-pole PMSM with double-layer windings.

Thus, the EMF phasors belong to the same phase can be selected according to the number of phases from the star of slots. To make the resultant EMF balanced per phase, the number of EMF phasors in different phases should be identical, and hence, to achieve DTP winding configuration, n_s should be an integer multiple of 6. As slot number $N_s = t \cdot n_s$, in DTP PMSMs, N_s also should be an integer multiple of 6.

2.2.2 Distribution Factor and Phase Shift Angle

Before assigning the coils in the phase winding in DTP PMSMs, it should be mentioned that the two winding sets in the DTP PMSMs are named as Winding 1 and Winding 2 in the following analyses for convenience. The first winding set, Winding 1, is composed by Phases

A1, B1, C1, which are marked with light yellow, light red, and light green, respectively. Similarly, the second winding set, Winding 2, is composed by Phases A2, B2, C2, which are marked with dark yellow, dark red, and dark green, respectively.

As mentioned above, in DTP PMSM, the number of spokes in the star of slots, n_s , is an integer multiple of 6. Assuming that $n_s = 6k$ (k is an integer), k can denote the number of spokes per phase. For example, as shown in Fig. 2.1, n_s is 12 in a 12-slot/10-pole PMSM, and hence, when it is equipped with DTP windings, each phase has two EMF phasors ($k = 2$). In the star of slots, to select the k spokes of the same phase, various phase shift angles should be considered. The resultant distribution factor also differs with different phase shift angles. In this sub-section 2.2.2, the analyses will only focus on the PMSMs with electrical periodicity number, $t = 1$, and in these machines, $n_s = N_s/t = N_s$, $k = n_s/6 = N_s/6$.

2.2.2.1 Phase shift angle = 0°

In DTP PMSMs, to select the coils of the two winding sets with phase shift angle = 0° , the 60° phase belt can be utilized in the star of slots, which is the same with that in STP PMSMs. For example, in a 12-slot/10-pole PMSM, as shown in Fig. 2.3 (a), the spokes in the star of slots can be selected based on the 60° phase belt, as shown in Fig. 2.3 (b). It should be mentioned that when the coils are wound in reverse direction, the corresponding spokes will also be shown in opposite direction. Hence, Spoke 1 in Fig. 2.3 (b) can represent the EMF phasors of Coil 1 and Coil -7 simultaneously.

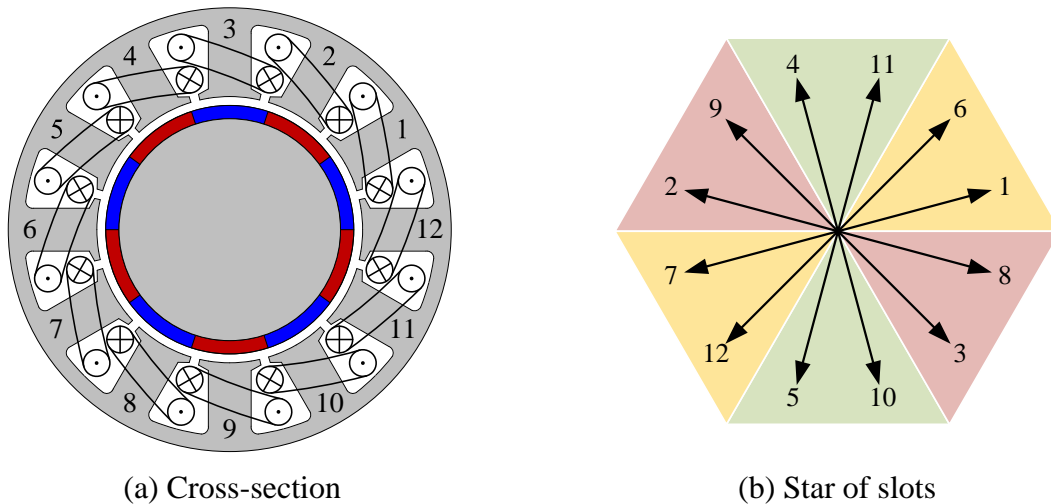


Fig. 2.3 Cross-section and star of slots of 12-slot/10-pole PMSM with 60° phase belt.

Based on the star of slots given in Fig. 2.3 (b), it can be found that there are various approaches to achieve DTP windings with phase shift angle $= 0^\circ$. Phase A1 can be composed by Coil 1 and Coil 6, and it can also be composed by Coil 1 and Coil -12, or by Coil -7 and Coil 6, or by Coil -7 and Coil -12. Similarly, for other phases, there are various options to choose corresponding coils. Considering that each three-phase winding set contains three phases, the resultant choice of coils of the two three-phase winding sets can be even more complicated.

In [BAR10], for a 12-slot/10-pole PMSM, two feasible DTP winding configurations with phase shift angle $= 0^\circ$ were discussed and compared. As the two DTP winding configurations are both equipped with double-layer (DL) windings, the two DTP winding configurations are named as DL-1 and DL-2, respectively. For DL-1, the stars of slots are of the two winding sets are shown in Fig. 2.4 (a) and (b), and the resultant winding layouts are given in Fig. 2.4 (c). Similarly, for DL-2, the detailed information can be found in Fig. 2.5.

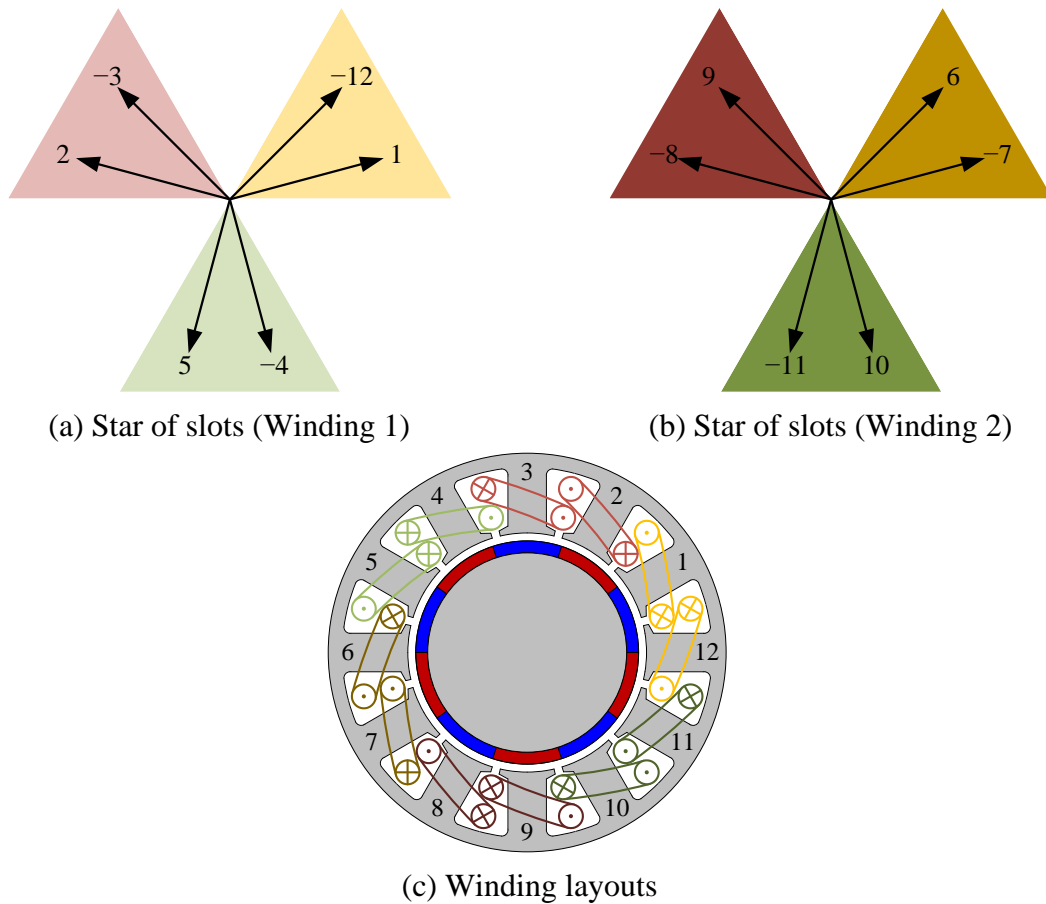


Fig. 2.4 Stars of slots and winding layouts of DTP 12-slot/10-pole PMSM with phase shift angle $= 0^\circ$ (DL-1).

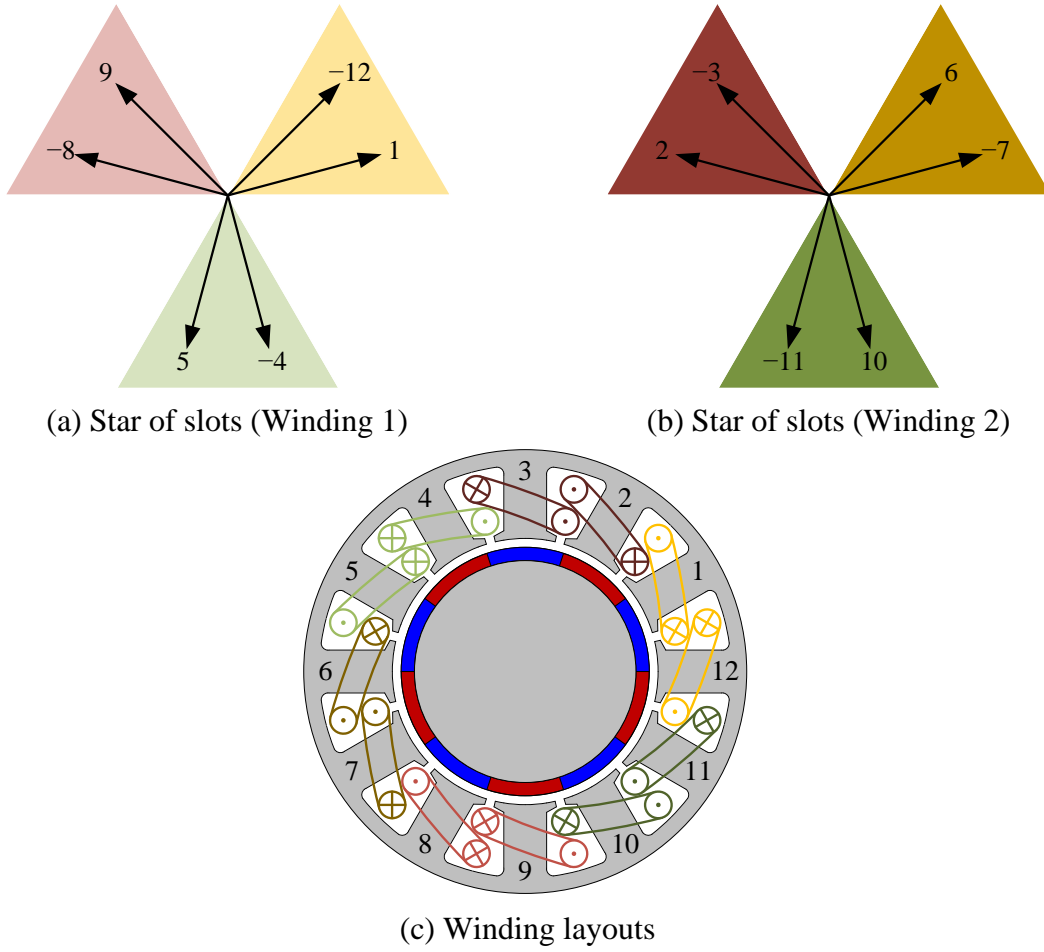


Fig. 2.5 Stars of slots and winding layouts of DTP 12-slot/10-pole PMSM with phase shift angle = 0° (DL-2).

Since phase shift angle = 0° , the currents in Phases A1, B1, C1 are equal to those in Phases A2, B2, C2 under healthy condition. Hence, it can be predicted that the electromagnetic performances of DTP PMSMs with DL-1 and DL-2 winding configurations are identical under healthy conditions. However, when one three-phase winding set is open-circuited and the DTP PMSMs are operated by the remaining winding set, the electromagnetic performances of DL-1 and DL-2 winding configurations will be different. Assuming that Winding 2 is open-circuited, the remaining windings in DL-1 and DL-2 machines are shown in Fig. 2.6 (a) and (b), respectively. It can be expected that the DL-2 winding configuration can produce less unbalanced radial force than the DL-1 counterpart under this condition, as reported and experimentally validated in [BAR10].

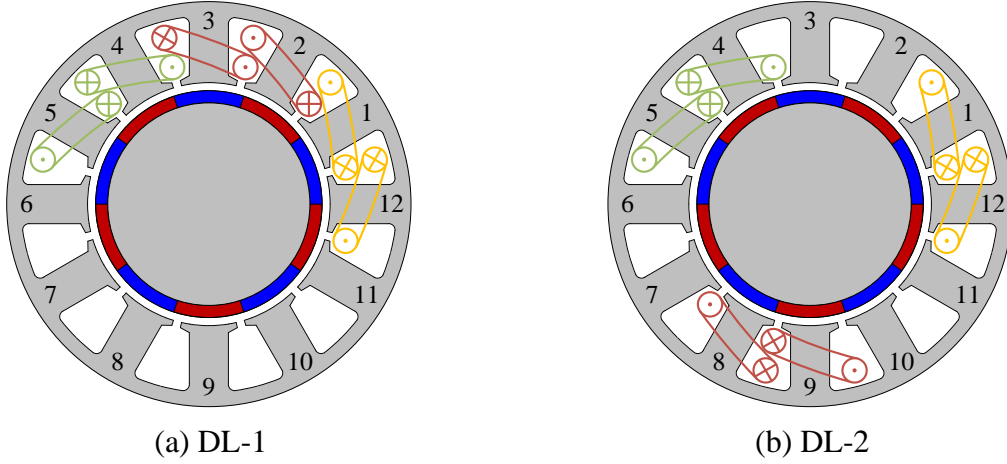


Fig. 2.6 Winding layouts of DTP 12-slot 10-pole PMSM with phase shift angle = 0° under single three-phase open-circuit condition.

In the 12-slot/10-pole PMSM, the number of spokes per phase, k , is 2, which is even. An 18-slot/14-pole PMSM, in which $k = 3$, is also given as follows, as another example for the conditions when k is odd. For the 18-slot/14-pole PMSM with double layer concentrated windings, the winding layouts are shown in Fig. 2.7 (a). To achieve phase shift angle = 0° , the spokes in the star of slots are selected using the 60° phase belt, as shown in Fig. 2.7 (b).

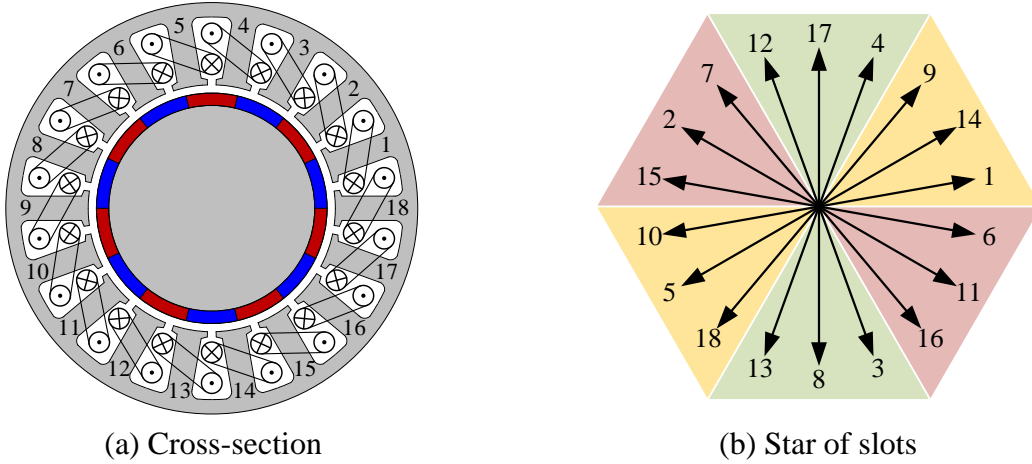


Fig. 2.7 Cross-section and star of slots of 18-slot/14-pole PMSM with 60° phase belt.

Similarly, there are various feasible methods to distinguish the coils for the two winding sets based on the star of slots shown in Fig. 2.7 (b). Considering the symmetricity of the two three-phase winding sets, one feasible winding configuration is selected as shown in Fig. 2.8. It can be seen that the adjacent coils always belong to different winding sets. Compared with other winding configurations, in which adjacent coils may belong to the same winding set, the winding configuration given in Fig. 2.8 can exhibit better torque capability under single three-phase open-circuit condition.

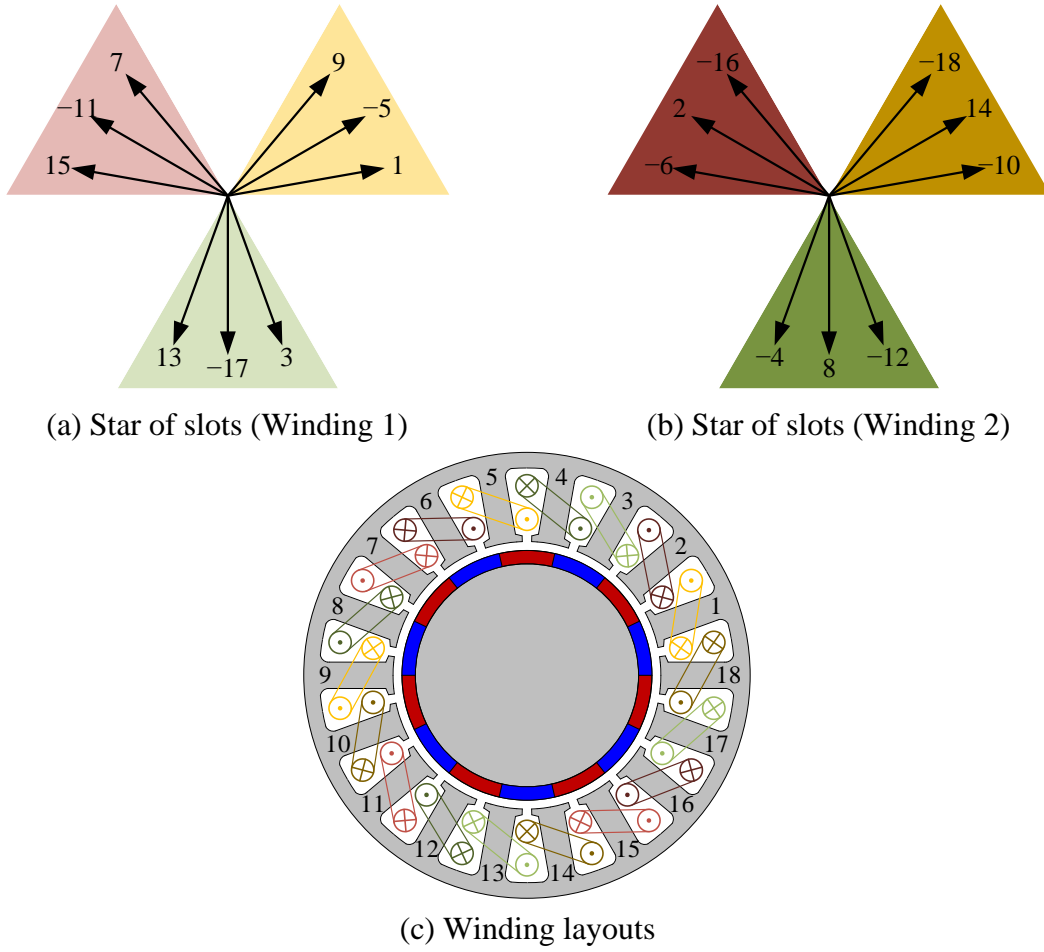


Fig. 2.8 Stars of slots and winding layouts of DTP 18-slot/14-pole PMSM with phase shift angle = 0° .

For each winding set, the distribution factors can be computed according to the selections of spokes in the star of slots. From Fig. 2.3 to Fig. 2.8, it can be concluded that in DTP PMSMs, when phase shift angle = 0° , the spokes are selected based on the 60° phase belt, which is identical to that in STP PMSMs. Hence, in DTP PMSMs with phase shift angle = 0° , the calculations of distribution factors are also identical to those in STP counterparts. As the number of spokes per phase is k , and the angular displacement between adjacent spokes is $360^\circ/N_s$, the distribution factor can be obtained as

$$K_d = \frac{\sin\left(k \frac{360^\circ}{2N_s}\right)}{k \sin\left(\frac{360^\circ}{2N_s}\right)} = \frac{\sin(30^\circ)}{k \sin\left(\frac{30^\circ}{k}\right)} \quad (2.2)$$

2.2.2.2 Phase shift angle = 30°

In DTP PMSMs, besides the 0° phase shift angle, another popular phase shift angle is 30°. To achieve the 30° phase shift angle, the star of slots should be analysed with the 30° phase belt, and hence, the star of slots can be separated into 12 sectors. To make the resultant EMF phasors balanced, N_s should be an integer multiple of 12. As $N_s = 6k$, in other words, 30° phase shift angle is feasible only when k is even.

For example, in a 12-slot/10-pole PMSM, the double-layer concentrated windings are shown in Fig. 2.9 (a), and the star of slots can be analysed with the 30° phase belt, as shown in Fig. 2.9 (b). The resultant star of slots of the two winding sets and the resultant winding layouts are shown in Fig. 2.10.

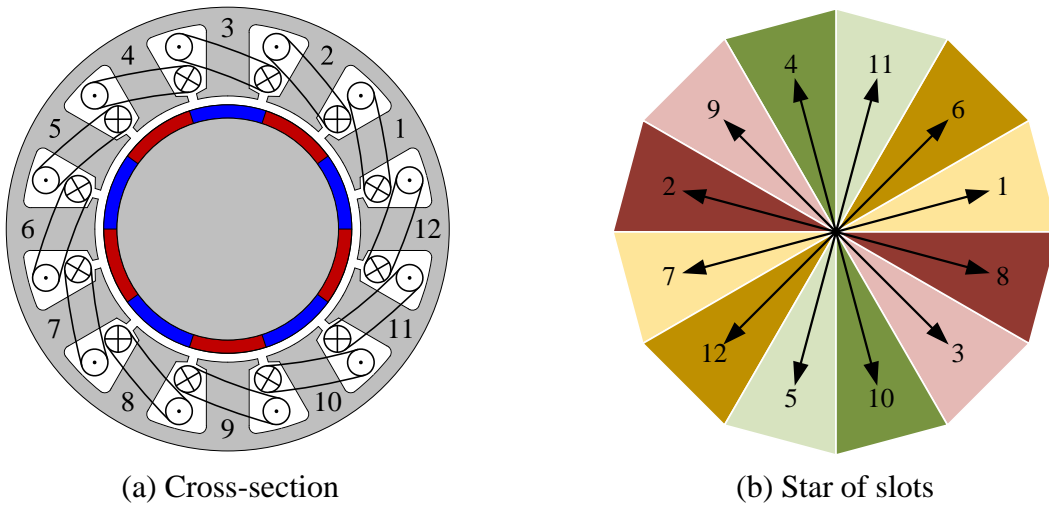
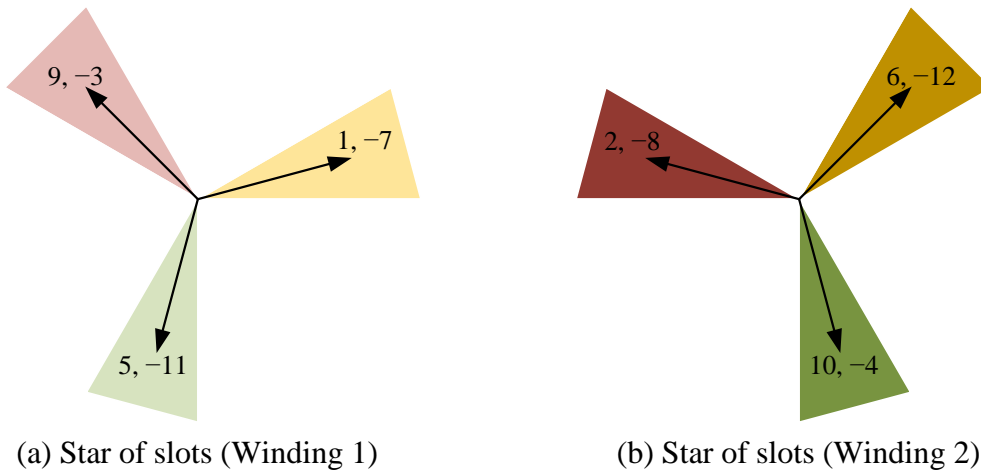
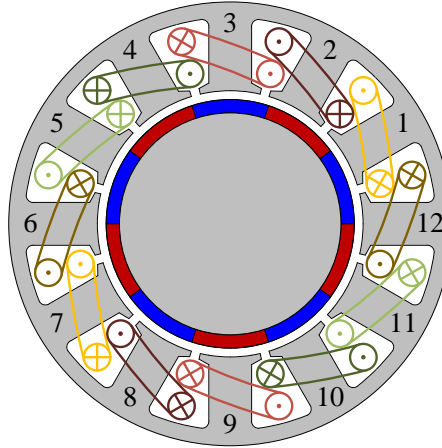


Fig. 2.9 Cross-section and star of slots of 12-slot/10-pole PMSM with 30° phase belt.

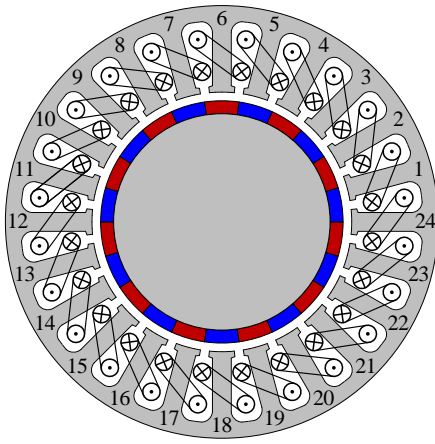




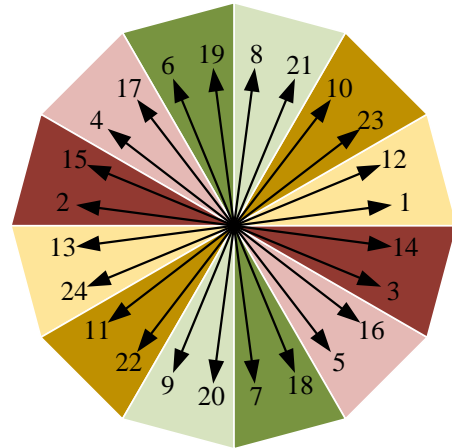
(c) Winding layouts

Fig. 2.10 Stars of slots and winding layouts of DTP 12-slot/10-pole PMSM with phase shift angle = 30° .

Taking a 24-slot/22-pole PMSM as another example, since $N_s = 24$, $2p = 22$, it can be obtained that $k = 24/6 = 4$. Since k is even, the 30° phase shift angle is feasible. The cross-section of the 24-slot/22-pole PMSM with double layer concentrated windings is shown in Fig. 2.11 (a), and the star of slots with the 30° phase belt is shown in Fig. 2.11 (b). Based on Fig. 2.11, the stars of slots of the two winding sets and the resultant winding layouts of the DTP 24-slot/22-pole PMSM with phase shift angle = 30° can be obtained, as shown in Fig. 2.12.



(a) Cross-section



(b) Star of slots

Fig. 2.11 Cross-section and star of slots of 24-slot/22-pole PMSM with 30° phase belt.

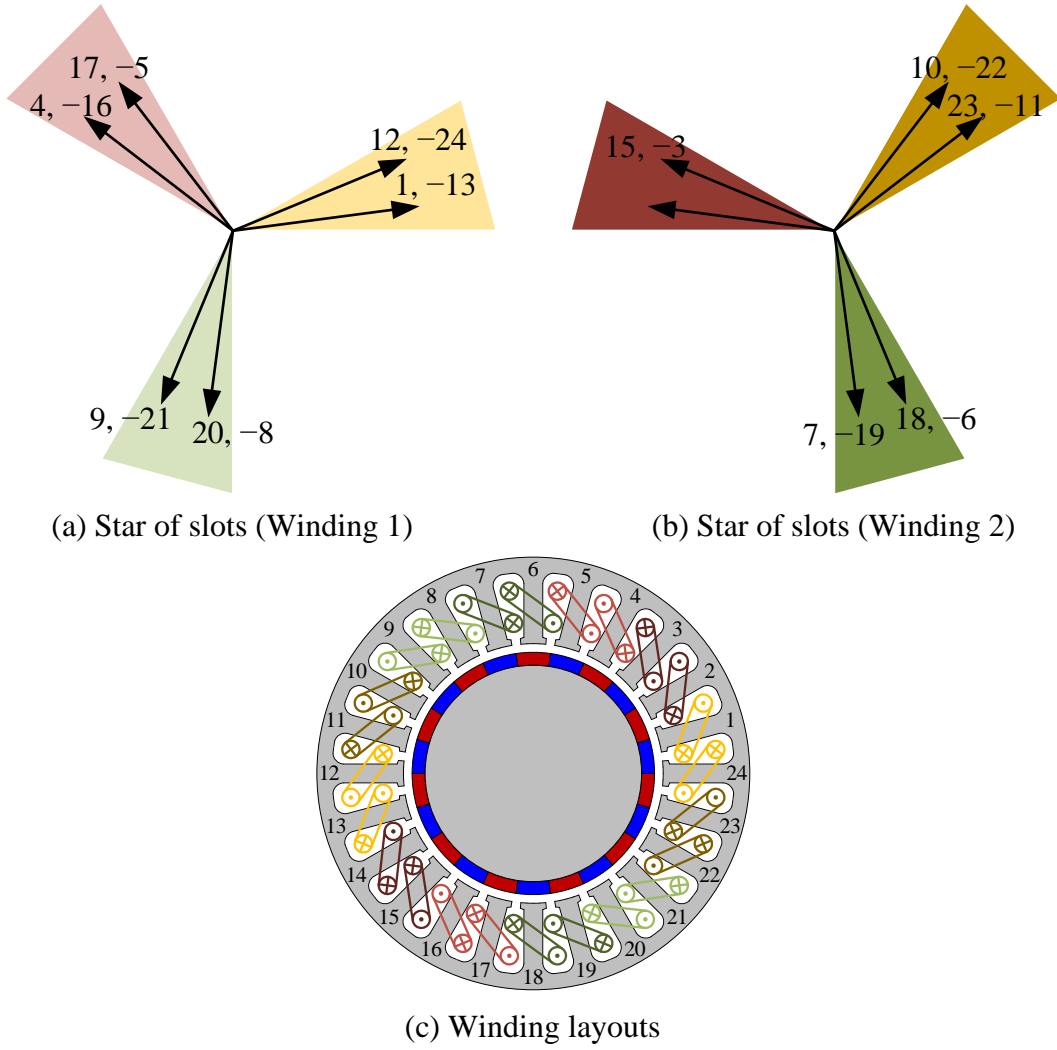


Fig. 2.12 Stars of slots and winding layouts of DTP 24-slot/22-pole PMSM with phase shift angle = 30° .

Overall, it can be concluded that in DTP PMSMs, only when N_s is an integer multiple of 12, the 30° phase shift angle could be feasible. From Fig. 2.9 (b) and Fig. 2.11 (b), it can further be found that when phase shift angle = 30° , the opposite spokes belong to the same phase. Hence, in DTP PMSMs with phase shift angle = 30° , the distribution factor can be computed with halved number of spokes per phase, which is $k/2$, and the angular displacement between adjacent spokes is still $360/N_s$. Thus, the resultant distribution factor can be calculated as

$$K_d = \frac{\sin\left(\frac{k}{2} \cdot \frac{360^\circ}{2N_s}\right)}{\frac{k}{2} \sin\left(\frac{360^\circ}{2N_s}\right)} = \frac{2 \sin(15^\circ)}{k \sin\left(\frac{30^\circ}{k}\right)} \quad (2.3)$$

2.2.2.3 Phase shift angle = slot-pitch angle

To achieve the conventional 0° and 30° phase shift angles, the spokes in the star of slots are selected using the 60° and 30° phase belts, respectively. Actually, besides using the 60° and 30° phase belts, the spokes of the two winding sets can also be selected alternately from the star of slots, and thus, the two winding sets will be shifted by $360^\circ/N_s$, which is the angular displacement between the adjacent spokes in the star of slots. As the phase shift angle under this condition equals $360^\circ/N_s$, this condition is called as “slot-pitch angle” in this chapter.

In 12-slot/10-pole PMSMs, N_s is 12, and hence, the slot-pitch angle is $360^\circ/12 = 30^\circ$. Thus, the DTP winding configuration with phase shift angle = 30° , shown in Fig. 2.9 and Fig. 2.10, can be seen as an example of DTP PMSMs with phase shift angle = slot-pitch angle.

Another example is given based on a 24-slot/22-pole PMSM. As N_s is 24, the slot-pitch angle is 15° in this machine. When the machine is equipped with double layer concentrated windings, as shown in Fig. 2.13 (a), the spokes of the two winding sets can be selected from the star of slots using 15° phase belt, as shown in Fig. 2.13 (b). Based on Fig. 2.13, the stars of slots of the two winding sets and the resultant winding layouts of the DTP 24-slot/22-pole PMSM with phase shift angle = 15° can be obtained, as shown in Fig. 2.14.

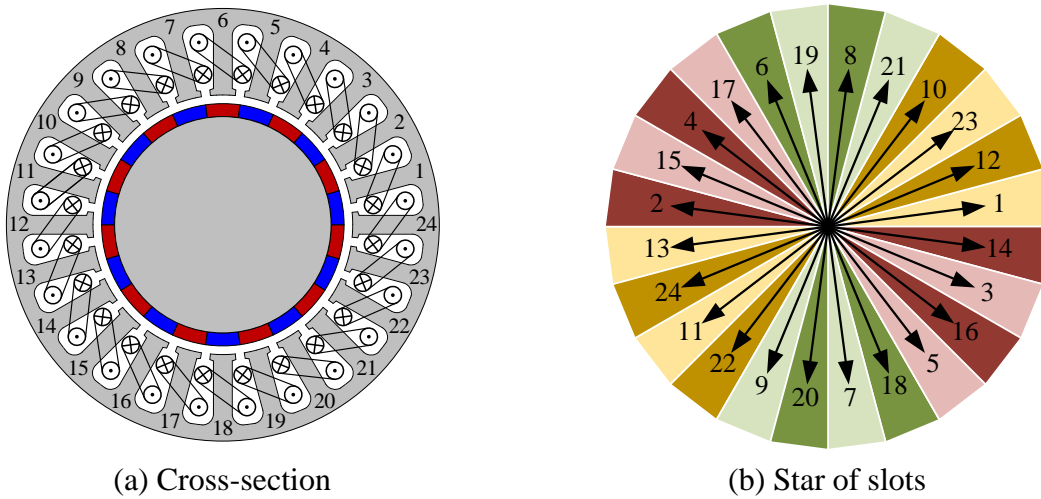


Fig. 2.13 Cross-section and star of slots of 24-slot/22-pole PMSM with 15° phase belt.

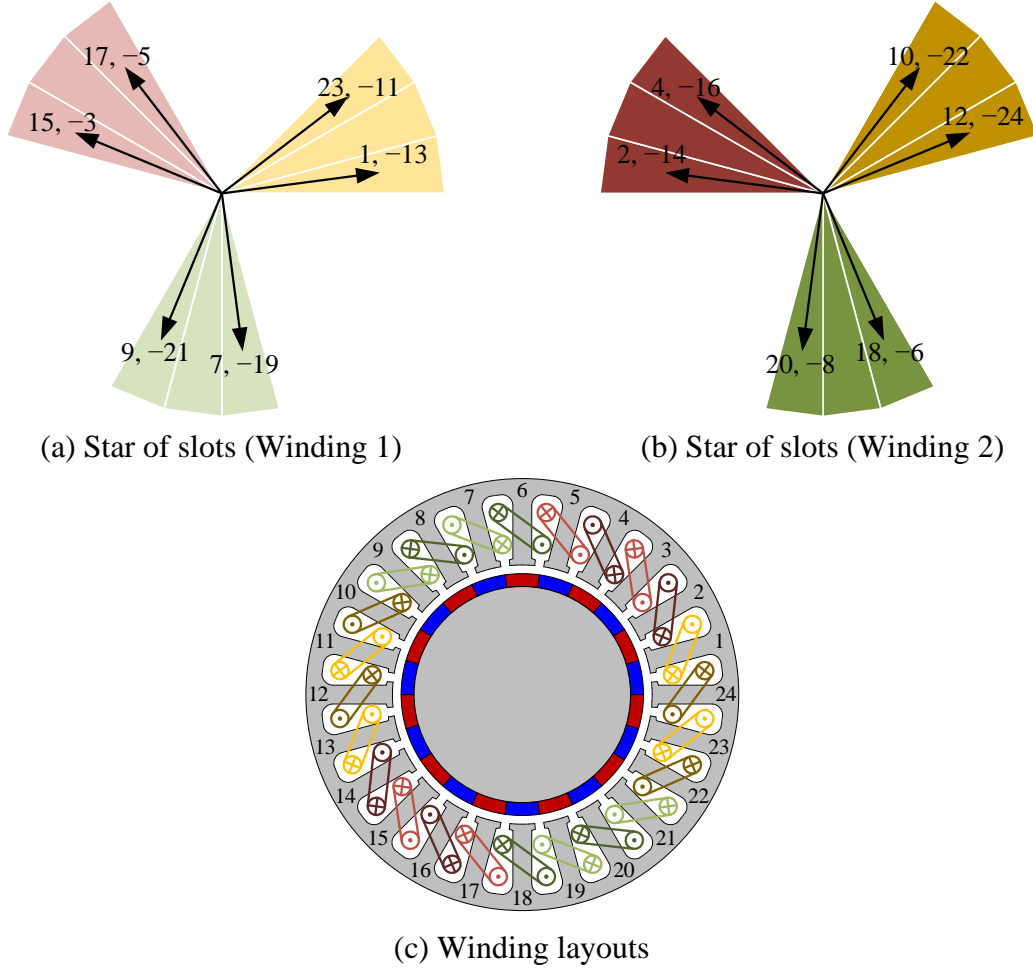


Fig. 2.14 Stars of slots and winding layouts of DTP 24-slot/22-pole PMSM with phase shift angle = 15° .

From Fig. 2.12 and Fig. 2.14, it can be observed that in the DTP 24-slot/22-pole PMSM, when phase shift angle = 30° , adjacent coils may belong to the same winding set; but when phase shift angle = 15° , adjacent coils always belong to different winding sets. Hence, it can be expected that when the DTP 24-slot/22-pole PMSM is operated under single three-phase open-circuit condition, the winding configuration with 15° phase shift angle can exhibit better torque performance than the counterpart with 30° phase shift angle, especially when the currents are high, as reported and validated by FE method and experiments in [XU19].

Besides the foregoing examples, i.e., 12-slot/10-pole PMSM ($k = 2$) and 24-slot/22-pole PMSMs ($k = 4$), another example, an 18-slot/14-pole PMSM, in which $k = 3$, is also given as follows, for the conditions when k is odd. As N_s is 18, the slot-pitch angle is 20° in this machine. The cross-section of the 18-slot/14-pole PMSM with double layer concentrated windings is shown in Fig. 2.15 (a), and the spokes of the two winding sets can be selected from the star of

slots using 20° phase belt, as shown in Fig. 2.15 (b). Based on Fig. 2.15, in the 18-slot/14-pole PMSM, the DTP winding configuration with phase shift angle = 20° can be obtained, and the stars of slots of two winding sets and the resultant winding layouts are shown in Fig. 2.16.

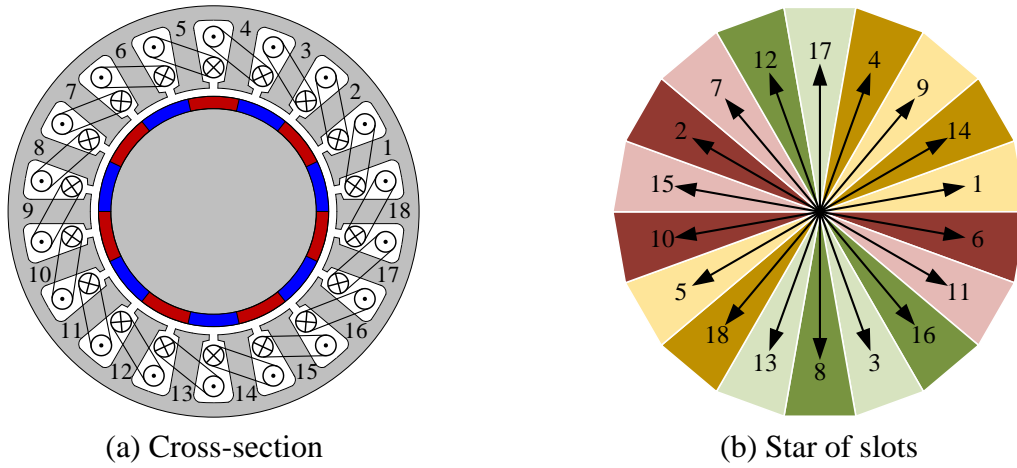


Fig. 2.15 Cross-section and star of slots of 18-slot/14-pole PMSM with 20° phase belt.

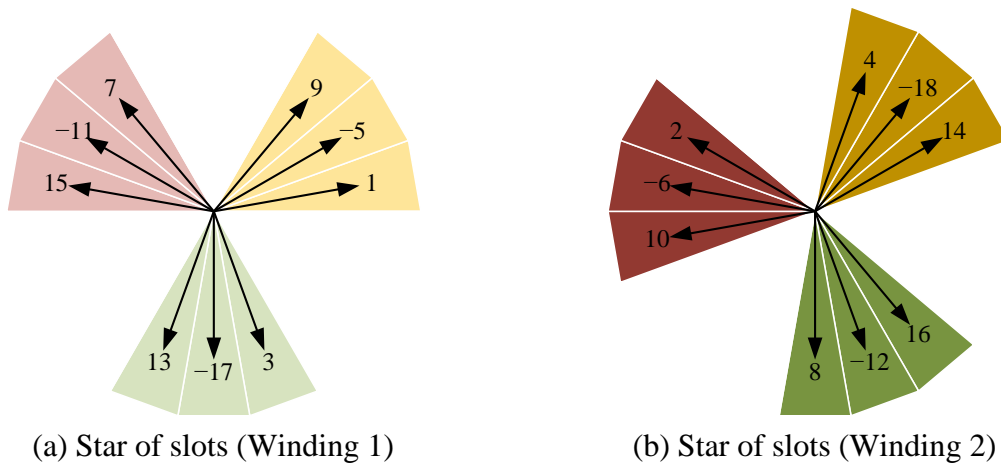


Fig. 2.16 Stars of slots and winding layouts of DTP 18-slot/14-pole PMSM with phase shift angle = 20° .

From Fig. 2.14 (b) and Fig. 2.16 (b), it can be observed that for the conditions with phase shift angle = slot-pitch angle, the calculations of distribution factors are different when k is even and odd. When k is even, opposite spokes belong to the same phase, and thus, the distribution factor can be computed based on $k/2$ spokes and the angular displacement between the adjacent spokes is $2 \times 360^\circ / N_s$. However, when k is odd, opposite spokes belong to different phases, and thus, the distribution factor still needs to be computed based on k spokes, but the angular displacement between the adjacent spokes is $360^\circ / N_s$. Hence, in DTP PMSMs with phase shift angle = slot-pitch angle, the calculation of distribution factors depends on the number of spokes per phase, k , as

$$K_d = \begin{cases} \frac{\sin\left(\frac{k}{2} \frac{360^\circ}{2N_s}\right)}{\frac{k}{2} \sin\left(\frac{360^\circ}{2N_s}\right)} = \frac{2 \sin(15^\circ)}{k \sin\left(\frac{30^\circ}{k}\right)}, \text{ when } k \text{ is even} \\ \frac{\sin\left(k \frac{360^\circ}{2N_s}\right)}{k \sin\left(\frac{360^\circ}{2N_s}\right)} = \frac{\sin(30^\circ)}{k \sin\left(\frac{30^\circ}{k}\right)}, \text{ when } k \text{ is odd} \end{cases} \quad (2.4)$$

2.2.2.4 Discussions about other phase shift angles

From previous sub-sections 2.2.2.2 and 2.2.2.3, it was found that the 30° phase shift angle is the slot-pitch angle for DTP PMSMs with $N_s = 12$, and the 30° phase shift angle is feasible for all DTP PMSMs with N_s is an integer multiple of 12. Similarly, since the 20° phase shift angle is the slot-pitch angle for DTP PMSMs with $N_s = 18$, it can be inferred that the 30° phase shift angle is feasible for all DTP PMSMs with N_s is an integer multiple of 18. The 15° phase shift angle is feasible for all DTP PMSMs with N_s is an integer multiple of 24 and the 10° phase shift angle is feasible for all DTP PMSMs with N_s is an integer multiple of 36. It can be further derived that when $N_s = N_{s0}$, the slot-pitch angle is $360^\circ / N_{s0}$, and then phase shift angle = $360^\circ / N_{s0}$, is feasible for all DTP PMSMs with N_s is an integer multiple of N_{s0} .

It should also be mentioned that in the DTP windings with phase shift angle = 0° , when all the coils in Winding 2 are wound in the reverse direction, the two winding sets can be seen as shifted by 60° . For example, the winding configuration of DTP 12-slot/10-pole PMSM with phase shift angle = 0° (DL-2) shown in Fig. 2.5, can be changed into a DTP winding configuration with phase shift angle = 60° , as shown in Fig. 2.17. Hence, it can also be concluded in DTP winding configuration, 0° and 60° phase shift angles are equivalent. To achieve the 0° and 60° phase shift angles, N_s , should be an integer multiple of 6.

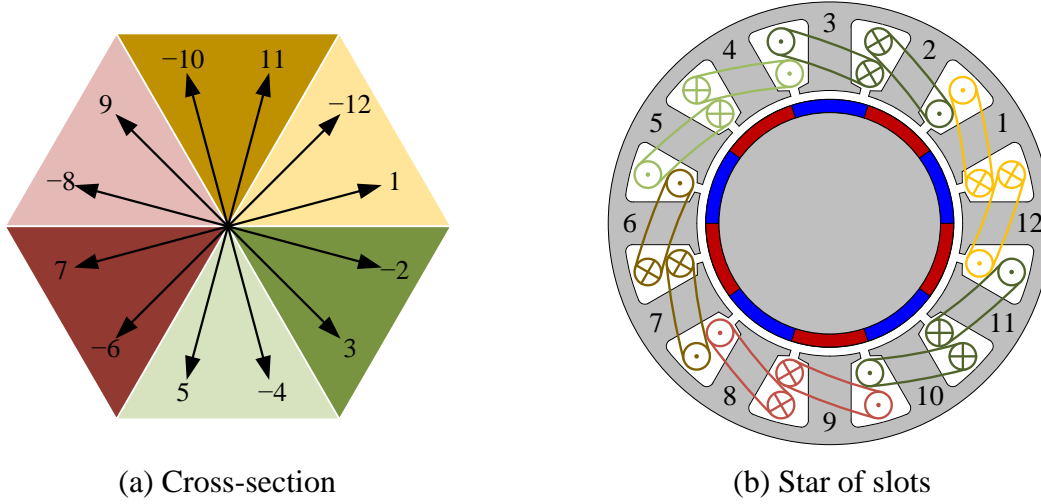


Fig. 2.17 Star of slots and winding layouts of DTP 12-slot/10-pole PMSM with phase shift angle = 60° .

In general, it can be summarized that feasibility of DTP winding configurations in PMSMs with different slot/pole number combinations mainly depends on the number of spokes in the star of slots, n_s . When the electrical periodicity number, $t = 1$, the number of spokes in the star of slots, n_s , equals to the number of slots, N_s , and the number of spokes per phase, $k = N_s/6$. When k is an integer, DTP winding configuration is feasible, and the phase shift angle could be $0^\circ/60^\circ$ and $60^\circ/k$ (slot-pitch angle). Besides $0^\circ/60^\circ$ and $60^\circ/k$, when k is even (an integer multiple of 2), the phase shift angle can also be 30° ($60^\circ/2$); when k is an integer multiple of 3, the phase shift angle can also be 20° ($60^\circ/3$), etc. For different phase shift angles, the requirements on k and N_s in DTP PMSMs are summarized in Table 2.1.

It should be mentioned that although the requirements on pole pair number, p , are not listed directly in the table, there is an implicit restriction: to achieve the phase shift angles shown in the table, t should be 1, in other words, the selection of p should make $\text{GCD}(N_s, p)$ equal to 1. Thus, for DTP PMSMs with $N_s = 36$ and $t = 1$ (e.g. 36-slot/2-pole, 36-slot/10-pole, 36-slot/14-pole, 36-slot/22-pole, 36-slot/26-pole, 36-slot/30-pole, 36-slot/34pole, ...), the feasible phase shift angles include $0^\circ/60^\circ$, 30° , 20° , and 10° . For DTP PMSMs with $N_s = 36$ and $t \neq 1$ (e.g. 36-slot/4-pole, 36-slot/6-pole, 36-slot/8-pole 36-slot/12-pole, 36-slot/16-pole, ...), the feasible phase shift angles should be found from their one electrical periodicity counterparts. Similarly, when $t = 1$, for different N_s , the feasible phase shift angles can be summarized, as shown in Table 2.2.

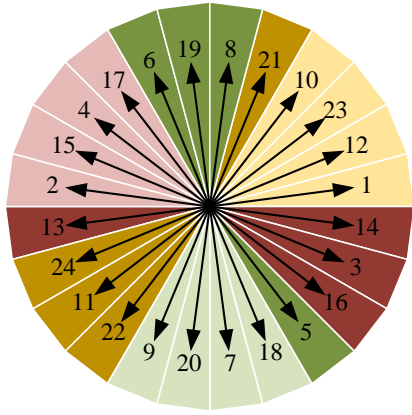
Table 2.1 Requirements on k and N_s in DTP PMSMs for different phase shift angles

| Phase shift angle | k | $N_s (t = 1)$ |
|-------------------|----------------------------|--|
| 0°/60° | Integer (Multiple of 1) | 6, 12, 18, 24, 30, 36, 42, 48, 54, 60, 66, 72, ... |
| 30° | Even (Multiple of 2) | 12, 24, 36, 48, 60, 72, ... |
| 20° | Multiple of 3 | 18, 36, 54, 72, 90, 108, ... |
| 15° | Multiple of 4 | 24, 48, 72, 96, 120, 144, ... |
| 12° | Multiple of 5 | 30, 60, 90, 120, 150, 180, ... |
| 10° | Multiple of 6 | 36, 72, 108, 144, 180, 216, ... |
| ... | | ... |

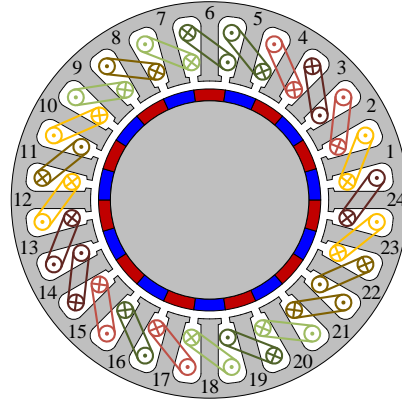
Table 2.2 Feasible phase shift angles for different $N_s (t = 1)$ in DTP PMSMs

| $N_s (t = 1)$ | k | Feasible phase shift angles (°) |
|---------------|-----|---------------------------------|
| 6 | 1 | 0/60 |
| 12 | 2 | 0/60, 30 |
| 18 | 3 | 0/60, 20 |
| 24 | 4 | 0/60, 15, 30 |
| 30 | 5 | 0/60, 12 |
| 36 | 6 | 0/60, 10, 20, 30 |
| ... | ... | ... |

In addition to the aforementioned methods, the coil EMF phasors of the two winding sets can also be selected using the unbalanced phase belt method. When using the unbalanced phase belt method, the coils of Winding 1 are still selected based on the 60° phase belt, but without the consideration of reverse spokes. The coils of Winding 2 are then selected according to phase shift angle and utilizing reverse spokes. Two examples are given based on the 24-slot/22-pole PMSM, as shown in Fig. 2.18 (phase shift angle = 15°) and Fig. 2.19 (phase shift angle = 30°) respectively. It can be found that with the unbalanced phase belt method, the phase shift angle can be any integer multiple of the slot-pitch angle. In Table 2.2, the feasible phase shift angles for different N_s with the conventional balanced phase belt are summarized; but with the unbalanced phase belt, even more phase shift angles become feasible. However, since the spokes of the same phase are still distributed in one 60° sector when using unbalanced phase belt method, the distribution factors are still identical to those with phase shift angle = 0°/60°. Hence, the unbalanced phase belt method cannot improve distribution factor, but only provides some more freedoms in control strategies. In the following investigation about different phase shift angles, the windings are still assigned using the conventional balanced phase belt method, instead of this unbalanced phase belt method.

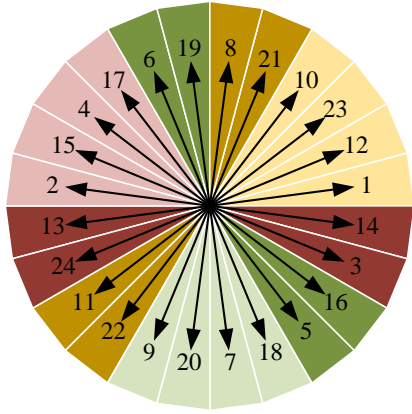


(a) Star of slots

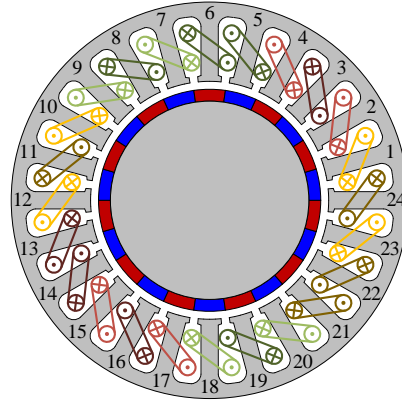


(b) Winding layouts

Fig. 2.18 Star of slots and winding layouts of DTP 24-slot/22-pole PMSM with phase shift angle = 15° using unbalanced phase belt.



(a) Star of slots



(b) Winding layouts

Fig. 2.19 Star of slots and winding layouts of DTP 24-slot/22-pole PMSM with phase shift angle = 30° unbalanced phase belt.

In summary, based on the foregoing analyses, for PMSMs with different slot/pole number combinations, the feasibility of DTP winding configuration can be obtained from electrical periodicity number, t , and the number of spokes in the star of slots, n_s . The feasible phase shift angles can be obtained from the number of spokes per phase in the star of slots, k . For the PMSMs with double layer windings, when slot number (N_s) ≤ 36 and pole number ($2p$) ≤ 30 , the electrical periodicity number, t , the number of spokes in the star of slots, n_s , are summarized in Table 2.3. When n_s is an integer multiple of 6, the numbers of spokes per phase, k , are also provided. In the table, the cases when n_s is an integer multiple of 6 are marked with light blue, and the cases when t is even and N_s is an odd multiple of 3 are marked with light yellow. Based on the table, it can be concluded that DTP winding configurations are feasible in PMSMs with coloured slot/pole number combinations.

Table 2.3 Electrical periodicity number, t , number of spokes in star of slots, n_s , number of spokes per phase, k , for PMSMs with different slot/pole number combinations

| $N_s \backslash 2p$ | | 6 | 12 | 18 | 24 | 30 | 36 |
|---------------------|-------|---|----|----|----|----|----|
| 2 | t | 1 | 1 | 1 | 1 | 1 | 1 |
| | n_s | 6 | 12 | 18 | 24 | 30 | 36 |
| | k | 1 | 2 | 3 | 4 | 5 | 6 |
| 4 | t | 2 | 2 | 2 | 2 | 2 | 2 |
| | n_s | 3 | 6 | 9 | 12 | 15 | 18 |
| | k | - | 1 | - | 2 | - | 3 |
| 6 | t | 3 | 3 | 3 | 3 | 3 | 3 |
| | n_s | 2 | 4 | 6 | 8 | 10 | 12 |
| | k | - | - | 1 | - | - | 2 |
| 8 | t | 2 | 4 | 2 | 4 | 2 | 4 |
| | n_s | 3 | 3 | 9 | 6 | 15 | 9 |
| | k | - | - | - | 1 | - | - |
| 10 | t | 1 | 1 | 1 | 1 | 5 | 1 |
| | n_s | 6 | 12 | 18 | 24 | 6 | 36 |
| | k | 1 | 2 | 3 | 4 | 1 | 6 |
| 12 | t | 6 | 6 | 6 | 6 | 6 | 6 |
| | n_s | 1 | 2 | 3 | 4 | 5 | 6 |
| | k | - | - | - | - | - | 1 |
| 14 | t | 1 | 1 | 1 | 1 | 1 | 1 |
| | n_s | 6 | 12 | 18 | 24 | 30 | 36 |
| | k | 1 | 2 | 3 | 4 | 5 | 6 |
| 16 | t | 2 | 4 | 2 | 8 | 2 | 4 |
| | n_s | 3 | 3 | 9 | 3 | 15 | 9 |
| | k | - | - | - | - | - | - |
| 18 | t | 3 | 3 | 9 | 3 | 3 | 9 |
| | n_s | 2 | 4 | 2 | 8 | 10 | 4 |
| | k | - | - | - | - | - | - |
| 20 | t | 2 | 2 | 2 | 2 | 10 | 2 |
| | n_s | 3 | 6 | 9 | 12 | 3 | 18 |
| | k | - | 1 | - | 2 | - | 3 |
| 22 | t | 1 | 1 | 1 | 1 | 1 | 1 |
| | n_s | 6 | 12 | 18 | 24 | 30 | 36 |
| | k | 1 | 2 | 3 | 4 | 5 | 6 |
| 24 | t | 6 | 12 | 6 | 12 | 6 | 12 |
| | n_s | 1 | 1 | 3 | 2 | 5 | 3 |
| | k | - | - | - | - | - | - |

| | | | | | | | |
|----|-------|---|----|----|----|----|----|
| 26 | t | 1 | 1 | 1 | 1 | 1 | 1 |
| | n_s | 6 | 12 | 18 | 24 | 30 | 36 |
| | k | 1 | 2 | 3 | 4 | 5 | 6 |
| 28 | t | 2 | 2 | 2 | 2 | 2 | 2 |
| | n_s | 3 | 6 | 9 | 12 | 15 | 18 |
| | k | - | 1 | - | 2 | - | 3 |
| 30 | t | 3 | 3 | 3 | 3 | 15 | 3 |
| | n_s | 2 | 4 | 6 | 8 | 2 | 12 |
| | k | - | - | 1 | - | - | 2 |

Notes:

n_s is an integer multiple of 6 t is even and n_s is an odd multiple of 3

Table 2.4 Feasible phase shift angles for DTP PMSMs with different slot/pole number combinations

| $2p \backslash N_s$ | | 6 | 12 | 18 | 24 | 30 | 36 |
|---------------------|--|----|------|------|---------|------|------------|
| 2 | | 0 | 0/30 | 0/20 | 0/15/30 | 0/12 | 0/10/20/30 |
| 4 | | 0 | 0 | 0 | 0/30 | 0 | 0/20 |
| 6 | | ** | ** | 0 | ** | ** | 0/30 |
| 8 | | 0 | 0 | 0 | 0 | 0 | 0 |
| 10 | | 0 | 0/30 | 0/20 | 0/15/30 | 0 | 0/10/20/30 |
| 12 | | ** | ** | 0 | ** | ** | 0 |
| 14 | | 0 | 0/30 | 0/20 | 0/15/30 | 0/12 | 0/10/20/30 |
| 16 | | 0 | 0 | 0 | 0 | 0 | 0 |
| 18 | | ** | ** | ** | ** | ** | ** |
| 20 | | 0 | 0 | 0 | 0/30 | 0 | 0/20 |
| 22 | | 0 | 0/30 | 0/20 | 0/15/30 | 0/12 | 0/10/20/30 |
| 24 | | ** | ** | 0 | ** | ** | 0 |
| 26 | | 0 | 0/30 | 0/20 | 0/15/30 | 0/12 | 0/10/20/30 |
| 28 | | 0 | 0 | 0 | 0/30 | 0 | 0/20 |
| 30 | | ** | ** | 0 | ** | ** | 0/30 |

Notes:

** Unfeasible slot/pole combinations for DTP PMSMs.

t is even and n_s is an odd multiple of 3

$k = 1$ $k = 2$ $k = 3$ $k = 4$ $k = 5$ $k = 6$

As mentioned before, in the cases when t is even and n_s is an odd multiple of 3, the windings in one electrical periodicity belong to the same winding set and the two winding sets are assigned according to different electrical periodicities. The phase shift angle is always 0° in these cases. In the cases when n_s is an integer multiple of 6, the feasible phase shift angles depend on k , as shown in Table 2.2, and details have been discussed in this sub-section before. The feasible phase shift angles for DTP PMSMs with different slot/pole number combinations are summarized, as shown in Table 2.4. It should be mentioned that as 0° phase shift angle is equivalent to 60° phase shift angle, 60° phase shift angles are not presented in the following tables and analyses.

Overall, for PMSMs with different slot/pole number combinations, the feasibility of DTP winding configuration and all the feasible phase shift angles are summarized in Table 2.3 and Table 2.4. The distribution factors can also be computed based on the slot/pole number combination and the specific phase shift angle.

For the cases when t is even and n_s is an odd multiple of 3, the windings are selected with the same method as that in conventional STP PMSMs and the phase shift angle is 0° . Considering that n_s is odd in these cases, the distribution factor can be calculated as [BIA06a]

$$K_d = \frac{\sin\left(\frac{n_s}{3} \frac{180^\circ}{2n_s}\right)}{\frac{n_s}{3} \sin\left(\frac{180^\circ}{2n_s}\right)} = \frac{3 \sin(30^\circ)}{n_s \sin\left(\frac{90^\circ}{n_s}\right)} \quad (2.5)$$

For the cases when n_s is an integer multiple of 6, i.e., an even multiple of 3, the 0° phase shift angle is always feasible and the distribution factor under this condition can be obtained as

$$K_d = \frac{\sin\left(\frac{n_s}{6} \frac{360^\circ}{2n_s}\right)}{\frac{n_s}{6} \sin\left(\frac{360^\circ}{2n_s}\right)} = \frac{6 \sin(30^\circ)}{n_s \sin\left(\frac{180^\circ}{n_s}\right)} = \frac{\sin(30^\circ)}{k \sin\left(\frac{30^\circ}{k}\right)} \quad (2.6)$$

For the cases when n_s is an integer multiple of 6, the phase shift angle = slot-pitch angle ($360^\circ/n_s$, $60^\circ/k$) it also feasible, the calculation of distribution factor needs considering k is odd or even. When k is odd, the distribution factor is identical to that in the 0° phase shift angle condition, but when k is even, the distribution factor is different from that in the 0° counterpart. Hence, when slot-pitch angle is utilized in the DTP winding configuration, the distribution factor can be calculated as

$$K_d = \begin{cases} \frac{\sin\left(\frac{n_s}{12} \frac{360^\circ}{n_s}\right)}{\frac{n_s}{12} \sin\left(\frac{360^\circ}{n_s}\right)} = \frac{12 \sin(30^\circ)}{n_s \sin\left(\frac{360^\circ}{n_s}\right)} = \frac{2 \sin(30^\circ)}{k \sin\left(\frac{60^\circ}{k}\right)}, & \text{when } k \text{ is even} \\ \frac{\sin\left(\frac{n_s}{6} \frac{360^\circ}{2n_s}\right)}{\frac{n_s}{6} \sin\left(\frac{360^\circ}{2n_s}\right)} = \frac{6 \sin(30^\circ)}{n_s \sin\left(\frac{180^\circ}{n_s}\right)} = \frac{\sin(30^\circ)}{k \sin\left(\frac{30^\circ}{k}\right)}, & \text{when } k \text{ is odd} \end{cases} \quad (2.7)$$

In addition, when n_s is an integer multiple of 12, the 30° phase shift angle is also feasible, and the distribution factor under this condition is

$$K_d = \frac{\sin\left(\frac{n_s}{12} \frac{360^\circ}{2n_s}\right)}{\frac{n_s}{12} \sin\left(\frac{360^\circ}{2n_s}\right)} = \frac{12 \sin(15^\circ)}{n_s \sin\left(\frac{180^\circ}{n_s}\right)} = \frac{2 \sin(15^\circ)}{k \sin\left(\frac{30^\circ}{k}\right)} \quad (2.8)$$

It can also be summarized that when $n_s = 6k$ and k is odd, feasible phase shift angles include 0° and slot-pitch angle $(60^\circ/k)$, and distribution factor is

$$K_d = \frac{\sin\left(\frac{n_s}{6} \frac{360^\circ}{2n_s}\right)}{\frac{n_s}{6} \sin\left(\frac{360^\circ}{2n_s}\right)} = \frac{6 \sin(30^\circ)}{n_s \sin\left(\frac{180^\circ}{n_s}\right)} = \frac{\sin(30^\circ)}{k \sin\left(\frac{30^\circ}{k}\right)} \quad (2.9)$$

When $n_s = 6k$ and k is even, feasible phase shift angles include 0° , 30° and slot-pitch angle $(60^\circ/k)$, and distribution factor is

$$K_d = \begin{cases} \frac{6 \sin(30^\circ)}{n_s \sin\left(\frac{180^\circ}{n_s}\right)} = \frac{\sin(30^\circ)}{k \sin\left(\frac{30^\circ}{k}\right)}, & \text{when } \beta = 0^\circ \\ \frac{12 \sin(30^\circ)}{n_s \sin\left(\frac{360^\circ}{n_s}\right)} = \frac{2 \sin(30^\circ)}{k \sin\left(\frac{60^\circ}{k}\right)}, & \text{when } \beta = \frac{60^\circ}{k} \\ \frac{12 \sin(15^\circ)}{n_s \sin\left(\frac{180^\circ}{n_s}\right)} = \frac{2 \sin(15^\circ)}{k \sin\left(\frac{30^\circ}{k}\right)}, & \text{when } \beta = 30^\circ \end{cases} \quad (2.10)$$

From (2.10), it can be further deduced that when n_s is an integer multiple of 12,

$$\frac{K_d(\beta = 30^\circ)}{K_d(\beta = 0^\circ)} = \frac{2 \sin(15^\circ)}{\sin(30^\circ)} = \frac{1}{\cos(15^\circ)} \approx 1.0353 \quad (2.11)$$

Hence, it can be expected that in DTP PMSMs, when n_s is an integer multiple of 12, both 0° and 30° phase shift angles are feasible, and the DTP winding configuration with 30° phase shift angle can produce higher fundamental back EMF amplitude and hence higher average torque than the counterpart with 0° phase shift angle by about 3.53% due to the improvement in winding factor.

Overall, when t is even and n_s is an odd multiple of 3, the 0° phase shift angle is always feasible. The corresponding distribution factors can be computed based on (2.5), as shown in Table 2.5.

Table 2.5 Feasible phase shift angles and corresponding distribution factors for DTP PMSMs (n_s is an odd multiple of 3)

| n_s | Phase shift angle ($^\circ$) | Distribution factor, K_d |
|-------|--------------------------------|----------------------------|
| 3 | 0 | 1.000 |
| 9 | 0 | 0.960 |
| 15 | 0 | 0.957 |

Based on (2.9) and (2.10), when n_s is an integer multiple of 6, the feasible phase shift angles and corresponding distribution factors are summarized in Table 2.6.

Table 2.6 Feasible phase shift angles and corresponding distribution factors for DTP PMSMs (n_s is an integer multiple of 6)

| n_s | k | Phase shift angle ($^\circ$) | Distribution factor, K_d |
|-------|-----|--------------------------------|----------------------------|
| 6 | 1 | 0 | 1.000 |
| 12 | 2 | 0 | 0.966 |
| | | 30 | 1.000 |
| 18 | 3 | 0 | 0.960 |
| | | 20 | 0.960 |
| 24 | 4 | 0 | 0.958 |
| | | 15 | 0.968 |
| | | 30 | 0.991 |
| 30 | 5 | 0 | 0.957 |
| | | 12 | 0.957 |
| 36 | 6 | 0 | 0.956 |
| | | 10 | 0.960 |
| | | 20 | 0.956 |
| | | 30 | 0.990 |

2.2.3 Pitch Factor and Coil Pitch

In DTP PMSMs, the calculation of pitch factor is the same as that in conventional STP PMSMs. Pitch factor is independent of winding assignments and can be calculated only based on the slot/pole numbers and coil pitch number, y . The diagram of coil-pitch with coil pitch number $= y$ is shown in Fig. 2.20. It can be seen that the coil span angle is $360^\circ \cdot y/N_s$ in mechanical, and hence, for the v -th harmonic, the coil span angle is $360^\circ \cdot vy/N_s$. As the pitch factor is calculated based on the coil span angle. For the v -th harmonic, the pitch factor can be obtained as

$$K_{pv} = \sin\left(\frac{360^\circ vy}{2N_s}\right) = \sin\left(\frac{180^\circ vy}{N_s}\right) \quad (2.12)$$

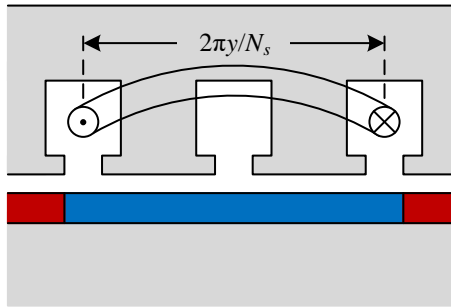


Fig. 2.20 Diagram of pole-pitch and coil-pitch in PMSMs.

Since the working harmonic of the N_s -slot/ $2p$ -pole PMSM is the p -th harmonic, the pitch factor of the working harmonic is

$$K_{pv} = \sin\left(\frac{180^\circ py}{N_s}\right) \quad (2.13)$$

With (2.13), the pitch factors of PMSMs with different slot/pole number combinations considering coil pitch number varying from 1 to 4 are listed in Table 2.7. In the table, the pitch factors higher than 0.866 ($\cos 30^\circ$) are marked with pink background. It should be mentioned that as the feasibility of DTP winding configuration is not considered in the calculation of pitch factor, some cells in Table 2.7 are zero, which suggests that the specific combinations of slot, pole and coil-pitch are unfeasible.

Table 2.7 Pitch factors (K_p) of PMSMs with different slot/pole number combinations and different coil pitch numbers

| $2p \backslash N_s$ | 6 | 12 | 18 | 24 | 30 | 36 |
|---------------------|-------|-------|-------|-------|-------|-------|
| $y = 1$ | | | | | | |
| 2 | 0.500 | 0.259 | 0.174 | 0.131 | 0.105 | 0.087 |
| 4 | 0.866 | 0.500 | 0.342 | 0.259 | 0.208 | 0.174 |
| 6 | 1.000 | 0.707 | 0.500 | 0.383 | 0.309 | 0.259 |
| 8 | 0.866 | 0.866 | 0.643 | 0.500 | 0.407 | 0.342 |
| 10 | 0.500 | 0.966 | 0.766 | 0.609 | 0.500 | 0.423 |
| 12 | 0.000 | 1.000 | 0.866 | 0.707 | 0.588 | 0.500 |
| 14 | 0.500 | 0.966 | 0.940 | 0.793 | 0.669 | 0.574 |
| 16 | 0.866 | 0.866 | 0.985 | 0.866 | 0.743 | 0.643 |
| 18 | 1.000 | 0.707 | 1.000 | 0.924 | 0.809 | 0.707 |
| 20 | 0.866 | 0.500 | 0.985 | 0.966 | 0.866 | 0.766 |
| 22 | 0.500 | 0.259 | 0.940 | 0.991 | 0.914 | 0.819 |
| 24 | 0.000 | 0.000 | 0.866 | 1.000 | 0.951 | 0.866 |
| 26 | 0.500 | 0.259 | 0.766 | 0.991 | 0.978 | 0.906 |
| 28 | 0.866 | 0.500 | 0.643 | 0.966 | 0.995 | 0.940 |
| 30 | 1.000 | 0.707 | 0.500 | 0.924 | 1.000 | 0.966 |
| $y = 2$ | | | | | | |
| 2 | 0.866 | 0.500 | 0.342 | 0.259 | 0.208 | 0.174 |
| 4 | 0.866 | 0.866 | 0.643 | 0.500 | 0.407 | 0.342 |
| 6 | 0.000 | 1.000 | 0.866 | 0.707 | 0.588 | 0.500 |
| 8 | 0.866 | 0.866 | 0.985 | 0.866 | 0.743 | 0.643 |
| 10 | 0.866 | 0.500 | 0.985 | 0.966 | 0.866 | 0.766 |
| 12 | 0.000 | 0.000 | 0.866 | 1.000 | 0.951 | 0.866 |
| 14 | 0.866 | 0.500 | 0.643 | 0.966 | 0.995 | 0.940 |
| 16 | 0.866 | 0.866 | 0.342 | 0.866 | 0.995 | 0.985 |
| 18 | 0.000 | 1.000 | 0.000 | 0.707 | 0.951 | 1.000 |
| 20 | 0.866 | 0.866 | 0.342 | 0.500 | 0.866 | 0.985 |
| 22 | 0.866 | 0.500 | 0.643 | 0.259 | 0.743 | 0.940 |
| 24 | 0.000 | 0.000 | 0.866 | 0.000 | 0.588 | 0.866 |
| 26 | 0.866 | 0.500 | 0.985 | 0.259 | 0.407 | 0.766 |
| 28 | 0.866 | 0.866 | 0.985 | 0.500 | 0.208 | 0.643 |
| 30 | 0.000 | 1.000 | 0.866 | 0.707 | 0.000 | 0.500 |

Continued on next page

| $y = 3$ | | | | | | |
|---------|-------|-------|-------|-------|-------|-------|
| 2 | 1.000 | 0.707 | 0.500 | 0.383 | 0.309 | 0.259 |
| 4 | 0.000 | 1.000 | 0.866 | 0.707 | 0.588 | 0.500 |
| 6 | 1.000 | 0.707 | 1.000 | 0.924 | 0.809 | 0.707 |
| 8 | 0.000 | 0.000 | 0.866 | 1.000 | 0.951 | 0.866 |
| 10 | 1.000 | 0.707 | 0.500 | 0.924 | 1.000 | 0.966 |
| 12 | 0.000 | 1.000 | 0.000 | 0.707 | 0.951 | 1.000 |
| 14 | 1.000 | 0.707 | 0.500 | 0.383 | 0.809 | 0.966 |
| 16 | 0.000 | 0.000 | 0.866 | 0.000 | 0.588 | 0.866 |
| 18 | 1.000 | 0.707 | 1.000 | 0.383 | 0.309 | 0.707 |
| 20 | 0.000 | 1.000 | 0.866 | 0.707 | 0.000 | 0.500 |
| 22 | 1.000 | 0.707 | 0.500 | 0.924 | 0.309 | 0.259 |
| 24 | 0.000 | 0.000 | 0.000 | 1.000 | 0.588 | 0.000 |
| 26 | 1.000 | 0.707 | 0.500 | 0.924 | 0.809 | 0.259 |
| 28 | 0.000 | 1.000 | 0.866 | 0.707 | 0.951 | 0.500 |
| 30 | 1.000 | 0.707 | 1.000 | 0.383 | 1.000 | 0.707 |
| $y = 4$ | | | | | | |
| 2 | 0.866 | 0.866 | 0.643 | 0.500 | 0.407 | 0.342 |
| 4 | 0.866 | 0.866 | 0.985 | 0.866 | 0.743 | 0.643 |
| 6 | 0.000 | 0.000 | 0.866 | 1.000 | 0.951 | 0.866 |
| 8 | 0.866 | 0.866 | 0.342 | 0.866 | 0.995 | 0.985 |
| 10 | 0.866 | 0.866 | 0.342 | 0.500 | 0.866 | 0.985 |
| 12 | 0.000 | 0.000 | 0.866 | 0.000 | 0.588 | 0.866 |
| 14 | 0.866 | 0.866 | 0.985 | 0.500 | 0.208 | 0.643 |
| 16 | 0.866 | 0.866 | 0.643 | 0.866 | 0.208 | 0.342 |
| 18 | 0.000 | 0.000 | 0.000 | 1.000 | 0.588 | 0.000 |
| 20 | 0.866 | 0.866 | 0.643 | 0.866 | 0.866 | 0.342 |
| 22 | 0.866 | 0.866 | 0.985 | 0.500 | 0.995 | 0.643 |
| 24 | 0.000 | 0.000 | 0.866 | 0.000 | 0.951 | 0.866 |
| 26 | 0.866 | 0.866 | 0.342 | 0.500 | 0.743 | 0.985 |
| 28 | 0.866 | 0.866 | 0.342 | 0.866 | 0.407 | 0.985 |
| 30 | 0.000 | 0.000 | 0.866 | 1.000 | 0.000 | 0.866 |

Based on (2.13) and Table 2.7, the optimized coil pitch number for PMSMs with different slot/pole number combinations can be obtained from the view of pitch factor, as shown in Table 2.8. It can be seen that the optimized coil pitch number is around $(N_s/2p)$ in terms of slot-pitch. It also should be mentioned that considering the relatively shorter end-winding lengths in concentrated windings, for the conditions with $2p > N_s$, the optimized coil pitch numbers are all selected as 1 in the table.

Table 2.8 Optimized coil pitch numbers for PMSMs with different slot/pole number combinations

| $2p \backslash N_s$ | 6 | 12 | 18 | 24 | 30 | 36 |
|---------------------|---|----|----|----|----|----|
| 2 | 3 | 6 | 9 | 12 | 15 | 18 |
| 4 | 1 | 3 | 4 | 6 | 7 | 9 |
| 6 | 1 | 2 | 3 | 4 | 5 | 6 |
| 8 | 1 | 1 | 2 | 3 | 4 | 4 |
| 10 | 1 | 1 | 2 | 2 | 3 | 4 |
| 12 | 1 | 1 | 1 | 2 | 2 | 3 |
| 14 | 1 | 1 | 1 | 2 | 2 | 3 |
| 16 | 1 | 1 | 1 | 1 | 2 | 2 |
| 18 | 1 | 1 | 1 | 1 | 2 | 2 |
| 20 | 1 | 1 | 1 | 1 | 1 | 2 |
| 22 | 1 | 1 | 1 | 1 | 1 | 2 |
| 24 | 1 | 1 | 1 | 1 | 1 | 1 |
| 26 | 1 | 1 | 1 | 1 | 1 | 1 |
| 28 | 1 | 1 | 1 | 1 | 1 | 1 |
| 30 | 1 | 1 | 1 | 1 | 1 | 1 |

Notes:

$y = 1$
 $y = 2$
 $y = 3$
 $y = 4$

With the optimized coil pitch numbers given in Table 2.8, the pitch factors for different slot/pole number combinations are shown in Table 2.9. The pitch factors higher than 0.966 ($\cos 15^\circ$) are marked with pink background.

Table 2.9 Pitch factors (K_p) of PMSMs with different slot/pole number combinations and different coil pitch numbers

| $2p \backslash N_s$ | 6 | 12 | 18 | 24 | 30 | 36 |
|---------------------|-------|-------|-------|-------|-------|-------|
| 2 | 1.000 | 1.000 | 1.000 | 1.000 | 1.000 | 1.000 |
| 4 | 0.866 | 1.000 | 0.985 | 1.000 | 0.995 | 1.000 |
| 6 | 1.000 | 1.000 | 1.000 | 1.000 | 1.000 | 1.000 |
| 8 | 0.866 | 0.866 | 0.985 | 1.000 | 0.995 | 0.985 |
| 10 | 0.500 | 0.966 | 0.985 | 0.966 | 1.000 | 0.985 |
| 12 | 0.000 | 1.000 | 0.866 | 1.000 | 0.951 | 1.000 |
| 14 | 0.500 | 0.966 | 0.940 | 0.966 | 0.995 | 0.966 |
| 16 | 0.866 | 0.866 | 0.985 | 0.866 | 0.995 | 0.985 |
| 18 | 1.000 | 0.707 | 1.000 | 0.924 | 0.951 | 1.000 |
| 20 | 0.866 | 0.500 | 0.985 | 0.966 | 0.866 | 0.985 |
| 22 | 0.500 | 0.259 | 0.940 | 0.991 | 0.914 | 0.940 |
| 24 | 0.000 | 0.000 | 0.866 | 1.000 | 0.951 | 0.866 |
| 26 | 0.500 | 0.259 | 0.766 | 0.991 | 0.978 | 0.906 |
| 28 | 0.866 | 0.500 | 0.643 | 0.966 | 0.995 | 0.940 |
| 30 | 1.000 | 0.707 | 0.500 | 0.924 | 1.000 | 0.966 |

However, it still should be noticed that the optimized coil pitch numbers and pitch factors shown in Table 2.8 and Table 2.9 are selected from the view of enhancing pitch factors only. In practice, it is usually preferred to use lower coil pitch number, because the short-pitched windings can shorten end-winding length and reduce high order MMF harmonics. For example, $y = 1$ is selected for the 24-slot/14-pole PMSM in [ZHU19] (fractional-slot concentrated windings), and $y = 5$ is selected for the 48-slot/8-pole Prius 2010 machine (integer-slot distributed windings). Hence, it is necessary to consider coil pitch number thoughtfully in the design of DTP PMSMs.

2.2.4 Resultant Winding Factor

Based on the analyses above, for PMSMs with different slot/pole number combinations, all the feasible phase shift angles and corresponding winding factors are summarized in Table 2.10.

Table 2.10 Feasible phase shift angles and corresponding winding factors for DTP PMSMs with different slot/pole number combinations and optimized coil pitch numbers

| $N_s \backslash 2p$ | 6 | | 12 | | 18 | | 24 | | 30 | | 36 | |
|---------------------|-------------------|-------|-------------------|-------|-------------------|-------|-------------------|-------|-------------------|-------|-------------------|-------|
| | $\beta(^{\circ})$ | K_w | $\beta(^{\circ})$ | K_w | $\beta(^{\circ})$ | K_w | $\beta(^{\circ})$ | K_w | $\beta(^{\circ})$ | K_w | $\beta(^{\circ})$ | K_w |
| 2 | 0 | 1.000 | 0 | 0.966 | 0/20 | 0.960 | 0 | 0.958 | 0/12 | 0.957 | 0/20 | 0.956 |
| | | | 30 | 1.000 | | | 15 | 0.966 | | | 10 | 0.960 |
| | | | | | | | 30 | 0.991 | | | 30 | 0.990 |
| 4 | 0 | 0.866 | 0 | 1.000 | 0 | 0.945 | 0 | 0.966 | 0 | 0.951 | 0/20 | 0.960 |
| | | | | | | | 30 | 1.000 | | | | |
| 6 | ** | | ** | | 0 | 1.000 | ** | | ** | | 0 | 0.966 |
| | | | | | | | | | | | 30 | 1.000 |
| 8 | 0 | 0.866 | 0 | 0.866 | 0 | 0.945 | 0 | 1.000 | 0 | 0.951 | 0 | 0.945 |
| 10 | 0 | 0.500 | 0 | 0.933 | 0/20 | 0.945 | 0 | 0.925 | 0 | 1.000 | 0/20 | 0.942 |
| | | | 30 | 0.966 | | | 15 | 0.933 | | | 10 | 0.945 |
| | | | | | | | 30 | 0.958 | | | 30 | 0.975 |
| 12 | ** | | ** | | 0 | 0.866 | ** | | ** | | 0 | 1.000 |
| 14 | 0 | 0.500 | 0 | 0.966 | 0/20 | 0.902 | 0 | 0.925 | 0/12 | 0.951 | 0/20 | 0.924 |
| | | | 30 | 0.966 | | | 15 | 0.933 | | | 10 | 0.927 |
| | | | | | | | 30 | 0.958 | | | 30 | 0.956 |
| 16 | 0 | 0.866 | 0 | 0.866 | 0 | 0.945 | 0 | 0.866 | 0 | 0.951 | 0 | 0.945 |
| 18 | ** | | ** | | ** | | ** | | ** | | ** | |
| 20 | 0 | 0.866 | 0 | 0.500 | 0 | 0.945 | 0 | 0.933 | 0 | 0.866 | 0/20 | 0.945 |
| | | | | | | | 30 | 0.966 | | | | |
| 22 | 0 | 0.500 | 0 | 0.250 | 0/20 | 0.902 | 0 | 0.949 | 0/12 | 0.874 | 0/20 | |
| | | | 30 | 0.259 | | | 15 | 0.958 | | | 10 | |
| | | | | | | | 30 | 0.983 | | | 30 | |
| 24 | ** | | ** | | 0 | 0.866 | ** | | ** | | 0 | 0.866 |
| 26 | 0 | 0.500 | 0 | 0.250 | 0/20 | 0.735 | 0 | 0.949 | 0/12 | 0.936 | 0/20 | 0.867 |
| | | | 30 | 0.259 | | | 15 | 0.958 | | | 10 | 0.870 |
| | | | | | | | 30 | 0.983 | | | 30 | 0.897 |
| 28 | 0 | 0.866 | 0 | 0.500 | 0 | 0.617 | 0 | 0.933 | 0 | 0.951 | 0/20 | 0.902 |
| | | | | | | | 30 | 0.966 | | | | |
| 30 | ** | | ** | | 0 | 0.500 | ** | | ** | | 0 | 0.933 |
| | | | | | | | | | | | 30 | 0.966 |

Notes:

** Unfeasible slot/pole combinations for DTP PMSMs.

 t is even and N_s is an odd multiple of 3

 $k = 1$ $k = 2$ $k = 3$ $k = 4$ $k = 5$ $k = 6$

In summary, in Section 2.2, the winding assignments and winding factors of DTP winding configurations in PMSMs are investigated systemically based on the star of slots. Different slot/pole number combinations, different phase shift angles, and different coil pitch numbers are all considered. For a PMSM with any slot/pole number combination, the feasible phase shift angles and corresponding winding layouts and distribution factors can be obtained from sub-section 2.2.2. The optimized coil pitch number and corresponding pitch factor are shown in sub-section 2.2.3. Subsection 2.2.4 provides a comprehensive table, including the feasible phase shift angles and corresponding winding factors for different slot/pole number combinations. Thus, the potentials of different DTP winding configurations can be quickly compared from the view of winding factors based on Table 2.10.

2.3 Attenuation Factor for Two Three-Phase Winding Sets

2.3.1 Attenuation Factor Caused by Spatial Shifting

In Section 2.2, the winding layouts of DTP winding configuration in PMSMs are obtained from the star of slots to enhance the winding factor of the working harmonic. In fact, the two winding sets in DTP PMSMs can also be distributed according to the concept of “stator shifting”. In [DAJ11], it is introduced that the process to realize stator shifting contains the steps below:

- Divide the original windings into two separate winding sets;
- Both windings are identical and supplied by identical currents;
- The second winding set is shifted mechanically for a specific angle referred to the first winding set.

Hence, when utilizing stator shifting in PMSMs, the two winding sets are shifted in spatial, but fed with identical currents without time shifting. When the two winding sets are connected in series, and supplied by one inverter, the PMSM is still a STP PMSM. When the two winding sets are supplied by two separate inverters, the whole windings can be seen as DTP windings with phase shift angle = 0° . In [RED14], the effects of stator shifting on the resultant stator MMF harmonics are investigated in detail, and the effects of the spatial shifting on different MMF harmonics are explained by the “attenuation factor”, K_a . For the ν -th harmonic, the final winding factor considering spatial shifting is $K_{w\nu-final}$,

$$K_{wv-final} = K_{wv-initial} \cdot K_{av} \quad (2.14)$$

where $K_{wv-initial}$ is the initial winding factor of the v -th harmonic in one winding set, and K_{av} is the attenuation factor of the v -th harmonic.

Assuming that the magnitudes of the v -th harmonics of Windings 1 and 2 are F_{v1} and F_{v2} respectively, since the two winding sets are identical in winding configurations, it can be obtained that

$$|F_{v1}| = |F_{v2}| \quad (2.15)$$

The resultant v -th MMF component of the whole windings, F_v , is the vectorial sum of F_{v1} and F_{v2} :

$$\vec{F}_v = \vec{F}_{v1} + \vec{F}_{v2} \quad (2.16)$$

Assuming that the spatial shifting angle between the two winding sets is α , in electric degree. For the v -th MMF components, the spatial shifting angle is $v\alpha$ in electric degree. Hence, the relationship between F_v , F_{v1} , and F_{v2} can be reflected geometrically in Fig. 2.21.

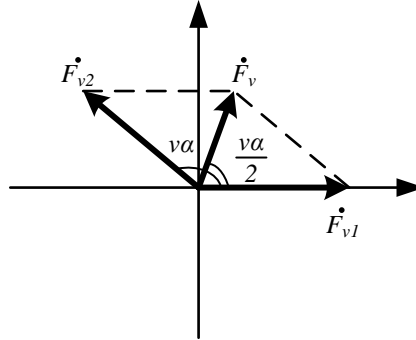


Fig. 2.21 Geometrical relationship between the v -th MMF components of different winding sets in PMSM with spatial shifting angle $= \alpha$.

From Fig. 2.21, the attenuation factor for the v -th MMF components, K_{av} , can be obtained as the ratio of the vectorial sum of F_{v1} and F_{v2} to the arithmetic sum of F_{v1} and F_{v2} , as

$$K_{av} = \frac{|\vec{F}_{v1} + \vec{F}_{v2}|}{|F_{v1}| + |F_{v2}|} = \frac{2 \left| \cos\left(\frac{v\alpha}{2}\right) \right| |F_{v1}|}{2|F_{v1}|} = \left| \cos\left(\frac{v\alpha}{2}\right) \right| \quad (2.17)$$

Thus, in PMSMs with spatial shifted windings, the attenuation factors for different MMF harmonics can be computed based on spatial shifting angle using (2.17). The variations of the attenuation factors of the 1st, 5th, and 7th MMF harmonics with spatial shifting angle are provided in Fig. 2.22 as examples.

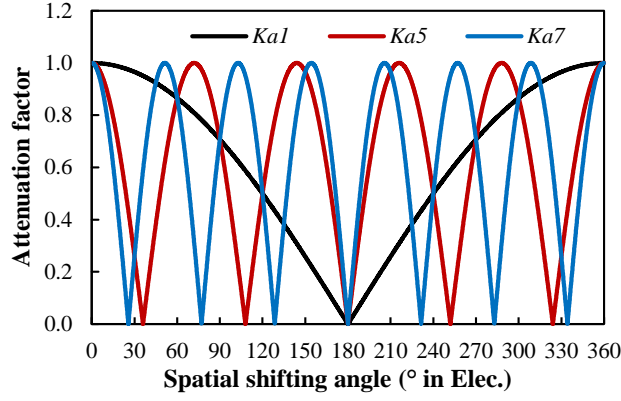
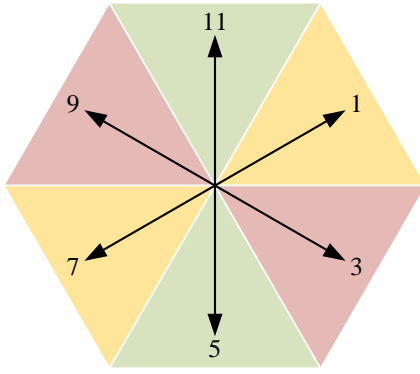


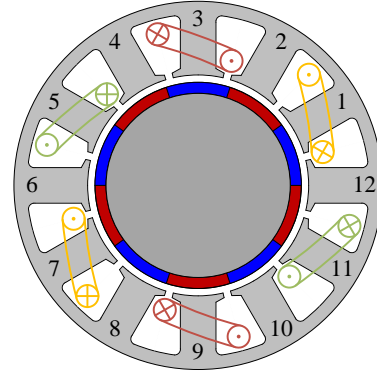
Fig. 2.22 Variations of attenuation factors of different MMF harmonic orders with spatial shifting angle.

It can be observed from Fig. 2.22 that when a proper spatial shifting angle is selected, it is feasible to minimize the non-working harmonics without much sacrifice on the working harmonic. For example, when the 5th harmonic is the working harmonic, the spatial shifting angle can be set as 77.14°. When $\alpha = 77.14^\circ$, $K_{a5} = 0.975$ and $K_{a7} = 0$, and hence the 7th harmonics of the two winding sets can be cancelled completely, while the 5th harmonics are reduced by only 2.5%. When the 7th harmonic is the working harmonic, the spatial shifting angle can be set as 108°, with which $K_{a5} = 0$ and $K_{a7} = 0.951$. The 5th harmonics are cancelled completely, while the 7th harmonics are reduced by only 4.9% under this condition.

However, it should be mentioned that the actual spatial shifting angle between the two winding sets is usually limited by the number of slots and the stator configuration. For example, the 77.14° spatial shifting is selected to reduce the 7th harmonics in the 24-slot/10-pole PMSM in [DAJ11], but to achieve the 77.14° spatial shifting, the stator teeth widths are unequal. Another example is given based on the 12-slot/10-pole PMSM. For the 12-slot/10-pole PMSM with double-layer windings, the whole armature windings can be seen as composed by two single-layer winding sets with a specific spatial shifting angle. The first winding set can be designed based on the star of slots, as shown in Fig. 2.23. Based on the first winding set shown Fig. 2.23 (b), the second single-layer three-phase winding set can be arranged using different spatial shifting angles, as presented in Fig. 2.24. As the stator teeth widths are identical in the machine, the spatial shifting angle (α) can only be chosen from 30°, 90°, and 150°.

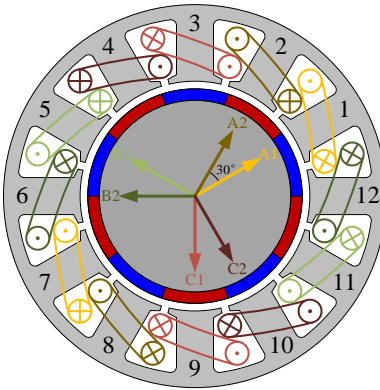


(a) Star of slots

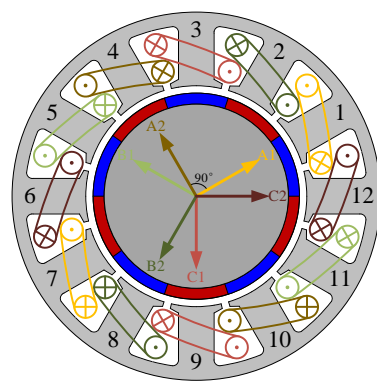


(b) Winding layouts

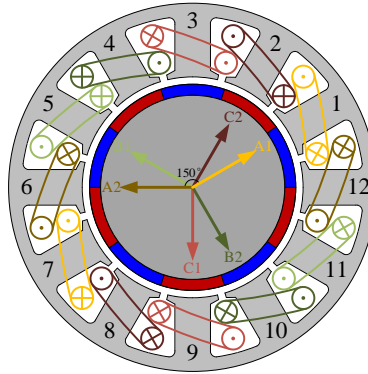
Fig. 2.23 Star of slots and winding layouts of 12-slot/10-pole PMSM with single layer three-phase windings.



(a) $\alpha = 30^\circ$



(b) $\alpha = 90^\circ$



(c) $\alpha = 150^\circ$

Fig. 2.24 Winding layouts of 12-slot/10-pole PMSM with two sets of single-layer three-phase windings using different spatial shifting angles.

From Fig. 2.22, the attenuation factors of the 1st, 5th, and 7th harmonics with $\alpha = 30^\circ$, 90° , and 150° can be obtained, as summarised in Table 2.11. It can be seen that to enhance the working harmonic (the 5th harmonic), the 150° spatial shifting should be selected among 30° , 90° , and 150° candidates.

Table 2.11 Attenuation factors of 1st, 5th, and 7th harmonics in 12-slot/10-pole PMSM with different spatial shifting angles

| Spatial shifting angle, α ($^\circ$ in Elec.) | 30 | 90 | 150 |
|---|-------|-------|--------------|
| K_{a1} | 0.966 | 0.707 | 0.259 |
| K_{a5} | 0.259 | 0.707 | 0.966 |
| K_{a7} | 0.259 | 0.707 | 0.966 |

2.3.2 Attenuation Factor Caused by Spatial and Time Shifting

In the 12-slot/10-pole PMSM, it should be noticed that when choosing spatial shifting angle = 150° , the resultant winding layouts is shown in Fig. 2.24 (c), which looks identical to that shown in Fig. 2.10 (DTP windings with phase shift angle = 30°). In fact, the DTP winding configurations with phase shift angle = 30° shown in Fig. 2.10 is composed by two three-phase windings, and the two winding sets are shifted by 150° in spatial and 30° in time. Hence, it is still necessary to further investigate the effects of spatial and time shifting angles on the resultant MMF production. In [CHE14a], a generic approach to calculate MMF in PMSMs with multiple three-phase winding sets was introduced. Based on [CHE14a], the concept “attenuation factor” is extended by considering spatial and time shifting angles simultaneously in this sub-section.

The MMF acting across the air gap produced by Winding 1 can be obtained as

$$F_1(\theta, t) = N_{A1}(\theta)i_{A1}(t) + N_{B1}(\theta)i_{B1}(t) + N_{C1}(\theta)i_{C1}(t) \quad (2.18)$$

where $N_{A1}(\theta)$, $N_{B1}(\theta)$, and $N_{C1}(\theta)$ are the turn functions of the PMSM, $i_{A1}(t)$, $i_{B1}(t)$ and $i_{C1}(t)$ are the currents fed in the three-phase winding set. With the utilization of winding factor, the windings are seen as full-pitch windings, and thus, the winding turn function and phase current of Phase A1 are shown in Fig. 2.25.

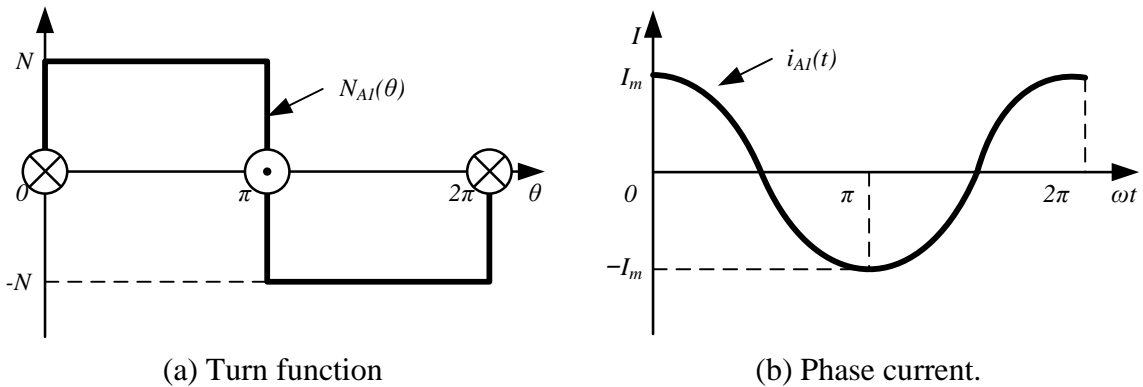


Fig. 2.25 Winding turn function and current of Phase A1.

From Fig. 2.25, the Fourier series of the winding turn functions of Phase A1, B1 and C1 can be expressed as

$$\begin{aligned} N_{A1}(\theta) &= \sum_{v=1,3,5,\dots}^{\infty} \frac{4N}{v\pi} \sin(v\theta) \\ N_{B1}(\theta) &= \sum_{v=1,3,5,\dots}^{\infty} \frac{4N}{v\pi} \sin\left[v\left(\theta + \frac{2\pi}{3}\right)\right] \\ N_{C1}(\theta) &= \sum_{v=1,3,5,\dots}^{\infty} \frac{4N}{v\pi} \sin\left[v\left(\theta - \frac{2\pi}{3}\right)\right] \end{aligned} \quad (2.19)$$

where N is the number of turns per coil, and θ is the rotor position.

Since Winding 1 is fed with balanced three-phase sinusoidal currents, i.e.

$$\begin{aligned} i_{A1}(t) &= I_m \cos(\omega t) \\ i_{B1}(t) &= I_m \cos\left(\omega t - \frac{2\pi}{3}\right) \\ i_{C1}(t) &= I_m \cos\left(\omega t + \frac{2\pi}{3}\right) \end{aligned} \quad (2.20)$$

where I_m is the peak value of phase currents, ω , t are the fundamental radian frequency and the time.

In a balanced three-phase winding set, MMF components rotate clockwise and anti-clockwise according to harmonic order. To be more specific, for the v -harmonics with $v = 1, 7, 13, 19, (6k+1, k \text{ is a natural number}) \dots$, the MMF rotates clockwise, and for the v -harmonics with $v = 5, 11, 17, (6k-1, k \text{ is a positive integer}) \dots$, the MMF rotates anti-clockwise. By using a negative number to denote negative rotation direction, the resultant MMF produced by Winding 1 can be expressed as

$$F_1(\theta, t) = \frac{6NI_m}{\pi} \sum_{v=1,-5,7,\dots}^{\infty} \frac{k_{wv}}{v} \sin(v\theta - \omega t) \quad (2.21)$$

where K_{wv} is the initial winding factor for the v -th harmonic in Winding 1.

For the second three-phase winding set in the DTP PMSM, the spatial and time shifting angles are illustrated in Fig. 2.25. It can be seen that Winding 2 leads Winding 1 by α in space, and the currents in Winding 2 are advanced than those in Winding 1 by β in time.

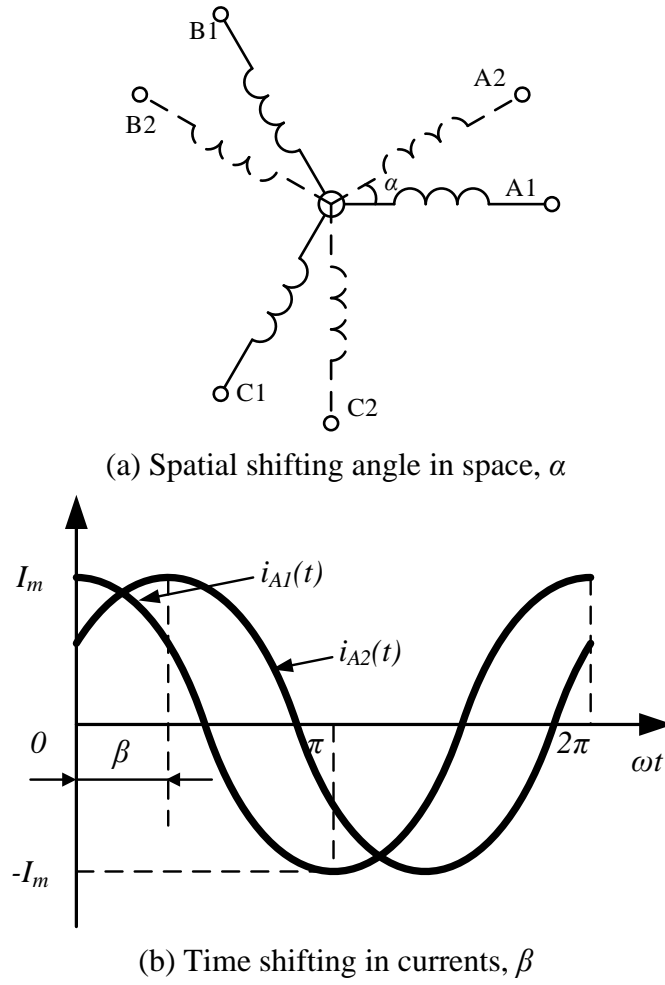


Fig. 2.26 Scheme of space and time displacements between two 3-phase winding sets.

According to (2.21) and the spatial and time displacements shown in Fig. 2.26, the resultant MMF produced by Winding 2 can be expressed as

$$F_2(\theta, t) = \frac{6NI_m}{\pi} \sum_{v=1, -5, 7, \dots}^{\infty} \frac{k_{wv}}{v} \sin[v(\theta + \alpha) - (\omega t - \beta)] \quad (2.22)$$

Therefore, the overall MMF along the air gap is the sum of those produced by Winding 1 and Winding 2, as

$$\begin{aligned} F(\theta, t) &= F_1(\theta, t) + F_2(\theta, t) \\ &= \frac{6NI_m}{\pi} \sum_{v=1, -5, 7, \dots}^{\infty} \frac{k_{wv}}{v} \{\sin(v\theta - \omega t) + \sin[v(\theta + \alpha) - (\omega t + \beta)]\} \\ &= \frac{6NI_m}{\pi} \sum_{v=1, -5, 7, \dots}^{\infty} \frac{k_{wv}}{v} [\sin(v\theta - \omega t) + \sin(v\theta - \omega t + v\alpha + \beta)] \end{aligned} \quad (2.23)$$

In (2.23), it can be obtained that the resultant ν -th MMF component in the DTP PMSM can be calculated as

$$\begin{aligned}
F_\nu(\theta, t) &= F_{\nu 1}(\theta, t) + F_{\nu 2}(\theta, t) \\
&= \frac{6NI_m k_{w\nu}}{\pi} \frac{1}{\nu} [\sin(\nu\theta - \omega t) + \sin(\nu\theta - \omega t + \nu\alpha + \beta)] \\
&= \frac{6NI_m k_{w\nu}}{\pi} \frac{1}{\nu} [\sin(\nu\theta - \omega t) + \sin(\nu\theta - \omega t) \cos(\nu\alpha + \beta) \\
&\quad + \cos(\nu\theta - \omega t) \sin(\nu\alpha + \beta)] \\
&= \frac{6NI_m k_{w\nu}}{\pi} \frac{1}{\nu} \left\{ \sin(\nu\theta - \omega t) \left[\sin^2\left(\frac{\nu\alpha + \beta}{2}\right) + \cos^2\left(\frac{\nu\alpha + \beta}{2}\right) \right. \right. \\
&\quad \left. \left. + \cos^2\left(\frac{\nu\alpha + \beta}{2}\right) - \sin^2\left(\frac{\nu\alpha + \beta}{2}\right) \right] + \cos(\nu\theta - \omega t) \right. \\
&\quad \left. \cdot 2 \sin\left(\frac{\nu\alpha + \beta}{2}\right) \cos\left(\frac{\nu\alpha + \beta}{2}\right) \right\} \tag{2.24} \\
&= \frac{6NI_m k_{w\nu}}{\pi} \frac{1}{\nu} \left[\sin(\nu\theta - \omega t) \cdot 2 \cos^2\left(\frac{\nu\alpha + \beta}{2}\right) + \cos(\nu\theta - \omega t) \right. \\
&\quad \left. \cdot 2 \sin\left(\frac{\nu\alpha + \beta}{2}\right) \cos\left(\frac{\nu\alpha + \beta}{2}\right) \right] \\
&= \frac{6NI_m k_{w\nu}}{\pi} \frac{1}{\nu} 2 \cos\left(\frac{\nu\alpha + \beta}{2}\right) \\
&\quad \cdot \left[\sin(\nu\theta - \omega t) \cos\left(\frac{\nu\alpha + \beta}{2}\right) + \cos(\nu\theta - \omega t) \sin\left(\frac{\nu\alpha + \beta}{2}\right) \right] \\
&= \frac{6NI_m k_{w\nu}}{\pi} \frac{1}{\nu} 2 \cos\left(\frac{\nu\alpha + \beta}{2}\right) \sin\left(\nu\theta - \omega t + \frac{\nu\alpha + \beta}{2}\right)
\end{aligned}$$

The resultant ν -th MMF component of the two winding sets obtained in (2.24) can also be expressed as

$$F_\nu(\theta, t) = \frac{6(2N)I_m k_{w\nu} \cos\left(\frac{\nu\alpha + \beta}{2}\right)}{\pi} \frac{1}{\nu} \sin\left[\nu\left(\theta + \frac{\alpha}{2}\right) - \left(\omega t - \frac{\beta}{2}\right)\right] \tag{2.25}$$

Meanwhile, according to (2.21), the ν -th MMF component produced by Winding 1 is

$$F_{\nu 1}(\theta, t) = \frac{6NI_m k_{w\nu}}{\pi} \frac{1}{\nu} \sin(\nu\theta - \omega t) \tag{2.26}$$

Hence, with spatial and time shifting angles simultaneously, the attenuation factor of the ν -th MMF harmonic can be calculated as

$$K_{av} = \frac{|\dot{F}_{\nu 1} + \dot{F}_{\nu 2}|}{|\dot{F}_{\nu 1}| + |\dot{F}_{\nu 2}|} = \frac{|\dot{F}_\nu|}{2|\dot{F}_{\nu 1}|} = \frac{\left| 2k_{w\nu} \cos\left(\frac{\nu\alpha + \beta}{2}\right) \right|}{2|k_{w\nu}|} = \left| \cos\left(\frac{\nu\alpha + \beta}{2}\right) \right| \tag{2.27}$$

In (2.27), it can be seen that both spatial shifting angle, α , and time shifting angle, β , are taken into consideration in the attenuation factor. In practice, the time shifting angle between the two winding sets is usually obtained according to the spatial shifting between the two winding sets. To be more specific, to enhance the winding factor of the working harmonic, the time shifting angle is set as the advancing angle of Winding 2 to Winding 1. For example, for the 12-slot/10-pole PMSM with spatial shifting angle = 30° , 90° , and 150° , as presented in Fig. 2.24, the stars of slots for the 5th harmonic (working harmonic) are shown in Fig. 2.27. For the case with spatial shifting angle, α , is 30° , the time shifting angle, β , should be the advancing angle of Spoke 2 (Phase A2) to Spoke 1 (Phase A1), which is 150° . Similarly, for the case when α is 90° , β is 90° ; and when α is 150° , β is 30° , respectively.

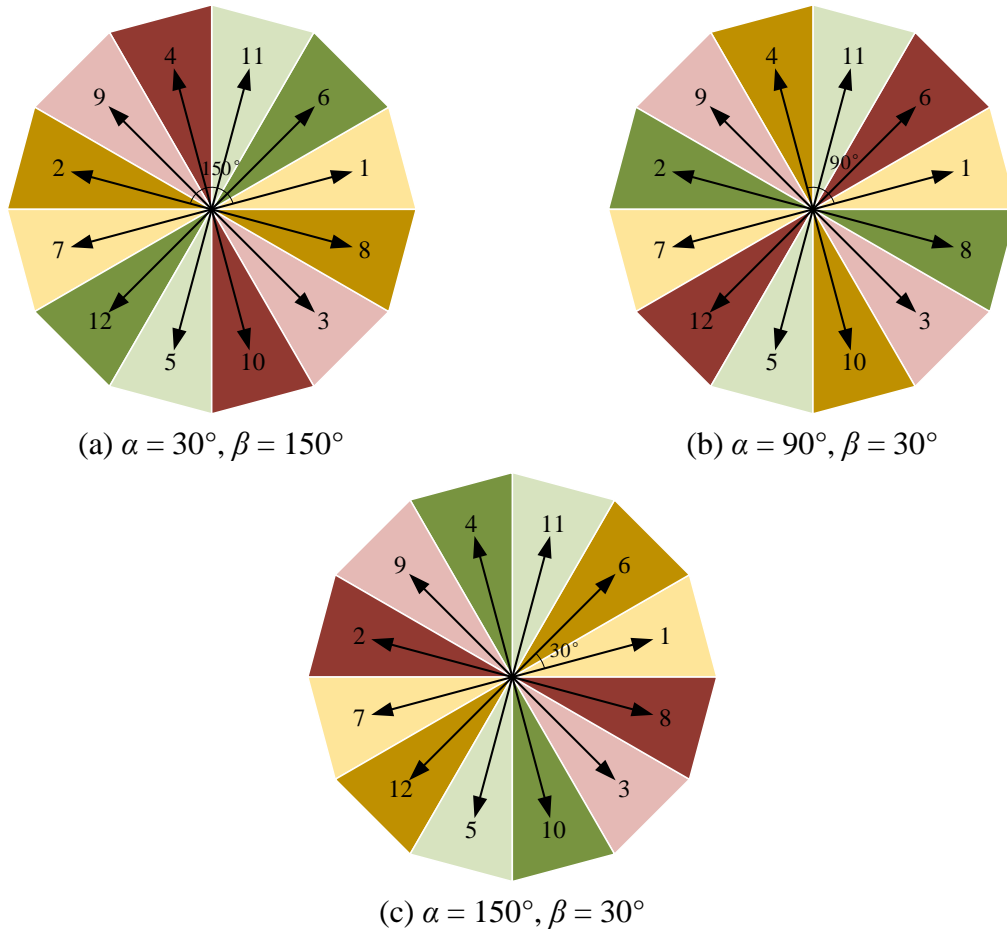


Fig. 2.27 Winding layouts of 12-slot/10-pole PMSM with two sets of single-layer three-phase windings using different spatial shifting angles.

Thus, in the 12-slot/10-pole PMSM with two winding sets, when the spatial and time shifting angles vary, the resultant attenuation factor can be calculated as summarized in Table 2.12. For any harmonic order, when $K_{av} = 0$, the corresponding harmonic order will be eliminated under

this condition. From Table 2.12, it can be seen that the DTP winding configurations with both spatial and time shifting angles can eliminate some MMF harmonic contents effectively without any sacrifice on working harmonic order.

Table 2.12 Attenuation factors of different harmonics in 12-slot/10-pole DTP PMSM with different spatial and time shifting angles

| Spatial shifting angle, α (° in Elec.) | 30 | | 90 | | 150 | |
|--|--|-------|-------|-------|-------|-------|
| Time shifting angle, β (° in Elec.) | 0 | 150 | 0 | 90 | 0 | 30 |
| Harmonic order, ν | Attenuation factor, $K_{av} = \left \cos\left(\frac{\nu\alpha+\beta}{2}\right) \right $ | | | | | |
| 1 | 0.966 | 0.000 | 0.707 | 0.000 | 0.259 | 0.000 |
| -5 | 0.259 | 1.000 | 0.707 | 1.000 | 0.966 | 1.000 |
| 7 | 0.259 | 1.000 | 0.707 | 1.000 | 0.966 | 1.000 |
| -11 | 0.966 | 0.000 | 0.707 | 0.000 | 0.259 | 0.000 |
| 13 | 0.966 | 0.000 | 0.707 | 0.000 | 0.259 | 0.000 |
| -17 | 0.259 | 1.000 | 0.707 | 1.000 | 0.966 | 1.000 |
| 19 | 0.259 | 1.000 | 0.707 | 1.000 | 0.966 | 1.000 |

In summary, in this section, the concept of “attenuation factor”, which was proposed in [RED14] to describe the effects of the two winding sets with specific spatial shifting angle on the resultant MMF is extended by considering both spatial and time shifting angles.

It also should be mentioned that as shown in Fig. 2.27, when the two winding sets are shifted by a specific spatial shifting angle, the time shifting angle between the currents in the two winding sets is also determined. When the currents fed in the two winding sets obey the time shifting angle obtained before, the currents can be called as “in phase currents” [BAR10]. Most existing papers and Section 2.2 only focus on the effects of DTP windings with “in phase currents”, but the attenuation factor introduced in this section makes it possible to investigate the effects of DTP windings on resultant MMF field with “out phase currents”.

Overall, in DTP PMSMs, with the extended attenuation factor, the influences of any spatial and time shifting angles between the two winding sets on the resultant MMF production can be predicted simply according to different harmonic order, without the need of complicated computation or simulations.

2.4 FE and Experimental Validation

2.4.1 Machine and Winding Configuration

In this section, the analyses of winding assignments, winding factors and attenuation factors in DTP PMSMs presented before, are validated based on a 24-slot/22-pole DTP PMSM. Different phase shift angles are considered. The effects of the different DTP winding configurations on different harmonic orders are firstly calculated using winding factors and attenuation factors. The calculated results are validated by the FE simulation results, and then the FE simulation results are validated by experimental results.

As introduced in Section 2.2 and can be found from Table 2.4, for the 24-slot/22-pole PMSM, feasible phase shift angles include 0° , 15° , and 30° . For different phase shift angles, the detailed winding layouts can be obtained from the star of slots, as shown in Fig. 2.28.

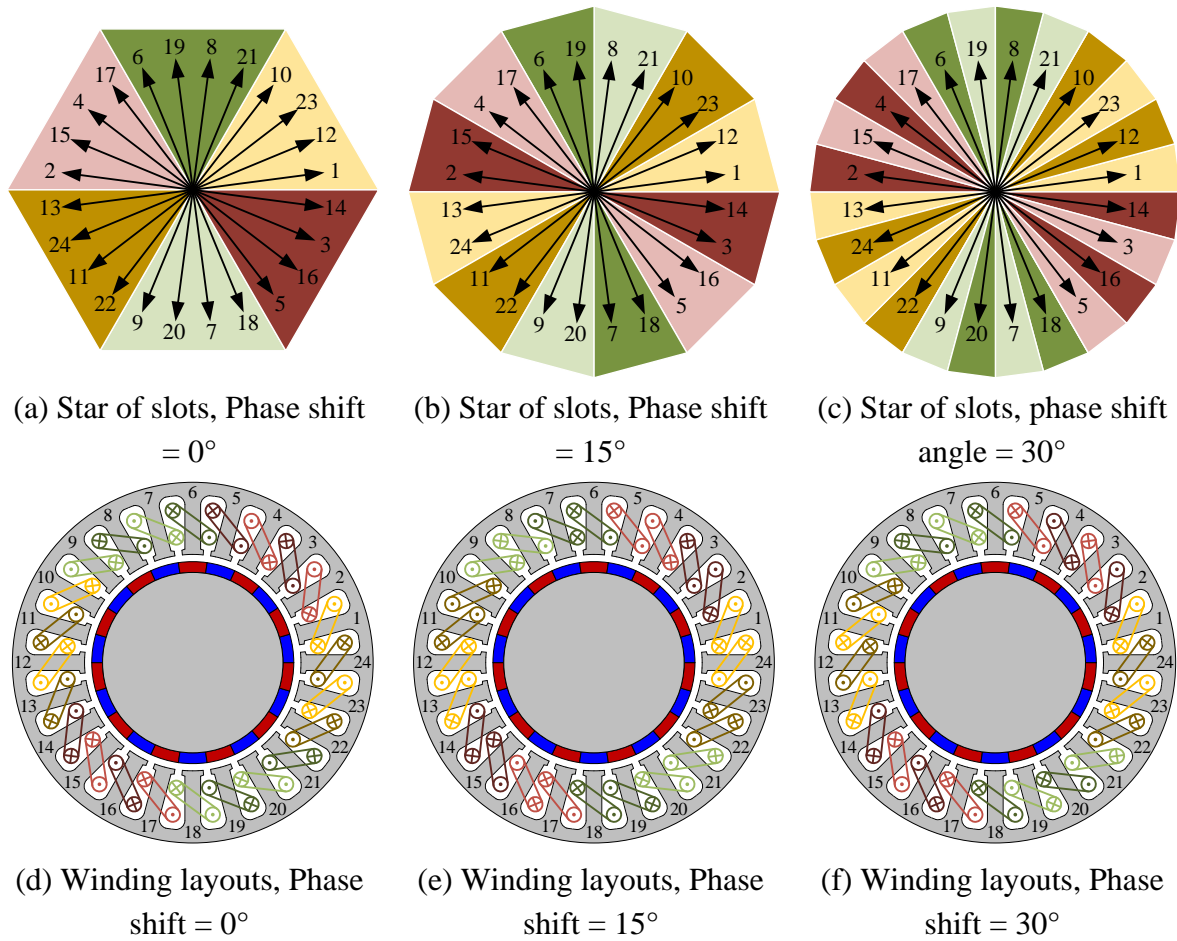


Fig. 2.28 Star of slots and winding layouts of 24-slot/22-pole DTP PMSM with different phase shift angles.

2.4.2 FE Validation

From Fig. 2.10, it can be found that in the investigated 24-slot/22-pole DTP PMSM, the winding factors of the working harmonics with 0° , 15° , and 30° phase shift angles are 0.949, 0.958, 0.983, respectively. It can be expected that compared with the counterpart with phase shift angle = 0° , the amplitude of the back EMF can be improved by 0.83% when the phase shift angle = 15° , or by 3.53% when the phase shift angle = 30° .

From Fig. 2.28 (a), it can be observed that when phase shift angle is 0° , the spatial shifting angle is the angular displacement from Slot 1 to Slot 13, which is 180° . For the conditions with 0° phase shift angle, the time shifting angle should be 0° . However, as the coils of Slots 13, 24, 11, 22 are wound reversely, the actual time shifting angle is 180° . Similarly, the spatial and time shifting angles with different phase shift angles can be observed from Fig. 2.28. When phase shift angle = 15° , spatial shifting angle = 165° and time shifting angle = 15° ; When phase shift angle = 30° , spatial shifting angle = 330° and time shifting angle = 30° . Then, the attenuation factors of different MMF harmonics in different DTP winding configurations are calculated, as shown in Table 2.13.

Table 2.13 Attenuation factors of different harmonics in 24-slot/22-pole DTP PMSM with different phase shift angles

| Phase shift angle | 0° | 15° | 30° |
|----------------------------------|--|-------------|-------------|
| Spatial shifting angle, α | 180° | 165° | 330° |
| Time shifting angle, β | 180° | 15° | 30° |
| Harmonic order, v | Attenuation factor, $K_{av} = \left \cos\left(\frac{v\alpha + \beta}{2}\right) \right $ | | |
| 1 | 1 | 0 | 1 |
| -5 | 1 | 0.707 | 0 |
| 7 | 1 | 0.707 | 0 |
| -11 | 1 | 1 | 1 |
| 13 | 1 | 1 | 1 |
| -17 | 1 | 0.707 | 0 |
| 19 | 1 | 0.707 | 0 |

From Table 2.13, it can be predicted that the two winding sets in the DTP windings with 0° phase shift cannot affect any of the resultant MMF harmonics. The DTP windings with 15° phase shift can eliminate the 1st harmonic and reduce the 5th, 7th, 17th, and 19th harmonics. The DTP windings with 30° phase shift can eliminate the 5th, 7th, 17th, and 19th harmonics.

With different phase shift angles, the air-gap MMF contents in the DTP PMSM are calculated by normalized currents and 2D FE simulations using JMAG. The waveforms and spectra of the calculated and FE simulated MMF distributions are shown in Fig. 2.29. It can be seen that the FE simulated results agree well with the calculated results.

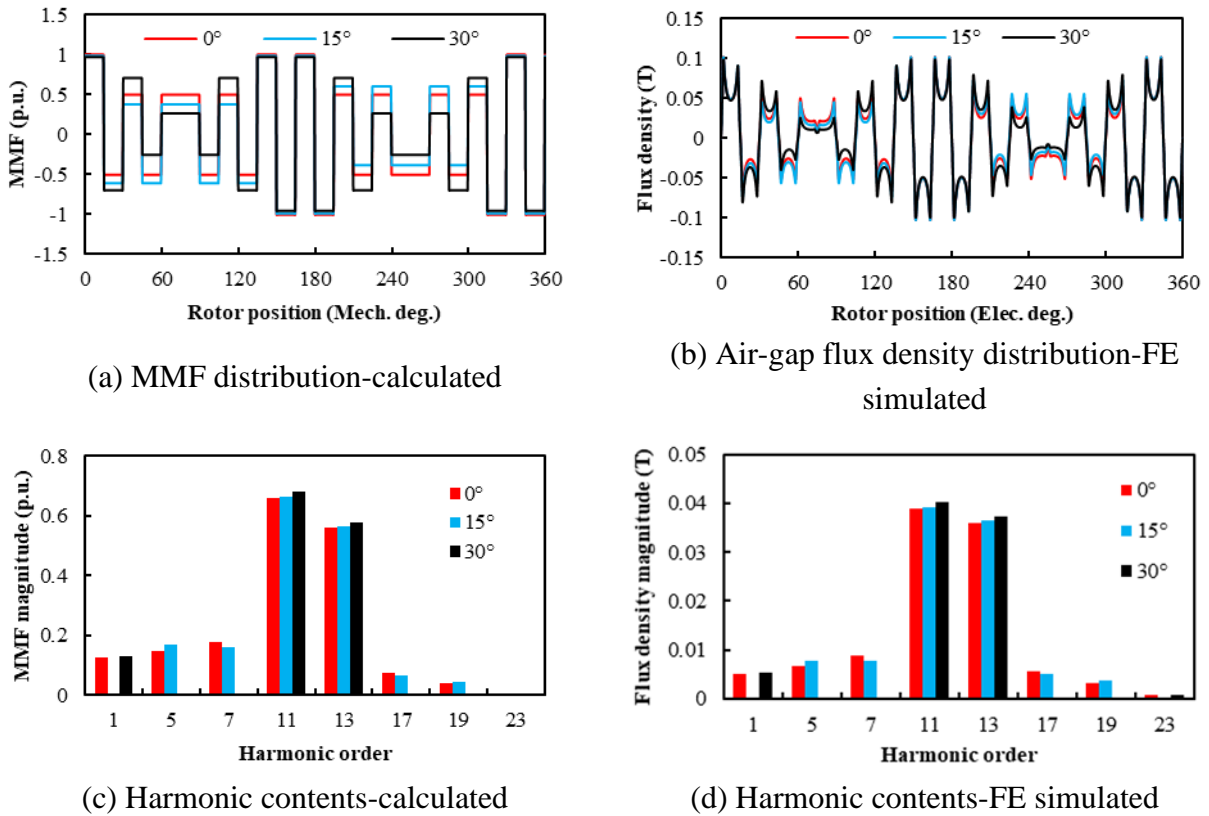


Fig. 2.29 Comparison of calculated and FE simulated MMF contents in 24-slot 22-pole DTP PMSMs with different phase shift angles.

From Fig. 2.29, the 15° and 30° phase shift angles can improve the amplitude of the 11th harmonic in the benchmark DTP PMSM with 0° phase shift. The elimination effects of DTP windings on specific harmonics can also be observed and completely agree with the prediction obtained from Table 2.13.

Overall, the effects of different DTP winding configurations on the stator MMF distributions and the resultant performance of PMSMs can be predicted by the calculations of winding factors and attenuation factors. The winding factors and attenuation factors introduced in this chapter are validated by FE simulation results.

2.4.3 Experimental Validation

The benchmark 24-slot/22-pole DTP PMSM is fabricated and tested considering different phase shift angles in [XU19]. The main design specifications are given in Table 2.14. The stator and rotor of the prototype are shown in Fig. 2.30 (a) and (b), respectively.

Table 2.14 Main design specifications of benchmark 24-slot/22-pole DTP PMSM

| Parameters | Value | Parameters | Value |
|--------------------|-------|--------------------------|-------|
| Stator slot number | 24 | Rotor pole number | 22 |
| Stator OD, mm | 90 | Rotor OD, mm | 60 |
| Stator ID, mm | 62.8 | Rotor ID, mm | 28 |
| Tooth width, mm | 3.4 | PM thickness, mm | 3 |
| Yoke thickness, mm | 3.3 | PM remanence, T | 1.2 |
| Stack length, mm | 25 | PM relative permeability | 1.05 |



(a) Stator



(b) Rotor

Fig. 2.30 Photos of 24-slot/22-pole DTP PMSM prototype.

As the experiments need to be conducted with various DTP winding configurations (Phase shift angle = 0° , 15° , and 30°), the terminals of all coils are connected to three connector blocks according to phases (Phases A1 and A2 in one connector block; Phases B1 and B2 in one connector block; and Phases C1 and C2 in one connector block) to switch winding connections between different DTP winding configurations. The connector blocks of the prototype is shown in Fig. 2.31 and the test rig is shown Fig. 2.32.

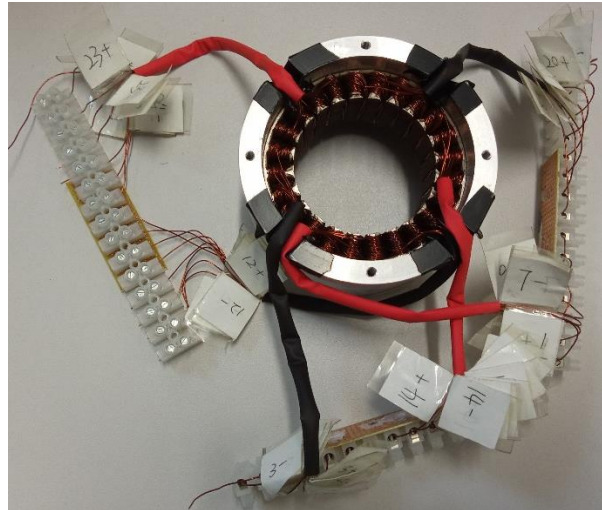


Fig. 2.31 Picture of connector blocks of prototype.

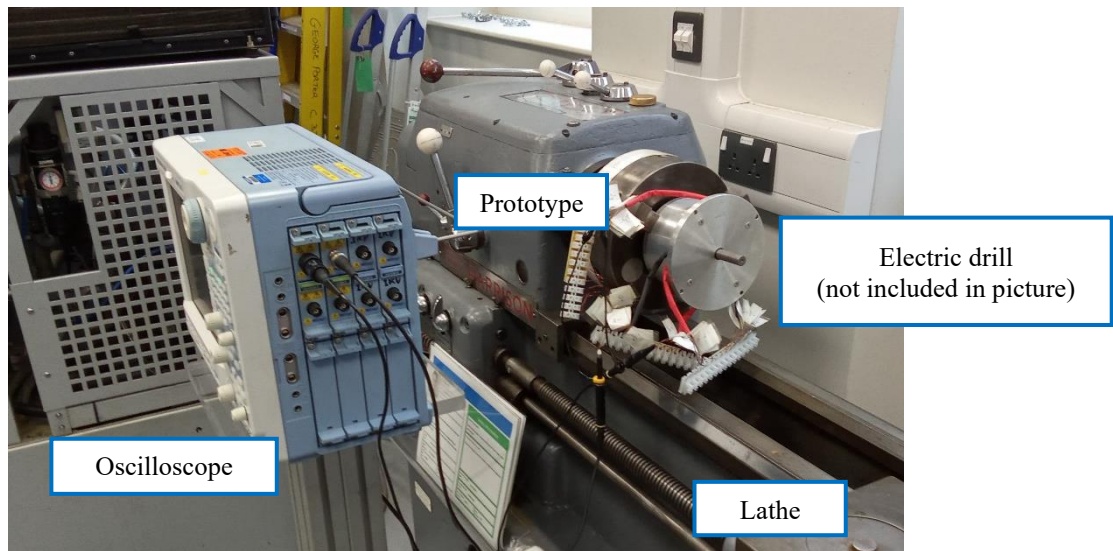
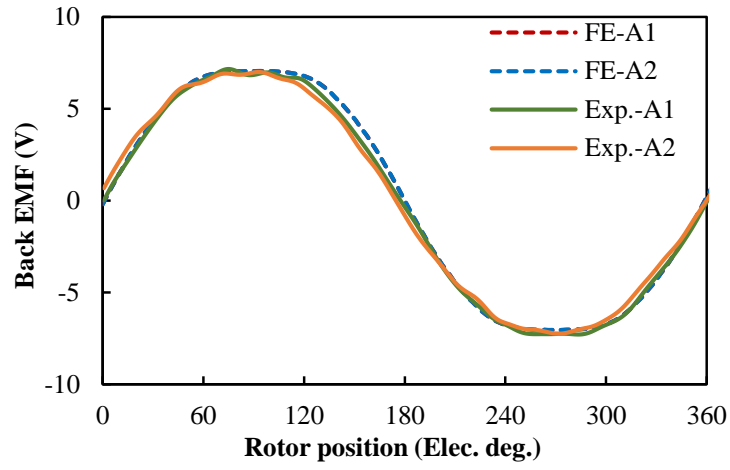


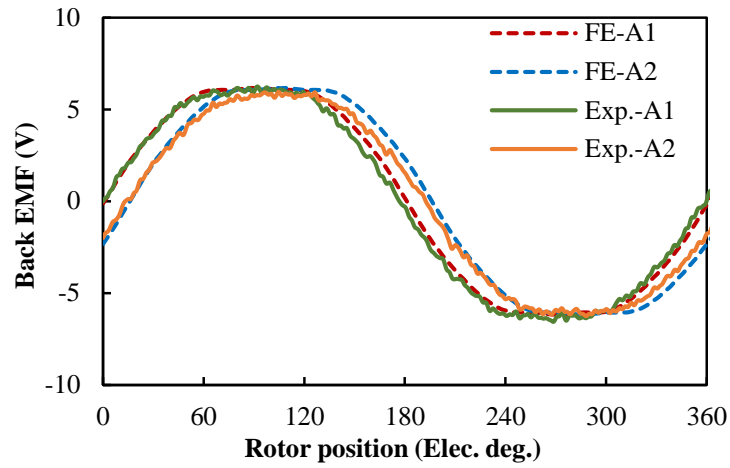
Fig. 2.32 Picture of test rig.

Although the air-gap flux density distributions cannot be measured directly, the back EMF waveforms of Phases A1 and A2 with different phase shift angles can be measured, as shown in Fig. 2.33. The FE simulated phase back EMFs are also presented in Fig. 2.33. Good agreements between FE simulation results and measured results can be observed. The different phase shift angles (0° , 15° , and 30°) can also be seen clearly from Fig. 2.33.

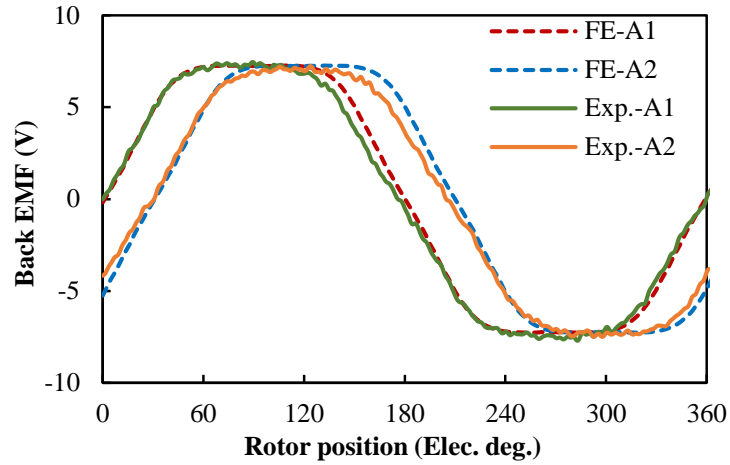
Thus, the correctness of the FE models utilized in this section is validated by the experimental results. Considering that the winding factor and attenuation factor calculations can be validated by FE method, the calculation results can also be validated by the experimental results.



(a) Phase shift angle = 0°



(b) Phase shift angle = 15°



(b) Phase shift angle = 30°

Fig. 2.33 Phase back EMF waveform comparisons between FE and measured results of 24-slot/22-pole DTP PMSM with different phase shift angles at 1000 rpm.

2.5 Conclusion

In this chapter, the feasibility of DTP winding configuration in PMSMs is analysed systematically based on the star of slots. Different slot/pole number combinations, different phase shift angles, different coil pitch numbers are all considered. The feasible DTP winding configurations and corresponding winding factors are summarized and shown according to slot/pole number combinations in Table 2.10.

In addition, in DTP PMSMs, the two winding sets are shifted by a spatial shifting angle, and the currents in the two winding sets are shifted by a time shifting angle. The effects of spatial and time shifting angles on the resultant MMF harmonics are examined simultaneously by extending the concept of “attenuation factor”. With the extended attenuation factor, the effects of any spatial and time shifting angles on different MMF harmonic orders can be predicted directly without the need of complicated calculation and simulations.

Finally, the DTP winding assignments, winding factors, and attenuation factors introduced in this chapter are validated by FE and experimental results.

CHAPTER 3

COMPARISON OF DIFFERENT WINDING CONFIGURATIONS FOR DUAL THREE-PHASE PMSMS IN ELECTRIC VEHICLES

In this section, two dual three-phase winding configurations, i.e. single-layer full-pitched (SF) and double-layer short-pitched (DS) windings, are compared based on the Toyota Prius 2010 permanent magnet synchronous machine (PMSM). It is found that the winding configuration with SF windings can improve average torque and reduce torque ripple in constant torque range. The winding configuration with DS windings has better torque performance in constant power range. The electromagnetic performances of the two winding configurations when one winding set is excited and the other one is open-circuited are also compared. The DS winding configuration shows much better performance under this condition. Overall, the dual three-phase winding configuration with DS windings is preferred for dual three-phase PMSMs in electric vehicles. A Toyota Prius 2010 PMSM equipped with DS windings was manufactured to verify the analyses presented in this section.

3.1 Introduction

In recent decades, electric vehicles (EVs) have attracted more and more attention with the concerns about global greenhouse gas emissions and the unstable supplies of fossil fuels. Since electrical machines are one of the most important components in the propulsion system in EVs, developing a high-performance machine specialized for EVs can greatly improve the overall performance of the vehicles. Among different kinds of machines, permanent magnet synchronous machine (PMSM) is regarded as a suitable choice for EV machines, as it has inherent high torque capacity, high torque density, and high efficiency [ZHU07] [ZHU17b] [CHA08] [SAN12] [YAN17a].

To further improve the performance of PMSMs, the dual three-phase (DTP) winding configuration is introduced, and some research has been conducted based on DTP PMSMs [BAR10] [ZHE12] [PAT14] [CHE14a] [ABD15]. Compared with conventional single three-phase (STP) machines, the advantages of DTP PMSMs include:

- Higher torque. The winding factors of the original windings can be improved by the DTP winding configuration [BAR10] [XU18];
- Lower torque ripple. The specific torque harmonics produced by the two winding sets can be cancelled with each other, and the stator MMF harmonics are significantly reduced by DTP windings [ABD15] [CHE14a];
- Higher efficiency. Due to the reduced stator MMF harmonic contents of DTP windings, the PM eddy losses in the DTP machines are lower than those in the STP counterpart. Considering that DTP windings can improve the output torque/power, the efficiency can be increased by the DTP winding configuration [ABD16a];
- Better fault-tolerant capacity. There are two separate winding sets in DTP windings, and hence, the loss of one winding set will not lead to the failure of the whole system. The DTP machine can be operated with the remaining healthy winding set [BAR11b] [ZHE12] [ZHE13].

Besides the advantages listed above, the ratings per phase are reduced with the increase in phase number. The vibration of PWM frequency can also be reduced by two parallel inverters in a DTP machine [MIY18] [ZHA20] [WAN20d]. Moreover, the two winding sets provide more control freedoms in a machine system, and thus, more control strategies can be utilized, and the performance of DTP machines can be further improved [ZHU21a].

However, most of the existing literature only focuses on fractional-slot PMSM, not the most widely employed machines in EVs, i.e., integral-slot PMSMs. Since fractional-slot PMSMs and integral-slot PMSMs have different slot/pole number combinations, their winding layouts are also different. The coil pitch number in fractional-slot PMSMs is usually relatively small. When the coil pitch number equals 1, the windings can also be called tooth coils or non-overlapping concentrated windings. For integral-slot PMSMs, the coil pitch number is around the number of slots per pole. These windings are called overlapping distributed windings. Considering the differences in slot/pole number combinations and winding configurations between fractional-slot PMSMs and integral-slot PMSMs, the conclusion obtained from fractional-slot PMSMs may not be used in integral-slot PMSMs directly. Thus, it is still meaningful to analyse the electromagnetic performance of integral-slot DTP PMSMs and compare it with that of the STP counterpart.

In this section, the Toyota Prius 2010 machine, which is a 48-slot/8-pole IPMSM, is chosen as the benchmark. For the 48 slot/8-pole IPMSM, two DTP winding configurations have been proposed in existing literature [PAT13] [YAN19a]. The DTP winding configuration with single-layer full-pitch windings (DTP-SF) was introduced in [YAN19a]. However, the differences between the original short-pitched windings and the proposed full-pitched windings are not considered thoughtfully. The DTP winding configuration with double-layer short-pitched windings (DTP-DS) can be found in [PAT15]. However, the electromagnetic performance of DTP-DS has not been presented comprehensively in existing papers, and the proposed DTP-DS winding configuration has never been compared with the conventional STP winding configuration in the Toyota Prius 2010 IPM machine.

In this section, the two DTP winding configurations are compared with each other for the first time, and both of them are compared with the original STP winding configuration. The comparisons are made using the finite element (FE) method over the whole speed range because the electromagnetic characteristics of the IPMSMs with these winding configurations can be affected obviously by rotation speed. Furthermore, for DTP-SF and DTP-DS machines, even if one three-phase winding set is open-circuited (OC), they still can be operated with the remaining three-phase winding set. To compare their electromagnetic performances under this condition, the comparison carried out under the three-phase OC condition is also considered. From the comparative studies given in this section, the DTP-DS winding configuration is preferred for the Toyota Prius 2010 PMSM and a prototype equipped with DTP-DS windings was fabricated and tested.

This chapter is structured as follows. The details of different winding configurations are provided in Section 3.2. In Section 3.3, the electromagnetic performances of these winding configurations are compared under healthy conditions in various aspects, including output torque capacity, torque ripple, torque-speed characteristic, efficiency, and so on. In Section 3.4, the electromagnetic performances of two DTP winding configurations are compared under three-phase OC conditions in similar aspects. The experimental verification is given in Section 3.6, followed by the conclusions in Section 3.7.

3.2 Winding Configurations

The Toyota Prius 2010 machine is well known for its excellent performance and has been investigated by researchers all over the world in recent years [BUR11] TAN16]. The cross-section of the machine with a 48-slot stator and an 8-pole V-type IPM rotor is presented in Fig. 3.1. The detailed design specifications of the Prius 2010 machine can be found in [BUR11], and the main parameters are shown in Table 3.1. The detailed characteristics of the magnets were investigated in [BUR11]. The diminishing nature of the remanent flux density and coercivity with increasing temperature can be observed. However, in this chapter, the simulations are calculated using JMAG-Designer, which is a simulation software for the development and design of electrical devices provided by JSOL [JMA23]. To simplify the calculation in simulations, the ideal permanent magnet material ‘NdFeB_Br = 1.2T’ is chosen as the magnets in the JMAG model, and B_r and μ_r of ‘NdFeB_Br = 1.2T’ are fixed at 1.2T and 1.05, respectively. Further, in the JMAG model, ‘35H270’ is chosen as the stator and rotor core materials, and the calculated iron losses in this paper are based on the properties of ‘35H270’ in JMAG software.

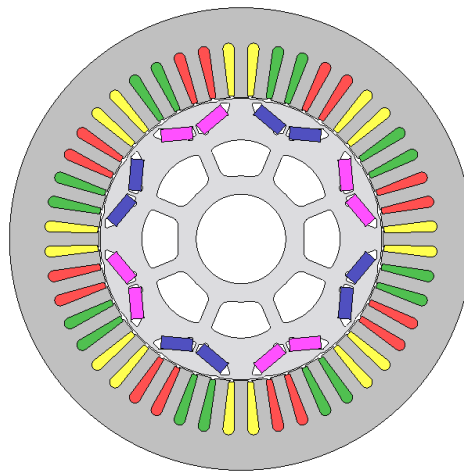


Fig. 3.1 Cross-section of the Toyota Prius 2010 machine.

Table 3.1 Design specifications of Toyota Prius 2010 machine

| | | | |
|-------------------------|-------|--------------------------|---------------------------------|
| Number of stator slots | 48 | Number of rotor poles | 8 |
| Stator OD, mm | 264 | Rotor OD, mm | 160.44 |
| Stator ID, mm | 161.9 | Rotor lamination ID, mm | 51 |
| Stator stack length, mm | 50.8 | Lamination thickness, mm | 0.305 |
| Slot depth, mm | 30.9 | Slot opening, mm | 1.88 |
| Phase resistance, Ohm | 0.077 | Magnet dimensions, mm | $49.3 \times 17.88 \times 7.16$ |

3.2.1 Winding Arrangements

The stator windings equipped in the Toyota Prius 2010 PMSM are 5-slot-pitched single-layer three-phase windings, as shown in Fig. 3.2 (a). In 48-slot/8-pole PMSMs, the number of slots per pole is 6. Hence, the original 5-slot-pitched windings in the Toyota Prius 2010 PMSM are short-pitched windings, which can reduce MMF harmonics and end-winding length. The diagram of coil electromotive force (EMF) phasors is given in Fig. 3.2(b). It can be seen that there is no phase shift between the coil EMF phasors of the same phase. In other words, the original three-phase windings cannot be transferred into two three-phase windings with a 30° phase shift directly.

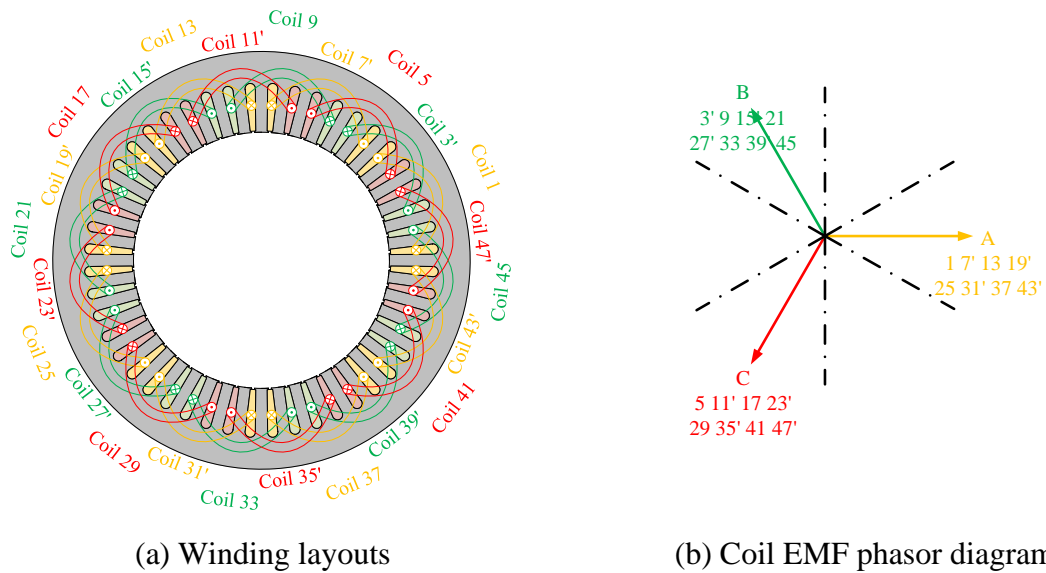
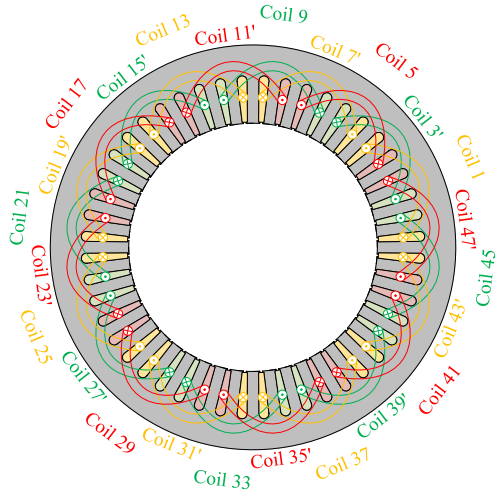
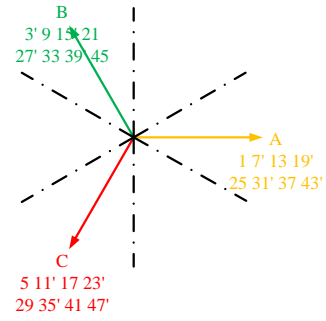


Fig. 3.2 Winding arrangements of Toyota Prius 2010 IPM machine.

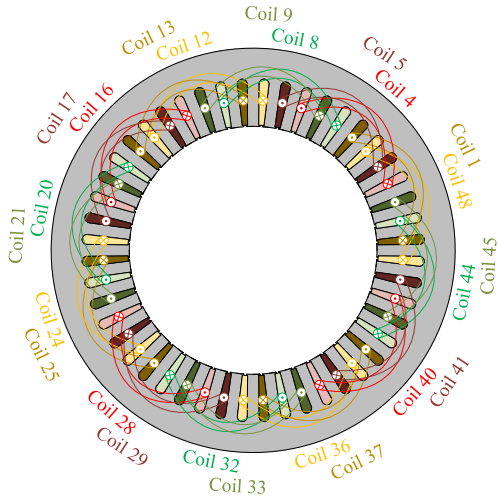
As is well-known in existing literature [BAR10], the DTP winding configuration with a 30° phase shift can improve output torque and reduce torque harmonics at the same time in PMSMs. To realize the advantages of the 30° DTP configuration in 48-slot/8-pole IPMSMs, two DTP winding configurations have been proposed. Different from the original single-layer short-pitched windings, the stator windings utilized in the two DTP winding configurations are single-layer full-pitched (SF) windings and double-layer short-pitched (DS) windings, respectively. In this section, the original STP and the two DTP winding configurations are designated as the STP, DTP-SF, and DTP-DS, respectively. The winding connections and coil EMF phasor diagrams of the STP, DTP-SF and DTP-DS machines are shown in Fig. 3.3.



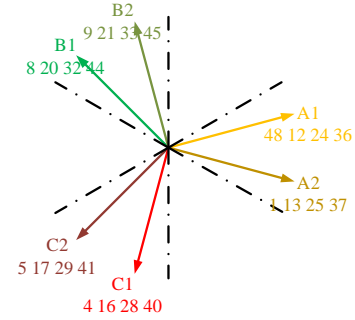
(a) STP-Winding layouts



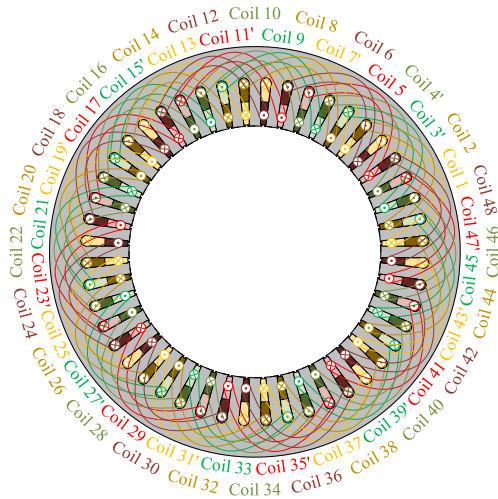
(b) STP-Coil EMF phasor diagram



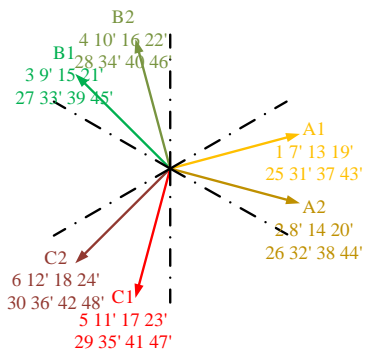
(c) DTP-SF-Winding layouts



(d) DTP-SF-Coil EMF phasor diagram



(e) DTP-DS-Winding layouts



(f) DTP-DS-Coil EMF phasor diagram

Fig. 3.3 Winding layouts and coil EMF phasor diagrams of STP, DTP-SF, DTP-DS PMSMs.

In the STP machine, as shown in Fig. 3.3(a), the coils of Phase A are Coils 1, 7', 13, 19', 25, 31', 37, and 43'. The interval between adjacent coils is 6 slot pitches in space, which is 180° in electrical degree, and hence, compared with Coils 1, 13, 25, and 37, Coils 7, 19, 31, and 43 are opposite connected. Thus, all the coils of Phase A in the STP machine share the same back EMF phases, as shown in Fig. 3.3(b). The detailed winding layouts of the DTP-SF winding configuration are shown in Fig. 3.3(c), it can be observed that the coil pitch number is 6 and the two three-phase winding sets are displaced by one slot in space, which is 30° in electric. Thus, the back EMFs induced in Coils 48, 12, 24, and 36 are advanced to those in Coils 1, 13, 25, and 37 by 30° in electric, as illustrated in Fig. 3.3(d). In the DTP-DS machine, the double-layer windings can be seen as duplicated from the original windings in the STP machine, and the new winding set is shifted by one slot pitch, as shown in Fig. 3.3(e). All the coils of Phase A in the STP machine, Coils 1, 7, 13, 19, 25, 31, 37, and 43, belong to Phase A1 in the DTP-DS machine, and the new Coils 2, 8, 14, 20, 26, 32, 38, and 44 belong to Phase A2. Thus, Phase A2 lags behind Phase A1 by one slot pitch, which is 30° in electric.

3.2.2 Winding Specifications

Besides the difference in winding arrangements, the drive systems for STP and DTP (DTP-SF and DTP-DS) PMSMs are also different, as shown in Fig. 3.4. For STP PMSMs, the inverters are three-phase six-switch voltage source inverters (VSI). However, for DTP PMSMs, the machines are fed by two separate three-phase inverters and the two inverters are parallel connected.

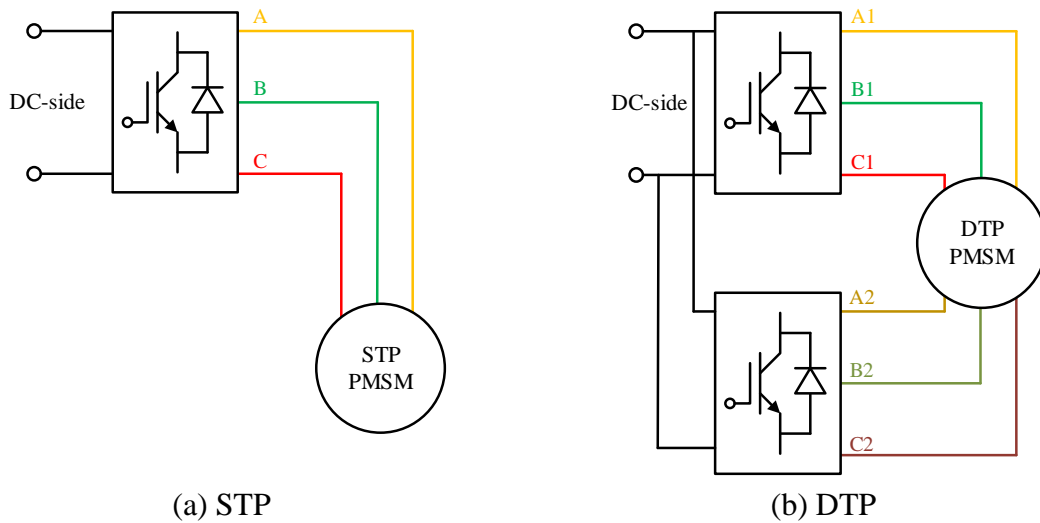


Fig. 3.4 Schematics of drive systems for STP and DTP PMSMs.

Hence, the total output power of DTP PMSMs can be split into two parts and provided by two separate inverters. When the inverters for STP and DTP PMSMs share the same DC-link voltage, the phase currents in DTP PMSMs can be halved from those in STP PMSMs for the equivalent output.

In the researched STP machine (Toyota Prius 2010 machine), the maximum phase current is set as 236A_{pk} and the DC-link voltage is rated at 650V_{dc}. Hence, for the DTP-SF and DTP-DS machines, the maximum phase current is 118A_{pk} and the DC-link voltage is 650V_{dc}. The lower current requirement suggests that cheaper power devices can be utilized in the inverters for DTP PMSMs. Thus, although the number of switches is doubled in the DTP drive system compared with the STP counterpart, the total cost is still lower than twice the original cost.

Based on the aforementioned discussions, the detailed specifications of STP, DTP-SF, and DTP-DS winding configurations are summarized in Table 3.2. It can be seen that since the current requirement is halved in the DTP-SF and DTP-DS windings compared with the STP counterpart, the number of wires per turn is changed from 12 (in STP windings) to 6 (in DTP-SF and DTP-DS windings). It also should be noticed that due to different winding layouts, as shown in Fig. 3.3, the number of coils per phase is 8 in STP and DTP-DS windings, but only 4 in DTP-SF windings. To keep the resultant ampere-turns the same with STP and DTP-DS counterparts, the number of turns per coil in DTP-SF windings is doubled from 11 to 22. Thus, the number of turns per phase keeps 88 in STP, DTP-SF, and DTP-DS windings. Another difference between STP, DTP-SF, and DTP-DS winding configurations is coil pitch number, which is 5 in STP and DTP-DS machines and 6 in DTP-SF machines.

Table 3.2 Specifications of STP, DTP-SF, and DTP-DS winding configurations

| | STP | DTP-SF | DTP-DS |
|----------------------------|-----|--------|--------|
| Number of phases | 3 | 6 | 6 |
| Wires in parallel per turn | 12 | 6 | 6 |
| Turns in series per coil | 11 | 22 | 11 |
| Coils in series per phase | 8 | 4 | 8 |
| Coil pitch number | 5 | 6 | 5 |

Based on the specifications shown in Table 3.2, the phase resistances of DTP-SF and DTP-DS windings can be estimated according to the phase resistance of the STP windings.

It is known that the resistance of a conductor can be computed as

$$R = \rho \frac{l}{A} \quad (3.1)$$

where l is the length of the conductor, A is the cross-sectional area of the conductor, and ρ is the electrical resistivity of the conductor. To obtain phase resistances of the DTP-SF and DTP-DS windings, the relationships of their total winding length and cross-sectional area to those of STP windings should be estimated firstly.

From Table 3.2, it is reported that the number of strands of wires per turn is 12 in STP windings and only 6 in DTP-SF and DTP-DS windings. Hence, the cross-sectional area of DTP-SF and DTP-DS windings is half of that of STP windings.

To obtain the relationships between the total winding lengths of STP, DTP-SF, and DTP-DS windings, the end-windings are assumed as semi-circular in shape, and then, the schematics of the short-pitched and full-pitched coils are plotted in Fig. 3.5.

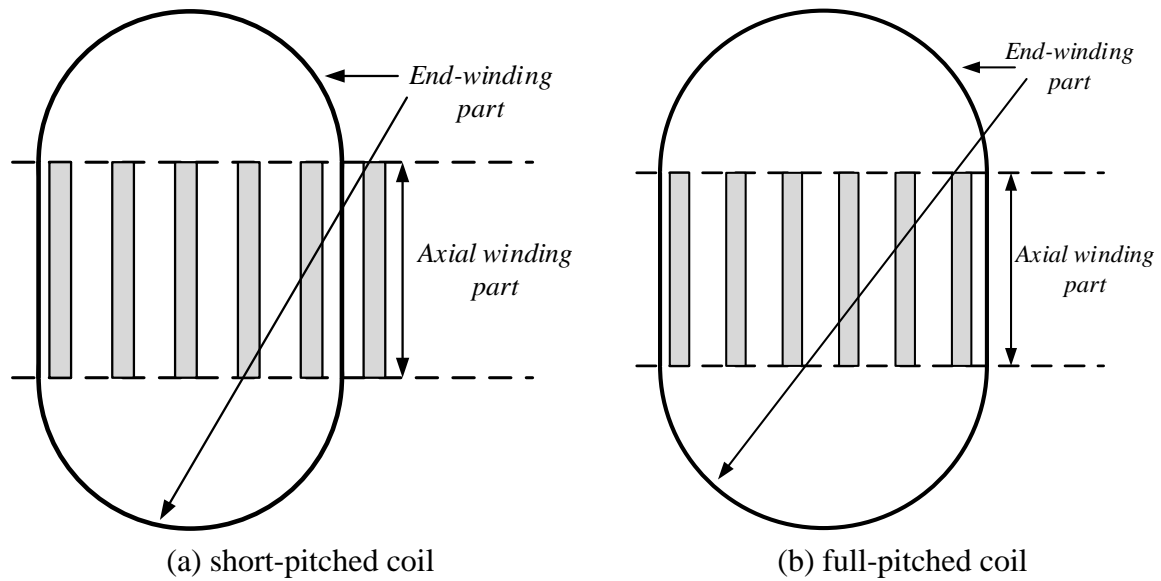


Fig. 3.5 Schemes of short-pitched and full-pitched coils.

Fig. 3.5, it can be seen that both short-pitched and full-pitched coils can be divided into two parts: the axial winding part and the end-winding part. The length of the axial winding part is the stator's axial length. The length of the end-winding part can be calculated based on the stator's inner diameter, slot depth, and coil pitch number, and these data can be found in Table 3.1.

The coil sides are assumed at the center of slots, and thus, the equivalent radius of each coil side, r_e , is the sum of the stator's inner radius and a half of the slot depth, as

$$r_e = \frac{50.8}{2} + \frac{39.6}{2} = 96.4 \text{ mm} \quad (3.2)$$

as shown in Fig. 3.6.

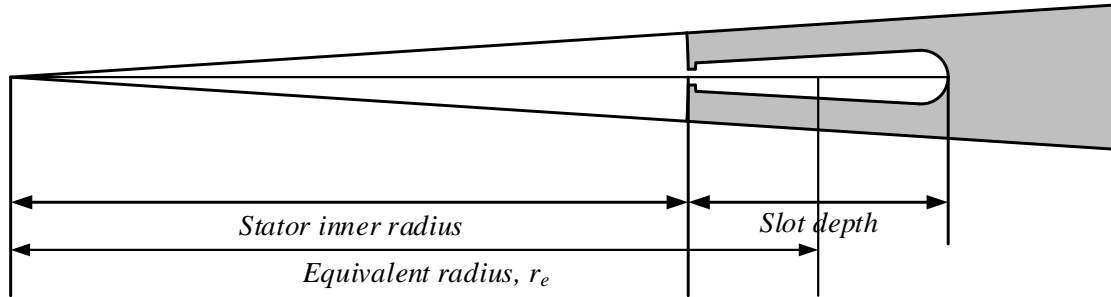


Fig. 3.6 Schematic of the equivalent radius of the coil side.

Then, the distance between the two coil sides in short-pitched coil, l_{cs-s} , and that in full-pitched coil, l_{cs-f} , can be obtained according to their different coil pitch numbers,

$$l_{cs-s} = 5 \frac{2\pi r_e}{48} \approx 63.10 \text{ mm} \quad (3.3)$$

$$l_{cs-f} = 6 \frac{2\pi r_e}{48} \approx 75.71 \text{ mm} \quad (3.4)$$

From Fig. 3.5, it can be seen that the diameter of end-winding is the distance between the two coil sides. Hence, the length of each end-winding part in short-pitched coil, l_{ew-s} , and that in full-pitched coil, l_{ew-f} , can be calculated as

$$l_{ew-s} = \frac{1}{2} \pi l_{cs-s} \approx 99.11 \text{ mm} \quad (3.5)$$

$$l_{ew-f} = \frac{1}{2} \pi l_{cs-f} \approx 118.93 \text{ mm} \quad (3.6)$$

Assuming the stator axial length is l_a , the total length of one short-pitched coil, l_s , and that of one full-pitched coil, l_f , are

$$l_s = 2l_a + 2l_{ew-s} = 299.82 \text{ mm} \quad (3.7)$$

$$l_f = 2l_a + 2l_{ew-f} = 339.46 \text{ mm} \quad (3.8)$$

As mentioned above, due to different wire numbers, the cross-sectional area of DTP-SF is half of that of STP windings. Furthermore, since STP and DTP-DS windings share the same short-pitched coils and the same coil numbers per phase, the two windings have the same total

winding lengths. Hence, the phase resistance of DTP-DS windings can be estimated from the phase resistance of STP windings (0.077Ohm), as

$$R_{DTP-DS} = \frac{A_{STP}}{A_{DTP}} R_{STP} = \frac{12A_{wire}}{6A_{wire}} 0.077 = 0.154 \text{ Ohm} \quad (3.9)$$

where A_{wire} is the cross-sectional area of a wire strand. For DTP-SF windings, since they share the same cross-sectional area and number of coils per phase with DTP-DS windings, the phase resistance can be estimated directly based on the winding lengths of the shorted-pitched and full-pitched coils, as

$$R_{DTP-SF} = \frac{l_f}{l_s} R_{DTP-DS} = \frac{339.46}{299.82} 0.154 \approx 0.174363 \text{ Ohm} \quad (3.10)$$

Besides the phase resistances, the total axial lengths of STP, DTP-SF, and DTP-DS windings can also be obtained based on Fig. 3.5. The total axial length of the short-pitched windings, l_{ta-s} , and that of full-pitched windings, l_{ta-f} , can be estimated as

$$l_{ta-s} = l_a + 2 \frac{l_{cs-s}}{2} \approx 50.80 + 63.10 = 113.90 \text{ mm} \quad (3.11)$$

$$l_{ta-f} = l_a + 2 \frac{l_{cs-f}}{2} \approx 50.80 + 75.71 = 126.51 \text{ mm} \quad (3.12)$$

Overall, the axial length and the phase resistance of different winding configurations are summarized in Table 3.3.

Table 3.3 Estimated key parameters of STP, DTP-SF, and DTP-DS windings

| | STP | DTP-SF | DTP-DS |
|-------------------------|--------|----------|--------|
| Total axial length (mm) | 113.90 | 126.51 | 113.90 |
| Phase resistance (Ohm) | 0.077 | 0.174363 | 0.154 |

As shown in Table 3.3, compared with DTP-DS windings, the phase resistance in DTP-SF machines is increased by 13.2%, and the total axial length is also raised by 11.1%. It is suggested that the DTP-DS winding configuration is better than the DTP-SF counterpart in efficiency and machine size because the higher phase resistance implies higher copper loss under the same phase currents and the longer axial length denotes the machine's larger size.

Based on the calculations shown above, it can be summarized that the total volumes of copper wires utilized in STP and DTP-DS machines are identical. However, the DTP-SF machine needs more copper wires, 13.2% higher than the counterparts, due to the longer coil pitch. In

other words, the cost of winding connections in the DTP-SF machine is higher than the other two counterparts. It should be mentioned that the analyses presented here are only based on estimations. The actual winding length and machine size can be further optimized in design and assembling processes. However, it can still be concluded that compared with the DTP-SF counterpart, the DTP-DS winding configuration has inherent advantages in winding resistance and machine size due to the shorter pitched windings.

3.3 Electromagnetic Performance under Healthy Condition

To reveal the merits and demerits of different winding configurations, the electromagnetic performances of Toyota Prius 2010 machines with STP, DTP-SF, and DTP-DS windings are analysed using 2D FE method in JMAG Designer. Because of the 48-slot/8-pole topology of the investigated machine, the electrical periodicity within the machine is 4. Hence, the flux distributions are identical every quarter machine and the electromagnetic performance of different winding configurations can be obtained from 1/4 models, as shown in Fig. 3.7.

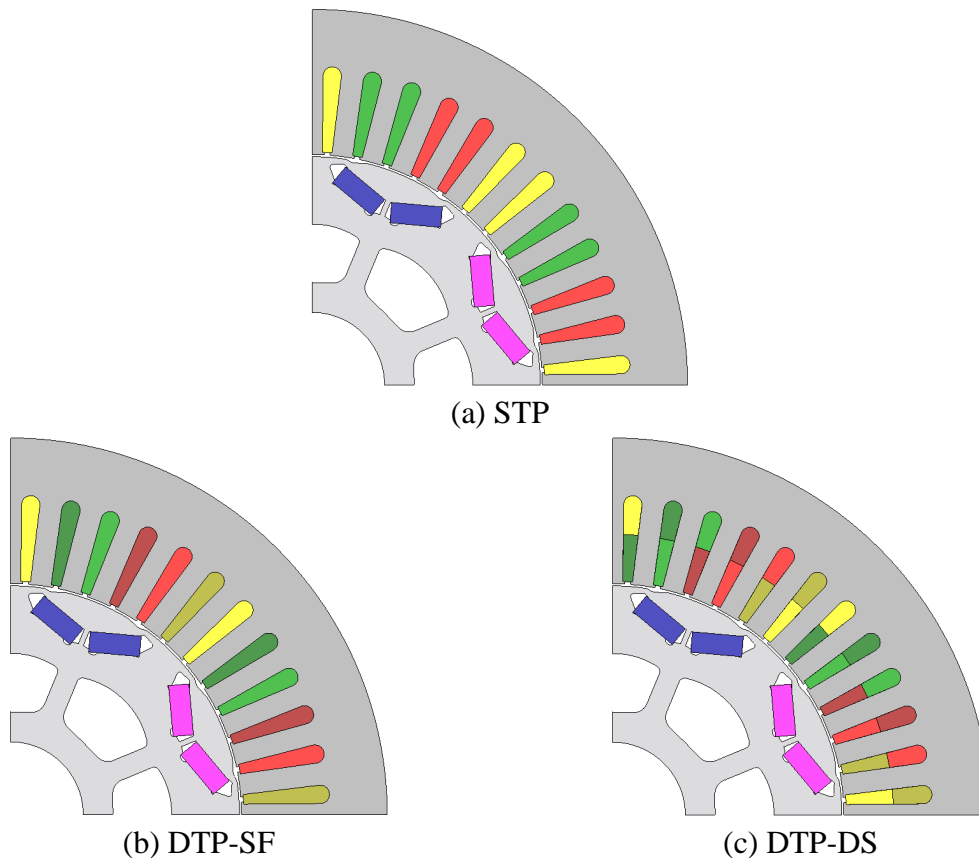


Fig. 3.7 FE models of Prius 2010 machine with different winding configurations.

3.3.1 Winding Factor

For all winding configurations, winding factor is the product of distribution factor and pitch factor. The distribution factors can be obtained from the coil EMF phasor diagrams shown in Fig. 3.3, and the pitch factors are determined by slot/pole number combination and coil pitch number. In Fig. 3.3(b), (d), and (f), it can be seen that in STP, DTP-SF, and DTP-DS windings, the EMF phasors of the same phase overlap each other. Hence, the distribution factors of the three winding configurations are all 1. Pitch factor can be obtained from the ratio of coil-pitch to pole-pitch. Thus, for the full-pitched windings (DTP-SF), the pitch factor is 1, and for the short-pitched windings (STP and DTP-DS), the pitch factors are 0.966. The winding factors of STP, DTP-SF, and DTP-DS winding configurations are calculated and listed in Table 3.4.

Table 3.4 Winding factors of STP, DTP-SF, and DTP-DS winding configurations

| | STP | DTP-SF | DTP-DS |
|----------------------------|-------|--------|--------|
| Distribution factor, k_d | 1 | 1 | 1 |
| Pitch factor, k_p | 0.966 | 1 | 0.966 |
| Winding factor, k_w | 0.966 | 1 | 0.966 |

From Table 3.4, it can be found that the resultant winding factors for STP, DTP-SF, and DTP-DS winding configurations are 0.966, 1, and 0.966, respectively. Compared with STP counterpart, DTP-SF winding configuration can improve winding factor by about 3.53%, but DTP-DS winding configuration remains the same.

However, it should be noticed that Table 3.4 only shows the winding factors of the fundamental components in one winding set in different winding configurations. Since there are two winding sets in DTP-SF and DTP-DS machines and the resultant stator MMF is produced by the two winding sets, it is still necessary to evaluate winding factors of the higher-order harmonics and the mutual effects between the two winding sets. The detailed calculation methods for winding factors of higher-order harmonics in one winding set and the resultant winding factors after two winding sets are fed with time-shifted phase currents were discussed in the previous section.

The effects of DTP winding configurations on resultant stator MMF harmonics can also be obtained from the ideal stator MMF distributions. The waveforms and spectra of the ideal stator MMF distributions in STP, DTP-SF, and DTP-DS machines are calculated, as shown in Fig. 3.8. It can be seen that the DTP-SF winding configuration still has higher fundamental component than STP and DTP-DS counterparts. Furthermore, the fifth and seventh harmonics

in DTP-SF and DTP-DS winding configurations are totally eliminated by the 30° -shifted two winding sets. Thus, it can further be inferred that the sixth torque ripple can also be totally eliminated in DTP-SF and DTP-DS machines [ZHA95] [BAR10] [ZHU21a].

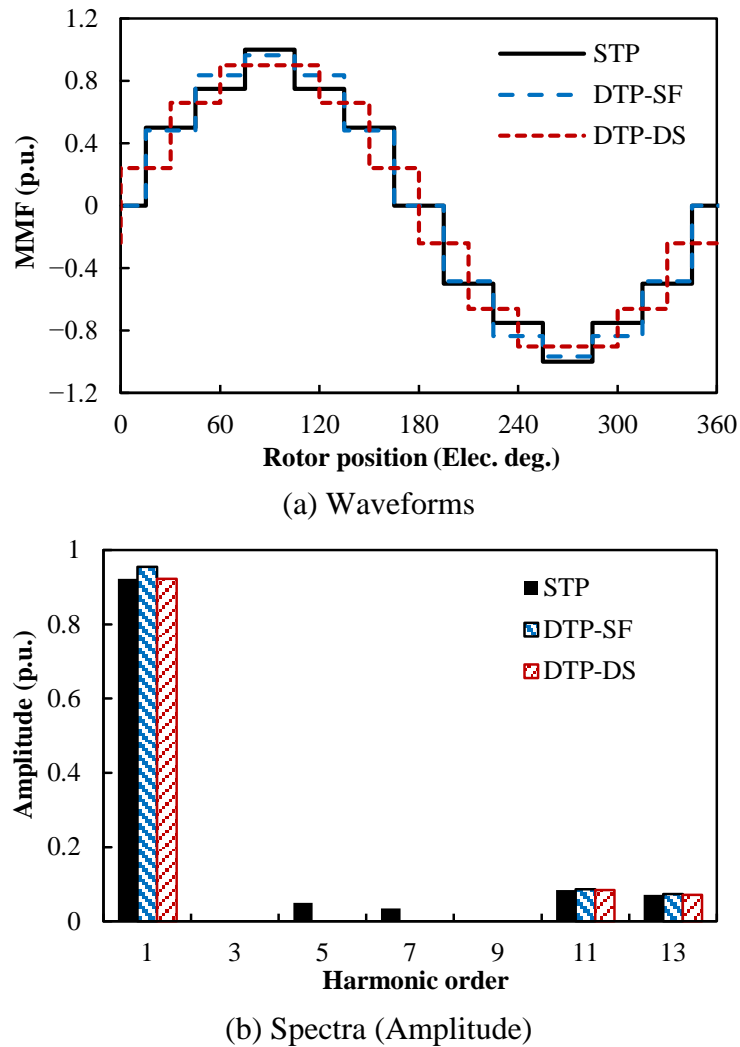
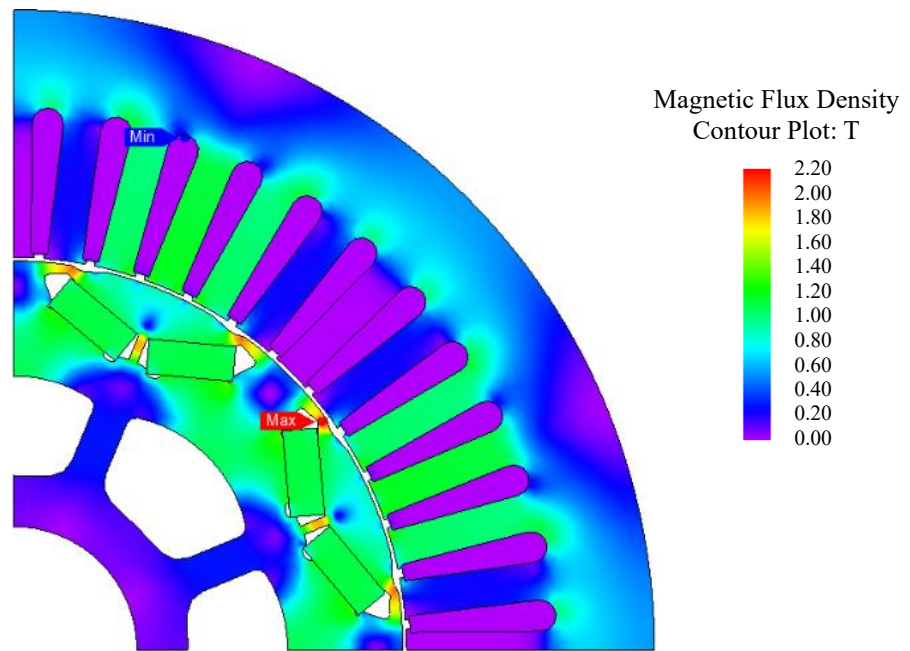


Fig. 3.8 Ideal stator MMF distributions for STP, DTP-SF, and DTP-DS winding configurations.

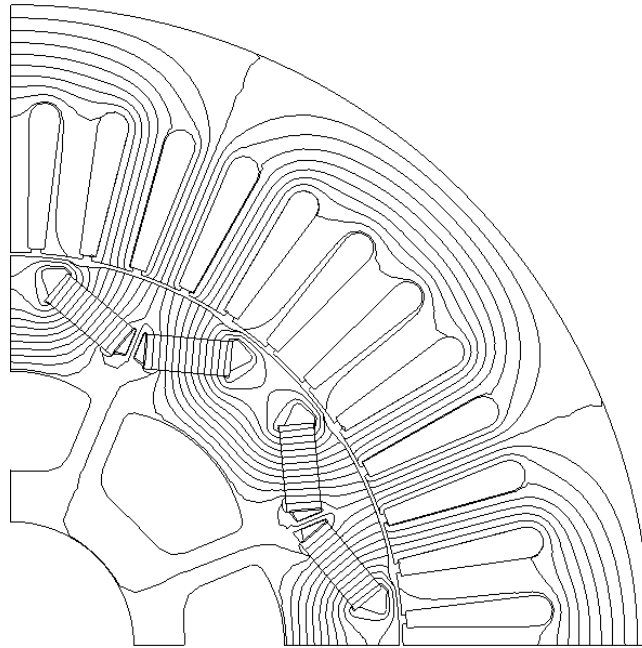
3.3.2 Open-circuit (OC) performance

3.3.2.1 Flux Distributions

Under OC condition, all the flux in the PMSM is provided by the magnets in the rotor, and thus, different winding configurations have no influence on flux distribution performance under OC condition. The flux density contour and flux line distribution of the Prius 2010 machine under OC condition are plotted in Fig. 3.9(a) and (b), respectively. The waveform and spectrum of the radial air-gap flux density in the machine are shown in Fig. 3.10(a) and (b), respectively.

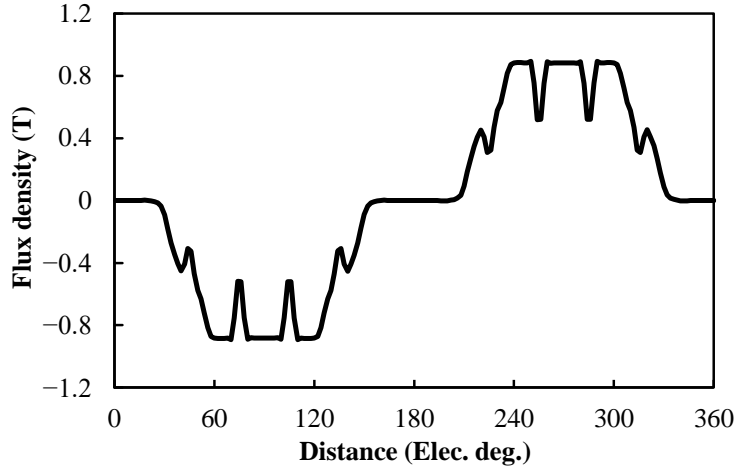


(a) Flux density distribution

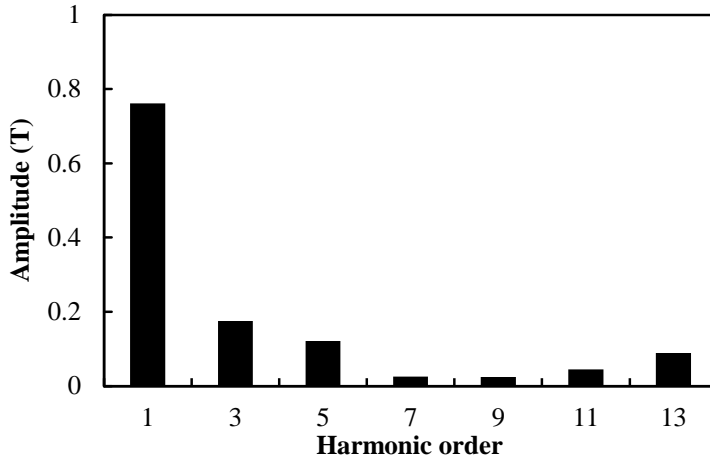


(b) Flux line distribution

Fig. 3.9 Flux density distribution of Prius 2010 machine under OC condition.



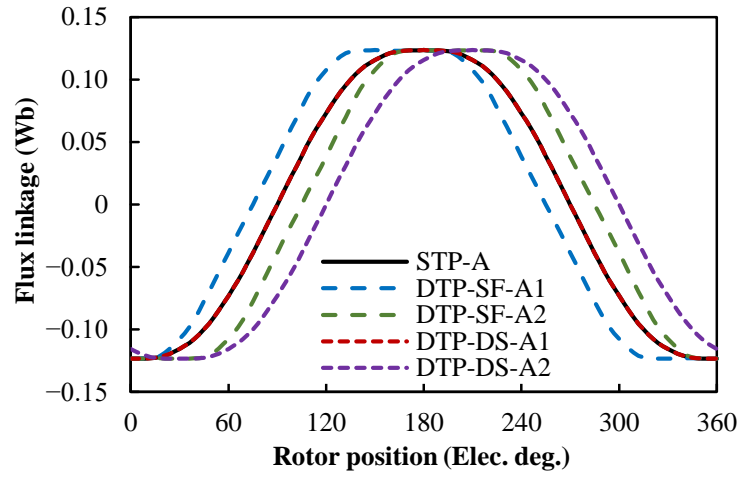
(a) Waveforms



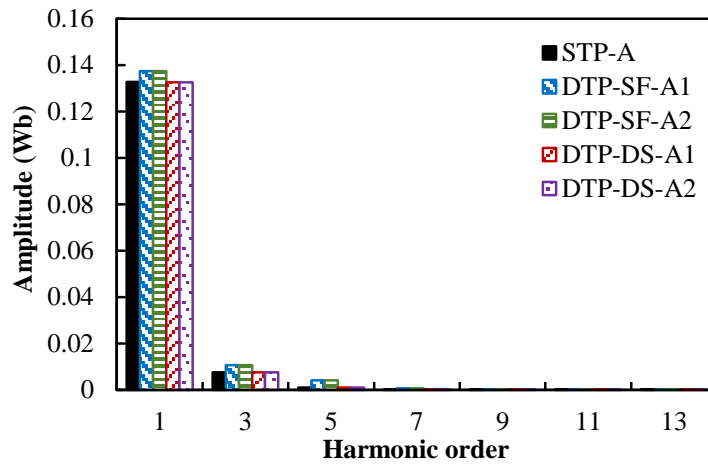
(b) Spectra (Amplitude)

Fig. 3.10 Radial air-gap flux density distribution of Prius 2010 machine under OC condition.

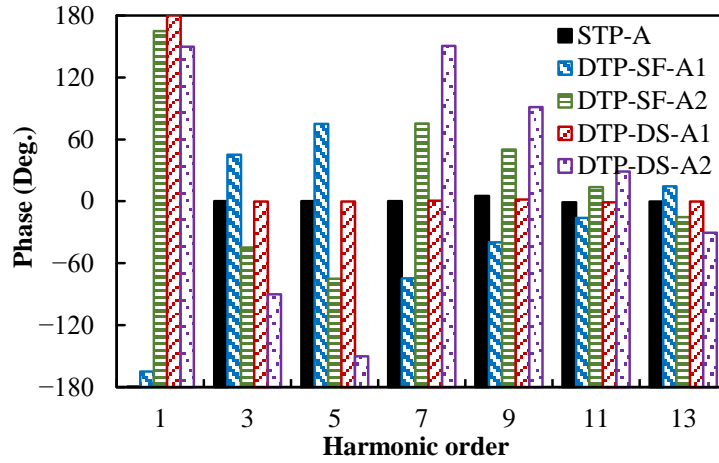
Although different winding configurations share the same flux density distributions under OC conditions, due to different winding connections, their flux-linkages are different. The waveforms and spectra of phase flux linkages in STP, DTP-SF and DTP-DS windings under OC condition are shown in Fig. 3.11. The phase shifting angle (30°) between the two winding sets can be clearly seen from Fig. 3.11(c). It can be seen that the flux linkage curve of Phase A in STP windings is completely overlapped with that of Phase A1 in DTP-DS windings, because the first three-phase winding set in DTP-DS windings has identical layouts with that in STP windings, as presented in Fig. 3.3. Thus, STP and DTP-DS winding configurations have identical phase flux-linkage harmonic contents, but DTP-SF winding configuration has slightly higher fundamental components than STP and DTP-DS counterparts.



(a) Waveforms



(b) Spectra (Amplitude)

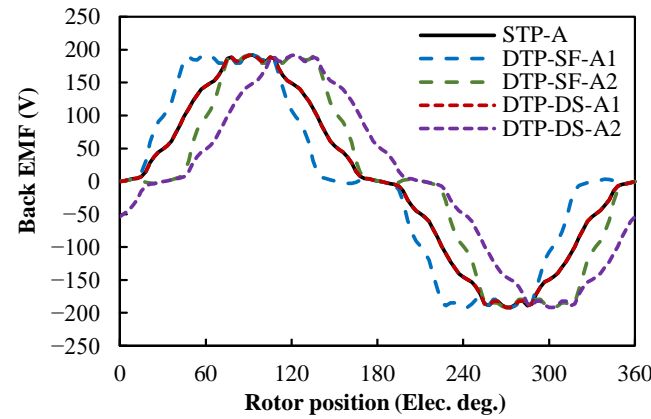


(c) Spectra (Phase)

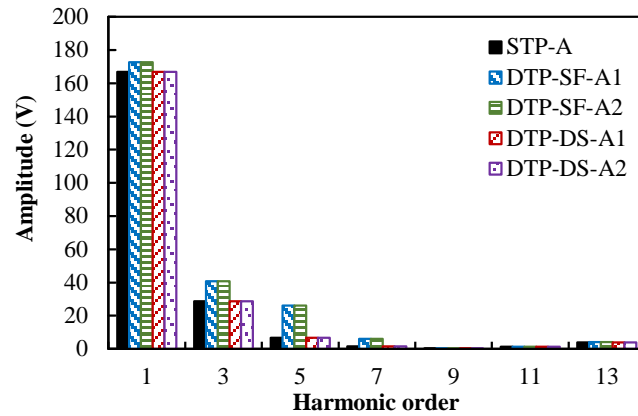
Fig. 3.11 Phase flux linkages of different winding configurations under OC condition.

3.3.2.2 Back EMF

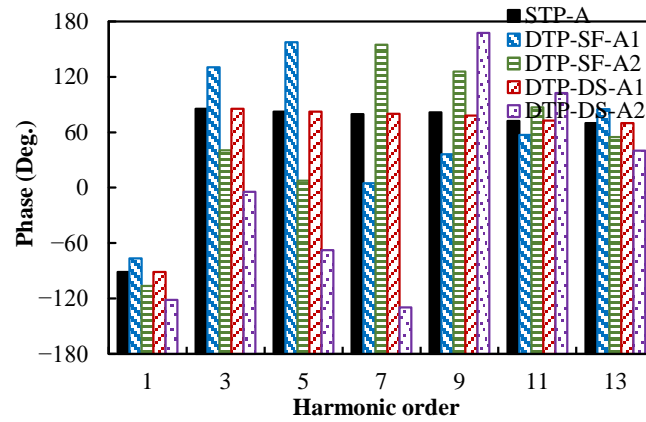
Under OC condition, the phase back EMFs in STP, DTP-SF, and DTP-DS machines at 3000rpm are compared in Fig. 3.12. It can be seen that STP and DTP-DS winding configurations have identical harmonic contents in phase back EMFs, and DTP-SF winding configuration has higher magnitudes in the 1st, 3rd, 5th, and 7th harmonics than STP and DTP-DS counterparts.



(a) Waveforms



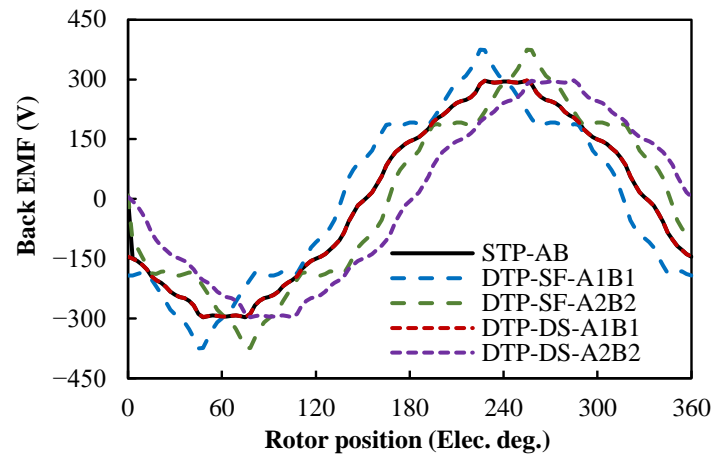
(b) Spectra (Amplitude)



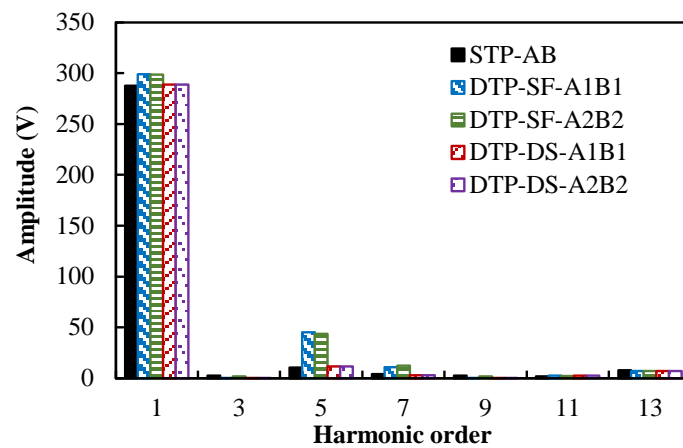
(c) Spectra (Phase)

Fig. 3.12 Phase back EMFs of different winding configurations at 3000rpm.

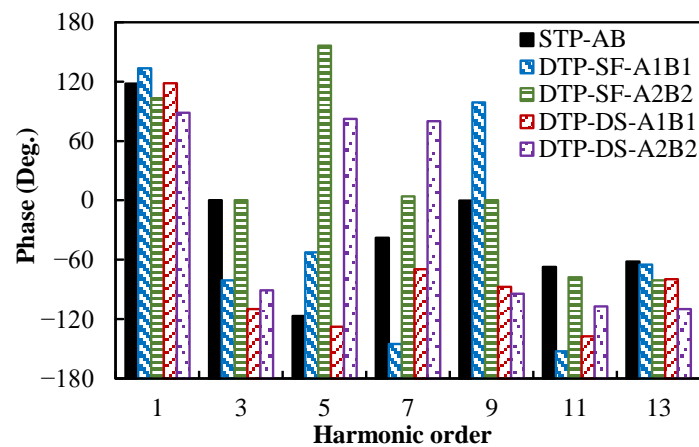
Based on Fig. 3.12, the line-to-line back EMFs of STP, DTP-SF, and DTP-DS winding configurations are compared in Fig. 3.13. The harmonic contents in line-to-line back EMFs are almost the same to those in phase back EMFs except that all the triple harmonics (the 3rd and 9th, etc. harmonics) are eliminated due to the symmetric three-phase winding layouts.



(a) Waveforms



(b) Spectra (Amplitude)

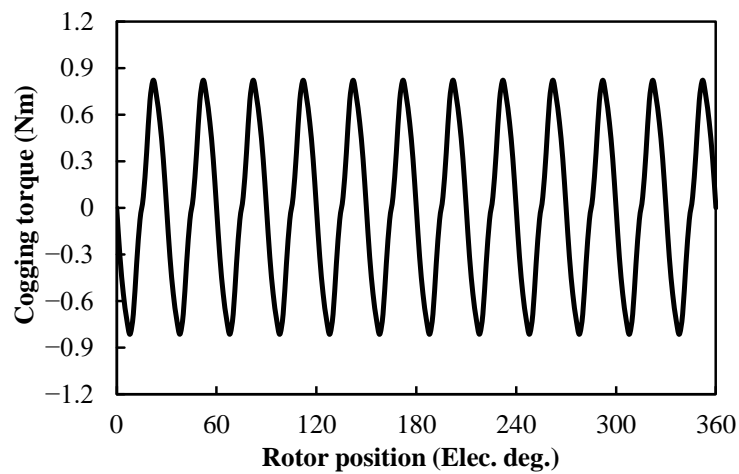


(c) Spectra (Phase)

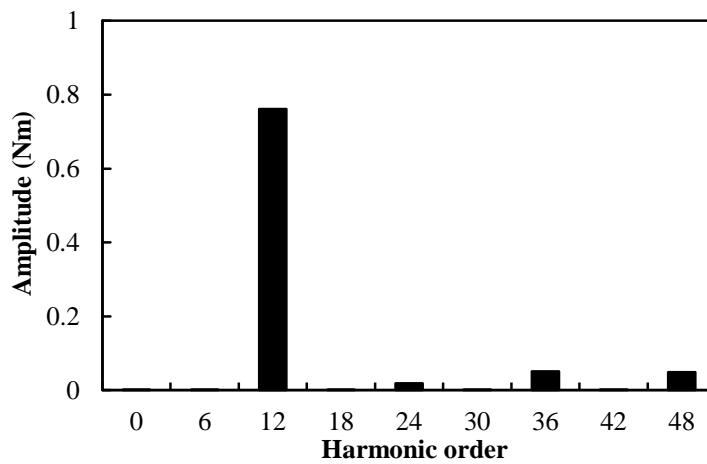
Fig. 3.13 Line-to-line back EMFs of different winding configurations at 3000rpm.

3.3.2.3 Cogging Torque

As cogging torque is not associated with armature windings, different winding configurations cannot affect cogging torque characteristic of the benchmark machine. The waveform and spectrum of the cogging torque in Toyota Prius 2010 machine are shown in Fig. 3.14. Due to the 48-slot/8-pole number combination, the fundamental order of cogging torque in the benchmark machine is 48 in mechanical angle (the smallest common multiple between slot number and pole number) and 12 in electric angle [ZHU00]. From Fig. 3.14, it can be seen that the dominant harmonic in cogging torque is the 12th harmonic.



(a) Waveform



(b) Spectrum

Fig. 3.14 Cogging torque of Toyota Prius 2010 machine.

3.3.3 Torque Performance

3.3.3.1 Average Torque-Current Advancing Angle Characteristics

Since an IPM rotor is employed in the benchmark PMSM, the output torque varies evidently with current advancing angle. Hence, the optimal current advancing angle for the maximum output torque should be chosen specially for STP, DTP-SF, and DTP-DS winding configurations to make full use of the PM and reluctance torque components in these PMSMs.

To produce the largest torque, phase currents should be set as the maximum values, i.e., 236Apk in STP windings and 118Apk in DTP-SF and DTP-DS windings. Since there are two winding sets in DTP-SF and DTP-DS winding configurations, and the two winding sets are shifted by 30° in electric, in the following sections, the current advancing angles for DTP winding configurations only denote the average values of the actual current advancing angles in the two winding sets. Thus, the average torque-current advancing angle characteristics of STP, DTP-SF, and DTP-DS winding configurations can be compared in Fig. 3.15, and the detailed values are listed in Table 3.5. It can be seen that compared with STP counterpart, both DTP-SF and DTP-DS winding configurations can improve average torque when using the same current advancing angle. As predicted by winding factors, DTP-SF winding configuration can produce the highest average torque among the three winding configurations. However, it can also be found that in the STP, DTP-SF, and DTP-DS PMSMs, the optimal current angles for the maximum average torque are all about 50° . In other words, DTP winding configurations cannot affect the optimal current advancing angle in STP PMSMs.

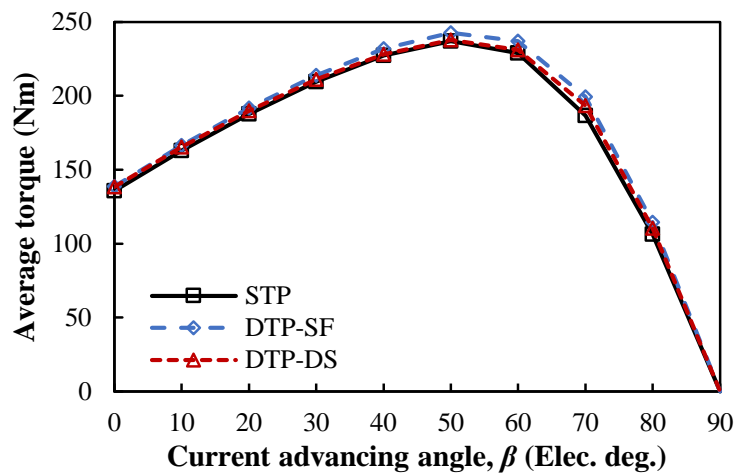


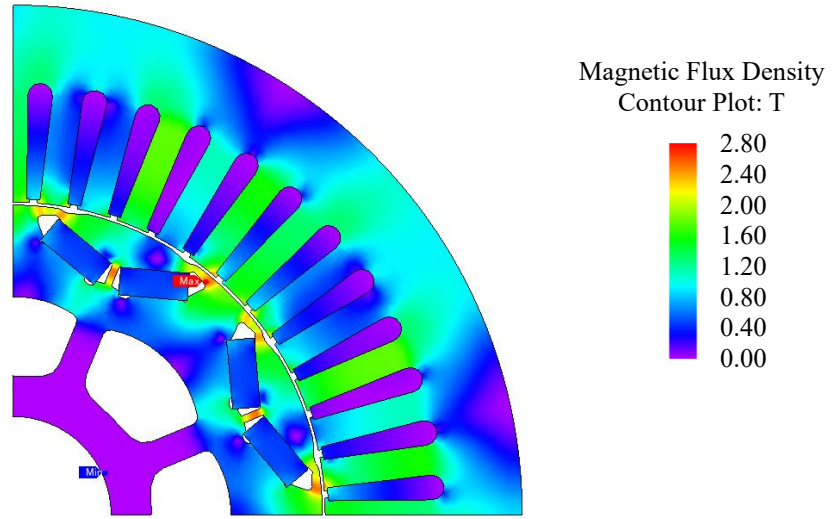
Fig. 3.15 Average torque-current advancing angle characteristics of different winding configurations.

Table 3.5 Comparison of average torque-current advancing angle characteristics of different winding configurations ($I_A = 236\text{A}$)

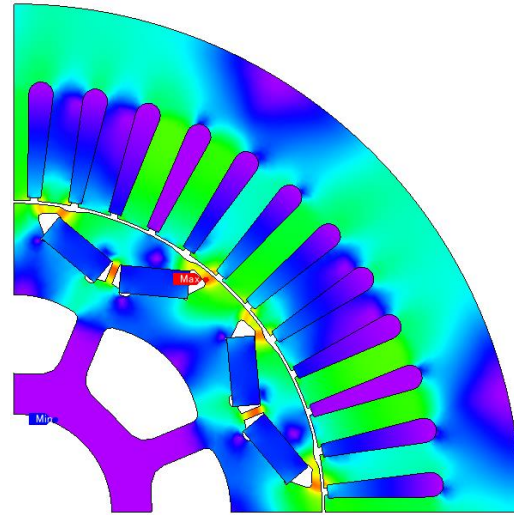
| | STP | DTP-SF | | DTP-DS | |
|---|---------------------|---------------------|--------------------------|---------------------|--------------------------|
| Current advancing angle, β ($^\circ$) | Average Torque (Nm) | Average Torque (Nm) | Improvement from STP (%) | Average Torque (Nm) | Improvement from STP (%) |
| 0 | 135.88 | 138.67 | +2.06 | 138.48 | +1.92 |
| 10 | 163.01 | 166.38 | +2.06 | 165.43 | +1.49 |
| 20 | 187.79 | 191.65 | +2.06 | 189.87 | +1.11 |
| 30 | 209.48 | 213.82 | +2.07 | 211.06 | +0.76 |
| 40 | 227.27 | 232.01 | +2.08 | 228.14 | +0.38 |
| 50 | 236.99 | 242.79 | +2.45 | 237.77 | +0.33 |
| 60 | 228.95 | 236.96 | +3.50 | 231.18 | +0.97 |
| 70 | 186.76 | 199.30 | +6.72 | 193.35 | +3.53 |
| 80 | 106.33 | 114.45 | +7.64 | 110.31 | +3.75 |
| 90 | -0.01 | -0.01 | - | -0.05 | - |

It also should be noticed from Table 3.5 that although DTP-DS winding configuration shares identical winding factors with STP counterpart, the average torque produced by STP PMSM can still be improved slightly by using DTP-DS windings, especially when current advancing angle is close to 90° . This phenomenon is caused by the different flux distributions and different winding layouts in STP and DTP PMSMs, and will be explained in details under the condition $I_A = 236\text{A}$, $\beta = 80^\circ$.

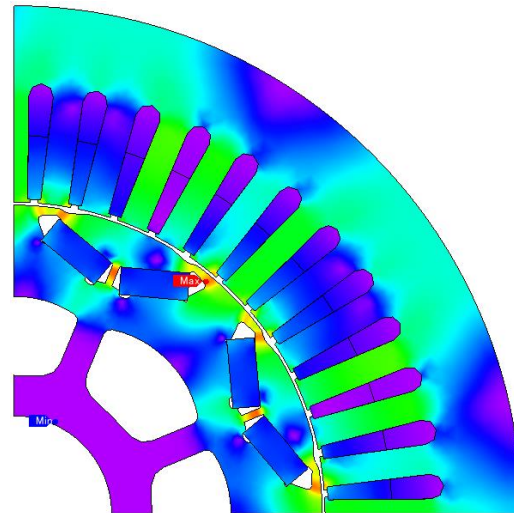
As shown in Table 3.5, under the condition $I_A = 236\text{A}$, $\beta = 80^\circ$, the average torque produced by STP PMSM can be improved by 7.64% and 3.75%, respectively in DTP-SF and DTP-DS PMSMs. To further investigate how STP and DTP winding configurations affect the resultant torque performance in PMSMs, the flux distributions of STP, DTP-SF and DTP-DS PMSMs under the condition $I_A = 236\text{A}$, $\beta = 80^\circ$, are shown in Fig. 3.16. It can be seen that the flux density distributions of different winding configurations are similar with each other under this condition. It is very difficult to find the differences between different winding configurations from Fig. 3.16. Hence, Fig. 3.17 provides the radial air-gap flux density waveforms and spectra of different winding configurations under this condition. From Fig. 3.17, it can be seen that since STP, DTP-SF, and DTP-DS windings have different stator MMFs, the amplitudes of the fundamental components in DTP-SF and DTP-DS PMSMs are slightly higher than that in STP counterpart. In addition, it also should be noticed that the phases of the fundamental components in DTP PMSMs are shifted a little compared with that in STP counterpart, which also contributes to the resultant average torque improvements.



(a) STP

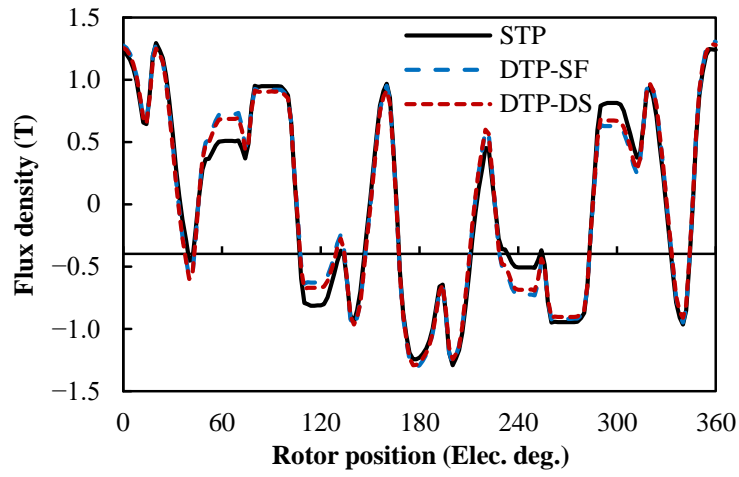


(b) DTP-SF

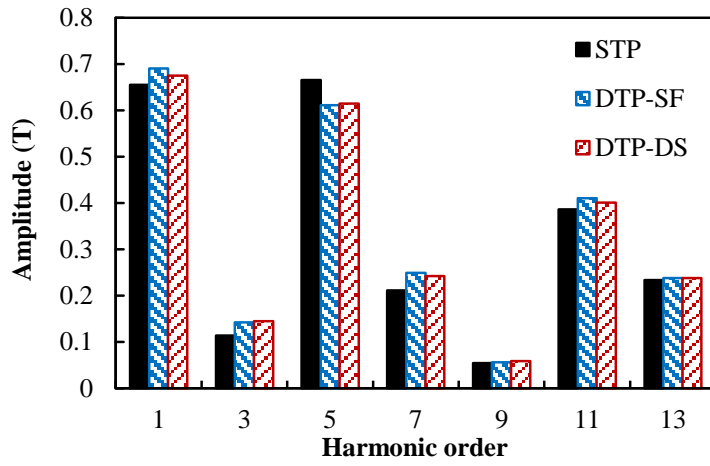


(c) DTP-DS

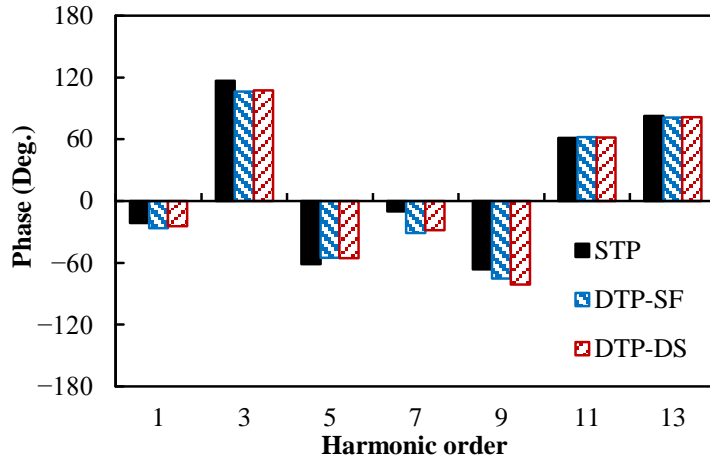
Fig. 3.16 Flux density distributions of different winding configurations at $I_A = 236\text{A}$, $\beta = 80^\circ$.



(a) Waveforms



(b) Spectra (Amplitude)

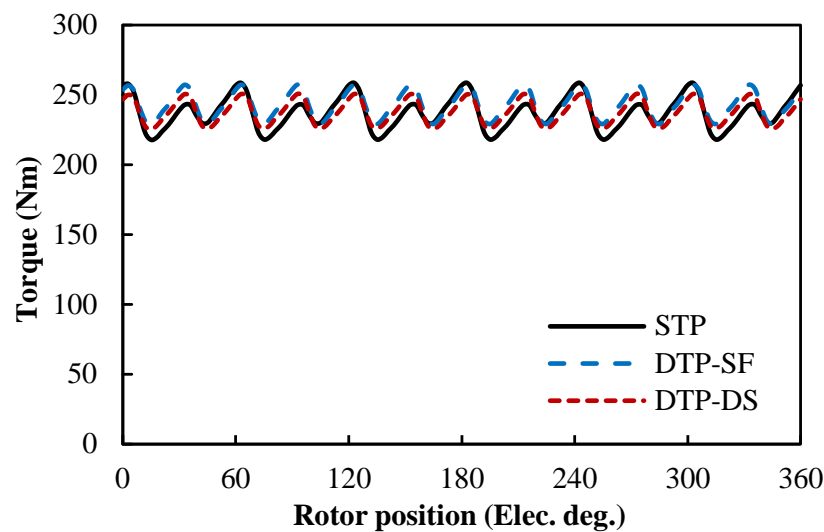


(c) Spectra (Phase)

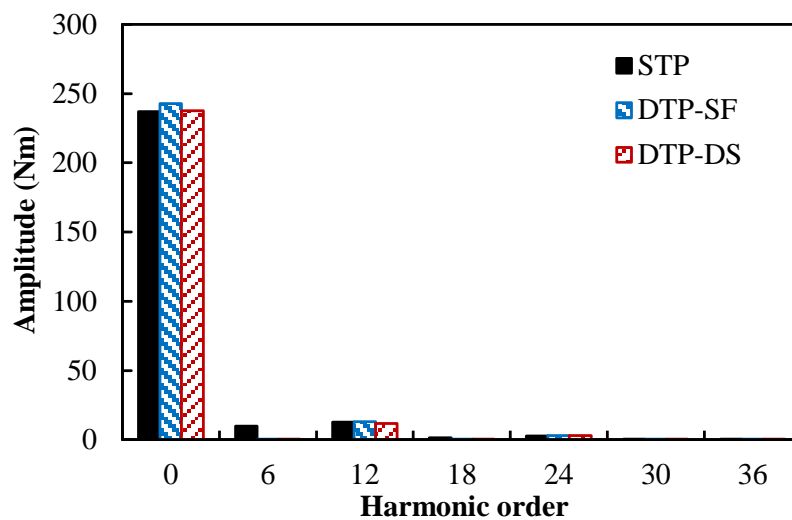
Fig. 3.17 Radial air-gap flux density distributions of different winding configurations at $I_A = 236\text{A}$, $\beta = 0^\circ$.

3.3.3.2 Instantaneous Torque Characteristics under Maximum Torque Condition

Based on Fig. 3.15 and Table 3.5, 50° is chosen as the optimal current advancing angles for STP, DTP-SF, and DTP-DS PMSMs for the maximum torque conditions. The waveforms and spectra of the instantaneous torque in STP, DTP-SF, and DTP-DS PMSMs are given in Fig. 3.18. The average torques and torque ripples of different winding configurations are listed in Table 3.6. Compared with STP counterpart, not only average torque can be improved by DTP winding configurations, but also torque ripples can be reduced significantly by using DTP windings.



(a) Waveforms



(b) Spectra (Amplitude)

Fig. 3.18 Instantaneous torque performance of different winding configurations under maximum torque condition.

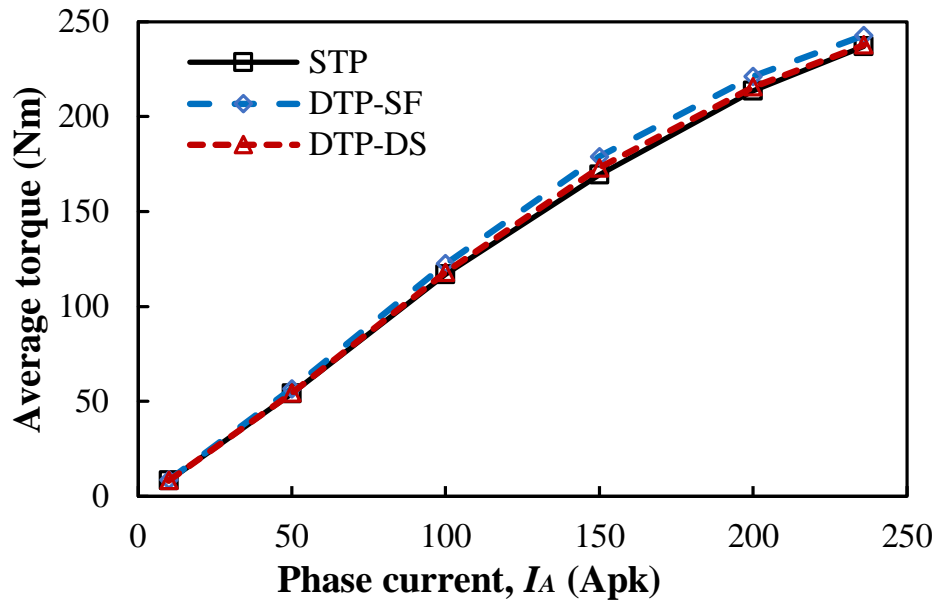
Table 3.6 Comparison of instantaneous torque performance of different winding configurations under maximum torque condition

| | STP | DTP-SF | DTP-DS |
|--------------------------|--------|--------|--------|
| Average torque | 236.98 | 242.80 | 237.75 |
| Improvement with STP (%) | - | +2.45 | +0.33 |
| Torque ripple (Nm) | 34.11 | 20.46 | 18.54 |
| Torque ripple (%) | 14.39 | 8.43 | 7.80 |

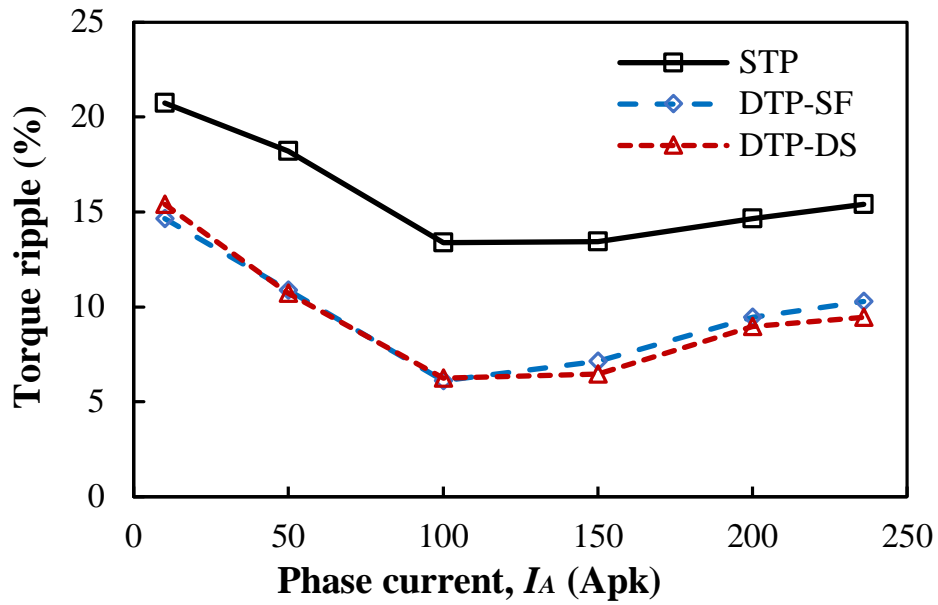
From Fig. 3.18(b), it can be observed that the dominant torque harmonics in STP PMSM are the 6th and 12th harmonics, while in DTP-SF and DTP-DS PMSMs, only the 12th harmonics are the dominant torque harmonics. In other words, with the utilization of DTP-SF and DTP-DS winding configurations, the 6th torque harmonics can be totally eliminated. Hence, both DTP-SF and DTP-DS winding configurations can reduce on-load torque ripples significantly.

3.3.3.3 Average Torque and Torque Ripple–Current Amplitude Characteristics

Besides the maximum torque condition, the torque characteristics of STP, DTP-SF, and DTP-DS winding configurations under other excitation conditions are also investigated. It should be mentioned again that in the following sections, only the amplitudes and phases of the phase currents in STP PMSM are utilized to describe load conditions, the actual phase current amplitudes in DTP-SF and DTP-DS PMSMs are only a half of that in STP counterpart, and the actual phase current phases in the two winding sets in DTP-SF and DTP-DS PMSMs are shifted by 30° in electric. Assuming I_A is varied from 10, 50, 100, 150, 200 to 236A_{pk}, and β varied from 0°, 10°, 20°, 30°, 40°, 50°, 60°, 70°, 80°, and 90°, the torque characteristics of the STP, DTP-SF, and DTP-DS PMSMs can be obtained separately using FE method. When the PMSMs are controlled using a maximum torque per ampere (MTPA) strategy, the variations of the average torque and torque ripple of different winding configurations with phase current amplitude can be shown in Fig. 3.19 and the detailed values are listed in Table 3.7.



(a) Average torque



(b) Torque ripple

Fig. 3.19 Average torque- and torque ripple-phase current amplitude characteristics of different winding configurations when using MTPA strategy.

Table 3.7 Comparison of torque characteristics of different winding configurations with different phase current amplitudes

| I_A (Apk) | | STP | DTP-SF | DTP-DS |
|-------------|--------------------------|--------|--------|--------|
| 10 | Average torque (Nm) | 8.27 | 8.57 | 8.26 |
| | Improvement with STP (%) | - | +3.73 | -0.02 |
| | Torque ripple (Nm) | 1.71 | 1.26 | 1.27 |
| | Torque ripple (%) | 20.73 | 14.65 | 15.40 |
| 50 | Average torque | 54.13 | 56.63 | 54.26 |
| | Improvement with STP (%) | - | +4.63 | +0.25 |
| | Torque ripple (Nm) | 9.85 | 6.16 | 5.82 |
| | Torque ripple (%) | 18.19 | 10.87 | 10.73 |
| 100 | Average torque | 116.79 | 122.52 | 118.05 |
| | Improvement with STP (%) | - | +4.91 | +1.08 |
| | Torque ripple (Nm) | 15.62 | 7.50 | 7.37 |
| | Torque ripple (%) | 13.38 | 6.12 | 6.24 |
| 150 | Average torque | 169.51 | 178.91 | 172.92 |
| | Improvement with STP (%) | - | +5.55 | +2.01 |
| | Torque ripple (Nm) | 22.80 | 12.77 | 11.19 |
| | Torque ripple (%) | 13.45 | 7.14 | 6.47 |
| 200 | Average torque | 213.46 | 221.18 | 215.68 |
| | Improvement with STP (%) | - | +3.61 | +1.04 |
| | Torque ripple (Nm) | 31.24 | 20.88 | 19.33 |
| | Torque ripple (%) | 14.64 | 9.44 | 8.96 |
| 236 | Average torque | 236.99 | 242.79 | 237.77 |
| | Improvement with STP (%) | - | +2.45 | +0.33 |
| | Torque ripple (Nm) | 36.52 | 24.97 | 22.49 |
| | Torque ripple (%) | 15.41 | 10.28 | 9.46 |

According to Table 3.7, compared with STP counterpart the variations of the average torque improvements in DTP-SF and DTP-DS PMSMs with phase current amplitude are shown in Fig. 3.20. From Fig. 3.19 and Fig. 3.20, it can be generally concluded that both DTP-SF and DTP-DS winding configurations can improve the average torque and reduce torque ripples in STP PMSM. It also should be noticed that both DTP-SF and DTP-DS winding configurations can always reduce on-load torque ripples, but only DTP-SF winding configuration can always improve average torque, no matter what excitation is. DTP-DS winding configuration can only improve average torque a little when using suitable phase currents. It is also noteworthy that when $I_A = 150\text{A}$, the torque improvements of DTP-SF and DTP-DS PMSMs are 5.59% and 2.02%, respectively, which are much higher than the theoretical increases in winding factors

(3.53% in DTP-SF winding configuration and 0% in DTP-DS winding configuration). It indicates that the real torque improvements caused by DTP winding configurations can be much higher than theoretical increases in winding factors under specific on-load conditions.

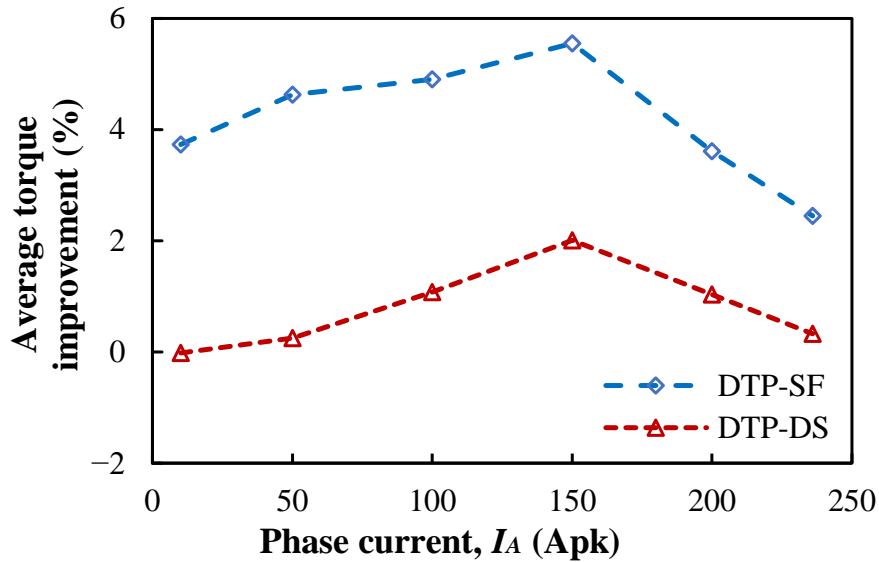


Fig. 3.20 Average torque improvement-phase current amplitude characteristics of DTP-SF and DTP-DS winding configurations when using MTPA strategy.

3.3.3.4 Torque and Power Speed Characteristics

In the analyses above, the speeds of STP, DTP-SF, and DTP-DS PMSMs are fixed at 3000 rpm. The performances of different winding configurations under other speeds, especially high-speed conditions, have not been considered. Hence, it is necessary to calculate the torque and power-speed envelopes of STP, DTP-SF, and DTP-DS winding configurations.

Further, since PMSMs are constrained by DC voltage under high-speed conditions and on-load back EMFs can be calculated by using d- and q-axis inductances in PMSMs, the d- and q-axis inductances of different winding configurations should be calculated firstly. With the method proposed in [QI09], the effects of d-axis currents on d-axis flux linkages are considered to improve the accuracy of the calculations. Assuming that I_d varies from -240A to 0A and I_q varies from 0A to 240A, the variations of d- and q-axis inductances with different winding configurations and different d- and q-axis current combinations can be obtained, as shown in Fig. 3.21. It can be observed that both d- and q-axis currents can affect d- and q-axis inductances evidently.

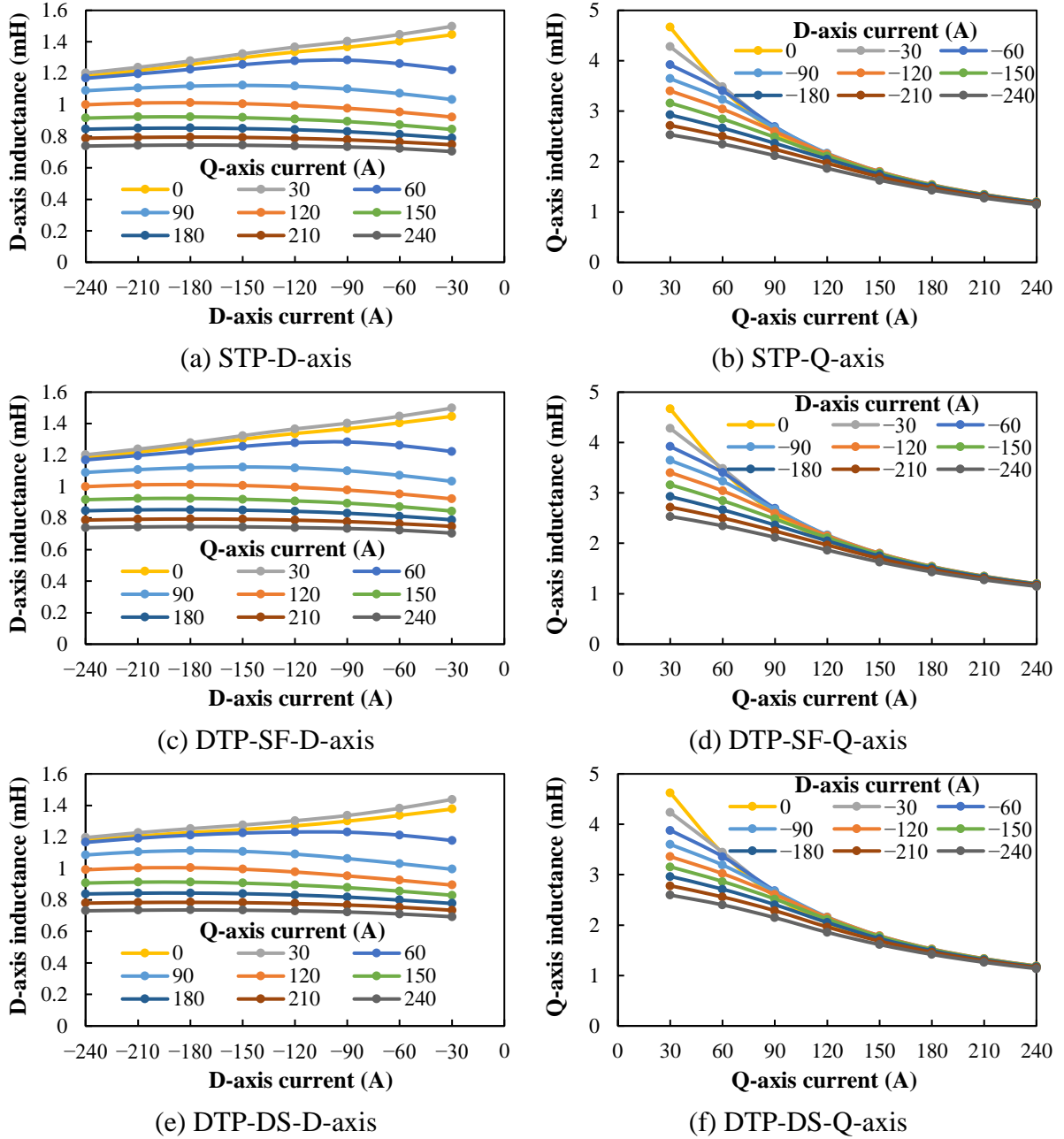
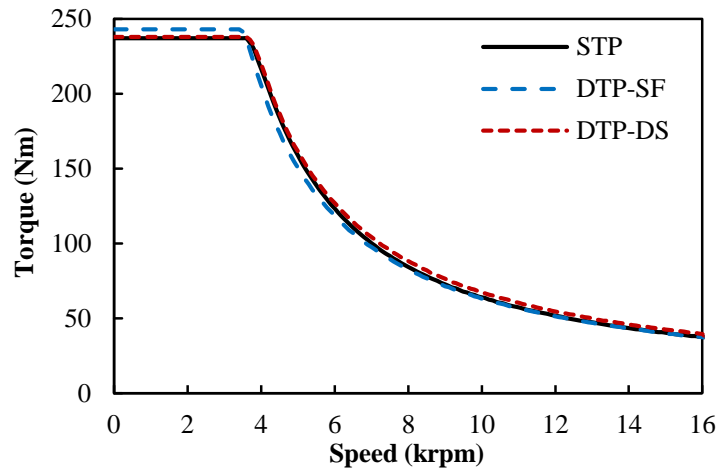


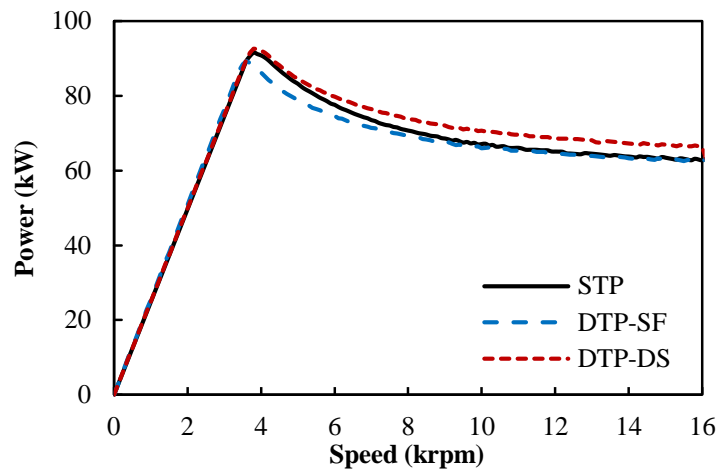
Fig. 3.21 Variations of d- and q-axis inductances with different winding configurations and different d- and q-axis current combinations.

In the calculation, the DC voltage is fixed at 650 V, and the phase currents are limited at 236Apk in STP windings and 118Apk in DTP windings. The torque and power-speed envelopes of STP, DTP-SF, and DTP-DS winding configurations are shown in Fig. 3.22. It should be mentioned that the powers shown in Fig. 3.22(b) are the output power of these PMSMs. Input powers of different PMSMs need take losses into consideration, and the analyses of losses will be presented sub-section 3.3.4. In Fig. 3.22, the STP, DTP-SF, and DTP-DS PMSMs are operated at two ranges, i.e., constant torque range and constant power range. When the speed is lower

than the base speed, the PMSM is operated to produce the highest average torque according to the limits of phase currents, but when the speed is higher than the base speed, the highest average torque is limited by DC voltage. As shown in Fig. 3.22, the base speed is 3500, 3400, and 3600 rpm for STP, DTP-SF, and DTP-DS PMSMs, respectively. Thus, DTP-DS winding configuration can only increase base speed slightly.



(a) Torque-speed envelope

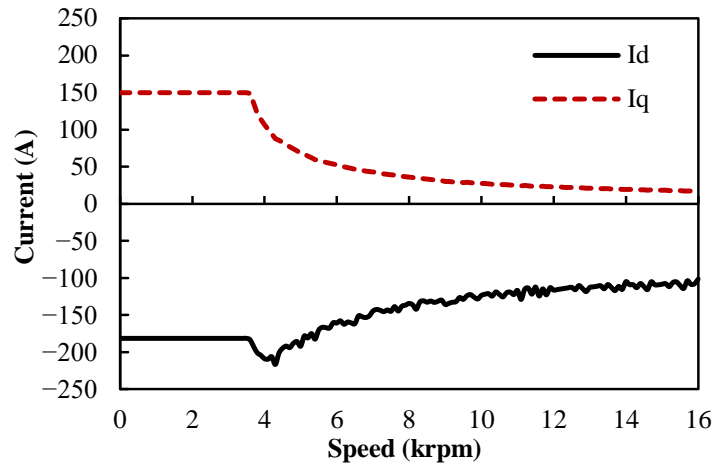


(b) Power-speed envelope

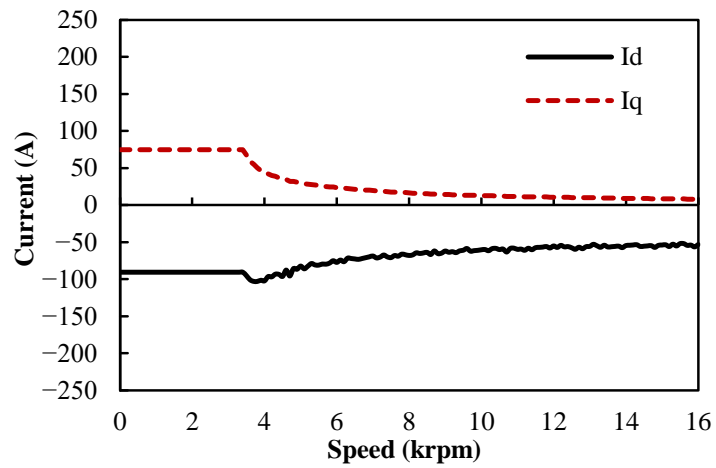
Fig. 3.22 Torque- and power-speed envelopes of different winding configurations.

From Fig. 3.22, it can be seen that, DTP-SF winding configuration has the highest average torque in constant torque range. However, DTP-DS winding configuration has the highest output power in constant power range. Under the same speed, the higher output power of DTP-DS PMSM suggests that DTP-DS PMSM can produce the highest average torque among the three PMSMs.

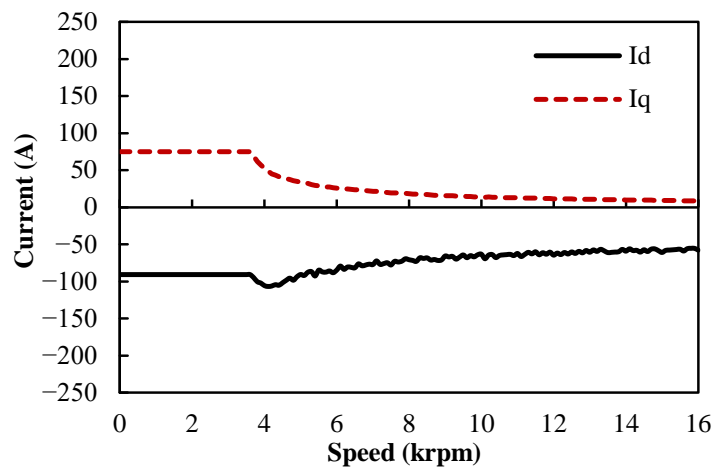
Actually, to obtain the torque- and power-speed envelopes shown in Fig. 3.22, the maximum d- and q-axis currents of STP, DTP-SF and DTP-DS winding configurations at different speeds are calculated before, as shown in Fig. 3.23.



(a) STP



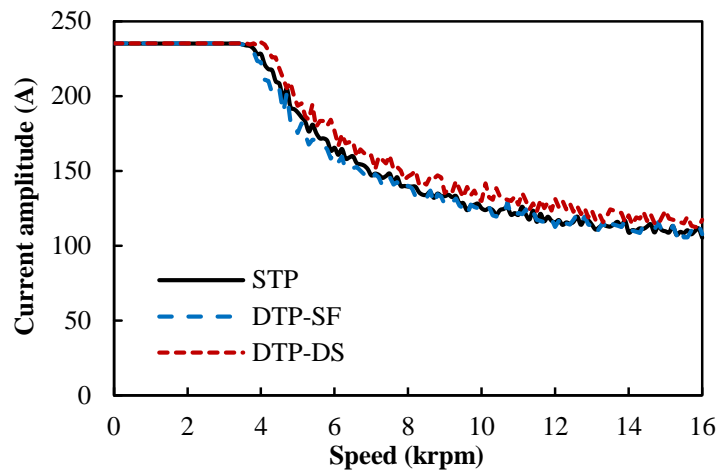
(b) DTP-SF



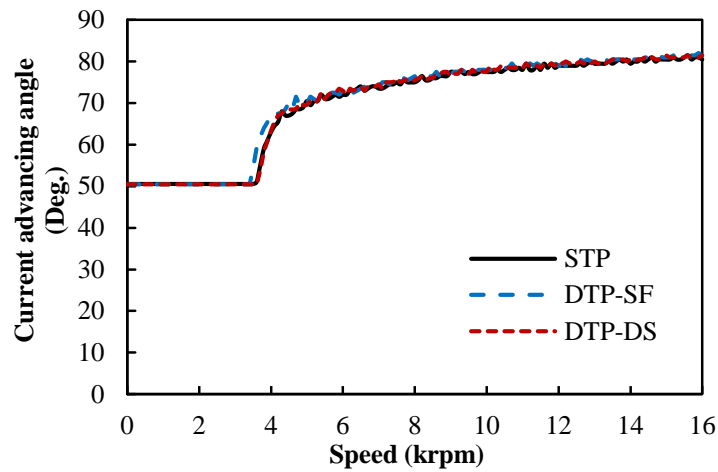
(c) DTP-DS

Fig. 3.23 d- and q-axis currents of different winding configurations over entire speed range.

According to the d- and q-axis currents shown in Fig. 3.23, the amplitudes and current advancing angles of the phase currents in STP, DTP-SF, and DTP-DS winding configurations over the entire speed range are shown in Fig. 3.24(a) and (b), respectively. In Fig. 3.24(a), the phase current amplitudes for DTP-SF and DTP-DS windings are doubled from the actual values for the convenience of the comparison to STP counterpart. It also should be mentioned that the curves shown in Fig. 3.24 are not very smooth, because the number of cases used in the calculation is only 81. The back EMF and output torque over the entire excitation range are fitted based on 81 cases using interpolation function, which results in some small errors between estimated values and real results. These small errors cause the small pulsations in the current amplitude– and current advancing angle–speed curves in Fig. 3.24.



(a) Current amplitude



(b) Current advancing angle

Fig. 3.24 Amplitudes and advancing angles of phase currents in different winding configurations over entire speed range.

From Fig. 3.24(a) and (b), it can be found that the amplitudes of phase currents in DTP-DS windings can be higher than those in DTP-SF and STP windings under high-speed conditions, while the current angles of different winding configurations are very similar with each other. Considering that under high-speed conditions, the phase back EMFs are limited by DC voltage, the higher phase currents in DTP-DS windings result in larger output torque in DTP-DS PMSM in constant power range.

Overall, it can be concluded that DTP-SF winding configuration produces the highest average torque in constant torque range and DTP-DS winding configuration can produce the highest average torque in constant power range, although both are not very significant.

3.3.4 Loss and Efficiency

3.3.4.1 Loss and Efficiency under Maximum Torque Condition

In this sub-section, the losses of STP, DTP-SF, and DTP-DS winding configurations under the maximum torque condition are calculated firstly. The total losses in PMSMs are classified into copper loss, iron loss, PM eddy loss, and mechanical loss. The losses and efficiencies of PMSMs are calculated using the method in [CHU15].

Copper loss is calculated by using Joule's law, as

$$P_{Cu} = 3R_0 I_a^2 \quad (3.13)$$

where R_0 is the phase resistance of the DTP windings, and I_a is the phase current amplitude.

For a specific speed, iron loss and PM eddy loss are calculated by the FE software, JMAG, according to the properties of materials. In this research, the lamination material is '35H270', and the PM material is 'NdFeB_Br = 1.2T'. However, it should be mentioned for other speeds, iron losses should be estimated based on the hysteresis and eddy current iron losses at the base speed, as

$$P_{Fe} = P_{Hyst-base} \frac{f}{f_{base}} + P_{Eddy-base} \left(\frac{f}{f_{base}} \right)^2 \quad (3.14)$$

where $P_{Hyst-base}$ and $P_{Eddy-base}$ are the hysteresis and eddy current iron losses at the base speed. f and f_{base} are the frequencies of the operating condition and the base speed.

Although STP, DTP-SF, and DTP-DS PMSMs have different winding configurations, their mechanical structures are identical. Hence, all the three PMSMs share the same mechanical loss characteristics, which can be estimated using the measured results in [HSU04], as

$$P_{Me} = 0.26f + 0.00103f^2 \quad (3.15)$$

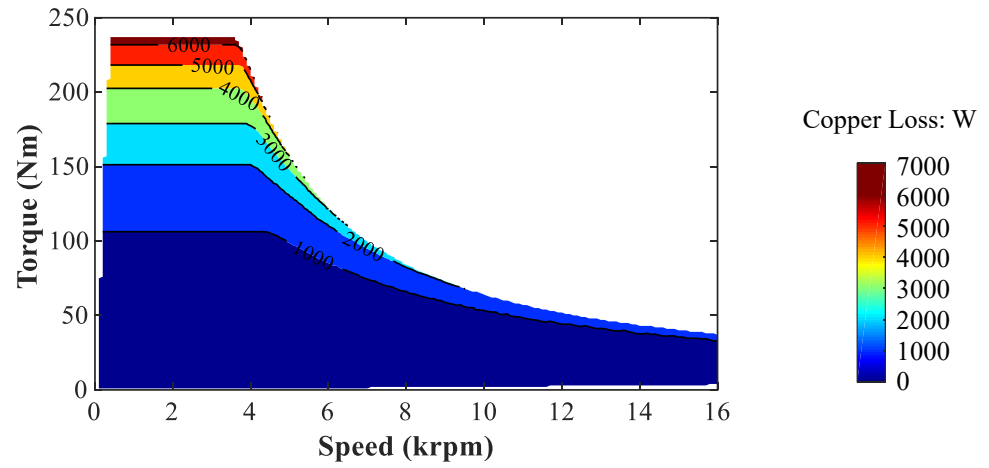
Overall, the loss and efficiency characteristics of STP, DTP-SF, and DTP-DS PMSMs under the maximum torque condition can be summarized and compared in Table 3.8. It can be seen that copper loss is the most dominant loss among all kinds of losses. Compared with STP and DTP-DS windings, the larger phase resistance of the full-pitched windings in DTP-SF windings results in larger copper loss and lower efficiency. From Table 8, it can also be seen that compared with STP counterpart, PM eddy losses can be reduced significantly by using DTP windings. This phenomenon can be explained by the reduced stator MMF harmonics produced by DTP windings. However, since PM eddy loss is much smaller than copper loss, the reduction in PM eddy loss in DTP-DS winding configuration can only increase its efficiency very little, but it may affect the rotor temperature significantly.

Table 3.8 Loss and efficiency of different winding configurations under maximum torque condition

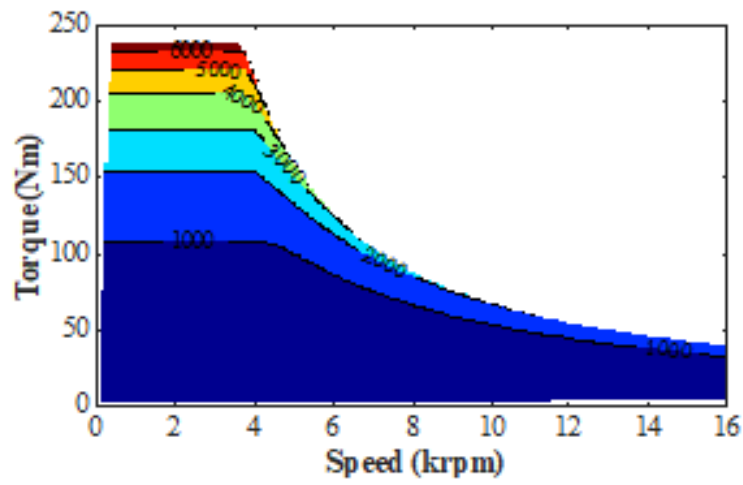
| | STP | DTP-SF | DTP-DS |
|---------------------|----------|----------|----------|
| Speed (rpm) | 3000 | 3000 | 3000 |
| Average torque (Nm) | 236.99 | 242.77 | 237.78 |
| Copper loss (W) | 6432.89 | 7283.49 | 6432.89 |
| Iron loss (W) | 373.12 | 373.12 | 370.24 |
| PM eddy loss (W) | 108.17 | 52.35 | 56.06 |
| Mechanical loss (W) | 93.20 | 93.20 | 93.20 |
| Output power (W) | 74452.60 | 76267.14 | 74700.57 |
| Total loss (W) | 7007.38 | 7802.16 | 6952.39 |
| Input power (W) | 81459.98 | 84069.30 | 81652.96 |
| Efficiency (%) | 91.40 | 90.72 | 91.49 |

3.3.4.2 Loss and Efficiency Maps

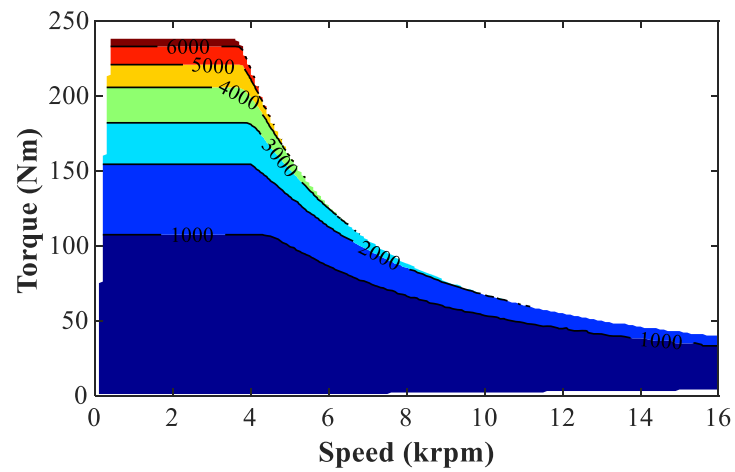
Based on the calculations above, the losses and efficiencies of STP, DTP-SF, and DTP-DS winding configurations under the entire speed range can be obtained. The copper loss maps and iron loss maps of these winding configurations are calculated firstly, as shown in Fig. 3.25 and Fig. 3.26, respectively.



(a) STP

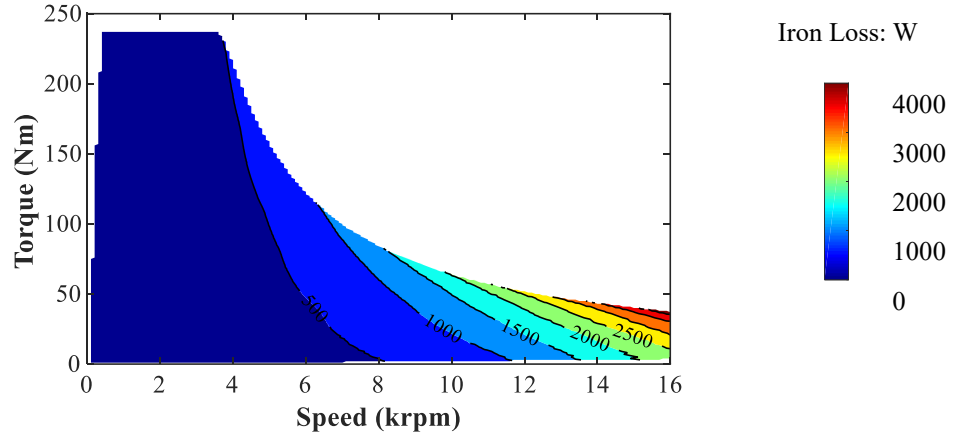


(b) DTP-SF

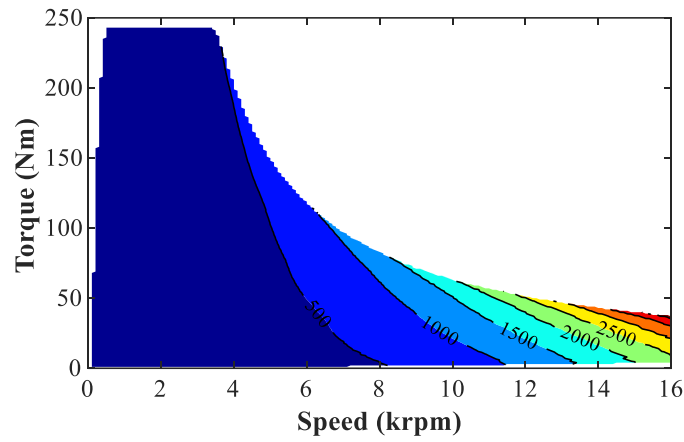


(c) DTP-DS

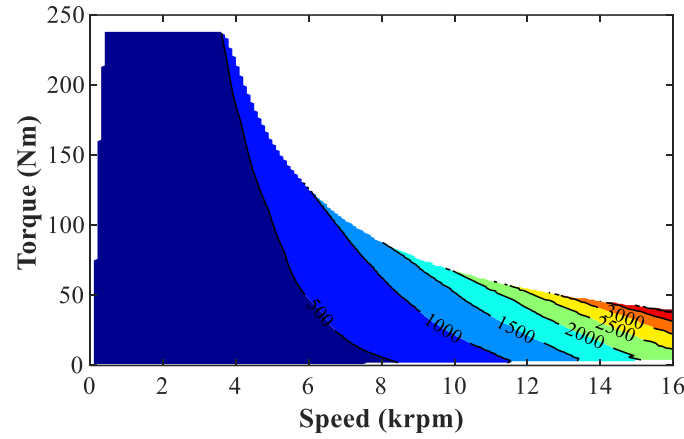
Fig. 3.25 Copper loss maps of different winding configurations.



(a) STP



(b) DTP-SF



(c) DTP-DS

Fig. 3.26 Iron loss maps of different winding configurations.

As shown in Table 3.8, PM eddy current loss only accounts for a small part of total losses in all investigated PMSMs. Considering that it is difficult to obtain PM eddy current loss under different speeds, PM eddy current loss is neglected in calculation of the efficiency maps.

For mechanical loss, in the investigated PMSMs, the variation of mechanical loss with speed can be obtained from (3.15), as shown in Fig. 3.27.

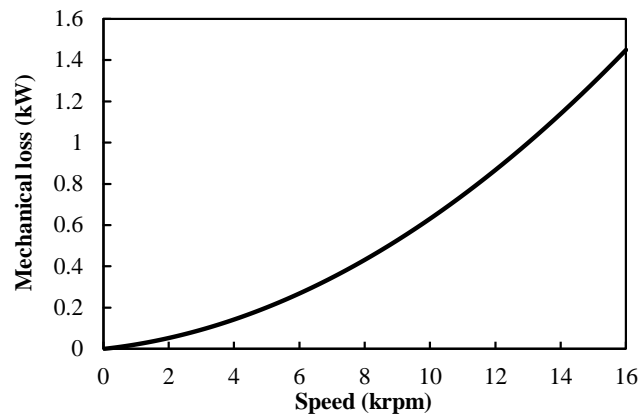
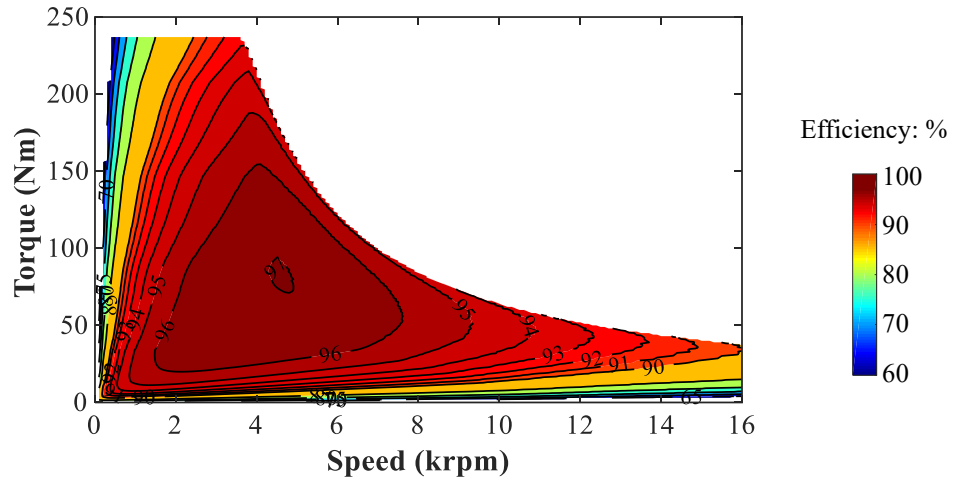


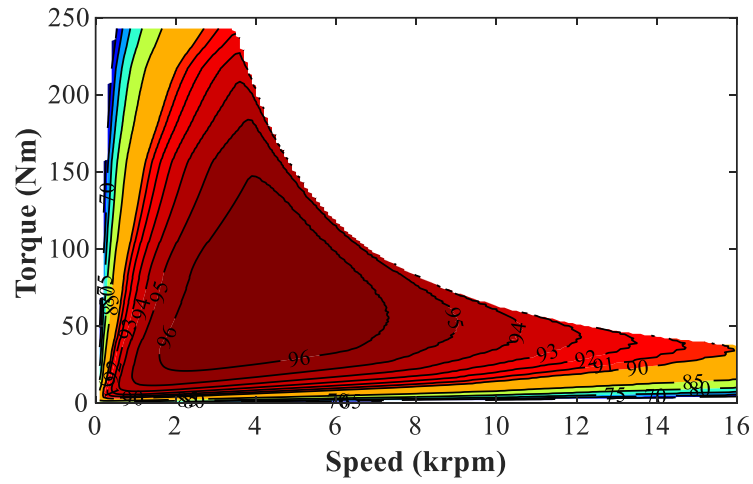
Fig. 3.27 Variation of mechanical loss with speed.

Based on Fig. 3.25, Fig. 3.26, and Fig. 3.27, the efficiency maps of STP, DTP-SF, and DTP-DS winding configurations are shown in Fig. 3.28. It can be seen that the highest efficiency in STP and DTP-DS PMSMs can reach 97%, while the highest efficiency in DTP-SF counterpart is 96%. Furthermore, the high-efficiency (97%) range in DTP-DS PMSM is slightly larger than that in the STP PMSM.

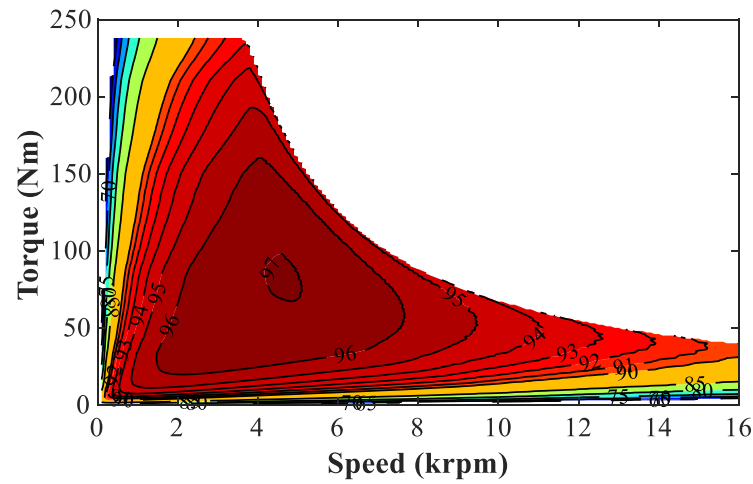
To better show the differences between the efficiency maps of DTP and STP PMSMs, the efficiency difference maps between DTP and STP PMSMs are shown in Fig. 3.29. For DTP-SF PMSM, the efficiency difference is almost zero over the whole range. However, for DTP-DS PMSM, the efficiency difference is positive in most of the whole range. It indicates that the overall efficiency of DTP-SF PMSM is slightly lower than that of STP counterpart, while DTP-DS winding configuration can improve the efficiency in STP PMSM over the whole operating region. It also should be noticed that almost all the efficiency differences shown in Fig. 3.29 are lower than $\pm 0.5\%$, which suggests that the influences of DTP-SF and DTP-DS winding configurations on resultant efficiency are not obvious.



(a) STP



(b) DTP-SF



(c) DTP-DS

Fig. 3.28 Efficiency maps of different winding configurations.

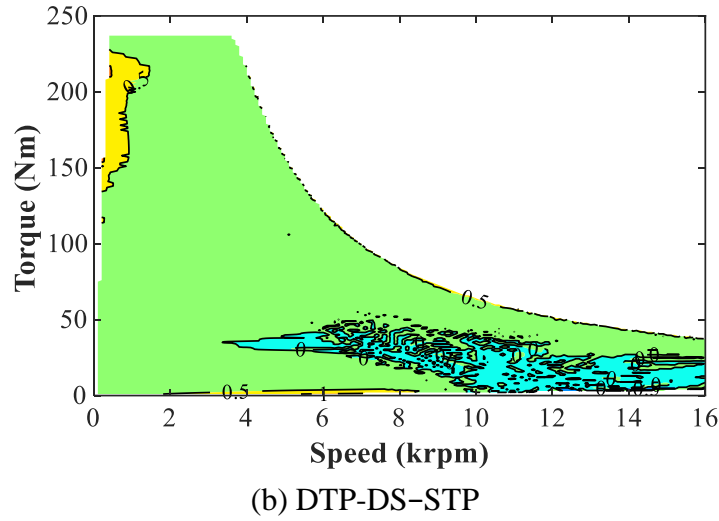
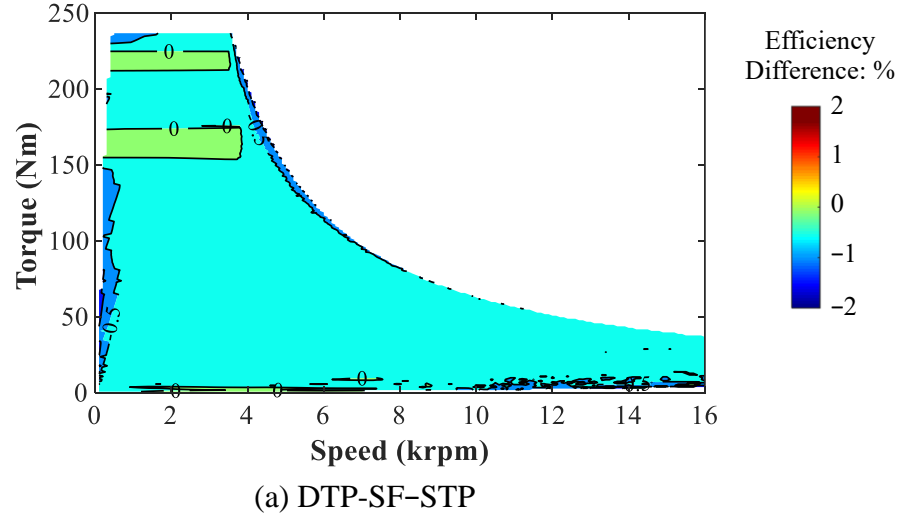


Fig. 3.29 Differences between efficiency maps of DTP and STP winding configurations.

3.3.5 Summary

In this sub-section, the electromagnetic performances of PMSMs with STP, DTP-SF, and DTP-DS winding configurations are compared comprehensively using 2D FE method. The comparison includes flux density distribution, back EMF performance, torque and power characteristics, loss and efficiency performance. From the analyses above, it is found that both DTP-SF and DTP-DS winding configurations can improve average torque and reduce torque ripples in the researched STP PMSM. Specifically, DTP-SF winding configuration is more suitable for constant torque range, as the torque improvement in the DTP-SF winding configuration is higher than that in the DTP-DS counterpart. The DTP-DS winding configuration is preferred for constant power range because it can produce higher output torque with lower torque pulsation under high-speed conditions.

3.4 Electromagnetic Performance under 3-phase OC Condition

Since DTP windings are composed of two separate three-phase winding sets, the failure of one winding set will not lead to the failure of the whole system, and DTP machines can run with only one three-phase winding set. Hence, the operation condition, where one three-phase winding set is excited and one three-phase winding set is open-circuited, which is designated as ‘3-ph OC condition’ in the following sections, should be paid extract attentions in DTP PMSMs. However, it also should be mentioned that although the performance under 3-ph OC condition indicates the fault-tolerant capability of the DTP winding configuration, the ‘3-ph OC condition’ does not only mean fault condition. For example, when peak performance is not required, it is possible to only partially excite the PMSM to improve overall efficiency by reducing copper, iron and inverter losses. Hence, better electromagnetic performance under 3-ph OC condition denotes more than better fault-tolerant capability.

3.4.1 Winding Layouts

Based on the winding connections shown in Fig. 3.3, assuming the second winding sets in DTP-SF and DTP-DS winding configurations are open-circuited, the layouts of the remaining winding set are shown in Fig. 3.30. It can be observed that the opposite parts of the stator are wound by the windings of the same phase. The radial forces produced by the opposite windings can be balanced, and hence, there will be no unbalanced radial force in the DTP PMSMs under three-phase OC condition.

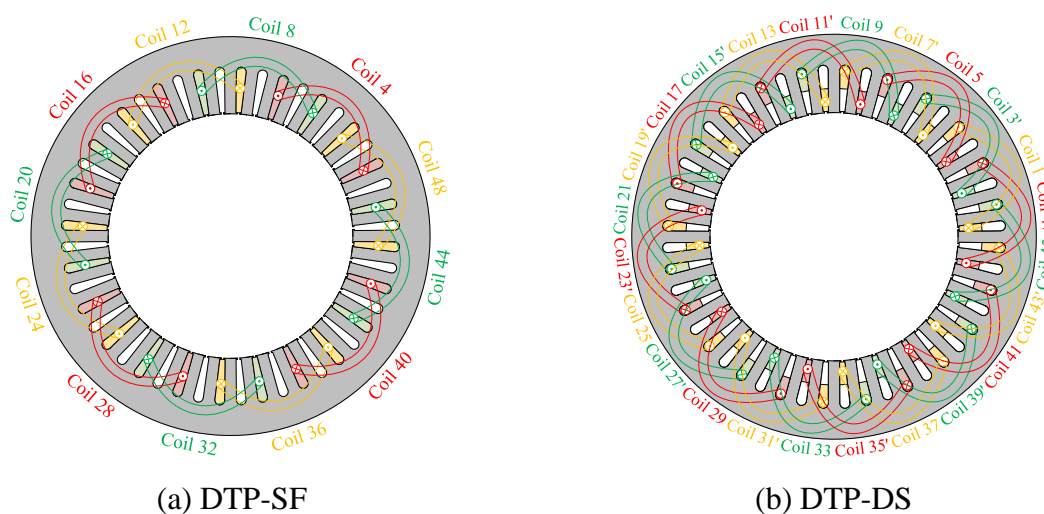


Fig. 3.30 Winding layouts of remaining winding set in DTP PMSMs under 3-ph OC condition.

Additionally, it should be noticed that the winding layouts of the remaining winding set in DTP-DS PMSM is exactly identical to the original windings in the Toyota Prius 2010 machine. It can be expected that DTP-DS winding configuration can have better performance than DTP-SF counterpart under 3-ph OC condition.

3.4.2 Torque Performance

3.4.2.1 Instantaneous Torque Characteristics under Maximum Torque Condition

The instantaneous torque characteristics of DTP-SF and DTP-DS winding configurations are examined under the maximum torque condition firstly. To find the optimal current advancing angles for the maximum average torque under 3-ph OC condition in the two DTP winding configurations, the phase current in the remaining winding set is set as 118Apk, the average torque-current advancing angle characteristics of DTP-SF and DTP-DS PMSMs are shown in Fig. 3.33. From Fig. 3.31, 40° is chosen as the optimal current advancing angle for the maximum torque condition in both DTP-SF and DTP-DS PMSMs.

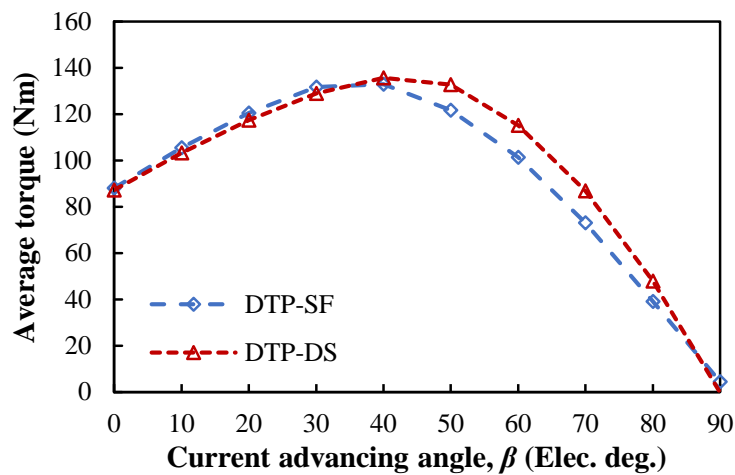
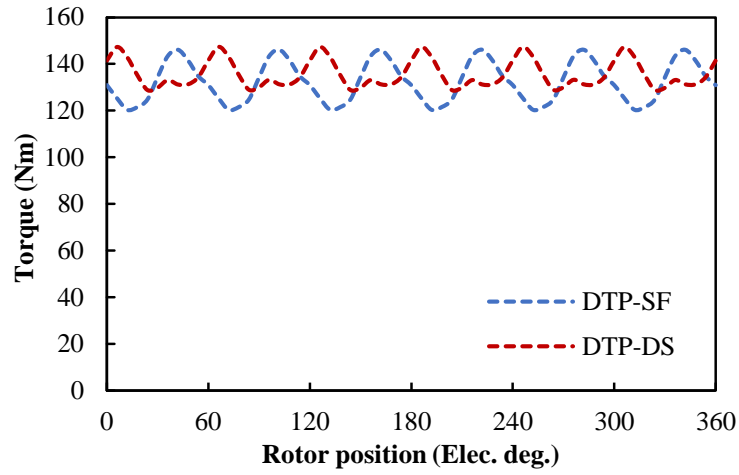
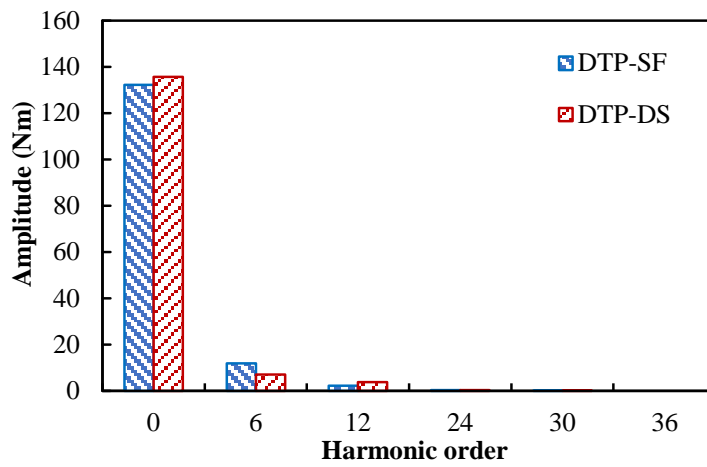


Fig. 3.31 Average torque-current advancing angle characteristics of different winding configurations under 3-ph OC condition.

With the maximum phase currents and the optimal current advancing angles, the waveforms and spectra of the instantaneous torque under 3-ph OC maximum torque condition are shown in Fig. 3.32 and the key characteristics are listed in Table 3.9. It can be seen that under 3-ph OC maximum torque condition, the maximum average output produced by DTP-DS winding configuration is higher than that produced by DTP-SF counterpart. Furthermore, the on-load torque ripple in DTP-DS PMSM is also lower than that in DTP-SF counterpart.



(a) Waveforms



(b) Spectra (Amplitude)

Fig. 3.32 Instantaneous torque performance of different winding configurations under 3-ph OC maximum torque condition.

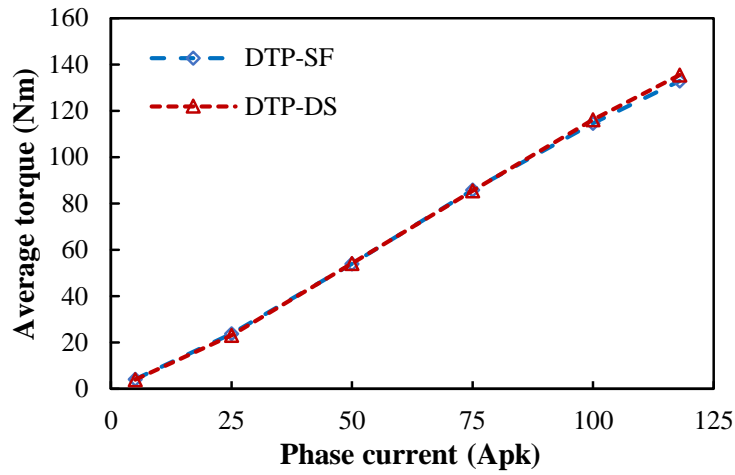
Table 3.9 Comparison of instantaneous torque characteristics of different winding configurations under 3-ph maximum torque OC condition

| | DTP-SF | DTP-DS |
|---------------------|--------|--------|
| Average torque (Nm) | 132.35 | 135.56 |
| Torque ripple (Nm) | 25.76 | 18.49 |
| Torque ripple (%) | 19.46 | 13.64 |

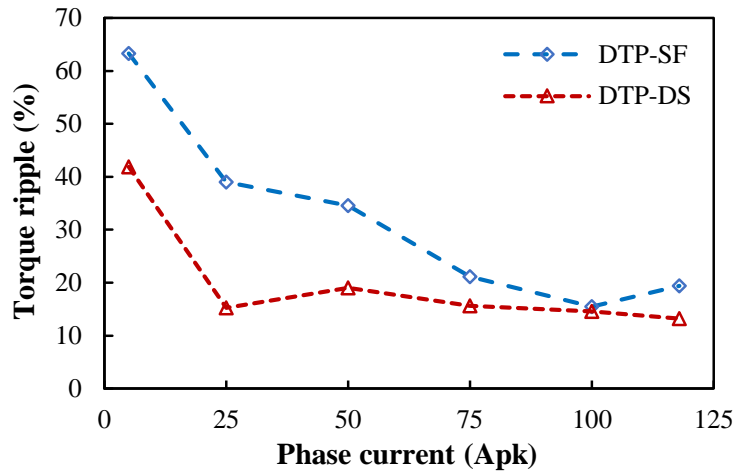
In Fig. 3.32(b), the 6th torque harmonics cannot be eliminated in DTP PMSMs under 3-ph OC condition, but the amplitude of the 6th torque harmonic in DTP-DS PMSM is significantly lower than that in DTP-SF counterpart. This phenomenon should be attributed to the short-pitched windings in DTP-DS winding configuration, which significantly reduce the winding factors for the 5th and 7th harmonics. Overall, compared with DTP-SF counterpart, DTP-DS configuration exhibits higher average torque and lower torque ripple under this condition.

3.4.2.2 Average Torque and Torque Ripple–Current Amplitude Characteristics

Similar to the analyses under healthy condition, when phase current is varied from 5, 25, 50, 75, 100, to 118Apk in DTP-SF and DTP-DS PMSMs under 3-ph OC condition, the optimal current advancing angles can be achieved by using MTPA control strategy. With the optimal current advancing angles, the variations of average torque and torque ripple with phase current amplitude can be obtained, as shown in Fig. 3.31. From Fig. 3.33, it can be seen that the average torques produced by the two DTP winding configurations are similar with each other, but the torque ripple in DTP-DS PMSM is obviously lower than that in DTP-SF counterpart.



(a) Average torque

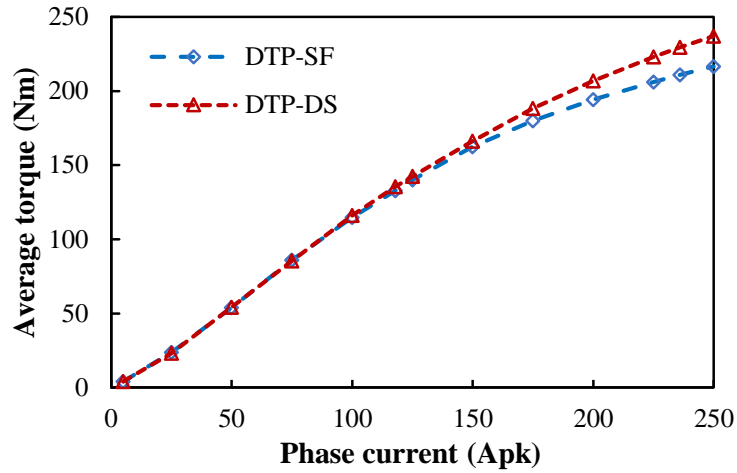


(b) Torque ripple

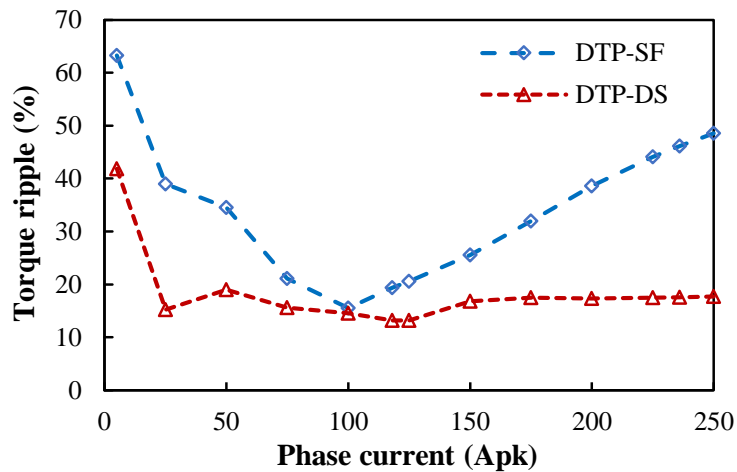
Fig. 3.33 Average torque- and torque ripple-phase current amplitude characteristics of different winding configurations under 3-ph OC condition when using MTPA strategy.

Considering that in DTP PMSMs, under 3-ph OC condition, the phase currents in the remaining winding set can be doubled to try to keep the original output torque [XU19]. The average torque and torque ripple characteristics of DTP-SF and DTP-DS PMSMs with phase current varying

from 5 to 250Apk are all considered, as shown in Fig. 3.34. It can be seen that with the increase of phase currents, DTP-DS winding configuration shows higher average torque than DTP-SF counterpart, and DTP-DS winding configuration keeps showing lower torque ripples than DTP-SF counterpart. Thus, it can be concluded that DTP-DS winding configuration is preferred for the 3-ph OC condition, no matter what excitation is.



(a) Average torque



(b) Torque ripple

Fig. 3.34 Average torque- and torque ripple-phase current amplitude characteristics of different winding configurations under 3-ph OC condition when using MTPA strategy considering over loading.

3.4.3 Loss and Efficiency

To make an all-around comparison between the electromagnetic performances of DTP-SF and DTP-DS winding configurations under 3-ph OC condition, their loss and efficiency performances are compared under maximum torque condition, as shown in Table 3.10. With higher output torque, DTP-DS PMSM shows higher output torque than DTP-SF counterpart.

In addition, the winding lengths of DTP-DS windings are also shorter than those of DTP-SF windings, and hence, the copper loss in DTP-DS PMSM is lower than that in DTP-SF counterpart. Furthermore, from Table 3.10, it can be found that the PM eddy loss in DTP-DS PMSM is also lower than that in DTP-SF PMSM, which should be attributed to the reduced MMF harmonics in DTP-DS PMSM. Thus, the overall efficiency of DTP-DS PMSM is significantly higher than that of DTP-SF counterpart by more than 2% under 3-ph maximum torque condition.

Table 3.10 Loss and efficiency of different winding configurations under 3-ph OC maximum torque condition

| | DTP-SF | DTP-DS |
|---------------------|----------|----------|
| Speed (rpm) | 3000 | 3000 |
| Average torque (Nm) | 132.35 | 135.56 |
| Copper loss (W) | 7283.49 | 6432.89 |
| Iron loss (W) | 245.53 | 247.14 |
| PM eddy loss (W) | 230.49 | 44.11 |
| Mechanical loss (W) | 93.20 | 93.20 |
| Output power (W) | 41578.68 | 42587.43 |
| Total loss (W) | 7852.70 | 6817.34 |
| Input power (W) | 49431.68 | 49404.77 |
| Efficiency (%) | 84.11 | 86.20 |

3.5 Summary

Based on the analyses presented in this sub-section, it can be summarized that DTP-DS winding configuration shows larger average torque and lower torque ripple than DTP-SF counterpart under 3-ph OC condition. Furthermore, the efficiency of DTP-DS PMSMS is also higher than that of DTP-SF counterpart under this condition. Compared with DTP-SF winding configuration, DTP-DS winding configuration is especially suitable for the applications which usually run under 3-ph OC condition.

3.6 Experimental Validation

According to the analyses above, it can be concluded that both DTP-SF and DTP-DS winding configurations can improve average torque and reduce torque ripple compared with STP counterpart, and DTP-DS winding configuration shows better performance in torque and

efficiency under high-speed and 3-ph OC conditions. To verify the analyses above, a Toyota Prius 2010 machine equipped with DTP-DS windings is manufactured and tested. The photos of the prototype and the test rig are shown in Fig. 3.35 and Fig. 3.36, respectively.



Fig. 3.35 Photos of DTP-DS prototype.

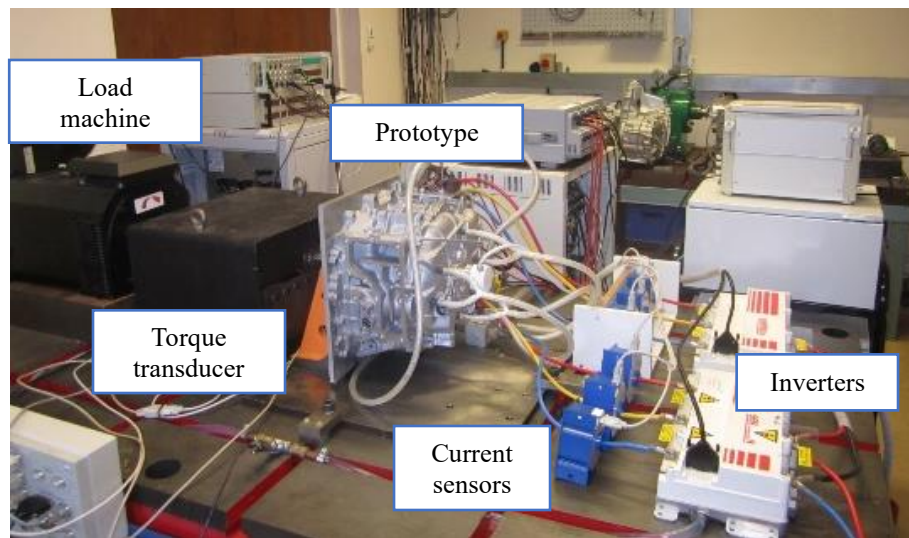


Fig. 3.36 Photo of test rig.

It should be mentioned 3D FE method is also utilized to improve the accuracy of FE simulations. The 3D model of the researched DTP-DS machine is shown in Fig. 3.37.

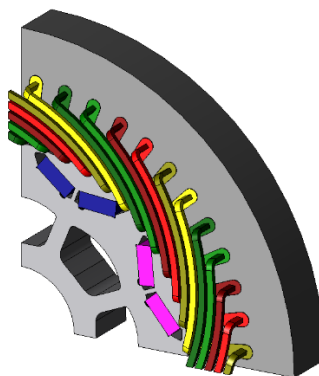
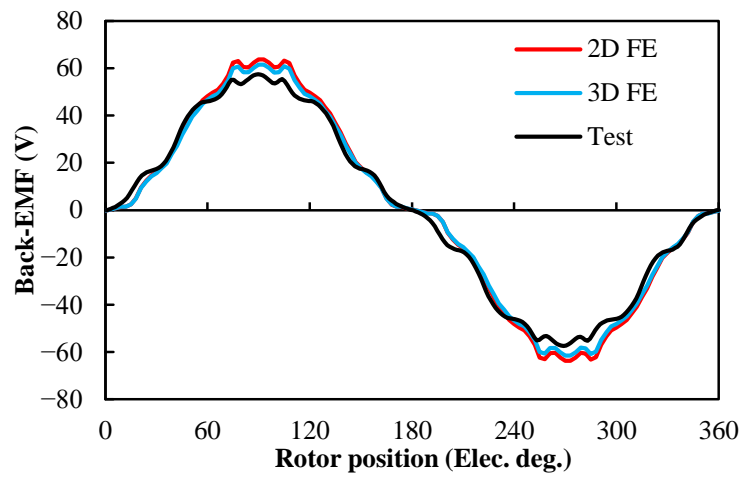
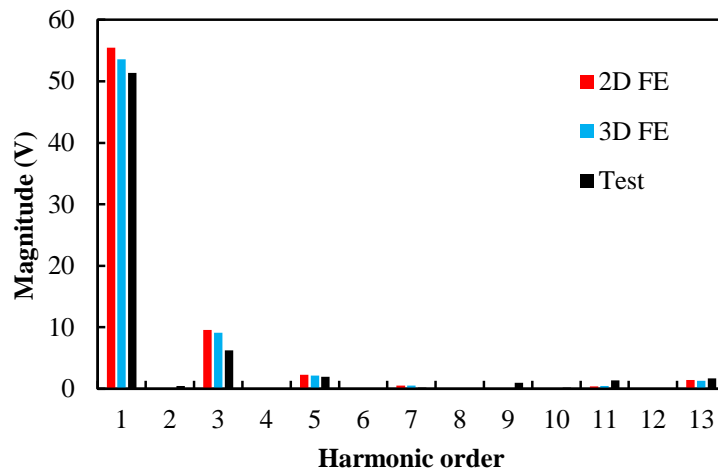


Fig. 3.37 3D model of DTP-DS prototype.

The back EMF performance of the prototype is tested at 1000 rpm. The waveforms and spectra of FE-predicted and tested phase back EMFs are shown in Fig. 3.38. It should be mentioned 3D FE method is also utilized to improve the accuracy of FE simulations. Although the tested back EMF is slightly lower than the FE-predicted values, it still can be found that the tested results agree well with FE-predicted results, and the 3D FE results can agree with the experimental results even better. It should be mentioned again that the magnet and core materials used in the FE models are not the actual materials equipped in the prototype. The precision of the FE simulations can be further improved with more accurate material properties. However, the agreements between simulated results and tested results shown in Fig. 3.38 are still good enough to confirm the correctness of the FE analyses.



(a) Waveforms



(b) Spectra (Amplitude)

Fig. 3.38 Phase back EMF comparison between FE and measured results at 1000 rpm.

The on-load experiment is carried out with phase currents varied from 20A_{pk} to 120A_{pk}. It should be mentioned that to simplify the operations, the $I_d = 0$ control strategy is utilized in the

experiments instead of the MTPA strategy. It also should be mentioned that since the bandwidth of the torque transducer is not high enough to capture high order torque harmonics, the accurate measurement of instantaneous torque is very difficult. Hence, only the variations of average torque with phase current amplitude are summarized and compared with FE-predicted results, as shown in Fig. 3.39. It can be seen that the measured average torque is slightly lower than the calculated results. In general, the FE-predicted average torques agree well with measured ones, especially the 3D FE-predicted results.

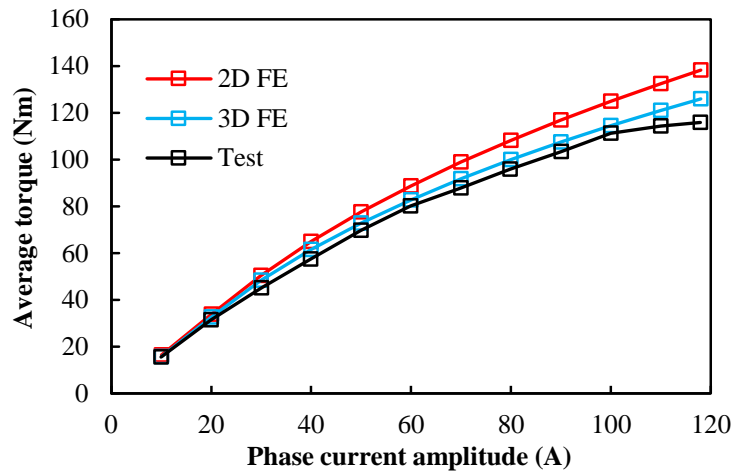


Fig. 3.39 Comparison of average torque characteristics between FE and measured results with $I_d = 0$ control strategy.

3.7 Conclusion

In this section, one STP and two DTP winding configurations (DTP-SF and DTP-DS) are analysed and compared based on Toyota Prius 2010 machine. The electromagnetic performances of the PMSM with STP, DTP-SF, and DTP-DS windings are simulated and compared in detail by considering various conditions. Then, a Toyota Prius 2010 machine equipped with DTP-DS windings was manufactured to validate the FE analyses. Some new findings can be obtained from this section, including:

- 1) Only DTP-SF winding configuration can improve the winding factor of the STP machine. DTP-DS windings share the same winding factors as STP windings.
- 2) In the constant torque region, DTP-SF windings can produce higher torque than DTP-DS and STP windings. The output torque of the DTP-DS machine is only slightly higher than that of the STP machine in this region. Both DTP-SF and DTP-DS winding configurations can

reduce torque ripples significantly, and the torque ripple in DTP-DS PMSM is even lower.

3) In the constant power region, DTP-DS windings show the largest torque output capacity and the lowest torque pulsation. However, the output torque of DTP-SF PMSM is even lower than that of the STP counterpart.

4) In DTP-SF windings, the full-pitched windings result in the highest copper loss among the three counterparts. Considering that the output torque of the DTP-DS machine is slightly higher than that of the STP machine, DTP-DS PMSM has a better efficiency performance than STP counterpart, and DTP-SF PMSM shows the worst efficiency performance.

5) The electromagnetic performances of DTP-SF and DTP-DS PMSMs under 3-ph OC condition show that DTP-DS winding configuration has better performance in almost all aspects, including average torque, torque ripple, and efficiency.

6) The stator and rotor cores and magnets of STP, DTP-SF, and DTP-DS machines are totally identical. The differences in overall costs only lie in the drive system and winding topologies. Compared with STP PMSM, DTP-SF and DTP-DS PMSMs need another two half-rating inverters and DTP-SF PMSM needs more copper wires due to the longer pitched windings.

Overall, the pros and cons of STP, DTP-SF, and DTP-DS machines are summarized in Table 3.11.

Table 3.11 Pros and cons of different winding configurations under maximum torque conditions

| STP | | DTP-SF | DTP-DS |
|------|---|--|--|
| Pros | <ul style="list-style-type: none"> • Simple winding connections • Simple drive system | <ul style="list-style-type: none"> • Highest torque under healthy condition | <ul style="list-style-type: none"> • Slightly higher torque under healthy condition (Compare with STP) |
| | | <ul style="list-style-type: none"> • Lower torque pulsation under healthy condition (Compare with STP) • Ability to run under three-phase OC condition | <ul style="list-style-type: none"> • Lower torque pulsation under healthy condition (Compare with STP) • Slightly higher efficiency (Compare with STP) • Highest torque under high-speed healthy condition • Ability to run under three-phase OC condition |

| | | | |
|------|---|---|---|
| | | | <ul style="list-style-type: none"> • Higher average torque and lower torque pulsation under three-phase OC condition (Compare with DTP-SF) |
| Cons | <ul style="list-style-type: none"> • Lower average torque and higher torque pulsation under healthy condition • Cannot run under three-phase OC condition | <ul style="list-style-type: none"> • Complex winding connections • Complex drive system • Largest winding usage • Worst efficiency performance • Lowest torque under high-speed healthy condition • Worse torque performance under three-phase OC condition (Compare with DTP-DS) | <ul style="list-style-type: none"> • Complex winding connections • Complex drive system |

Although DTP-SF winding configuration can increase the winding factor and produce the highest torque in the constant torque region, considering the advantages of DTP-DS winding configuration in average torque, torque ripple, and efficiency, especially under high-speed and 3-ph OC conditions, DTP-DS winding configuration is preferred for the DTP PMSMs utilized in EVs.

CHAPTER 4

TORQUE SEPARATION FOR DUAL THREE-PHASE PMSMs USING FROZEN PERMEABILITY METHOD

In existing paper [CHE14b], a method to separate the instantaneous torque components in STP PMSMs was proposed. However, the method to separate the instantaneous torque components in DTP PMSMs have not been analysed. In this chapter, an accurate model accounting for the mutual inductance between two winding sets is developed, and together with the utilization of frozen permeability method, a method to separate the instantaneous torque components in DTP PMSMs was introduced based on the method in [CHE14b]. It is found that in addition to the PM and reluctance torque components produced by the two winding sets separately, the mutual inductance between the two winding sets also contributes a lot to the overall output torque, as a reluctance torque component. With the frozen permeability method, the instantaneous torque components are separated appropriately, which can provide more insights for the design and control of DTP PMSMs.

4.1 Introduction

Due to high torque density and efficiency, PMSMs have attracted more and more attention in recent years. Among all PMSMs, DTP PMSMs have reduced MMF harmonics and inherent fault-tolerant capability, and hence, are especially suitable for applications, such as more electric aircrafts, electric vehicles, rail traction, and ship propulsion [LEV08] [SAL19] [ZHU21a].

In general, the produced torque of a PMSM can be separated into PM and reluctance torque components. PM torque component is produced by the interaction between armature fields and PM fields, and reluctance torque component is caused by the interaction between armature fields and rotor saliency. Thus, utilizing reluctance torque components appropriately can effectively improve the torque performance of PMSMs with even reduced PM consumption. Further, an accurate torque component separation method for DTP PMSMs can be of great importance in the design of DTP PMSMs.

In literature, a few methods have been presented to separate torque components in PMSMs, such as by assuming that flux-linkages only vary with q-axis current [QI09] or using frozen permeability (FP) method [KWA05] [CHU13a] [CHE14b]. In [KWA05], the non-linear saturation effects of d- and q-axis currents on d- and q-axis flux-linkages are analysed with FP method. Then, the average torque components in PMSMs can be separated using the method proposed in [CHU13a]. Based on foregoing analyses, in [CHE14b], a method to separate and reproduce instantaneous torque components in PMSMs under any load condition was proposed. However, all these papers separate torque components only in conventional STP PMSMs, without the consideration of DTP PMSMs. Since there are two three-phase winding sets in DTP PMSMs, and the resultant armature fields are produced by the two winding sets simultaneously, the torque components in DTP PMSMs are different from those in STP PMSMs. The effects of the two winding sets on PM and reluctance torque components still remain to be researched.

In this chapter, the torque separation method proposed in [CHE14b] is extended into DTP PMSMs, and the separated torque components in STP and DTP PMSMs are compared. The researched STP and DTP PMSMs are introduced in Section 4.2. An analytical model for DTP PMSMs, which accounts for the coupling effects between the two winding sets, is presented in Section 4.3. Based on the analytical model and with the help of FP method, the instantaneous torque of DTP PMSMs can be separated into PM and reluctance torque components, and the processes of the torque separation method are explained in detail in Section 4.4. Then, Section 4.5 shows the comparison of the separated torque components in STP and DTP PMSMs. Experimental validations are introduced in Section 4.6. Section 4.7 draws the conclusion.

4.2 Machine Configurations

In order to illustrate the processes of the torque separation method for DTP PMSMs, a DTP PMSM should be chosen as a benchmark machine in this chapter. In addition, to show the differences in PM and reluctance torque components between STP and DTP PMSMs, and those between different types of DTP configurations, all the three PMSMs researched in Chapter 3 (STP, DTP-SF, and DTP-DS PMSMs) are chosen as benchmark PMSMs in this chapter. The detailed design parameters of different PMSMs and the specifications of different winding conjurations can be found in Chapter 3, but also presented in Table 4.1 and Table 4.2 for convenience. The cross-sections of the benchmark STP and DTP PMSMs are shown in Fig. 4.1(a) to (c), respectively.

Table 4.1 Geometric Specifications of benchmark STP and DTP PMSMs

| | | | |
|-------------------------|-------|--------------------------|---------------------------------|
| Number of stator slots | 48 | Number of rotor poles | 8 |
| Stator OD, mm | 264 | Rotor OD, mm | 160.44 |
| Stator ID, mm | 161.9 | Rotor lamination ID, mm | 51 |
| Stator stack length, mm | 50.8 | Lamination thickness, mm | 0.305 |
| Slot depth, mm | 30.9 | Slot opening, mm | 1.88 |
| Phase resistance, Ohm | 0.077 | Magnet dimensions, mm | $49.3 \times 17.88 \times 7.16$ |

Table 4.2 Specifications of STP, DTP-SF, and DTP-DS winding configurations

| | STP | DTP-SF | DTP-DS |
|----------------------------|-----|--------|--------|
| Number of phases | 3 | 6 | 6 |
| Wires in parallel per turn | 12 | 6 | 6 |
| Turns in series per coil | 11 | 22 | 11 |
| Coils in series per phase | 8 | 4 | 8 |
| Coil pitch number | 5 | 6 | 5 |

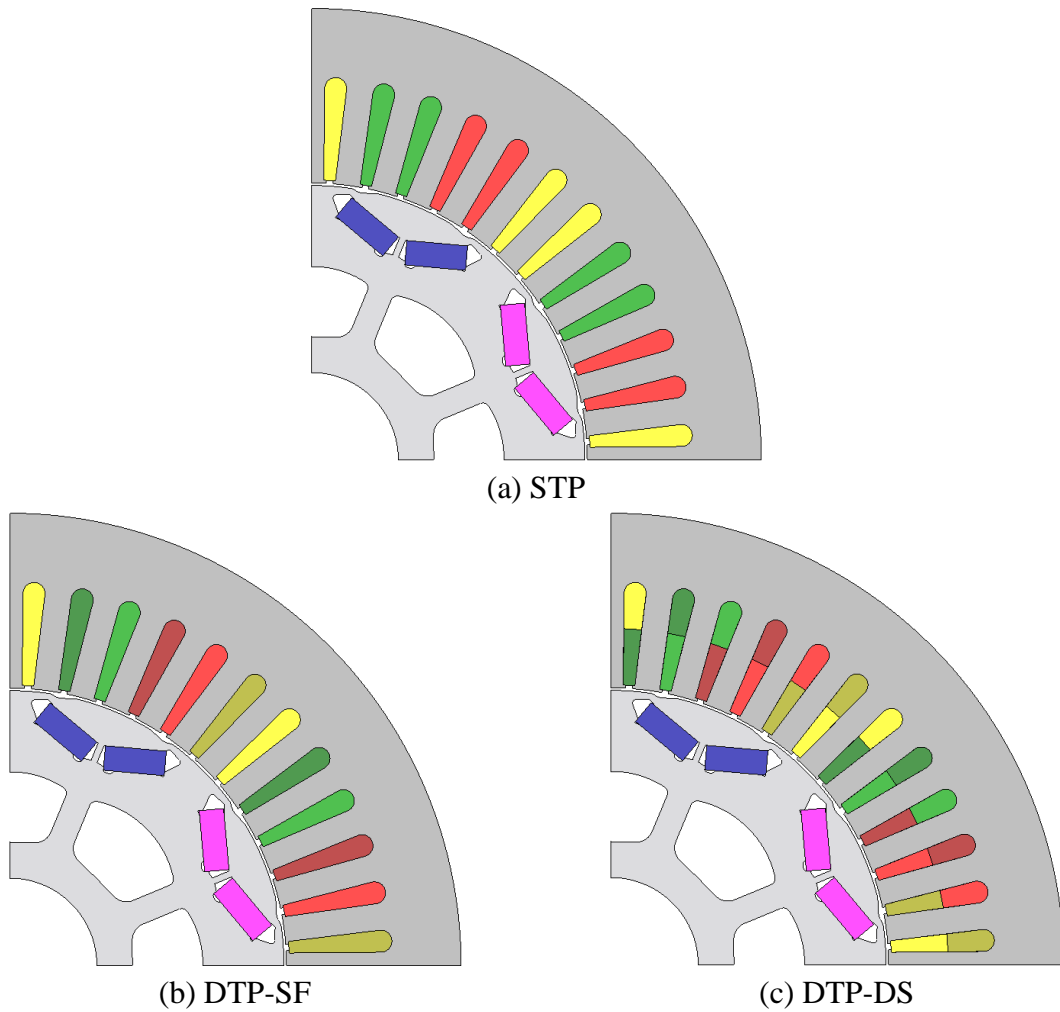


Fig. 4.1 Cross-sections of benchmark STP and DTP PMSMs.

4.3 Analytical Modelling and Torque Components for DTP PMSMs

Since the armature windings of DTP PMSMs are composed by two separated winding sets and each winding set has own d - and q -axes. In DTP PMSMs, magnetic cross coupling effect exists not only between d - and q -axes within the same winding set, but also between the d - and q -axes of the other winding set. Therefore, to account for all the cross-coupling effects in DTP PMSMs, besides the mutual inductances between the d - and q -axes within one winding set, the mutual inductances between the d - and q -axes of the two winding sets also should be included, and hence, the d - and q -axis flux linkages of the two winding sets can be calculated as [KAR12]

$$\begin{bmatrix} \psi_{d1} \\ \psi_{q1} \\ \psi_{d2} \\ \psi_{q2} \end{bmatrix} = \begin{bmatrix} \psi_{md1} \\ \psi_{mq1} \\ \psi_{md2} \\ \psi_{mq2} \end{bmatrix} + \begin{bmatrix} L_{d1} & M_{d1q1} & M_{d1d2} & M_{d1q2} \\ M_{q1d1} & L_{q1} & M_{q1d2} & M_{q1q2} \\ M_{d2d1} & M_{d2q1} & L_{d2} & M_{d2q2} \\ M_{q2d1} & M_{q2q1} & M_{q2d2} & L_{q2} \end{bmatrix} \begin{bmatrix} i_{d1} \\ i_{q1} \\ i_{d2} \\ i_{q2} \end{bmatrix} \quad (4.1)$$

where ψ is flux linkage, L is self-inductance, M is mutual inductance, and i is current. The subscripts $d1$, $q1$, $d2$, and $q2$ refer to the d - and q -axis components of Winding 1 and Winding 2, respectively. It can be seen that all the mutual inductances between the d - and q -axes in one winding set, and the mutual inductances between the d - and q -axes of the two winding sets are considered in the inductance matrix in (4.1). In addition, since the mutual inductance between $d1$ -axis to $q1$ -axis equals to that between $q1$ -axis to $d1$ -axis, it can be assumed that $M_{d1q1} = M_{q1d1} = M_1$, and similarly, other mutual inductances in (4.1) can be simplified as $M_{d1d2} = M_{d2d1} = M_2$, $M_{d1q2} = M_{q2d1} = M_3$, $M_{q1d2} = M_{d2q1} = M_4$, $M_{q1q2} = M_{q2q1} = M_5$, and $M_{d2q2} = M_{q2d2} = M_6$. Thus, the d - and q -axis flux linkages in DTP PMSMs can be calculated as

$$\begin{cases} \psi_{d1} = \psi_{md1} + L_{d1}i_{d1} + M_1i_{q1} + M_2i_{d2} + M_3i_{q2} \\ \psi_{q1} = \psi_{mq1} + M_1i_{d1} + L_{q1}i_{q1} + M_4i_{d2} + M_5i_{q2} \\ \psi_{d2} = \psi_{md2} + M_2i_{d1} + M_4i_{q1} + L_{d2}i_{d2} + M_6i_{q2} \\ \psi_{q2} = \psi_{mq2} + M_3i_{d1} + M_5i_{q1} + M_6i_{d2} + L_{q2}i_{q2} \end{cases} \quad (4.2)$$

Similar to STP PMSMs, the total electromagnetic torque produced by DTP PMSMs can also be estimated from the sum of the cross products of stator current vectors and stator flux linkage vectors in the two winding sets [KAR12], as

$$T_{em} = 1.5p(\psi_{d1}i_{q1} - \psi_{q1}i_{d1} + \psi_{d2}i_{q2} - \psi_{q2}i_{d2}) \quad (4.3)$$

Based on (4.2) and (4.3), the total electromagnetic torque of DTP PMSMs can be obtained as

$$T_{em} = 1.5p[\psi_{md1}i_{q1} - \psi_{mq1}i_{d1} + \psi_{md2}i_{q2} - \psi_{mq2}i_{d2} + (L_{d1} - L_{q1})i_{d1}i_{q1} + (L_{d2} - L_{q2})i_{d2}i_{q2} + M_1(i_{q1}i_{q1} - i_{d1}i_{d1}) + M_6(i_{q2}i_{q2} - i_{d2}i_{d2}) + (M_2 - M_5)(i_{d1}i_{q2} + i_{d2}i_{q1}) + (M_3 + M_4)(i_{q1}i_{q2} - i_{d1}i_{d2})] \quad (4.4)$$

where p is the number of pole pairs.

From (4.4), since PM torque components are produced by the interaction between armature fields and PM fields, the PM torque components produced by the two winding sets and rotor, can be separated as

$$T_{pm1} = 1.5p(\psi_{md1}i_{q1} - \psi_{mq1}i_{d1}) \quad (4.5)$$

$$T_{pm2} = 1.5p(\psi_{md2}i_{q2} - \psi_{mq2}i_{d2}) \quad (4.6)$$

$$T_{pm} = T_{pm1} + T_{pm2} \quad (4.7)$$

where T_{pm1} represents the PM torque component produced by the first winding set and the rotor, and T_{pm2} represents that produced by the second winding set and the rotor, respectively. T_{pm} represents the PM torque component of the whole DTP PMSM.

Similarly, since reluctance torque components are caused by the interaction between the armature fields and the rotor saliency, the reluctance torque in DTP PMSMs can be separated into three components as

$$T_{rel1} = 1.5p[(L_{d1} - L_{q1})i_{d1}i_{q1} + M_1(i_{q1}i_{q1} - i_{d1}i_{d1})] \quad (4.8)$$

$$T_{rel2} = 1.5p[(L_{d2} - L_{q2})i_{d2}i_{q2} + M_6(i_{q2}i_{q2} - i_{d2}i_{d2})] \quad (4.9)$$

$$T_{relm} = 1.5p[(M_2 - M_5)(i_{d1}i_{q2} + i_{d2}i_{q1}) + (M_3 + M_4)(i_{q1}i_{q2} - i_{d1}i_{d2})] \quad (4.10)$$

$$T_{relm} = T_{rel1} + T_{rel2} + T_{relm} \quad (4.11)$$

Considering that $M_1 = M_{d1q1} = M_{q1d1}$, and $M_2 = M_{d2q2} = M_{q2d2}$, T_{rel1} and T_{rel2} indicate the reluctance torque components, which are only influenced by the first and second winding sets respectively. All the inductances in (4.10), M_2 (M_{d1d2} , M_{d2d1}), M_3 (M_{d1q2} , M_{q2d1}), M_4 (M_{q1d2} , M_{d2q1}), and M_5 (M_{q1q2} , M_{q2q1}), are the mutual inductances between the two winding sets, which indicate the interactions between the two winding sets. Hence, T_{relm} represents the reluctance torque component that produced due to the differences in the mutual inductances between the two winding sets. T_{rel} represents the reluctance torque component of the whole DTP PMSM.

In (4.10), it can be inferred that when the two winding sets in DTP PMSMs are physically isolated, all the mutual inductances between the two winding sets (M_2 , M_3 , M_4 , and M_5) will be zero, and T_{relm} will also be zero. Only under this condition, the total reluctance torque of DTP PMSMs can be obtained as the sum of T_{rel1} and T_{rel2} . Otherwise, T_{relm} must be considered in the calculation of the total reluctance torque in DTP PMSMs.

Besides PM and reluctance torque components, as introduced and explained in [CHE14b], the interaction between rotor magnets and un-even reluctance in stator iron core can also contribute to the resultant output torque in DTP PMSMs. Thus, the total output torque of DTP PMSMs can be expressed as

$$\begin{aligned} T_{total} &= T_{em} + T_{mr} \\ &= T_{pm1} + T_{pm2} + T_{rel1} + T_{rel2} + T_{relm} + T_{mr} \end{aligned} \quad (4.12)$$

where T_{mr} represents the torque component, which is produced by rotor magnets and uneven reluctance in stator core.

Overall, as shown in (4.12), with the analytical model accounting for all cross-coupling effects in DTP PMSMs, the total output torque of DTP PMSMs can be separated into two PM torque components (T_{pm1} and T_{pm2}), three reluctance torque components (T_{rel1} , T_{rel2} , and T_{relm}), and one magnet-iron torque component (T_{mr}).

4.4 Torque Separation Method for DTP PMSMs

4.4.1 Calculate Relative Permeability Distribution

In this section, the torque separation method for DTP PMSMs is introduced based on the analytical model given in Section 4.3. DTP-SF PMSM under the condition (phase current amplitude, $I_{a1} = 118\text{A}$, current advancing angle, $\beta = 50^\circ$) is selected as an example to present the processes of the torque separation method. To employ FP method, the relative permeability distribution of DTP-SF machine under this load condition is firstly calculated step by step. The calculations are operated over a whole electric cycle, and the results are stored for the further analyses. In the researched PMSMs, 60 steps are calculated for one electric cycle, and the relative permeability distribution of DTP-SF machine at Step 1 is shown in Fig. 4.2.

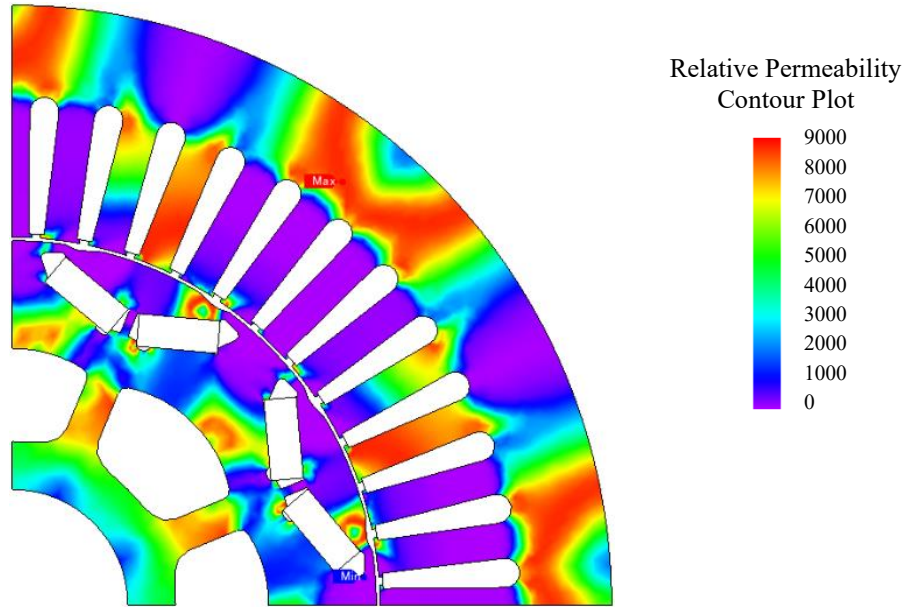


Fig. 4.2 Relative permeability distribution of DTP-SF PMSM at Step 1 under on-load condition ($I_{a1} = 118\text{A}$, $\beta = 50^\circ$).

4.4.2 Excitation Configurations of Different Cases

Under a specific on-load condition, after the relative permeability distributions of the researched DTP PMSM are calculated and stored step by step, the excitation configuration of the DTP PMSM should be changed according to Table 4.3, and then, the flux linkages and instantaneous torque waveforms obtained with different excitation configurations can be utilized to separate and reproduce the torque components in the DTP PMSM. It should be further explained that in Table 4.3, “ $i_{d1} = i_{d1}$, $i_{q1} = 0$ ” denotes that in the first winding set, the d -axis current is not changed, but the q -axis current is changed to 0. “*Magnets*” denotes that the rotor magnets are not changed, but “*No magnets*” means that all the rotor magnets are removed. Since the relative permeability distributions are obtained from the specific on-load condition, all the calculated results based on them have taken cross-saturation effects into consideration.

Table 4.3 Excitation configurations of different cases in torque separation method for DTP PMSMs

| Case | Excitation configurations |
|------|--|
| A | $i_{d1} = i_{d1}, i_{q1} = i_{q1}, i_{d2} = i_{d2}, i_{q2} = i_{q2}, \& \text{No magnets}$ |
| A1 | $i_{d1} = i_{d1}, i_{q1} = i_{q1}, i_{d2} = i_{q2} = 0, \& \text{No magnets}$ |
| A2 | $i_{d1} = i_{q1} = 0, i_{d2} = i_{d2}, i_{q2} = i_{q2}, \& \text{No magnets}$ |
| B1 | $i_{d1} = i_{d1}, i_{q1} = i_{d2} = i_{q2} = 0, \& \text{Magnets}$ |
| C1 | $i_{d1} = i_{d1}, i_{q1} = i_{d2} = i_{q2} = 0, \& \text{No magnets}$ |
| D1 | $i_{q1} = i_{q1}, i_{d1} = i_{d2} = i_{q2} = 0, \& \text{Magnets}$ |
| E1 | $i_{q1} = i_{q1}, i_{d1} = i_{d2} = i_{q2} = 0, \& \text{No magnets}$ |
| B2 | $i_{d2} = i_{d2}, i_{d1} = i_{q1} = i_{q2} = 0, \& \text{Magnets}$ |
| C2 | $i_{d2} = i_{d2}, i_{d1} = i_{q1} = i_{q2} = 0, \& \text{No magnets}$ |
| D2 | $i_{q2} = i_{q2}, i_{d1} = i_{q1} = i_{d2} = 0, \& \text{Magnets}$ |
| E2 | $i_{q2} = i_{q2}, i_{d1} = i_{q1} = i_{d2} = 0, \& \text{No magnets}$ |
| F | <i>Magnets</i> |

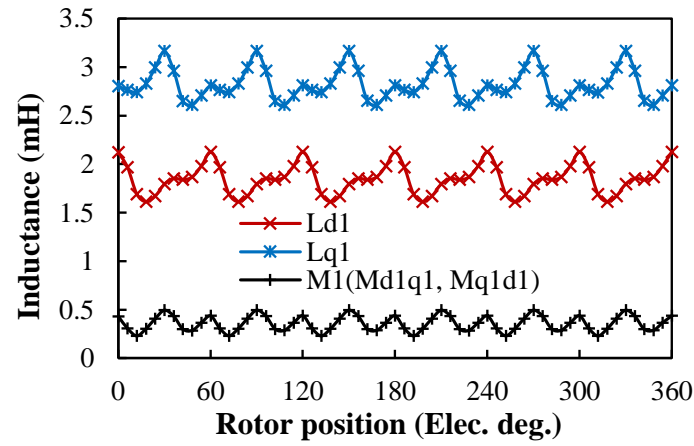
4.4.3 Flux Linkage Components of Different Cases

With the different excitation configurations given in Table 4.3 and based on (4.2), the components in the resultant d - and q -axis flux linkages of the researched DTP PMSM under different cases can be obtained, as shown in Table 4.4. It can be seen that under Cases C1, E1, C2, and E2, the d - and q -axis flux linkages only vary with one current component. Hence, for DTP PMSMs, the whole inductance matrix can be obtained from Cases C1, E1, C2, and E2.

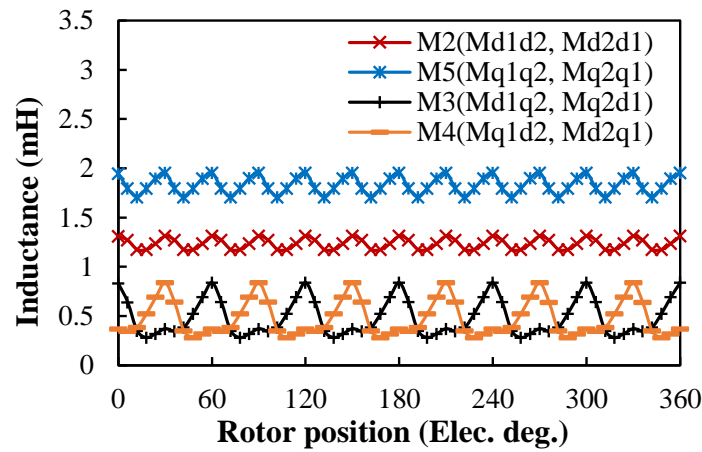
Table 4.4 Flux-linkage components of different cases in torque separation method for DTP PMSMs

| Case | Flux linkage components | | | |
|------|--|--|--|--|
| | ψ_{d1} | ψ_{q1} | ψ_{d2} | ψ_{q2} |
| A | $L_{d1}i_{d1} + M_1i_{q1} + M_2i_{d2} + M_3i_{q2}$ | $M_1i_{d1} + L_{q1}i_{q1} + M_4i_{d2} + M_5i_{q2}$ | $M_2i_{d1} + M_4i_{q1} + L_{d2}i_{d2} + M_6i_{q2}$ | $M_3i_{d1} + M_5i_{q1} + M_6i_{d2} + L_{q2}i_{q2}$ |
| A1 | $L_{d1}i_{d1} + M_1i_{q1}$ | $M_1i_{d1} + L_{q1}i_{q1}$ | $M_2i_{d1} + M_4i_{q1}$ | $M_3i_{d1} + M_5i_{q1}$ |
| A2 | $M_2i_{d2} + M_3i_{q2}$ | $M_4i_{d2} + M_5i_{q2}$ | $L_{d2}i_{d2} + M_6i_{q2}$ | $M_6i_{d2} + L_{q2}i_{q2}$ |
| B1 | $\psi_{md1} + L_{d1}i_{d1}$ | $\psi_{mq1} + M_1i_{d1}$ | $\psi_{md2} + M_2i_{d1}$ | $\psi_{mq2} + M_3i_{d1}$ |
| C1 | $L_{d1}i_{d1}$ | M_1i_{d1} | M_2i_{d1} | M_3i_{d1} |
| D1 | $\psi_{md1} + M_1i_{q1}$ | $\psi_{mq1} + L_{q1}i_{q1}$ | $\psi_{md2} + M_4i_{q1}$ | $\psi_{mq2} + M_5i_{q1}$ |
| E1 | M_1i_{q1} | $L_{q1}i_{q1}$ | M_4i_{q1} | M_5i_{q1} |
| B2 | $\psi_{md1} + M_2i_{d2}$ | $\psi_{mq1} + M_4i_{d2}$ | $\psi_{md2} + L_{d2}i_{d2}$ | $\psi_{mq2} + M_6i_{d2}$ |
| C2 | M_2i_{d2} | M_4i_{d2} | $L_{d2}i_{d2}$ | M_6i_{d2} |
| D2 | $\psi_{md1} + M_3i_{q2}$ | $\psi_{mq1} + M_5i_{q2}$ | $\psi_{md2} + M_6i_{q2}$ | $\psi_{mq2} + L_{q2}i_{q2}$ |
| E2 | M_3i_{q2} | M_5i_{q2} | M_6i_{q2} | $L_{q2}i_{q2}$ |
| F | ψ_{md1} | ψ_{mq1} | ψ_{mq1} | ψ_{mq2} |

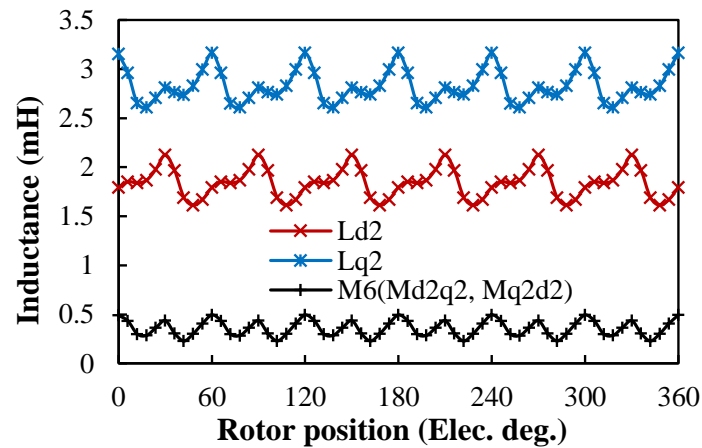
In the researched DTP-SF PMSM, under the on-load condition ($I_{a1} = 118\text{A}$, $\beta = 50^\circ$), the d - and q -axis flux linkages under Cases C1, E1, C2, and E2 are calculated with the stored relative permeability distributions, and then, the self and mutual inductances under these cases can be obtained. The variations of these inductances with rotor position are plotted in Fig. 4.3.



(a) L_{d1} , L_{q1} , and M_1



(b) M_2 , M_5 , M_3 , and M_4



(c) L_{d2} , L_{q2} , and M_6

Fig. 4.3 Variations of different inductances with rotor position.

As shown in Fig. 4.3, in the researched DTP-SF PMSM under the specific on-load condition, the average inductance matrix can be obtained, as

$$\begin{bmatrix} 1.84 & 0.36 & 1.24 & 0.48 \\ 0.36 & 2.82 & 0.47 & 1.83 \\ 1.24 & 0.47 & 1.84 & 0.36 \\ 0.48 & 1.83 & 0.36 & 2.83 \end{bmatrix} (mH) \quad (4.13)$$

From Fig. 4.3 and (4.13), it can be observed that the inductances in one winding set (L_{d1} , L_{q1} , and M_1 in the first winding set) are almost the same with those in the other winding set (L_{d2} , L_{q2} , and M_6 in the second winding set). Furthermore, it can be seen that M_2 (M_{d1d2} , M_{d2d1} , 1.24mH) and M_5 (M_{q1q2} , M_{q2q1} , 1.83mH) are only slightly lower than L_{d1} , L_{d2} (1.84mH) and L_{q1} , L_{q2} (2.82mH), which suggests that the cross-coupling effect between the two winding sets is very evident in the researched DTP PMSM.

4.4.4 Torque Separation and Reproduction

As the d - and q -axis flux linkages under different cases have been provided in Table 4.4, the electromagnetic torque produced under these conditions can be calculated using (4.4). In addition, under the cases with rotor magnets (Cases B1, D1, B2, D2, and F), besides electromagnetic torque, T_{mr} also exists in resultant total output torque. Hence, the torque components of the researched DTP PMSM under different cases can be summarized in Table 4.5. Then, the instantaneous torque waveforms of different torque components can be separated based on the instantaneous torque waveforms of the researched DTP PMSM under these cases.

According to (4.5), (4.6), (4.7) and Table 4.5, the PM torque components in DTP PMSMs can be obtained as

$$T_{pm1} = T_{B1} - T_{C1} + T_{D1} - T_{E1} - 2T_F \quad (4.14)$$

$$T_{pm2} = T_{B2} - T_{C2} + T_{D2} - T_{E2} - 2T_F \quad (4.15)$$

$$T_{pm} = T_{pm1} + T_{pm2} = T_{B1} - T_{C1} + T_{D1} - T_{E1} + T_{B2} - T_{C2} + T_{D2} - T_{E2} - 4T_F \quad (4.16)$$

In the DTP-SF PMSM under the specific on-load condition ($I_{a1} = 118A$, $\beta = 50^\circ$), the instantaneous torque waveforms of the PM torque components are shown in Fig. 4.4. It can be seen that the PM torque components caused by the two winding sets are shifted by 30° .

Table 4.5 Torque components of different cases in torque separation method for DTP PMSMs

| Case | Torque components |
|------|---|
| A | $1.5p[(L_{d1} - L_{q1})i_{d1}i_{q1} + (L_{d2} - L_{q2})i_{d2}i_{q2} + M_1(i_{q1}i_{q1} - i_{d1}i_{d1}) + M_6(i_{q2}i_{q2} - i_{d2}i_{d2}) + (M_2 - M_5)(i_{d1}i_{q2} + i_{d2}i_{q1}) + (M_3 + M_4)(i_{q1}i_{q2} - i_{d1}i_{d2})]$ |
| A1 | $1.5p[(L_{d1} - L_{q1})i_{d1}i_{q1} + M_1(i_{q1}i_{q1} - i_{d1}i_{d1})]$ |
| A2 | $1.5p[(L_{d2} - L_{q2})i_{d2}i_{q2} + M_6(i_{q2}i_{q2} - i_{d2}i_{d2})]$ |
| B1 | $1.5p(-\psi_{mq1}i_{d1} - M_1i_{d1}i_{d1}) + T_{mr}$ |
| C1 | $-1.5pM_1i_{d1}i_{d1}$ |
| D1 | $1.5p(\psi_{md1}i_{q1} + M_1i_{q1}i_{q1}) + T_{mr}$ |
| E1 | $1.5pM_1i_{q1}i_{q1}$ |
| B2 | $1.5p(-\psi_{mq2}i_{d2} - M_6i_{d2}i_{d2}) + T_{mr}$ |
| C2 | $-1.5pM_6i_{d2}i_{d2}$ |
| D2 | $1.5p(\psi_{md2}i_{q2} + M_6i_{q2}i_{q2}) + T_{mr}$ |
| E2 | $1.5pM_6i_{q2}i_{q2}$ |
| F | T_{mr} |

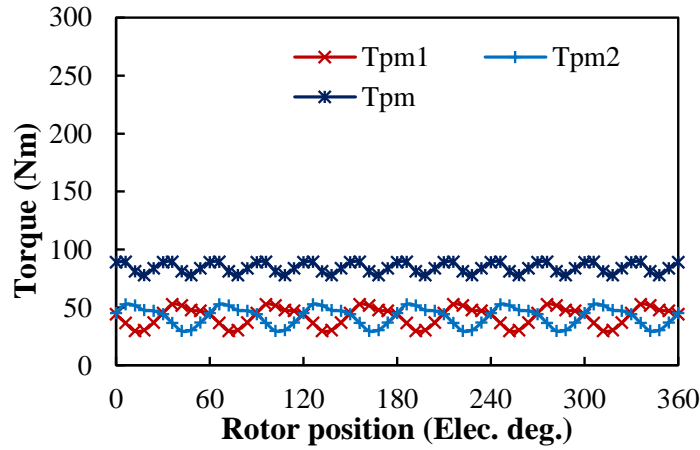


Fig. 4.4 Variations of PM torque components with rotor position in DTP-SF PMSM under on-load condition ($I_{a1} = 118\text{A}$, $\beta = 50^\circ$).

For reluctance torque components, from (4.8), (4.9), (4.10), (4.11), and Table 4.5, the reluctance torque components in DTP PMSMs can be obtained as

$$T_{rel} = T_A \quad (4.17)$$

$$T_{rel1} = T_{A1} \quad (4.18)$$

$$T_{rel2} = T_{A2} \quad (4.19)$$

$$T_{relm} = T_{rel} - T_{rel1} - T_{rel2} = T_A - T_{A1} - T_{A2} \quad (4.20)$$

It is worth noticing that T_{rel} , T_{rel1} and T_{rel2} can be obtained directly from the instantaneous torque waveforms under Cases A, A1, and A2. However, T_{relm} , which represents the reluctance torque

component produced due to the differences in mutual inductances between the two winding sets, can only be calculated as the difference between total reluctance torque (T_{rel}) and the sum of reluctance torque components produced by the two winding sets separately (T_{rel1} and T_{rel2}). In the researched DTP-SF PMSM, the instantaneous torque waveforms of the reluctance torque components are shown in Fig. 4.5.

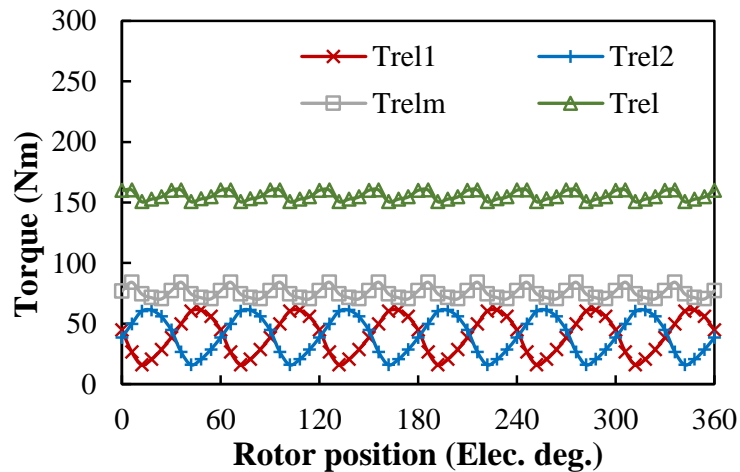


Fig. 4.5 Variations of reluctance torque components with rotor position in DTP-SF PMSM under on-load condition ($I_{a1} = 118\text{A}$, $\beta = 50^\circ$).

With the separated torque components, the total output torque of DTP PMSMs can be calculated as

$$\begin{aligned} T_{total} &= T_{rel} + T_{pm} + T_{mr} \\ &= T_A + T_{B1} - T_{C1} + T_{D1} - T_{E1} + T_{B2} - T_{C2} + T_{D2} - T_{E2} - 3T_F \end{aligned} \quad (4.21)$$

Based on the foregoing analyses, in the researched DTP-SF PMSM, the instantaneous torque waveforms of T_{total} , T_{pm} , T_{rel} , and T_{mr} are shown in Fig. 4.6. The output torque waveform of the DTP-SF PMSM, which is obtained from FE analyses directly, is also given in Fig. 4.6. It can be seen that the reproduced total output torque (T_{total}) agrees well with the direct FE results (T_{direct}). Thus, the correctness of the proposed torque separation method for DTP PMSMs can be validated.

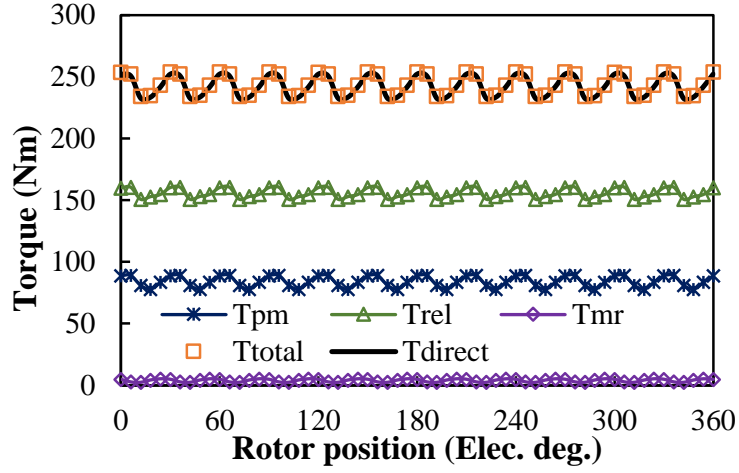


Fig. 4.6 Variations of different torque components with rotor position in DTP-SF PMSM under on-load condition ($I_{a1} = 118\text{A}$, $\beta = 50^\circ$).

4.5 Comparison of Torque Components in STP and DTP PMSMs

Since the torque separation method introduced in Section 4.4 is applicable for all DTP PMSMs, the torque components in DTP-DS PMSM can also be separated with the proposed method. To make a fair comparison, the on-load condition ($I_{a1} = 118\text{A}$, $\beta = 50^\circ$) is also chosen for the torque separation in DTP-DS PMSM. Under this condition, the instantaneous torque waveforms of the PM and reluctance torque components in DTP-DS PMSM are calculated and shown in Fig. 4.7 and Fig. 4.8, respectively.

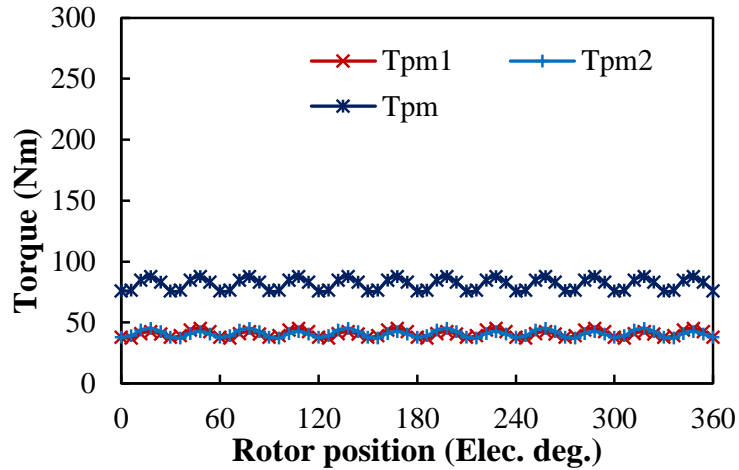


Fig. 4.7 Variations of PM torque components with rotor position in DTP-DS PMSM under on-load condition ($I_{a1} = 118\text{A}$, $\beta = 50^\circ$).

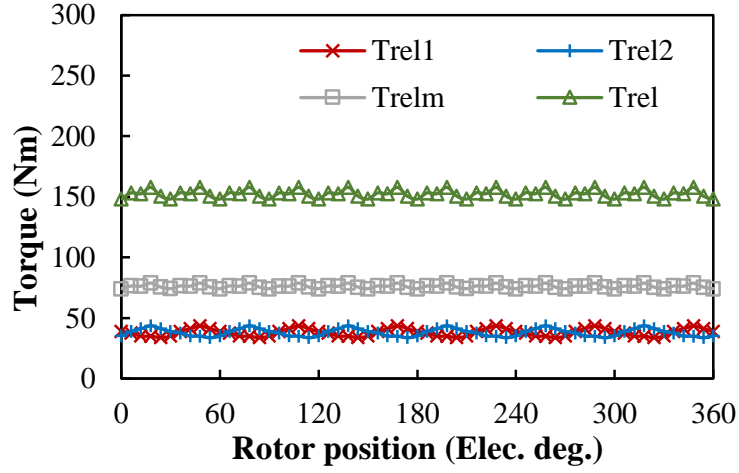


Fig. 4.8 Variations of reluctance torque components with rotor position in DTP-DS PMSM under on-load condition ($I_{a1} = 118\text{A}$, $\beta = 50^\circ$).

Based on Fig. 4.7 and Fig. 4.8, the total torque of DTP-DS PMSM can be reproduced by taking PM, reluctance, and magnet-iron torque components into consideration. The variations of these torque components with rotor position are shown in Fig. 4.9. The instantaneous torque waveform, which is calculated directly by FE method is also given in Fig. 4.9. It can be found that the reproduced total torque still agrees well with the directly-calculated total torque. Hence, the correctness of the proposed torque separation method for DTP PMSMs is validated again in another DTP PMSM.

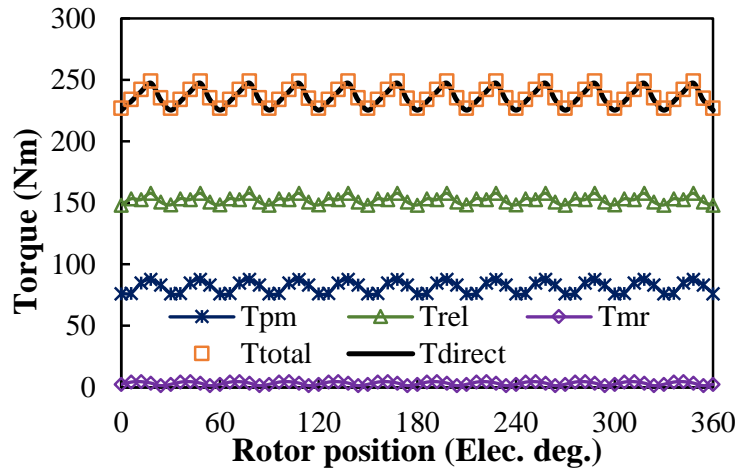


Fig. 4.9 Variations of different torque components with rotor position in DTP-DS PMSM under on-load condition ($I_{a1} = 118\text{A}$, $\beta = 50^\circ$).

The torque separation method for DTP PMSMs introduced in this chapter is extended from the method for STP PMSMs proposed in [CHE14b]. Utilizing the torque separation method in [CHE14b], the different torque components in the benchmark STP PMSM are separated under the specific on-load condition ($I_a = 236\text{A}$, $\beta = 50^\circ$), as shown in Fig. 4.9.

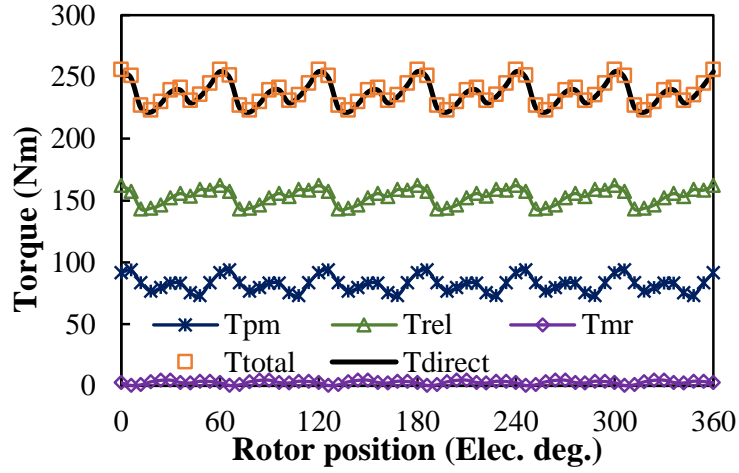


Fig. 4.10 Variations of different torque components with rotor position in STP PMSM under on-load condition ($I_a = 236\text{A}$, $\beta = 50^\circ$).

It should be mentioned that due to different winding configurations in STP and DTP PMSMs, the phase current amplitude in STP PMSM is doubled from those in DTP PMSMs for a fair comparison. Similarly, the instantaneous torque waveform obtained directly by FE method is also presented in Fig. 4.9 to show the effectiveness of the torque separation method in STP PMSMs.

From Fig. 4.6, Fig. 4.9, and Fig. 4.10, the different torque components in the benchmark STP, DTP-SF, and DTP-DS PMSMs can be summarized in Table 4.6. It should be noticed that the total average torques in Table 4.6 are obtained as the sum of the separated torque components, (4.21), which are slightly different from the average torques obtained directly from FE analyses (shown in Table 3.6). From Table 4.6, it can be found that although the detailed torque components in STP, DTP-SF, and DTP-DS PMSMs are different, the ratios of PM, reluctance, and magnet-iron torque components in total output torque in the three machines are very similar. In other words, DTP winding configuration cannot change the contributions of PM and reluctance torque components in total output torque in STP PMSMs. In addition, it can be found that in DTP-SF and DTP-DS PMSMs, the reluctance torque component produced by the mutual inductances between the two winding sets, T_{relm} , is the largest component among T_{pm1} , T_{pm2} , T_{rel1} , T_{rel2} , and T_{relm} . Hence, when separating torque components in DTP PMSMs, the cross-coupling effect between the two winding sets cannot be ignored.

Table 4.6 Comparison of torque components in STP, DTP-SF, and DTP-DS PMSMs

| | STP | | DTP-SF | | DTP-DS | |
|-------------|------------------------|--------------|------------------------|--------------|------------------------|--------------|
| | Average torque (Nm) | Ratio (%) | Average torque (Nm) | Ratio (%) | Average torque (Nm) | Ratio (%) |
| T_{pm1} | - | - | 42.08 | 17.26 | 40.81 | 17.20 |
| T_{pm2} | - | - | 42.09 | 17.26 | 40.81 | 17.20 |
| T_{pm} | 82.35 | 34.56 | 84.17 | 34.52 | 81.61 | 34.39 |
| T_{rel1} | - | - | 40.19 | 16.48 | 38.14 | 16.07 |
| T_{rel2} | - | - | 40.09 | 16.44 | 38.08 | 16.05 |
| T_{relm} | - | - | 75.48 | 30.96 | 76.20 | 32.11 |
| T_{rel} | 153.16 | 64.28 | 155.76 | 63.89 | 152.43 | 64.24 |
| T_{mr} | 2.76 | 1.16 | 3.88 | 1.59 | 3.24 | 1.37 |
| T_{total} | 238.27 | 100.00 | 243.81 | 100.00 | 237.29 | 100.00 |

4.6 Experimental Validation

In this chapter, all researches are conducted based on the results obtained by 2D FE method. Although 2D FE predicted results are considered fairly reliable nowadays, it is still necessary to experimentally validate at least one model in this chapter to avoid any error in modelling and FE simulations. Fortunately, the benchmark DTP-DS PMSM was fabricated and tested in Section 3.6. The correctness of the 2D FE analyses shown in this chapter can also be verified by the experiments presented in Section 3.6.

4.7 Conclusion

In this chapter, the output torque of DTP PMSMs is analysed analytically, accounting for the cross-coupling effect within and between different winding sets. It is found that the total output torque of DTP PMSMs can be separated into two PM torque components (T_{pm1} and T_{pm2}), three reluctance torque components (T_{rel1} , T_{rel2} , and T_{relm}), and one magnet-iron torque component (T_{mr}). Then, the different torque components in DTP PMSMs are separated by setting different excitation configurations in FE models with the help of FP method. It is found that the reluctance produced by the mutual inductance between the two winding sets contributes the most in the resultant output torque.

The precise torque separation results can provide more insights for the design and control of DTP PM machines. It also should be mentioned that the torque separation method proposed in this chapter can even be further extended to other PMSMs with multiple winding sets.

CHAPTER 5

INFLUENCE OF LOAD ON EFFECTIVENESS OF ROTOR SKEW IN STP IPMSMS AND SPMSMS

In this chapter, the influence of load on the effectiveness of rotor skew in interior and surface permanent magnet synchronous machines (PMSMs) is investigated and the optimal skew angles for minimum on-load torque ripple are obtained and compared under different load conditions. Both rotor continuous and step skews are considered. It is found that the effectiveness of rotor skew depends on electric loading and magnetic saturation, and thus, in general it is less effective in interior PMSM than in surface PMSM. The conventional skew angle, i.e., one on-load torque ripple periodicity, only works well in surface PMSM under light-load conditions. For surface PMSM under very heavy-load conditions, when the magnetic saturation becomes very severe due to high electric loading, or interior PMSM under all load conditions, there exists an optimal skew angle, which can result in higher average torque and lower torque ripple simultaneously than the conventional skew angle.

5.1 Introduction

Due to high torque/power density and high efficiency, permanent magnet synchronous machines (PMSMs) have been widely used in many industrial and domestic applications [HEN94] [ZHU07] [PYR08]. Since torque ripples directly affect speed smoothness, their reduction is important for some high-performance applications. Numerous studies have been carried out to minimize torque ripples in PMSMs, particularly under on-load conditions [JAH96] [ZHU00] [BIA02].

The techniques to reduce torque ripples can be generally classified into two categories [JAH96]: machine design method and control method. Since machine design method can minimize torque ripples inherently and ease control strategy, many design techniques have been proposed to reduce on-load torque ripples in the last decades, including stator slot and rotor pole number combination [ATA03] [HAN10], stator/rotor skew [PIR90] [CHE10] [ISL09] [URR10] [AZA12] [CHU13b] [CHU13c] [FEI13] [GE17] [OCA20] [CHE20b] [WAN20e] [XIN21] [ISL22], PM shaping [WAN10] [WAN14d] [DU19] [DU20], rotor iron shaping [BIA09]

[ALO11] [BIA15], and stator tooth shaping [YU14] [PET15]. Among all these torque ripple reduction techniques, rotor skew method is the most popular one, as they are simple and effective. Hence, the effectiveness of rotor skew in PMSMs under different load conditions will be the focus of this chapter.

In [AZA12], the on-load electromagnetic performance of PMSM with rotor skew is analysed, and it is reported that it is not adequate to use open-circuit parameters to reduce on-load torque ripples in rotor skew since the load affects back electromotive force (EMF) and cogging torque significantly. It is also reported in [ISL09] that the on-load torque ripples could even be increased by rotor skew. In [CHU13b], the influence of load on the effectiveness of rotor skew is investigated comprehensively in surface PMSMs (SPMSMs) and it is found that the effectiveness of rotor skew can be affected evidently by load, as the magnetic saturation is determined by electric loadings. Consequently, an improved skew method is proposed in [CHU13c], in which both current angle and skew angle are modified to make full use of the skewed rotor under on-load conditions. It is further reported in [GE17] that the optimal skew angle and axial lengths of rotor slices obtained by 2-dimension (2D) finite element (FE) method can be further improved by using 3D FE method to take end field leakages and interactions between axial adjacent rotor slices into consideration.

However, it should be noticed that [CHU13b] is only conducted in SPMSMs, the influence of load on the effectiveness of rotor skew in interior PMSMs (IPMSMs) still remains to be investigated and compared with that in SPMSMs. Further, in the improved skew method proposed in [CHU13c], the optimal current angle and skew angle are obtained by scanning different current angles and different skew angles, which is very complicated and time-consuming. In this chapter, a simplified approach to calculate torque performance of PMSMs after rotor skew is firstly introduced, and then the optimal current angle and skew angles under different load conditions can be obtained in IPMSM and SPMSM. Based on the foregoing analyses, the influences of load on the effectiveness of rotor skew in IPMSM and SPMSM are analysed and compared. Both continuous and step skews are considered. It is found that for SPMSM under over-load conditions and IPMSM under all load conditions, there exists a better skew angle, which can result in higher average torque and lower torque ripple simultaneously than the conventional idealized skew angle.

This chapter is organized as follows. In Section 5.2, the machine configurations of the benchmark IPMSM and SPMSM are introduced. In Section 5.3, the torque characteristics of IPMSM and SPMSM without rotor skew are presented and a simplified torque estimation approach was proposed based on the torque characteristics without rotor skew. In Section 5.4, the influences of load on the effectiveness of rotor continuous skew in IPMSM and SPMSM are investigated. Then, the influences of load on the effectiveness of rotor step skew in IPMSM and SPMSM are provided in Section 5.5. The experimental validation is provided in Section 5.6 and Section 5.7 is the conclusion.

5.2 Machine Configurations

In all slot/pole number combinations for PMSMs, 48-slot/8-pole is widely used in electric vehicles, such as Toyota Prius, Nissan Leaf, and Lexus LS, etc. [STA06] [BUR09] [BUR11] [SAT11]. In this chapter, the investigation of the effectiveness of rotor skew under different load conditions will be conducted based on Toyota Prius 2010 machine. However, since the original rotor of Toyota Prius 2010 machine is an IPM rotor, a SPM rotor is also designed purposely in order to make a comparison between IPMSM and SPMSM.

The geometric dimensions of Toyota Prius 2010 machine can be found from [BUR11] and the main design specifications are given in Table 5.1. The cross-section of Toyota Prius 2010 machine (benchmark IPMSM) is shown in Fig. 5.1(a). The newly-designed SPM rotor shares identical rotor outer diameter and PM volume with the original IPM rotor in Toyota Prius 2010 machine, and the thickness and width of the surface-mounted magnets are adjusted to produce the maximum average torque under the full-load condition of Toyota Prius 2010 (phase current, $I_a = 236\text{A}$). The main design specifications of the SPM rotor can also be found in Table 5.1 and the cross-sections of the benchmark SPMSM are shown in Fig. 5.1(b).

Table 5.1 Main design specifications of benchmark PMSMs

| Parameter | Dimension |
|---------------------------------|-----------|
| Stator slot / rotor pole number | 48/8 |
| Stator outer diameter, mm | 264 |
| Stator inner diameter, mm | 161.9 |
| Stator slot depth, mm | 30.9 |
| Stator slot opening, mm | 1.88 |
| Rotor outer diameter, mm | 160.44 |
| Rotor inner diameter, mm | 51 |
| Stack length, mm | 50.8 |
| Lamination thickness, mm | 0.305 |
| Magnet remanence, T | 1.2 |
| Magnet relative permeability | 1.05 |
| Magnet dimensions of IPM rotor | |
| Magnet thickness, mm | 7.16 |
| Magnet length, mm | 17.88 |
| Magnet dimensions of SPM rotor | |
| Magnet thickness, mm | 5.55 |
| Magnet pole-arc ratio | 0.76 |

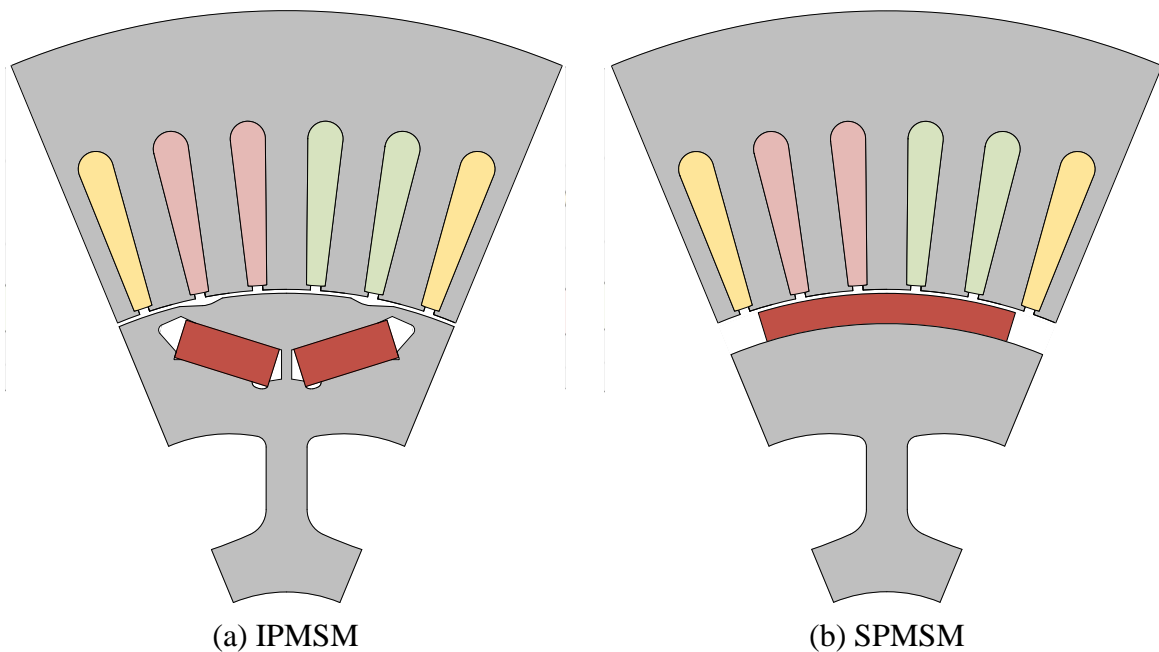


Fig. 5.1 Cross-sections of benchmark IPMSM and SPMSM.

5.3 Simplified Torque Estimation Approach

5.3.1 Torque Characteristics without Rotor Skew

Before investigating the effectiveness of rotor skew in PMSMs, the torque characteristics of the benchmark IPMSM and SPMSM without rotor skew under different load conditions are firstly examined. It should be mentioned that although the maximum phase current amplitude for Toyota Prius 2010 machine is 236A, to make the comparison systematic and comprehensive, open-circuit condition and nine on-load conditions (phase current amplitude, $I_a = 10, 50, 100, 150, 200, 236, 300, 400, 500\text{A}$) are investigated to cover the full load conditions, from light-load, heavy-load, full-load, to over-load. Furthermore, with the simplified torque estimation approach introduced in this section [MOG94], the torque characteristics of IPMSM and SPMSM after rotor skew can be obtained directly based on the torque characteristics before rotor skew.

In PMSMs, the open-circuit torque is also known as cogging torque. The waveforms and spectra of the cogging torque of IPMSM and SPMSM are shown in Fig. 5.2. Although the amplitudes of these torque harmonics are different, due to the same slot/pole number combination, the harmonic orders in cogging torque are the same as those in the IPMSM and SPMSM, i.e., 48 in mechanical, which is the smallest common multiple between the slot number Q_s , 48 and the pole number $2p$, 8; or 12 in electrical, because the great common divisor between Q_s and p is 4, the electrical degree in the benchmark PMSMs will be four times of mechanical degree [ZHU00].

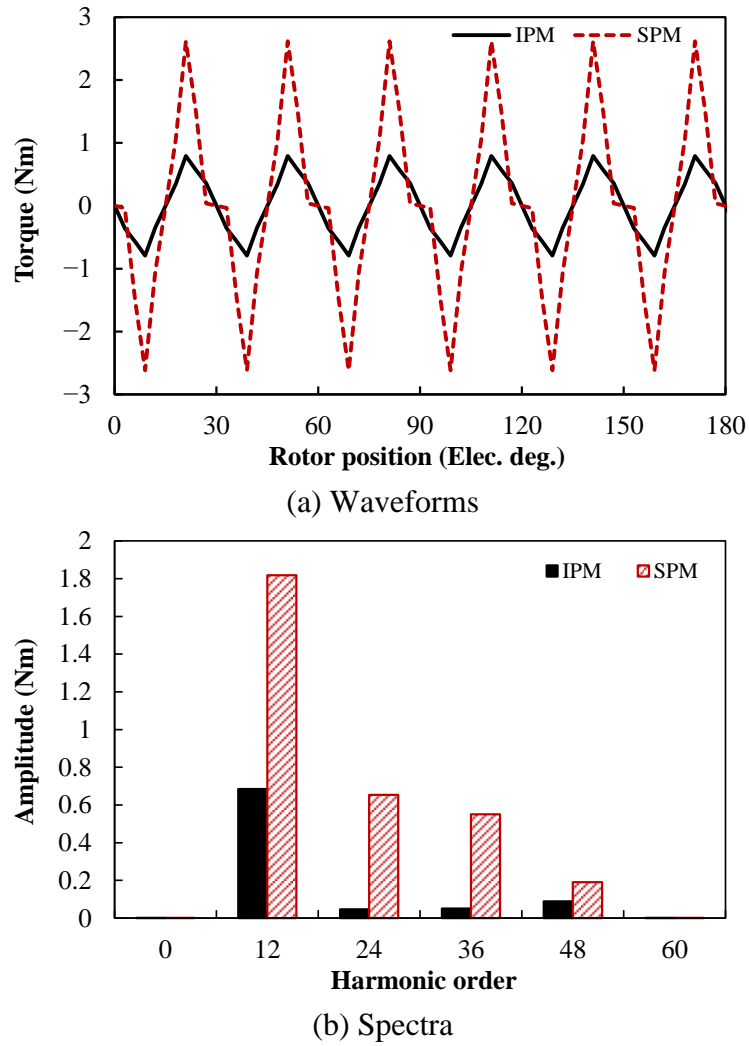
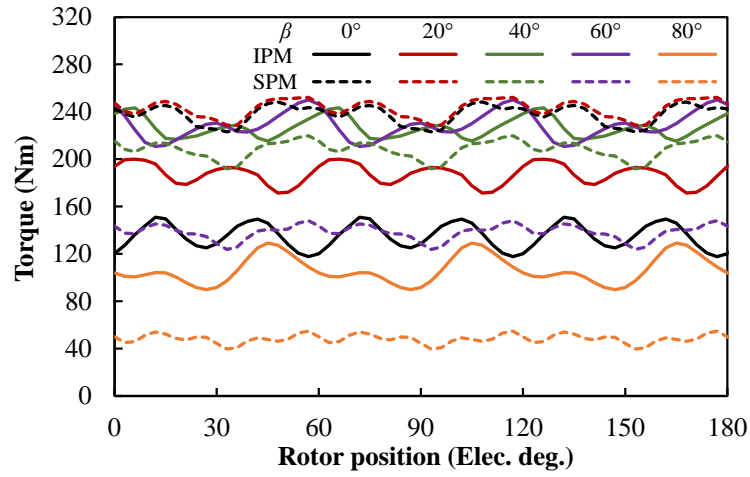
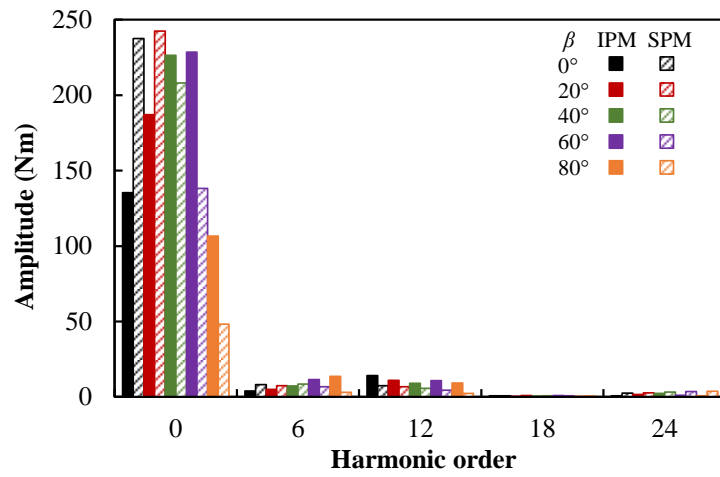


Fig. 5.2 Cogging torque characteristics of IPMSM and SPMSM under open-circuit condition.

Under on-load conditions, torque characteristics of PMSMs are affected by phase current amplitude (I_a) and current angle (β) simultaneously. In this chapter, current angle denotes current advancing angle, which is the advancing angle of the resultant phase current vector to the q -axis. For each phase current amplitude condition, the torque waveforms of the benchmark IPMSM and SPMSM with continuously-varied current angle are calculated firstly. For example, when phase current amplitude is 236A, the torque waveforms and spectra of the IPMSM and SPMSM with different current angles ($\beta = 0^\circ, 20^\circ, 40^\circ, 60^\circ$, and 80°) are given in Fig. 5.3(a) and (b), respectively.



(a) Waveforms



(b) Spectra

Fig. 5.3 Instantaneous torque characteristics of IPMSM and SPMSM with different current angles ($I_a = 236\text{A}$).

Based on Fig. 5.3, under the condition of $I_a = 236\text{A}$, the variations of average torque with current angle in IPMSM and SPMSM can be obtained, as shown in Fig. 5.4.

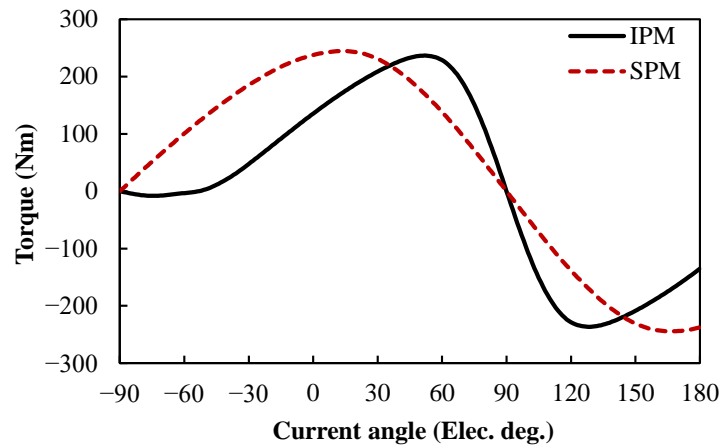


Fig. 5.4 Variations of average torque with current angle in IPMSM and SPMSM ($I_a = 236\text{A}$).

Similarly, when I_a is varied from 10A to 500A, the variations of average torque with current angle in IPMSM and SPMSM can be calculated, as shown in Fig. 5.5.

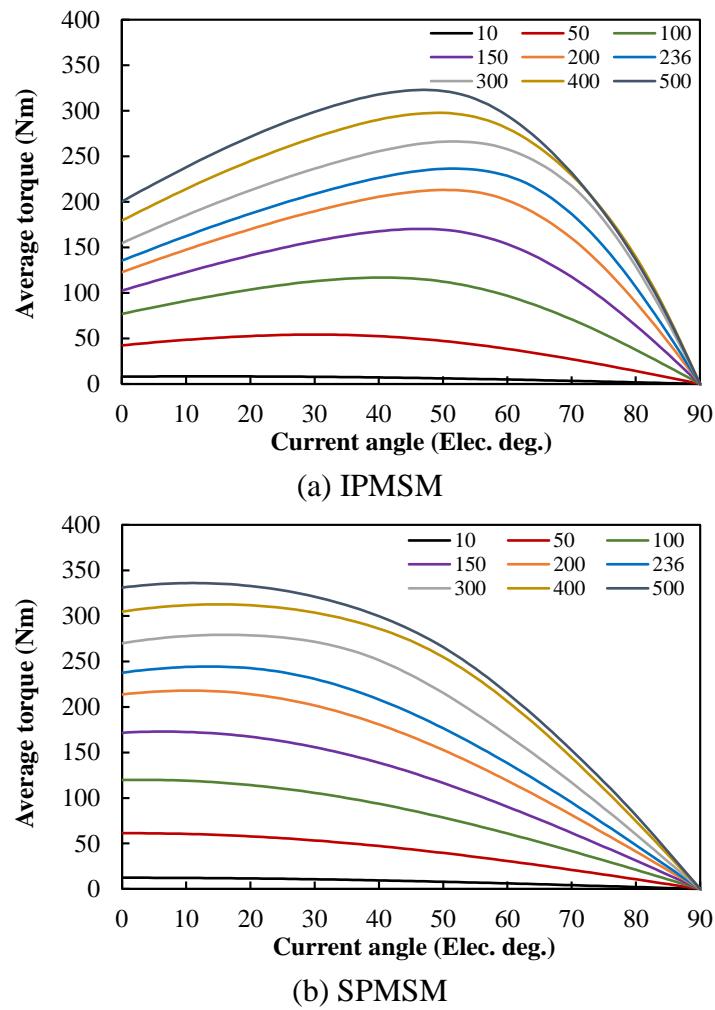


Fig. 5.5 Variations of average torque with current angle in IPMSM and SPMSM under different phase current amplitude conditions.

From Fig. 5.5, for any specific phase current amplitude, the optimal current angles for maximum average torque in IPMSM and SPMSM can be found, as summarized in Table 5.2.

Table 5.2 Optimal current angles for maximum average torque with different phase current amplitudes in IPMSM and SPMSM (Elec. deg.)

| Phase current amplitude (A) | IPMSM | SPMSM |
|-----------------------------|-------|-------|
| 10 | 13 | 0 |
| 50 | 30 | 1 |
| 100 | 41 | 3 |
| 150 | 47 | 6 |
| 200 | 50 | 11 |
| 236 | 52 | 13 |
| 300 | 52 | 16 |
| 400 | 49 | 15 |
| 500 | 47 | 11 |

Based on Table 5.2, without rotor skew, the influence of load on optimal current angle can be presented by the variations of the optimal current angles with phase current amplitude, as shown in Fig. 5.6. It can be seen that even in SPMSM, with the increase of electric loading, armature reaction and magnetic saturation become evident, which results in equivalent magnet saliency and the optimal current angle is larger than 0° .

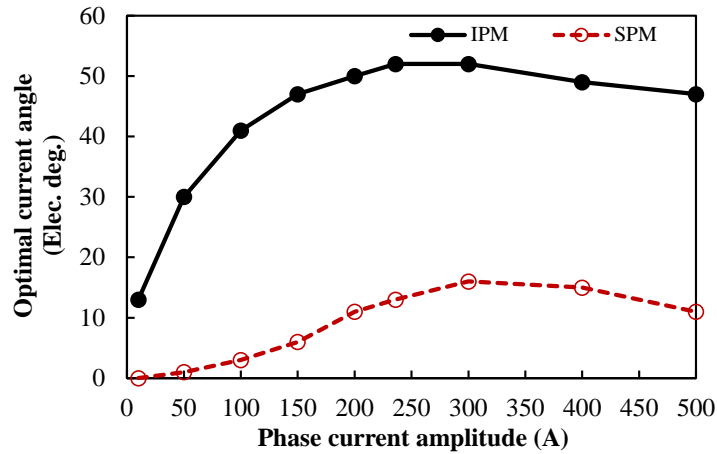


Fig. 5.6 Variations of optimal current angle with phase current amplitude in IPMSM and SPMSM.

With the optimal current angles shown in Fig. 5.6, the influences of load on average torque and torque ripple before rotor skew are shown in Fig. 5.7 (a) and (b). It can be seen that in both IPMSM and SPMSM, when phase current amplitude is higher than $200A_{pk}$, magnetic saturation becomes more severe and average torques are no longer linear with phase current amplitude. It can also be observed that compared with IPMSM, SPMSM can produce slightly higher average torque and lower torque ripples when phase current amplitude is higher than $300A_{pk}$, which suggests that SPMSM has better over-load torque performance.

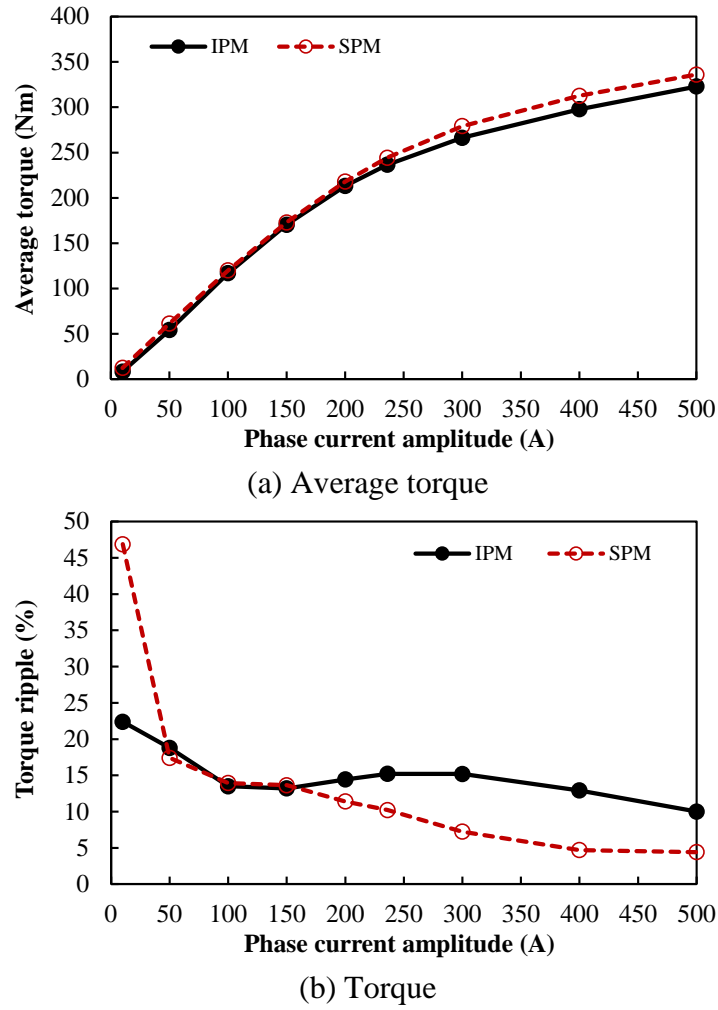


Fig. 5.7 Variations of average torque and torque ripple with phase current amplitude in IPMSM and SPMSM (with optimal current angles in Fig. 5.6)

5.3.2 Simplified Torque Estimation Approach

In this sub-section, following the analyses shown in [MOG94], a simplified torque estimation approach is introduced based on conventional multi-slice rotor model. The electromagnetic performances of IPMSM and SPMSM after rotor skews presented in this chapter are estimated by the simplified approach.

The continuous skewed rotor and the multi-slice model for the conventional and simplified approaches are illustrated in Fig. 5.8. In the conventional approach [CHU13b], the multi-slice rotor has a high slice number (also called as step number), and the shifting angle between rotor slices is determined by the skew angle and slice number. However, in the simplified approach, the slice number is determined by skew angle, to keep the shifting angle between rotor slices fixed.

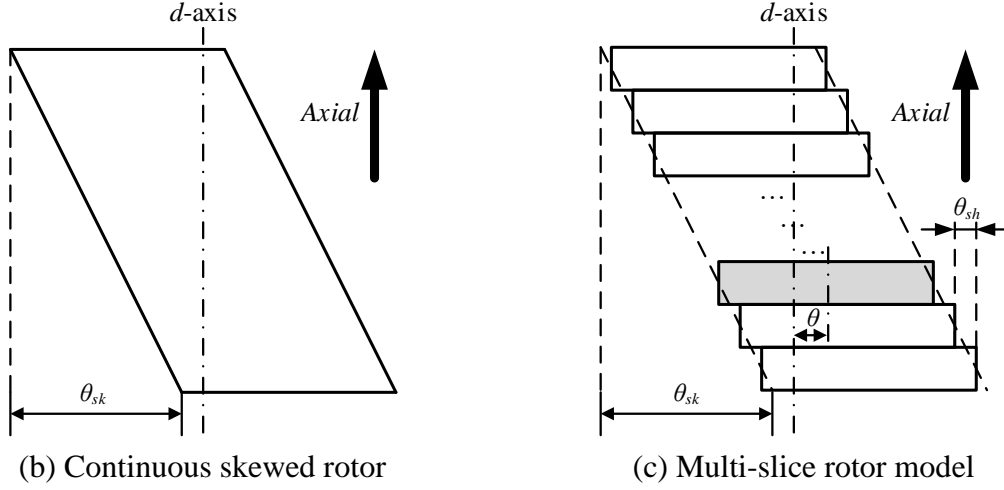


Fig. 5.8 Rotor axial arrangements of continuous skewed rotor, multi-slice rotor models for conventional and simplified torque estimation approaches.

Thus, in the conventional approach, when skew angle varies, the shifting angle between rotor slices varies as well, and the FE model has to be modified, which makes the analyses very complicated and time-consuming. However, in the simplified approach, for a specific current angle, the instantaneous torque of one rotor slice can be utilized for different skew angles. What is more, the instantaneous torque of one rotor slice with different current angles can be easily obtained from the torque waveforms of PMSMs without rotor skew. Thus, the resultant torque performances after rotor skew, considering different skew angles and different current angles can be obtained directly from the torque performances of PMSMs without rotor skew by using the simplified approach, without the need of modifying FE model frequently. The details of the simplified approach will be introduced as follows.

Although the rotor models in the conventional and simplified approaches are slightly different, the calculation methods of the resultant torque after rotor skew are identical in the two approaches. In Fig. 5.8, assuming skew angle is θ_{sk} in the continuous skewed rotor, the multi-slice rotor is composed by many rotor slices, and the rotor slices are displaced from $-\theta_{sk}/2$ to $+\theta_{sk}/2$ compared with the d -axis. In Fig. 5.8(b), since the greyed rotor slice is displaced from d -axis by θ , when the current angle for the whole rotor (d -axis) is β_0 , the equivalent current angle for the greyed rotor slice $\beta_0 + \theta$. Hence, the instantaneous torque of the greyed rotor slice can be obtained from the instantaneous torque produced by the un-skewed PMSM with current angle, $\beta = \beta_0 + \theta$, taking rotor slice axial length and waveform shifting due to shifted initial position into consideration, as

$$T_{rs}(\beta_0, \theta) = \frac{1}{N_s} T(\beta = \beta_0 + \theta, \theta_0 = -\theta) \quad (5.1)$$

where $T_{rs}(\beta_0, \theta)$ is the instantaneous torque produced by one rotor slice, when the current angle for the whole rotor is β_0 , and the displacement from the rotor slice to d -axis is θ . N_s is slice number. $T(\beta, \theta_0)$ is the instantaneous torque produced by the un-skewed PMSM rotor when current angle is β , and torque waveform shifting is θ_0 .

Thus, based on (5.1), the resultant torque after rotor continuous skew, T_{sk} , can be calculated as

$$T_{sk} = \frac{1}{\theta_{sk}} \int_{-\theta_{sk}/2}^{\theta_{sk}/2} T(\beta = \beta_0 + \theta, \theta_0 = -\theta) d\theta \quad (5.2)$$

It should be mentioned that (5.1) and (5.2) work for both the conventional and simplified approaches, the difference between the two approaches lies in the configuration of the rotor slices. For example, assuming the slice number, N_s , is 15 in the conventional approach, and the shifting angle between rotor slices, θ_{sh} , is 1° in the simplified approach, for the conditions with skew angle = 3° and 18° , the initial shifting positions of the rotor slices in the conventional and simplified multi-slice rotor models are summarized in Table 5.3. It should be mentioned that to simplify the calculations, the central rotor slice should be placed at the d -axis of the rotor (initial position = 0°). Thus, when the calculated slice number is even in the simplified approach, for example, when skew angle = 18° , the calculated slice number is 18, the resultant torque is calculated from a 19 (slice number+1)-slice model, but only halves of the torques produced by the first and the last rotor sides are utilized in the calculations. Hence, the -9° and 9° rotor slices are marked in brackets in Table 5.3. It can be clearly seen that in the conventional approach, when skew angle varies from 3° to 18° , the initial positions of almost all rotor slices need to be modified, but in the simplified approach, when skew angle varies from 3° to 18° , the selection of rotor slices is changed, but the initial positions of all rotor slices do not need to be modified. Furthermore, it can be inferred that with the simplified approach, based on the torque waveforms of the un-skewed PMSMs (current angle internal = 1°), the resultant torque waveform of PMSMs after rotor skew, considering different skew angles (every 1°) and different current angles (every 1°) can be obtained.

Table 5.3 Rotor slice initial positions in conventional and simplified multi-slice rotor models

| Skew angle (°) | Approach | Slice number, N_s | Shifting angle between rotor slices, θ_{sh} (°) | Rotor slice initial positions (°) |
|----------------|--------------|---------------------|--|--|
| 3 | Conventional | 15 | 0.2 | -1.4, -1.2, -1, -0.8, -0.6, -0.4, -0.2, 0, 0.2, 0.4, 0.6, 0.8, 1, 1.2, 1.4 |
| | Simplified | 3 | 1 | -1, 0, 1 |
| 18 | Conventional | 15 | 1.2 | -8.4, -7.2, -6, -4.8, -3.6, -2.4, -1.2, 0, 1.2, 2.4, 3.6, 4.8, 6, 7.2, 8.4 |
| | Simplified | 18 | 1 | (-9), -8, -7, -6, -5, -4, -3, -2, -1, 0, 1, 2, 3, 4, 5, 6, 7, 8, (9) |

5.3.3 Verification with Conventional Approach

In this section, the resultant instantaneous torque waveforms of PMSMs after rotor continuous skew can be obtained by the simplified approach are compared with those obtained by the conventional approach to verify the effectiveness of the simplified approach.

From Table 5.3, under the condition (IPMSM with $I_a = 236A$, $\beta_0 = 45^\circ$, and $\theta_{sk} = 3^\circ$), when using the conventional approach, 15 cases ($\beta_0 = 45^\circ$, $\theta_0 = -1.4^\circ, -1.2^\circ, -1^\circ, -0.8^\circ, -0.6^\circ, -0.4^\circ, -0.2^\circ, 0^\circ, 0.2^\circ, 0.4^\circ, 0.6^\circ, 0.8^\circ, 1^\circ, 1.2^\circ$, and 1.4°) are needed in the FE analyses of the un-skewed IPMSM. However, when using the simplified approach, only 3 cases ($\beta_0 = 45^\circ$, $\theta_0 = -1^\circ, 0^\circ, 1^\circ$) are needed in the FE analyses of the un-skewed IPMSM. Further, the torque waveforms of the 3 cases ($\beta_0 = 45^\circ$, $\theta_0 = -1^\circ, 0^\circ$, and 1°) can be obtained from the torque waveforms of other 3 cases ($\beta_0 = 44^\circ, 45^\circ$, and 46° , $\theta_0 = 0^\circ$), as illustrated in Fig. 5.9.

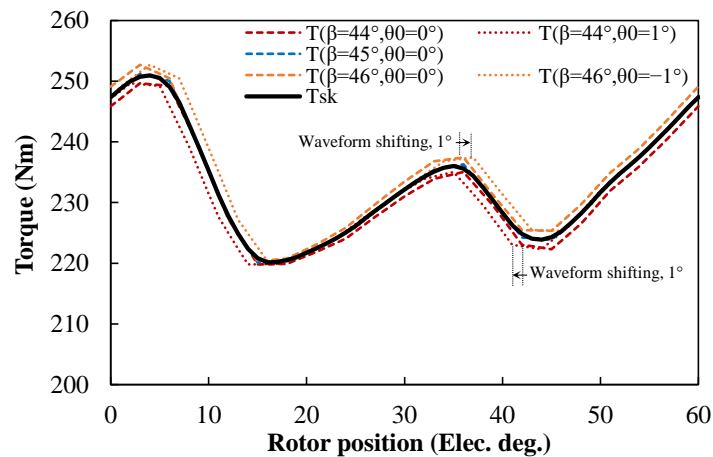
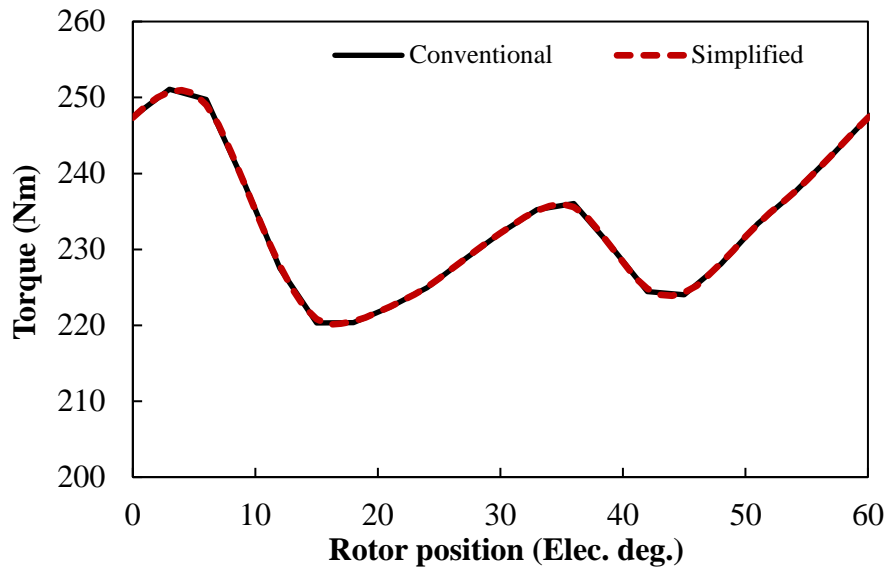
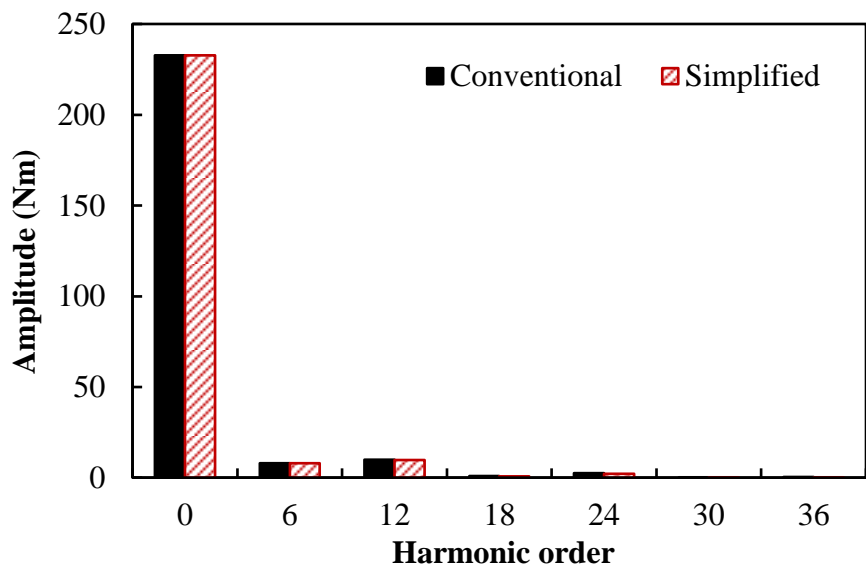


Fig. 5.9 Instantaneous torque waveform of IPMSM with rotor continuous skew obtained by simplified approach ($I_a = 236A$, $\beta_0 = 45^\circ$, and $\theta_{sk} = 3^\circ$).

Based on Table 5.3 and Fig. 5.9, the instantaneous torque performances of IPMSM after rotor continuous skew obtained by the conventional and simplified approaches are compared under different skew angle conditions, as shown Fig. 5.10 and Fig. 5.11.

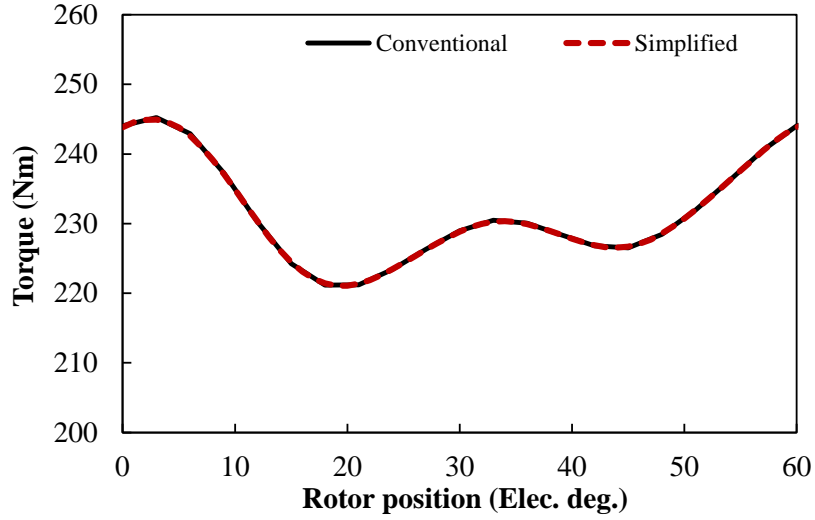


(a) Waveforms

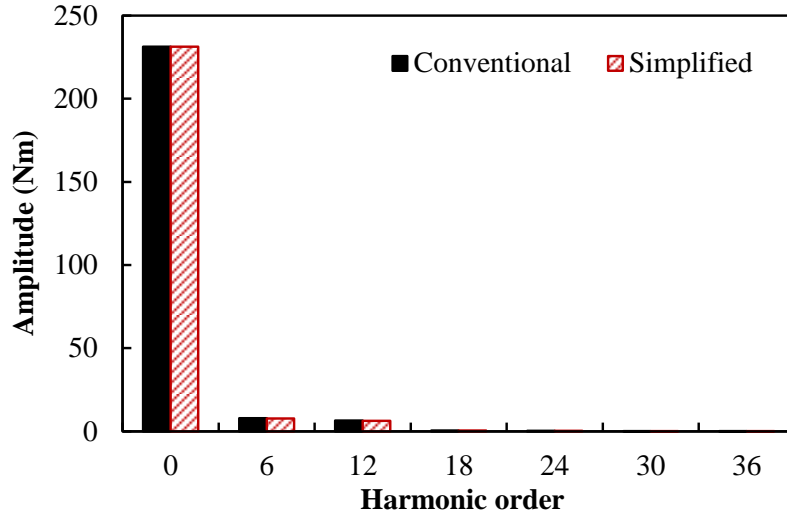


(b) Spectra

Fig. 5.10 Comparison of instantaneous torques obtained by conventional and simplified approaches (IPMSM, $I_a = 236\text{A}$, $\beta_0 = 45^\circ$, and $\theta_{sk} = 3^\circ$).



(a) Waveforms



(b) Spectra

Fig. 5.11 Comparison of instantaneous torques obtained by conventional and simplified approaches (IPMSM, $I_a = 236\text{A}$, $\beta_0 = 45^\circ$, and $\theta_{sk} = 18^\circ$).

It can be seen that the instantaneous torque waveforms obtained by the conventional and simplified approaches are almost totally identical. Hence, the simplified approach can achieve similar results compared with the conventional approach, but with much lighter burdens in calculations. It also should be noticed that when skew angle is small, for example, 3° , the rotor slice number will also be small in the simplified approach, but since the smaller skew angle has lower effects on resultant torque characteristics after rotor skew, the resultant torque performances obtained by the conventional and simplified approaches are still almost the same.

Fig. 5.12 Variations of average torque and torque ripple with skew angle and current angle in IPMSM obtained by simplified approach ($I_a = 236\text{A}$).

From Fig. 5.12(a), it can be found that for the conditions with current angle larger than 80° , the average torques are very small, and hence, the torque ripples will be very high. To avoid these extremely high torque ripples, the torque ripples higher than 40% are not displayed in Fig. 5.12(b).

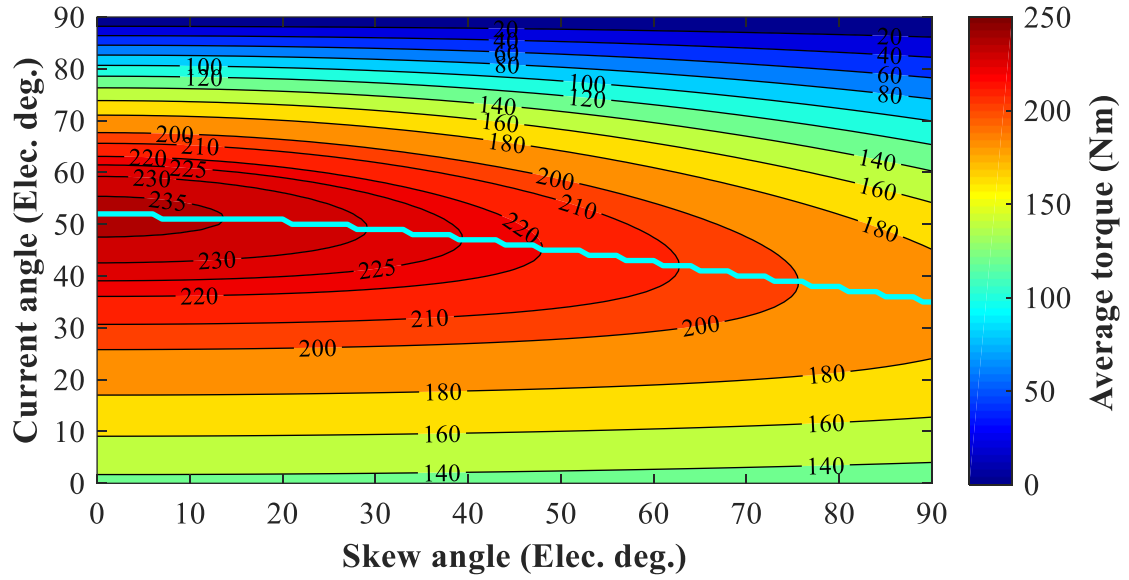
In conclusion, based on multi-slice rotor model, a simplified approach to estimate torque performance after rotor continuous skew is introduced in this section. Different from the multi-slice rotor model in the conventional approach, which has a fixed slice number, the multi-slice rotor model in the simplified approach has a fixed shifting angle between rotor slices. Thus, the torque characteristic of every rotor slice can be obtained directly from the un-skewed PMSM and the precision of the simplified approach can be greatly improved by minimizing current angle interval in the FE analyses of the un-skewed PMSM. Although the slice number will be very small when skew angle is very small in the simplified approach, considering that smaller skew angle has relatively lower effect on the resultant torque characteristic after rotor skew, the inaccuracy of the simplified approach in small skew angles still can be acceptable.

5.4 Influences of Load in Rotor Continuous Skew

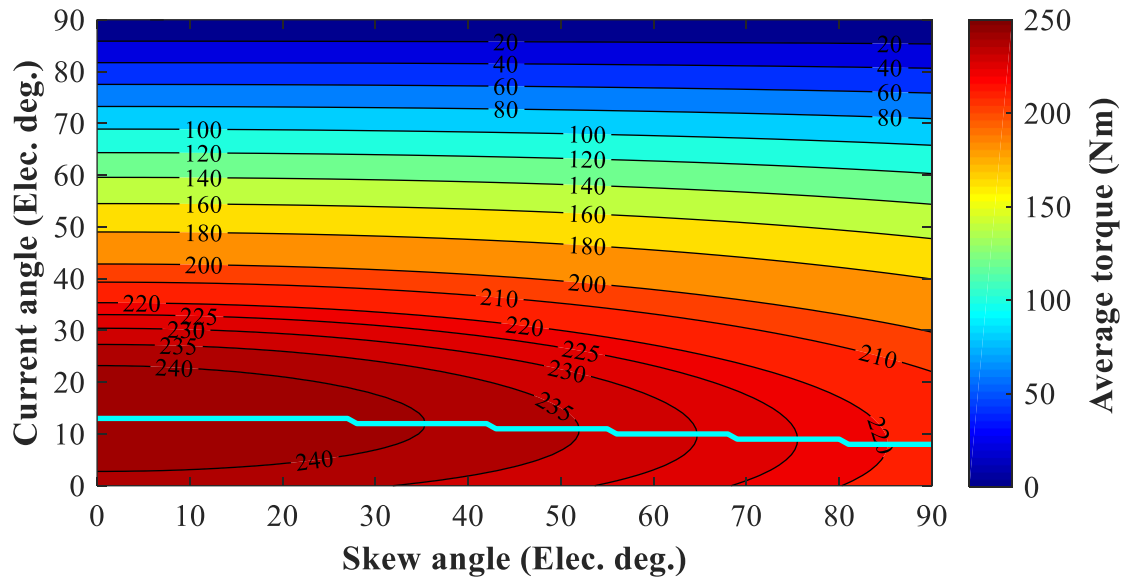
5.4.1 Optimal Current and Skew Angles for Specific Load Condition

5.4.1.1 Selection of Optimal Current Angle

In the benchmark IPMSM, when the phase current amplitude is 236A, based on the variation of average torque with skew angle and current angle, as shown in Fig. 5.12(a), for different skew angle, the optimal current angle for the maximum average torque can be obtained, as presented in Fig. 5.13(a). Similarly, in the benchmark SPMSM, when phase current amplitude is 236A, the optimal current angles for different skew angles can also be achieved based on the variation of average torque with skew angle and current angle, as shown in Fig. 5.13(b).



(a) IPMSM



(b) SPMSM

Fig. 5.13 Variations of average torque with skew angle and current angle in IPMSM and SPMSM after rotor continuous skew ($I_a = 236\text{A}$).

Based on Fig. 5.13, the variations of optimal current angles with skew angle in IPMSM and SPMSM are compared under the specific load condition ($I_a = 236\text{A}$) in Fig. 5.14. It can be seen that when $I_a = 236\text{A}$, the optimal current angles in IPMSM and SPMSM all become smaller with the increase of skew angle.

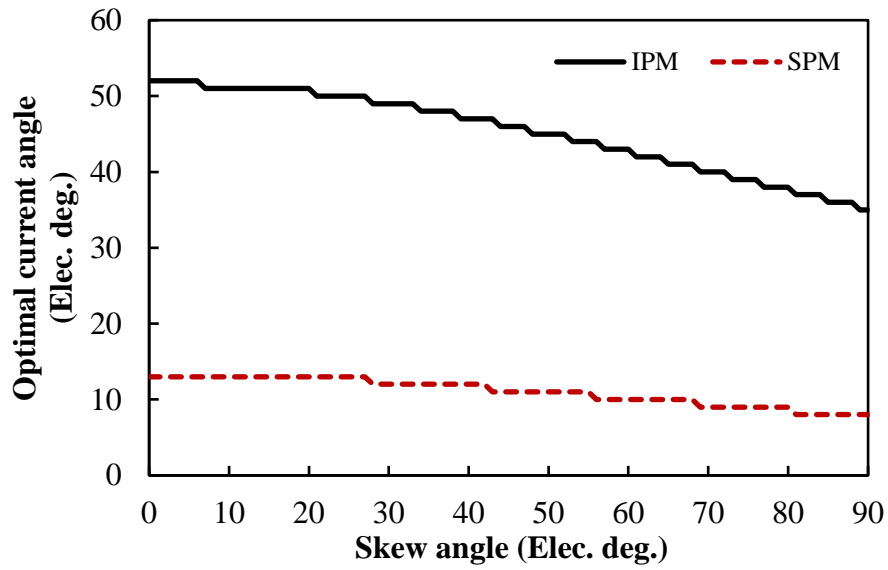
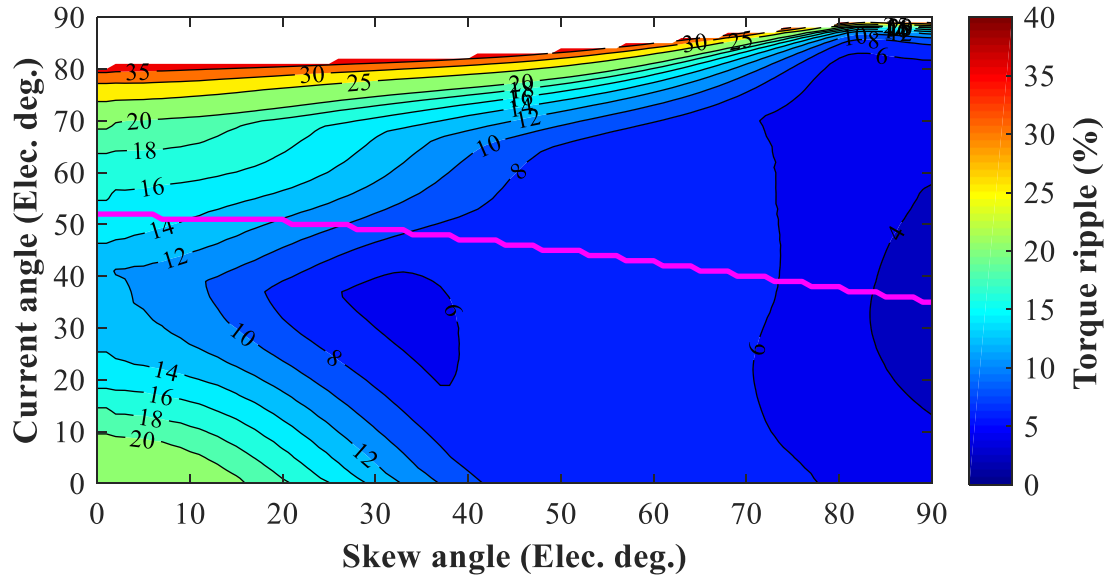


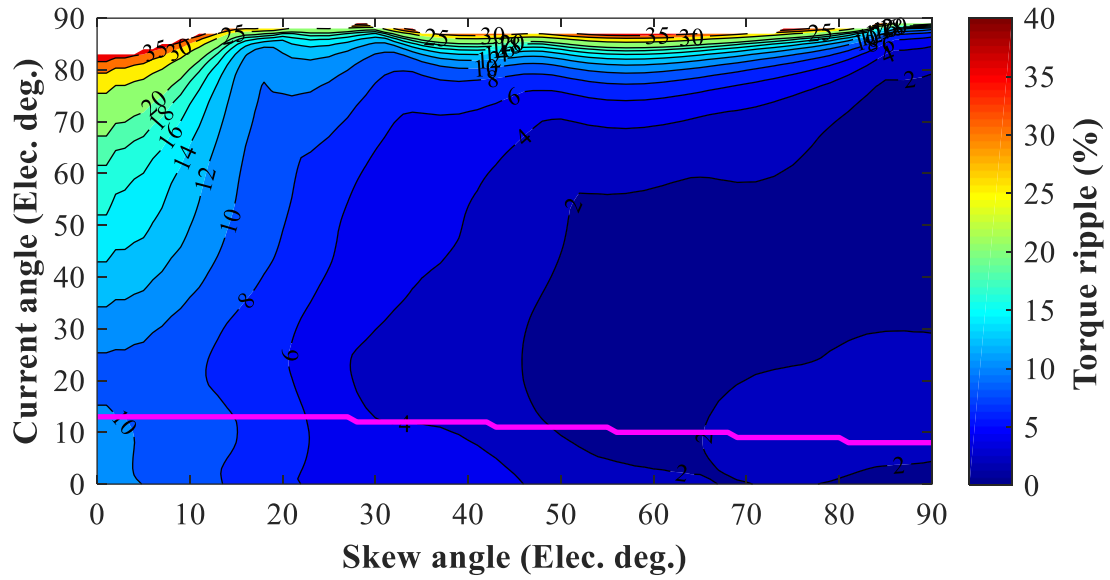
Fig. 5.14 Variations of optimal current angle with skew angle in IPMSM and SPMSM after rotor continuous skew ($I_a = 236A$).

5.4.1.2 Selection of Optimal Skew Angle

Under the specific load condition ($I_a = 236A$), the variations of torque ripples with skew angle and current angle in IPMSM and SPMSM are shown together in Fig. 5.15. When using the optimal current angles, the variations of torque ripple with skew angle in IPMSM and SPMSM can be obtained from the polylines of optimal current angles in Fig. 5.15.



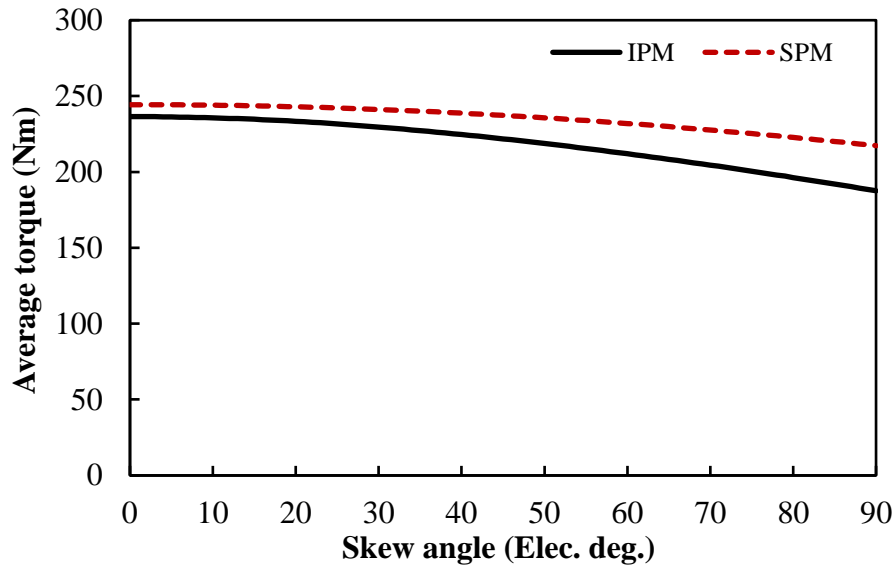
(a) IPMSM



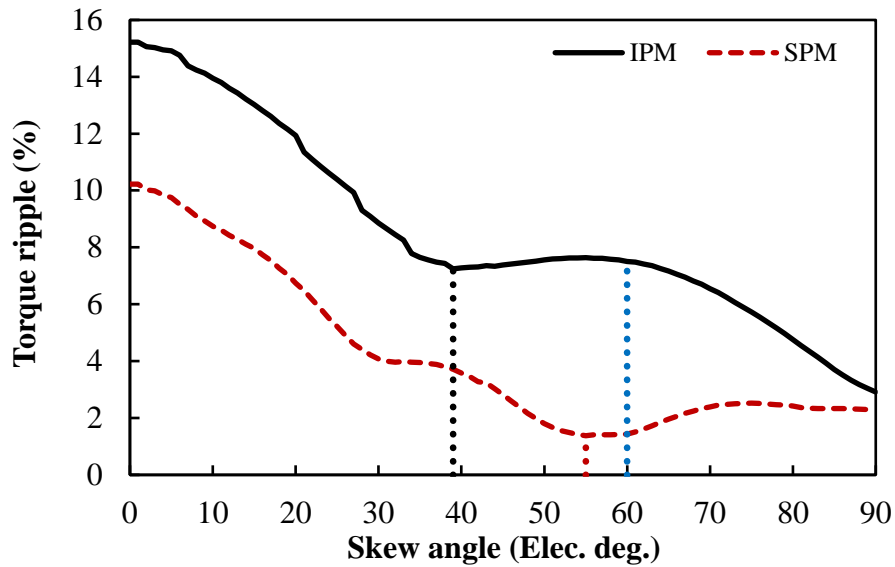
(b) SPMSM

Fig. 5.15 Variations of torque ripple with skew angle and current angle in IPMSM and SPMSM after rotor continuous skew ($I_a = 236A$).

With the optimal current angles given in Fig. 5.14, the resultant average torque and torque ripple versus skew angle characteristics of IPMSM and SPMSM can be obtained from Fig. 5.13 and Fig. 5.15, as shown in Fig. 5.16(a) and (b), respectively.



(a) Average torque



(b) Torque ripple

Fig. 5.16 Variations of average torque and torque ripple with skew angle in IPMSM and SPMSM after rotor continuous skew and using optimal current angles ($I_a = 236A$).

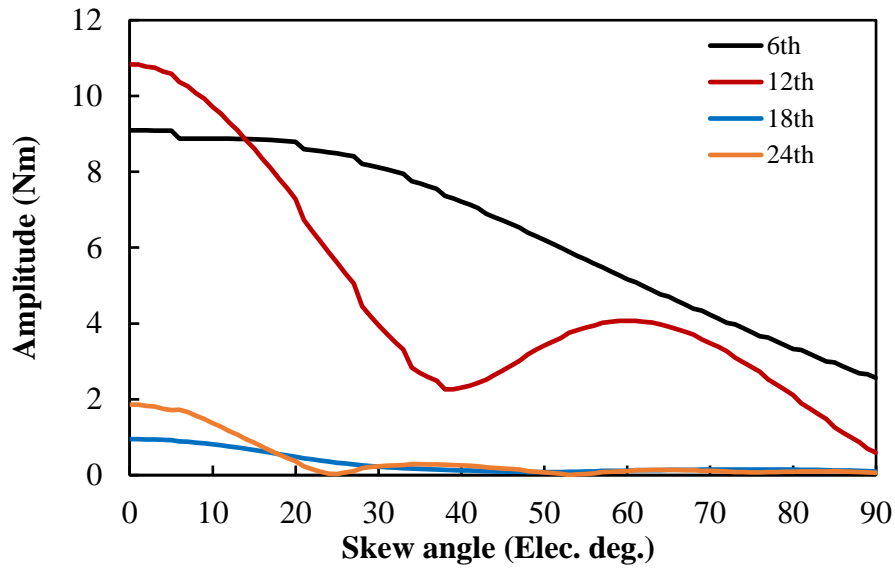
From Fig. 5.3, it was found that the one periodicity for on-load torque ripple is 60° in the benchmark IPMSM and SPMSM, and hence, the conventional skew angle for the benchmark IPMSM and SPMSM is 60° . However, from Fig. 5.16, it can be found that in IPMSM and SPMSM, some skew angles lower than 60° can produce higher average torque and lower torque ripple than the conventional skew angle, 60° . In this chapter, for any load condition, the skew angle, which is not larger than 60° and can produce the lowest torque ripple, is selected as the optimal skew angle. Thus, under the condition ($I_a = 236A$), 39° and 56° can be selected as the optimal skew angles for the minimum torque ripple in the benchmark IPMSM and SPMSM

respectively based on Fig. 5.16(b). The detailed torque characteristics of IPMSM and SPMSM with conventional and optimal skew angles are summarized in Table 5.4. It should be noticed that “skew angle = 0°” denotes the conditions without rotor skew.

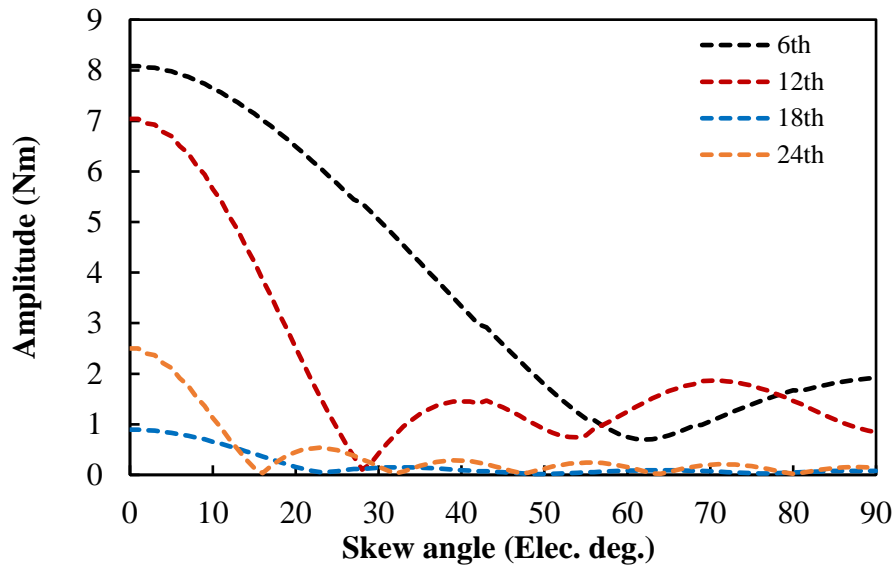
Table 5.4 Torque characteristics of IPMSM and SPMSM after rotor continuous skew using different skew angles ($I_a = 236A$)

| | Skew angle (°) | Optimal current angle (°) | Average torque (Nm) | Torque ripple (%) |
|-------|----------------|---------------------------|---------------------|-------------------|
| IPMSM | 0 | 52 | 236.50 | 15.22 |
| | 60 | 43 | 211.99 | 7.51 |
| | 39 | 47 | 225.22 | 7.25 |
| SPMSM | 0 | 13 | 244.36 | 10.22 |
| | 60 | 10 | 231.96 | 1.43 |
| | 55 | 11 | 233.90 | 1.38 |

To further investigate the effects of skew angle on different torque harmonics in IPMSM and SPMSM, the variations of different torque harmonic amplitudes with skew angle in IPMSM and SPMSM are calculated, as shown in Fig. 5.17. It can be observed that under load conditions, the effects of skew angle on different amplitudes are different from the theoretical predictions. For example, it is expected that the 12th torque harmonics in PMSMs should be reduced significantly with 30deg skew angle. In fact, in IPMSMs, due to the influences of electric loadings, the 12th torque harmonic can only be reduced significantly with around 40deg skew angle; but in SPMSMs, although electric loadings can also affect the effectiveness of rotor skew, the 12th torque harmonic can still be reduced significantly with around 30deg skew angle. This phenomenon can further be explained by the different effects of step skew on different torque harmonic order components under load conditions, which was reported previously in [CHU13b]. Considering that the resultant torque ripples are composed by different torque harmonic order components, the resultant optimal skew angle for a specific load condition can only be obtained by scanning different skew angles and different current angles. In the benchmark IPMSM and SPMSM, when phase current amplitude is 236A, the resultant optimal skew angle is 43° in IPMSM, and 55° in SPMSM.



(a) IPMSM



(b) SPMSM

Fig. 5.17 Variations of different torque harmonic amplitudes with skew angle in IPMSM and SPMSM after rotor continuous skew and using optimal current angles ($I_a = 236A$).

5.4.2 Effects of Load in Interior and Surface PMSMs

5.4.2.1 Effects of Load on Optimal Current Angle

Based on section 5.4.1.1, when the phase current amplitude is varied from 10A, 50A, 100A, 150A, 200A, 236A, 300A, 400A, to 500A, the variations of the optimal current angles with skew angle can be obtained by using the simplified torque estimation approach, as shown in Fig. 5.18. It can be seen that under on-load conditions, in both IPMSM and SPMSM, the optimal current angle always becomes smaller when the skew angle becomes larger. Compared

with that in SPMSM, the optimal current angle in IPMSM varies more evidently with skew angle.

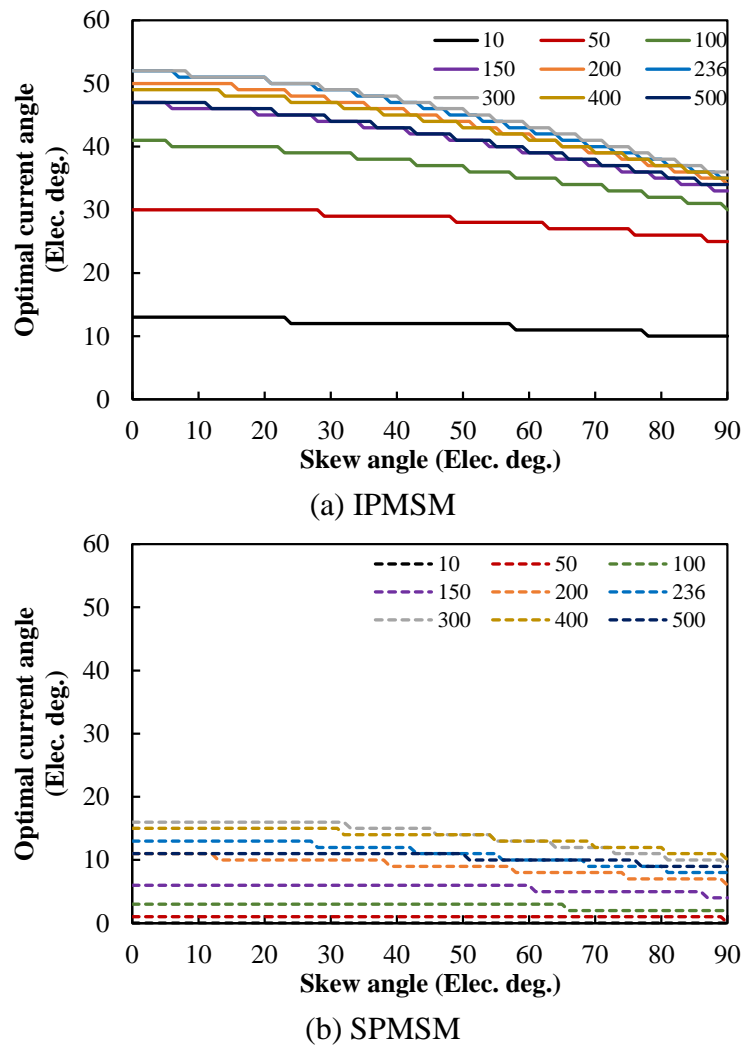


Fig. 5.18 Variations of optimal current angles with skew angle in IPMSM and SPMSM after rotor continuous skew under different phase current amplitude conditions

From Fig. 5.18, for any skew angle, the variation of the optimal current angle with phase current amplitude can also be obtained. For example, when the skew angle is 0° (without skew) and 60° (one on-load torque ripple periodicity, conventional skew angle), the effects of load on optimal current angle are compared in Fig. 5.19. It can be observed that in both IPMSM and SPMSM, the optimal current angles obtained from un-skewed PMSMs are no longer suitable for skewed PMSMs. Thus, when using rotor skew to reduce torque ripples in PMSMs, it is always necessary to re-calculate optimal current angles according to skew angle under different load conditions.

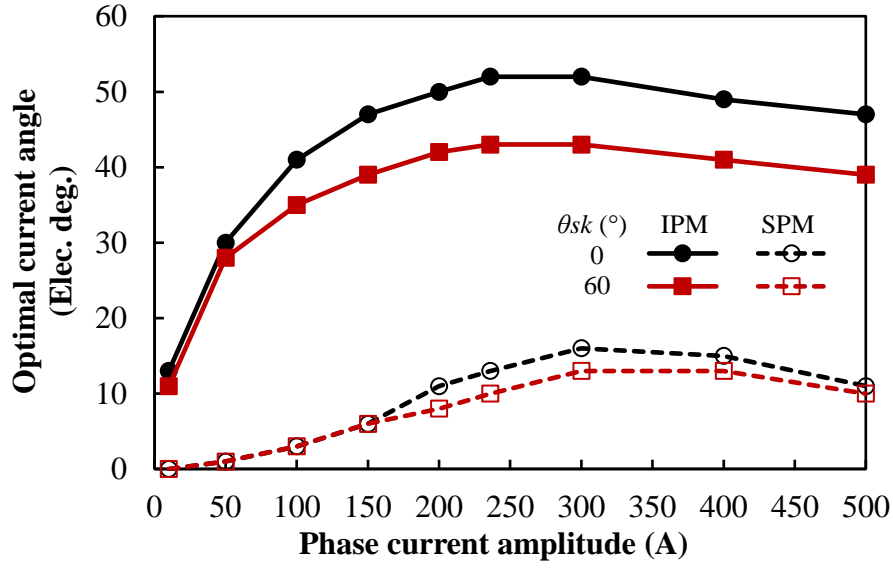
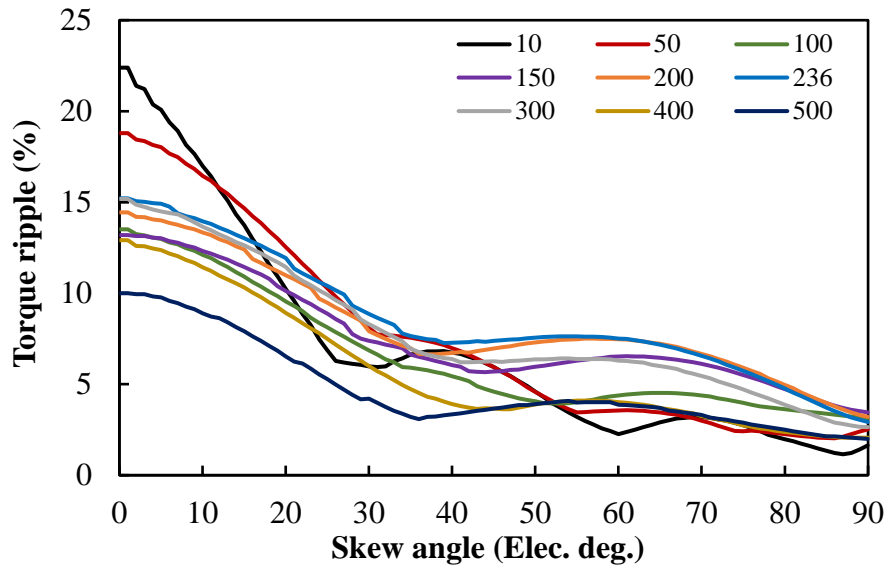


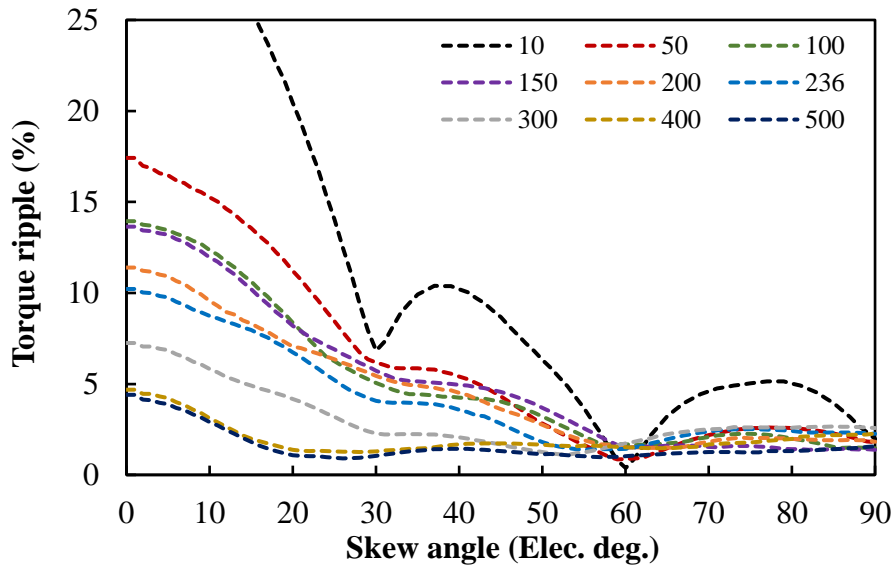
Fig. 5.19 Variations of optimal current angles with phase current amplitude in IPMSM and SPMSM after rotor continuous skew when using different skew angles.

5.4.2.2 Effects of Load on Optimal Skew Angle

For varied skew angle, with the optimal current angles given in Fig. 5.18, the variations of torque ripples with skew angle in IPMSM and SPMSM after rotor continuous skew under different phase current amplitude conditions are calculated, as shown in Fig. 5.20. Based on the torque ripple versus skew angle characteristics of IPMSM and SPMSM under different load conditions shown in Fig. 5.20, the optimal skew angles for the minimum torque ripple under these load conditions can be derived, as introduced in section 5.4.1.2 and shown in Table 5.5. Besides the optimal skew angles and the corresponding optimal current angles, the average torque and torque ripple characteristics of IPMSM and SPMSM after rotor continuous skew when using optimal skew angles are also provided in Table 5.5.



(a) IPMSM



(b) SPMSM

Fig. 5.20 Variations of torque ripple with skew angle in IPMSM and SPMSM after rotor continuous skew and using optimal current angles under different phase current amplitude conditions.

Table 5.5 Optimal skew angles for minimum torque ripple in IPMSM and SPMSM when using rotor continuous skew under different load conditions

| Machine type | Phase current amplitude (A) | Optimal skew angle (°) | Optimal current angle (°) | Average torque (Nm) | Torque ripple (%) |
|--------------|-----------------------------|------------------------|---------------------------|---------------------|-------------------|
| IPMSM | 10 | 60 | 11 | 7.84 | 2.26 |
| | 50 | 55 | 28 | 49.51 | 3.45 |
| | 100 | 53 | 36 | 105.30 | 3.93 |
| | 150 | 44 | 42 | 152.36 | 5.67 |
| | 200 | 37 | 46 | 190.20 | 6.64 |
| | 236 | 39 | 47 | 211.99 | 7.25 |
| | 300 | 42 | 47 | 240.41 | 6.21 |
| | 400 | 47 | 44 | 269.25 | 3.62 |
| | 500 | 36 | 44 | 291.53 | 3.07 |
| SPMSM | 10 | 60 | 0 | 11.80 | 0.38 |
| | 50 | 60 | 1 | 58.61 | 0.86 |
| | 100 | 60 | 3 | 114.14 | 1.68 |
| | 150 | 60 | 6 | 164.02 | 1.50 |
| | 200 | 60 | 8 | 206.43 | 1.55 |
| | 236 | 55 | 11 | 233.90 | 1.38 |
| | 300 | 53 | 14 | 270.06 | 1.11 |
| | 400 | 28 | 15 | 310.15 | 1.26 |
| | 500 | 26 | 11 | 333.76 | 0.91 |

From Table 5.5, the variations of optimal skew angle with phase current amplitude in IPMSM and SPMSM after rotor continuous skew are shown in Fig. 5.21. It can be seen that in SPMSM, only when $I_a \geq 236\text{A}$ and the SPMSM is operated under over-load conditions, the optimal skew angle is no longer 60° . However, in IPMSM, the optimal skew angle is no longer 60° when $I_a \geq 50\text{A}$. Hence, the conventional skew angle is more suitable for SPMSM.

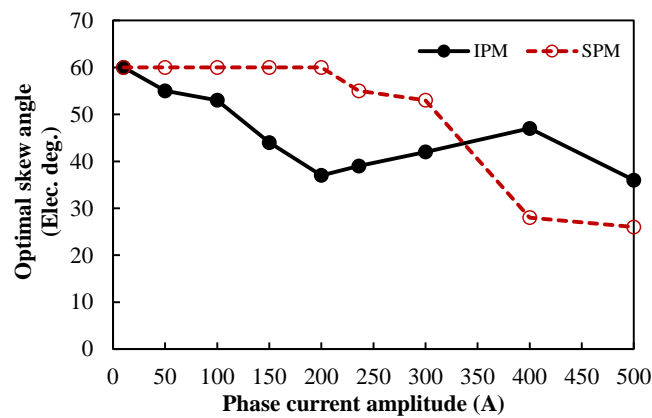


Fig. 5.21 Variations of optimal skew angle with phase current amplitude in IPMSM and SPMSM with rotor continuous skew

5.4.2.3 Effects of Load on Torque Characteristics with Conventional and Optimal Skew Angles

To compare the effectiveness of the conventional and optimal skew angles, the average torque and torque ripple characteristics of IPMSM and SPMSM after rotor continuous skew when using conventional and optimal skew angles are compared in Fig. 5.22. For convenience, the torque characteristics of IPMSM and SPMSM before rotor skew are also shown in Fig. 5.22, as represented by “ $\theta_{sk} = 0^\circ$ ”. Considering that average torque and torque ripple vary a lot under different load conditions, the ratios of resultant average torque and torque ripple after rotor continuous skew to those without rotor skew are also calculated. The variations of average torque and torque ripple ratios with phase current amplitude in IPMSM and SPMSM are shown in Fig. 5.23. It can be seen that compared with the conventional skew angle, 60° , the optimal skew angle can reduce on-load torque ripples and improve average torque simultaneously.

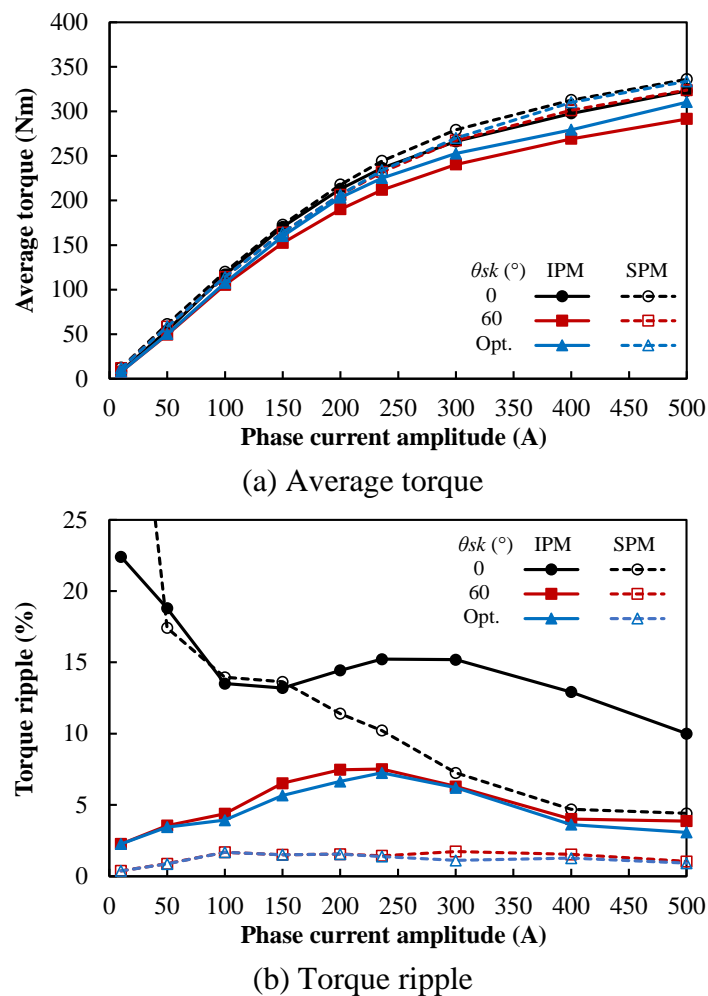
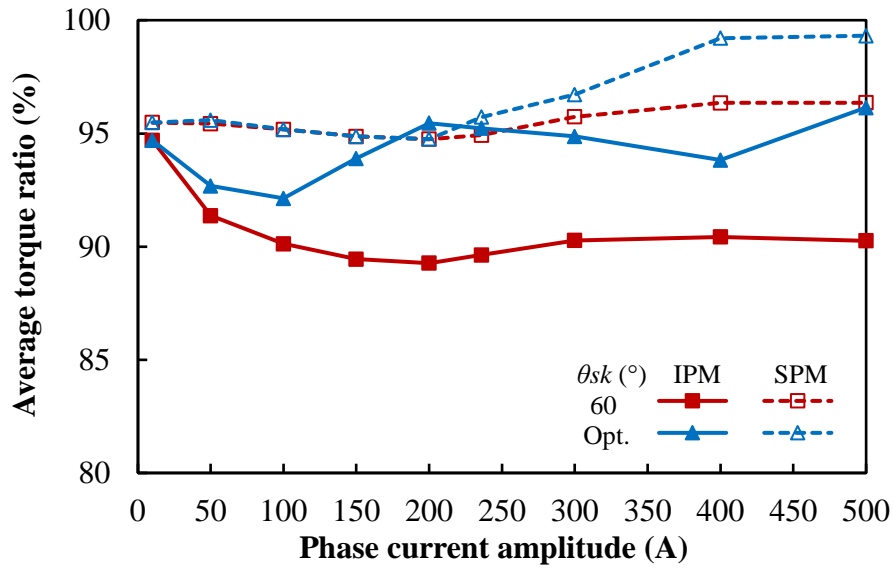
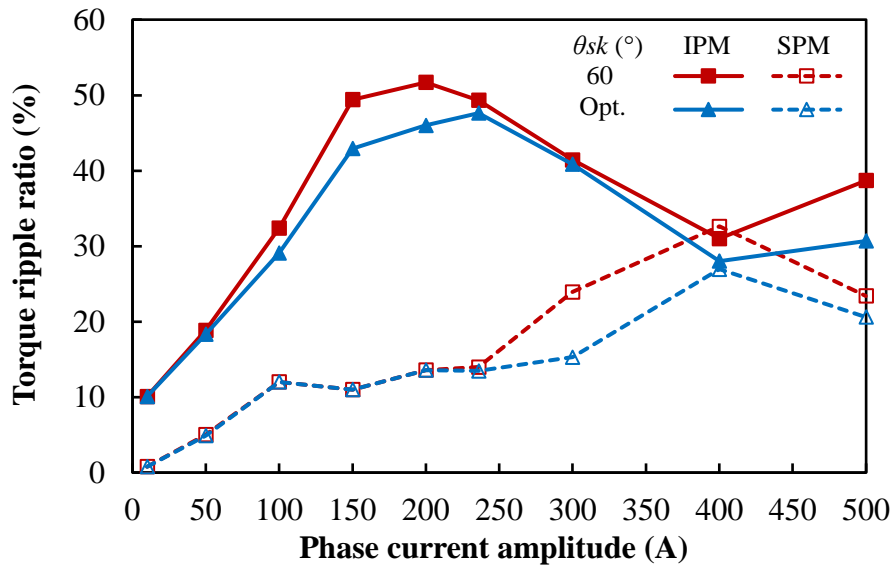


Fig. 5.22 Variations of average torque and torque ripple with phase current amplitude in IPMSM and SPMSM after rotor continuous skew when using different skew angles.



(a) Average torque ratio



(b) Torque ripple ratio

Fig. 5.23 Variations of average torque and torque ripple ratios with phase current amplitude in IPMSM and SPMSM after rotor continuous skew when using different skew angles.

Overall, it can be summarized that when rotor continuous skew is utilized in PMSMs for torque ripple reduction, it is always necessary to analyse the torque characteristic after rotor skew considering different skew angles and different current angles under different load conditions, especially in IPMSMs. It is found that for SPMSM under very heavy load conditions, when the magnetic saturation becomes very severe due to high electric loading, or interior PMSM under all load conditions, there exists an optimal skew angle, which can result in higher average torque and lower torque ripple simultaneously than the conventional skew angle.

5.5 Influences of Load in Rotor Step Skew

In fact, considering the difficulties in manufacturing continuously-skewed rotors, rotor step skew is a more practical approach for torque ripple reduction in PMSMs. In this section, the effects of load on optimal current angle and optimal skew angle, and the effectiveness of conventional and optimal skew angles are investigated in IPMSM and SPMSM based on 2-step and 3-step skews.

5.5.1 Simplified Torque Estimation Approach in Rotor Step Skew

The axial arrangements of 2- and 3-step skewed rotors are shown in Fig. 5.24. It can be seen that with the skew angle θ_{sk} , the shifting angle, θ_{sh} , between rotor slices is $\theta_{sk}/2$ in a 2-step skewed rotor, and $\theta_{sk}/3$ in a 3-step skewed rotor.

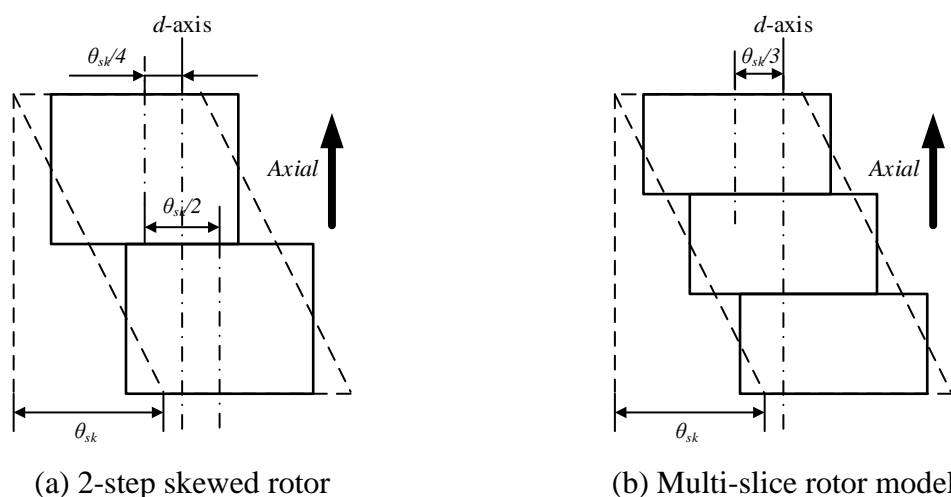


Fig. 5.24 Rotor axial arrangements of step skewed rotors.

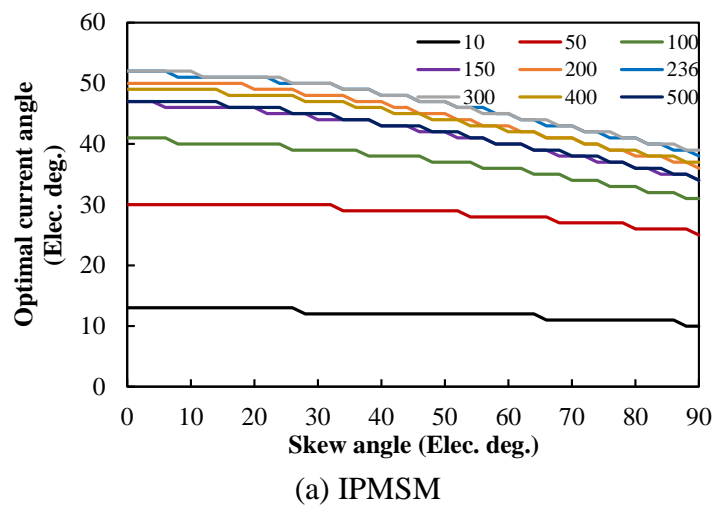
The instantaneous torque waveforms of PMSMs after rotor step skew can also be obtained by (5.1) and (5.2). However, since the torque performances of the un-skewed PMSMs are calculated every 1° in current angle in this chapter, when using the simplified approach to estimate the torque performance after rotor step skew, the skew angle should be an integer multiple of 2° in 2-step skew, or an integer multiple of 3° in 3-step skew, to make the shifting angle between rotor slices keep integer. Hence, in this section, the skew angle is varied from $0^\circ, 2^\circ, 4^\circ, \dots$ to 90° in 2-step skew, and from $0^\circ, 3^\circ, 6^\circ, \dots$ to 90° in 3-step skew. It also should be noticed that when using the simplified torque estimation approach to predict torque performance of PMSMs with rotor step skew, the axial flux leakages were not considered. In

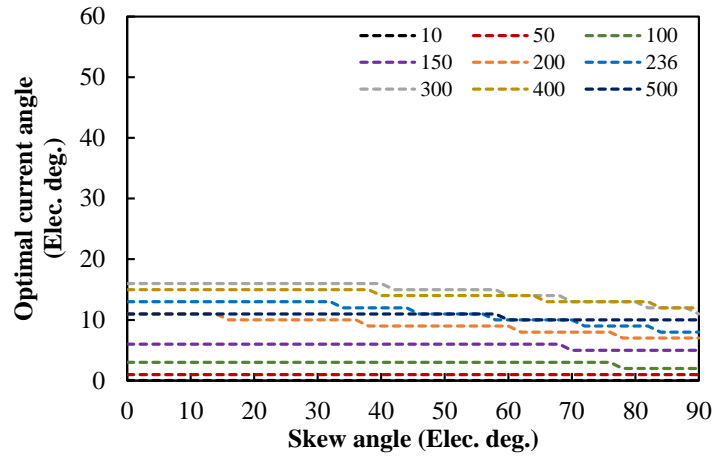
fact, due to the large amounts of flux leakages between adjacent rotor steps, the actual air-gap flux densities will be slower than predictions and the resultant output torque will also be reduced. To solve this problem, one solution is to add non-magnetic spacers between rotor steps [EAS97]. However, as this problem is out of the scope of this thesis, it will be not considered in Chapters 5 and 6.

5.5.2 Effects of Load in Interior and Surface PMSMs

5.5.2.1 Effects of Load on Optimal Current Angle

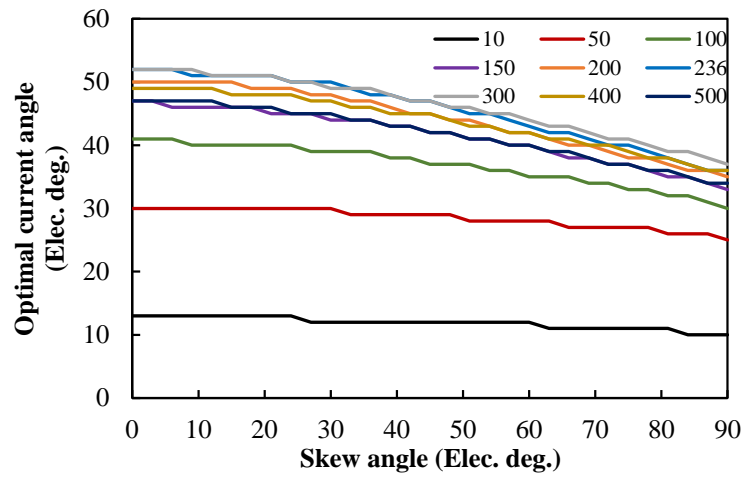
In the benchmark IPMSM and SPMSM, when the phase current amplitude is varied from 10A, 50A, 100A, 150A, 200A, 236A, 300A, 400A, to 500A, the average torque and torque ripple characteristics of PMSMs after rotor 2-step and 3-step skews are firstly calculated using the simplified approach, considering different skew angles and different current angles. Then, similar to the analyses in rotor continuous skew, under different load conditions, the optimal current angle for the maximum average torque can be selected according to skew angle in rotor step skew. The variations of optimal current angles with skew angle in IPMSM and SPMSM after rotor 2-step and 3-step skews under different phase current amplitude conditions are presented in Fig. 5.25 and Fig. 5.26.



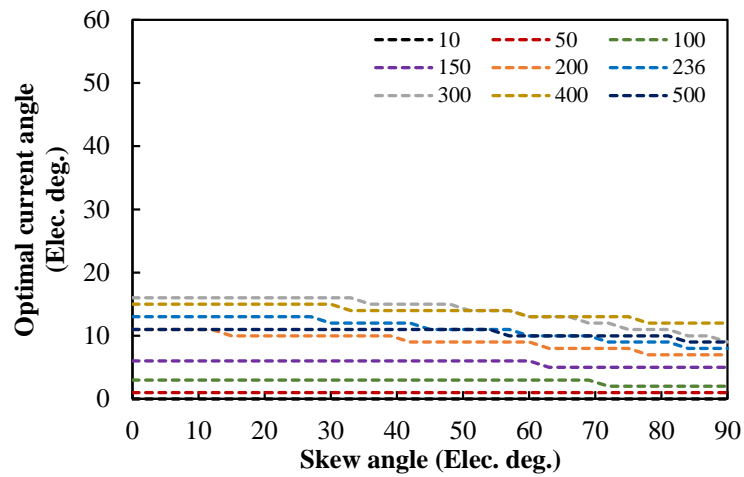


(b) SPMSM

Fig. 5.25 Variations of optimal current angles with skew angle in IPMSM and SPMSM after rotor 2-step skew under different phase current amplitude conditions.



(a) IPMSM



(b) SPMSM

Fig. 5.26 Variations of optimal current angles with skew angle in IPMSM and SPMSM after rotor 3-step skew under different phase current amplitude conditions.

Based on Fig. 5.18, Fig. 5.25, and Fig. 5.26, for any specific skew angle, the variations of the optimal current angles with phase current amplitude in rotor continuous, 2-step, and 3-step skews can be found and compared. For example, when the skew angle is 60° , the optimal current angles in different rotor skew methods are compared in Fig. 5.27. It can be found that under different load conditions, even for the same skew angle, the optimal current angles in rotor continuous, 2-step, and 3-step skews are still not identical. However, it also should be noticed that the differences between the optimal current angles in different rotor skew methods are very small, especially between those in rotor continuous and 3-step skews. In other words, the influences of load on optimal current angle in rotor step skew are close to those in rotor continuous skew.

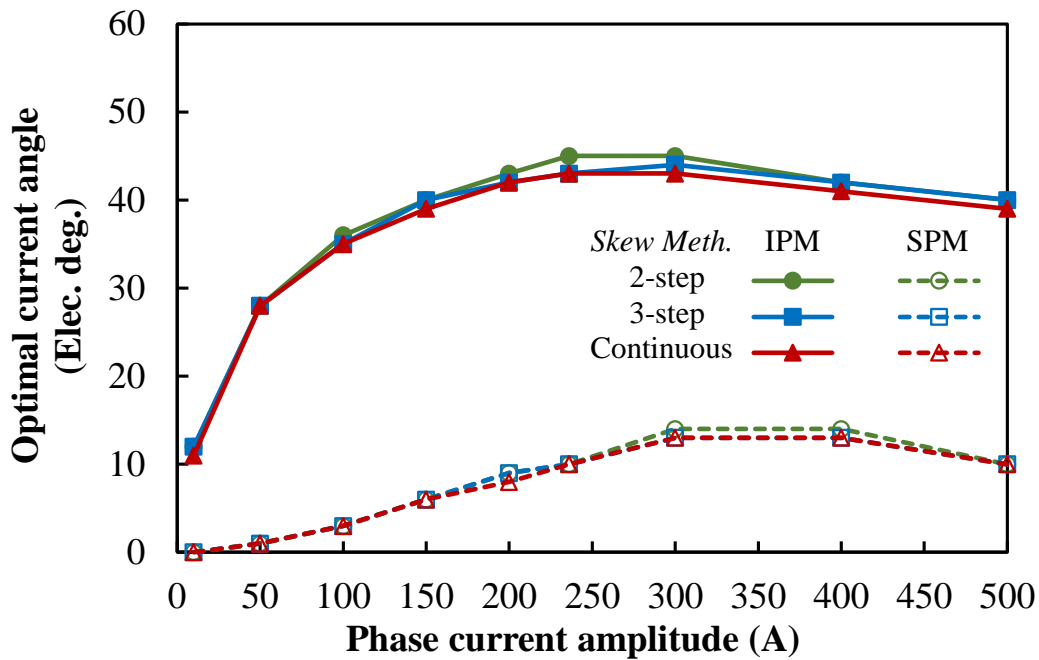


Fig. 5.27 Variations of optimal current angle with phase current amplitude in IPMSM and SPMSM using rotor continuous, 2-step, and 3-step skews ($\theta_{sk} = 60^\circ$).

5.5.2.2 Effects of Load on Optimal Skew Angle

Similar to the analyses in rotor continuous skew, as shown in 5.4.2.2, under different load conditions, the optimal skew angle for the maximum torque ripple can be obtained from the variations of torque ripples with skew angle under these load conditions. In rotor 2-step and 3-step skews, with the optimal current angles given in Fig. 5.25 and Fig. 5.26, the torque ripple versus skew angle characteristics of IPMSM and SPMSM under different phase current amplitude conditions are calculated, as summarized in Fig. 5.28 and Fig. 5.29.

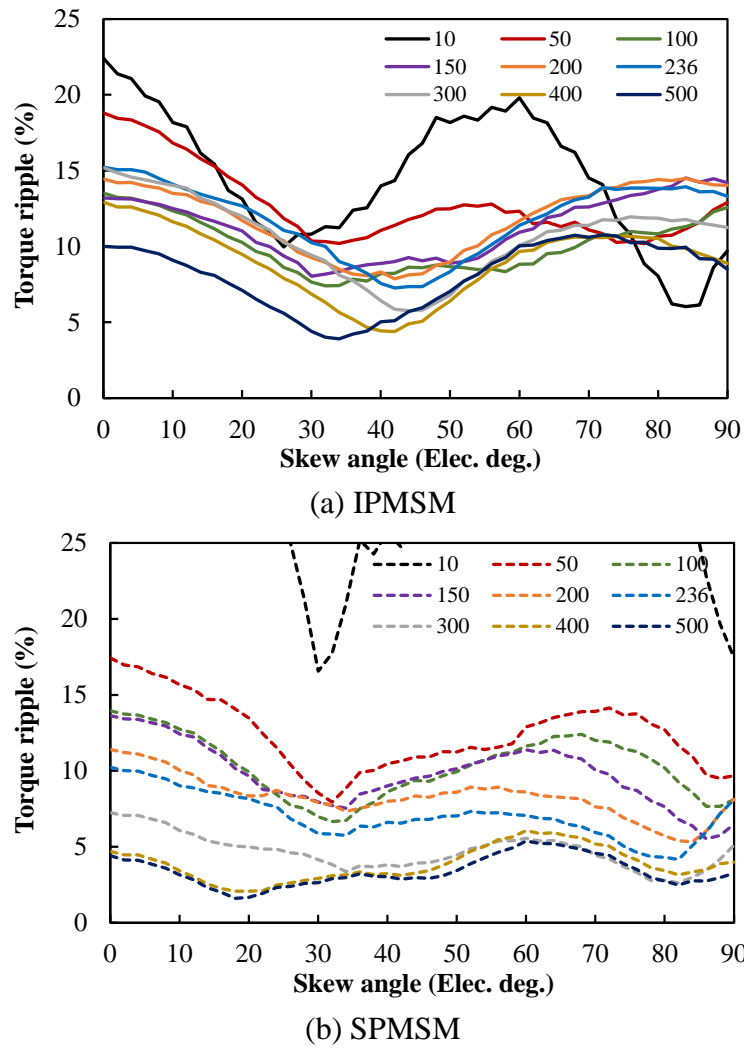
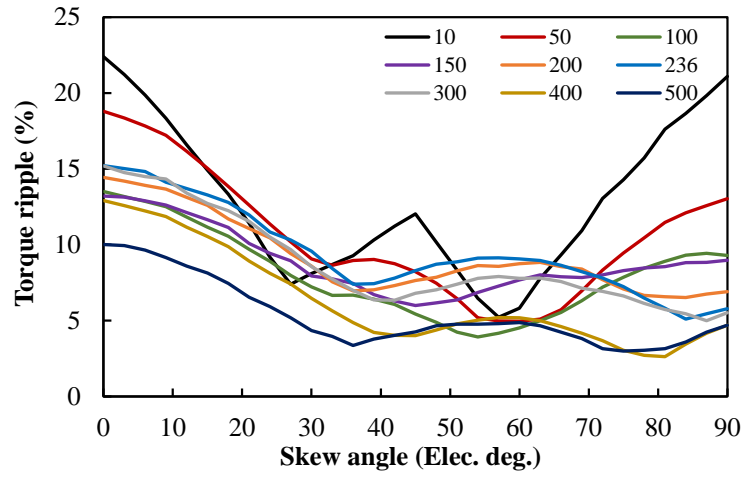
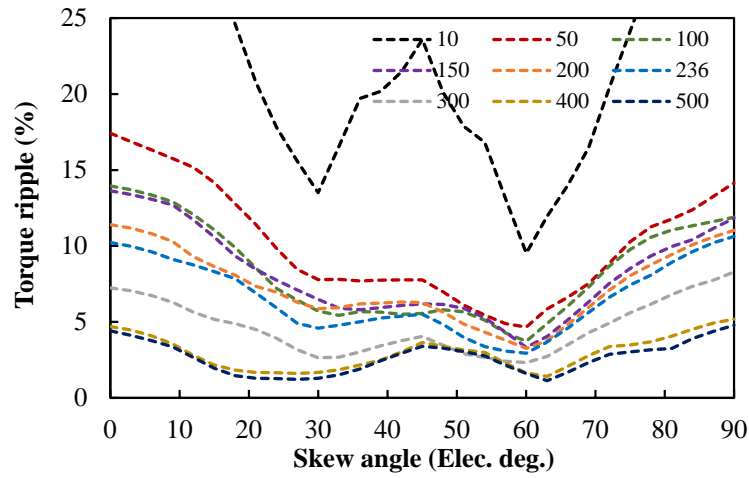


Fig. 5.28 Variations of torque ripple with skew angle in IPMSM and SPMSM after rotor 2-step skew and using optimal current angles under different phase current amplitude conditions.



(a) IPMSM



(b) SPMSM

Fig. 5.29 Variations of torque ripple with skew angle in IPMSM and SPMSM after rotor 3-step skew and using optimal current angles under different phase current amplitude conditions.

From Fig. 5.28 and Fig. 5.29, in rotor 2-step and 3-step skews, the optimal skew angles for different phase current amplitudes can be obtained, as summarized in Table 5.6. Similar to Table 5.5, for any optimal skew angle, the corresponding optimal current angle, average torque and torque ripple characteristics after rotor skew are also presented in Table 5.6.

Table 5.6 Optimal skew angles for minimum torque ripple in IPMSM and SPMSM when using different rotor skew methods under different load conditions

| Machine type | Phase current amplitude (A) | Skew method | Optimal skew angle (°) | Optimal current angle (°) | Average torque (Nm) | Torque ripple (%) |
|--------------|-----------------------------|-------------|------------------------|---------------------------|---------------------|-------------------|
| IPMSM | 10 | 2-step | 26 | 13 | 8.21 | 9.96 |
| | | 3-step | 57 | 12 | 7.92 | 5.22 |
| | | Cont. | 60 | 11 | 7.84 | 2.26 |
| | 50 | 2-step | 34 | 29 | 52.98 | 10.19 |
| | | 3-step | 60 | 28 | 49.98 | 4.96 |
| | | Cont. | 55 | 28 | 49.51 | 3.45 |
| | 100 | 2-step | 32 | 39 | 114.17 | 7.39 |
| | | 3-step | 54 | 36 | 108.27 | 3.91 |
| | | Cont. | 53 | 36 | 105.30 | 3.93 |
| | 150 | 2-step | 30 | 44 | 166.41 | 8.03 |
| | | 3-step | 45 | 42 | 160.59 | 6.00 |
| | | Cont. | 44 | 42 | 152.36 | 5.67 |
| | 200 | 2-step | 42 | 46 | 203.97 | 7.86 |
| | | 3-step | 36 | 47 | 204.83 | 6.96 |
| | | Cont. | 37 | 46 | 190.20 | 6.64 |
| | 236 | 2-step | 42 | 48 | 226.84 | 7.27 |
| | | 3-step | 36 | 48 | 227.92 | 7.40 |
| | | Cont. | 39 | 47 | 211.99 | 7.25 |
| | 300 | 2-step | 44 | 48 | 255.14 | 5.76 |
| | | 3-step | 42 | 47 | 254.10 | 6.35 |
| | | Cont. | 42 | 47 | 240.41 | 6.21 |
| | 400 | 2-step | 42 | 45 | 286.41 | 4.39 |
| | | 3-step | 45 | 45 | 282.49 | 4.01 |
| | | Cont. | 47 | 44 | 269.25 | 3.62 |
| | 500 | 2-step | 34 | 44 | 314.61 | 3.90 |
| | | 3-step | 36 | 44 | 311.86 | 3.35 |
| | | Cont. | 36 | 44 | 291.53 | 3.07 |
| SPMSM | 10 | 2-step | 30 | 0 | 12.26 | 16.57 |
| | | 3-step | 60 | 0 | 11.86 | 9.52 |
| | | Cont. | 60 | 0 | 11.80 | 0.38 |
| | 50 | 2-step | 32 | 1 | 60.71 | 7.95 |
| | | 3-step | 60 | 1 | 58.82 | 4.66 |
| | | Cont. | 60 | 1 | 58.61 | 0.86 |
| | 100 | 2-step | 32 | 3 | 118.67 | 6.65 |
| | | 3-step | 60 | 3 | 114.75 | 3.72 |
| | | Cont. | 60 | 3 | 114.14 | 1.68 |

| | | | | | |
|-----|--------|----|----|--------|------|
| 150 | 2-step | 34 | 6 | 170.66 | 7.54 |
| | 3-step | 60 | 6 | 164.96 | 3.33 |
| | Cont. | 60 | 6 | 164.02 | 1.50 |
| 200 | 2-step | 34 | 10 | 214.99 | 7.32 |
| | 3-step | 60 | 9 | 207.59 | 3.26 |
| | Cont. | 60 | 8 | 206.43 | 1.55 |
| 236 | 2-step | 34 | 12 | 241.38 | 5.75 |
| | 3-step | 60 | 10 | 233.29 | 2.94 |
| | Cont. | 55 | 11 | 233.90 | 1.38 |
| 300 | 2-step | 34 | 16 | 276.55 | 3.36 |
| | 3-step | 60 | 13 | 268.89 | 2.33 |
| | Cont. | 53 | 14 | 270.06 | 1.11 |
| 400 | 2-step | 18 | 15 | 311.86 | 2.07 |
| | 3-step | 27 | 15 | 310.59 | 1.60 |
| | Cont. | 28 | 15 | 310.15 | 1.26 |
| 500 | 2-step | 18 | 11 | 335.22 | 1.60 |
| | 3-step | 27 | 11 | 333.86 | 1.21 |
| | Cont. | 26 | 11 | 333.76 | 0.91 |

Based on Table 5.6, in IPMSM and SPMSM, the effects of phase current amplitude on optimal skew angle in rotor 2-step, 3-step and continuous skews are compared in Fig. 5.30. It can be concluded that in all rotor skew methods, the optimal skew angle can be affected significantly by load. It also should be noticed that the optimal skew angles in rotor continuous and 3-step skews are close to each other, but the optimal skew angle in rotor 2-step skew is different from those in rotor continuous and 3-step skews.

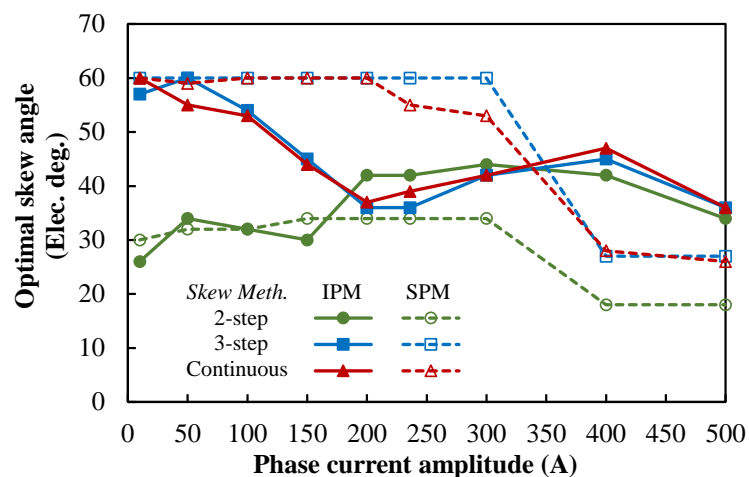


Fig. 5.30 Variations of optimal skew angle with phase current amplitude in IPMSM and SPMSM when using rotor continuous, 2-step, and 3-step skew methods.

5.5.2.3 Effects of Load on Torque Characteristics with Optimal Skew Angles

Similar to Fig. 5.30, based on Table 5.6, the variations of average torque and torque ripple characteristics of IPMSM and SPMSM with phase current amplitude when using rotor 2-step, 3-step, and continuous skews are compared in Fig. 5.31.

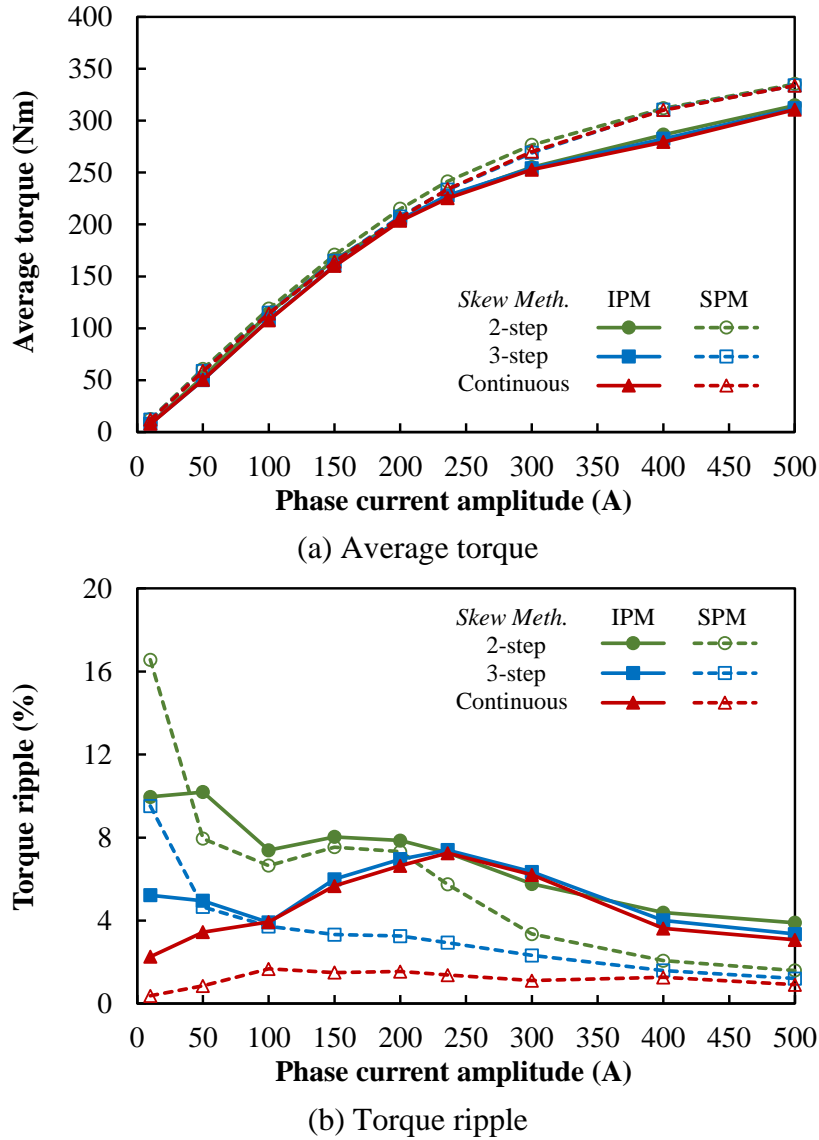
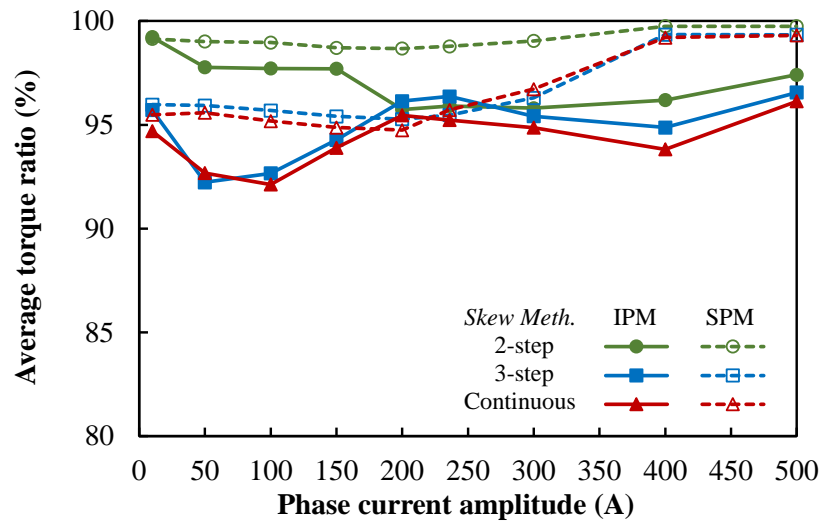


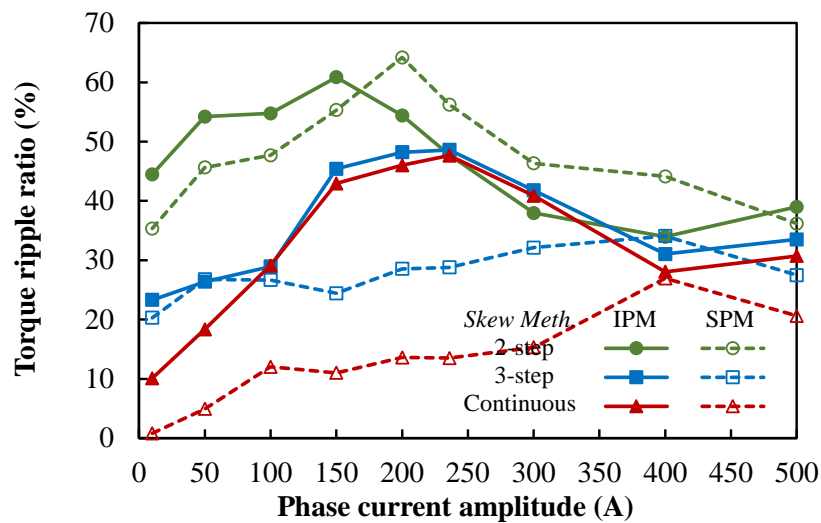
Fig. 5.31 Variations of average torque and torque ripple with phase current amplitude in IPMSM and SPMSM with rotor continuous, 2-step, and 3-step skew methods

The ratios of resultant average torque and torque ripple after rotor skew to those before rotor skew are also presented in Fig. 5.32 for clarity. From Fig. 5.32, it can be clearly seen that rotor 2-step skew can produce higher average torque, albeit with higher torque ripple, than rotor 3-step and continuous skews. It also should be noticed that in SPMSM, rotor continuous skew can achieve much lower torque ripple than rotor 3-step skew, but in IPMSM, rotor 3-step skew

shows similar effectiveness with rotor continuous skew in both average torque and torque ripple. In other words, in IPMSM, rotor 3-step skew can result in similar torque ripple reduction with rotor continuous skew, it is not necessary to improve the effectiveness of rotor skew by adding step number.



(a) Average torque ratio



(b) Torque ripple ratio

Fig. 5.32 Variations of average torque and torque ripple ratios with phase current amplitude in IPMSM and SPMSM with rotor continuous, 2-step, and 3-step skew methods.

5.6 Experimental Validation

In this chapter, all research findings are obtained based on the results obtained by 2D FE method. Although 2D FE predicted results are considered fairly reliable today, it is still necessary to experimentally validate at least one model in this chapter to avoid any error in

modelling and FE analysis. Hence, the FE predicted electromagnetic performances of the benchmark IPM machine (Toyota Prius 2010 machine) without rotor skew are compared with the measured results under open-circuit and on-load conditions to verify the correctness of the FE analyses used in this chapter. The photos of the benchmark IPM machine and the test rig are provided in Fig. 5.33.

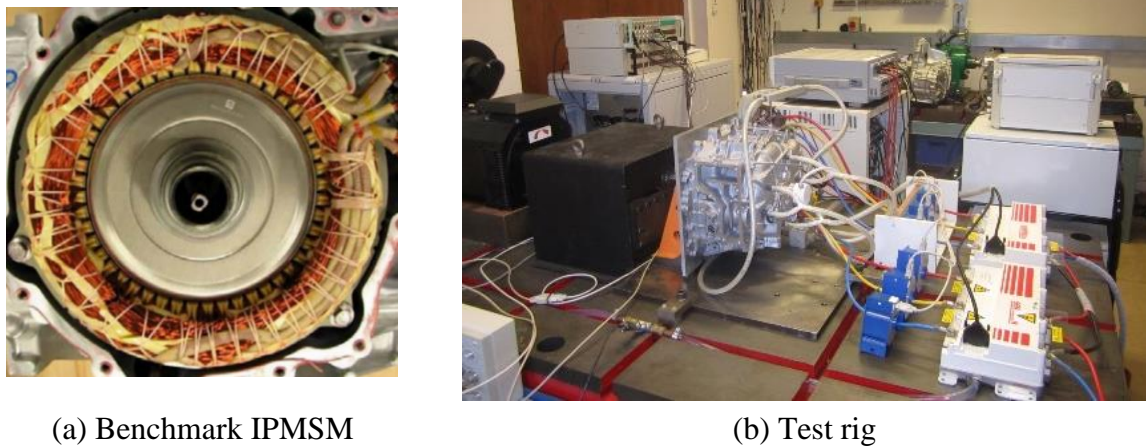


Fig. 5.33 Photos of benchmark IPMSM and test rig.

Under open-circuit condition, the predicted and measured phase back EMF (RMS values) of the benchmark IPMSM are compared in Fig. 5.34. It can be seen that the results obtained by 2D FE method directly are slightly higher than measured results, since the end-winding effects and the flux leakages cannot be considered in 2D FE analyses.

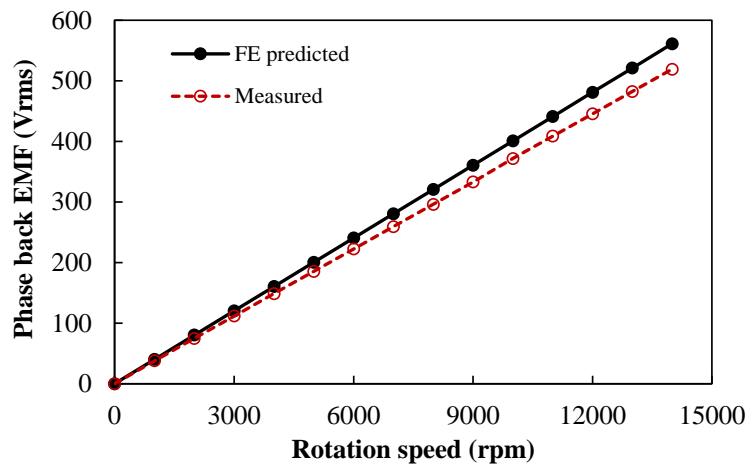
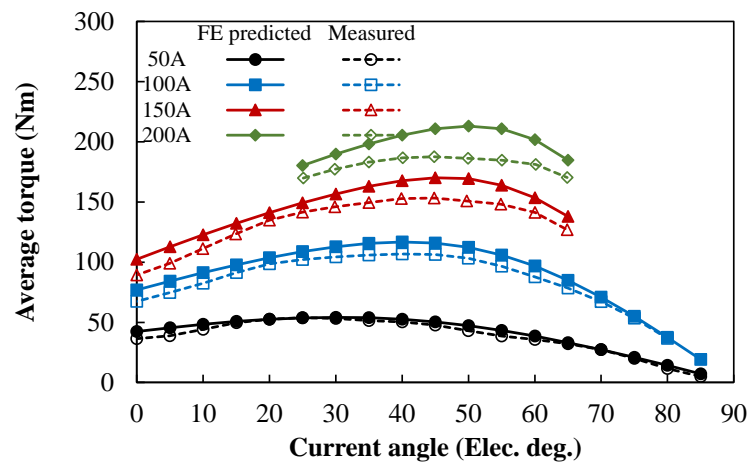
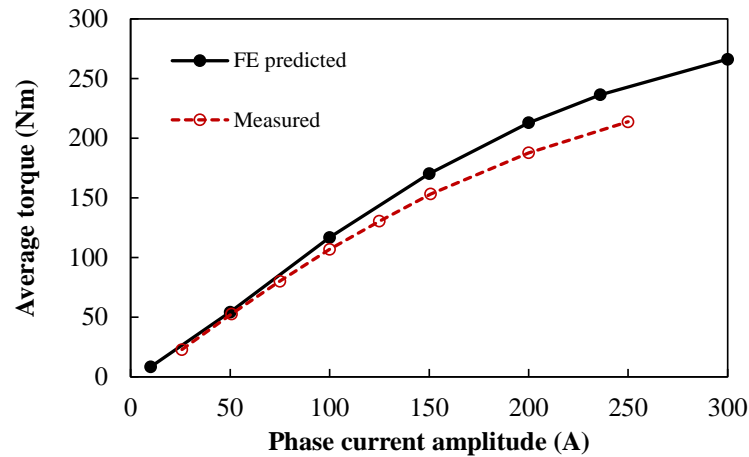


Fig. 5.34 Comparison of FE predicted and measured phase back EMFs in benchmark IPMSM under open-circuit condition.

Under on-load conditions, the FE predicted and measured average torque versus current angle characteristics and the average torque versus phase current amplitude characteristics of the benchmark IPMSM are compared in Fig. 5.35. It can be seen that the measured results agree well with FE predicted results, especially when phase current amplitude $\leq 100\text{A}$. When phase current amplitude $\geq 150\text{A}$, the measured average torque is slightly lower than FE predicted result, which suggests that the actual magnetic saturation in the benchmark IPMSM could be even more severe than FE predictions.



(a) Average torque-current angle characteristics



(b) Average torque-phase current amplitude characteristics

Fig. 5.35 Comparison of FE predicted and measured on-load torque characteristics in benchmark IPMSM.

Consequently, considering the agreement between FE predicted and measured characteristics in the benchmark IPMSM, the reliability of the analysis results presented in this chapter can be confirmed by the experiments.

5.7 Conclusion

In this chapter, the influences of load on the effectiveness of rotor continuous and step skews are investigated in 48-slot/8-pole IPMSM and SPMSM. A simplified approach to estimate torque performance of PMSMs after rotor skew was introduced based on the conventional multi-slice rotor model, and then the optimal current angle and optimal skew angle under different load conditions can be obtained and compared by using the simplified approach. It is found that the effectiveness of rotor skew depends on electric loading and magnetic saturation, and thus, in general it is less effective in IPMSM than in SPMSM. It is also found that the conventional skew angle, i.e., one on-load torque ripple periodicity, only works well in SPMSM under light-load conditions. For SPMSM under very heavy-load conditions, when the magnetic saturation becomes very severe due to high electric loading, or IPMSM under all load conditions, an optimal skew angle can be found, which can result in higher average torque and lower torque ripple simultaneously than the conventional skew angle.

CHAPTER 6

INFLUENCE OF LOAD ON EFFECTIVENESS OF ROTOR SKEW IN DTP IPMSMs AND SPMSMs

In chapter 5, the effectiveness of rotor skew in interior and surface STP PMSMs has been investigated. In this chapter, the effectiveness of rotor skew in interior and surface DTP PMSMs will be investigated and compared with that in STP PMSMs. The influences of load on the optimal skew angle for the minimum on-load torque ripple in STP and DTP PMSMs are also investigated and compared. Both rotor continuous skew and step skew are considered in the analyses. It is found that similar to STP PMSMs, the effectiveness of rotor skew on torque ripple reduction also depends on electric loading and magnetic saturation in DTP PMSMs, and thus, in general it is less effective in IPMSM than in SPMSM. As the on-load torque harmonic contents in STP and DTP PMSMs are different (the 6th torque harmonics which exist in STP PMSMs are eliminated in DTP PMSMs), the conventional skew angles, i.e., one on-load torque ripple periodicity, in STP and DTP PMSMs are also different, being 60° in STP PMSMs and 30° in DTP PMSMs. As the optimal skew angles for the minimum on-load torque ripple can be obtained under different load conditions in DTP PMSMs, it can be further found that the optimal skew angles in DTP SPMSM are close to the conventional skew angle. However, the optimal skew angles in DTP IPMSM are quite different from the conventional skew angle, but close to those in STP IPMSM.

6.1 Introduction

In recent years, PMSMs have been widely researched due to their advantages of high power/torque density, high efficiency, and have been utilized in many industrial and domestic applications [HEN94] [ZHU07] [PYR08]. Since torque ripples can affect speed smoothness directly, the reduction of torque ripples is especially important for some high-performance applications and many studies have been carried out to minimize torque ripples in PMSMs, particularly under on-load conditions [JAH96] [ZHU00] [BIA02].

In general, the techniques to reduce torque ripples can be generally classified into two categories [JAH96]: machine design method and control method. These techniques have been

reviewed in detail in Section 1.3. It can be concluded that among all the techniques for reducing torque ripples, choosing suitable machine topology to reduce inherent torque harmonic contents is the most important one, and rotor skew is the most popular one. As DTP winding configuration can eliminate some torque harmonics in conventional STP PMSMs [BAR10] [ABD15] [XU18], it can be expected that the combination of DTP winding configuration and rotor skew can result in significant torque ripple reduction. However, it should be noticed that rotor skew has never been analysed comprehensively in DTP PMSMs, and hence, the effectiveness of rotor skew in DTP PMSMs under different load conditions will be the focus of this chapter.

In this chapter, the torque characteristics of DTP IPMSM and SPMSM after rotor skew are calculated using the simplified approach introduced in Section 5.3. The optimal current angles and optimal skew angles under different load conditions are obtained from the calculations. With the optimal current and skew angles, the resultant torque characteristics after rotor skew are compared under different load conditions. Both rotor continuous skew and step skew are considered. The effectiveness of rotor skew in DTP PMSMs is compared with that in STP PMSMs as well in this chapter.

This chapter is organized as follows. In Section 6.2, the machine configurations of the benchmark DTP IPMSM and SPMSM are introduced. In Section 6.3, the torque characteristics of DTP IPMSM and SPMSM without rotor skew are shown and compared with those of STP IPMSM and SPMSM. Then, the influences of load on optimal current angle, optimal skew angle, and the resultant torque characteristics in rotor continuous skew in DTP IPMSM and SPMSM are investigated and compared with those in STP IPMSM and SPMSM in Section 6.4. The influences of load on optimal current angle, optimal skew angle, and the resultant torque characteristics in rotor step skew in DTP IPMSM and SPMSM are provided in Section 6.5. The experimental validation is introduced in Section 6.6. Section 6.7 is the conclusion.

6.2 Machine Configurations

In this chapter, the effectiveness of rotor skew in DTP PMSMs is analysed. The Toyota Prius 2010 machine is chosen as the benchmark IPMSM and the SPMSM designed in Section 5.2 is chosen as the benchmark SPMSM. Thus, the results obtained in DTP PMSMs can be compared fairly with those in STP PMSMs. It also should be mentioned that as introduced in Section 5.2,

since the DTP-DS winding configuration has better efficiency and better fault-tolerant capability than the DTP-SF counterpart, the DTP-DS winding configuration is chosen as the winding configurations of the benchmark DTP PMSMs. The key geometric parameters are given in Table 5.1, and the cross-sections of the benchmark DTP IPMSM and SPMSM are shown in Fig. 6.1, respectively.

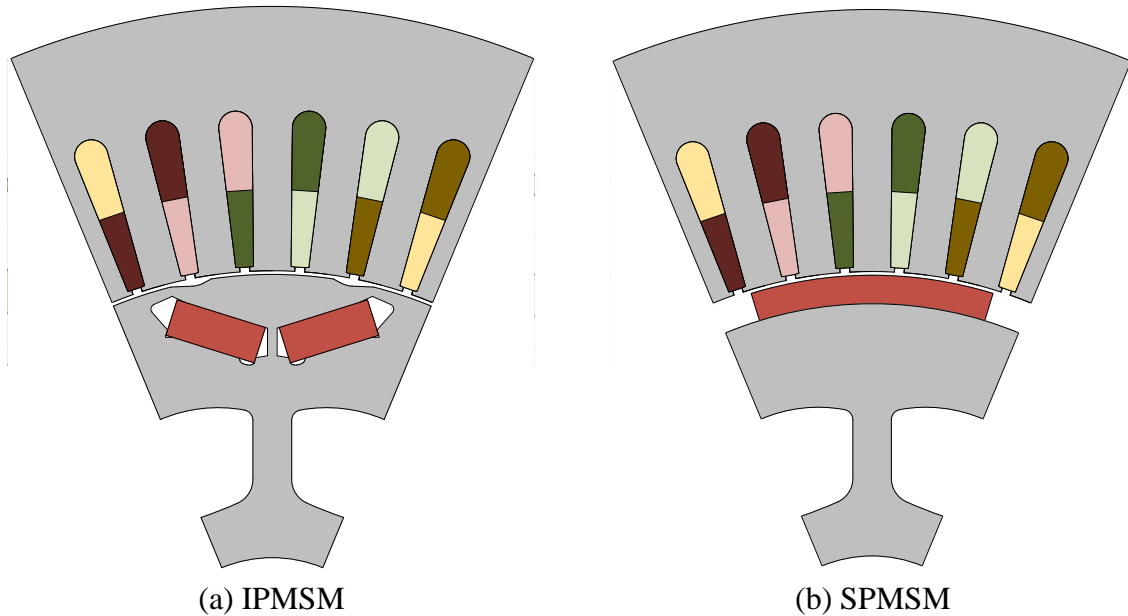
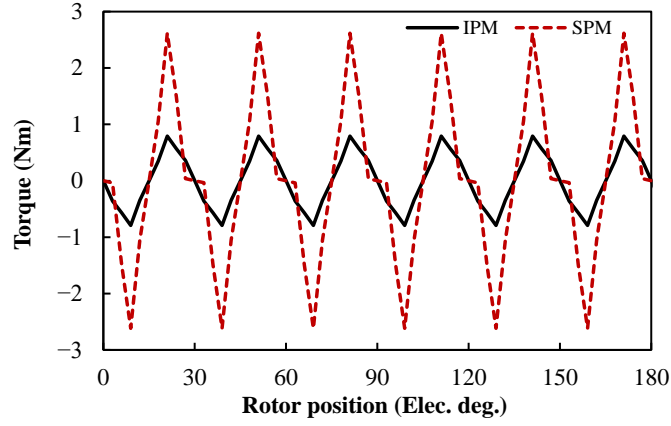


Fig. 6.1 Cross-sections of benchmark DTP IPMSM and SPMSM.

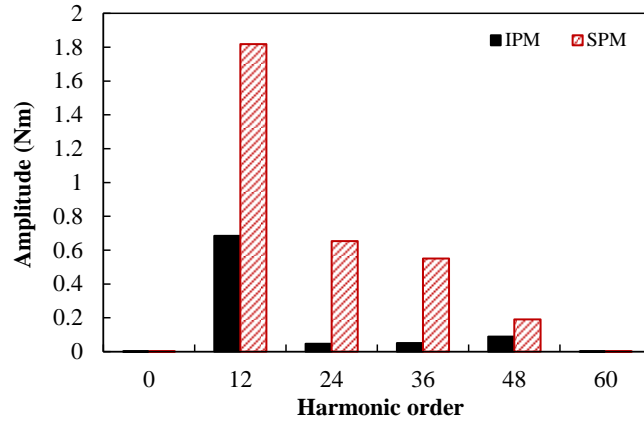
6.3 Torque Characteristics without Rotor Skew

In this section, the torque characteristics of DTP IPMSM and SPMSM before rotor skew are firstly calculated based on 2D FE method under different load conditions. As introduced in Section 3.3, the torque characteristics after rotor skew can be obtained from the torque characteristics before rotor skew. In addition, considering that the torque characteristics of STP IPMSM and SPMSM have been calculated and presented in Section 3.3, the torque characteristics of STP and DTP PMSMs are also compared in this section.

Since winding configuration cannot affect the open-circuit torque (cogging torque) of STP and DTP PMSMs, the open-circuit torque in DTP IPMSM and SPMSM are identical with those in STP IPMSM and SPMSM, as shown in shown in Fig. 6.2. Since the SPMSM is designed to without the consideration of cogging torque, SPMSM has much higher cogging torque amplitudes. To be more specific, the harmonic orders of IPMSM and SPMSM are identical, but the amplitudes of different torque harmonic orders are different.



(a) Waveforms

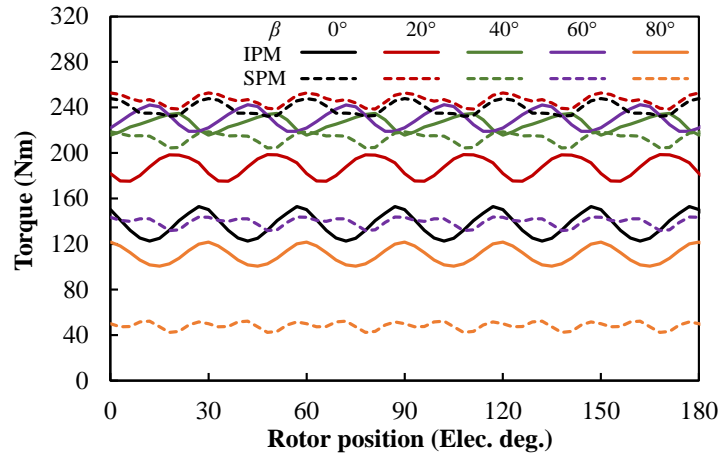


(b) Spectra

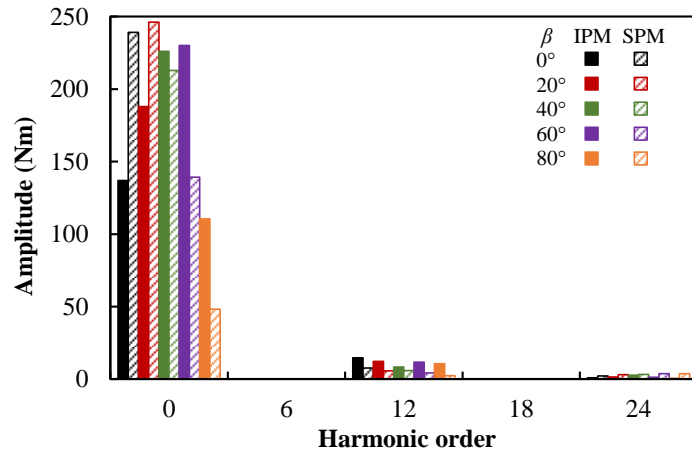
Fig. 6.2 Cogging torque characteristics of IPMSM and SPMSM under open-circuit condition.

In the analyses of torque characteristics in STP IPMSM and SPMSM, nine on-load conditions (phase current amplitude, $I_a = 10, 50, 100, 150, 200, 236, 300, 400, 500\text{A}$) are selected to cover the full load conditions, from light-load, heavy-load, full-load, to over-load. Similar to the analyses in STP PMSMs, considering that the winding configurations of STP and DTP PMSMs are different, the phase current amplitudes of DTP PMSMs are halved from those in STP PMSMs. Hence, the phase current amplitudes of the nine on-load conditions are selected as $I_{a1} = 5, 25, 50, 75, 100, 118, 150, 200, 250\text{A}$.

To illustrate the effects of current angle (current advancing angle) on torque characteristics in DTP IPMSM and SPMSM, the instantaneous torque waveforms of the benchmark DTP IPMSM and SPMSM with fixed phase current amplitude ($I_{a1} = 118\text{A}$) and varied current angles ($\beta = 0^\circ, 20^\circ, 40^\circ, 60^\circ, \text{ and } 80^\circ$) are shown in Fig. 6.3Fig. 5.3. It can be seen that the 6th torque harmonics are completely eliminated by the DTP windings, and the dominant torque harmonics in DTP IPMSM and SPMSM are the 12th torque harmonics.



(a) Waveforms



(b) Spectra

Fig. 6.3 Instantaneous torque characteristics of IPMSM and SPMSM with different current angles ($I_{a1} = 118\text{A}$).

Based on Fig. 6.3, for the fixed phase current amplitude, $I_{a1} = 118\text{A}$, the variations of average torque with current angle in DTP IPMSM and SPMSM are shown in Fig. 6.4.

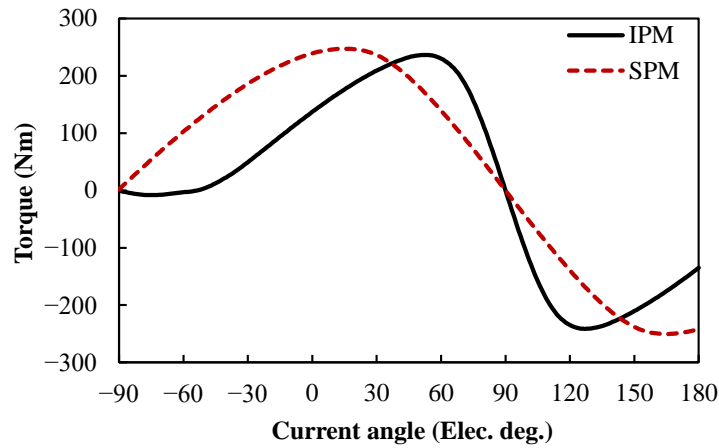


Fig. 6.4 Variations of average torque with current angle in IPMSM and SPMSM ($I_{a1} = 118\text{A}$).

It should be mentioned that β is varied from -90° to 180° and the interval is 1° in Fig. 6.4 to provide more information for the following analyses of rotor skew with different current and skew angles.

For other load conditions, the variations of average torque with current angle (β is varied from 0° to 90°) in DTP IPMSM and SPMSM are shown in Fig. 6.5 (a) and (b), respectively. From Fig. 6.5, the optimal current angle for the maximum average torque under different load conditions can be summarized in Table 6.1. It should be noticed that the optimal current angles in STP IPMSM and SPMSM are also provided in Table 6.1 for comparison. It can be seen that although the average torque-current angle characteristics of STP and DTP PMSMs are almost the same, their optimal current angles are not identical.

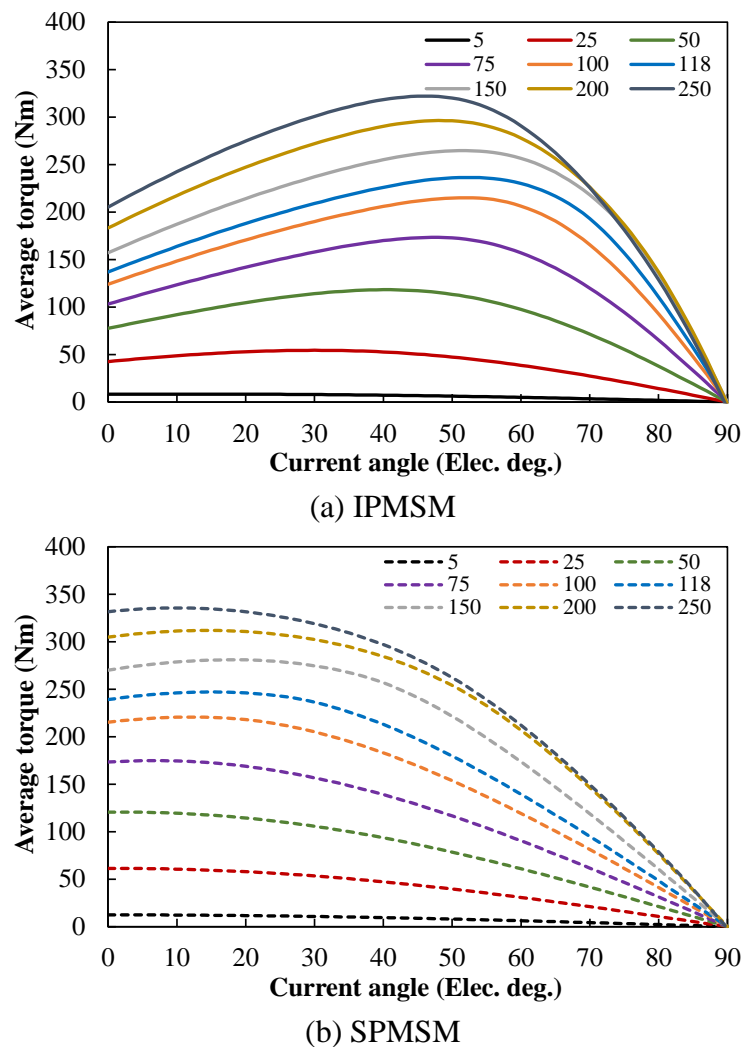


Fig. 6.5 Variations of average torque with current angle in DTP IPMSM and SPMSM under different phase current amplitude conditions.

Table 6.1 Optimal current angles for maximum average torque with different phase current amplitudes in STP and DTP PMSMs (Elec. deg.)

| Phase current amplitude (A) | IPMSM | | SPMSM | |
|-----------------------------|-------|-----|-------|-----|
| | STP | DTP | STP | DTP |
| 5 | 13 | 13 | 0 | 0 |
| 25 | 30 | 30 | 1 | 1 |
| 50 | 41 | 40 | 3 | 2 |
| 75 | 47 | 47 | 6 | 7 |
| 100 | 50 | 52 | 11 | 12 |
| 118 | 52 | 53 | 13 | 15 |
| 150 | 52 | 51 | 16 | 18 |
| 200 | 49 | 48 | 15 | 14 |
| 250 | 47 | 46 | 11 | 10 |

Based on Table 6.1, the influences of load on optimal current angle in DTP IPMSM and SPMSM are shown as the optimal current angle-phase current amplitude characteristics in Fig. 6.6, and compared with those in STP IPMSM and SPMSM in Fig. 6.7. It should be noticed that in Fig. 6.7 and the following figures, which include both STP and DTP PMSMs, the horizontal axis only denotes the phase current amplitude in DTP PMSMs. Due to the halved winding turn number in STP PMSMs compared with that in DTP counterpart, for the same load condition, the actual phase currents in STP PMSMs should be doubled from those in DTP PMSMs, e.g., 118A in DTP PMSMs, and 236A in STP PMSMs. As mentioned above, even under the same load condition, the optimal current angles in STP and DTP PMSMs are not exactly the same.

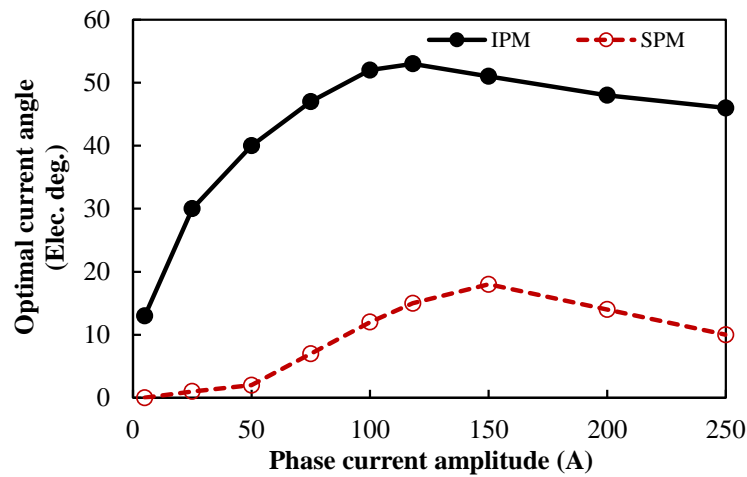


Fig. 6.6 Variations of optimal current angle with phase current amplitude in DTP IPMSM and SPMSM.

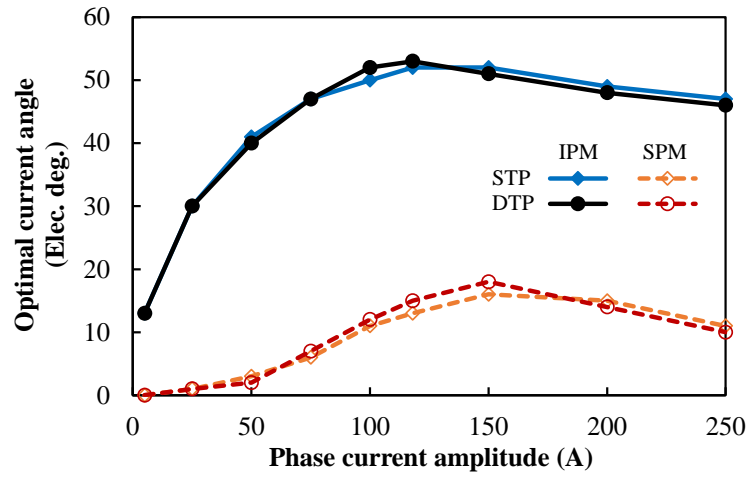


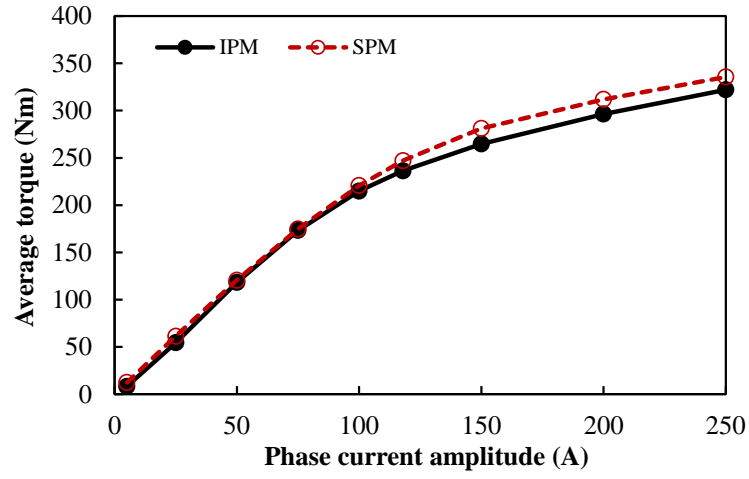
Fig. 6.7 Variations of optimal current angle with phase current amplitude in STP and DTP IPMSM and SPMSM.

With the optimal current angles given in Table 6.1, the average torque and torque ripple characteristics of STP and DTP PMSMs under different load conditions are summarized in Table 6.2.

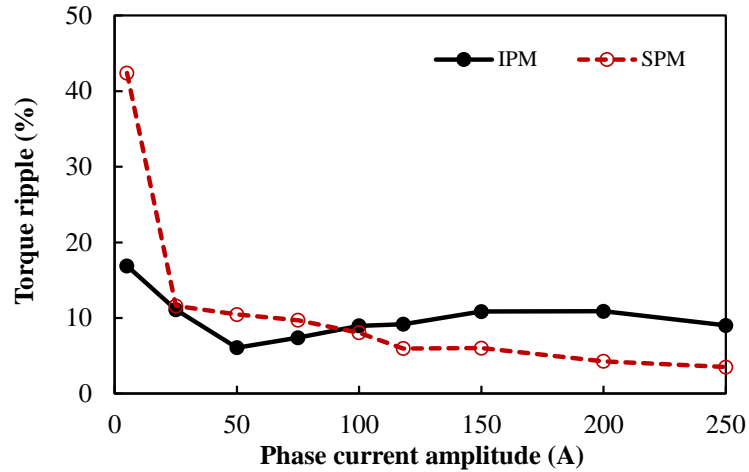
Table 6.2 Torque characteristics of STP and DTP PMSMs with different phase currents and optimal current angles

| Phase current amplitude (A) | Item | IPMSM | | SPMSM | |
|--------------------------------|---------------------|--------|--------|--------|--------|
| | | STP | DTP | STP | DTP |
| 5 | Average torque (Nm) | 8.28 | 8.28 | 12.36 | 12.36 |
| | Torque ripple (%) | 22.40 | 16.89 | 46.87 | 42.41 |
| 25 | Average torque (Nm) | 54.19 | 54.38 | 61.31 | 61.39 |
| | Torque ripple (%) | 18.80 | 11.11 | 17.42 | 11.60 |
| 50 | Average torque (Nm) | 116.84 | 118.17 | 119.92 | 120.58 |
| | Torque ripple (%) | 13.51 | 6.07 | 13.95 | 10.46 |
| 75 | Average torque (Nm) | 170.33 | 173.34 | 172.89 | 174.83 |
| | Torque ripple (%) | 13.20 | 7.39 | 13.64 | 9.71 |
| 100 | Average torque (Nm) | 213.05 | 214.99 | 217.88 | 220.70 |
| | Torque ripple (%) | 14.44 | 8.96 | 11.40 | 8.06 |
| 118 | Average torque (Nm) | 236.50 | 236.45 | 244.36 | 247.18 |
| | Torque ripple (%) | 15.22 | 9.18 | 10.22 | 5.97 |
| 150 | Average torque (Nm) | 266.31 | 264.75 | 279.22 | 281.06 |
| | Torque ripple (%) | 15.19 | 10.85 | 7.24 | 6.03 |
| 200 | Average torque (Nm) | 297.76 | 296.33 | 312.63 | 311.93 |
| | Torque ripple (%) | 12.92 | 10.89 | 4.69 | 4.28 |
| 250 | Average torque (Nm) | 322.97 | 322.09 | 336.06 | 335.64 |
| | Torque ripple (%) | 10.00 | 9.03 | 4.41 | 3.52 |

From Table 6.2, the influences of load on average torque and torque ripple characteristics in DTP IPMSM and SPMSM are shown as the average torque- and torque ripple-phase current amplitude characteristics in Fig. 6.8, and compared with those in STP IPMSM and SPMSM in Fig. 6.9. In this chapter, since DTP-DS winding configuration is chosen for comparison with the benchmark DTP PMSMs, instead of DTP-SF counterpart compared with STP IPMSM and SPMSM, the benchmark DTP IPMSM and SPMSM have very similar average torque and lower torque ripple performances, as introduced in Section 3. From Fig. 6.9 (b), it can be further observed that in both IPMSM and SPMSM, although DTP winding configuration can reduce on-load torque ripples in STP counterparts, but with the increase of electric loading ($I_{a1} > 300\text{A}$), the torque ripple characteristics of STP and DTP PMSMs become similar with each other.

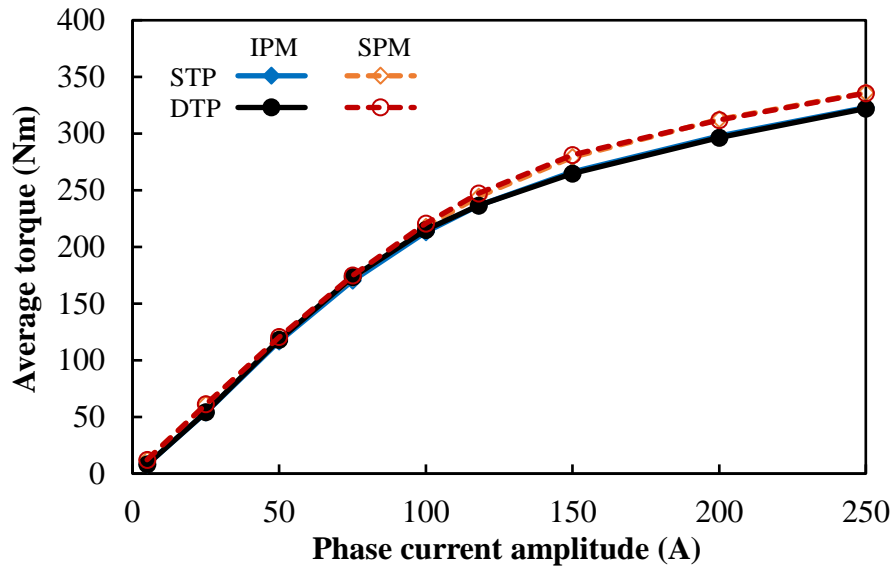


(a) Average torque

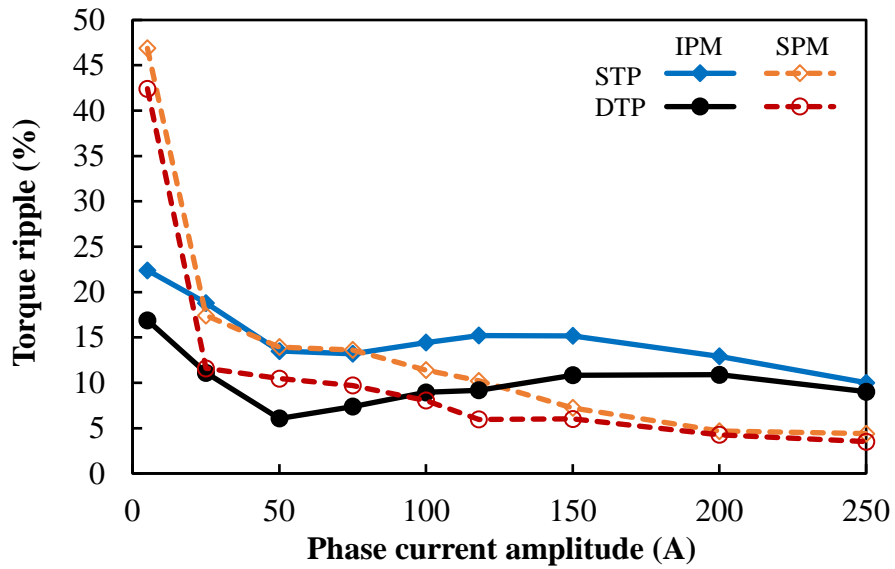


(b) Torque ripple

Fig. 6.8 Variations of average torque and torque ripple with phase current amplitude in DTP IPMSM and SPMSM when using optimal current angles.



(a) Average torque



(b) Torque ripple

Fig. 6.9 Variations of average torque and torque ripple with phase current amplitude in STP and DTP PMSMs when using optimal current angles.

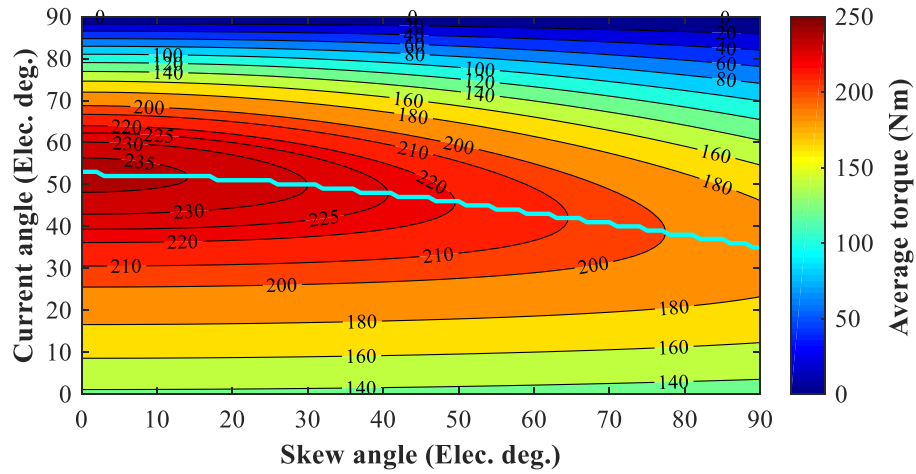
6.4 Influences of Load in PMSMs with Rotor Continuous Skew

In Section 5.3, a simplified approach to estimate the torque performance of PMSMs after rotor continuous skew is introduced in detail. The simplified approach is utilized in STP PMSMs in Section 5.4, but actually it is also applicable in DTP PMSMs. In this section, the instantaneous torque waveforms of DTP PMSMs with different current and skew angles are firstly calculated using the simplified approach, as explained in Section 5.3. Then, the optimal current angle and optimal skew angle under any specific load condition can be selected based on the calculation results. Thus, the effects of load on optimal current angle and optimal skew angle, average torque and torque ripple in DTP PMSMs can be obtained and compared with those in STP PMSMs.

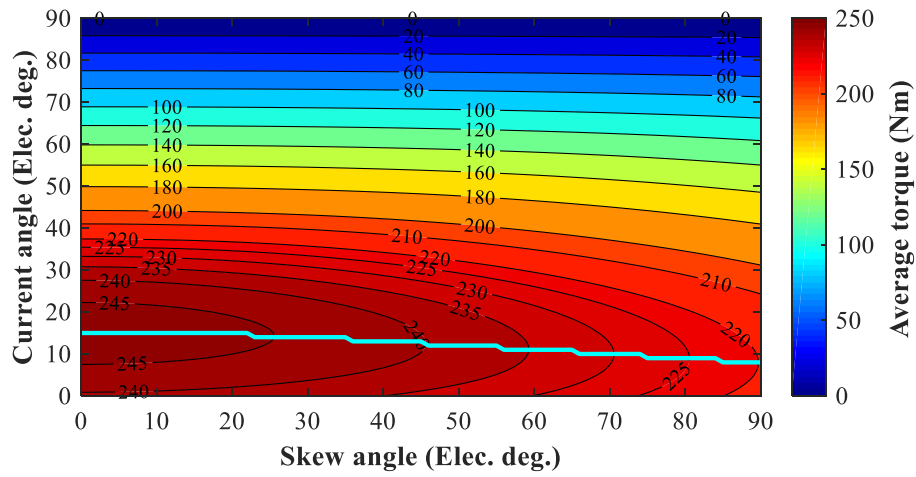
6.4.1 Selection of Optimal Current Angle and Optimal Skew Angle for Specific Load Condition

Similar to the analyses of STP PMSMs, in this chapter, the optimal current angle is selected for the maximum average torque and the optimal skew angle is selected for the minimum torque ripple. To achieve the optimal current angle and optimal skew angle, the instantaneous torque waveforms of DTP PMSMs after rotor continuous skew with different current and skew angles are calculated using the simplified approach introduced in Section 5.3.

When the phase current amplitude is fixed at 118A, the variations of average torque of DTP IPMSM and SPMSM with different current and skew angles are shown in Fig. 6.10 (a) and (b), respectively. From Fig. 6.10, for any skew angle, the optimal current angle for the maximum average torque can be obtained. Thus, in DTP IPMSM and SPMSM, under the condition of $I_{a1} = 118\text{A}$, the optimal current angle-skew angle characteristics are marked as polylines in Fig. 6.10 and compared in Fig. 6.11. It can be seen the optimal current angles in DTP IPMSM and SPMSM both become smaller with the increase of skew angle.



(a) IPMSM



(b) SPMSM

Fig. 6.10 Variations of average torque with skew angle and current angle in DTP IPMSM and SPMSM after rotor continuous skew ($I_{a1} = 118A$).

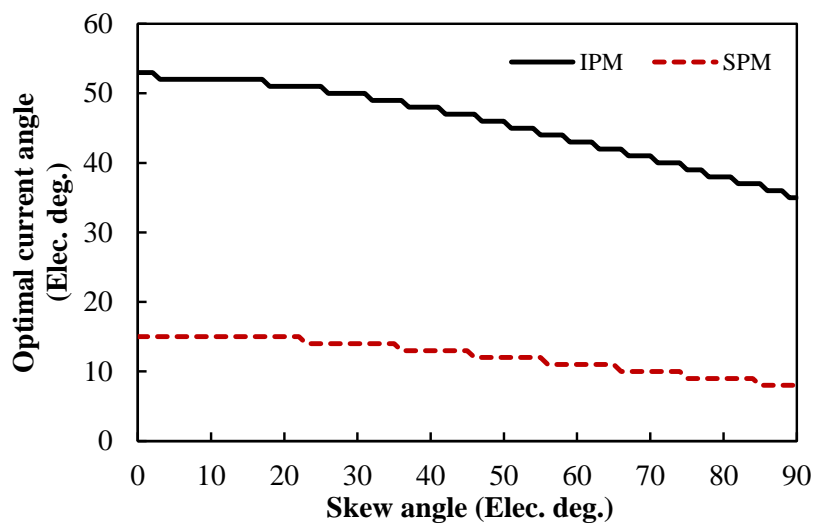


Fig. 6.11 Variations of optimal current angle with skew angle in DTP IPMSM and SPMSM after rotor continuous skew ($I_{a1} = 118A$).

For the same load condition in STP PMSMs, when the phase current amplitude is 236A, the variation of optimal current angle with skew angle under this condition was calculated in Section 5.4.1. Thus, the optimal current angle-skew angle characteristics of STP and DTP PMSMs can be compared in Fig. 6.12. It can be seen that although the optimal current angles in STP and DTP PMSMs are not exactly the same, the variations of optimal current angle with skew angle in STP and DTP PMSMs are quite similar.

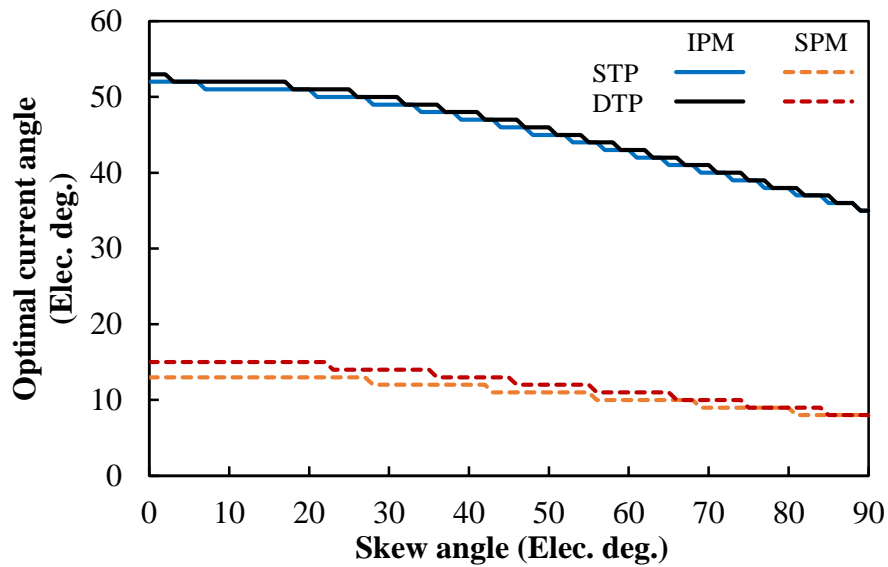
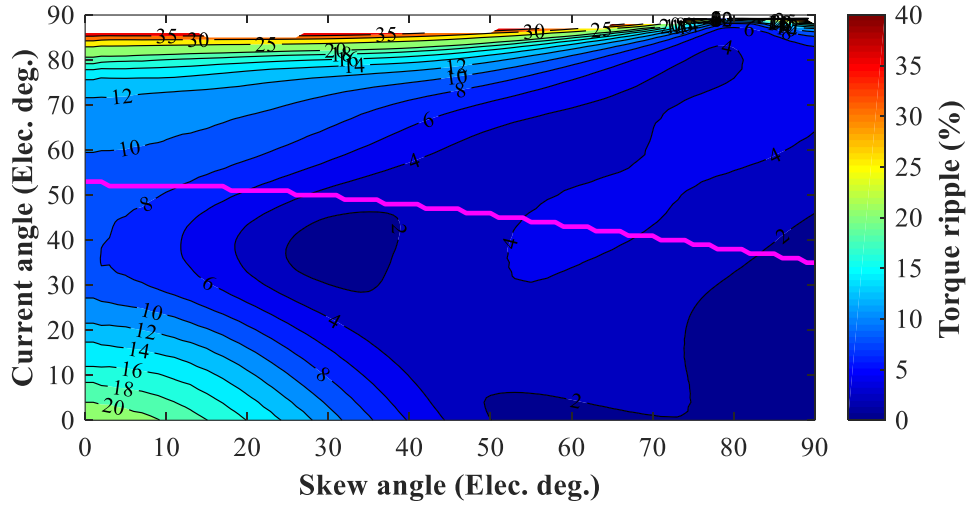
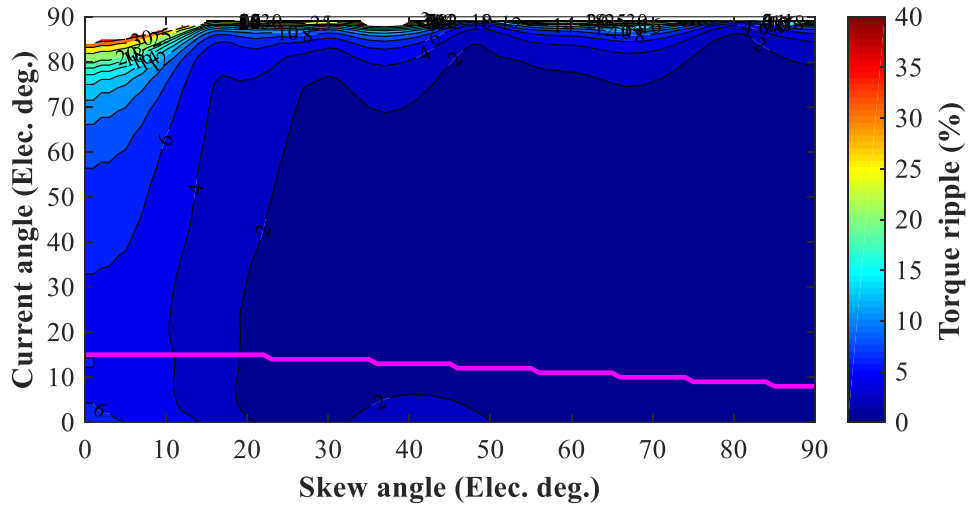


Fig. 6.12 Variations of optimal current angle with skew angle in STP and DTP PMSMs after rotor continuous skew.

Besides average torque, when the phase current amplitude is fixed at 118A, the variations of torque ripple of DTP IPMSM and SPMSM with different current and skew angles are shown in Fig. 6.13 (a) and (b), respectively.



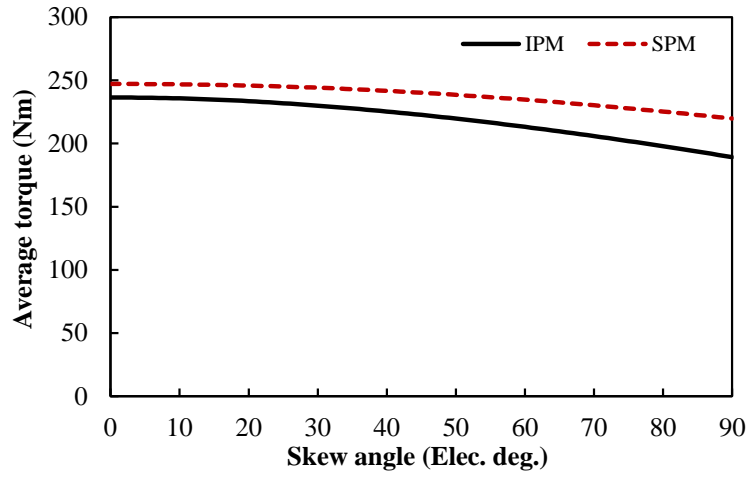
(a) IPMSM



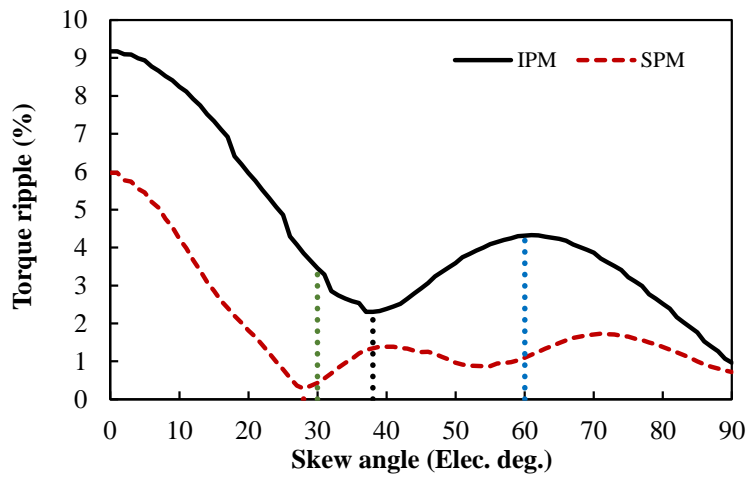
(b) SPMSM

Fig. 6.13 Variations of torque ripple with skew angle and current angle in DTP IPMSM and SPMSM after rotor continuous skew ($I_{a1} = 118\text{A}$).

As mentioned above, the optimal current angle for any skew angle can be obtained from Fig. 6.11. With the optimal current angles, the variations of average torque and torque ripple with skew angle in DTP IPMSM and SPMSM can be obtained from Fig. 6.10 and Fig. 6.13, respectively, and the results are shown in Fig. 6.14 (a) and (b), respectively.



(a) Average torque



(b) Torque ripple

Fig. 6.14 Variations of average torque and torque ripple with skew angle in DTP IPMSM and SPMSM after rotor continuous skew and using optimal current angles ($I_{a1} = 118\text{A}$).

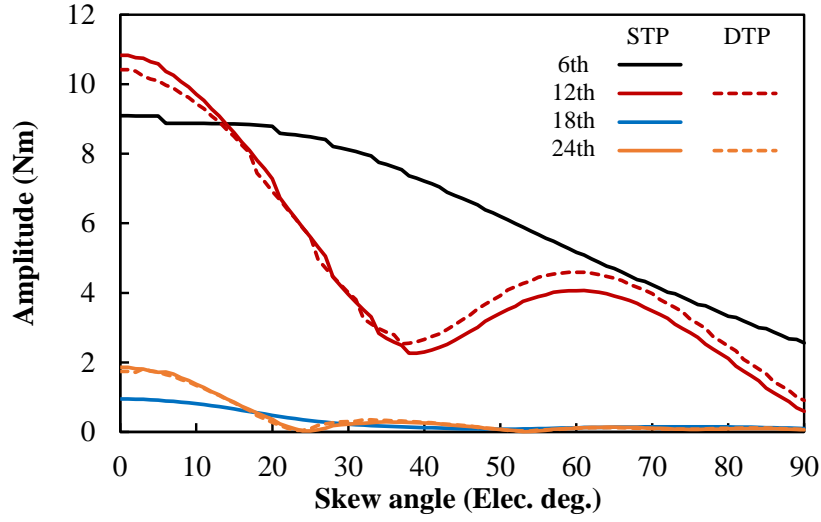
Since the dominant torque harmonics in DTP IPMSM and SPMSM are the 12th torque harmonics, the conventional skew angle (one periodicity for on-load torque ripple) for DTP IPMSM and SPMSM should be 30°. However, from Fig. 6.14, it can be observed that the lowest torque ripple is not achieved with 30° skew angle in both DTP IPMSM and SPMSM. Considering that the larger the skew angle, the lower the resultant average torque, the optimal skew angle is chosen from the angles less than 60° in this chapter. Hence, the skew angle $\leq 60^\circ$ and can produce the lowest torque ripple is chosen as the optimal skew angle for the minimum torque ripple. From Fig. 6.14 (b), under the specific load condition ($I_{a1} = 118\text{A}$), the optimal skew angle is 38° for DTP IPMSM and 28° for DTP SPMSM, respectively. For some typical skew angles (0°, without rotor skew; 30°, conventional skew angle for DTP PMSMs; 60°, conventional skew angle for STP PMSMs; and the optimal skew angle), the average torque and

torque ripple characteristics of DTP IPMSM and SPMSM are summarized and compared in Table 6.3. It can be seen that the optimal skew angle can produce the lowest torque ripple among all these skew angles. It also should be mentioned that the optimal skew angle in DTP SPMSM (28°) is close to the conventional skew angle (30°), but the optimal skew angle in DTP IPMSM (38°) is relatively away from the conventional skew angle (30°). Considering that in STP IPMSM and SPMSM, under the same load condition, the conventional skew angle is 60° , but the optimal skew angle is 39° in STP IPMSM and 55° in STP SPMSM. It can be concluded that in both STP and DTP PMSMs, the conventional skew angle works better in reducing torque ripples in SPMSMs than in IPMSMs. For IPMSMs under this load condition, the optimal skew angles in STP and DTP IPMSMs are very similar with each other.

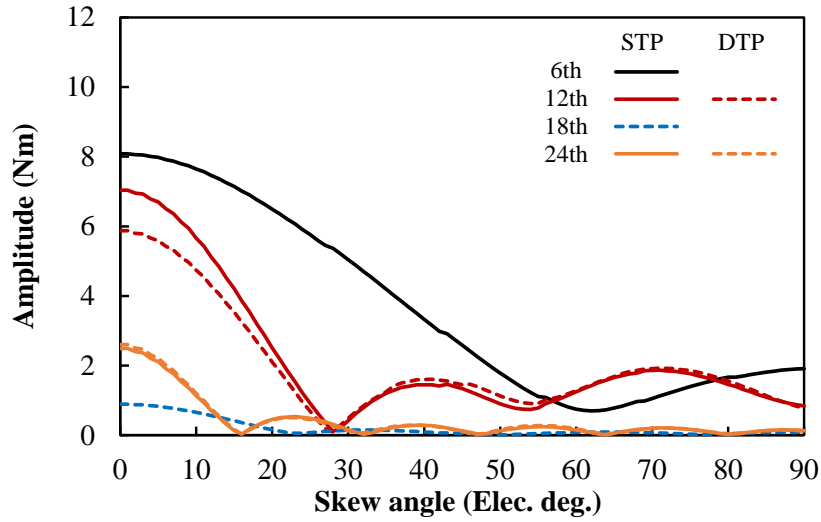
Table 6.3 Torque characteristics of DTP IPMSM and SPMSM after rotor continuous skew using different skew angles ($I_{a1} = 118\text{A}$)

| | Skew angle ($^\circ$) | Optimal current angle ($^\circ$) | Average torque (Nm) | Torque ripple (%) |
|-------|-------------------------|------------------------------------|---------------------|-------------------|
| IPMSM | 0 | 53 | 236.45 | 9.18 |
| | 30 | 50 | 229.98 | 3.46 |
| | 38 | 48 | 226.35 | 2.30 |
| | 60 | 43 | 213.21 | 4.32 |
| SPMSM | 0 | 15 | 247.18 | 5.97 |
| | 28 | 14 | 244.56 | 0.28 |
| | 30 | 14 | 244.16 | 0.43 |
| | 60 | 11 | 234.70 | 1.10 |

To find out the reason why the optimal skew angles are different in STP and DTP PMSMs under this load condition, the influences of skew angle on different torque harmonic orders in STP and DTP IPMSMs are shown in Fig. 6.15 (a), and those in STP and DTP SPMSMs are shown in Fig. 6.15 (b), respectively. It can be seen that although the torque harmonic contents in STP and DTP PMSMs are different, for the same torque harmonic order, the effects of skew angle on the torque harmonic amplitudes are almost the same in STP and DTP PMSMs.



(a) IPMSM



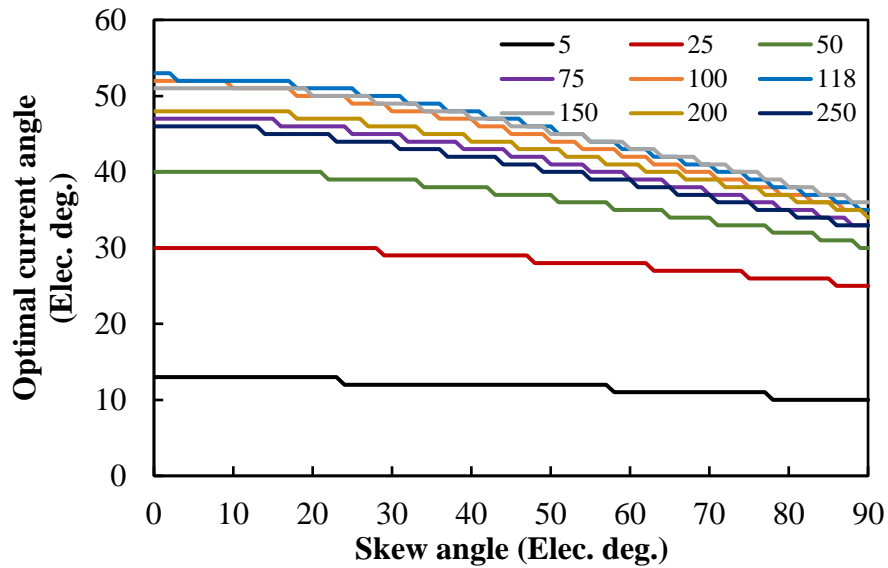
(b) SPMSM

Fig. 6.15 Variations of different torque harmonic amplitudes with skew angle in DTP PMSMs after rotor continuous skew and using optimal current angles ($I_{a1} = 118\text{A}$).

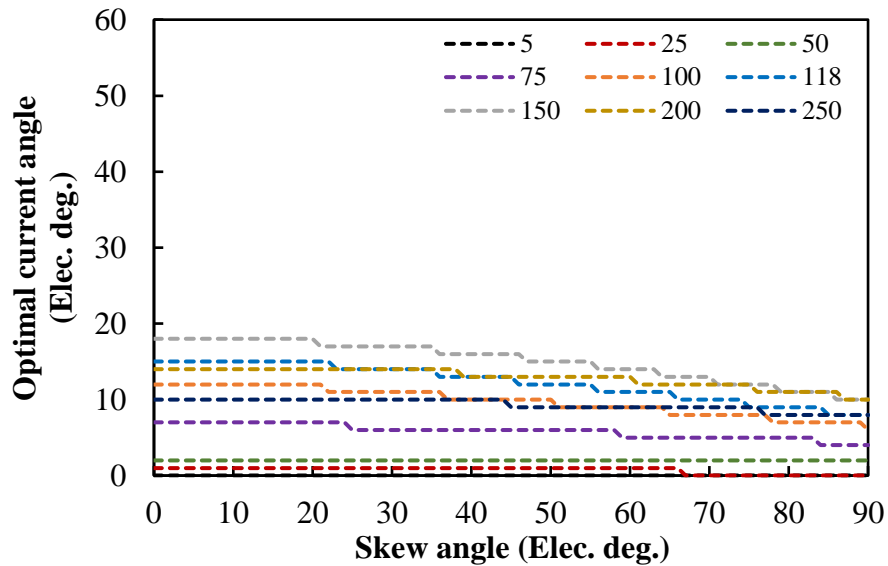
Further, it can be observed that for the same torque harmonic order, to achieve similar reduction effect, the skew angles in IPMSMs should be larger than those in SPMSMs. For example, in STP and DTP SPMSMs, 28° skew angle can reduce the 12th torque harmonics significantly, while in STP and DTP IPMSMs, only 38° skew angle can reduce the 12th torque harmonics effectively. Similarly, in STP SPMSM, 60° skew angle can reduce the 6th torque harmonic significantly, but in STP IPMSM, the 6th torque harmonic cannot be reduced effectively by skew angles smaller than 60° . Hence, in STP IPMSM, the optimal skew angle is mainly determined by the 12th torque harmonic. As the optimal skew angle in DTP IPMSM is also mainly determined by the 12th torque harmonic, the optimal skew angles in STP and DTP IPMSMs are almost the same under this condition.

6.4.2 Effects of Load on Optimal Current Angle

Based on the analyses in Section 6.4.1, for DTP IPMSM and SPMSM, when the phase current amplitude is varied from 5, 25, 50, 75, 100, 118, 150, 200, 250A, the variations of the optimal current angles with skew angle are shown in Fig. 6.16. It can be seen that compared with SPMSM, the optimal current angle in IPMSM varies more evidently with skew angle.



(a) IPMSM



(b) SPMSM

Fig. 6.16 Variations of optimal current angles with skew angle in IPMSM and SPMSM after rotor continuous skew under different phase current amplitude conditions.

Based on Fig. 6.16, for any skew angle, the relationship between the optimal current angle and the phase current amplitude can be obtained. For some typical skew angles (0° , without rotor skew; 30° , conventional skew angle for DTP PMSMs; 60° , conventional skew angle for STP PMSMs; and the optimal skew angle), the effects of load on the optimal current angle can be presented by the variations of the optimal current angle with phase current amplitude, as shown in Fig. 6.17. It can be found that in both DTP IPMSM and SPMSM, the optimal current angles need to be re-calculated according to skew angles after rotor skew.

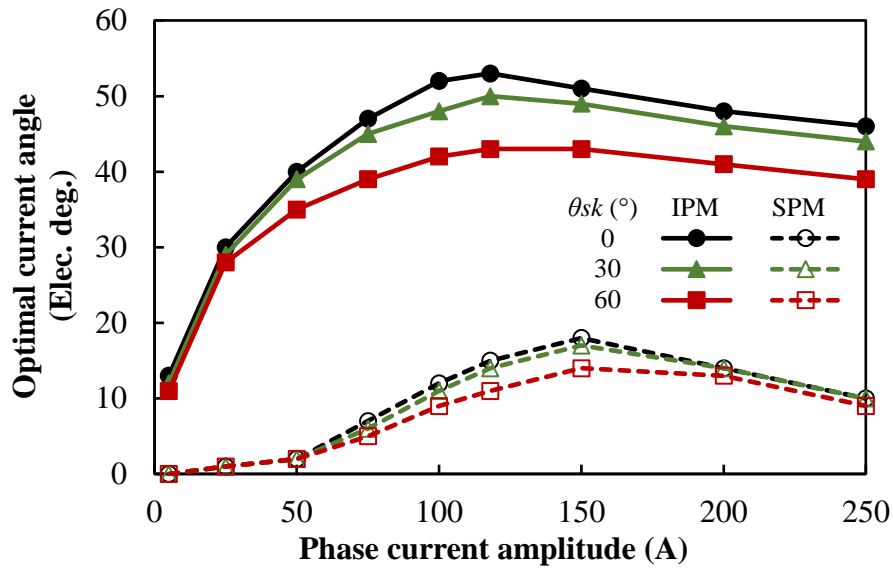
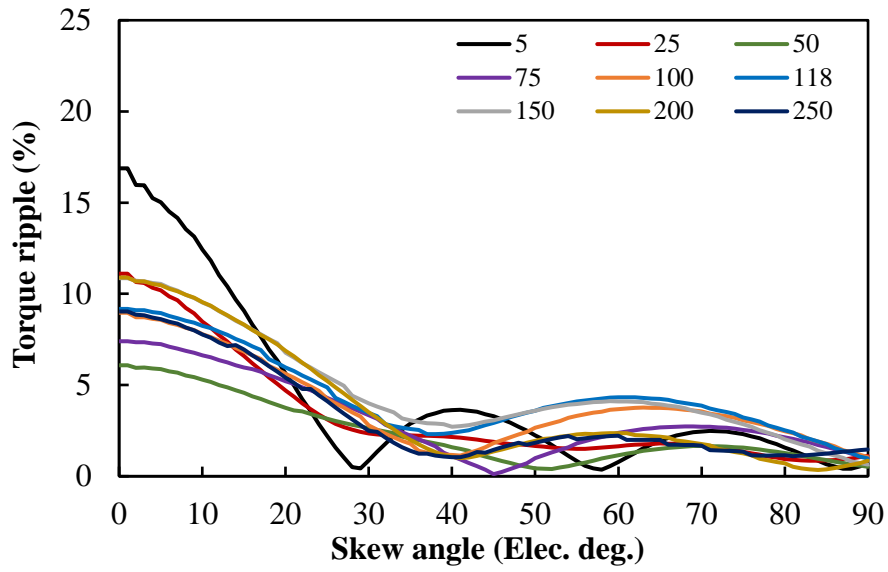


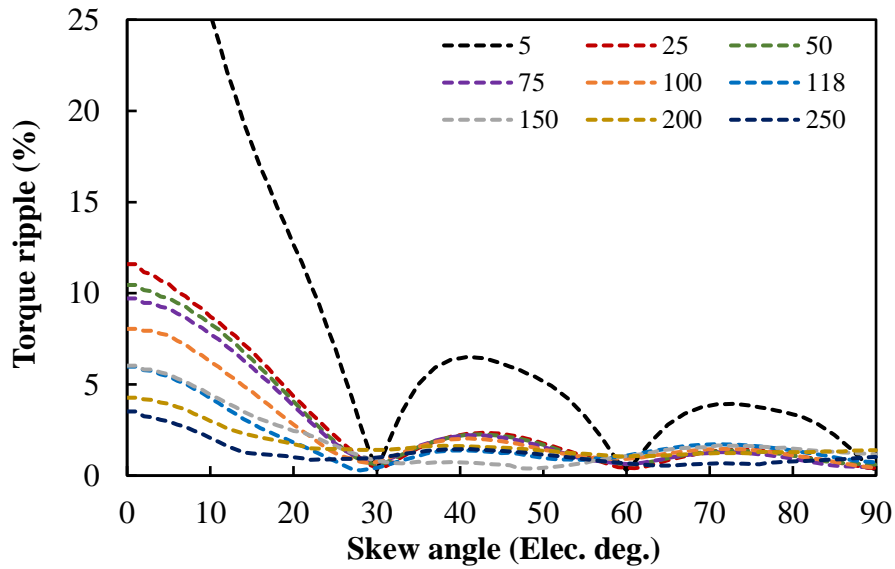
Fig. 6.17 Variations of optimal current angles with phase current amplitude in IPMSM and SPMSM after rotor continuous skew when using different skew angles.

6.4.3 Effects of Load on Optimal Skew Angle

With the optimal current angles given in Fig. 6.16, the variations of torque ripples with skew angle in DTP IPMSM and SPMSM after rotor continuous skew under different load conditions are calculated, as shown in Fig. 6.18 (a) and (b), respectively.



(a) IPMSM



(b) SPMSM

Fig. 6.18 Variations of torque ripple with skew angle in IPMSM and SPMSM after rotor continuous skew and using optimal current angles under different phase current amplitude conditions.

From Fig. 6.18, the optimal skew angles for the minimum torque ripple in DTP IPMSM and SPMSM can be obtained under these load conditions. The optimal skew angles and the corresponding optimal current angles, average torques, and torque ripples are summarized in Table 6.4.

Table 6.4 Optimal skew angles for minimum torque ripple in DTP IPMSM and SPMSM when using rotor continuous skew under different load conditions

| Machine type | Phase current amplitude (A) | Optimal skew angle (°) | Optimal current angle (°) | Average torque (Nm) | Torque ripple (%) |
|--------------|-----------------------------|------------------------|---------------------------|---------------------|-------------------|
| IPMSM | 5 | 58 | 11 | 7.87 | 0.34 |
| | 25 | 55 | 28 | 50.40 | 1.49 |
| | 50 | 52 | 36 | 108.99 | 0.39 |
| | 75 | 45 | 42 | 161.88 | 0.10 |
| | 100 | 41 | 46 | 203.33 | 1.13 |
| | 118 | 38 | 48 | 226.35 | 2.30 |
| | 150 | 40 | 47 | 253.13 | 2.71 |
| | 200 | 41 | 44 | 282.67 | 0.99 |
| | 250 | 41 | 42 | 306.87 | 1.03 |
| SPMSM | 5 | 30 | 0 | 12.22 | 0.31 |
| | 25 | 30 | 1 | 60.68 | 0.42 |
| | 50 | 30 | 2 | 119.06 | 0.60 |
| | 75 | 30 | 6 | 172.32 | 0.73 |
| | 100 | 29 | 11 | 217.86 | 0.69 |
| | 118 | 28 | 14 | 244.56 | 0.28 |
| | 150 | 49 | 15 | 273.22 | 0.40 |
| | 200 | 60 | 13 | 300.85 | 1.04 |
| | 250 | 60 | 9 | 323.63 | 0.67 |

From Table 6.4, the effects of load on optimal skew angle in rotor continuous skew can be observed from the variations of optimal skew angle with phase current amplitude in DTP IPMSM and SPMSM, as shown in Fig. 6.19. The optimal skew angle-phase current amplitude characteristics of DTP IPMSM and SPMSM are also compared with those in STP counterparts, as shown in Fig. 6.20. It can be seen that the optimal skew angles in STP and DTP IPMSMs are close to each other under all load conditions, but the optimal skew angles in STP and DTP SPMSMs are quite different under all load conditions.

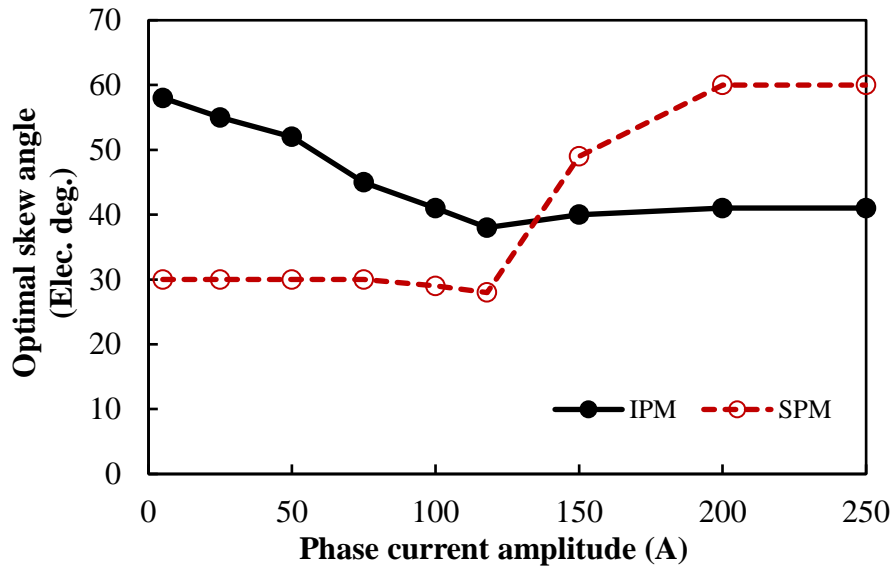


Fig. 6.19 Variations of optimal skew angle with phase current amplitude in IPMSM and SPMSM with rotor continuous skew

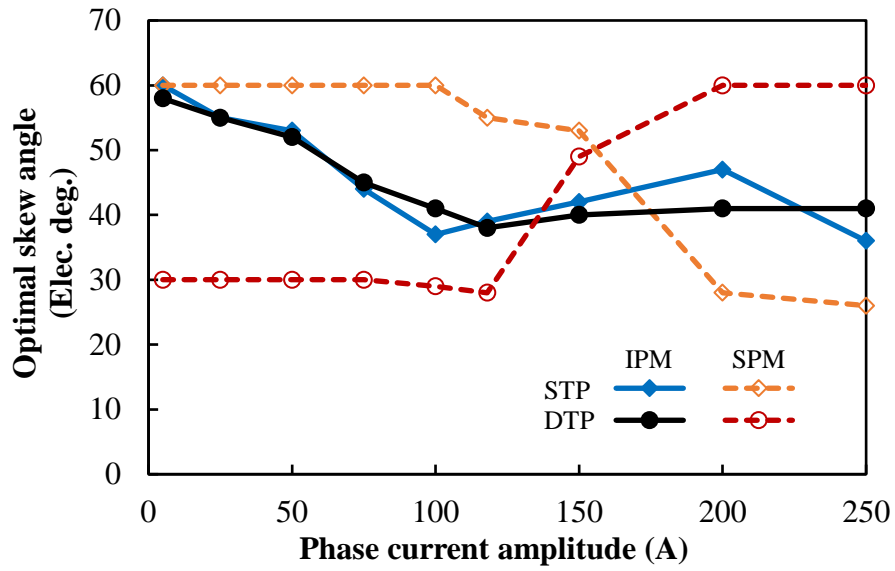
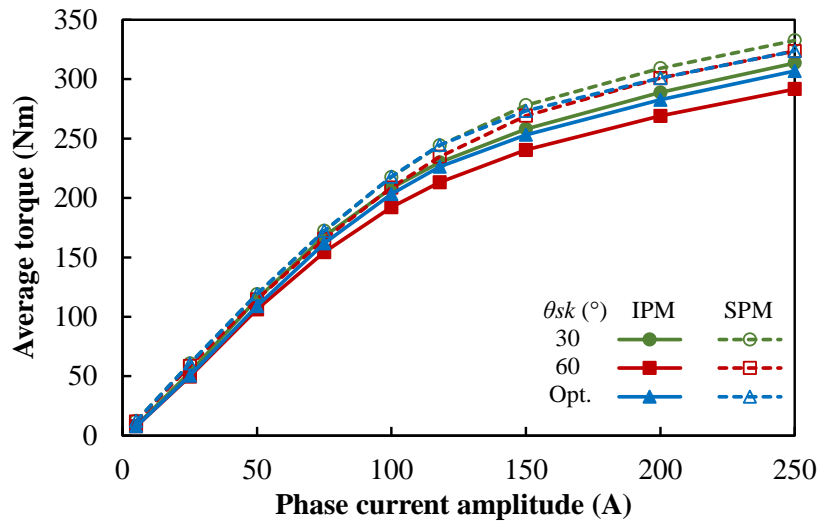


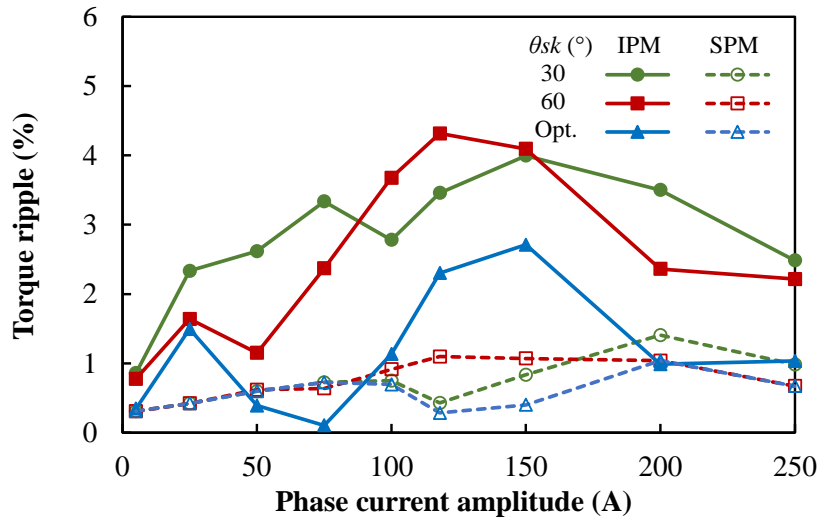
Fig. 6.20 Variations of optimal skew angle with phase current amplitude in IPMSM and SPMSM with rotor continuous skew

6.4.4 Effects of Load on Torque Characteristics with Conventional and Optimal Skew Angles

In Table 6.4, besides the optimal skew angles and the optimal current angles, the average torque and torque ripple characteristics of DTP IPMSM and SPMSM after rotor continuous skew when using the optimal skew and current angles are also provided. Hence, for rotor continuous skew, the effects of load on average torque and torque ripple characteristics in DTP IPMSM and SPMSM can be presented as the variations of average torque and torque ripple with phase current amplitude, as shown in Fig. 6.21. It should be mentioned that besides the optimal skew angles, the conventional skew angles (30° and 60°) are also considered in Fig. 6.21.



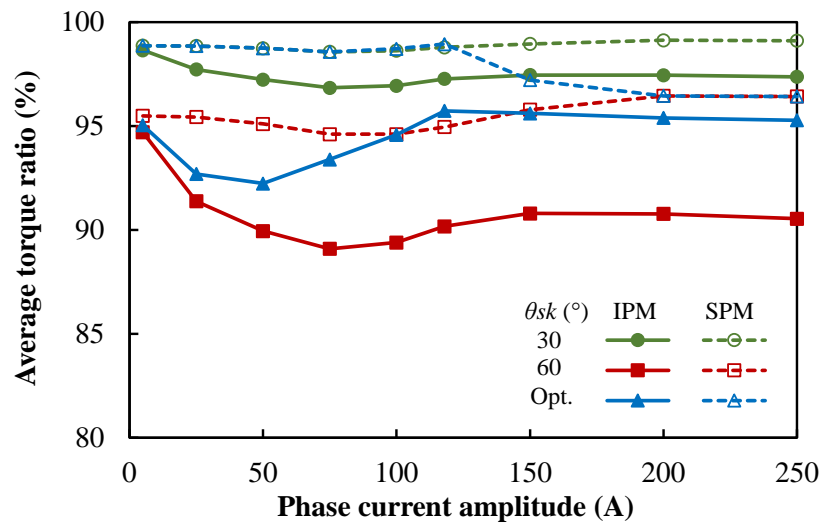
(a) Average torque ratio



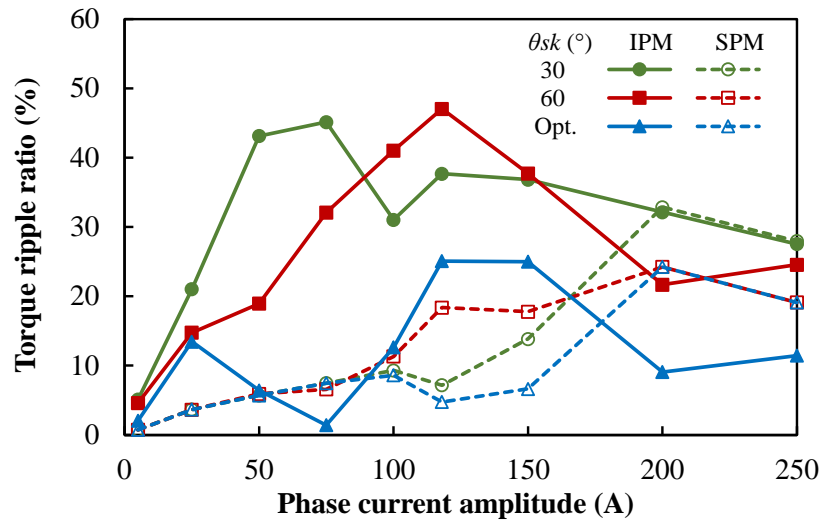
(b) Torque ripple

Fig. 6.21 Variations of average torque and torque ripple with phase current amplitude in DTP IPMSM and SPMSM after rotor continuous skew when using different skew angles.

To better present the effectiveness of rotor continuous skew with different skew angles in DTP IPMSM and SPMSM, the ratios of average torque and torque ripple after rotor skew to those before rotor skew are also calculated under different load conditions. In DTP IPMSM and SPMSM, for 30°, 60°, and the optimal skew angle, the variations of average torque and torque ripple ratios with phase current amplitude are shown in Fig. 6.22. It can be concluded that in DTP IPMSM and SPMSM, the rotor continuous skew can still reduce on-load torque ripples effectively. Compared with conventional skew angles, the optimal skew angles introduced in this chapter can result in even better torque ripple performance.



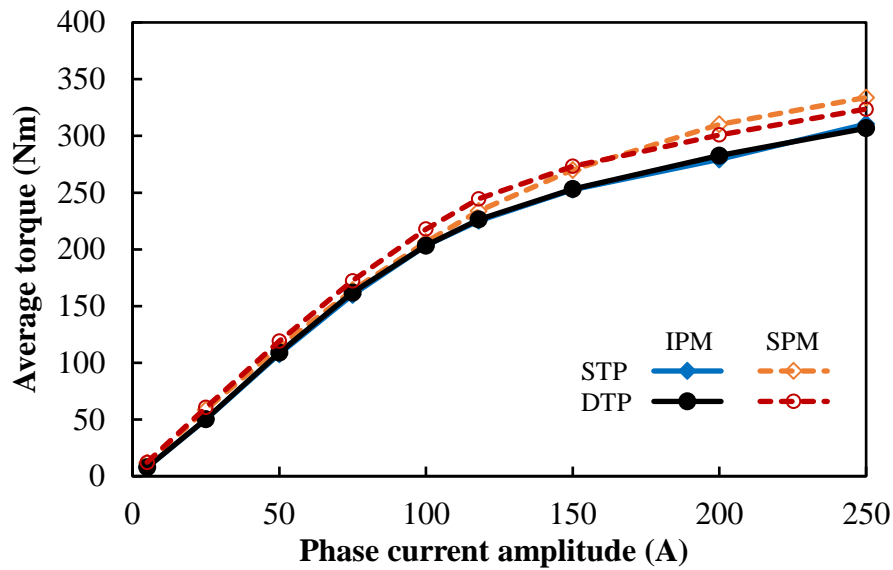
(a) Average torque ratio



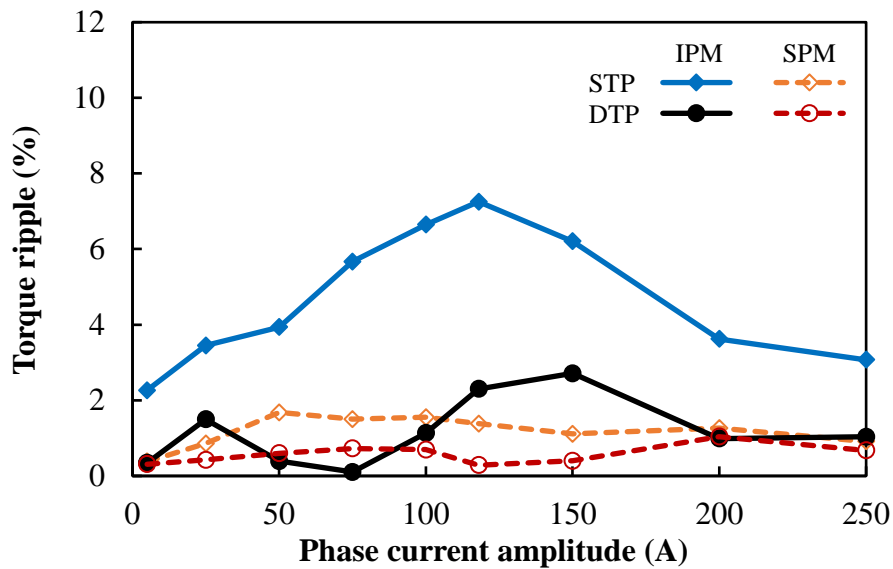
(b) Torque ripple ratio

Fig. 6.22 Variations of average torque and torque ripple ratios with phase current amplitude in DTP IPMSM and SPMSM after rotor continuous skew when using different skew angles.

To compare the effectiveness of rotor continuous skew in STP and DTP PMSMs, the average torque-, torque ripple-, average torque ratio-, and torque ripple ratio-phase current amplitude characteristics in STP and DTP PMSMs are compared in Fig. 6.23 and Fig. 6.24. Only the optimal skew angles are considered in the comparison. From Fig. 6.24 (b), it should be noticed that although DTP PMSMs have inherent lower torque ripples than STP counterparts, as shown in Fig. 6.9 (b), the torque ripple reductions caused by rotor continuous skew in DTP PMSMs are still more evident than those in STP PMSMs.

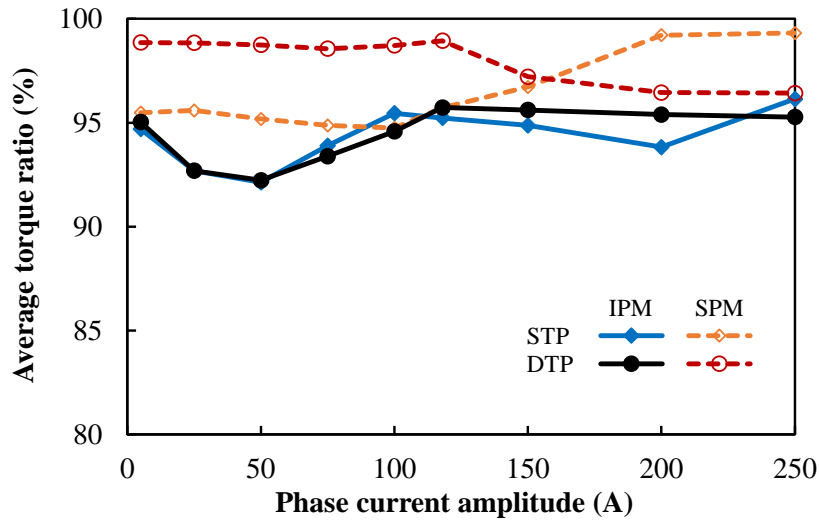


(a) Average torque ratio

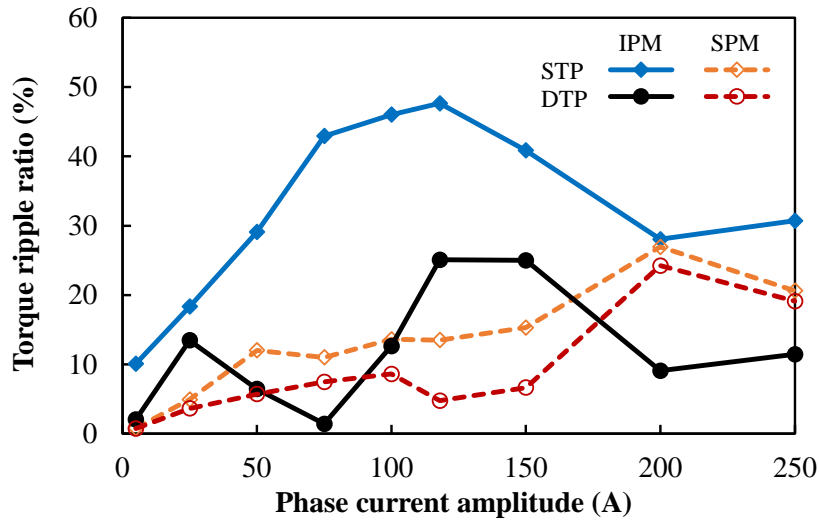


(b) Torque ripple

Fig. 6.23 Comparisons of average torque- and torque ripple-phase current amplitude characteristics in STP and DTP PMSMs after rotor continuous skew when using optimal skew angles.



(a) Average torque ratio



(b) Torque ripple ratio

Fig. 6.24 Comparisons of average torque ratio- and torque ripple ratio-phase current amplitude characteristics in STP and DTP PMSMs after rotor continuous skew when using optimal skew angles.

6.5 Influences of Load in PMSMs with Rotor Step Skew

Considering the difficulties in manufacturing continuously-skewed rotors, rotor step skew is more practical than rotor continuous skew in practice. Hence, it is still necessary to investigate the effectiveness of rotor step skew in DTP PMSMs under different load conditions. In this section, the influences of load on optimal current angle, optimal skew angle, average torque, and torque ripples in DTP IPMSM and SPMSM are investigated. 2-step and 3-step rotor skews are considered. The results in PMSMs with rotor step skew are also compared with those in PMSMs with rotor continuous skew in this section.

6.5.1 Effects of Load on Optimal Current Angle

Similar to the analyses in PMSMs with rotor continuous skew, for different load conditions, the instantaneous torque waveforms of DTP IPMSM and SPMSM with different skew angles and different current angles are firstly calculated in rotor 2-step and 3-step skews. Then, the optimal current angles for maximum average torque can be derived for different skew angles. In the benchmark DTP IPMSM and SPMSM, when the phase current amplitude is varied from 5, 25, 50, 75, 100, 118, 150, 200, to 250A, the variations of the optimal current angles with skew angle are shown in Fig. 6.25 for rotor 2-step skew, and in Fig. 6.26 for rotor 3-step skew.

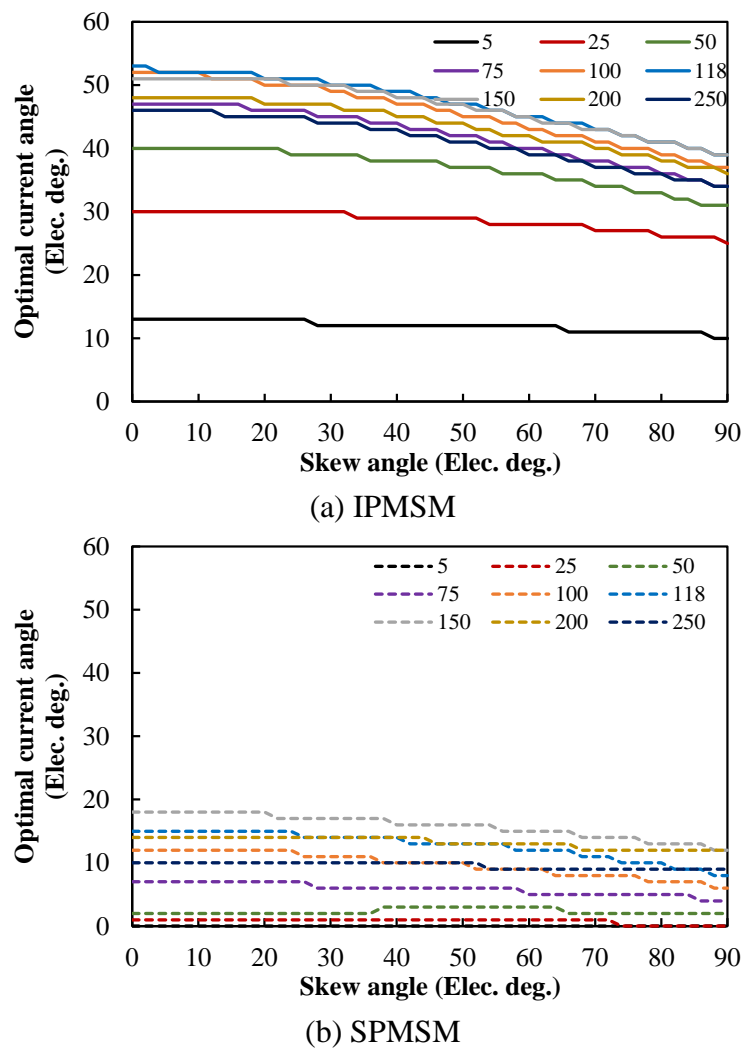


Fig. 6.25 Variations of optimal current angles with skew angle in DTP IPMSM and SPMSM after rotor 2-step skew under different phase current amplitude conditions.

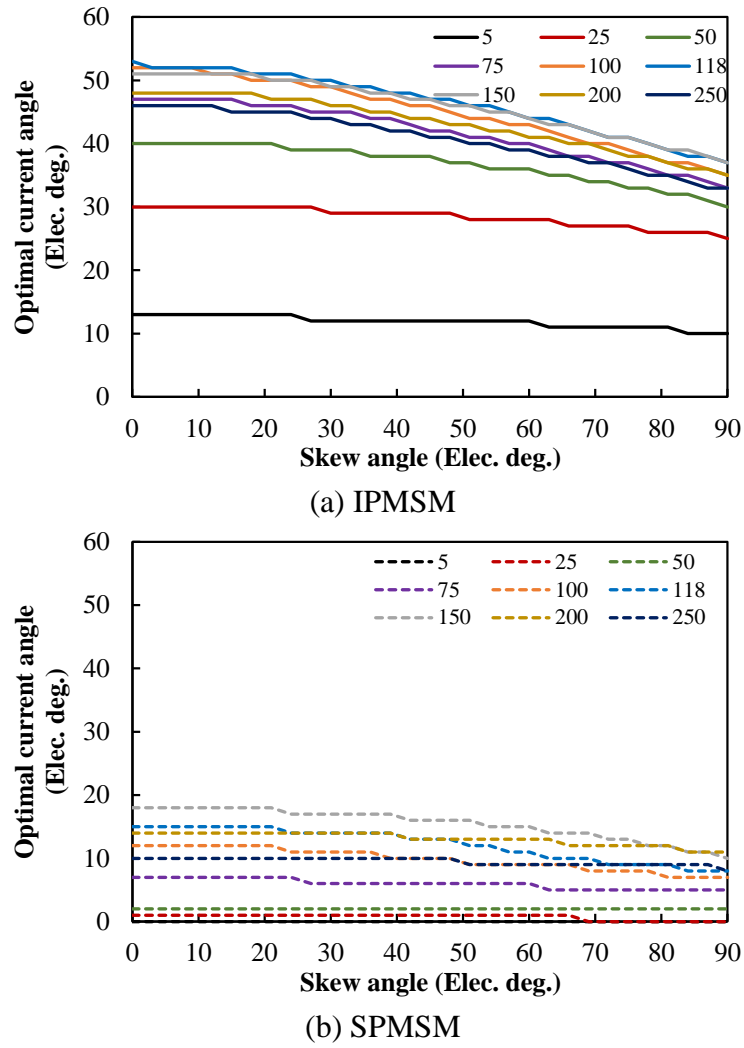


Fig. 6.26 Variations of optimal current angles with skew angle in DTP IPMSM and SPMSM after rotor 3-step skew under different phase current amplitude conditions.

Based on the foregoing analyses, for any skew angle, the optimal current angle for rotor continuous, 2-step, and 3-step skews can be found from Fig. 6.16, Fig. 6.25, and Fig. 6.26, respectively. Hence, for rotor continuous, 2-step, and 3-step skews in DTP PMSMs, the influences of load on optimal current angle can be reflected by the variations of the optimal current angles with phase current amplitude, as shown in Fig. 6.27. It can be seen that although the optimal current angles in rotor continuous, 2-step, and 3-step skews are not identical, the differences between them are very small. Hence, the influences of load on optimal current angle in rotor step skew are similar to those in rotor continuous skew in DTP PMSMs.

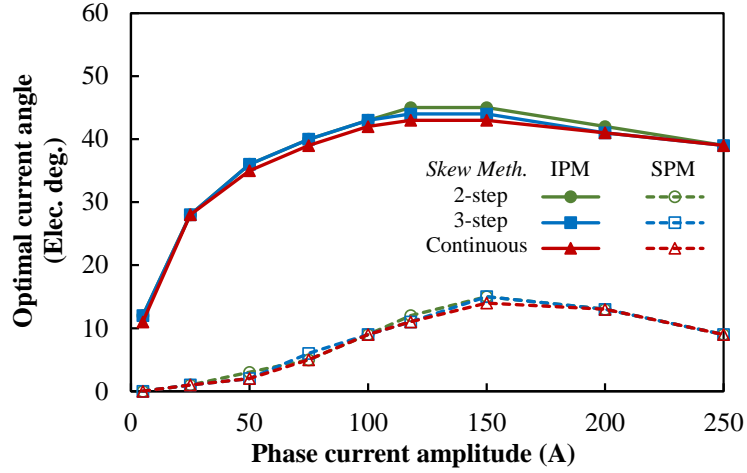
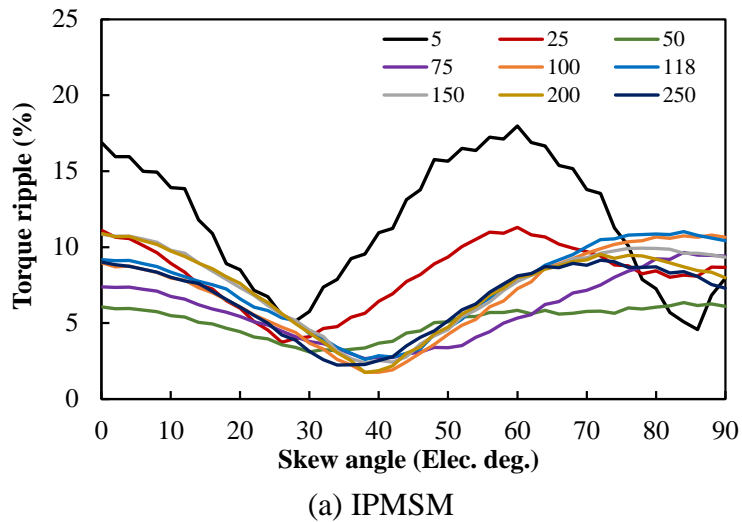
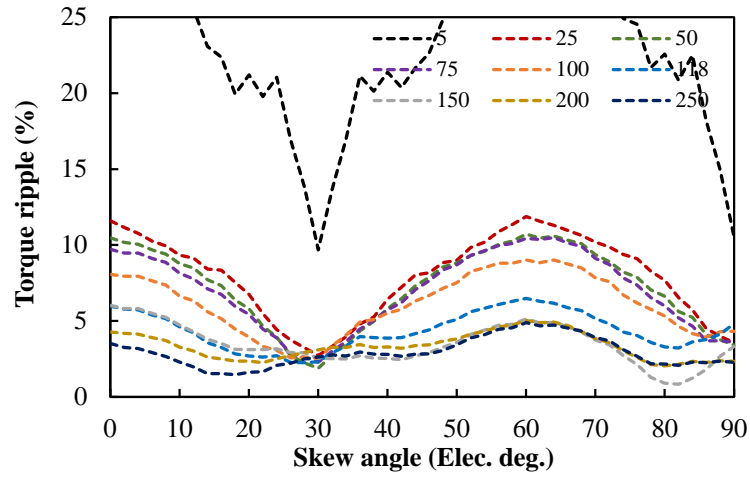


Fig. 6.27 Variations of optimal current angle with phase current amplitude in DTP IPMSM and SPMSM using rotor continuous, 2-step, and 3-step skews ($\theta_{sk} = 60^\circ$).

6.5.2 Effects of Load on Optimal Skew Angle

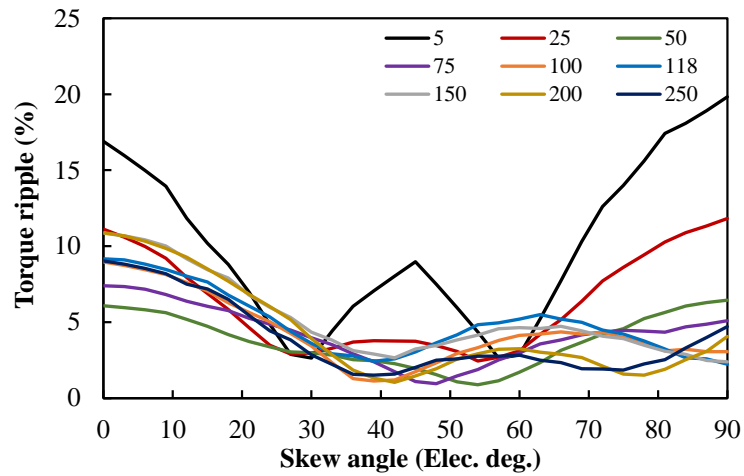
Similar to the analyses in rotor continuous skew, with the optimal current angles given in Fig. 6.25 and Fig. 6.26, the torque ripple-skew angle characteristics of DTP IPMSM and SPMSM with rotor 2-step and 3-step skews under different load conditions ($I_{a1} = 5, 25, 50, 75, 100, 118, 150, 200, \text{ to } 250\text{A}$) are shown in Fig. 6.28 and Fig. 6.29, respectively. Thus, the optimal skew angles for the minimum torque ripple, which can produce the lowest torque ripple among all skew angles $\leq 60^\circ$, can be obtained from Fig. 6.28 and Fig. 6.29. For the load conditions with different phase current amplitudes (5, 25, 50, 75, 100, 118, 150, 200, 250A), the optimal skew angles and corresponding optimal current angles, average torque, and torque ripple in rotor continuous, 2-step, and 3-step skews are summarized in Table 6.5.



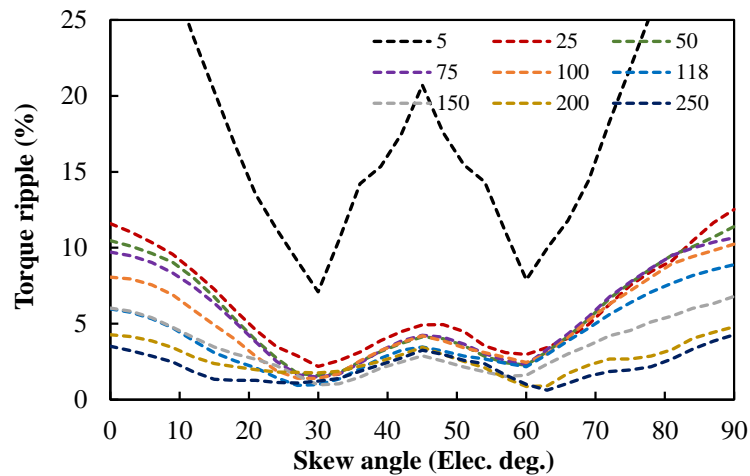


(b) SPMSM

Fig. 6.28 Variations of torque ripple with skew angle in IPMSM and SPMSM after rotor 2-step skew and using optimal current angles under different phase current amplitude conditions.



(a) IPMSM



(b) SPMSM

Fig. 6.29 Variations of torque ripple with skew angle in IPMSM and SPMSM after rotor 3-step skew and using optimal current angles under different phase current amplitude conditions.

Table 6.5 Optimal skew angles for minimum torque ripple in IPMSM and SPMSM when using different rotor skew methods under different load conditions

| Machine type | Phase current amplitude (A) | Skew method | Optimal skew angle (°) | Optimal current angle (°) | Average torque (Nm) | Torque ripple (%) |
|--------------|-----------------------------|-------------|------------------------|---------------------------|---------------------|-------------------|
| IPMSM | 5 | 2-step | 28 | 12 | 8.20 | 5.13 |
| | | 3-step | 30 | 12 | 8.18 | 2.63 |
| | | Cont. | 58 | 11 | 7.87 | 0.86 |
| | 25 | 2-step | 26 | 30 | 53.67 | 3.73 |
| | | 3-step | 54 | 28 | 50.93 | 2.45 |
| | | Cont. | 55 | 28 | 50.40 | 2.33 |
| | 50 | 2-step | 30 | 39 | 115.67 | 3.10 |
| | | 3-step | 54 | 36 | 109.29 | 0.89 |
| | | Cont. | 52 | 36 | 108.99 | 2.62 |
| | 75 | 2-step | 38 | 44 | 166.93 | 2.66 |
| | | 3-step | 48 | 42 | 161.72 | 0.95 |
| | | Cont. | 45 | 42 | 161.88 | 3.33 |
| | 100 | 2-step | 38 | 48 | 207.53 | 1.76 |
| | | 3-step | 39 | 47 | 205.47 | 1.13 |
| | | Cont. | 41 | 46 | 203.33 | 2.78 |
| | 118 | 2-step | 38 | 49 | 228.93 | 2.61 |
| | | 3-step | 39 | 48 | 227.04 | 2.42 |
| | | Cont. | 38 | 48 | 226.35 | 3.46 |
| | 150 | 2-step | 38 | 49 | 256.86 | 2.39 |
| | | 3-step | 42 | 47 | 253.45 | 2.66 |
| | | Cont. | 40 | 47 | 253.13 | 4.00 |
| | 200 | 2-step | 38 | 46 | 287.40 | 1.74 |
| | | 3-step | 42 | 44 | 283.57 | 1.03 |
| | | Cont. | 41 | 44 | 282.67 | 3.50 |
| | 250 | 2-step | 34 | 44 | 314.04 | 2.23 |
| | | 3-step | 39 | 42 | 309.71 | 1.52 |
| | | Cont. | 41 | 42 | 306.87 | 2.48 |
| SPMSM | 5 | 2-step | 30 | 0 | 12.26 | 9.69 |
| | | 3-step | 30 | 0 | 12.24 | 7.10 |
| | | Cont. | 30 | 0 | 12.22 | 0.31 |
| | 25 | 2-step | 30 | 1 | 60.86 | 2.72 |
| | | 3-step | 30 | 1 | 60.76 | 2.19 |
| | | Cont. | 30 | 1 | 60.68 | 0.42 |
| | 50 | 2-step | 30 | 2 | 119.43 | 1.89 |
| | | 3-step | 30 | 2 | 119.23 | 1.59 |
| | | Cont. | 30 | 2 | 119.06 | 0.60 |

| | | | | | |
|-----|--------|----|----|--------|------|
| 75 | 2-step | 30 | 6 | 172.90 | 2.30 |
| | 3-step | 30 | 6 | 172.59 | 1.48 |
| | Cont. | 30 | 6 | 172.32 | 0.73 |
| 100 | 2-step | 30 | 11 | 218.45 | 2.53 |
| | 3-step | 30 | 11 | 217.99 | 1.40 |
| | Cont. | 29 | 11 | 217.86 | 0.69 |
| 118 | 2-step | 28 | 14 | 245.24 | 2.25 |
| | 3-step | 27 | 14 | 245.03 | 0.93 |
| | Cont. | 28 | 14 | 244.56 | 0.28 |
| 150 | 2-step | 42 | 16 | 276.75 | 2.44 |
| | 3-step | 30 | 17 | 278.43 | 0.98 |
| | Cont. | 49 | 15 | 273.22 | 0.40 |
| 200 | 2-step | 22 | 14 | 310.81 | 2.25 |
| | 3-step | 60 | 13 | 302.19 | 0.87 |
| | Cont. | 60 | 13 | 300.85 | 1.04 |
| 250 | 2-step | 18 | 10 | 334.81 | 1.46 |
| | 3-step | 60 | 9 | 325.03 | 1.00 |
| | Cont. | 60 | 9 | 323.63 | 0.67 |

From Table 6.5, the variations of the optimal skew angle with phase current amplitude in DTP IPMSM and SPMSM for rotor continuous, 2-step, and 3-step skews are compared in Fig. 6.30. It can be seen that in DTP SPMSM, the optimal skew angles for rotor continuous, 2-step, and 3-step skews are all about 30° when phase current amplitude is smaller than 118A. Since $I_{a1} = 118\text{A}$ is the full-load condition for the benchmark DTP PMSMs, it can be concluded that in DTP SPMSM, the conventional skew angle (30°) can achieve very good torque reduction effects under light-, heavy- and full-load conditions. Only when DTP SPMSM is operated under over-load conditions, it is necessary to use other optimal skew angles. However, in DTP IPMSM, the optimal skew angles for rotor continuous, 2-step, and 3-step skews are different, especially under light-load conditions. Hence, it is necessary to check and modify skew angles when using different skew methods in DTP IPMSM under different load conditions.

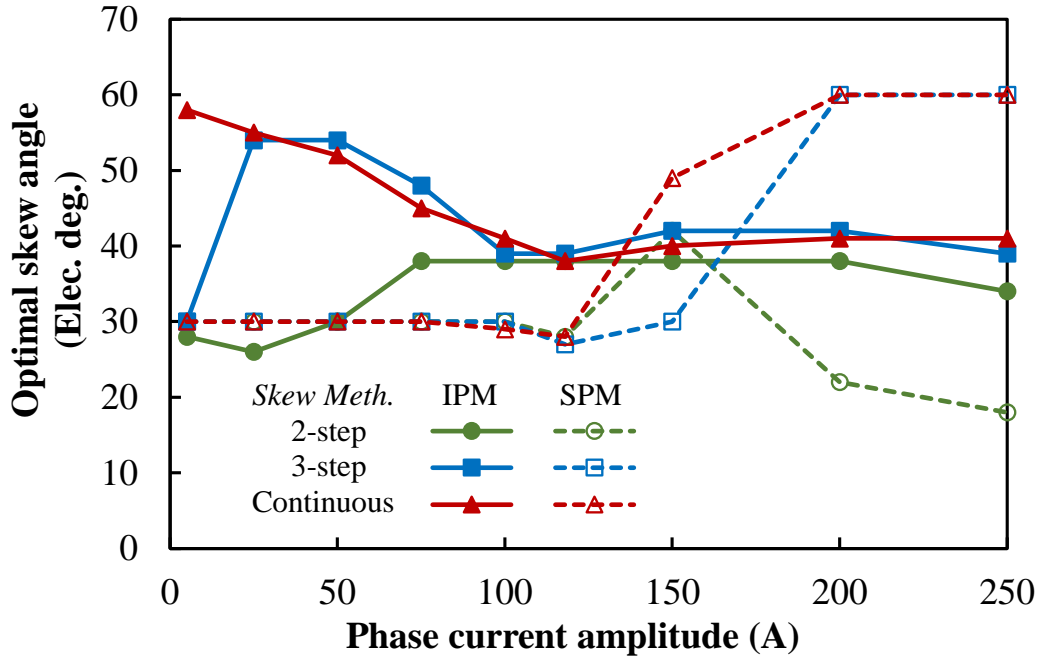
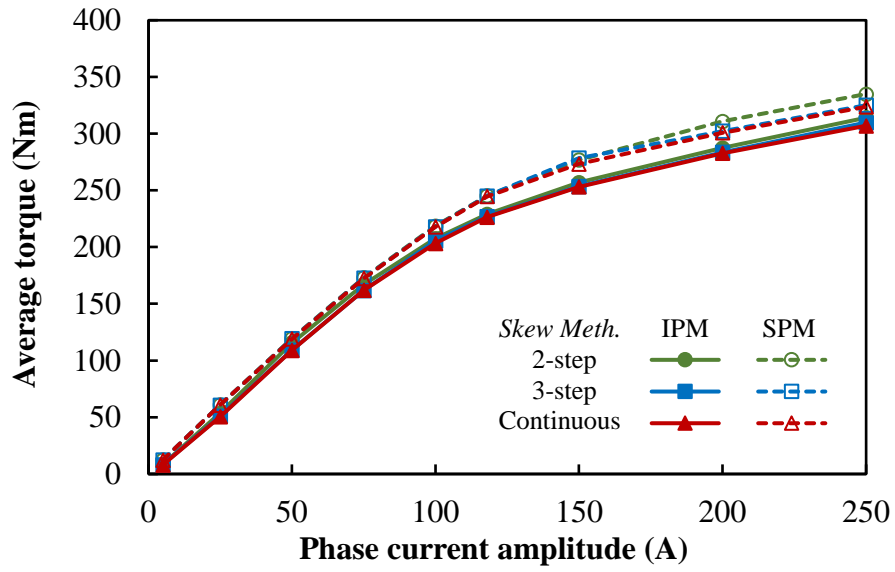


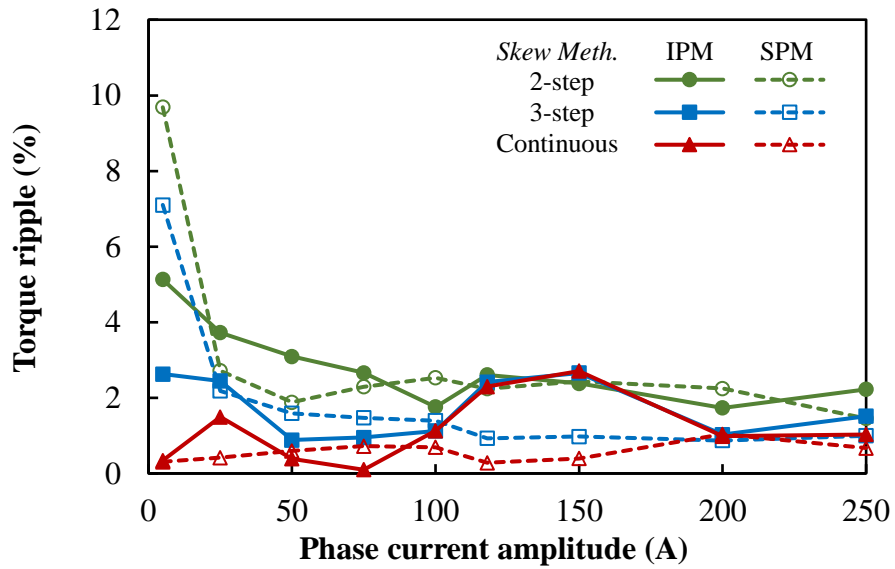
Fig. 6.30 Variations of optimal skew angle with phase current amplitude in IPMSM and SPMSM when using rotor continuous, 2-step, and 3-step skew methods.

6.5.3 Effects of Load on Torque Characteristics with Optimal Skew Angles

In rotor continuous, 2-step, and 3-step skews, with the optimal skew angles shown in Table 6.5, the average torque and torque ripple characteristics of DTP IPMSM and SPMSM under different load conditions can also be found from Table 6.5. Hence, the variations of average torque and torque ripple characteristics of DTP IPMSM and SPMSM with phase current amplitude in rotor continuous, 2-step, and 3-step skews can be obtained, as shown in Fig. 6.31. To show the effectiveness of different skew methods, the ratios of resultant average torque and torque ripple after rotor skew to those before rotor skew are presented in Fig. 6.32 for comparison. It can be seen that rotor 2-step skew can produce higher average torque than the other two methods, but has higher torque ripple simultaneously. In addition, since the optimal skew angles in rotor 3-step and continuous skews are very similar with each other, the resultant average torques produced by DTP PMSMs with rotor 3-step and continuous skews are also similar with each other, as shown in Fig. 6.32 (a). However, from Fig. 6.32 (b), it can be observed that in both DTP IPMSM and SPMSM, the more the step number is, the lower the resultant torque ripple will be, especially under light-load conditions. Compared with 3-step skew, rotor continuous skew can achieve similar average torque with lower torque ripple.

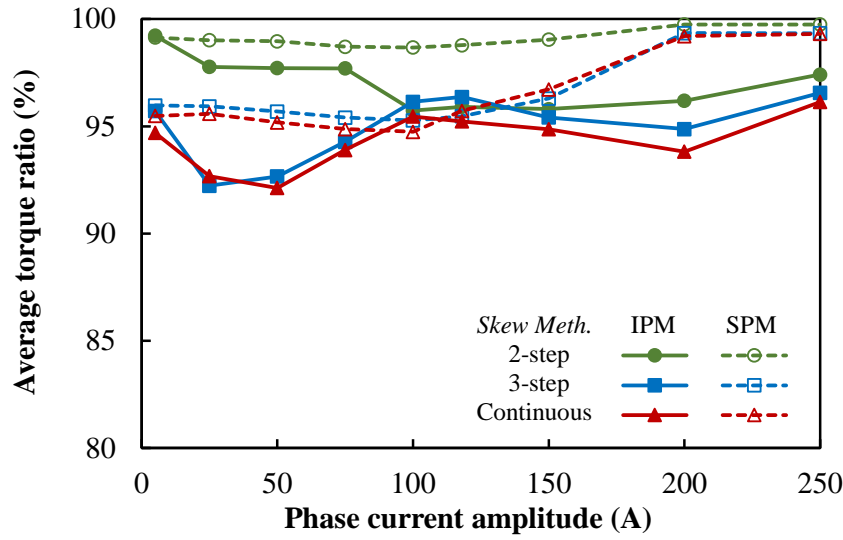


(a) Average torque

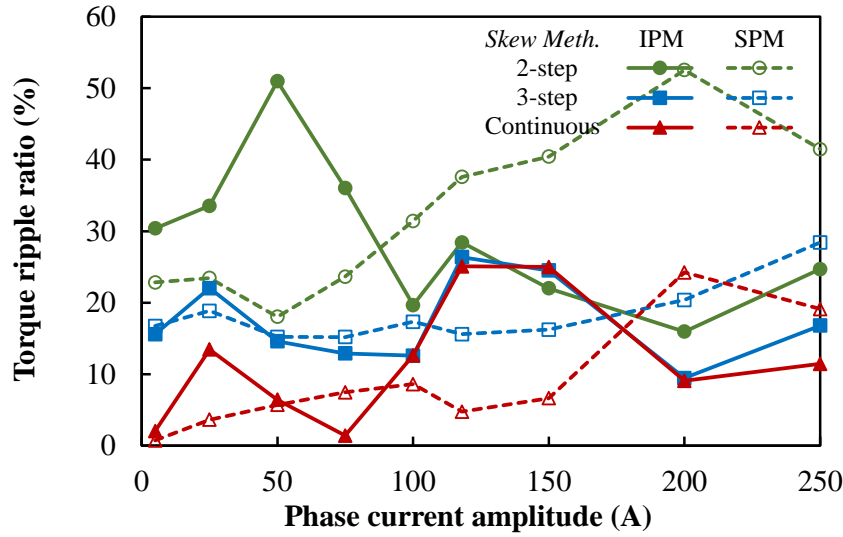


(b) Torque ripple

Fig. 6.31 Variations of average torque and torque ripple with phase current amplitude in DTP IPMSM and SPMSM with rotor continuous, 2-step, and 3-step skew methods.



(a) Average torque ratio



(b) Torque ripple ratio

Fig. 6.32 Variations of average torque and torque ripple ratios with phase current amplitude in DTP IPMSM and SPMSM with rotor continuous, 2-step, and 3-step skew methods.

6.6 Experimental Validation

In this chapter, the investigations are conducted based on the calculation results obtained by 2D FE method in JMAG. As mentioned above, to avoid errors in modelling and FE analysis, it is ideal to experimentally validate at least one model in the investigation.

Fortunately, the benchmark DTP IPMSM is the Toyota Prius 2010 machine equipped with DTP-DS windings, which was proposed and tested in Chapter 3. In Section 3.7, a good agreement between 2D FE and tested results was observed, and hence, the conclusions obtained from 2D FE analyses of the benchmark DTP PMSMs in this chapter are also reliable.

6.7 Conclusion

The influences of load on the effectiveness of rotor continuous and step skews in DTP interior and surface PMSMs are investigated based on 48-slot/8-pole DTP IPMSM and SPMSM. The DTP-DS winding configuration is chosen for the benchmark DTP IPMSM and SPMSM. The results obtained in DTP PMSMs are compared with those in STP PMSMs as well. The analyses show that similar to the conclusion obtained in STP PMSMs, for DTP PMSMs, the effectiveness of rotor skew on torque ripple reduction also depends on electric loading and magnetic saturation, and it is less effective in DTP IPMSM than in DTP SPMSM. Since the 6th torque harmonics in STP PMSMs are completely eliminated by the DTP winding configuration, the dominant torque harmonics in DTP PMSMs are the 12th harmonics, and hence, the conventional skew angles are 30° in DTP PMSMs. Compared with the optimal skew angles obtained from the analyses, it is further found that the conventional skew angle is only suitable for DTP SPMSM under normal load condition (from light-load, heavy-load to full-load conditions). For DTP SPMSM under over-load condition and DTP IPMSM under all load conditions, optimal skew angles are different from the conventional skew angle and need to be re-calculated according to load conditions.

CHAPTER 7

ANALYSIS OF TORQUE CHARACTERISTICS IN DUAL THREE-PHASE PMSMS WITH ASYMMETRIC IPM ROTOR

In this chapter, torque characteristics of dual three-phase (DTP) permanent magnet synchronous machines (PMSMs) with asymmetric interior permanent magnet (AIPM) rotors are investigated and compared with those with symmetrical interior permanent magnet (IPM) rotors. Electromagnetic performances of DTP PMSMs with symmetrical and asymmetric IPM rotors are compared in many aspects, including air-gap flux density, back EMF, cogging torque, torque, loss, and efficiency. It is found that in DTP PMSMs, AIPM rotors can achieve significant torque improvements under both healthy and single three-phase open-circuit conditions. A prototype is fabricated and tested to verify the theoretical analyses.

7.1 Introduction

In recent years, multi-phase PMSMs have been widely researched due to their advantages of high power/torque density, high efficiency, reduced current/power rating per phase, and enhanced fault-tolerance capability [JAH95] [ZHU07] [LEV08] [ZHU21a]. Compared with other types of multi-phase PMSMs, dual three-phase (DTP) PMSMs have attracted more attention since commercial standard three-phase inverters can be employed directly and the control strategy is relatively easier in DTP PMSMs [BAR11b], [ZHE13] [XU18]. In addition, considering the independent two winding sets in DTP PMSMs, the faults in one three-phase winding set will not lead to the full loss of torque output and the fault-tolerant control strategy in DTP PMSMs is also easier than other multi-phase PMSMs [BAR11b] [ZHE12].

Regardless of winding configuration, the rotors in DTP PMSMs can be generally classified into surface permanent magnet (SPM) rotors [BAR10] [ZHE12] [ZHE13] [ABD15] [DEM16] [XU18] [XU19] [FEN22] [LI19c] [LI20a] and interior permanent magnet (IPM) rotors [BAR10] [PAT14] [CHE18] [ZHU19]. Compared with IPM rotors, the PMs in SPM rotors are placed closer to air-gap and the flux leakages in SPM rotors are smaller, and hence, SPM rotors usually feature with high torque density [BAR10]. However, the d- and q-axis inductances are

almost the same in SPM rotors. Thus, SPM rotors cannot produce reluctance torque, and due to low winding inductance, PMSMs with SPM rotors usually suffer from low flux-weakening capacities [ABD16a]. In IPM rotors, the existence of rotor saliency makes it possible to utilize both PM torque and reluctance torque at the same time [CHE18] [ZHU19]. What is more, the PMs in IPM rotors are buried in rotor cores, there is no need to consider glass/carbon fibre-banding under high-speed conditions. Thus, IPM rotors are especially suitable for variable-speed applications, such as electric vehicles [PAT14] [ZHU19].

To further improve the torque performances of PMSMs with IPM rotors, asymmetric IPM (AIPM) rotor topologies were introduced in some papers [ZHA14] [ZHA15a] [ZHA15b] [ZHA17b] [ZHA18b] [XIN19] [ALS16] [LIU17] [YAN17b] [YAN19b] [ZEN19] [JI19] [XIA20] [XIA21] [XIA22]. In [ZHA14] and [XIA20], the adoption of assisted flux barriers in V-type IPM machines displaces the axis of reluctance torques, which increases the average torque. In [ZHA15a] [XIN19] [YAN19b] [JI19], the asymmetric magnet and flux barrier were optimized synchronously in PM assisted synchronous reluctance machines. The axes of the PM and reluctance torque components can also be shifted closer by combining different types of rotor topologies [ZHA15b] [ZHA17b] [ZHA18b] [ALS16] [LIU17] [ZEN19] [XIA22]. For example, the asymmetric inset SPM rotor structures introduced in [ZHA15b] and [ALS16] can be seen as compositions of SPM rotor and reluctance rotor. In addition, besides in circumferential direction, SPM rotor and reluctance rotor can also be composed together in axial direction [YAN17b] [ZHA17b] [ZHA18b]. Besides the combination of SPM and reluctance rotors, asymmetric rotors can also be combined by SPM and IPM rotors [LIU17] or by different types of IPM rotors (e.g. I-type and spoke-type PMs in [ZEN19], V-type and spoke-type PMs in [XIA22]). All these asymmetric rotor designs can shift the reluctance torque axis closer to PM torque axis in PMSMs, and thus, utilization ratios of PM and reluctance torque components can be improved simultaneously.

However, all existing papers only focus on conventional single three-phase (STP) winding configuration, the effects of AIPM rotors on electromagnetic characteristics in DTP PMSMs have not been analysed before. Therefore, this chapter aims to fill the gap by investigating and comparing the influences of IPM and AIPM rotors on electromagnetic performances in DTP PMSMs. Both healthy and single three-phase open-circuit (3-ph OC) conditions are considered.

This chapter is organized as follows. In Section 7.2, the topologies and working principles of the analysed DTP PMSMs with IPM and AIPM rotors are described. Then, the electromagnetic performances of DTP PMSMs with IPM and AIPM rotors are compared under healthy condition in Section 7.3, and under 3-ph OC condition in Section 7.4. In Section 7.5, a prototype of DTP PMSM with AIPM rotor was fabricated and tested to verify the analyses. Finally, some conclusions are drawn in Section 7.6.

7.2 Machine Configuration and Operation Principle

In this chapter, the effects of AIPM rotors in DTP PMSMs are investigated based on Toyota Prius 2010 machine and the results are compared with those obtained with the original symmetrical IPM rotor. Considering that the original windings of Toyota Prius 2010 machine are STP windings, the DTP winding configuration for Toyota Prius 2010 machine will also be introduced in this section.

7.2.1 Machine Configuration

For the benchmark PMSM, Toyota Prius 2010 machine, the slot/pole number combination is 48-slot/8-pole, and the original armature windings are single-layer short-pitched STP windings [BUR11]. Compared with STP winding configuration, DTP winding configuration with 30° phase shift can improve average torque and reduce torque ripples inherently. Hence, to enhance the torque performance of the original Toyota Prius 2010 machine, two DTP winding configurations (DTP-SF and DTP-DS) were proposed and compared in Chapter 3 and [WAN22]. In this chapter, the single-layer full-pitched DTP (DTP-SF) winding configuration is selected for further analyses due to its advantages of enhanced average torque capability and easier manufacture. The winding arrangement and the coil electromotive force (EMF) phasor diagram of the single-layer full-pitched DTP windings are shown in Fig. 7.1(a) and (b), respectively. The phase shift angle, 30° , can be observed clearly from the coil EMF phasor diagram in Fig. 7.1(b).

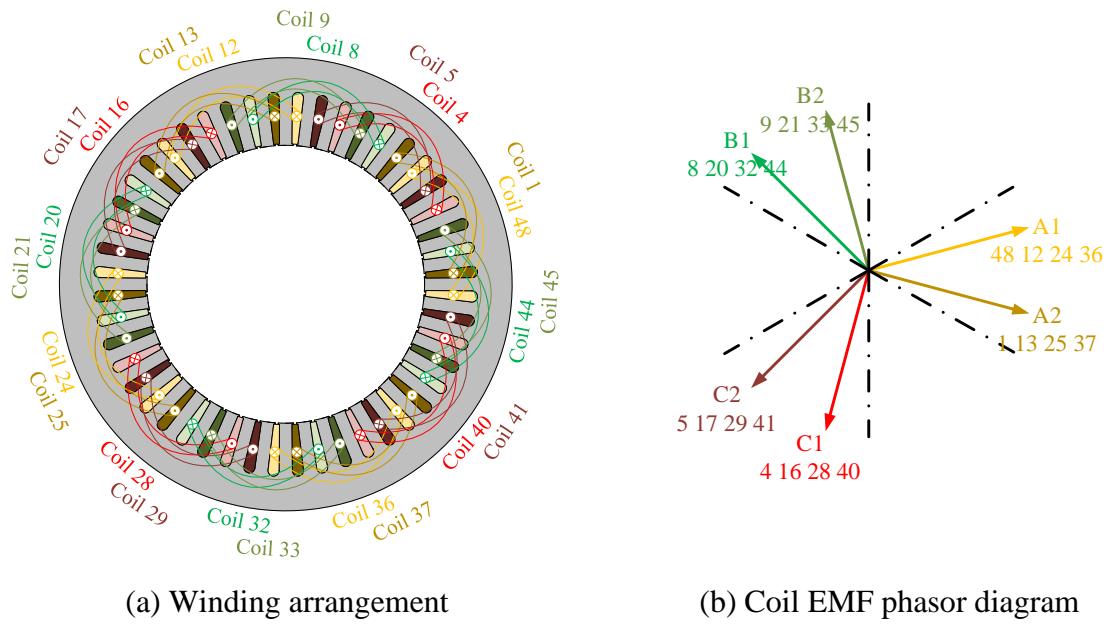


Fig. 7.1 Winding configuration of DTP windings in benchmark PMSM.

The AIPM rotor analysed in this chapter was firstly proposed in [XIA21], which was also designed based on Toyota Prius 2010 machine, and featured with skewed V-type PMs and flux barriers outside PMs. The cross-sections of the benchmark DTP PMSMs with the original symmetrical IPM rotor (designated as IPM rotor in the rest of this chapter) and the AIPM rotor are illustrated in Fig. 7.2(a) and (b), respectively. The detailed geometric dimensions of Toyota Prius 2010 machine, including the stator and the IPM rotor and the AIPM rotor can be found from [BUR11] and [XIA21], respectively, and some key geometric parameters are listed in Table 7.1 for convenience.

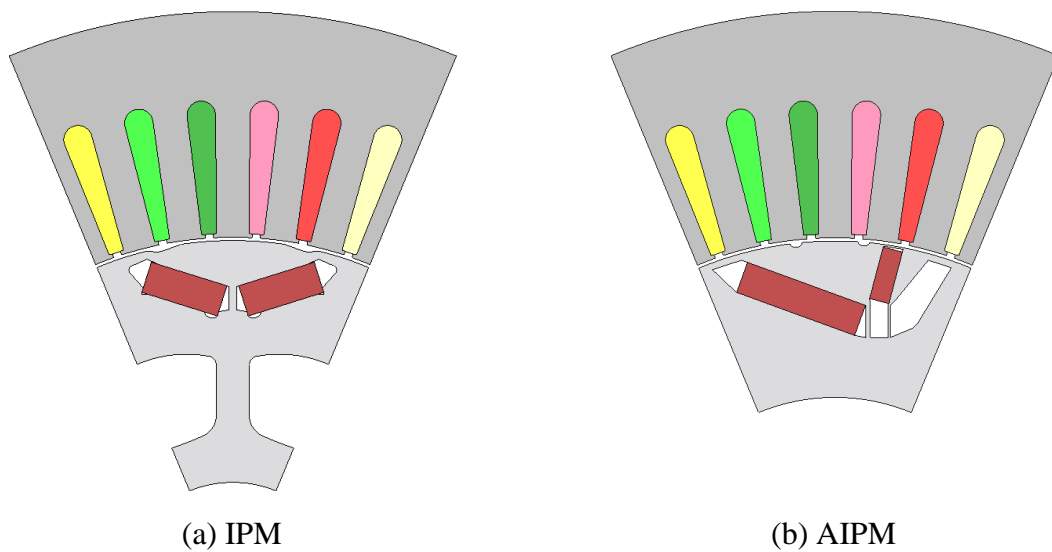


Fig. 7.2 Cross-sections of DTP PMSMs with IPM and AIPM rotors.

Table 7.1 Main design specifications of benchmark PMSMs

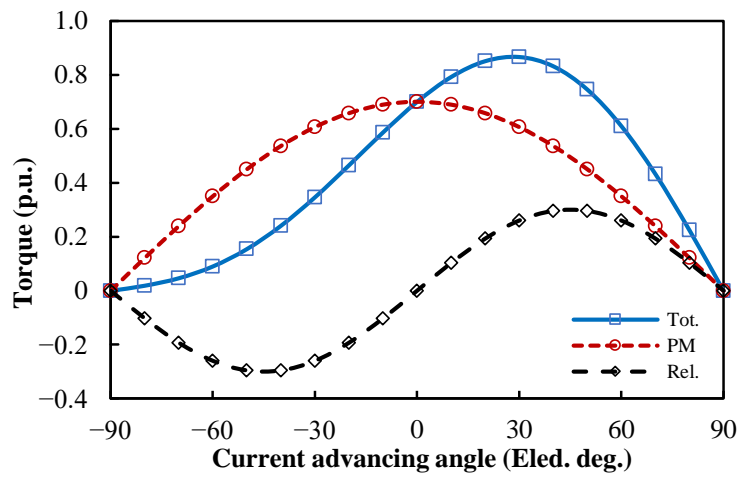
| Parameters | Values |
|--------------------------|--------|
| Stator | |
| Stator OD, mm | 264 |
| Stator ID, mm | 161.9 |
| Stack length, mm | 50.8 |
| Slot depth, mm | 30.9 |
| Slot opening, mm | 1.88 |
| IPM rotor | |
| Rotor OD, mm | 160.4 |
| Rotor ID, mm | 51 |
| Stack length, mm | 50.8 |
| PM length, mm | 17.88 |
| PM thickness, mm | 7.16 |
| PM remanence, T | 1.2 |
| PM relative permeability | 1.05 |
| AIPM rotor | |
| Rotor OD, mm | 160.4 |
| Rotor ID, mm | 90 |
| Stack length, mm | 50.8 |
| Large PM length, mm | 28.3 |
| Large PM thickness, mm | 7.2 |
| Small PM length, mm | 12 |
| Small PM thickness, mm | 4.5 |
| PM remanence, T | 1.2 |
| PM relative permeability | 1.05 |

7.2.2 Operation Principle

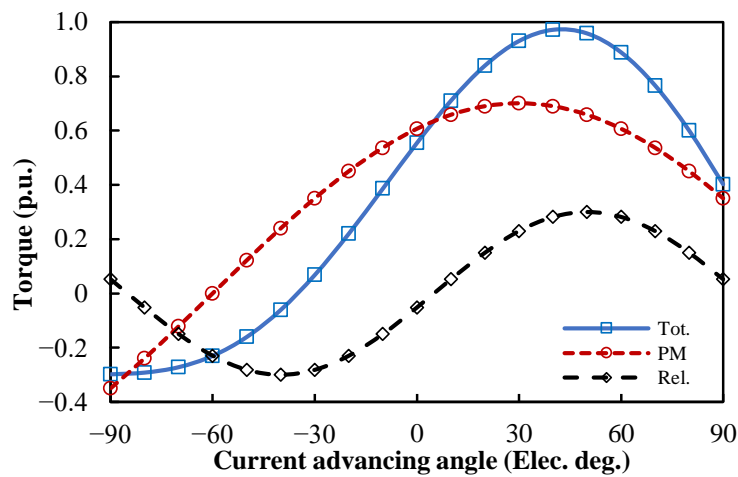
The operation principle of STP PMSMs with AIPM rotors was introduced in detail in [ZHU22]. Although the winding configurations of DTP PMSMs are different from those of STP counterparts, the output torques of DTP and STP PMSMs are both composed by PM and reluctance torque components. PM torque component is produced by the interaction between armature windings and PM magnetic field, while reluctance torque is produced due to rotor saliency. Thus, the operation principle of DTP PMSMs with AIPM rotors is still identical to that of STP PMSMs.

Compared with IPM rotor, AIPM rotor shifts the axis of PM magnetic field and changes rotor saliency simultaneously. Hence, the optimal current advancing angles for the maximum

average torque in DTP IPM machines are no longer suitable for DTP AIPM machines. With appropriate AIPM rotor designs, the optimal current advancing angles for the maximum PM and reluctance torque components can be much closer to each other. Thus, compared with IPM machine, PM and reluctance torque components can be utilized more effectively with the same current advancing angle in AIPM machine. To further illustrate the difference between the torque components in PMSMs with IPM and AIPM rotors, the torque components versus current advancing angle characteristics in PMSMs with IPM and AIPM rotors are plotted in Fig. 7.3. Compared with IPM counterpart, the magnetic field shifting (MFS) effect caused by AIPM rotor makes it possible for AIPM machine to produce higher average torque. In the researched AIPM rotor, as shown in Fig. 7.2(b), the different sizes of two interior PMs and the extra flux barrier can make the MFS effect even more evident.



(a) IPM



(b) AIPM

Fig. 7.3 Torque components of PMSMs with different rotors.

7.3 Electromagnetic Performance under Healthy Condition

In this section, the electromagnetic performances of the benchmark DTP PMSMs with IPM and AIPM rotors are compared, including air-gap flux density, back EMF, cogging torque, torque, loss, and efficiency. It should be mentioned that all the analyses presented below are based on the results obtained from JMAG-Designer by using 2-demenision (2D) finite element (FE) method.

7.3.1 Open-Circuit Characteristics

The flux density and flux line distributions of the DTP PMSMs with IPM and AIPM rotors under OC condition are firstly calculated and compared, as shown in Fig. 7.4 and Fig. 7.5, respectively. In Fig. 7.5, due to the middle small magnet and the outside flux barrier in one AIPM rotor pole, the closed flux lines around the small magnet can be observed.

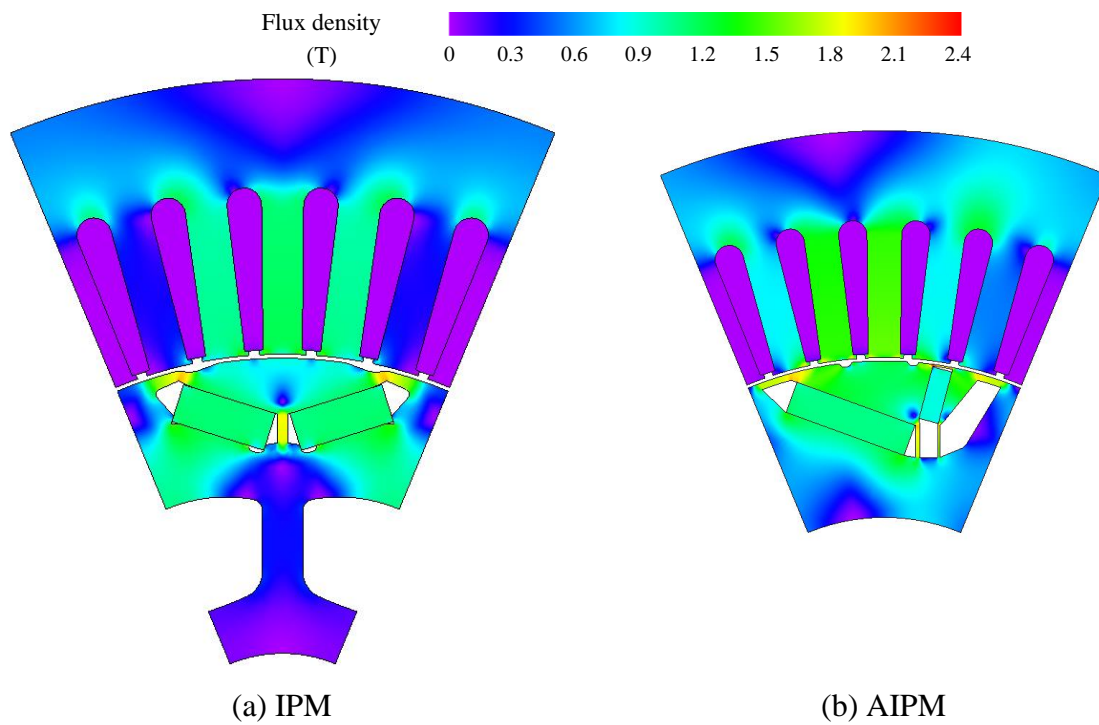


Fig. 7.4 Flux density distributions of DTP PMSMs with different rotors under OC condition.

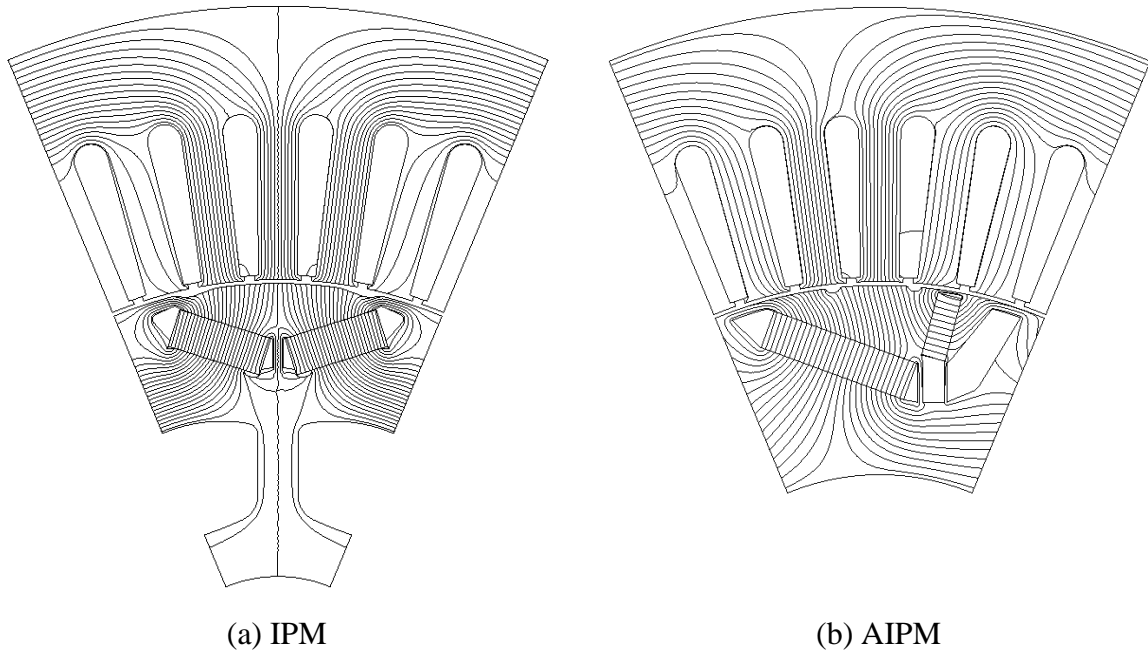
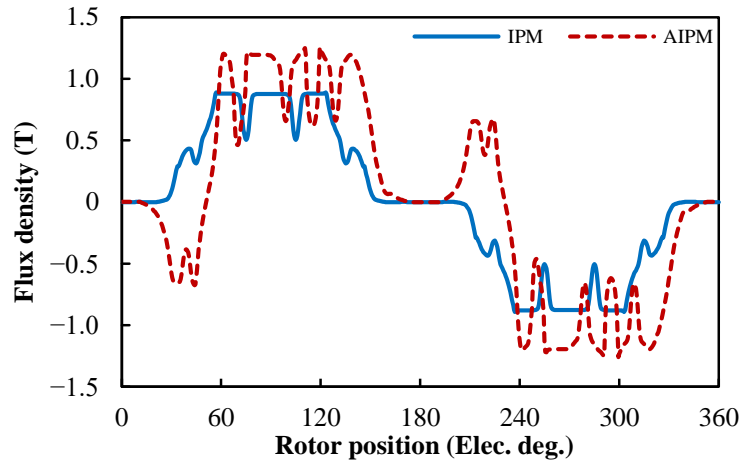
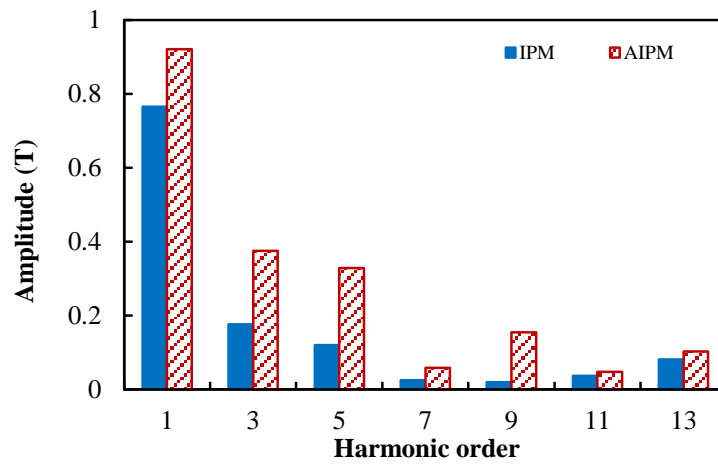


Fig. 7.5 Flux line distributions of DTP PMSMs with different rotors under OC condition.

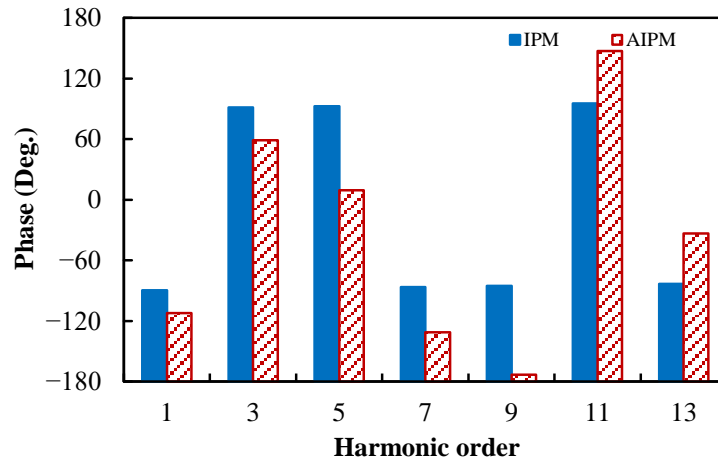
The waveforms and spectra of the radial air-gap flux densities under OC condition are shown in Fig. 7.6(a) and (b). In Fig. 7.6(a), the fluctuations in the waveform of AIPM machine can be explained by the closed flux lines around small magnets in AIPM rotor. From Fig. 7.6(b), it can be clearly seen that AIPM rotor has higher fundamental component, which can be attribute to the flux-focusing effect caused by the flux barrier in the AIPM rotor. However, AIPM machine also shows more harmonic contents compared with IPM counterpart, which may result in larger eddy current loss in AIPM machine. Hence, the flux density distributions of the benchmark PMSMs under OC condition suggest that the loss and efficiency of the DTP PMSMs with IPM and AIPM rotors need more attention in the following analyses.



(a) Waveforms



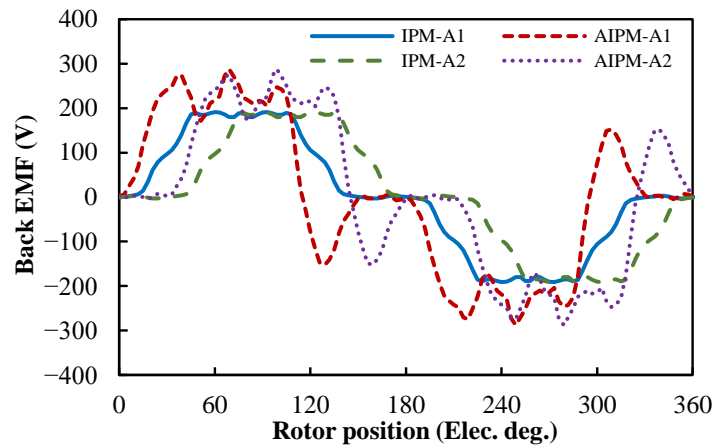
(b) Spectra (Amplitude)



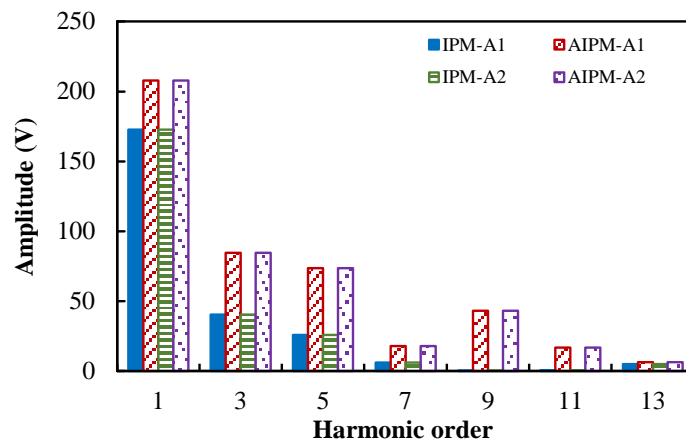
(c) Spectra (Phase)

Fig. 7.6 Radial air-gap flux densities of DTP PMSMs machines with different rotors under OC condition.

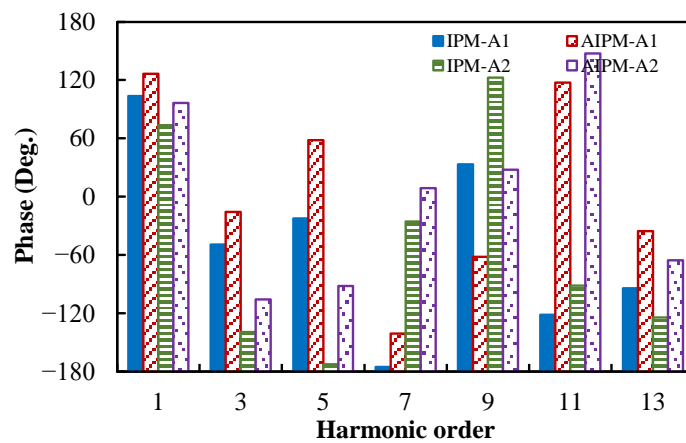
Assuming rotor speed is 3000rpm, the waveforms and spectra of phase back electromotive forces (EMFs) of Phases A1 and A2 are shown in Fig. 7.7. From Fig. 7.7(b), it can be seen that similar to the conclusions obtained from air-gap flux densities, the amplitude of the fundamental back EMF in AIPM machine is about 20% higher than that in the IPM machine.



(a) Waveforms



(b) Spectra (Amplitude)



(c) Spectra (Phase)

Fig. 7.7 Phase back EMFs of DTP PMSMs with different rotors at 3000rpm.

For DTP PMSMs with IPM and AIPM rotors, the waveforms and spectra of the cogging torques are given in Fig. 7.8(a) and (b). Due to the same slot/pole number combination, the fundamental orders of cogging torque in IPM and AIPM machines are exactly the same, which is 48 in mechanical angle (the smallest common multiple between slot number, 48, and pole number, 8) and 12 in electric angle [ZHU00], but the amplitudes of the same harmonic order are different in IPM and AIPM machines. In the researched DTP PMSMs, the cogging torque produced by AIPM rotor is much larger than that produced by IPM rotor.

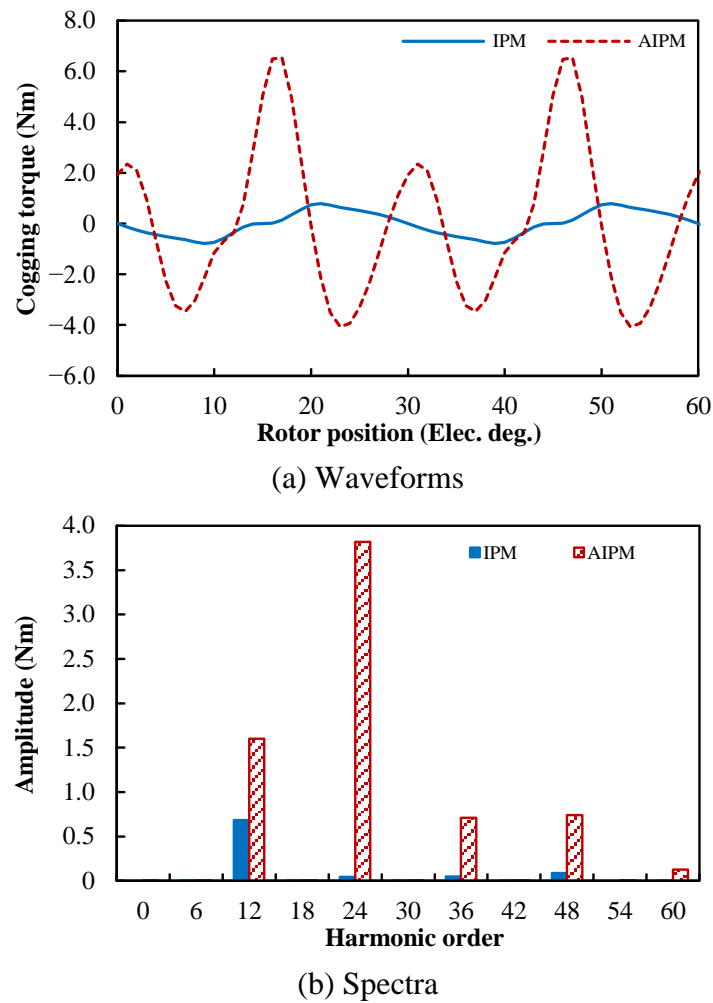


Fig. 7.8 Cogging torques of DTP PMSMs with different rotors.

7.3.2 Torque Characteristics

7.3.2.1 Torque Component-Current Advancing Angle Characteristics

Since the most featured difference between IPM and AIPM machines lies in the torque components-current advancing angle characteristics, the variations of PM and reluctance

torque components with current advancing angle in DTP IPM and AIPM machines are compared firstly in this sub-section. As discussed in Section 3.2, considering that the maximum phase current amplitude in the original STP Toyota Prius 2010 machine is 236A and winding turns are doubled in DTP benchmark machines, the maximum phase current amplitude for DTP PMSMs is 118A.

In DTP PMSMs with IPM and AIPM rotors, the variations of average torque with current advancing angle under the condition with $I_{A1} = 118A$ are firstly plotted in Fig. 7.9. It can be seen that in IPM and AIPM machines, the maximum average torques are obtained with current advancing angle = 53° , and 62° , respectively. With the help of frozen permeability method [CHU13a] [CHE14b] [WAN20a], PM and reluctance torque components can be separated from total average torque, and thus, the variations of PM and reluctance torque components with current advancing angle are also presented in Fig. 7.9. It can be found that the optimal current advancing angles for the maximum PM torque component are 24° in IPM machine, and 53° in AIPM machine. While the optimal current advancing angles for the maximum reluctance torque component are 58° in IPM machine, and 65° in AIPM machine. The optimal current advancing angles for different torque components are summarized in Table 7.2. It can be seen that in IPM machine, the difference between the optimal current advancing angles for the maximum PM and reluctance torque components is 34° , but in AIPM machine, the difference is only 12° . In other words, compared with DTP IPM machine, PM and reluctance torque components can be better utilized by using AIPM rotor.

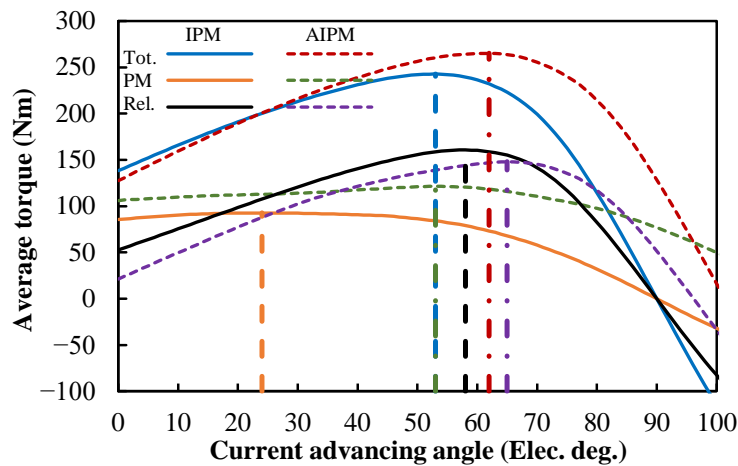


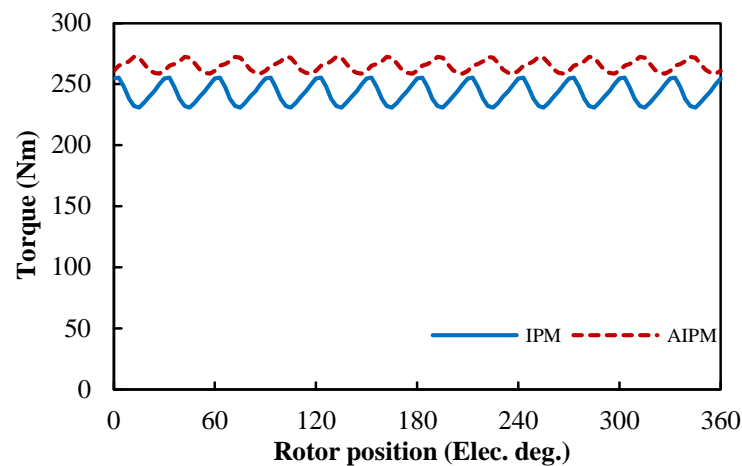
Fig. 7.9 Torque component-current advancing angle characteristics of DTP PMSMs with IPM and AIPM rotors ($I_{A1} = 118A$).

Table 7.2 Maximum torque components and optimal current advancing angles of DTP PMSMs with IPM and AIPM rotors ($I_{Al} = 118\text{A}$)

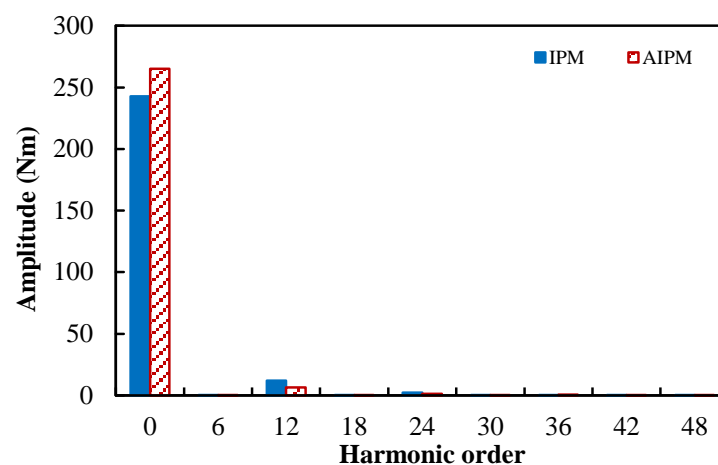
| Torque component | Maximum value (Nm) | | Optimal current advancing angle ($^{\circ}$) | |
|------------------|--------------------|--------|--|------|
| | IPM | AIPM | IPM | AIPM |
| Tot. torque | 242.77 | 265.22 | 53 | 62 |
| PM torque | 92.73 | 121.40 | 24 | 53 |
| Rel. torque | 160.70 | 147.87 | 58 | 65 |

7.3.2.2 Instantaneous Torque Characteristics under Maximum Torque Condition

From Fig. 7.9 and Table 7.2, the optimal current advancing angles for the maximum average torque are 53° , and 62° respectively, in IPM and AIPM machines. With the optimal current advancing angles, the waveforms and spectra of the instantaneous torque in DTP PMSMs with IPM and AIPM rotors under maximum torque condition are shown in Fig. 7.10.



(a) Waveforms



(b) Spectra

Fig. 7.10 Instantaneous torque waveforms and spectra of DTP PMSMs with IPM and AIPM rotors ($I_{Al} = 118\text{A}$ pk).

Based on Fig. 7.10, the average torque and torque ripple characteristics of PMSMs under this condition are summarized in Table 7.3. It can be seen that compared with DTP IPM machine, AIPM rotor can increase average torque by 9.25% and reduce torque ripple by 47.62% under this condition. Furthermore, since the researched DTP PMSMs are modified from the benchmark machines proposed in [XIA21] by changing winding configurations. The torque characteristics of STP PMSMs with IPM and AIPM rotors under maximum torque condition provided in [XIA21], as shown in Table 7.4, are comparable to the results obtained in this chapter. It can be seen that in STP PMSMs, AIPM rotor can increase average torque by 8.35% and reduce torque ripple by 34.08% under maximum torque condition. Hence, compared with STP counterpart, DTP PMSM can achieve better improvement in average torque and more reduction in torque ripple by employing AIPM rotor.

Table 7.3 Torque characteristics of DTP IPM and AIPM machines ($I_{A1} = 118\text{Apk}$)

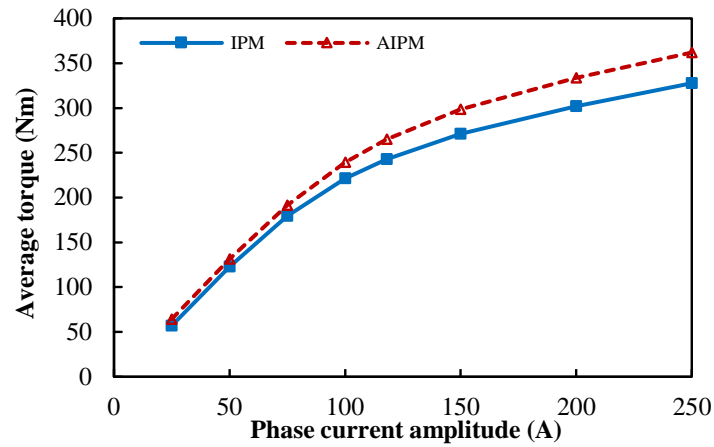
| | IPM | AIPM | Change |
|----------------------|--------|--------|---------|
| Average torque (Nm) | 242.77 | 265.22 | +9.25% |
| Peak-peak value (Nm) | 24.28 | 13.89 | -42.78% |
| Torque ripple (%) | 10.00 | 5.24 | -47.62% |

Table 7.4 Torque characteristics of STP IPM and AIPM machines ($I_A = 236\text{Apk}$)

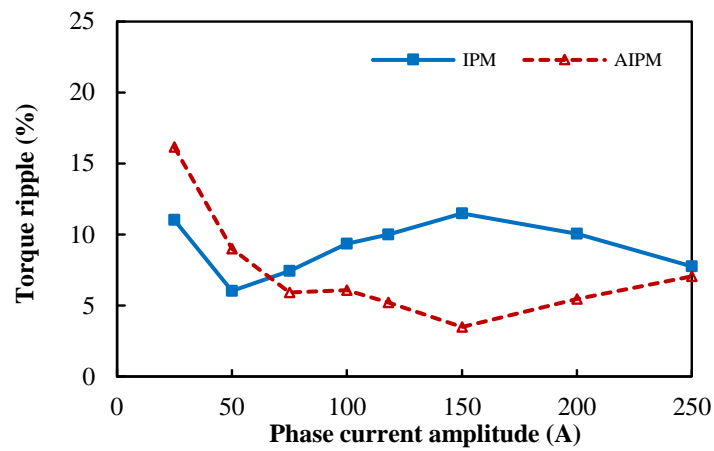
| | IPM | AIPM | Change |
|----------------------|--------|--------|---------|
| Average torque (Nm) | 236.50 | 256.26 | +8.35% |
| Peak-peak value (Nm) | 35.99 | 25.71 | -28.58% |
| Torque ripple (%) | 15.22 | 10.03 | -34.08% |

7.3.2.3 Average Torque and Torque Ripple–Current Amplitude Characteristics

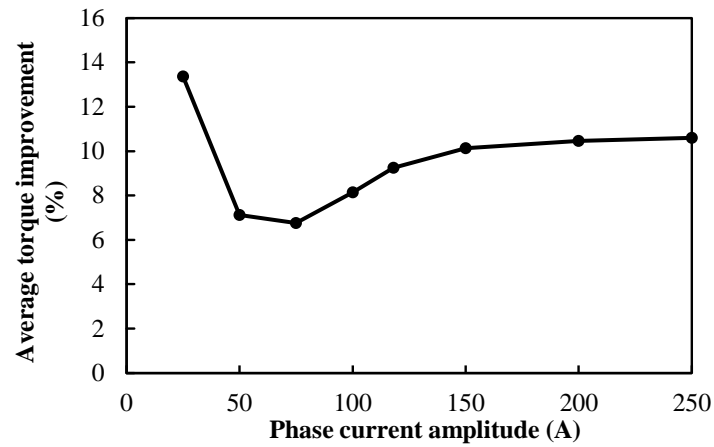
In the researched DTP IPM and AIPM machines, assuming I_{A1} varies from 25Apk to 250Apk to cover the load conditions from light-load to over-load, the optimal current advancing angles for different phase current amplitudes in DTP IPM and AIPM machines can also be obtained by using the maximum torque per amplitude (MTPA) control strategy. Thus, the variations of average torques and torque ripples with phase current amplitude are obtained as shown in Fig. 7.11(a) and (b), respectively. It can be seen that the average torque of DTP PMSM can always be improved significantly by using AIPM rotor and the variation of average torque improvement with phase current amplitude is also presented in Fig. 7.11(c). In addition, from Fig. 7.11(b), when phase current $\geq 75\text{Apk}$, not only the average torque can be improved, the torque ripple can also be reduced by employing AIPM rotor. Hence, AIPM rotor can greatly improve the torque performance of DTP PMSM under different load conditions.



(a) Average torque



(b) Torque ripple

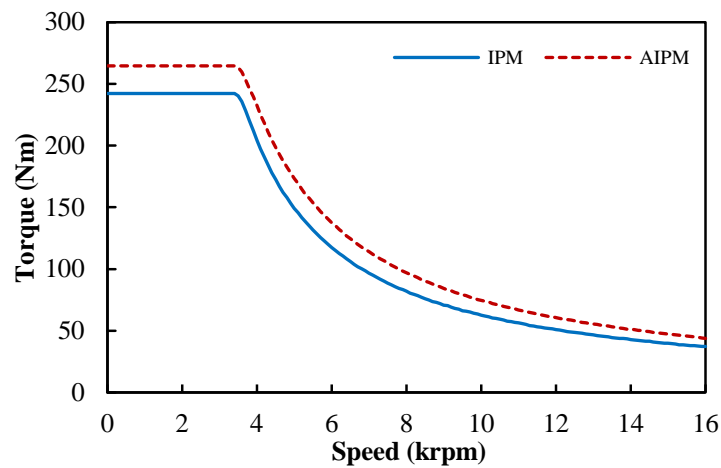


(c) Average torque improvement

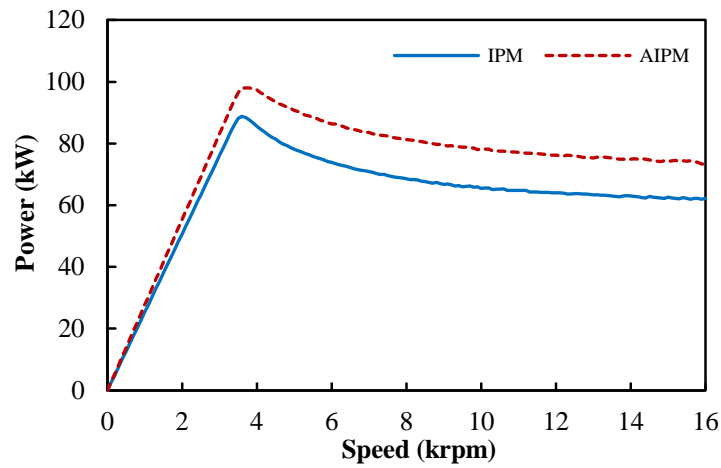
Fig. 7.11 Variations of torque characteristics with phase current amplitude in DTP PMSMs with IPM and AIPM rotors when using MTPA strategy.

7.3.2.4 Torque- and Power-Speed Characteristics

To analyse the torque performance of DTP PMSMs with IPM and AIPM rotors at other speeds, the torque and power-speed curves of DTP IPM and AIPM PMSMs are calculated under the constraints (DC-side voltage $\leq 650\text{Vdc}$ and phase current $\leq 118\text{A}$), as shown in Fig. 7.12. The variations of d - and q -axis currents (I_d and I_q), and phase currents (I_a) with speed are shown in Fig. 7.13. From Fig. 7.12, it can be clearly seen that AIPM machine can produce higher torque than the IPM counterpart over the entire speed range.

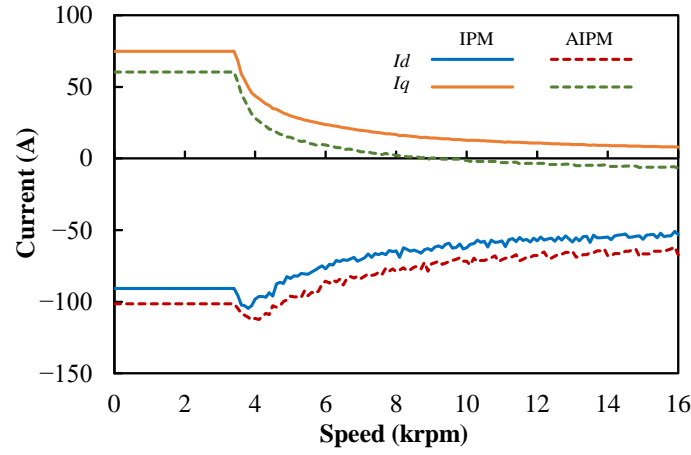


(a) Torque-speed curves

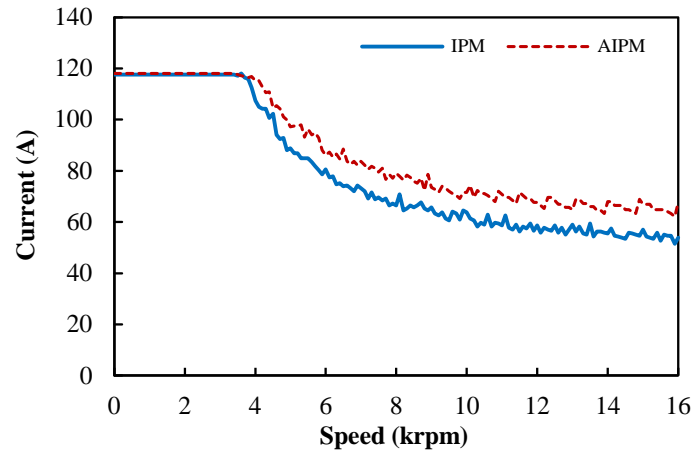


(b) Power-speed curves

Fig. 7.12 Torque and power-speed curves of DTP PMSMs with IPM and AIPM rotors.



(a) I_d - and I_q -speed curves



(b) I_a -speed curves

Fig. 7.13 Current-speed curves of DTP PMSMs with IPM and AIPM rotors.

7.3.3 Loss and Efficiency

7.3.3.1 Loss and Efficiency under Maximum Torque Condition

As introduced in Section 3.3, the losses in DTP PMSMs with IPM and AIPM rotors are classified into copper loss, iron loss, PM eddy current loss, and mechanical loss.

Copper loss is calculated by using Joule's law, as

$$P_{Cu} = 3R_0 I_a^2 \quad (7.1)$$

where R_0 is the phase resistance of the DTP windings, and I_a is the phase current amplitude.

For the conditions with speed = 3000rpm, iron losses, including hysteresis and eddy current iron losses, are obtained directly from JMAG-Designer. For other speeds, iron losses are estimated based on the iron losses obtained at 3000rpm, as

$$P_{Fe} = P_{Hyst-base} \frac{f}{f_{base}} + P_{Eddy-base} \left(\frac{f}{f_{base}} \right)^2 \quad (7.2)$$

where $P_{Hyst-base}$ and $P_{Eddy-base}$ are the hysteresis and eddy current iron losses at the base speed. f and f_{base} are the frequencies of the operating condition and the base speed.

PM eddy current losses are obtained from JMAG-Designer directly as well, and mechanical losses are estimated by [HSU04]

$$P_{Me} = 0.26f + 0.00103f^2 \quad (7.3)$$

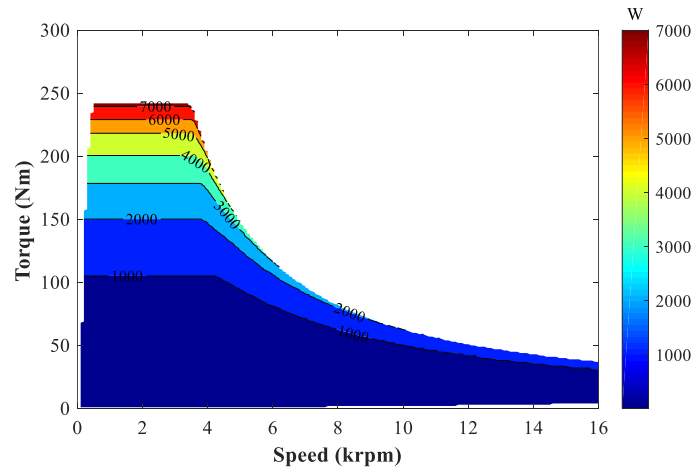
Overall, the loss and efficiency characteristics of DTP PMSMs with IPM and AIPM rotors under maximum torque condition ($I_{Al} = 118\text{Apk}$, speed = 3000rpm) are summarized and compared in Table 7.5. It can be seen that copper loss is the most dominant loss in both IPM and AIPM machines. Since IPM and AIPM machines share the same stator and armature windings, the copper losses of the two DTP PMSMs are identical. Due to similar iron losses in IPM and AIPM machines, and the slightly higher PM eddy current loss in AIPM machine, the total loss in AIPM machine is only slightly higher than that in IPM counterpart. However, considering that the output torque and output power of the AIPM machine is obviously larger than those of IPM counterpart, and AIPM machine still has higher overall efficiency than IPM counterpart under maximum torque condition.

Table 7.5 Loss and efficiency of DTP PMSMs with IPM and AIPM rotors ($I_{al} = 118\text{Apk}@3000\text{rpm}$)

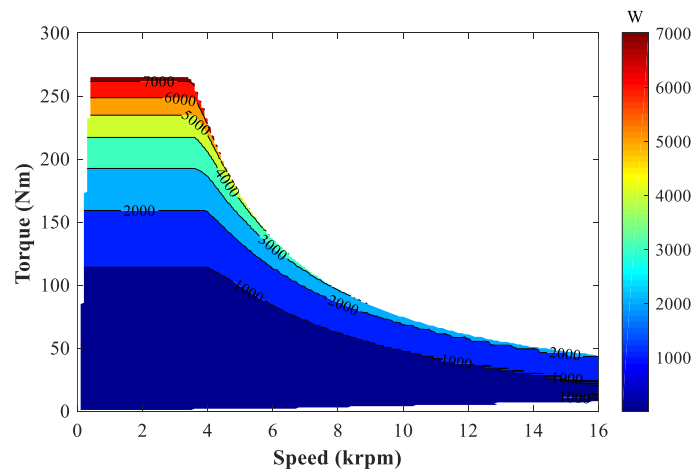
| | IPM | AIPM |
|----------------------------|---------|---------|
| Average output torque (Nm) | 242.76 | 265.21 |
| Output power (kW) | 76.27 | 83.32 |
| Copper loss (W) | 7283.49 | 7283.49 |
| Stator iron loss (W) | 338.27 | 325.81 |
| Rotor iron loss (W) | 28.62 | 27.49 |
| Total iron loss (W) | 366.89 | 353.30 |
| PM eddy current loss (W) | 63.28 | 86.05 |
| Mechanical loss (W) | 93.20 | 93.20 |
| Total loss (kW) | 7.81 | 7.82 |
| Efficiency (%) | 90.71 | 91.42 |

7.3.3.2 Loss and Efficiency Maps

Based on (7.1), (7.2), Fig. 7.12, and Fig. 7.13, the copper loss and iron loss maps of DTP PMSMs with IPM and AIPM rotors can be calculated, as shown in Fig. 7.14 and Fig. 7.15, respectively.



(a) IPM



(b) AIPM

Fig. 7.14 Copper loss maps of DTP PMSMs with IPM and AIPM rotors.

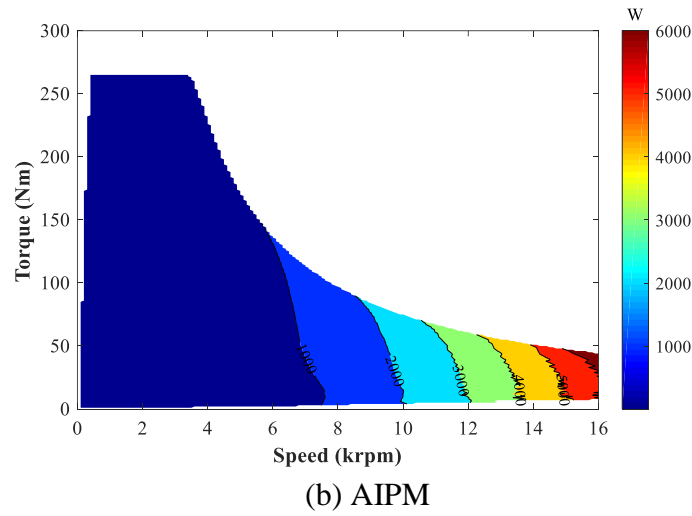
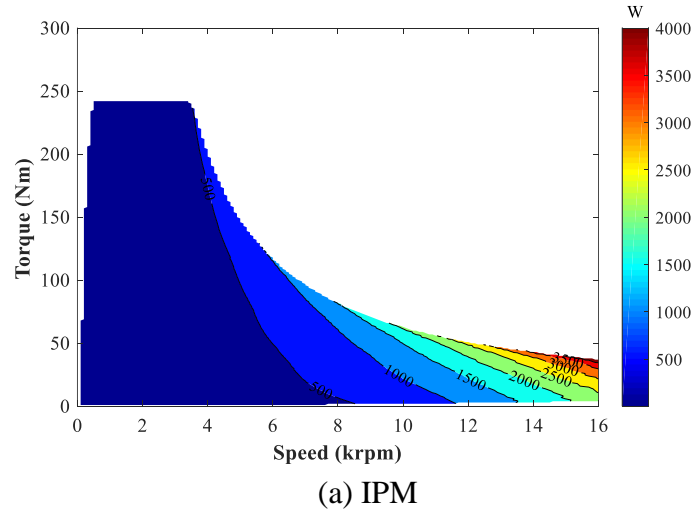


Fig. 7.15 Iron loss maps of DTP PMSMs with IPM and AIPM rotors.

The mechanical losses of DTP IPM and AIPM machines at different speeds can be calculated by using (7.3), as shown in Fig. 7.16.

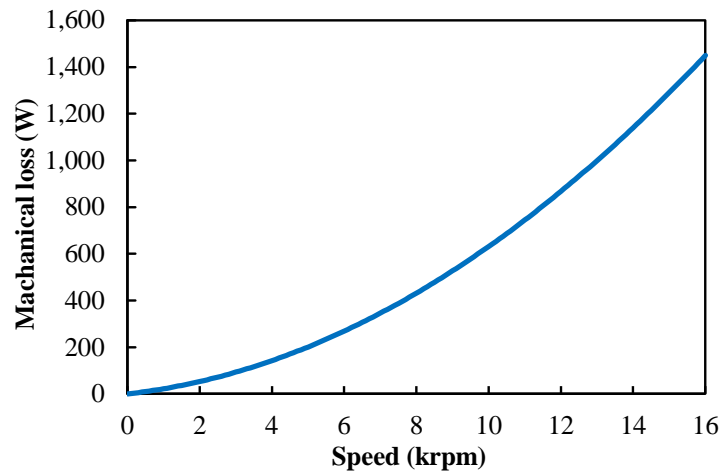
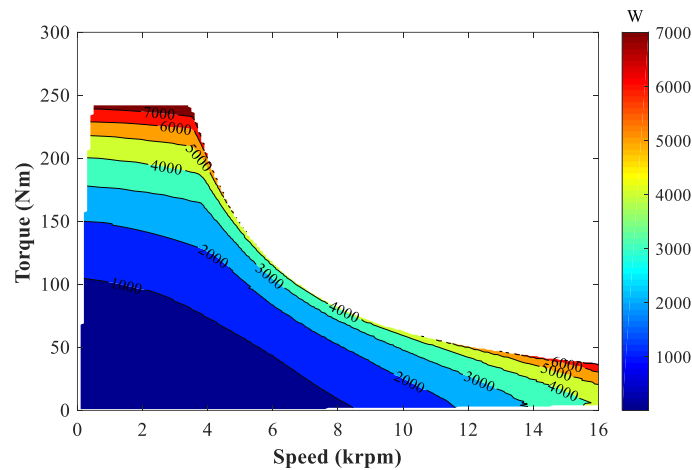
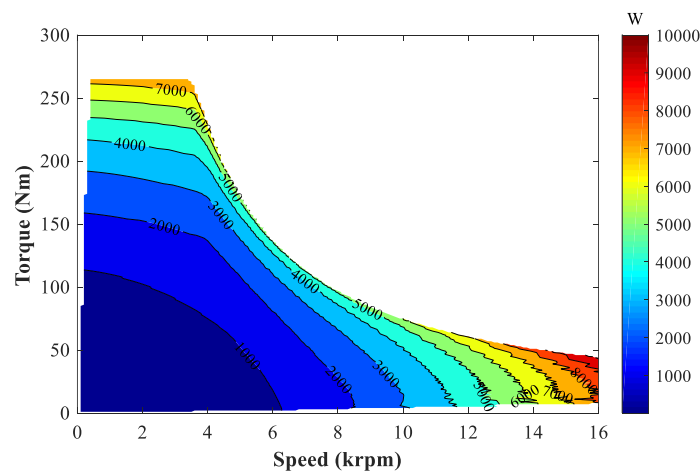


Fig. 7.16 Mechanical loss of DTP PMSMs with IPM and AIPM rotors.

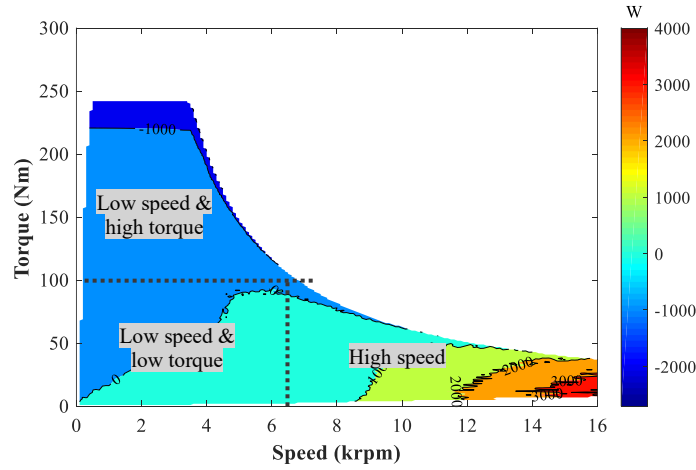
Considering that PM eddy current loss at other speeds cannot be estimated directly from base speed and PM eddy current loss is very small in total loss, as indicated in Table 7.5, the ignorance of PM eddy current loss in the calculation of resultant efficiency is still acceptable. Thus, when ignoring PM eddy current loss, the total loss maps of the DTP IPM and AIPM machines can be obtained from Fig. 7.14, Fig. 7.15, and Fig. 7.16, as shown in Fig. 7.17. The total loss difference between AIPM and IPM machines is also given in Fig. 7.17(c). In Fig. 7.17(c), the operating conditions can be classified into three conditions, i.e., low speed & low torque, low speed & high torque, and high speed conditions. It can be observed that under high speed conditions, iron loss is the dominant loss and the AIPM machine has higher total loss, while under low speed & high torque conditions, copper loss is the dominant loss and the IPM machine has higher total loss. Under low speed & low torque conditions, the AIPM and IPM machines show similar total losses.



(a) IPM



(b) AIPM



(c) Total loss difference (AIPM–IPM).

Fig. 7.17 Total loss maps of DTP PMSMs with IPM and AIPM rotors.

It should be noticed that the iron loss in AIPM machine is higher than that in IPM counterpart under high speed and low speed & low torque conditions, as shown in Fig. 7.15, but in Table 7.5, it was reported that the iron loss of AIPM machine is slightly lower than that in IPM counterpart under maximum torque (low speed & high torque) condition. Hence, it is necessary to further analyse the effects of electric loadings and speeds on iron losses in DTP IPM and AIPM machines.

Assuming phase currents varying from 0 (OC) to 250Apk, the iron losses of DTP PMSMs with IPM and AIPM rotors at 3000rpm are compared in Fig. 7.18. It can be seen that the iron loss in DTP AIPM machine is higher than that in IPM counterpart when phase currents are low (≤ 50 Apk), but lower than in the IPM counterpart when phase currents are high (≥ 75 Apk).

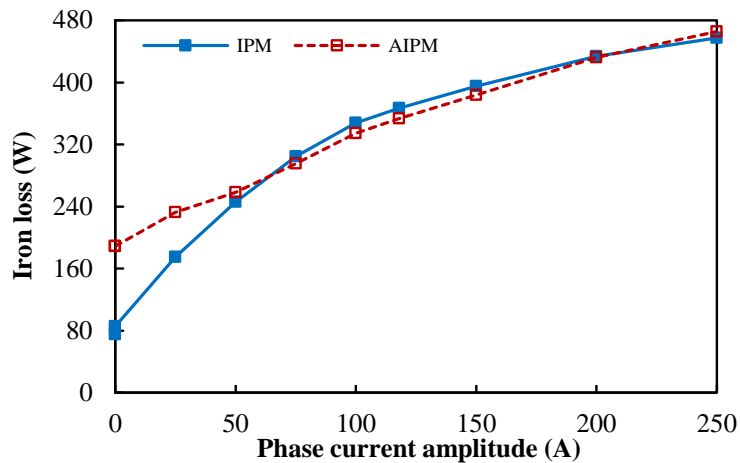
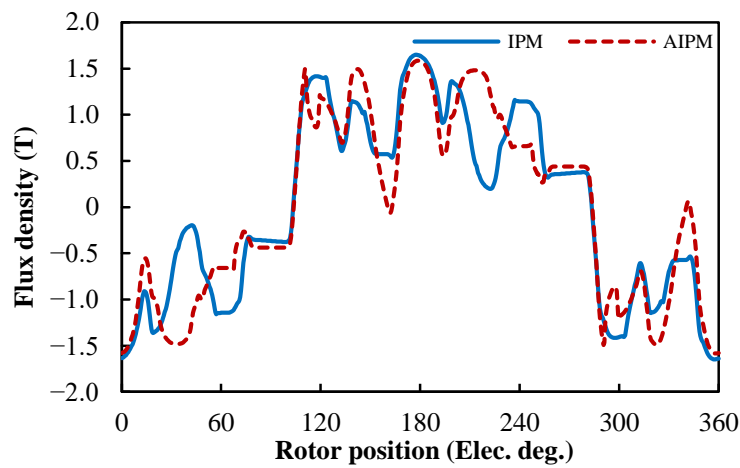
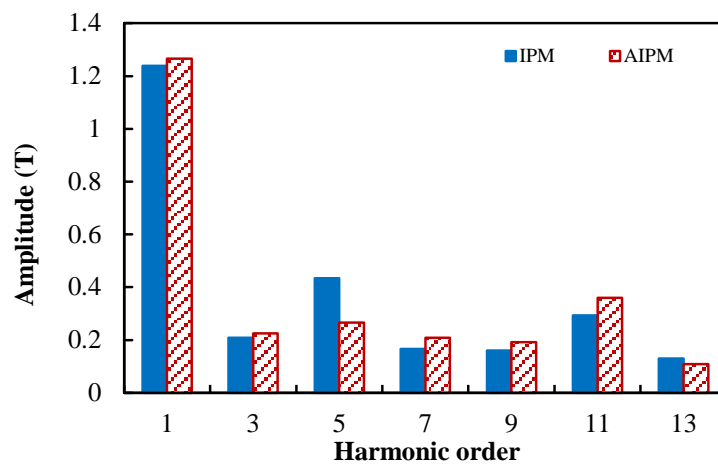


Fig. 7.18 Variations of iron losses with phase current amplitude in DTP PMSMs with IPM and AIPM rotors.

This phenomenon can be explained by the different air-gap MMF harmonic contents in the AIPM and IPM machines. When electric loading is low, the air-gap MMF is mainly produced by rotor PMs. Under OC condition, the air-gap flux densities of the DTP AIPM and IPM machines are shown in Fig. 7.6. From Fig. 7.6(b), it can be seen that AIPM machine has much higher fundamental component (0.77T in IPM machine, and 0.92T in AIPM machine) and more abundant harmonic contents (THD = 42.66% in IPM machine, 68.42% in AIPM machine). Hence, the iron loss of the DTP AIPM machine is significantly higher than that in the DTP IPM machine under low-load conditions. However, with the increase of phase currents, the air-gap flux densities of the DTP AIPM and IPM machines are mainly affected by armature windings, and less affected by rotor PMs. Under maximum torque condition ($I_{A1} = 118\text{A}$), the radial air-gap flux densities of DTP PMSMs with IPM and AIPM rotors are compared in Fig. 7.19.



(a) Waveforms

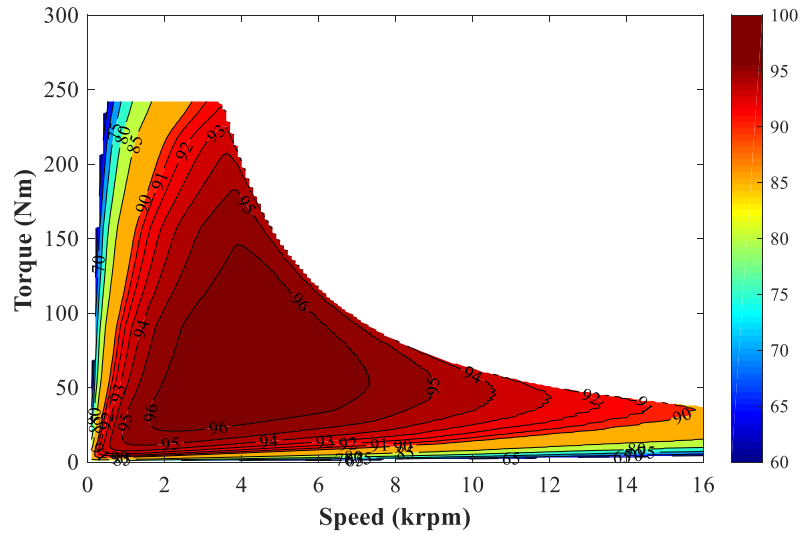


(b) Spectra

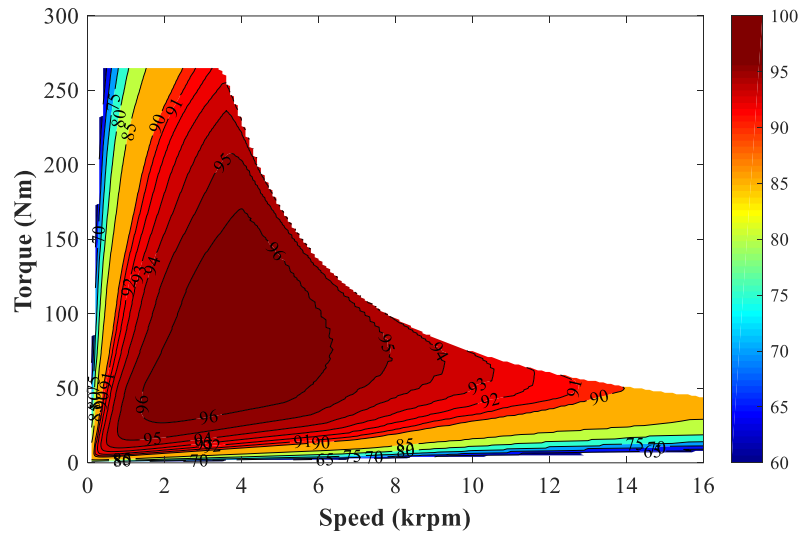
Fig. 7.19 Radial air-gap flux densities of DTP PMSMs machines with different rotors under maximum torque condition.

It can be seen that the air-gap flux densities of the DTP IPM and AIPM machines are close to each other under this condition. In addition, due to different rotor layouts, the harmonic contents in AIPM machine are even lower than those in IPM counterpart under this condition (THD = 41.57% in IPM machine, 38.44% in AIPM machine). As a result, compared with IPM counterpart, DTP AIPM machine shows higher iron loss when electric loading is low (under low speed & low torque, and high speed conditions) and lower iron loss when electric loading is high (under low speed & high torque condition).

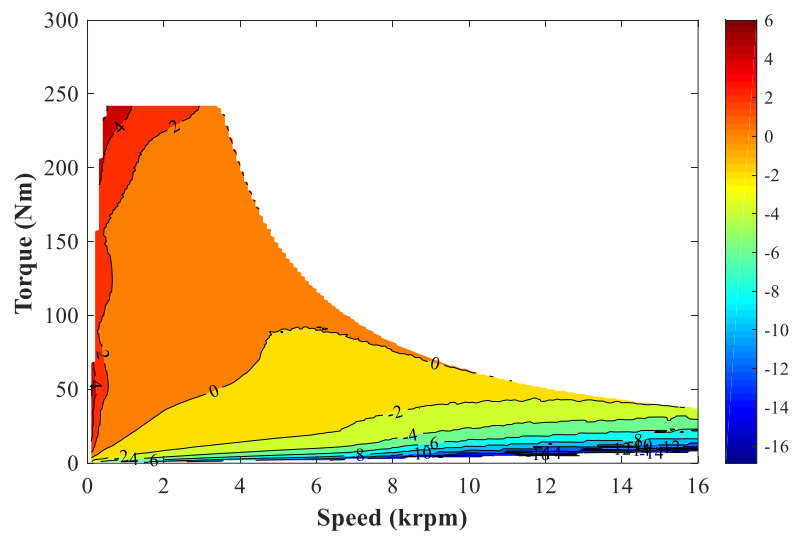
Based on Fig. 7.17, the efficiency maps of DTP PMSMs with IPM and AIPM rotors can be obtained, as shown in Fig. 7.20(a) and (b), respectively. The efficiency difference between the AIPM and IPM machines is also presented Fig. 7.20(c). It can be summarized that DTP IPM and AIPM machines show higher efficiencies under different operating conditions. Due to the more abundant PM MMF harmonics in DTP AIPM machine, DTP AIPM machine shows higher iron loss and lower efficiency than IPM counterpart under high speed condition. However, when electric loading is higher, the iron losses due to armature reaction field become more significant and hence the iron losses in IPM and AIPM machines become similar to each other. Considering that DTP AIPM machine can produce the same output torque with IPM counterpart with smaller phase currents, and lower copper losses, DTP AIPM machine exhibits higher efficiency than IPM counterpart under low speed & high torque condition.



(a) IPM



(b) AIPM



(c) Efficiency difference (AIPM-IPM)

Fig. 7.20 Efficiency maps of DTP PMSMs with IPM and AIPM rotors.

7.4 Electromagnetic Performance under 3-ph OC Condition

Since the two three-phase winding sets in DTP PMSMs are connected independently, any fault in one three-phase winding set will not result in the failure of total torque output and DTP PMSMs can still operate with the remaining three-phase winding set. In addition, DTP PMSMs sometimes could be operated by only one winding set to reduce copper, iron, and inverter losses. Hence, the torque characteristics of the researched PMSM with IPM and AIPM rotors under single three-phase OC (3-ph OC) condition are important for DTP PMSMs, and will be investigated and compared in this section.

7.4.1 Torque Characteristics

7.4.1.1 Torque Component-Current Advancing Angle Characteristics

As mentioned above, in the researched IPM and AIPM machines, the maximum phase current amplitude is 118A. When the phase current amplitude is 118A under 3-ph OC condition ($I_{A1} = 118\text{A}$, $I_{A2} = 0$), the variations of total torque, PM torque, and reluctance torque with current advancing angle are shown in Fig. 7.21 and the optimal current advancing angles under this condition can be summarized in Table 7.6. It can be seen that the difference between the optimal current advancing angles for the maximum PM and reluctance torque components is 25° in IPM machine, and it is 19° in AIPM machine. Hence, under 3-ph OC condition, the MFS effect still can be observed in AIPM machine and AIPM rotor can still improve average torque.

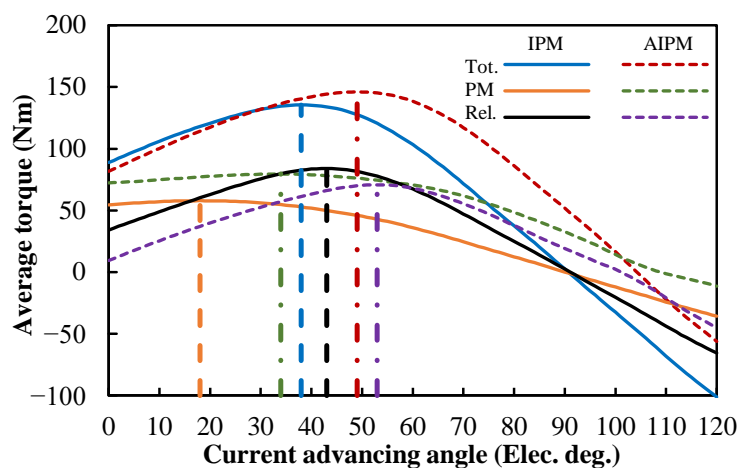


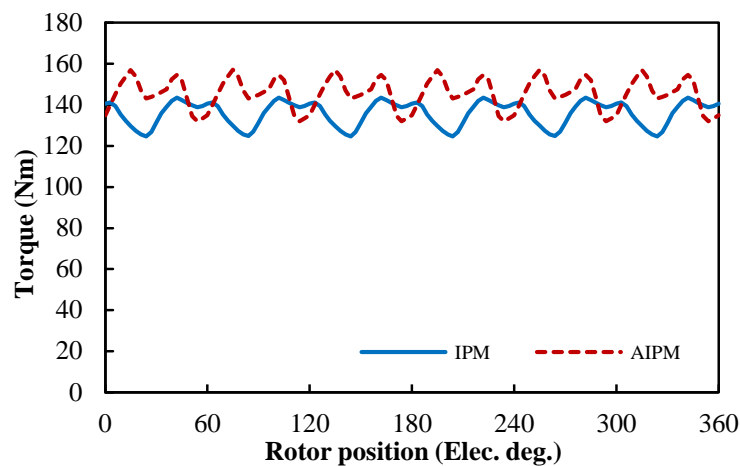
Fig. 7.21 Torque component-current advancing angle characteristics of DTP PMSMs with IPM and AIPM rotors under single three-phase OC condition (3-ph OC, $I_{A1} = 118\text{A}$).

Table 7.6 Maximum torque components and optimal current advancing angles of DTP PMSMs with IPM and AIPM rotors (3-ph OC, $I_{Al} = 118\text{A}$)

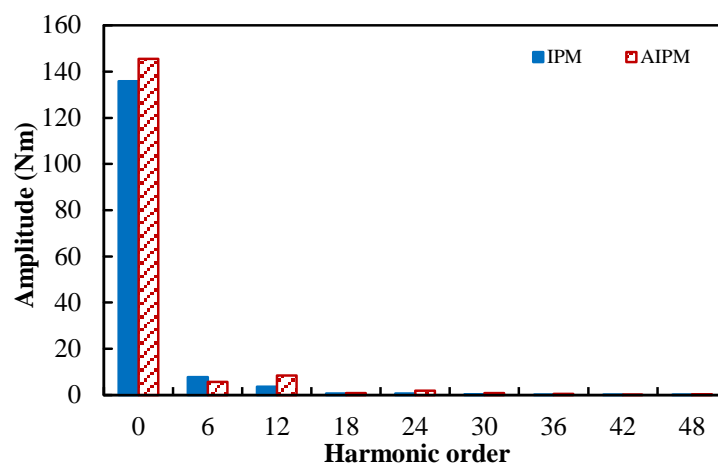
| Torque component | Maximum value (Nm) | | Optimal current advancing angle (°) | |
|------------------|--------------------|--------|-------------------------------------|------|
| | IPM | AIPM | IPM | AIPM |
| Tot. torque | 135.53 | 146.09 | 38 | 49 |
| PM torque | 57.88 | 79.45 | 18 | 34 |
| Rel. torque | 83.99 | 70.82 | 43 | 53 |

7.4.1.2 Instantaneous Torque Characteristics under Maximum Torque Condition

From Table 7.6, under 3-ph OC condition, the optimal current advancing angles for the maximum average torque is 38° in IPM machine and 49° in AIPM machine, respectively. The waveforms and spectra of the instantaneous torque in the DTP PMSMs with IPM and AIPM rotors under 3-ph OC maximum torque condition are shown in Fig. 7.22.



(a) Waveforms



(b) Spectra

Fig. 7.22 Instantaneous torque waveforms and spectra of DTP PMSMs with IPM and AIPM rotors under 3-ph OC maximum torque condition.

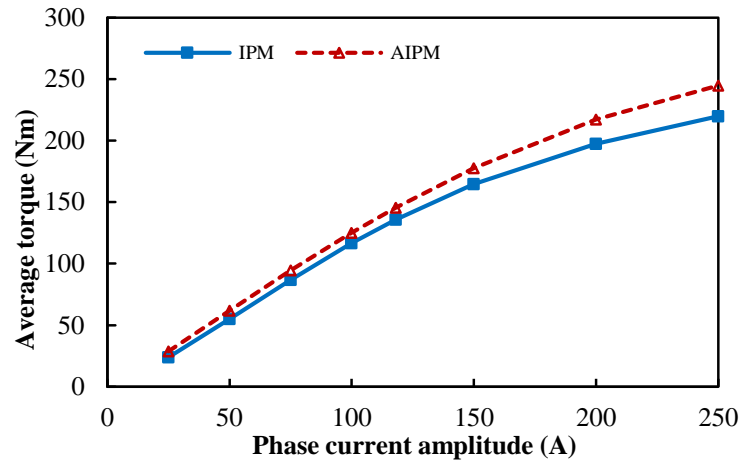
From Fig. 7.22, the torque characteristics are summarized in Table 7.7. It can be seen that the average torque of IPM machine can still be improved significantly by employing AIPM rotor, but the torque ripple is increased slightly by using AIPM rotor.

Table 7.7 Torque characteristics of DTP IPM and AIPM machines under three-phase OC maximum torque condition

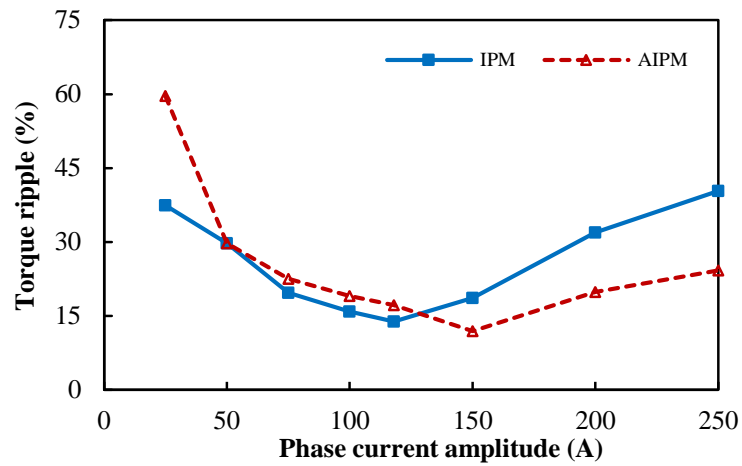
| | IPM | AIPM | Change |
|----------------------|--------|--------|---------|
| Average torque (Nm) | 135.80 | 145.54 | +7.17% |
| Peak-peak value (Nm) | 18.79 | 25.09 | +33.54% |
| Torque ripple (%) | 13.83 | 17.24 | |

7.4.1.3 Average Torque and Torque Ripple–Current Amplitude Characteristics

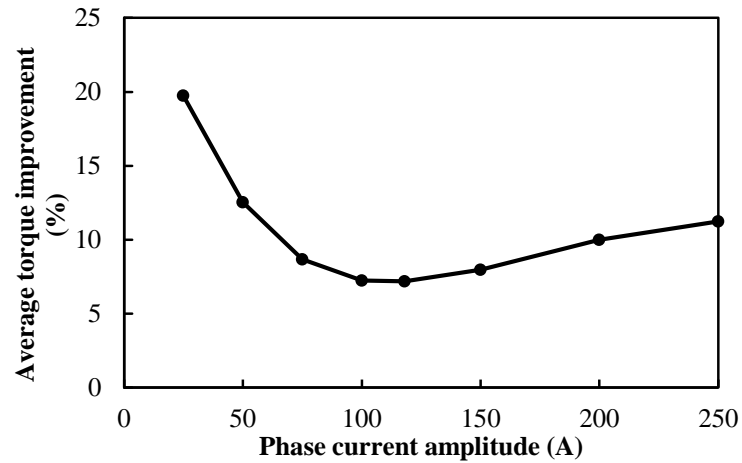
Similar to the analyses under healthy condition, when one three-phase winding set is open-circuited and I_{AI} varies from 25A_{pk} to 250A_{pk}, the variations of average torque and torque ripples with phase current amplitude in DTP IPM and AIPM machines are shown Fig. 7.23(a) and (b), respectively. It can be seen that the average torque of IPM machine can still be improved by employing AIPM rotor, and with different phase current amplitudes, the torque improvements are presented summarized in Fig. 7.23(c).



(a) Average torque



(b) Torque ripple



(c) Average torque improvement.

Fig. 7.23 Variations of torque characteristics with phase current amplitude in DTP PMSMs with IPM and AIPM rotors under 3-ph OC condition using MTPA control strategy.

However, from Fig. 7.23(b), the torque ripples of IPM machines can only be reduced by employing AIPM rotor when phase current $\geq 150\text{A}$. Considering that the maximum phase current amplitude is 118A in the researched machine, it can be concluded that AIPM rotor can still achieve significant torque improvement, but cannot reduce torque ripples in DTP PMSM under 3-ph OC condition.

7.4.2 Loss and Efficiency

Similar to the analyses under healthy condition, the loss and efficiency characteristics of DTP PMSMs with IPM and AIPM rotors under 3-ph maximum torque condition are summarized and compared in Table 7.8. It can be seen that the total losses in IPM and AIPM machines are still very close to each other under 3-ph OC condition. Since AIPM machine can produce higher output torque and higher output power under this condition, AIPM machine still shows slightly higher overall efficiency than IPM counterpart under 3-ph maximum torque condition.

Table 7.8 Loss and efficiency of DTP PMSMs with IPM and AIPM rotors under 3-ph maximum torque condition

| | IPM | AIPM |
|----------------------------|---------|---------|
| Average output torque (Nm) | 135.80 | 145.53 |
| Output power (kW) | 42.66 | 45.72 |
| Copper loss (W) | 3641.75 | 3641.75 |
| Stator iron loss (W) | 321.02 | 308.92 |
| Rotor iron loss (W) | 26.84 | 25.34 |
| Total iron loss (W) | 347.87 | 334.25 |
| PM eddy current loss (W) | 51.95 | 52.17 |
| Mechanical loss (W) | 93.20 | 93.20 |
| Total loss (kW) | 4.13 | 4.12 |
| Efficiency (%) | 91.16 | 91.73 |

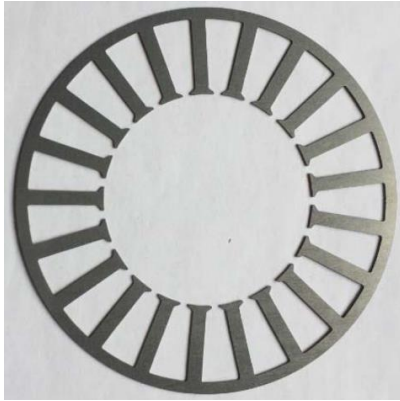
7.5 Experimental Validation

Considering the difficulties in manufacturing and testing a large prototype, which shares the same size with Toyota Prius 2010 machine, a small-scale 24-slot/4-pole prototype with an AIPM rotor was fabricated and tested to verify the FE analyses presented in this chapter. Some key design specifications of the prototype are given in Table 7.9.

Table 7.9 Main Design Specifications of 24-slot/4-pole Prototype DTP AIPM Machine

| Parameters | Values |
|--------------------------|--------|
| Stator | |
| Stator OD, mm | 100.0 |
| Stator ID, mm | 50.0 |
| Stack length, mm | 50.0 |
| Slot depth, mm | 18.5 |
| Slot opening, mm | 2.0 |
| AIPM rotor | |
| Rotor OD, mm | 48.0 |
| Rotor ID, mm | 14.0 |
| Stack length, mm | 50.0 |
| Large PM length, mm | 15.5 |
| Large PM thickness, mm | 3.5 |
| Small PM length, mm | 5.5 |
| Small PM thickness, mm | 2.0 |
| PM remanence, T | 1.23 |
| PM relative permeability | 1.04 |

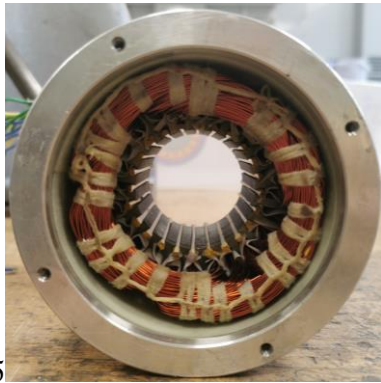
The pictures of the DTP AIPM prototype are given in Fig. 7.24 and the test rig is shown in Fig. 7.25.



(a) Stator lamination



(b) Rotor lamination



(c) Stator



(d) Rotor

Fig. 7.24 Pictures of prototype DTP PMSM with AIPM rotor.

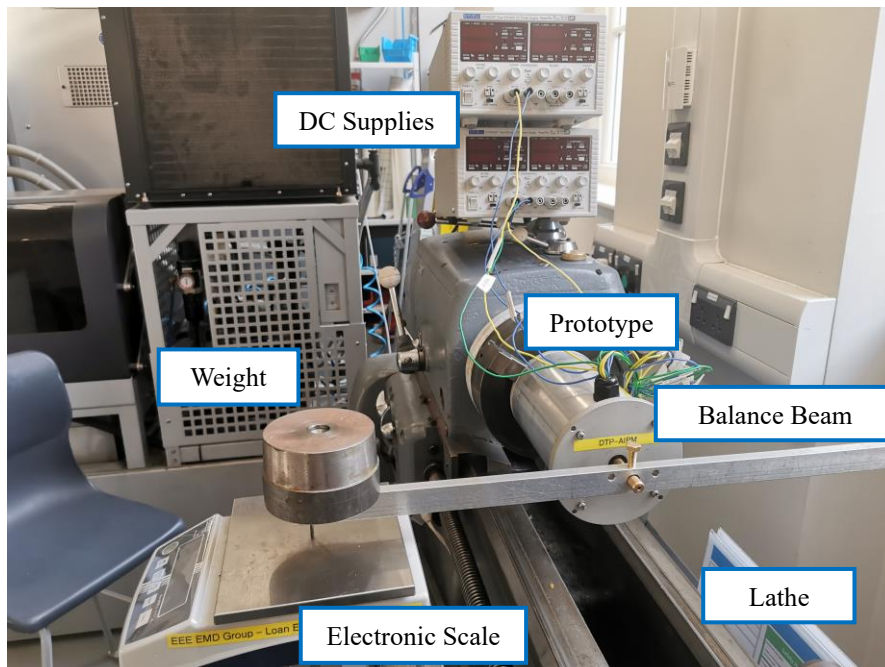
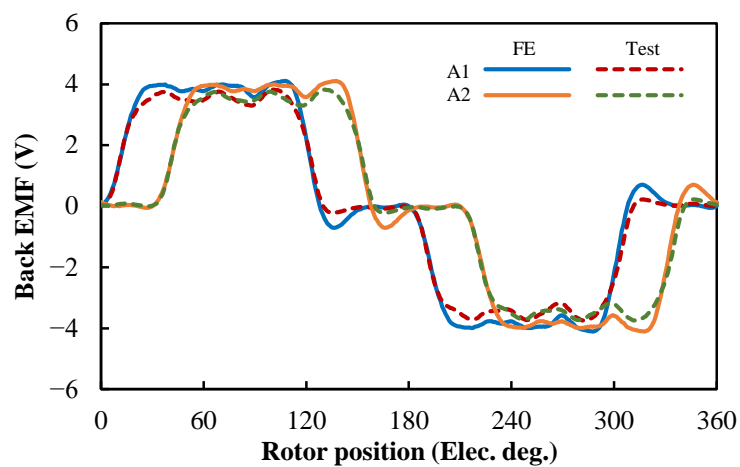
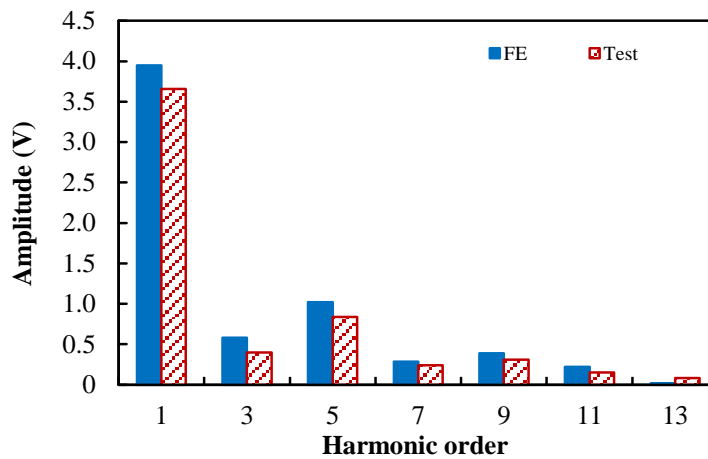


Fig. 7.25 Picture of test rig.

The FE predicted and measured waveforms and spectra of phase back EMFs are compared in Fig. 7.26. For the prototype machine, the phase back EMFs exhibit significant harmonics due to the asymmetric rotor layout. In Fig. 7.26(a), an asymmetric in the half waveform can be observed due to the small magnet between the large magnet and the flux barrier. It can also be found from Fig. 7.26(b) that the measured fundamental and harmonic amplitudes are lower than the FE predicted results, which could be due to the neglect of end effects in 2D FE calculations. Although the AIPM rotor is not symmetrical from the view of one rotor pole, the whole rotor is still symmetrical as the four rotor poles share the same cyclic layout, and thus, there is no even harmonic in resultant phase back EMFs.



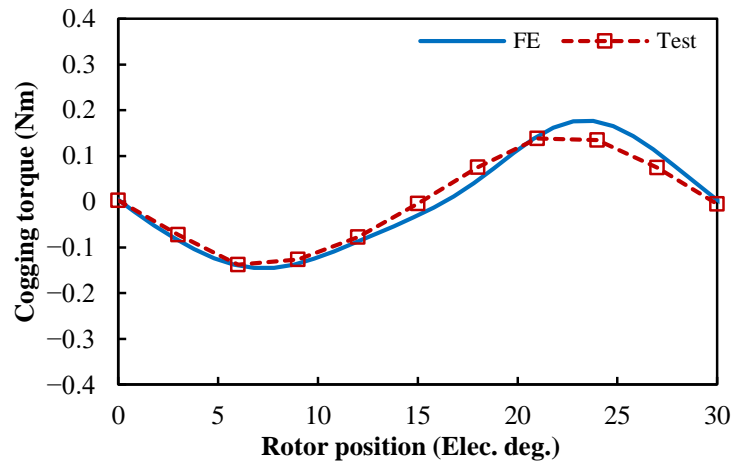
(a) Waveforms



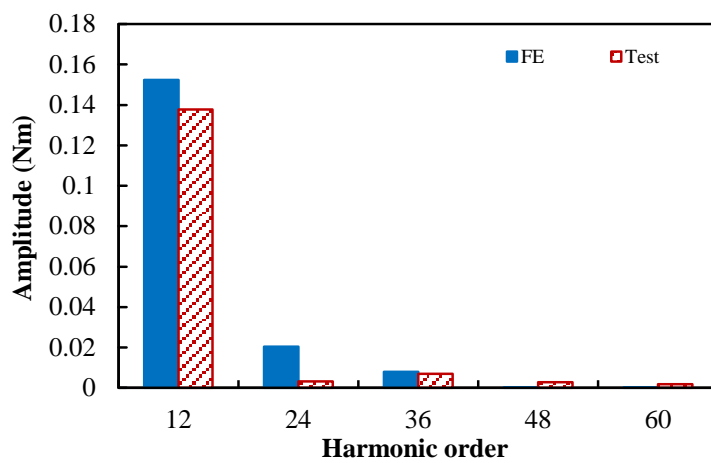
(b) Spectra

Fig. 7.26 Phase back EMF comparison between FE predicted and measured results at 200rpm.

The FE predicted and measured waveform and spectra cogging torque are shown in Fig. 7.27. The cogging torque is measured by using the method proposed in [ZHU09]. Identical to that in the 48-slot/8-pole PMSMs, the fundamental order of cogging torque is 12 in electric for the 24-slot/4-pole prototype. The measured cogging torque validates the order number of the FE predicted results, but the measured cogging torque amplitude is much smaller than predictions, which could be caused by the errors in iron bridges when manufacturing rotor laminations.



(a) Waveforms



(b) Spectra

Fig. 7.27 Cogging torque comparison between FE predicted and measured results.

To validate the FE analyses under on-load conditions, the two three phase winding sets of the prototype are supplied by direct currents, and the static torque versus rotor position waveforms are measured under different current values. It should be noticed that due to the 30° phase shift between the two winding sets, the phase currents in the two winding sets are different at the same time, as shown in Fig. 7.28. The direct currents in different phases are assigned as $I_{A1}=I_{dc}$, $I_{B1}=I_{C1}=-0.5I_{dc}$, $I_{A2}=0.866I_{dc}$, $I_{B2}=0$, and $I_{C2}=-0.866I_{dc}$. To achieve the aforementioned currents, two DC supplies are utilized, as shown in Fig. 7.25. The first winding set is supplied by a DC supply with I_{dc} . Phases B1 and C1 windings are connected in parallel firstly and then connected with Phase A1 winding in series. The second winding set is supplied by another DC supply with $0.866I_{dc}$ which is supplied to series connected Phases A2 and C2 windings. Phase B2 winding is not supplied with current.

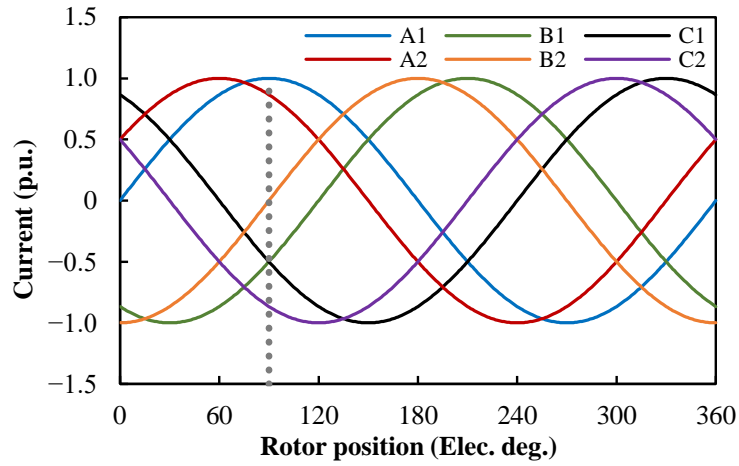
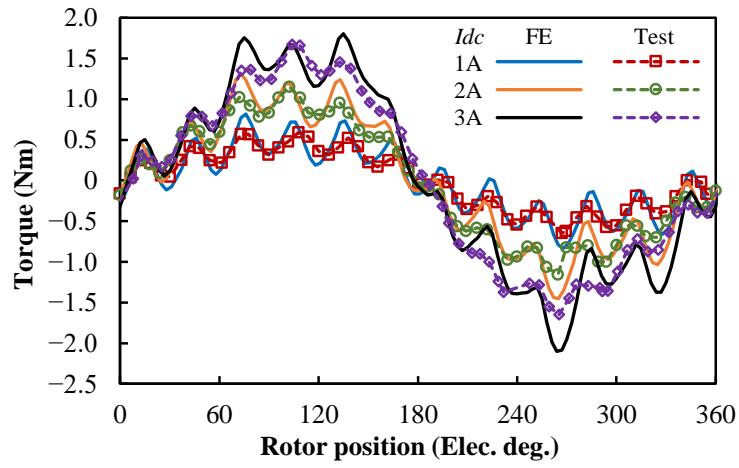
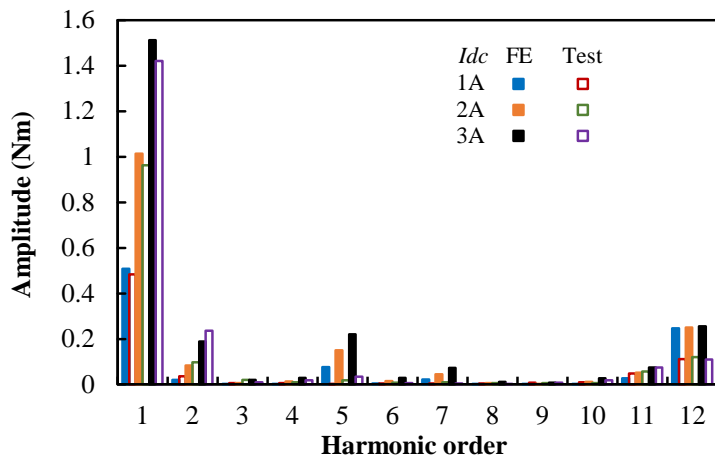


Fig. 7.28 Phase currents for DTP PMSM.

The FE predicted and measured waveforms and spectra of static torque versus rotor position characteristics of the prototype machine with different I_{dc} values are compared in Fig. 7.29. The corresponding variations of the fundamental amplitudes of static torque with I_{dc} are compared in Fig. 7.30. It can be seen that the measured results are only slightly lower than the FE predicted results, due to the neglecting of end-winding effects in 2D FE calculations. Overall, the good agreement between the FE predicted and tested results under OC and on-load conditions confirms the accuracies of the FE analyses and conclusions in this chapter.



(a) Waveforms



(b) Spectra

Fig. 7.29 Static torque comparison between FE predicted and measured results with different I_{dc} values.

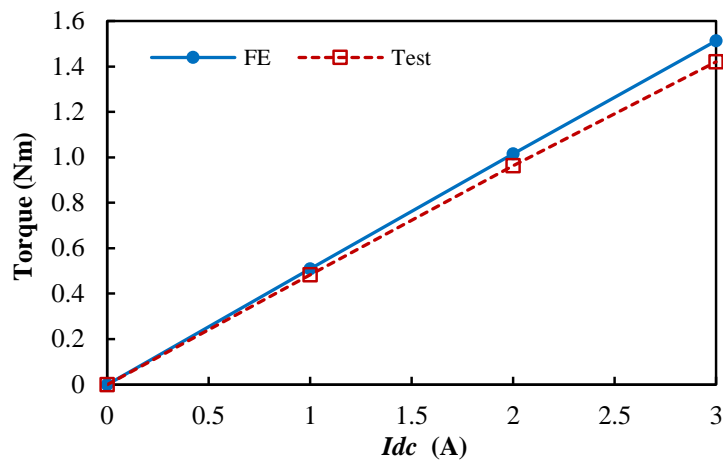


Fig. 7.30 Variations of FE predicted and measured fundamental static torque amplitudes with I_{dc} .

7.6 Conclusion

In this chapter, the effects of AIPM rotors on the electromagnetic performance of DTP PMSMs are investigated based on Toyota Prius 2010 machine. The electromagnetic performances of DTP PMSM with AIPM rotor are compared with those obtained with IPM rotor. Both healthy and 3-ph OC conditions are considered. It is found that the MFS effect still exists in DTP PMSMs no matter under healthy or 3-ph OC condition, and thus, the average torque can still be improved significantly by employing AIPM rotor. Furthermore, it is found that in DTP PMSMs, the average torque improvement by AIPM rotor is higher than that in STP PMSMs.

Overall, the benefits of AIPM rotors in STP PMSMs, such as higher average torque and lower torque ripple still exist in DTP PMSMs and the torque improvement can still be achieved even under 3-ph OC condition in DTP PMSMs.

In addition, it is also found that due to the more abundant PM MMF harmonics in DTP AIPM machine, DTP AIPM machines show higher iron loss and lower efficiency than IPM counterpart when electric loading is low. However, when electric loading is higher, the iron losses due to armature reaction field become more significant and the difference between the iron losses in IPM and AIPM machines becomes smaller. As a result, DTP AIPM machine exhibits higher efficiency than DTP IPM machine under low speed & high torque condition. Therefore, compared with IPM rotors, the application of AIPM rotors to electric vehicles may be limited, since electric vehicles usually require not only high torque density but also high efficiency under low speed & low torque conditions.

CHAPTER 8

GENERAL CONCLUSION AND FUTURE WORK

Compared with conventional STP PMSMs, DTP PMSMs are featured with better fault-tolerant, power sharing, and torque capabilities, as well as better efficiency performance. Besides that, they still preserve the merits of PMSMs, i.e. high torque density, high power density, and high efficiency. Hence, DPT PMSMs have been regarded as a promising candidate for machines utilized in electric vehicles in recent years. In this thesis, the electromagnetic performance of DTP PMSMs are investigated, with particular reference to torque capability and torque ripple for electric vehicle applications. Some general research approaches in designing and analysing DTP PMSMs are proposed with examples and some design techniques are specifically examined based on a benchmark Toyota Prius 2010 IPM machine. The general conclusions and future work are summarized as follows.

8.1 General Conclusion

8.1.1 General Winding Configuration Technique of DTP PMSMs

A generic winding configuration technique of DTP PMSMs is firstly developed in Chapter 2 based on the star of slots. Different slot/pole number combinations, phase shift angles, and coil pitch numbers are all considered. Thus, for PMSMs with different slot/pole number combinations, all feasible phase shift angles and corresponding winding factors can be obtained with the proposed method, as summarized in Table 2.10, and presented again in Table 8.1. Thus, for a PMSM with any slot/pole number combination, all feasible DTP winding configurations can be found directly from the table. Additionally, as winding factors of different DTP winding configurations are also given in the table, the electromagnetic performances of these DTP winding configurations can be predicted and compared quickly based on the table.

Table 8.1 Feasible phase shift angles and corresponding winding factors for DTP PMSMs with different slot/pole number combinations and optimized coil pitch numbers

| $\begin{matrix} N_s \\ 2p \end{matrix}$ | 6 | | 12 | | 18 | | 24 | | 30 | | 36 | |
|---|-------------------|-------|-------------------|-------|-------------------|-------|-------------------|-------|-------------------|-------|-------------------|-------|
| | $\beta(^{\circ})$ | K_w | $\beta(^{\circ})$ | K_w | $\beta(^{\circ})$ | K_w | $\beta(^{\circ})$ | K_w | $\beta(^{\circ})$ | K_w | $\beta(^{\circ})$ | K_w |
| 2 | 0 | 1.000 | 0 | 0.966 | 0/20 | 0.960 | 0 | 0.958 | 0/12 | 0.957 | 0/20 | 0.956 |
| | | | 30 | 1.000 | | | 15 | 0.966 | | | 10 | 0.960 |
| | | | | | | | 30 | 0.991 | | | 30 | 0.990 |
| 4 | 0 | 0.866 | 0 | 1.000 | 0 | 0.945 | 0 | 0.966 | 0 | 0.951 | 0/20 | 0.960 |
| | | | | | | | 30 | 1.000 | | | | |
| 6 | ** | | ** | | 0 | 1.000 | ** | | ** | | 0 | 0.966 |
| | | | | | | | | | | | 30 | 1.000 |
| 8 | 0 | 0.866 | 0 | 0.866 | 0 | 0.945 | 0 | 1.000 | 0 | 0.951 | 0 | 0.945 |
| 10 | 0 | 0.500 | 0 | 0.933 | 0/20 | 0.945 | 0 | 0.925 | 0 | 1.000 | 0/20 | 0.942 |
| | | | 30 | 0.966 | | | 15 | 0.933 | | | 10 | 0.945 |
| | | | | | | | 30 | 0.958 | | | 30 | 0.975 |
| 12 | ** | | ** | | 0 | 0.866 | ** | | ** | | 0 | 1.000 |
| 14 | 0 | 0.500 | 0 | 0.966 | 0/20 | 0.902 | 0 | 0.925 | 0/12 | 0.951 | 0/20 | 0.924 |
| | | | 30 | 0.966 | | | 15 | 0.933 | | | 10 | 0.927 |
| | | | | | | | 30 | 0.958 | | | 30 | 0.956 |
| 16 | 0 | 0.866 | 0 | 0.866 | 0 | 0.945 | 0 | 0.866 | 0 | 0.951 | 0 | 0.945 |
| 18 | ** | | ** | | ** | | ** | | ** | | ** | |
| 20 | 0 | 0.866 | 0 | 0.500 | 0 | 0.945 | 0 | 0.933 | 0 | 0.866 | 0/20 | 0.945 |
| | | | | | | | 30 | 0.966 | | | | |
| 22 | 0 | 0.500 | 0 | 0.250 | 0/20 | 0.902 | 0 | 0.949 | 0/12 | 0.874 | 0/20 | |
| | | | 30 | 0.259 | | | 15 | 0.958 | | | 10 | |
| | | | | | | | 30 | 0.983 | | | 30 | |
| 24 | ** | | ** | | 0 | 0.866 | ** | | ** | | 0 | 0.866 |
| 26 | 0 | 0.500 | 0 | 0.250 | 0/20 | 0.735 | 0 | 0.949 | 0/12 | 0.936 | 0/20 | 0.867 |
| | | | 30 | 0.259 | | | 15 | 0.958 | | | 10 | 0.870 |
| | | | | | | | 30 | 0.983 | | | 30 | 0.897 |
| 28 | 0 | 0.866 | 0 | 0.500 | 0 | 0.617 | 0 | 0.933 | 0 | 0.951 | 0/20 | 0.902 |
| | | | | | | | 30 | 0.966 | | | | |
| 30 | ** | | ** | | 0 | 0.500 | ** | | ** | | 0 | 0.933 |
| | | | | | | | | | | | 30 | 0.966 |

Notes:

** Unfeasible slot/pole combinations for DTP PMSMs.

■ t is even and N_s is an odd multiple of 3

■ $k=1$ ■ $k=2$ ■ $k=3$ ■ $k=4$ ■ $k=5$ ■ $k=6$

As shown in Table 1.1, 48-slot/8-pole is the most popular slot/pole combination for PMSMs in electric vehicles right now. Based on the proposed DTP winding configuration technique, two DTP winding configurations, i.e., single-layer full-pitched one (DTP-SF) and double-layer short-pitched one (DTP-DS), are proposed for 48-slot/8-pole PMSMs. The two DTP winding configurations are analysed and compared with STP counterpart under healthy and three-phase open-circuit conditions based on the Toyota Prius 2010 IPM machine, as shown in Fig. 8.1.

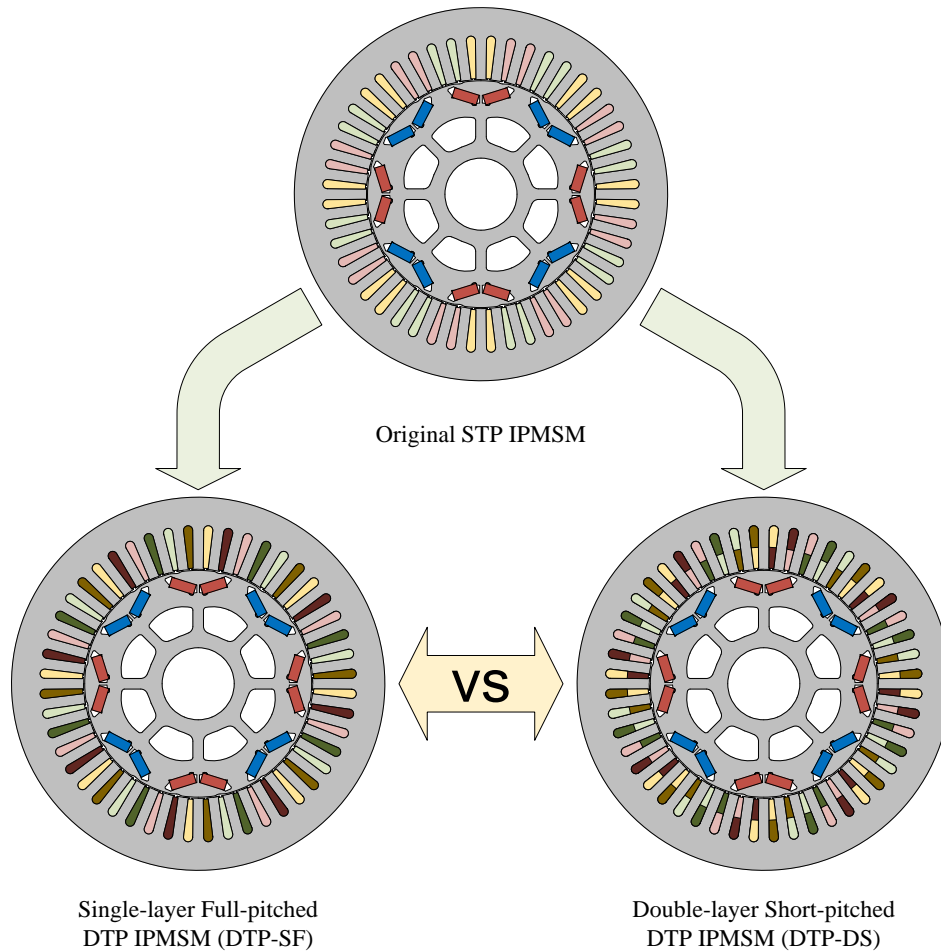


Fig. 8.1 Comparison of 48-slot/8-pole IPMSM with different winding configurations.

The comparison shows that DTP-DS winding configuration is advantageous in average torque, torque ripple, and efficiency, especially under high-speed and three-phase open-circuit conditions. Hence, it is suggested that DTP-DS winding configuration is preferred for DTP PMSMs to be used in electrical vehicles. A Prius 2010 machine with the proposed DTP-DS windings is fabricated and tested to verify the FE analyses.

8.1.2 Extension of Some Analysing Methods to DTP PMSMs

8.1.2.1 Attenuation Factor

In STP PMSMs, the concept of “attenuation factors” is utilized to describe the effects of stator shifting angle on different MMF orders. In DTP PMSMs, the two winding sets are shifted by a spatial shifting angle in space, and by a time shifting angle in currents. Hence, the concept of “attenuation factors” needs to be extended to DTP PMSMs by considering spatial and time shifting angles synchronously. Assuming that a PMSM has two three-phase winding sets, the spatial shifting angle between the two winding sets is α , and the time shifting angle between the currents in the two winding sets is β , as illustrated in Fig. 8.2.

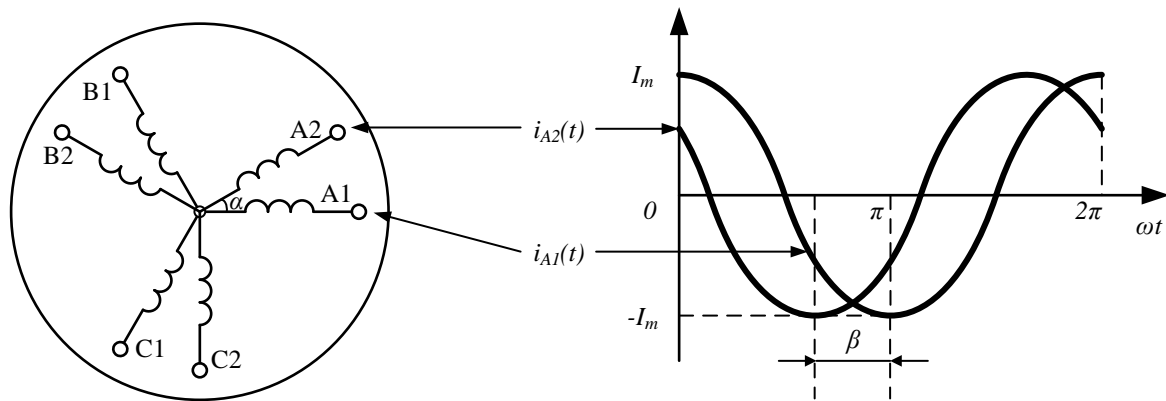


Fig. 8.2 DTP PMSM with spatial shifting angle, α , and time shifting angle, β .

When the two winding sets are connected in series and fed by one inverter, the machine is a STP PMSM. The attenuation factor, which only considers the effects of spatial shifting angle, is given in [RED14], as:

$$K_{av} = \left| \cos\left(\frac{v\alpha}{2}\right) \right| \quad (8.1)$$

When the two winding sets are fed by two separate inverters with a time shifting angle, β . The attenuation factor, which considers the effects of spatial and time shifting angles synchronously, is given in Chapter 2, as:

$$K_{av} = \left| \cos\left(\frac{v\alpha + \beta}{2}\right) \right| \quad (8.2)$$

Hence, the attenuation factor in STP PMSMs, (8.1), can be seen as a special case of the attenuation factor in DTP PMSMs, (8.2), with $\beta = 0$.

8.1.2.2 Torque Separation Method

The instantaneous torque separation method in STP PMSMs proposed in [CHE14b] is extended to DTP PMSMs in Chapter 4, by considering the cross-coupling effects within and between the two winding sets. As there are two winding sets in DTP PMSMs, the total out torque can be separated into more torque components, and the number of excitation cases needed for the torque separation is increased from 6 to 12. The instantaneous torque separation methods in STP and DTP PMSMs are illustrated and compared in Fig. 8.3.

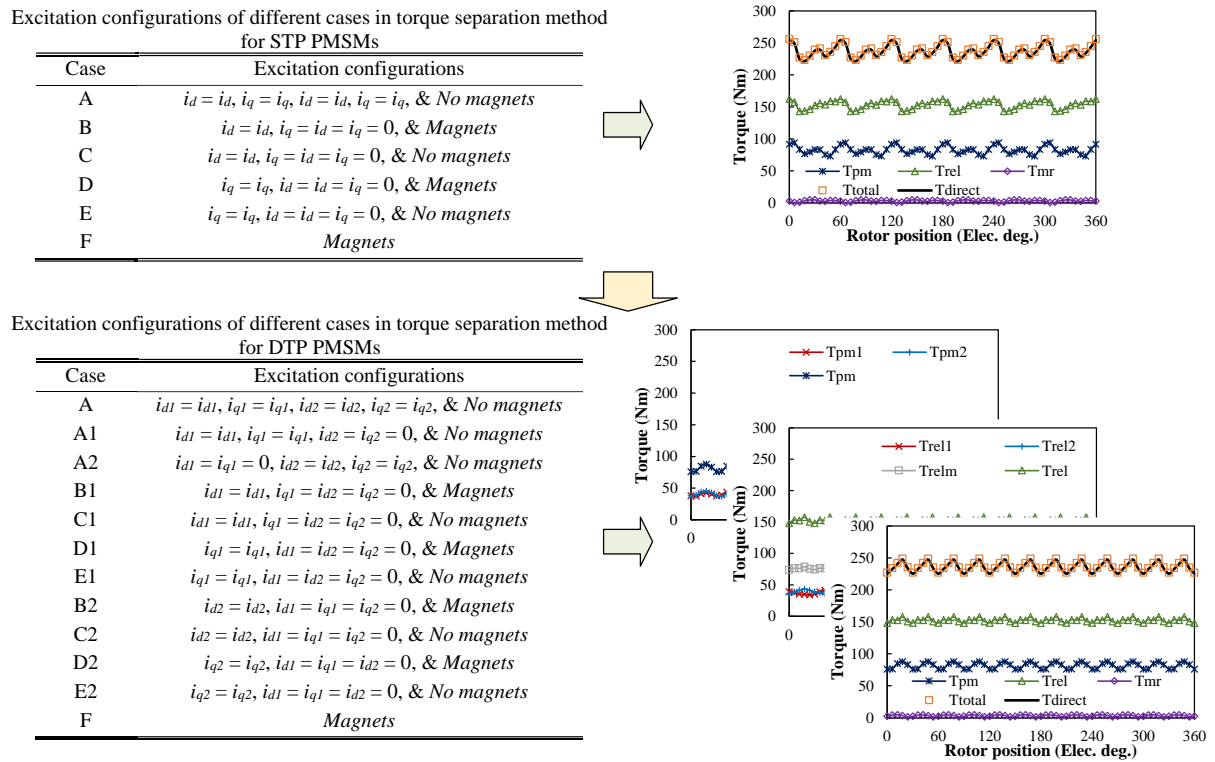


Fig. 8.3 Comparison of instantaneous torque separation methods in STP and DTP PMSMs.

An example is conducted in the Toyota Prius 2010 IPM machine with STP and DTP-DS windings, and the torque separation results are also given in Fig. 8.3. Under the researched full-load condition, it is found the reluctance torque component produced by the mutual inductance between the two winding sets contributes the most to the resultant output torque in the DTP PMSM.

8.1.3 Comparison of some design techniques in STP and DTP PMSMs

8.1.3.1 Rotor Skew

A simplified approach to estimate torque performance of PMSMs with rotor skew is firstly developed in Chapter 5. With the simplified approach, based on the Toyota Prius 2010 IPM machine and a SPMSM designed based on the Prius machine, the torque performances of STP and DTP IPMSM and SPMSM with continuously-varied skew angles are calculated under various load conditions, as shown in Fig. 8.4.

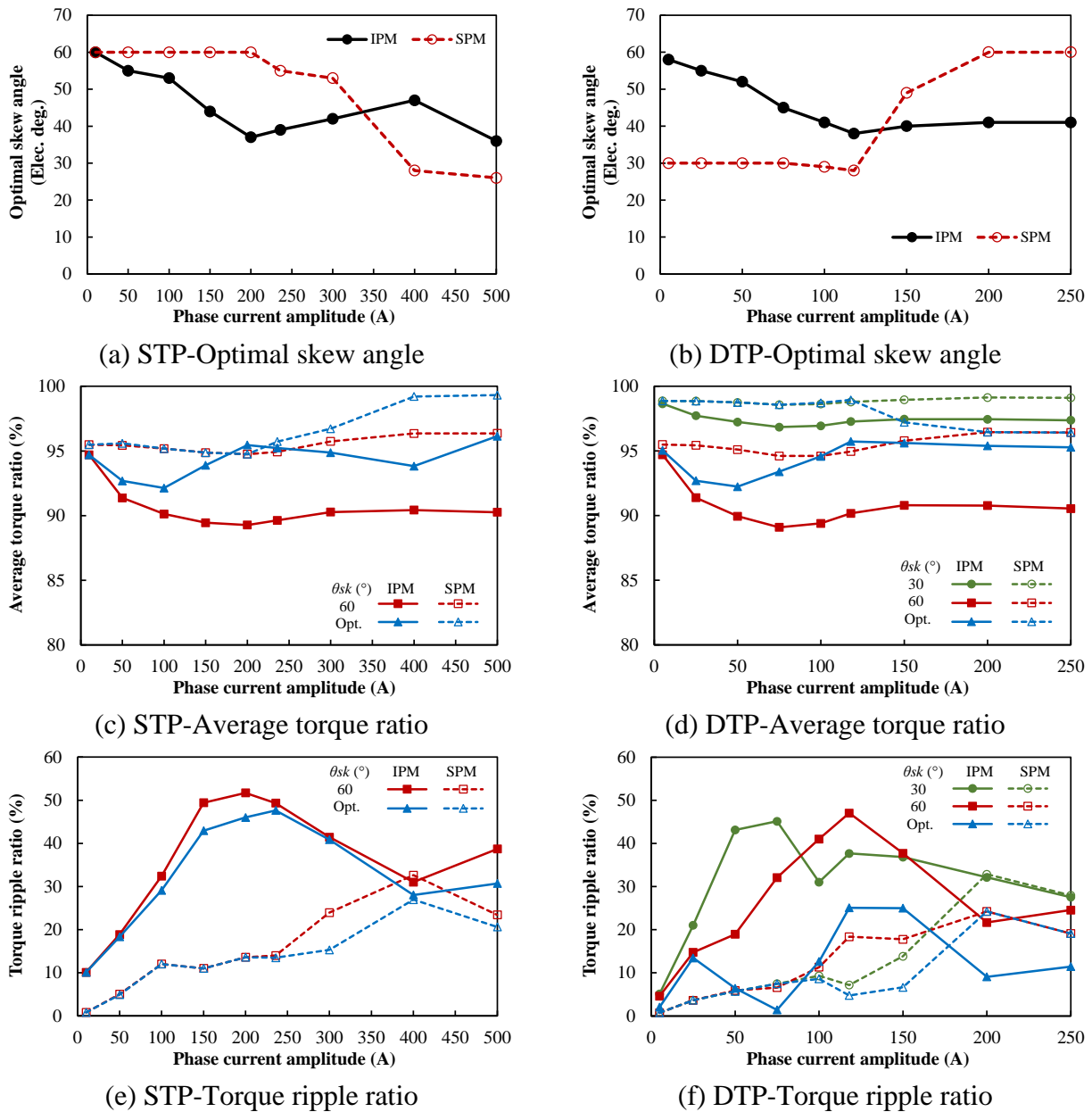


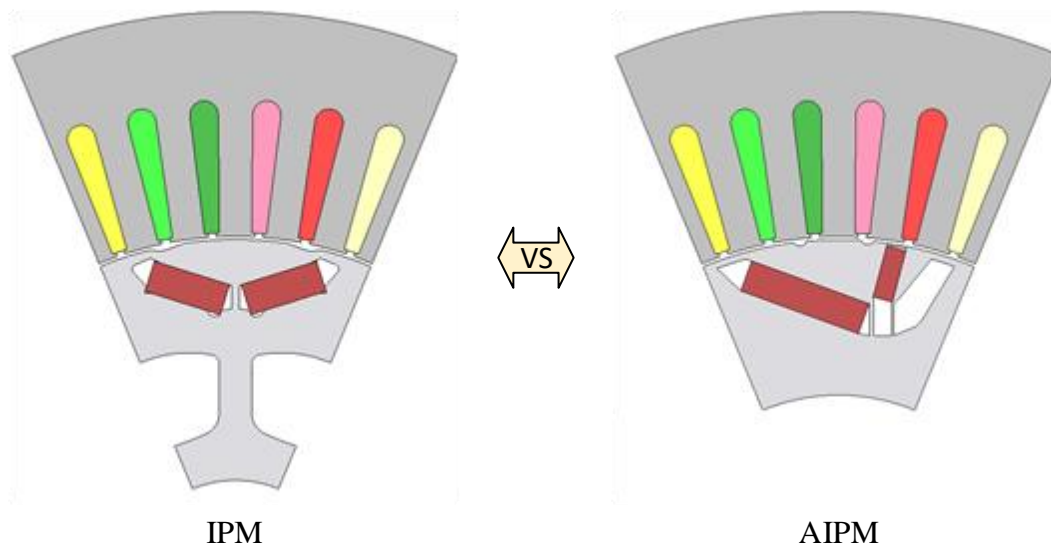
Fig. 8.4 Variations of optimal skew angle, average torque ratio, and torque ripple ratio with phase current amplitude in STP and DTP SPMSM and IPMSM.

It is found that the effectiveness of rotor skew in STP and DTP SPMSMs and IPMSMs depends on electric loading and magnetic saturation, especially in IPMSMs. The optimal skew angles in STP and DTP PMSMs accounting for the effects of loads are calculated based on the aforementioned analyses. The variations of the optimal skew angle with phase current amplitude in STP and DTP SPMSM and IPMSM are shown in Fig. 8.4 (a) and (b). The effects of the conventional and optimal skew angles on average torque and torque ripple are presented by average torque ratios and torque ripple ratios in Fig. 8.4 (c) to (f).

It should be mentioned that in the STP PMSMs, the phase current for full-load condition is 236A_{pk}; in the DTP PMSMs, the phase current for full-load condition is 118A_{pk}. From Fig. 8.4 (a) and (b), it can be found that for STP and DTP SPMSMs, even considering the effects of load, the optimal skew angles are still very close to the conventional skew angles, i.e., 60° in STP SPMSMs, and 30° in DTP PMSMs, except over-load conditions. However, for STP and DTP IPMSMs, the optimal skew angles are quite different from conventional skew angles, even under light-load conditions. The torque performances with different skew angles are shown in Fig. 8.4 (c) to (f). Compared with conventional skew angles, the proposed optimal skew angles can improve average torque and reduce torque ripples in both STP and DTP PMSMs.

8.1.3.2 AIPM Rotor Configuration

Finally, the effects of AIPM rotors, which are under extensive investigation in STP PMSMs [XIA21], on the electromagnetic performance of DTP PMSMs are evaluated, as illustrated in Fig. 8.5. The torque characteristics of the IPM and AIPM rotors in STP and DTP PMSMs are also shown illustrated in Fig. 8.5.



| Torque Characteristics of STP IPM and AIPM Machines ($I_A = 236\text{Apk}$) | | | |
|---|--------|--------|---------|
| | IPM | AIPM | Change |
| Average torque (Nm) | 236.50 | 256.26 | +8.35% |
| Peak-peak value (Nm) | 35.99 | 25.71 | -28.58% |
| Torque ripple (%) | 15.22 | 10.03 | -34.08% |

| Torque Characteristics of DTP IPM and AIPM Machines ($I_A = 118\text{Apk}$) | | | |
|---|--------|--------|---------|
| | IPM | AIPM | Change |
| Average torque (Nm) | 242.77 | 265.22 | +9.25% |
| Peak-peak value (Nm) | 24.28 | 13.89 | -42.78% |
| Torque ripple (%) | 10.00 | 5.24 | -47.62% |

Fig. 8.5 Comparison of IPM and AIPM rotors in STP and DTP PMSMs.

It reveals that in DTP PMSMs, AIPM rotors can still enhance average torque can reduce torque ripples. However, further investigation on loss and efficiency finds that the AIPM rotor increases iron loss and decreases overall efficiency in various operating conditions. Hence, the application of AIPM rotors to DTP PMSMs in electric vehicles may be limited and less attractive than the application to STP PMSMs.

8.2 Future Work

Based on the above analyses and conclusions, some future work are summarized as follows:

(1) Investigation of parasitic effects of DTP PMSMs

As this thesis only focuses on the electromagnetic performance of DTP PMSMs, some more in-depth analyses can be continued, e.g. thermal field, mechanical stress, rotor dynamics, acoustic noise and vibration behaviours.

(2) Investigation of DTP PMSMs with different slot/pole number combinations and different rotor configurations

Although 48-slot/8-pole is the most popular machine topology for PMSMs in electric vehicles, some other slot/pole combinations are still utilized in electric vehicle machines, as shown in Table 1.1. Considering that different rotor configurations can also affect the electromagnetic performances of DTP PMSMs, it is still necessary to extend the investigation of DTP PMSMs into other slot/pole number combinations and other rotor configurations.

(3) Investigation of more design/optimization techniques in DTP PMSMs

Besides rotor skew method shown in this thesis, more machine design/optimization techniques, such as rotor surface shaping, PM shaping and segmentation, auxiliary slot, and other AIPM rotor designs etc. can also be utilized in DTP PMSMs to further improve their electromagnetic performances. The investigations of these design/optimization techniques in DTP PMSMs can provide more insights for the design of DTP PMSMs.

(4) Sensitivity analysis of torque performances of DTP PMSMs to manufacturing and assembly tolerances.

REFERENCES

- [ABD15] A. S. Abdel-Khalik, S. Ahmed, and A. M. Massoud, "Low space harmonics cancelation in double-layer fractional slot winding using dual multiphase winding," *IEEE Trans. Magn.*, vol. 51, no. 5, Art no. 8104710, May 2015.
- [ABD16a] A. S. Abdel-Khalik, S. Ahmed, and A. M. Massoud, "A six-phase 24-slot/10-pole permanent-magnet machine with low space harmonics for electric vehicle applications," *IEEE Trans. Magn.*, vol. 52, no. 6, Art no. 8700110, June 2016.
- [ABD16b] A. S. Abdel-Khalik, S. Ahmed, and A. M. Massoud, "Effect of multilayer windings with different stator winding connections on interior PM machines for EV applications," *IEEE Trans. Magn.*, vol. 52, no. 2, Art no. 8100807, Feb. 2016.
- [ABD16c] A. S. Abdel-Khalik, S. Ahmed, and A. Massoud, "Application of stator shifting to five-phase fractional-slot concentrated winding interior permanent magnet synchronous machine," *IET Electr. Power Appl.*, vol. 10, no. 7, pp. 681–690, Aug. 2016.
- [ABD18] A. S. Abdel-Khalik, S. Gadoue and S. Ahmed, "A nine-phase six-terminal fractional-slot-winding for interior permanent-magnet machines with low space harmonics," *2018 XIII Int. Conf. Electr. Mach. (ICEM)*, Alexandroupoli, Greece, 2018, pp. 499-505.
- [AGA20] E. Agamloh, A. Jouanne, and A. Yokochi, "An overview of electric machine trends in modern electric vehicles," *Machines*, vol. 8, no. 2, pp. 20, Apr. 2020.
- [ALO11] N. P. Alotto, M. Barcaro, N. Bianchi, and M. Guarnieri, "Optimization of interior PM motors with machine rotor flux barriers," *IEEE Trans. Magn.*, vol. 47, no. 5, pp. 958-961, May 2011.
- [ALS16] J. Y. Alsawalhi and S. D. Sudhoff, "Design optimization of asymmetric salient permanent magnet synchronous machines," *IEEE Trans. Energy Convers.*, vol. 31, no. 4, pp. 1315-1324, Dec. 2016.

- [ARM09] E. Armando, P. Guglielmi, G. Pellegrino, M. Pastorelli, and A. Vagati, "Accurate modeling and performance analysis of IPM-PMASR motors," *IEEE Trans. Ind. Appl.*, vol. 45, no. 1, pp. 123-130, Jan.-Feb. 2009.
- [ATA00] K. Atallah, D. Howe, P. H. Mellor, and D. A. Stone, "Rotor loss in permanent magnet brushless AC machines," *IEEE Trans. Ind. Appl.*, vol. 36, no. 6, pp. 1612–1618, Nov.-Dec. 2000.
- [ATA03] K. Atallah, J. Wang, and D. Howe, "Torque-ripple minimization in modular permanent-magnet brushless machines," *IEEE Trans. Ind. Appl.*, vol. 39, no. 6, pp. 1689-1695, Nov.-Dec. 2003.
- [AZA12] Z. Azar, Z. Q. Zhu, and G. Ombach, "Influence of electric loading and magnetic saturation on cogging torque, back-EMF and torque ripple of PM machines," *IEEE Trans. Magn.*, vol. 48, no. 10, pp. 2650-2658, 2012.
- [BAR09] M. Barcaro, N. Bianchi, and F. Magnussen, "Configurations of fractional-slot IPM motors with dual three-phase winding," *2009 IEEE Int. Electr. Mach. Drives Conf. (IEMDC)*, Miami, FL, USA, 2009, pp. 936-942.
- [BAR10] M. Barcaro, N. Bianchi, and F. Magnussen, "Analysis and tests of a dual three-phase 12-slot 10-pole permanent-magnet motor," *IEEE Trans. Ind. Appl.*, vol. 46, no. 6, pp. 2355-2362, Nov.-Dec. 2010.
- [BAR11a] M. Barcaro, N. Bianchi, and F. Magnussen, "Six-phase supply feasibility using a PM fractional-slot dual winding machine," *IEEE Trans. Ind. Appl.*, vol. 47, no. 5, pp. 2042-2050, Sept.-Oct. 2011.
- [BAR11b] M. Barcaro, N. Bianchi, and F. Magnussen, "Faulty operations of a PM fractional-slot machine with a dual three-phase winding," *IEEE Trans. Ind. Electron.*, vol. 58, no. 9, pp. 3825–3832, Sept. 2011.
- [BAR12] M. Barcaro, N. Bianchi, and F. Magnussen, "Permanent-magnet optimization in permanent-magnet-assisted synchronous reluctance motor for a wide constant-power speed range," *IEEE Trans. Ind. Electron.*, vol. 59, no. 6, pp. 2495-2502, June 2012.

- [BEN11] J. W. Bennett, B. C. Mecrow, D. J. Atkinson, and G. J. Atkinson, "Safety-critical design of electromechanical actuation systems in commercial aircraft," *IET Electr. Power Appl.*, vol. 5, no. 1, pp. 37-47, Jan. 2011.
- [BIA00] N. Bianchi, S. Bolognani, and B. J. Chalmers, "Salient-rotor PM synchronous motors for an extended flux-weakening operation range," *IEEE Trans. Ind. Appl.*, vol. 36, no. 4, pp. 1118-1125, July-Aug. 2000.
- [BIA02] N. Bianchi and S. Bolognani, "Design techniques for reducing the cogging torque in surface-mounted PM motors," *IEEE Trans. Ind. Appl.*, vol. 38, no. 5, pp. 1259-1265, 2002.
- [BIA06a] N. Bianchi and M. Dai Pre, "Use of the star of slots in designing fractional-slot single-layer synchronous motors," *IEE Electr. Power Appl.*, vol. 153, no. 3, pp. 459-466, May 2006.
- [BIA06b] N. Bianchi, S. Bolognani, and G. Grezzani, "Design considerations for fractional-slot winding configurations of synchronous machines," *IEEE Trans. Ind. Appl.*, vol. 42, no. 4, pp. 997-1006, July-Aug. 2006.
- [BIA06c] N. Bianchi, M. D. Pre, and S. Bolognani, "Design of a fault-tolerant IPM motor for electric power steering," *IEEE Trans. Veh. Technol.*, vol. 55, no. 4, pp. 1102-1111, July 2006.
- [BIA08] N. Bianchi, S. Bolognani, and M. D. Dai Pre, "Impact of stator winding of a five-phase permanent-magnet motor on postfault operations," *IEEE Trans. Ind. Electron.*, vol. 55, no. 5, pp. 1978-1987, 2008.
- [BIA09] N. Bianchi, S. Bolognani, D. Bon, and M. Dai Pre, "Rotor flux-barrier design for torque ripple reduction in synchronous reluctance and PM-assisted synchronous reluctance motors," *IEEE Trans. Ind. Appl.*, vol. 45, no. 3, pp. 921-928, May-June 2009.
- [BIA15] N., Bianchi, M. Degano, and E. Fornasiero, "Sensitivity analysis of torque ripple reduction of synchronous reluctance and interior PM motors," *IEEE Trans. Ind. Appl.*, vol. 51, no. 1, pp. 187-195, Jan. 2015.

- [BIN06] A. Binder, T. Schneider, and M. Klohr, "Fixation of buried and surface-mounted magnets in high-speed permanent-magnet synchronous machines," *IEEE Trans. Ind. Appl.*, vol. 42, no. 4, pp. 1031-1037, July-Aug. 2006.
- [BOL04] I. Boldea, L. Tutelea and C. I. Pitic, "PM-assisted reluctance synchronous motor/generator (PM-RSM) for mild hybrid vehicles: electromagnetic design," *IEEE Trans. Ind. Appl.*, vol. 40, no. 2, pp. 492-498, Mar.-Apr. 2004.
- [BRA52] M. W. Brainard, "Synchronous machines with rotating permanent-magnet fields, part I, characteristics and mechanical construction," *AIEE Trans.*, vol. 71, pt. III, pp. 670-676, Aug. 1952.
- [BUR09] T. A. Burress, C. L. Coomer, S. L. Campbell, A. A. Wereszczak, J. P. Cunningham, L. D. Marlino, L. E. Seiber, and H. T. Lin, "Evaluation of the 2008 Lexus LS 600h hybrid synergy drive system," *ORNL/TM-2008/185*, Oak Ridge National Lab., TN, USA, 2009.
- [BUR11] T. A. Burress, S. L. Campbell, C. L. Coomer, C. W. Ayers, A. A. Wereszczak, J. P. Cunningham, L. D. Marlino, L. E. Seiber, and H. T. Lin, "Evaluation of the 2010 Toyota Prius hybrid synergy drive system," *ORNL/TM-2010/253*, Oak Ridge National Lab., TN, USA, 2011.
- [CAO12] W. P. Cao, B. C. Mecrow, G. J. Atkinson, J. W. Bennett, and D. J. Atkinson, "Overview of electric motor technologies used for more electric aircraft (MEA)," *IEEE Trans. Ind. Electron.*, vol. 59, no. 9, pp. 3523-3531, Sept. 2012.
- [CHA08] K. T. Chau, C. C. Chan, and C. Liu, "Overview of permanent-magnet brushless drives for electric and hybrid electric vehicles," *IEEE Trans. Ind. Electron.*, vol. 55, no. 6, pp. 2246-2257, June 2008.
- [CHA96] B. J. Chalmers, L. Musaba, and D. F. Gosden, "Variable-frequency synchronous motor drives for electric vehicles," *IEEE Trans. Ind. Appl.*, vol. 32, no.4, pp. 896-903, 1996.
- [CHE10] H. S. Chen, D. G. Dorrell, and M. C. Tsai, "Design and operation of interior permanent-magnet motors with two axial segments and high rotor saliency," *IEEE Trans. Magn.*, vol. 46, no. 9, pp. 3664-3675, Sept. 2010.

- [CHE11a] M. Cheng, W. Hua, J. Zhang, and W. Zhao, "Overview of stator-permanent magnet brushless machines," *IEEE Trans. Ind. Electron.*, vol. 58, no. 11, pp. 5087-5101, Nov. 2011, doi: 10.1109/TIE.2011.2123853.
- [CHE11b] Q. Chen, G. Liu, W. Gong, and W. Zhao, "A new fault-tolerant permanent-magnet machine for electric vehicle applications," *IEEE Trans. Magn.*, vol. 47, no. 10, pp. 4183–4186, 2011.
- [CHE14a] X. Chen, J. Wang, and V. I. Patel, "A generic approach to reduction of magnetomotive force harmonics in permanent-magnet machines with concentrated multiple three-phase windings," *IEEE Trans. Magn.*, vol. 50, no. 11, Art no. 8103604, Nov. 2014.
- [CHE14b] X. Chen, J. Wang, V. I. Patel, P. Lazari, L. Chen, and P. Lombard, "Reluctance torque evaluation for interior permanent magnet machines using frozen permeability," *Int. Conf. Power Electr. Mach. & Drives (PEMD)*, Manchester, UK, 2014.
- [CHE15] X. Chen, J. Wang, B. Sen, P. Lazari, and T. Sun, "A high-fidelity and computationally efficient model for interior permanent-magnet machines considering the magnetic saturation, spatial harmonics, and iron loss effect," *IEEE Trans. Ind. Electron.*, vol. 62, no. 7, pp. 4044-4055, July 2015.
- [CHE16] X. Chen, J. Wang, V. I. Patel, and P. Lazari, "A nine-phase 18-slot 14-pole interior permanent-magnet machine with low space harmonics for electric vehicle applications," *IEEE Trans. Energy Convers.*, vol. 31, no. 3, pp. 860-871, Sept. 2016.
- [CHE17] L. Cheng, Y. Sui, P. Zheng, Z. Yin, and C. Wang, "Investigation of low space harmonic six-phase PMSM with FSCWs for electric vehicle applications," *2017 IEEE Transp. Electr. Conf. Expo, Asia-Pacific (ITEC Asia-Pacific)*, Harbin, China, Aug. 2017.
- [CHE18] L. Cheng, Y. Sui, P. Zheng, Z. Yin, and C. Wang, "Influence of stator MMF harmonics on the utilization of reluctance torque in six-phase PMA-SynRM with FSCW," *Energies*, vol. 11, no. 1, pp. 108, Jan. 2018.

- [CHE20] Q. Chen, Y. Yan, G. Liu, and G. Xu, "Design of a new fault-tolerant permanent magnet machine with optimized salient ratio and reluctance torque ratio," *IEEE Trans. Ind. Electron.*, vol. 67, no. 7, pp. 6043-6054, July 2020.
- [CHE20] W. Chen, J. Ma, G. Wu, and Y. Fang, "Torque ripple reduction of a salient-pole permanent magnet synchronous machine with an advanced step-skewed rotor design," *IEEE Access*, vol. 8, pp. 118989-118999, 2020.
- [CHE98] J. Y. Chen and C. Z. Chen, "Investigation of a new AC electrical machine winding," *IEE Proc. Electr. Power Appl.*, vol. 145, no. 2, pp. 125-132, Mar. 1998.
- [CHU13a] W. Q. Chu and Z. Q. Zhu, "Average torque separation in permanent magnet synchronous machines using frozen permeability," *IEEE Trans. Magn.*, vol. 49, no. 3, pp. 1202-1210, 2013.
- [CHU13b] W. Q. Chu and Z. Q. Zhu, "Investigation of torque ripples in permanent magnet synchronous machines with skewing," *IEEE Trans. Magn.*, vol. 49, no. 3, pp. 1211-1220, 2013.
- [CHU13c] W. Q. Chu and Z. Q. Zhu, "Reduction of on-load torque ripples in permanent magnet synchronous machines by improved skewing," *IEEE Trans. Magn.*, vol. 49, no. 7, pp. 3822-3825, 2013.
- [CHU15] W. Q. Chu, Z. Q. Zhu, J. Zhang, X. Liu, D. A. Stone, and M. P. Foster, "Investigation on operational envelopes and efficiency maps of electrically excited machines for electrical vehicle applications," *IEEE Trans. Magn.*, vol. 51, no. 4, pp. 1-10, Apr. 2015.
- [CIS10a] M. V. Cistelecan, F. J. T. E. Ferreira, and M. Popescu, "Three phase tooth-concentrated multiple-layer fractional windings with low space harmonic content," *2010 IEEE Energy Convers. Cong. Expo. (ECCE)*, 2010.
- [CIS10b] M. V. Cistelecan, F. J. T. E. Ferreira, and M. Popescu, "Adjustable flux three-phase AC machines with combined multiple-step star-delta winding connections," *IEEE Trans. Energy Convers.*, vol. 25, no. 2, pp. 348-355, June 2010.

- [CRO02] J. Cros and P. Viarouge, "Synthesis of high performance PM motors with concentrated windings," *IEEE Trans. Energy Convers.*, vol. 17, no. 2, pp. 248–253, June 2002.
- [DAJ11] G. Dajaku and D. Gerling, "A novel 24-slots/10-poles winding topology for electric machines," *Proc. Int. Electr. Mach. Drives Conf. (IEMDC)*, Niagara Falls, ON, Canada, pp. 65-70, May 2011.
- [DAJ12] G. Dajaku and D. Gerling, "Efficiency improvements of electric machines for automotive application," *World Electr. Veh. J.*, vol. 5, no. 2, pp.520-526, June 2012.
- [DAJ13] G. Dajaku and D. Gerling, "A novel tooth concentrated winding with low space harmonic contents," *2013 Int. Electr. Mach. Drives Conf. (IEMDC)*, Chicago, IL, USA, 2013, pp. 755-760.
- [DAJ21] G. Dajaku, "Advanced multi-phase fractional slot concentrated windings: characteristics and potentials," *Electr. Eng.*, vol. 103, no. 1, pp. 397–406, Feb. 2021.
- [DAM13] A. Damiano, I. Marongiu, A. Monni, and M. Porru, "Design of a 10 MW multi-phase PM synchronous generator for direct-drive wind turbines," *Proc. 39th Annu. Conf. IEEE Ind. Electron. Soc. (IECON)*, Vienna, Austria, 2013, pp. 5266-5270.
- [DEM16] Y. Demir and M. Aydin, "A novel dual three-phase permanent magnet synchronous motor with asymmetric stator winding," *IEEE Trans. Magn.*, vol. 52, no. 7, Art no. 8105005, July 2016.
- [DEM17] Y. Demir and M. Aydin, "A novel asymmetric and unconventional stator winding configuration and placement for a dual three-phase surface PM motor," *IEEE Trans. Magn.*, vol. 53, no. 11, Art no. 8111805, Nov. 2017.
- [DEM19] Y. Demir, E. Yolacan, A. M. EL-Refaie and M. Aydin, "Investigation of different winding configurations and displacements of a nine-phase permanent-magnet-synchronous motor with unbalanced AC winding structure," *IEEE Trans. Ind. Appl.*, vol. 55, no. 4, pp. 3660-3670, July-Aug. 2019.

- [DEO97] R. P. Deodhar, S. Andersson, I. Boldea, and T. J. E. Miller, "The flux-reversal machine: a new brushless doubly-salient permanent-magnet machine," *IEEE Trans. Ind. Appl.*, vol. 33, no. 4, pp. 925–934, July-Aug. 1997.
- [DHU18] H. Dhulipati, S. Mukundan, W. Li, J. Tjong, and N. C. Kar, "Investigation of phase angle displacements in six-phase PMSM with concentrated windings for reduced MMF harmonics," *2018 21st Int. Conf. Electr. Mach. Syst. (ICEMS)*, Jeju, South Korea, 2018, pp. 308-313.
- [DOU59] J. F. H. Douglas, "Induction motors with permanent magnet excitation," *Electr. Eng.*, vol. 78, no. 12, pp. 1195-1195, Dec. 1959.
- [DU19] Z. S. Du and T. A. Lipo, "High torque density and low torque ripple shaped-magnet machines using sinusoidal plus third harmonic shaped magnets," *IEEE Trans. Ind. Appl.*, vol. 55, no. 3, pp. 2601-2610, May-June 2019.
- [DU20] Z. S. Du and T. A. Lipo, "Reducing torque ripple using axial pole shaping in interior permanent magnet machines," *IEEE Trans. Ind. Appl.*, vol. 56, no. 1, pp. 148-157, Jan.-Feb. 2020.
- [EAS97] J. F. Eastham, D. M. Ionel, M. J. Balchin, T. Betzer, and E. Demeter, "Finite element analysis of an interior-magnet brushless DC machine, with a step-skewed rotor," *IEEE Trans. Magn.*, vol. 33, no. 2, pp. 2117–2119, Mar. 1997.
- [ELR08] A. M. El-Refaie and T. M. Jahns, "Impact of winding layer number and magnet type on synchronous surface PM machines designed for wide constant-power speed range operation," *IEEE Trans. Energy Convers.*, vol. 23, no. 1, pp. 53-60, Mar. 2008.
- [ELR10] A. M. EL-Refaie, "Fractional-slot concentrated-windings synchronous permanent magnet machines: opportunities and challenges," *IEEE Trans. Ind. Electron.*, vol. 57, no. 1, pp. 107-121, Jan. 2010.
- [FEI13] W. Fei and Z. Q. Zhu, "Comparison of cogging torque reduction in permanent magnet brushless machines by conventional and herringbone skewing techniques," *IEEE Trans. Energy Convers.*, vol. 28, no. 3, pp. 664-674, Mar. 2013.

- [FEN22] J. H. Feng, P. L. Xu, Z. Q. Zhu, S. S. Wang, B. Shao, Y. Xiao, S. Guo, Y. Li, and S. Feng, "Comparative study of dual 3-phase permanent magnet machines with coil span of two slot-pitches," *IET Electr. Power Appl.*, vol. 16, no. 12, pp. 1426-1438, Dec. 2022.
- [GE17] X. Ge, Z. Q. Zhu, G. Kemp, D. Moule, and C. Williams, "Optimal step-skew methods for cogging torque reduction accounting for three-dimensional effect of interior permanent magnet machines," *IEEE Trans. Energy Convers.*, vol. 32, no. 1, pp. 222-232, Mar. 2017.
- [GOP00] T. Gopalarathnam, H. A. Toliyat, and J. C. Moreira, "Multi-phase fault-tolerant brushless DC motor drives," *Conf. Rec. IAS Annu. Meeting*, Rome, Italy, Oct. 2000, pp. 1683-1688.
- [GUG13] P. Guglielmi, B. Boazzo, E. Armando, G. Pellegrino, and A. Vagati, "Permanent-magnet minimization in PM-assisted synchronous reluctance motors for wide speed range," *IEEE Trans. Ind. Appl.*, vol. 49, no. 1, pp. 31-41, Jan.-Feb. 2013.
- [GUO22] L. Guo, J. Xu, S. Wu, X. Xie, and H. Wang, "Analysis and design of dual three-phase fractional-slot permanent magnet motor with low space harmonic," *IEEE Trans. Magn.*, vol. 58, no. 1, Art no. 8100112, Jan. 2022.
- [HAL80] K. Halbach, "Design of permanent magnet multi-pole magnets with oriented rare earth cobalt material," *Nucl. Instr. and Meth.*, vol.169, no.1, pp.1- 10, 1980.
- [HAN10] S. H. Han, T. M. Jahns, W. L. Soong, M. K. Güven, and M. S. Illindala, "Torque ripple reduction in interior permanent magnet synchronous machines using stators with odd number of slots per pole pair," *IEEE Trans. Energy Convers.*, vol. 25, no. 1, pp. 118-127, Mar. 2010.
- [HAN57] D. J. Hanrahan and D. S. Toffolo, "Permanent magnet generators, part I-theory," *AIEE Trans.*, vol. 76, pt. III, pp. 1098-1103, Dec. 1957.
- [HAY98] J. A. Haylock, B. C. Mecrow, A. G. Jack, and D. J. Atkinson, "Operation of a fault tolerant PM drive for an aerospace fuel pump application," *IEE Proc.*

Electr. Power Appl., vol. 145, no. 5, pp. 441-448, Sept. 1998.

- [HEN94] J. R. Hendershot and T. J. E. Miller, *Design of brushless permanent magnet motors*, Magna Physics Pub., 1994.
- [HOA97] E. Hoang, A. H. Ben-Ahmed, and J. Lucidarme, "Switching flux permanent magnet poly-phase synchronous machines," *Proc. 7th Eur. Conf. Power Electron. Appl. (EPC)*, 1997, vol. 3, pp. 903-908.
- [HON80] V. B. Honsinger, "Performance of polyphase permanent magnet machines," *IEEE Trans. Power App. Syst.*, vol. PAS-99, no. 4, pp. 1510-1518, July 1980.
- [HON82] V. B. Honsinger, "The fields and parameters of interior type AC permanent magnet machines," *IEEE Trans. Power App. Syst.*, vol. PAS-101, no. 4, pp. 867-876, Apr. 1982.
- [HON98] Y. Honda, T. Higaki, S. Morimoto, and Y. Takeda, "Rotor design optimisation of a multi-layer interior PM synchronous motor," *IEE Proc. Electr. Power Appl.*, vol.145, no.2, pp.119-124, 1998.
- [HSU04] J. S. Hsu, C. W. Ayers, C. L. Coomer, R. H. Wiles, S. L. Campbell, K. T. Lowe, and R. T. Michelhaugh, "Report on Toyota/Prius motor torque-capability, torque-property, no-load back EMF, and mechanical losses," *Oak Ridge Nat. Lab.*, U.S. Dept. Energy, 2004.
- [HU17a] Y. Hu, S. Zhu, and C. Liu, "Magnet eddy-current loss analysis of interior PM machines for electric vehicle application," *IEEE Trans. Magn.*, vol. 53, no. 11, Art no. 7402904, Nov. 2017.
- [HU17b] Y. Hu, Z. Q. Zhu, and M. Odavic, "Comparison of two-individual current control and vector space decomposition control for dual three-phase PMSM," *IEEE Trans. Ind. Appl.*, vol. 53, no. 5, pp. 4483-4492, Sept.-Oct. 2017.
- [HU18] Y. Hu, S. Zhu, C. Liu, and K. Wang, "Electromagnetic performance analysis of interior PM machines for electric vehicle applications," *IEEE Trans. Energy Convers.*, vol. 33, no. 1, pp. 199-208, Mar. 2018.

- [HUA22] J. Huang, Y. Sui, Z. Yin, S. Yang, and P. Zheng, "Five-phase hybrid single/double layer fractional slot winding pmsm for torque improvement under third harmonic current injection condition," *IEEE Trans. Magn.*, vol. 58, no. 8, Art no. 8204206, Aug. 2022.
- [HUG70] A. Hughes, "New 3-phase winding of low m.m.f.-harmonic content," *Proc. IEE*, vol. 117, no. 8, pp. 1657-1666, 1970.
- [ISH06] D. Ishak, Z. Q. Zhu and D. Howe, "Comparison of PM brushless motors, having either all teeth or alternate teeth wound," *IEEE Trans. Energy Convers.*, vol. 21, no. 1, pp. 95-103, March 2006.
- [ISL09] R. Islam, I. Husain, A. Fardoun, and K. McLaughlin, "Permanent-magnet synchronous motor magnet designs with skewing for torque ripple and cogging torque reduction," *IEEE Trans. Ind. Appl.*, vol. 45, no. 1, pp. 152-160, 2009.
- [ISL20] M. S. Islam, M. A. Kabir, R. Mikail, and I. Husain, "Space-shifted wye–delta winding to minimize space harmonics of fractional-slot winding," *IEEE Trans. Ind. Appl.*, vol. 56, no. 3, pp. 2520-2530, May-June 2020.
- [ISL22] M. S. Islam, A. Shrestha, and M. Islam, "Effect of step skew in synchronous reluctance machines for high performance applications," *2022 IEEE Energy Convers. Cong. Expo. (ECCE)*, Detroit, MI, USA, 2022.
- [JAC96] A. G. Jack, B. C. Mecrow, and J. A. Haylock, "A comparative study of permanent magnet and switched reluctance motors for high-performance fault-tolerant applications," *IEEE Trans. Ind. Appl.*, vol. 32, no. 4, pp. 889-895, July-Aug. 1996.
- [JAH86] T. M. Jahns, G. B. Kliman, and T. W. Neumann, "Interior permanent-magnet synchronous motors for adjustable-speed drives," *IEEE Trans. Ind. Appl.*, vol. IA-22, no. 4, pp. 738-747, July 1986.
- [JAH87] T. M. Jahns, "Flux-weakening regime operation of an interior permanent-magnet synchronous motor drive," *IEEE Trans. Ind. Appl.*, vol. IA-23, no. 4, pp. 681-689, July 1987.

- [JAH96] T. M. Jahns and W. L. Soong, "Pulsating torque minimization techniques for permanent magnet AC motor drives – a review," *IEEE Trans. Ind. Electron.*, vol. 43, no. 2, pp. 321–330, Apr. 1996.
- [JEO19] C. L. Jeong, Y. K. Kim and J. Hur, "Optimized design of PMSM with hybrid-type permanent magnet for improving performance and reliability," *IEEE Trans. Ind. Appl.*, vol. 55, no. 5, pp. 4692-4701, Sept.-Oct. 2019.
- [JI19] Z. Ji, H. Li, Z. Chen, T. Yu, L. Liu, and M. Ma, "Design and optimization of permanent magnet assisted synchronous reluctance motor for better torque performance," *22nd Int. Conf. Electr. Mach. Syst. (ICEMS)*, Harbin, China, 2019.
- [JMA23] JMAG User Support. Available online: <https://www.jmag-international.com/supports/> (accessed on 12 Sept. 2023).
- [KAL13] S. Kallio, M. Andriollo, A. Tortella, and J. Karttunen, "Decoupled d-q model of double-star interior-permanent-magnet synchronous machines," *IEEE Trans. Ind. Electron.*, vol. 60, no. 6, pp. 2486-2494, June 2013.
- [KAN22] L. Kang and Y. Chen, "Optimal design of 9-phase permanent magnet synchronous generator with low voltage change rate for diesel railway vehicles," *IEEE Trans. Veh. Technol.*, vol. 71, no. 3, pp. 2681-2690, Mar. 2022.
- [KAR12] J. Karttunen, S. Kallio, P. Peltoniemi, P. Silventoinen, and O. Pyrhönenet, "Dual three-phase permanent magnet synchronous machine supplied by two independent voltage source inverters," *Proc. Int. Symp. Power Electron. Electr. Drives, Autom. Motion (SPEEDAM)*, Sorrento, Italy, June 2012, pp. 741-747.
- [KAR17] J. Karttunen, S. Kallio, J. Honkanen, P. Peltoniemi, and P. Silventoinen, "Partial current harmonic compensation in dual three-phase pmsms considering the limited available voltage," *IEEE Trans. Ind. Electron.*, vol. 64, no. 2, pp. 1038-1048, Feb. 2017.
- [KIM13] K. C. Kim and S. H. Jeon, "Analysis on correlation between cogging torque and torque ripple by considering magnetic saturation," *IEEE Trans. Magn.*, vol. 49, no. 5, pp. 2417-2420, May 2013.

- [KWA05] S. Y. Kwak, J. K. Kim, and H. K. Jung, “Characteristic analysis of multilayer-buried magnet synchronous motor using fixed permeability method,” *IEEE Trans. Energy Convers.*, vol. 20, no. 3, pp. 549-555, 2005.
- [LEV08] E. Levi, “Multiphase electric machines for variable-speed applications,” *IEEE Trans. Ind. Electron.*, vol. 55, no. 5, pp. 1893–1909, May 2008.
- [LI03] Yong Li, Jibin Zou, and Yongping Lu, “Optimum design of magnet shape in permanent-magnet synchronous motors,” *IEEE Trans. Magn.*, vol. 39, no. 6, pp. 3523-3526, Nov. 2003.
- [LI17] G. J. Li, B. Ren, and Z. Q. Zhu, “Design guidelines for fractional slot multiphase modular permanent magnet machines,” *IET Electr. Power Appl.*, vol. 11, no. 6, pp. 1023–1031, 2017.
- [LI19a] Y. Li, H. Yang, H. Lin, S. Fang, and W. Wang, “A novel magnet-axis-shifted hybrid permanent magnet machine for electric vehicle applications,” *Energies*, vol. 12, no. 4, pp. 641–653, 2019.
- [LI19b] Y. X. Li, Z. Q. Zhu, X. M. Wu, A. S. Thomas, and Z. Y. Wu, “Comparative study of modular dual 3-phase permanent magnet machines with overlapping/non-overlapping windings,” *IEEE Trans. Ind. Appl.*, vol. 55, no. 4, pp. 3566-3576, July-Aug. 2019.
- [LI19c] Y. X. Li, Z. Q. Zhu, A. S. Thomas, Z. Y. Wu, and X. M. Wu, “Novel modular fractional slot permanent magnet machines with redundant teeth,” *IEEE Trans. Magn.*, vol. 55, no. 9, Art no. 8204810, Sept. 2019.
- [LI20a] Y. X. Li, Z. Q. Zhu, and A. S. Thomas, “Generic slot and pole number combinations for novel modular permanent magnet dual 3-phase machines with redundant teeth,” *IEEE Trans. Energy Convers.*, vol. 35, no. 3, pp. 1676-1687, Sept. 2020.
- [LI20b] F. Li, K. Wang, J. Zhang, and F. Zeng, “Effect of angle displacements on electromagnetic performance of dual three-phase consequent-pole permanent magnet machine,” *IET Electr. Power Appl.*, vol. 14, no. 7, pp. 1177–1185, 2020.

- [LI88] T. Li and G. Slemon, "Reduction of cogging torque in permanent magnet motors," *IEEE Trans. Magn.*, vol. 24, no. 6, pp. 2901-2903, Nov. 1988.
- [LIA95] Y. Liao, F. Liang, and T. A. Lipo, "A novel permanent magnet motor with doubly salient structure," *IEEE Trans. Ind. Appl.*, vol. 31, no. 5, pp. 1069-1078, Sept.-Oct. 1995.
- [LIB04] F. Libert and J. Soulard, "Investigation on pole-slot combinations for permanent-magnet machines with concentrated windings," *Proc. 16th Int. Conf. Electr. Mach. (ICEM)*, Cracow, Poland, 5-8 Sept. 2004.
- [LIU12] G. Liu, J. Yang, W. Zhao, J. Ji, Q. Chen, and W. Gong, "Design and analysis of a new fault-tolerant permanent-magnet Vernier machine for electric vehicles," *IEEE Trans. Magn.*, vol. 48, no. 11, pp. 4176-4179, Nov. 2012.
- [LIU16] X. Liu, H. Chen, J. Zhao, and A. Belahcen, "Research on the performances and parameters of interior PMSM used for electric vehicles," *IEEE Trans. Ind. Electron.*, vol. 63, no. 6, pp. 3533-3545, June 2016.
- [LIU17] G. Liu, G. Xu, W. Zhao, X. Du, and Q. Chen, "Improvement of torque capability of permanent-magnet motor by using hybrid rotor configuration," *IEEE Trans. Energy Convers.*, vol. 32, no. 3, pp. 953-962, 2017.
- [LOC07] F. Locment, E. Semail, and F. Piriou, "Design and study of a multiphase axial-flux machine," *IEEE Trans. Magn.*, vol. 42, no. 4, pp. 1427-1430, Apr. 2006.
- [LOV02] E. C. Lovelace, T. M. Jahns, and J. H. Lang, "A saturating lumped-parameter model for an interior PM synchronous machine," *IEEE Trans. Ind. Appl.*, vol. 38, no. 3, pp. 645-650, May-June 2002.
- [MAG03] F. Magnussen and C. Sadarangani, "Winding factors and Joule losses of permanent magnet machines with concentrated windings," *Proc. IEEE Int. Electr. Mach. Drives Conf. (IEMDC)*, Madison, WI, USA, June 2003, vol. 1, pp. 333-339.
- [MAG07] F. Magnussen and H. Lendenmann, "Parasitic effects in PM machines with concentrated windings," *IEEE Trans. Ind. Appl.*, vol. 43, no. 5, pp. 1223-1232, Sept.-Oct. 2007.

- [MAT10] A. Matyas, G. Aroquiadassou, C. Martis, A. Mpanda-Mabwe, and K. Biro, "Design of six-phase synchronous and induction machines for EPS," *Proc. 19th Int. Conf. Electr. Mach. (ICEM)*, Rome, Italy, Sept. 2010.
- [MCC87] M. McCaig and A. G. Clegg, "Permanent magnet materials," in *Permanent magnets in theory and practice*, 2nd ed. London, UK: Pentech Press, 1987, pp. 87-123.
- [MEC04] B. C. Mecrow, A. G. Jack, D. J. Atkinson, S. R. Green, G. J. Atkinson, A. King, and B. Green, "Design and testing of a four-phase fault-tolerant permanent-magnet machine for an engine fuel pump," *IEEE Trans. Energy Convers.*, vol. 19, no. 4, pp. 671–678, 2004.
- [MEC96] B. C. Mecrow, A. G. Jack, J. A. Haylock, and J. Coles, "Fault-tolerant permanent magnet machine drives", *IEE Proc. Electr. Power Appl.*, vol. 143, no. 6, pp. 437-442, Nov. 1996.
- [MER47] F. W. Merrill, "AlNiCo materials for small motor and generator fields," *Electrical Manufacturing*, vol. 39, pp. 78-83, 180-190, Mar. 1947.
- [MIY18] Y. Miyama, M. Ishizuka, H. Kometani, and K. Akatsu, "Vibration reduction by applying carrier phase-shift PWM on dual three-phase winding permanent magnet synchronous motor," *IEEE Trans. Ind. Appl.*, vol. 54, no. 6, pp. 5998-6004, Nov.-Dec. 2018.
- [MOG94] J. S. Moghani, J. F. Eastham, R. Akmese and R. J. Hill-Cottingham, "Three dimensional force prediction in a model linear brushless d.c. motor," *IEEE Trans. Magn.* vol 30, no. 6, pp. 4752-4754, 1994.
- [OCA20] O. Ocak, and M. Aydin, "An innovative semi-FEA based variable magnet-step-skew to minimize cogging torque and torque pulsations in permanent magnet synchronous motors," *IEEE Access*, vol. 8, pp. 210775-210783, 2020.
- [PAR05] L. Parsa and H. A. Toliyat, "Five-phase permanent-magnet motor drives," *IEEE Trans. Ind. Appl.*, vol. 41, no. 1, pp. 30–37, Jan. 2005.
- [PAR07] L. Parsa and H. A. Toliyat, "Fault-tolerant interior-permanent-magnet machines for hybrid electric vehicle applications," *IEEE Trans. Veh. Technol.*, vol. 56, no. 4, pp. 1546–1552, July 2007.

- [PAT13] V. I. Patel, J. Wang, W. Wang, and X. Chen, "Analysis and design of 6-phase fractional slot per pole per phase permanent magnet machines with low space harmonics," *2013 Int. Electr. Mach. Drives Conf. (IEMDC)*, Chicago, IL, USA, 2013, pp. 386-393.
- [PAT14] V. I. Patel, J. Wang, W. Wang, and X. Chen, "Six-phase fractional-slot-per-pole-per-phase permanent-magnet machines with low space harmonics for electric vehicle application," *IEEE Trans. Ind. Appl.*, vol. 50, no. 4, pp. 2554-2563, July-Aug. 2014.
- [PAT15] V. I. Patel, J. Wang, and S. S. Nair, "Demagnetization assessment of fractional-slot and distributed wound 6-phase permanent magnet machines," *IEEE Trans. Magn.*, vol. 51, no. 6, Art no. 8105511, June 2015.
- [PEL10] G. Pellegrino, P. Guglielmi, A. Vagati, and F. Villata, "Core losses and torque ripple in IPM machines: dedicated modeling and design tradeoff," *IEEE Trans. Ind. Appl.*, vol. 46, no. 6, pp. 2381-2391, Nov.-Dec. 2010.
- [PET15] I. Petrov, P. Ponomarev, Y. Alexandrova, and J. Pyrhonen, "Unequal teeth widths for torque ripple reduction in permanent magnet synchronous machines with fractional-slot non-overlapping windings," *IEEE Trans. Magn.*, vol. 51, no. 2, Feb. 2015.
- [PIR90] F. Piriou and A. Razek, "A model for coupled magnetic-electric circuits in electric machines with skewed slots," *IEEE Trans. Magn.*, vol. 26, no. 2, pp. 1096-1100, Mar. 1990.
- [POL99] H. Polinder and M. J. Hoeijmakers, "Eddy current losses in the segmented surface-mounted magnets of a PM machine," *Proc. IEE Electr. Power Appl.*, vol. 146, no. 3, pp. 261-266, May 1999.
- [PYR08] J. Pyrhonen, T. Jokinen, and V. Hrabovcova, *Design of rotating electrical machines*, WILEY, 2008.
- [QI09] G. Qi, J. T. Chen, Z. Q. Zhu, D. Howe, L. B. Zhou, and C. L. Gu, "Influence of skew and cross-coupling on flux-weakening performance of permanent-magnet brushless AC machines," *IEEE Trans. Magn.*, vol. 45, no. 5, pp. 2110-

2117, May 2009.

- [RAH12] M. A. Rahman, “History of interior permanent magnet motors [History],” *IEEE Ind. Appl. Mag.*, vol. 19, no. 1, pp. 10-15, Jan.-Feb. 2013.
- [RAH85] M. Rahman, T. Little, and G. Slemon, “Analytical models for interior-type permanent magnet synchronous motors,” *IEEE Trans. Magn.*, vol. 21, no. 5, pp. 1741-1743, Sept. 1985.
- [RAI98] G. M. Raimondi, R. D. McFarlane, C. M. Bingham, K. Atallah, D. Howe, P. H. Mellor, R. Capewell, and C. Whitley, “Large electromechanical actuation systems for flight control surfaces,” *Proc. IEE Colloq. All Electr. Aircr.*, London, UK, 1998, Art no. 260.
- [RED14] P. B. Reddy, K. K. Huh, and A. M. EL-Refaie, “Generalized approach of stator shifting in interior permanent-magnet machines equipped with fractional-slot concentrated windings,” *IEEE Trans. Ind. Electron.*, vol. 61, no. 9, pp. 5035-5046, Sept. 2014.
- [RED15] P. Reddy, A. M. El-Refaie, and K.-K. Huh, “Effect of number of layers on performance of fractional-slot concentrated-windings interior permanent magnet machines,” *IEEE Trans. Power Electron.*, vol. 30, no. 4, pp. 2205–2218, Apr. 2015.
- [REN15] Y. Ren and Z. Q. Zhu, “Enhancement of steady-state performance in direct-torque-controlled dual three-phase permanent-magnet synchronous machine drives with modified switching table,” *IEEE Trans. Ind. Electron.*, vol. 62, no. 6, pp. 3338-3350, June 2015.
- [RUB12] M. Ruba and D. Fodorean, “Analysis of fault-tolerant multiphase power converter for a nine-phase permanent magnet synchronous machine,” *IEEE Trans. Ind. Appl.*, vol. 48, no. 6, pp. 2092-2101, Nov.-Dec. 2012.
- [RUD23] I. A. Rudden, G. J. Li, D. K. Kana, Z. Q. Zhu, A. Duke, R. Clark, and A. Thomas, “Space harmonic cancellation in a dual three-phase SPM machine with star-delta windings,” *IEEE Trans. Energy Convers.*, (Early access).

- [SAL19] A. Salem and M. Narimani, "A review on multiphase drives for automotive traction applications," *IEEE Trans. Transp. Electrification*, vol. 5, no. 4, pp. 1329-1348, Dec. 2019.
- [SAN12] J. Santiago, H. Bernhoff, B. Ekergr ard, S. Eriksson, S. Ferhatovic, R. Waters, and M. Leijon, "Electrical motor drivelines in commercial all-electric vehicles: a review," *IEEE Trans. Veh. Technol.*, vol. 61, no. 2, pp. 475-484, Feb. 2012.
- [SAT11] Y. Sato, S. Ishikawa, T. Okubo, M. Abe, and K. Tamai, "Development of high response motor and inverter system for the Nissan Leaf electric vehicle," *SAE Int. Tech. Paper*, Art no. 2011-01-0350, 2011.
- [SAU51] R.M. Saunders and R.H. Weakley, "Design of Permanent-Magnet Alternators," *AIEE Trans.*, vol. 70, pt. II, pp. 1578-1581, 1951.
- [SAY83] M. G. Say, *Alternating Current Machines*, 5th ed. London, UK: Pitman Publishing, 1983.
- [SCH90] R. F. Schiferl and T. A. Lipo, "Power capability of salient pole permanent magnet synchronous motor in variable speed drive applications," *IEEE Trans. Ind. Appl.*, vol. 26, No. 1, pp. 115-123, 1990.
- [SCH97] N. Schofield, K. Ng, Z. Q. Zhu, and D. Howe, "Parasitic rotor losses in a permanent magnet brushless traction machine," *IEEE Int. Electr. Mach. Drives Conf. (IEMDC)*, Cambridge, UK, 1997, pp. 200–204.
- [SCU09] F. Scuiller, E. Semail, J. F. Charpentier, and P. Letellier, "Multi-criteria based design approach of multi-phase permanent magnet low-speed synchronous machines," *IET Electr. Power Appl.*, vol. 3, no. 2, pp. 102110, Mar. 2009.
- [SCU20] F. Scuiller, F. Becker, H. Zahr, and E. Semail, "Design of a bi-harmonic 7-phase PM machine with tooth-concentrated winding," *IEEE Trans. Energy Convers.*, vol. 35, no. 3, pp. 1567-1576, Sept. 2020.
- [SHA20] L. Shao, W. Hua, J. Soulard, Z. Zhu, Z. Wu, and M. Cheng, "Electromagnetic performance comparison between 12-phase switched flux and surface-mounted PM machines for direct-drive wind power generation," *IEEE Trans.*

Ind. Appl., vol. 56, no. 2, pp. 1408-1422, Mar.-Apr. 2020.

- [SHA23] B. Shao, Z. Q. Zhu, L. Yan, J. Feng, S. Guo, Y. Li, and L. Feng, "Torque ripple reduction for direct torque control of dual three-phase PMSM based on multiple virtual voltage vectors," *IEEE Trans. Energy Convers.*, vol. 38, no. 1, pp. 296-309, Mar. 2023.
- [SOO02] W. L. Soong and N. Ertugrul, "Field-weakening performance of interior permanent-magnet motors," *IEEE Trans. Ind. Appl.*, vol. 38, no. 5, pp. 1251-1258, Sept.-Oct. 2002.
- [STA06] R. H. Staunton, C. W. Ayers, L. D. Marlino, J. N. Chiasson, and T. A. Burrell, "Evaluation of 2004 Toyota Prius hybrid electric drive system," *ORNL/TM-2006-423*, Oak Ridge National Lab., TN, USA, May 2006.
- [STR52] F. Strauss, "Synchronous machines with rotating permanent-magnet fields," *AIEE Trans.*, vol. 71, pt. III, pp. 887-893, Oct. 1952.
- [SUN22] Y. Sun, W. Zhao, J. Ji, J. Zheng, and X. Song, "Effect of phase shift on inductance and short-circuit current in dual three-phase 48-slot/22-pole permanent-magnet machines," *IEEE Trans. Ind. Electron.*, vol. 69, no. 2, pp. 1135-1145, Feb. 2022.
- [TAN16] M. Taniguchi, T. Yashiro, K. Takizawa, S. Baba, M. Tsuchida, T. Mizutani, H. Endo, and H. Kimura, "Development of new hybrid transaxle for compact-class vehicles," *SAE Int. Tech. Paper*, Art no. 2016-01-1163, 2016.
- [URR10] J. C. Urresty, J. R. Riba, L. Romeral, and A. Garcia, "A simple 2-D finite-element geometry for analyzing surface-mounted synchronous machines with skewed rotor magnets," *IEEE Trans. Magn.*, vol. 46, no. 11, pp. 3948-3954, 2010.
- [WAN10] D. H. Wang, X. H. Wang, Y. B. Yang, and R. Zhang, "Optimization of magnetic pole shifting to reduce cogging torque in solid-rotor permanent-magnet synchronous motors," *IEEE Trans. Magn.*, vol. 46, no. 5, pp. 1228-1234, May 2010.
- [WAN14a] J. Wang, V. I. Patel, and W. Wang, "Fractional-slot permanent magnet

brushless machines with low space harmonic contents,” *IEEE Trans. Magn.*, vol. 50, no. 1, Art no. 8200209, Jan. 2014.

- [WAN14b] K. Wang, Z. Q. Zhu, and G. Ombach, “Torque improvement of five-phase surface-mounted permanent magnet machine using third-order harmonic,” *IEEE Trans. Energy Convers.*, vol. 29, no. 3, pp. 735-747, Sept. 2014.
- [WAN14c] K. Wang, Z. Q. Zhu, and G. Ombach, “Synthesis of high performance fractional-slot permanent-magnet machines with coil-pitch of two slot-pitches,” *IEEE Trans. Energy Convers.*, vol. 29, no. 3, pp. 758-770, Sept. 2014.
- [WAN14d] K. Wang, Z. Q. Zhu, G. Ombach, and W. Chlebosz, “Average torque improvement of interior permanent-magnet machine using 3rd harmonic in rotor shape,” *IEEE Trans. Ind. Electron.*, vol. 61, no. 9, pp. 5047–5057, Sept. 2014.
- [WAN15a] Y. Wang, R. Qu, and J. Li, “Multilayer windings effect on interior PM machines for EV applications,” *IEEE Trans. Ind. Appl.*, vol. 51, no. 3, pp. 2208-2215, May-June 2015.
- [WAN15b] K. Wang, Z. Q. Zhu, Y. Ren, and G. Ombach, “Torque improvement of dual three-phase permanent-magnet machine with third-harmonic current injection,” *IEEE Trans. Ind. Electron.*, vol. 62, no. 11, pp. 6833-6844, Nov. 2015.
- [WAN19] B. Wang, J. Wang, A. Griffio and Y. Shi, “Investigation into fault-tolerant capability of a triple redundant PMA SynRM drive,” *IEEE Trans. Power Electron.*, vol. 34, no. 2, pp. 1611-1621, Feb. 2019.
- [WAN20a] S. S. Wang, Z. Q. Zhu, A. Pride, R. Deodhar, and C. Umemura, “Torque separation for dual three-phase pm machines using frozen permeability method,” *Int. Conf. Power Electron. Mach. and Drives (PEMD)*, Nottingham (Online), UK, Dec. 2020, pp. 204-209.
- [WAN20b] K. Wang and H. Lin, “A novel 24-slot/10-pole dual three-phase fractional-slot overlapped winding for low non-working space harmonics and stator modularization,” *IEEE Access*, vol. 8, pp. 85490-85503, 2020.

- [WAN20c] K. Wang and H. Lin, “Modular permanent magnet synchronous machine with low space harmonic content,” *Energies*, vol. 13, no. 15, pp. 3924, Jan. 2020.
- [WAN20d] X. Wang, H. Yan, G. Sala, G. Buticchi, C. Gu, W. Zhao, L. Xu, and H. Zhang, “Selective torque harmonic elimination for dual three-phase PMSMs based on PWM carrier phase shift,” *IEEE Trans. Power Electron.*, vol. 35, no. 12, pp. 13255-13269, Dec. 2020.
- [WAN20e] X. Wang, X. Sun, and P. Gao, “Study on the effects of rotor-step skewing on the vibration and noise of a PMSM for electric vehicles,” *IET Electr. Power Appl.*, vol. 14, no. 1, pp. 131-138, 2020.
- [WAN22] S. S. Wang, Z. Q. Zhu, A. Pride, J. Shi, R. Deodhar, and C. Umemura, “Comparison of different winding configurations for dual three-phase interior PM machines in electric vehicles,” *World Electr. Veh. J.*, vol. 13, no. 3, pp. 51, Mar. 2022.
- [WAN99] C. Wang, S. A. Nasar, and I. Boldea, “Three-phase flux reversal machine (FRM),” *IEE Electr. Power Appl.*, vol. 146, no. 2, pp. 139-146, Mar. 1999.
- [XIA20] Y. Xiao, Z. Q. Zhu, J. T. Chen, D. Wu, and L.M. Gong, “A novel V-shape interior permanent magnet synchronous machine with asymmetric spoke-type flux barrier”, *Int. Conf. Electr. Mach. (ICEM)*, Gothenburg (Online), Sweden, Aug. 2020, pp. 382–388.
- [XIA21] Y. Xiao, Z. Q. Zhu, S. S. Wang, G. W. Jewell, J. T. Chen, D. Wu, and L. M. Gong, “A novel asymmetric interior permanent magnet machine for electric vehicles,” *IEEE Trans. Energy Conv.*, vol. 36, no. 3, pp. 2404-2415, Sept. 2021.
- [XIA22] Y. Xiao, Z. Q. Zhu, G. W. Jewell, J. T. Chen, D. Wu, and L. M. Gong, “A novel asymmetric interior permanent magnet synchronous machine,” *IEEE Trans. Ind. Appl.*, vol. 58, no. 3, pp. 3370-3382, May-June 2022.
- [XIN19] F. Xing, W. Zhao, and B. Kwon, “Design and optimisation of a novel asymmetric rotor structure for a PM-assisted synchronous reluctance machine,” *IET Electr. Power Appl.*, vol. 13, no. 5, pp. 573–580, May 2019.

- [XIN21] Z. Xing, X. Wang, and W. Zhao. "Cogging torque reduction based on segmented skewing magnetic poles with different combinations of pole-arc coefficients in surface-mounted permanent magnet synchronous motors," *IET Electr. Power Appl.*, vol. 15, no. 2, pp. 200-213, Feb. 2021.
- [XU18] P. L. Xu, J. H. Feng, S. Y. Guo, S. Feng, W. Chu, Y. Ren, and Z. Q. Zhu, "Analysis of dual three-phase permanent-magnet synchronous machines with different angle displacements," *IEEE Trans. Ind. Electron.*, vol. 65, no. 3, pp. 1941-1954, Mar. 2018.
- [XU19] P. L. Xu, Z. Q. Zhu, B. Shao, S. S. Wang, J. H. Feng, S. Y. Guo, Y. F. Li, and S. Z. Feng, "Analysis of dual 3-phase fractional-slot non-overlapping winding pm synchronous machines with different angle displacements," *2019 IEEE Energy Convers. Cong. Expo. (ECCE)*, Baltimore, MD, USA, Sept.-Oct. 2019, pp. 5616-5623.
- [YAN17a] Y. Yang, S. M. Castano, R. Yang, M. Kasprzak, B. Bilgin, A. Sathyan, H. Dadkhah, and A. Emadi, "Design and comparison of interior permanent magnet motor topologies for traction applications," *IEEE Trans. Transp. Electrific.*, vol. 3, no. 1, pp. 86-97, Mar. 2017.
- [YAN17b] H. Yang, Y. Li, H. Lin, Z. Q. Zhu, S. Lyu, H. Wang, S. Fang, and Y. Huang, "Novel reluctance axis shifted machines with hybrid rotors," *IEEE Energy Convers. Cong. Expo. (ECCE)*, Cincinnati, OH, USA, 2017, pp. 2362-2367.
- [YAN19a] R. Yang, N. Schofield, N. Zhao, and A. Emadi, "Dual three-phase permanent magnet synchronous machine investigation for battery electric vehicle power-trains," *J. Eng.*, vol. 2019, no. 17, pp. 3981-3985, June 2019.
- [YAN19b] H. Yang, W. Wang, H. Lin, Z. Q. Zhu, S. Lyu, and S. Niu, "A novel hybrid-pole interior PM machine with magnet-axis-shifting effect," *IEEE Int. Electr. Mach. & Drives Conf. (IEMDC)*, San Diego, CA, USA, 2019, pp. 273-279.
- [YAN22] L. Yan, Z. Q. Zhu, J. Qi, Y. Ren, C. Gan, S. Brockway, and C. Hilton, "Suppression of major current harmonics for dual three-phase PMSMs by virtual multi three-phase systems," *IEEE Trans. Ind. Electron.*, vol. 69, no. 6,

pp. 5478-5490, June 2022.

- [YU14] H. C. Yu, B. S. Yu, J. T. Yu, and C. K. Lin, "A dual notched design of radial-flux permanent magnet motors with low cogging torque and rare earth material," *IEEE Trans. Magn.*, vol. 50, no. 11, Art no. 8203104, Nov. 2014.
- [ZEN19] X. Zeng, L. Quan, X. Zhu, L. Xu, and F. Liu, "Investigation of an asymmetrical rotor hybrid permanent magnet motor for approaching maximum output torque," *IEEE Trans. Appl. Supercond.*, vol. 29, no. 2, Art no. 0602704, Jan. 2019.
- [ZHA14] W. Zhao, F. Zhao, T. A. Lipo, and B. I. Kwon, "Optimal design of a novel V-type interior permanent magnet motor with assisted barriers for the improvement of torque characteristics," *IEEE Trans. Magn.*, vol. 50, no. 11, Art no. 8104504, 2014.
- [ZHA15a] W. Zhao, D. Chen, T. A. Lipo, and B. Kwon, "Performance improvement of ferrite-assisted synchronous reluctance machines using asymmetrical rotor configurations," *IEEE Trans. Magn.*, vol. 51, no. 11, Art no. 8108504, Nov. 2015.
- [ZHA15b] W. Zhao, T. A. Lipo, and B. I. Kwon, "Optimal design of a novel asymmetrical rotor structure to obtain torque and efficiency improvement in surface inset PM motors," *IEEE Trans. Magn.*, vol. 51, no. 3, pp. 1-4, 2015.
- [ZHA17a] L. Zhang, Y. Fan, R. D. Lorenz, R. Cui, C. Li, and M. Cheng, "Design and analysis of a new five-phase brushless hybrid-excitation fault-tolerant motor for electric vehicles," *IEEE Trans. Ind. Appl.*, vol. 53, no. 4, pp. 3428-3437, July-Aug. 2017.
- [ZHA17b] W. Zhao, F. Xing, X. Wang, and T. A. Lipo, "Design and analysis of a novel PM-assisted synchronous reluctance machine with axially integrated magnets by the finite-element method," *IEEE Trans. Magn.*, vol. 53, no. 16, June 2017, Art. No. 8104104.
- [ZHA18a] W. Zhao, J. Zheng, J. Ji, S. Zhu, and M. Kang, "Star and delta hybrid connection of a FSCW PM machine for low space harmonics," *IEEE Trans.*

Ind. Electron., vol. 65, no. 12, pp. 9266-9279, Dec. 2018.

- [ZHA18b] W. Zhao, H. Shen, T. A. Lipo, and X. Wang, "A new hybrid permanent magnet synchronous reluctance machine with axially sandwiched magnets for performance improvement," *IEEE Trans. Energy Convers.*, vol. 33, no. 4, pp. 2018-2029, 2018.
- [ZHA95] Y. Zhao and T. A. Lipo, "Space vector PWM control of dual three-phase induction machine using vector space decomposition," *IEEE Trans. Ind. Appl.*, vol. 31, no. 5, pp. 1100-1109, Sept.-Oct. 1995.
- [ZHE11] P. Zheng, Y. Sui, J. Zhao, C. Tong, T. A. Lipo, and A. Wang, "Investigation of a novel five-phase modular permanent-magnet in-wheel motor," *IEEE Trans. Magn.*, vol. 47, no. 10, pp. 4084-4087, 2011.
- [ZHE12] P. Zheng, F. Wu, Y. Sui, P. Wang, Y. Lei, and H. Wang, "Harmonic analysis and fault-tolerant capability of a semi-12-phase permanent-magnet synchronous machine used for EVs," *Energies*, vol. 5, no. 9, pp. 3586-3607, Sept. 2012.
- [ZHE13] P. Zheng, F. Wu, Y. Lei, Y. Sui, and B. Yu, "Investigation of a novel 24-slot/14-pole six-phase fault-tolerant modular permanent-magnet in-wheel motor for electric vehicles," *Energies*, vol. 6, no. 10, pp. 4980-5002, Sept. 2013.
- [ZHO06] F. Zhou, J. Shen, W. Fei, and R. Lin, "Study of retaining sleeve and conductive shield and their influence on rotor loss in high-speed PM BLDC motors," *IEEE Trans. Magn.*, vol. 42, no. 10, pp. 3398-3400, Oct. 2006.
- [ZHU00] Z. Q. Zhu and D. Howe, "Influence of design parameters on cogging torque in permanent magnet machines," *IEEE Trans. Energy Convers.*, vol. 15, no. 4, pp. 407-412, Dec. 2000.
- [ZHU01] Z. Q. Zhu and D. Howe, "Halbach permanent magnet machines and applications: a review," *IEE Proc. Electr. Power Appl.*, vol. 148, no. 4, pp. 299-308, 2001.
- [ZHU07] Z. Q. Zhu and D. Howe, "Electrical machines and drives for electric, hybrid, and fuel cell vehicles," *Proc. IEEE*, vol. 95, no. 4, pp. 746-765, Apr. 2007.

- [ZHU09] Z. Q. Zhu, "A simple method for measuring cogging torque in permanent magnet machines," *Proc. IEEE Power Energy Soc. Gen. Meeting*, Calgary, AB, Canada, July 2009.
- [ZHU12] Z. Q. Zhu, "Recent advances on permanent magnet machines," *CES Trans.*, vol. 27, no. 3, pp. 1-1, Mar. 2012.
- [ZHU17a] X. Zhu, X. Wang, C. Zhang, L. Wang, and W. Wu, "Design and analysis of a spoke-type hybrid permanent magnet motor for electric vehicles," *IEEE Trans. Magn.*, vol. 53, no. 11, Art no. 8208604, Nov. 2017.
- [ZHU17b] Z. Q. Zhu, W. Q. Chu, and Y. Guan, "Quantitative comparison of electromagnetic performance of electrical machines for HEVs/EVs," *CES Trans. Electr. Mach. Syst.*, vol. 1, no. 1, pp. 37-47, Mar. 2017.
- [ZHU18] S. Zhu, Y. Hu, C. Liu, K. Wang and W. Chen, "Reduction of stator core loss in interior PM machines for electric vehicle applications," *IEEE Trans. Magn.*, vol. 54, no. 11, Art no. 8700405, Nov. 2018.
- [ZHU19] S. Zhu, T. Cox, Z. Xu, and C. Gerada, "Novel 24-slots14-poles fractional-slot concentrated winding topology with low-space harmonics for electrical machine," *J. Eng.*, vol. 2019, no. 17, pp. 3784-3788, 2019.
- [ZHU21a] Z. Q. Zhu, S. S. Wang, B. Shao, L. C. Yan, P. L. Xu, and Y. Ren, "Advances in dual-three-phase permanent magnet synchronous machines and control techniques," *Energies*, vol. 14, no. 22, pp. 7508, Nov. 2021.
- [ZHU21b] S. Zhu, W. Zhao, G. Liu, Y. Mao, and Y. Sun, "Effect of phase shift angle on radial force and vibration behavior in dual three-phase PMSM," *IEEE Trans. Ind. Electron.*, vol. 68, no. 4, pp. 2988-2998, April 2021.
- [ZHU22] Z. Q. Zhu and Y. Xiao, "Novel magnetic-field-shifting techniques in asymmetric rotor pole interior PM machines with enhanced torque density," *IEEE Trans. Magn.*, vol. 58, no. 2, Art no. 8100610, Feb. 2022.
- [ZHU92] Z. Q. Zhu and D. Howe, "Analytical prediction of the cogging torque in radial-field permanent magnet brushless motors," *IEEE Trans. Magn.*, vol. 28, no. 2, pp. 1371-1374, Mar. 1992.

APPENDIX I

PUBLICATIONS RESULTED FROM PHD STUDY

Journal Publications:

S. S. Wang, Z. Q. Zhu, A. Pride, J. Shi, R. Deodhar, and C. Umemura, “Comparison of different winding configurations for dual three-phase interior PM machines in electric vehicles,” *World Electr. Veh. J.*, vol. 13, no. 3, pp. 51, Mar. 2022.

Z. Q. Zhu, **S. S. Wang**, B. Shao, L. C. Yan, P. L. Xu, and Y. Ren, “Advances in dual-three-phase permanent magnet synchronous machines and control techniques,” *Energies*, vol. 14, no. 22, pp. 7508, Nov. 2021.

Y. Xiao, Z. Q. Zhu, **S. S. Wang**, G. W. Jewell, J. T. Chen, D. Wu, and L. M. Gong, “A novel asymmetric interior permanent magnet machine for electric vehicles,” *IEEE Trans. Energy Conv.*, vol. 36, no. 3, pp. 2404-2415, Sept. 2021.

J. H. Feng, P. L. Xu, Z. Q. Zhu, **S. S. Wang**, B. Shao, Y. Xiao, S. Guo, Y. Li, S. Feng, “Comparative study of dual 3-phase permanent magnet machines with coil span of two slot-pitches,” *IET Elec. Power Appl.*, vol. 16, no. 12, pp. 1426-1438, Dec. 2022.

Conference Publications:

S. S. Wang, Z. Q. Zhu, A. Pride, R. Deodhar, and C. Umemura, “Torque separation for dual three-phase pm machines using frozen permeability method,” *Int. Conf. Power Electron. Mach. and Drives (PEMD)*, Nottingham (Online), UK, 15-17 Dec. 2020; pp. 204-209.

P. L. Xu, Z. Q. Zhu, B. Shao, **S. S. Wang**, J. H. Feng, S. Y. Guo, Y. F. Li, S. Z. Feng, “Analysis of dual 3-phase fractional-slot non-overlapping winding pm synchronous machines with different angle displacements,” *2019 IEEE Energy Convers. Cong. Expo. (ECCE)*, Baltimore, MD, USA, 29 Sept.-3 Oct. 2019; pp. 5616-5623.